Journal of Applied Mathematics

Mathematical and Numerical Modeling of Flow and Transport

Guest Editors: Shuyu Sun, Eleanor W. Jenkins, Zhangxing (John) Chen, and Juergen Geiser

Mathematical and Numerical Modeling of Flow and Transport

Journal of Applied Mathematics

Mathematical and Numerical Modeling of Flow and Transport

Guest Editors: Shuyu Sun, Eleanor W. Jenkins, Zhangxing (John) Chen, and Juergen Geiser

Copyright © 2011 Hindawi Publishing Corporation. All rights reserved.

This is a special issue published in "Journal of Applied Mathematics." All articles are open access articles distributed under the Creative Commons Attribution License, which permits unrestricted use, distribution, and reproduction in any medium, provided the original work is properly cited.

Editorial Board

Said Abbasbandy, Iran
Mina B. Abd-El-Malek, Egypt
Mohamed A. Abdou, Egypt
Subhas Abel, India
Mostafa Adimy, France
Pankaj Agarwal, India
Carlos J. S. Alves, Portugal
Mohamad Alwash, USA
Igor Andrianov, Germany
Francis T. K. Au, Hong Kong
Olivier Bahn, Canada
Roberto Barrio, Spain
Alfredo Bellen, Italy
J. Biazar, Iran
Hester Bijl, The Netherlands
Joke G. Blom, The Netherlands
James Robert Buchanan, USA
J. C. Butcher, New Zealand
Xiao Chuan Cai, USA
Weiming Cao, USA
Alexandre Carvalho, Brazil
Song Cen, China
Qianshun Chang, China
Tai-Ping Chang, Taiwan
Xinfu Chen, USA
Jeng-Tzong Chen, Taiwan
Ke Chen, UK
Jen-Tzung Chien, Taiwan
Cheng-Sheng Chien, Taiwan
Md. Chowdhury, Malaysia
C. Conca, Chile
Alessandro Corsini, Italy
Livija Cveticanin, Serbia
Mohamed Darouach, France
Patrick De Leenheer, USA
Eric De Sturler, USA
Kai Diethelm, Germany
Vit Dolejsi, Czech Republic
Salah M. El-Sayed, Egypt
Meng Fan, China
Ya Ping Fang, China
Antonio J. M. Ferreira, Portugal
Michel Fliess, France
M. A. Fontelos, Spain
Luca Formaggia, Italy
V. A. Galaktionov, UK
Huijun Gao, China
B. Geurts, The Netherlands
Pablo González-Vera, Spain
Laurent Gosse, Italy
K. S. Govinder, South Africa
Jorge Luis Gracia, Spain
Yuantong Gu, Australia
Zhihong Guan, China
Nicola Guglielmi, Italy
Frederico G. Guimarães, Brazil
A. Gumel, Canada
Maoan Han, China
Ferenc Hartung, Hungary
Luis Javier Herrera, Spain
Ying U. Hu, France
Zhilong L. Huang, China
Kazufumi Ito, USA
Takeshi Iwamoto, Japan
George Jaiani, Georgia
Zhongxiao Jia, China
Yehia Khulief, Saudi Arabia
Jong H. Kim, Republic of Korea
Kazutake Komori, Japan
Vadim A. Krysko, Russia
Jin L. Kuang, Singapore
Miroslaw Lachowicz, Poland
Hak-Keung Lam, UK
Tak-Wah Lam, Hong Kong
Peter G. L. Leach, Greece
Wan-Tong Li, China
Jibin Li, China
Yongkun Li, China
Chong Lin, China
Leevan Ling, Hong Kong
Mingzhu Liu, China
Kang Liu, USA
Yansheng Liu, China
Fawang Liu, Australia
Chein-Shan Liu, Taiwan
Jose Luis Lopez, Spain
Julián López-Gómez, Spain
Shiping Lu, China
Gert Lube, Germany
Nazim I. Mahmudov, Turkey
Fazal M. Mahomed, South Africa
Oluwole D. Makinde, South Africa
F. Marcellán, Spain
Guiomar Martín-Herrán, Spain
Nicola Mastronardi, Italy
Michael Meylan, Australia
Alain Miranville, France
Jaime E. Munoz Rivera, Brazil
Javier Murillo, Spain
Roberto Natalini, Italy
Srinivasan Natesan, India
Khalida Inayat Noor, Pakistan
Donal O'Regan, Ireland
Martin Ostoja-Starzewski, USA
Turgut Öziş, Turkey
Claudio Padra, Argentina
Reinaldo Martinez Palhares, Brazil
Bozenna Pasik-Duncan, USA
Juan Manuel Peña, Spain
Ricardo Perera, Spain
Malgorzata Peszynska, USA
James F. Peters, Canada
Mark A. Petersen, South Africa
Miodrag Petković, Serbia
Vu Ngoc Phat, Vietnam
Andrew Pickering, Spain
Hector Pomares, Spain
Mario Primicerio, Italy
Morteza Rafei, The Netherlands
B. V. Rathish Kumar, India
Jacek Rokicki, Poland
Carla Roque, Portugal
Debasish Roy, India
Marcelo A. Savi, Brazil
Wolfgang Schmidt, Germany
Eckart Schnack, Germany

Mehmet Sezer, Turkey
Naseer Shahzad, Saudi Arabia
Fatemeh Shakeri, Iran
Hui-Shen Shen, China
Jian Hua Shen, China
Fernando Simões, Portugal
A. A. Soliman, Egypt
Yuri N. Sotskov, Belarus
Peter Spreij, The Netherlands
Niclas Strömberg, Sweden
Ray Kai Leung Su, Hong Kong
Jitao Sun, China
Wenyu Sun, China
Xianhua Tang, China
Marco Henrique Terra, Brazil
Alexander Timokha, Norway
Ch. Tsitouras, Greece
Kuppalapalle Vajravelu, USA
Alvaro Valencia, Chile
Nguyen Van Minh, USA
E. S. Van Vleck, USA
Ezio Venturino, Italy
Jesus Vigo-Aguiar, Spain
Yimin Wei, China
Junjie Wei, China
Li Weili, China
Martin Weiser, Germany
Adam Wittek, Australia
Dongmei Xiao, China
Yuesheng Xu, USA
Suh-Yuh Yang, Taiwan
Jianke Yang, USA
Jinyun Yuan, Brazil
Alejandro Zarzo, Spain
Guisheng Zhai, Japan
Jingxin Zhang, Australia
Hongyong Zhao, China
Shan Zhao, USA
Xiaoqiang Zhao, Canada
Renat Zhdanov, USA
J. Hoenderkamp, The Netherlands

Contents

Mathematical and Numerical Modeling of Flow and Transport, Shuyu Sun, Eleanor W. Jenkins, Zhangxing (John) Chen, and Juergen Geiser
Volume 2011, Article ID 901380, 4 pages

Adaptive Optimal *m*-Stage Runge-Kutta Methods for Solving Reaction-Diffusion-Chemotaxis Systems, Jui-Ling Yu
Volume 2011, Article ID 389207, 25 pages

Numerical Study of the Effect of a Power Plant Cooling Water Discharge in the Montevideo Bay, Mónica Fossati, Pablo Santoro, Santiago Urrestarazu, and Ismael Piedra-Cueva
Volume 2011, Article ID 970467, 23 pages

Numerical Analysis of Water Forced Convection in Channels with Differently Shaped Transverse Ribs, Oronzio Manca, Sergio Nardini, and Daniele Ricci
Volume 2011, Article ID 323485, 25 pages

Numerical Simulation of Solid Tumor Blood Perfusion and Drug Delivery during the "Vascular Normalization Window" with Antiangiogenic Therapy, Jie Lv, Jin-feng Cao, Yan Cai, Yu Zhou, Quan Long, Wei Yao, and Shi-xiong Xu
Volume 2011, Article ID 190371, 8 pages

Simulation of Thermomagnetic Convection in a Cavity Using the Lattice Boltzmann Model, Mahshid Hadavand and Antonio C. M. Sousa
Volume 2011, Article ID 538637, 14 pages

A Parallel Stochastic Framework for Reservoir Characterization and History Matching, Sunil G. Thomas, Hector M. Klie, Adolfo A. Rodriguez, and Mary F. Wheeler
Volume 2011, Article ID 535484, 19 pages

Computing Exponential for Iterative Splitting Methods: Algorithms and Applications, Jürgen Geiser
Volume 2011, Article ID 193781, 27 pages

Numerical Simulation of Pollutant Transport in Fractured Vuggy Porous Karstic Aquifers, Xiaolin Fan, Shuyu Sun, Wei Wei, and Jisheng Kou
Volume 2011, Article ID 498098, 41 pages

Multiscale Time-Splitting Strategy for Multiscale Multiphysics Processes of Two-Phase Flow in Fractured Media, Jisheng Kou, Shuyu Sun, and Bo Yu
Volume 2011, Article ID 861905, 24 pages

Implementing Estimation of Capacity for Freeway Sections, Chang-qiao Shao
Volume 2011, Article ID 941481, 9 pages

Modeling and Simulation of a Chemical Vapor Deposition, J. Geiser and M. Arab
Volume 2011, Article ID 641920, 25 pages

Radiative Mixed Convection over an Isothermal Cone Embedded in a Porous Medium with Variable Permeability, M. F. El-Amin, N. A. Ebrahiem, Amgad Salama, and Shuyu Sun
Volume 2011, Article ID 124590, 10 pages

Development of a Particle Interaction Kernel Function in MPS Method for Simulating Incompressible Free Surface Flow, Tony W. H. Sheu, Chenpeng Chiao, and Chinlong Huang
Volume 2011, Article ID 793653, 16 pages

Effects of Gravity and Inlet/Outlet Location on a Two-Phase Cocurrent Imbibition in Porous Media, M. F. El-Amin and Shuyu Sun
Volume 2011, Article ID 673523, 18 pages

Modeling and Analysis of Material Flows in Re-Entrant Supply Chain Networks Using Modified Partial Differential Equations, Fenglan He, Ming Dong, and Xiaofeng Shao
Volume 2011, Article ID 325690, 14 pages

A Stabilized Mixed Finite Element Method for Single-Phase Compressible Flow, Liyun Zhang and Zhangxin Chen
Volume 2011, Article ID 129724, 16 pages

An Analytical Solution of the Advection Dispersion Equation in a Bounded Domain and Its Application to Laboratory Experiments, M. Massabó, R. Cianci, and O. Paladino
Volume 2011, Article ID 493014, 14 pages

Hindawi Publishing Corporation
Journal of Applied Mathematics
Volume 2011, Article ID 901380, 4 pages
doi:10.1155/2011/901380

Editorial

Mathematical and Numerical Modeling of Flow and Transport

Shuyu Sun,[1] Eleanor W. Jenkins,[2] Zhangxing (John) Chen,[3] and Juergen Geiser[4]

[1] *Computational Transport Phenomena Laboratory (CTPL), Division of Physical Sciences and Engineering (PSE), King Abdullah University of Science and Technology (KAUST), Thuwal 23955-6900, Saudi Arabia*
[2] *Department of Mathematical Sciences, Clemson University, Clemson, SC 29634-0975, USA*
[3] *Schulich School of Engineering, University of Calgary, 2500 University Drive NW, Calgary, AB, Canada T2N 1N4*
[4] *Department of Mathematics, Humboldt-University of Berlin, Unter den Linden 6, 10099 Berlin, Germany*

Correspondence should be addressed to Shuyu Sun, shuyu.sun@kaust.edu.sa

Received 19 August 2011; Accepted 19 August 2011

Copyright © 2011 Shuyu Sun et al. This is an open access article distributed under the Creative Commons Attribution License, which permits unrestricted use, distribution, and reproduction in any medium, provided the original work is properly cited.

1. Introduction

Most processes in natural and engineered systems inherently involve flow and transport. From atoms to galaxies, from inorganic reactions to living organisms, from oceans to streambeds, flow and transport processes occur across a wide range of physical applications. Application areas include groundwater contamination, carbon sequestration, air pollution, petroleum exploration and recovery, weather prediction, drug delivery, material design, chemical separation processes, natural disaster assessments, and others. As a result of its importance in a variety of problems of interest, accurate and efficient numerical modeling of flow and transport is essential.

Interest in the numerical simulation of flow and transport mechanisms has increased in recent years along with the rapid increase in computational power. Spectacular advances in computer performance and emerging technologies of parallel distributed grids and GPU computing have provided flow and transport modelers with tools to simulate and study complex phenomena. However, efficient numerical algorithms, new mathematical formulations, and advanced computational techniques are required if researchers are to take full advantage of this progress and address new and existing challenges in flow and transport modeling and simulation. One particular challenge requires modelers to synthesize varied temporal and spatial scales at which flow and transport mechanisms operate. Nanoscale

changes tend to be fast, while geological changes occur over much larger time scales. Thus, algorithms that are optimal for one problem set need not be so for another. The physics associated with each process and often with each of the spatial and temporal scales are coupled, requiring that one take a global approach to developing appropriate numerical algorithms. For example, a numerical algorithm for a flow process should conserve mass locally, but it is imperative that this happen if the flow model is to be coupled to a transport model. Temporal integration methods for nanoscale simulations must be incorporated into the integration method used for larger scales. The list goes on.

2. Overview of Work Presented in this Special Issue

The papers presented in this special issue cover state-of-the-art simulations of flow and transport problems; they represent ongoing research projects on various important topics relevant to the modeling and computation of flow and transport. In particular, this special issue focuses on four important areas of complex flow and transport: (1) porous media flow and transport, (2) coupling of flow and transport to heat transfer, (3) flow and transport in chemical, biological, and sociological systems, and (4) new numerical algorithms to tackle challenges in flow and transport simulation. We outline each of the four areas below.

Porous media flow and transport is of great community interest because of its importance in oil production and environmental protection. A group of papers addresses various issues in this area. The paper entitled *"Numerical simulation of pollutant transport in fractured vuggy porous karstic aquifers"* contains an analysis of a mathematical model for contaminant transport in fractured vuggy porous media. The results show how different distributions of vugs and fractures impact the contaminant transport and the effluent outlet concentration. In the paper entitled *"A parallel stochastic framework for reservoir characterization and history matching,"* the authors consider the spatial distribution of parameters that characterize subsurface porous media, and they present an efficient, accurate, and parallel framework for estimating reservoir parameters. The methodology uses measurement data such as inferred phase pressures, phase concentrations, fluxes, and seismic and well-log data. The paper entitled *"An analytical solution of the advection dispersion equation in a bounded domain and its application to laboratory experiments"* is a study of the modeling of contaminant transport through a saturated porous medium under a uniform flow in a parallel plate geometry. A general solution of the advection dispersion equation in a porous medium is provided and used to examine experimental data acquired via a noninvasive technique. In *"Effects of gravity and inlet/outlet location on a two-phase cocurrent imbibition in porous media,"* the authors use a two-dimensional simulation tool to numerically investigate gravity and inlet/outlet location effects on two-phase cocurrent imbibition in a porous medium. Three different cases of side-, top-, and bottom-inlet location are considered.

Another group of papers contains analyses of flow and transport coupled with heat transfer. Incorporating heat transfer into a flow and transport system usually requires the addition of an energy balance equation. Models of fully coupled flow, transport, and heat transfer are useful in heat transfer enhancement technology, where, for example, transversal turbulators are used to enhance the heat transfer rate by reducing the thermal resistance near surfaces. The paper entitled *"Numerical analysis of water forced convection in channels with differently shaped transverse ribs"* addresses this particular application with a numerical investigation of turbulent water forced convection in a ribbed channel. A very realistic case study is included in the paper entitled *"Numerical study of the effect of a power plant cooling water*

discharge in the Montevideo Bay," where the authors present a finite-element based numerical simulation of the effects of power plant cooling water on the overall water temperature in the Río de la Plata River and Montevideo Bay. Simulations of thermomagnetic convection in a differentially heated square cavity using the single relaxation time lattice Boltzmann method are the focus of the paper entitled *"Simulation of thermomagnetic convection in a cavity using the Lattice Boltzmann model."* These models are important in understanding the cooling processes associated with microelectronic devices, which are becoming more ubiquitous each day. The paper entitled *"Radiative mixed convection over an isothermal cone embedded in a porous medium with variable permeability"* contains an analysis of the interaction of mixed convection with thermal radiation in an optical dense viscous fluid adjacent to an isothermal cone imbedded in a porous medium.

There is also a group of papers that addresses flow and transport mechanisms in application areas associated with chemical, biological, and sociological systems. In these complex systems, flow and transport often interact with other phenomena. In *"Modeling and simulation of a chemical vapor deposition,"* the authors consider a chemical system and propose a model on PE-CVD (plasma-enhanced chemical vapor deposition) processes for metallic bipolar plates. They also discuss the optimization of the processes for deposition of a heterogeneous layer of material on a metallic plate. A biological system is investigated in *"Numerical simulation of solid tumor blood perfusion and drug delivery during the "vascular normalization window" with antiangiogenic therapy,"* where the authors report on the influence of vascular normalization on solid tumor blood perfusion and drug delivery using a generated blood vessel network for simulations. A stochastic approach for estimating freeway capacity is the focus of *"Implementing estimation of capacity for freeway sections."* New approaches for predicting freeway capacities are necessary as demands on transportation systems increase in proportion to population densities. The subject of the paper entitled *"Modeling and analysis of material flows in re-entrant supply chain networks using modified partial differential equations"* is material flow in a supply chain. Supply chain networks are of great interest to industry, but their study is complicated by human interaction with the network. The authors begin the paper by reviewing the basic partial differential equation models for supply chain networks and follow by proposing a modified continuum model for reentrant supply chains. They demonstrate the usefulness of their model using numerical examples.

There is a group of papers that addresses advanced numerical methods, which are vital to resolving the many challenges associated with flow and transport simulation. In "*A stabilized mixed finite element method for single-phase compressible flow,"* the authors present and study a stabilized mixed finite element method for single-phase compressible flow through porous media. A moving particle solution for the Navier-Stokes equations is considered in *"Development of a particle interaction kernel function in MPS method for simulating incompressible free surface flow."* The authors study a kernel function that accounts for the interaction among moving particles within the particle method framework. In *"Multiscale time-splitting strategy for multiscale multiphysics processes of two-phase flow in fractured media,"* a multiscale time splitting strategy to simulate multiscale multiphysics processes of two-phase flow in fractured porous media is proposed and analyzed. This is especially useful when handling rapid changes of the pressure and saturation normally associated with fractured systems with capillarity. In *"Adaptive optimal m-stage Runge-Kutta methods for solving reaction-diffusion-chemotaxis systems,"* the author proposes an adaptive optimal time stepping strategy for the explicit m-stage Runge-Kutta method to solve reaction-diffusion-chemotaxis systems. *"Computing exponential for iterative splitting methods: algorithms and applications"* contains

a study of more general iterative splitting methods, and the author proposes efficient algorithms to solve the splitting schemes.

3. Conclusions

The progress in understanding flow and transport and their interaction with other physical, chemical, biological, and sociological processes is strongly dependent on adequacy, accuracy, and efficiency of numerical modeling and simulation. This special issue focuses on four important areas of flow and transport and it highlights new numerical algorithms to address conventional challenges of flow and transport simulation. The issue is not intended to be an exhaustive collection nor a survey of all of the current trends in flow and transport research; many additional significant research areas of flow and transport exist, and include, for example, coupling of different flows (e.g., coupling Stokes and Darcy flows), coupling of flow and transport in different scales (e.g., transport in molecular scale, pore scale, lab scale, and field scale), information flow (as opposed to material flow), and nonlinearity in flow and transport (non-Newtonian fluid, non-Darcy flow, etc.). Space limitations have prevented these important topics from being included here, but our hope is that they will be addressed in future special issues.

Acknowledgments

The authors would like to thank the participants of the special issue for their inspiring contributions, and the anonymous reviewers for their diligent work, which led to the high quality of the special issue. The Lead Guest Editor (S. Sun) would like to acknowledge KAUST faculty Baseline Research Fund (BRF) for supporting his research in flow and transport.

Shuyu Sun
Eleanor W. Jenkins
Zhangxing (John) Chen
Juergen Geiser

Hindawi Publishing Corporation
Journal of Applied Mathematics
Volume 2011, Article ID 389207, 25 pages
doi:10.1155/2011/389207

Research Article

Adaptive Optimal m-Stage Runge-Kutta Methods for Solving Reaction-Diffusion-Chemotaxis Systems

Jui-Ling Yu

Department of Financial and Computational Mathematics, Providence University, Taichung 43301, Taiwan

Correspondence should be addressed to Jui-Ling Yu, jlyu@pu.edu.tw

Received 15 December 2010; Accepted 26 April 2011

Academic Editor: Shuyu Sun

Copyright © 2011 Jui-Ling Yu. This is an open access article distributed under the Creative Commons Attribution License, which permits unrestricted use, distribution, and reproduction in any medium, provided the original work is properly cited.

We present a class of numerical methods for the reaction-diffusion-chemotaxis system which is significant for biological and chemistry pattern formation problems. To solve reaction-diffusion-chemotaxis systems, efficient and reliable numerical algorithms are essential for pattern generations. Along with the implementation of the method of lines, implicit or semi-implicit schemes are typical time stepping solvers to reduce the effect on time step constrains due to the stability condition. However, these two schemes are usually difficult to employ. In this paper, we propose an adaptive optimal time stepping strategy for the explicit m-stage Runge-Kutta method to solve reaction-diffusion-chemotaxis systems. Instead of relying on empirical approaches to control the time step size, variable time step sizes are given explicitly. Yet, theorems about stability and convergence of the algorithm are provided in analyzing robustness and efficiency. Numerical experiment results on a testing problem and a real application problem are shown.

1. Introduction and Background

The reaction-diffusion-chemotaxis system is the most common model used to describe chemical and biological processes and the most successful model used to describe the generation of pattern formations. Numerical simulation of such system is necessary because complicated chemotaxis terms and highly nonlinear reaction terms increase the difficulty on finding analytical solutions for realistic systems. Even though, some of the early chemotaxis models had analytical solution or one-dimensional simulation with reduced models [1, 2], the development of numerical methods for solving chemotaxis systems does not seem sufficient comparing with other type of PDEs systems. Since interesting patterns may emerge and evolve before they reach steady state [3–8], some particular heed needs to be paid to the

numerical methods to ensure that the numerical simulated patterns literally obey primary model equations [5, 8].

Chemotaxis is a directed motion, shown in motile organism, which moves toward or away from certain chemical or environment. It has been observed in microorganism, plants, animals, even in blood vessels of cancer tumors. For bacteria, chemotaxis was first discovered in the lab by Wilhelm Pfeffer and his associates in *E. coli*. in 1884 [9]. Besides the random motion of bacteria, they also show directed random movements in response to some higher concentration of oxygen. Keller and Segel [1] construct the first differential chemotaxis models. They extend the reaction-diffusion model with a convection term to simulate chemotaxis. Based on their work, many models are constructed, especially on the development of bacteria colonies [3–8, 10].

The general form of the reaction-diffusion-chemotaxis is given by [11].

$$u_t = D_u \Delta u + \nabla\left(u\chi(p)\nabla p\right) + f(p,u). \tag{1.1}$$

Here, u represents the microorganism (bacteria) density; p stands for chemoattractant concentration and is given or obtained from another equation. f is the reaction term which models the interactions between the chemicals. The diffusion term, $D_u \Delta u$, imitates the random motion of particles with positive constant diffusivity D_u. $\nabla \cdot (u\chi(p)\nabla p)$ describes the directed random movement of particles p that are modulated by the concentration gradient of the chemoattractant. The chemotaxis parameter function, χ, indicates the strength of the chemotaxis, which is given by the Keller-Segal model.

$$\chi(x) = \frac{C_0}{(C_1 + x)^s}, \tag{1.2}$$

where C_0 and C_1 are positive constants and $s \geq 1$ is an integer power. Observe that $\lim_{x\to\infty}\chi(x) = 0$ which indicates that particles tend to stay where they are when the local concentration of chemoattractant is large.

The basic idea for illustrating patterns using reaction-diffusion-chemotaxis systems is to demonstrate that eigenvalues of local linearization that are responsible for the growth (decay) can have positive (negative) real parts. Therefore, it can lead to growth at some places and decay at others, resulting in spatially inhomogeneous patterns [12, 13]. Based on this idea, we consider the method of lines (MOL) approach in this paper because it is not only the first step for construction of many numerical methods, but also provides good explanations about the generation of patterns through analyzing the positive (growth modes) and negative (decay modes) of eigenvalues. Other numerical methods used on the chemotaxis model include the fractional step method [14], the Alternating Direction Implicit (ADI) method [15, 16], and the optimal two-stage scheme [5, 8] listed here for readers's references.

The MOL approach reduces the partial differential equations to a system of ordinary differential equations (ODEs) by approximating spatial derivatives with numerous spatial discretization methods, for example, the finite difference, finite element, and spectral methods. The solution can be obtained after following some suitable time integrator. According to various spatial discretization features, the computation work can be facilitated by developing some more sophisticated robust and efficient adaptive time integrators [5, 8].

In this paper, we use standard finite differences of center difference for the Laplacian operator and upwind differences for the chemotaxis term. The reason for adapting upwind

differences is the stability concern. When the chemotaxis dominates, the system behaves more like a hyperbolic system. Then the upwind differences are more stable methods [17]. It is worth to mention that the following time-stepping scheme can also be applied to other discretization methods when the domain containing the eigenvalues is known or can be estimated. The general form of the resulting ODE system after spatial discretization reads

$$\frac{d\mathbf{u}}{dt} = M(t)\mathbf{u} + \mathbf{b}(\mathbf{t}), \tag{1.3}$$

where $M(t)$ is a time-dependent matrix and $\mathbf{b}(\mathbf{t})$ is a reaction vector which also depends on time.

Typically, the time integrator for (1.3) can be classified as implicit or explicit methods. Generally, the numerical scheme for solving implicit method is more complicated than explicit method since it often involves solving systems of algebraic equations or needs to deal with the inverse of matrices. Although implicit methods allow larger step size than explicit ones for those spatial discretization matrices only having eigenvalues with negative real parts, the computational cost may still be high due to the complicated implementation for implicit methods. Most importantly, the problem regarding time constrain still exists if the spatial matrices contain very positive real parts of eigenvalues; even for the implicit method the use of very small time steps is yet unpreventable in order to meet the stability condition. This situation is likely to occur for pattern formation problems for which the spatial discretization matrices comprise both positive and negative real parts for their eigenvalues [5, 8]. Besides, for pattern formation problems, those positive real eigenvalues are the unpredictable ones which evolve along with time. Bear these factors in mind, the explicit methods are actually better ones for the reaction-diffusion-chemotaxis systems.

In the present paper, we start with reviewing the explicit m-stage Runge-Kutta methods and then construct their adaptive optimal time steps to enhance the computation efficiency for the chemotaxis system. The optimal time step formulas are presentable and easy to calculate. Only some simple estimations about the bounds for the largest and smallest eigenvalues of the discretization spatial matrices are required at each time step. The numerical simulations on the test and realistic problems are provided. Comparison will be made in the testing problem to demonstrate that our method is not only stable but also more efficient than other similar methods, referring to CPU time and the number of iterations.

2. Optimal Time Steps for Explicit Runge-Kutta Methods

2.1. Time Independence ODEs Systems

Since interesting patterns are caused by the interaction between growth and decay modes, to analyze system (1.3) and relate it to the pattern formation model (1.1), one can do the local linearization property of the right-hand side of (1.3). The positive and negative real eigenvalues of the linearization matrix then, respectively, correspond to the growth and decay modes. Because of this reason, we will consider the corresponding ODEs induced from the chemotaxis system and introduce our idea by starting with the constant coefficients case, that is,

$$\frac{d\mathbf{u}}{dt} = M\mathbf{u} + \mathbf{b} \tag{2.1}$$

then generalize it to the time-dependent coefficients case. The general formulation of the m-stage Runge-Kutta method is

$$\begin{aligned} k_1 &= \mathbf{f}(t_n, \mathbf{u}_n), \\ k_q &= \mathbf{f}\left(t_n + \alpha_q \Delta t, \mathbf{u}_n + \Delta t_n \sum_{s=1}^{q-1} \beta_{qs} k_s \right), \quad q = 2, \ldots, m, \\ \alpha_q &= \sum_{s=1}^{q-1} \beta_{qs}, \\ \mathbf{u}_{n+1} &= \mathbf{u}_n + \Delta t_n \sum_{s=1}^{q} \gamma_s k_s, \quad q = 2, \ldots, m, \end{aligned} \tag{2.2}$$

where m is the stage number and $\alpha_q = \sum_{j=1}^{q-1} \beta_{qj},\ q = 2, \ldots, m$. The subscripts n and $n+1$ are the iteration level. For simplicity, we first look at the uniform time step size $\Delta t = t_n - t_{n-1}$ for all n. Then $\mathbf{u}_n \approx \mathbf{u}(\mathbf{x}_n)$ is the numerical solution at the nth step. Equations for the unknowns γ_s and β_{qs} can be obtained by matching terms with Taylor's expansion.

We choose single-step explicit methods, which basically are Runge-Kutta methods, because they are easy to implement and especially efficient for ODEs systems derived from the PDEs. The method is set to be explicit since the range of eigenvalues with negative real parts is measurable for chemotaxis systems. In [5, 8], we have developed adaptive two-stage time stepping scheme with optimum time step sizes for solving chemotaxis system and verified that it is reliable and more economical when comparing with other similar methods. We conjecture that the similar strategy used in [5, 8] could be used to derive optimal adaptive three- and four-stage methods. In the two-stage case, the size of the optimal step is determined by the root of the first-order equation hence it is absolute optimal within one time step. If our conjecture is correct, the sizes of optimal steps for higher-stage methods should be the roots of some higher-order equations. But, are these adaptive step sizes absolute optimal? And are they easy to be found as in the two-stage case?

To answer these questions, we begin our study with the three-stage Runge-Kutta method and set $\mathbf{b} = 0$ in (2.1). As in [5, 8], we first fix all the intermediate coefficients at $t = t_n$ for the three-stage Runge-Kutta method. The general time dependence case is proposed in the next section. Denoting $M = M(t_n)$ and applying (2.2) to the three-stage Runge-Kutta method with all the intermediate values being fixed at t_n, we arrive at

$$\begin{aligned} k_1 &= M\mathbf{u}_n, \\ k_2 &= M(1 + \alpha_2 \Delta t M)\mathbf{u}_n, \\ k_3 &= M\left(1 + \alpha_3 \Delta t M + \alpha_2 \beta_{32} \Delta t^2 M^2\right)\mathbf{u}_n, \end{aligned} \tag{2.3}$$

$$\mathbf{u}_{n+1} = \left(1 + \delta_1 \Delta t M + \delta_2 \Delta t^2 M^2 + \delta_3 \Delta t^3 M^3\right)\mathbf{u}_n, \tag{2.4}$$

where $\delta_i, i = 1, 2, 3$, are combinations of the coefficients β_{qs} and γ_s. Since $\mathbf{u}(t_{n+1}) = e^{M\Delta t}\mathbf{u}(t_n)$ and assuming $\mathbf{u}_n$ is exact up to the order Δt^3, we have $\delta_1 = 1$, $\delta_2 = (1/2!)$, $\delta_3 = (1/3!)$. Similar

arguments also hold for RK methods with other stages. Thus, if we treat it as a standard iterative method, (2.4) is a one-step method [18]:

$$\begin{aligned}\mathbf{u}_{n+1} &= \left[1 + \Delta t M + \frac{1}{2!}(\Delta t M)^2 + \cdots + \frac{1}{m!}(\Delta t M)^m\right]\mathbf{u}_n. \\ &= p_m(\Delta t)\mathbf{u}_n.\end{aligned} \tag{2.5}$$

In the case of $\mathbf{b} \neq 0$, (2.5) becomes

$$\mathbf{u}_{n+1} = p_m(\Delta t)\mathbf{u}_n + \left(1 + \frac{\Delta t}{2!}M + \cdots + \frac{\Delta t^m}{m!}M^{m-1}\right)\mathbf{b}. \tag{2.6}$$

Denote $\mathbf{v}$ as the solution by solving the system with the perturbated initial condition; we have

$$\mathbf{v}_{n+1} = p_m(\Delta t)\mathbf{v}_n + \left(1 + \frac{\Delta t}{2!}M + \cdots + \frac{\Delta t^m}{m!}M^{m-1}\right)\mathbf{b}. \tag{2.7}$$

From (2.6) and (2.7), the accumulation error can be written as

$$|\mathbf{u}_{n+1} - \mathbf{v}_{n+1}| = \left|p_m(\Delta t)\right| \times |\mathbf{u}_n - \mathbf{v}_n|. \tag{2.8}$$

Note that

$$p_m(\lambda) = 1 + \Delta t\lambda + \frac{1}{2!}(\Delta t\lambda)^2 + \cdots + \frac{1}{m!}(\Delta t\lambda)^m \tag{2.9}$$

is called the amplification factor, where λ is an eigenvalue of M. It is obtained when a scalar test problem, $u' = \lambda u$, is applied to the single-step method.

Suppose that $\lambda = a + bi = \mathrm{Re}\,\lambda + \mathrm{Im}\,\lambda i$. For pattern formation problems, what we are interested in is the long-term behavior of the solution vectors. It is important to ensure that observed patterns are accurate in the sense that they are not coming from the accumulation error of numerical schemes. We therefore make the following definition of stability.

Definition 2.1. An explicit single-step method is said to be stable if $|p_m(\lambda)| < 1$ when $a < 0$ and $|p_m(\lambda)| \leq 1 + a\Delta t + O(\Delta t)$ when $a \geq 0$.

Here $O(\Delta t)$ means higher order of Δt. Our definition is designed to guarantee appropriate numerical solutions for both decay and growth cases. Based on this definition, we get restrictions on the step size. Typically, time steps are restricted either when the scheme is explicit and $a < 0$ or when the scheme is implicit and $a > 0$ [5, 8]. Since the amplification factors are functions of complex numbers, it is sometimes difficult to analyze. The following theorem shows that the amplification factor can be approximated by simpler functions of a plus some error terms instead of functions of complex eigenvalues λ. Observe that the order of error terms indicated in Theorem 2.2 is the same as the truncation error of the m-stage Runge-Kutta method. Therefore, we can work with this simpler function without losing the order of accuracy.

2.1.1. Stability Analysis and the Optimization Method

The following theorem states that the m-stage Runge-Kutta method satisfies the stability condition automatically for $a > 0$ but needs constraints on Δt when $a < 0$.

Theorem 2.2. $|p_m(\lambda)|^2 = |p_m(a+bi)|^2 = (1+\Delta ta+(1/2)\Delta t^2a^2+\cdots+(1/m!)\Delta t^m a^m)^2+O(\Delta t^{m+1})$, *where* $m = 1,\ldots,4$.

Proof. The proof for $m = 1$ is straightforward, and the proof for $m = 2$ is in [5, 8]. For $m = 3$,

$$\begin{aligned}
\left|p_3(\lambda)\right|^2 &= \left(1+\Delta ta+\frac{\Delta t^2}{2}\left(a^2-b^2\right)+\frac{\Delta t^3}{6}\left(a^3-3ab^2\right)\right)^2 \\
&\quad+\left(\Delta tb+\Delta t^2ab+\frac{\Delta t^3}{6}\left(3a^2b-b^3\right)\right)^2 \\
&= \left(1+\Delta ta+\frac{1}{2}(\Delta ta)^2+\frac{1}{6}(\Delta ta)^3\right)^2-2(1+\Delta ta)\left(\frac{1}{2}\Delta t^2b^2+\frac{1}{2}\Delta t^3ab^2\right) \\
&\quad+O\left(\Delta t^4\right)+\left(\Delta tb+\Delta t^2ab+\frac{\Delta t^3}{6}\left(3a^2b-b^3\right)\right)^2 \\
&= \left(1+\Delta ta+\frac{1}{2}(\Delta ta)^2+\frac{1}{6}(\Delta ta)^3\right)^2 \\
&\quad-\Delta t^2b^2-2\Delta t^3ab^2+O\left(\Delta t^4\right)+\Delta t^2b^2+2\Delta t^3ab^2+O\left(\Delta t^4\right) \\
&= \left(1+\Delta ta+\frac{1}{2}(\Delta ta)^2+\frac{1}{6}(\Delta ta)^3\right)^2+O\left(\Delta t^4\right).
\end{aligned} \tag{2.10}$$

For $m = 4$,

$$\begin{aligned}
\left|p_4(\lambda)\right|^2 &= \left(1+\Delta ta+\frac{\Delta t^2}{2}\left(a^2-b^2\right)+\frac{\Delta t^3}{6}\left(a^3-3ab^2\right)+\frac{\Delta t^4}{24}\left(a^4-6a^2b^2+b^4\right)\right)^2 \\
&\quad+\left(\Delta tb+\Delta t^2ab+\frac{\Delta t^3}{6}\left(3a^2b-b^3\right)+\frac{\Delta t^4}{24}\left(4a^3b-4ab^3\right)\right)^2 \\
&= \left(1+\Delta ta+\frac{1}{2}(\Delta ta)^2+\frac{1}{6}(\Delta ta)^3+\frac{1}{24}(\Delta ta)^4\right)^2 \\
&\quad-2\left(1+\Delta ta+\frac{1}{2}(\Delta ta)^2+\frac{1}{6}(\Delta ta)^3+\frac{1}{24}(\Delta ta)^4\right) \\
&\quad*\left(\frac{1}{2}\Delta t^2b^2+\frac{1}{2}\Delta t^3ab^2+\frac{1}{4}\Delta t^4a^2b^2-\frac{1}{24}\Delta t^4b^4\right) \\
&\quad+\left(\frac{1}{2}\Delta t^2b^2+\frac{1}{2}\Delta t^3ab^2+\frac{1}{4}\Delta t^4a^2b^2-\frac{1}{24}\Delta t^4b^4\right)^2
\end{aligned}$$

$$
\begin{aligned}
&+\left(\Delta t b+\Delta t^2 ab+\frac{\Delta t^3}{6}\left(3a^2b-b^3\right)+\frac{\Delta t^4}{24}\left(4a^3b-4ab^3\right)\right)^2\\
&=\left(1+\Delta t a+\frac{1}{2}(\Delta t a)^2+\frac{1}{6}(\Delta t a)^3+\frac{1}{24}(\Delta t a)^4\right)^2\\
&\quad+\Delta t^4\left(-2a^2b^2+\frac{1}{12}b^4\right)-2\Delta t^3 ab^2-\Delta t^2 b^2+O\left(\Delta t^5\right)+\frac{1}{4}\Delta t^4 b^4+O\left(\Delta t^5\right)\\
&\quad+\Delta t^4\left(-\frac{1}{3}b^4+2a^2b^2\right)+2\Delta t^3 ab^2+\Delta t^2 b^2+O\left(\Delta t^5\right)\\
&=\left(1+\Delta t a+\frac{1}{2}(\Delta t a)^2+\frac{1}{6}(\Delta t a)^3+\frac{1}{24}(\Delta t a)^4\right)^2+O\left(\Delta t^5\right).
\end{aligned}
\tag{2.11}
$$

The geometric interpretation is that, for spatial matrices $M(t_n)$, the eigenvalues with negative real parts are assumed to be contained in the left-plane ellipse. Let us denote $1+\Delta t a+(1/2)\Delta t^2 a^2+\cdots+(1/m!)\Delta t^m a^m$ as $p_m(a,\Delta t)$. To examine whether numerically generated patterns truly obey the original models, one needs to verify if the negative modes ($a<0$) are diminished and positive modes ($a>0$) are growing accordingly. That is, when the negative modes occur, $p_m(a,\Delta t)$ is less than one, and is greater than one when the spatial matrix $M(t_n)$ happens to have positive modes. From $p_m(a,\Delta t)$, we find that when $a>0$, $p_m(a,\Delta t)$ is definitely greater than unity, hence the stability condition is automatically satisfied; when $a<0$, $p_m(a,\Delta t)$ is then possible to be less than unity. It is necessary to put the limitation on the time steps to ensure the stability condition $p_m(a,\Delta t)<1$ is preserved. Besides, the negative modes should be diminished in an effective way so that the computational cost can be reduced. Under these consideration, we derive the optimal time step which not only diminishes decay modes efficiently but also guarantees the stability conditions. Before moving on the theorems about showing how we get the optimal time steps for m-stage Runge-Kutta method, let us recall the Gerschgorin theorem [19]. It says that for matrices with real coefficients, the distribution for the real parts of eigenvalues can be estimated simply by the discs centered at the diagonal elements. So we can assume that the range of negative real parts of eigenvalues of the discretized spatial matrices is known. Here, only negative real eigenvalues are needed as they are the only ones responsible for the stability and restriction of the step sizes for explicit schemes. We are now ready to give relevant theorems for constructing optimal step sizes by effectively damping the negative modes. □

Theorem 2.3. *For $a<0$ and m being even, $p_m(a,\Delta t)>0$ and is concave up for all $\Delta t>0$.*

Proof. For $m=2$, it is a second-degree polynomial with a positive leading coefficient. The proof is straightforward. Note that $p_2(a,\Delta t)>0$.

Assume $p_{m-2}(a,\Delta t)>0$ for all even m. For m being even and $m>2$, we have

$$
\frac{\partial^2 p_m(a,\Delta t)}{\partial \Delta t^2}=a^2 p_{m-2}(a,\Delta t)>0. \tag{2.12}
$$

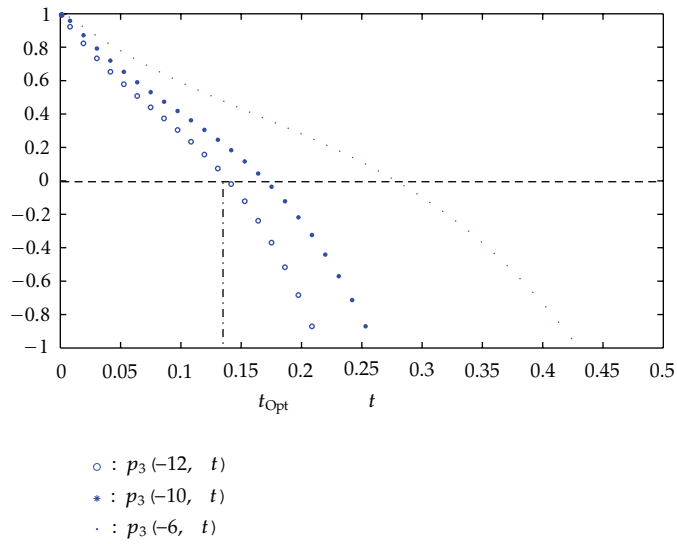

Figure 1: Graphs for $p_3(a, \Delta t)$ where $a = -6$: ·, $a = -10$: ∗, $a = -12$: ○.

It follows from mathematical induction, $\partial^2/\partial \Delta t^2 p_m(a, \Delta t) > 0$ for all even m. Hence, $p_m(a, \Delta t)$ is concave up w.r.t. Δt if m is even.

Moreover, $p_m(a, \Delta t) > 0$ for all even m, because $p_m(a, \Delta t) > \exp(a\Delta t) > 0$ for even m. □

Corollary 2.4. *For $a < 0$ and m being an odd number, $p_m(a, \Delta t) < 1$ and $p_m(a, \Delta t)$ is strictly decreasing for all $\Delta t > 0$.*

Proof. For $m = 1$, the proof is trivial. For $m > 1$, $p_m(a, 0) = 1$ and

$$\frac{\partial p_m(a, \Delta t)}{\partial \Delta t} = a p_{m-1}(a, \Delta t) < 0 \tag{2.13}$$

since $a < 0$ and $m - 1$ is an even number.

Therefore, we conclude $p_m(a, \Delta t) < 1$ for all odd m and $\Delta t > 0$. Moreover, $p_m(a, \Delta t)$ is strictly decreasing with respect to Δt. □

Theorem 2.5 (Case for m being odd). *Assume that $-a_{\max} \le a \le -a_{\min}$, where $a_{\max} > a_{\min} > 0$ are two positive numbers. Then the solution of the following min-max problem occurs at $\Delta t = \Delta t_{\text{opt}}$ in which Δt satisfies $f_m(-a_{\max}, \Delta t) = 0$, where m is an odd number. The min-max problem is stated as*

$$\min_{\Delta t > 0} \max_{-a_{\max} \le a \le -a_{\min}} p_m(a, \Delta t). \tag{2.14}$$

Proof. Note that $p_m(a_1, \Delta t) > p_m(a_2, \Delta t)$ if $a_1 > a_2$ and $a_1, a_2 < 0$. For any fixed Δt, the maximum of $p_m(a, \Delta t)$ is obtained at $p_m(-a_{\min}, \Delta t)$. So the min-max occurs when $p_m(-a_{\max}, \Delta t) = 0$. Since $p_m(a, \Delta t)$ is continuous, $p_m(a, 0) = 1 > 0$, and $p_m(a, \Delta t) < 0$ as

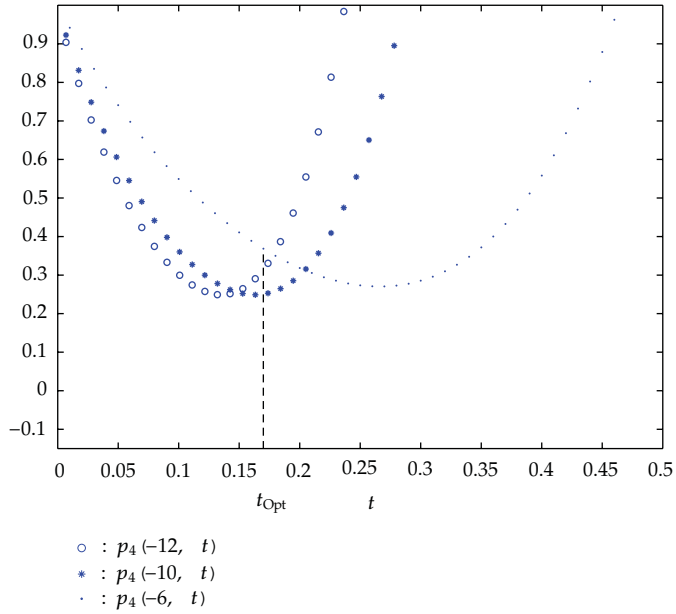

Figure 2: Graphs for $p_4(a, \Delta t)$ where $a = -6$: $\cdot$, $a = -10$: $*$, $a = -12$: $\circ$.

$\Delta t \to \infty$, the solution exists by Intermediate Value Theorem. Furthermore, from Corollary 2.4, $p_m(a, \Delta t)$ is monotone decreasing w.r.t. Δt, so the solution is unique. □

Theorem 2.6 (Case for m being even). *Assume that $-a_{\max} \le a \le -a_{\min}$, where $a_{\max} > a_{\min} > 0$ are two positive numbers. Then the solution of the following min-max problem occurs at $\Delta t = \Delta t_{\mathrm{opt}}$ in which Δt satisfies $p_m(-a_{\max}, \Delta t) = p_m(-a_{\min}, \Delta t)$, where m is an even number $(m = 2, 4)$. The min-max problem is stated as*

$$\min_{\Delta t > 0} \max_{-a_{\max} \le a \le -a_{\min}} p_m(a, \Delta t). \tag{2.15}$$

Proof. For each fixed a, $p_m(a, \Delta t)$ is a quadratic-like polynomial function in Δt. Then for any fixed Δt, the maximum of $p_m(a, \Delta t)$ is obtained at $p_m(-a_{\min}, \Delta t), \Delta t < \Delta t_{\mathrm{opt}}$, and at $p_m(-a_{\max}, \Delta t)$, $\Delta t > \Delta t_{\mathrm{opt}}$. So the minimax occurs when $p_m(-a_{\max}, \Delta t) = p_m(-a_{\min}, \Delta t)$, that is,

$$\sum_{i=0}^{m} \frac{(-a_{\max} \Delta t)^m}{m!} = \sum_{i=0}^{m} \frac{(-a_{\min} \Delta t)^m}{m!}. \tag{2.16}$$

This leads to the solution. □

Let us denote $g_m(\Delta t) = p_m(-a_{\max}, \Delta t) - p_m(-a_{\min}, \Delta t)$. The following theorem states that the optimal time step is unique for m being even. For m being odd, it is shown in Theorem 2.5.

Theorem 2.7. *If m is even, $g_m(\Delta t)$ has only one positive real solution.*

Proof.

$$\begin{aligned} g_m(\Delta t) &= \Delta t(a_{\max} - a_{\min})\left[\sum_{i=1}^{m}(-\Delta t)^{m-1}\frac{\left(a_{\max}^m - a_{\min}^m\right)}{m!(a_{\max} - a_{\min})}\right] \\ &= \Delta t(a_{\max} - a_{\min})q_m(\Delta t). \end{aligned} \tag{2.17}$$

It follows from (2.17) and the fact that $a_{\max} \neq a_{\min}$, to find the zeros of $g_m(\Delta t)$ is enough to solve $q_m(\Delta t) = 0$. Since $q_m(0) = 1$ and $q_m(\Delta t) < 0$ as Δt tends to infinity, positive real solutions hence exist for $g_m(\Delta t)$ by the Intermediate Value Theorem. Moreover, $q_m(\Delta t)$ is strictly decreasing (Figures 1 and 2). Therefore, the solution is unique. □

2.2. Time-Dependent ODEs Systems

In the previous section, we derived simpler forms of amplification factors as well as theorems for setting optimal time steps for constant ODEs systems. The optimal time step is obtained under the assumption that the intermediate values of Runge-Kutta methods are fixed at current time. Under the stability consideration, we continue our study on searching optimal time steps and relevant schemes when the ODEs system and Runge-Kutta methods are time dependent. The general form of the time dependent system is

$$\frac{d\mathbf{u}}{dt} = M(t)\mathbf{u} + \mathbf{b}(\mathbf{t}). \tag{2.18}$$

Derivation of Adaptive Optimal Time Step for the Three-Stage Runge-Kutta Method

We start with the three-stage Runge-kutta method. As before, we first set the reaction vector to be zero.

$$\begin{aligned} k_1 &= M_n\mathbf{u}_n, \\ k_2 &= M_{n+\alpha_2}\left(u_n + \beta_{21}\Delta t k_1\right), \\ k_3 &= M_{n+\alpha_3}\left(u_n + \Delta t\left(\beta_{31}k_1 + \beta_{32}k_2\right)\right), \\ \mathbf{u}_{n+1} &= \mathbf{u}_n + \Delta t\left(\gamma_1 k_1 + \gamma_2 k_2 + \gamma_3 k_3\right). \end{aligned} \tag{2.19}$$

Here, $M_n = M(t_n)$. Expand $M_{n+\alpha_i}$ at t_n by Taylor expansion, then $M_{n+\alpha_i} = M_n + \alpha_i\Delta t_n M_n' + ((\alpha_i\Delta t_n)^2/2!)M_n'' + O(\Delta t^3)$, where $i = 2, 3$.

Therefore,

$$k_1 = M_n\mathbf{u}_n,$$

$$k_2 = \left[M_n + \left(\alpha_2 M_n' + \beta_{21}M_n^2\right)\Delta t_n + \left(\frac{\alpha_2^2}{2}M_n'' + \alpha_2\beta_{21}M_n M_n'\right)\Delta t_n^2\right]\mathbf{u}_n + O\left(\Delta t_n^3\right),$$

$$k_3 = \Bigg[M_n + \alpha_3 M_n' \Delta t_n + \left(\beta_{31} + \beta_{32}\right) M_n^2 \Delta t_n + \frac{\alpha_3^2}{2} M_n'' \Delta t_n^2 + \left(\beta_{31}\alpha_3 + \beta_{32}(\alpha_2 + \alpha_3)\right) M_n' M_n \Delta t_n^2 + \beta_{32}\beta_{21} M_n^3 \Delta t_n^2 \Bigg] \mathbf{u}_n + O\left(\Delta t_n^3\right). \tag{2.20}$$

Since by consistency,

$$\begin{aligned} \sum_{i=1}^{3} \gamma_i &= 1, \\ \alpha_q &= \sum_{j=1}^{q-1} \beta_{qj}, \quad q = 2, 3, \\ \gamma_2 \alpha_2 + \gamma_3 \alpha_3 &= \frac{1}{2}, \\ \gamma_2 \alpha_2^2 + \gamma_3 \alpha_3^2 &= \frac{1}{3}, \\ \gamma_3 \alpha_2 \beta_{32} &= \frac{1}{6}. \end{aligned} \tag{2.21}$$

Followed by (2.20) and the consistency condition, (2.19) can be simplified as

$$\mathbf{u}_{n+1} = \mathbf{u}_n + \Bigg[M_n \Delta t_n + \frac{1}{2} M_n' \Delta t_n^2 + \frac{1}{6} M_n'' \Delta t_n^3 + \frac{1}{2} M_n^2 \Delta t_n^2 + \frac{1}{2} M_n' M_n \Delta t_n^3 + \frac{1}{6} M_n^3 \Delta t_n^3 \Bigg] \mathbf{u}_n + O\left(\Delta t_n^4\right). \tag{2.22}$$

Now, we assume

$$\begin{aligned} \sum_{i=1}^{3} \tau_i &= 1, \\ \tau_2 \mu + \tau_3 &= \frac{1}{2}, \\ \tau_2 \mu^2 + \tau_3 &= \frac{1}{3}. \end{aligned} \tag{2.23}$$

Then, we can rewrite (2.22) as

$$\mathbf{u}_{n+1} = \mathbf{u}_n + \Bigg[\left(\tau_1 + \tau_2 + \tau_3\right) M_n \Delta t_n + \left(\tau_2 \mu + \tau_3\right) M_n' \Delta t_n^2 + \frac{1}{2}\left(\tau_2 \mu^2 + \tau_3\right) M_n'' \Delta t_n^3 + \frac{1}{2}\left(\tau_1 + \tau_2 + \tau_3\right)^2 M_n^2 \Delta t_n^2 + \left(\tau_1 + \tau_2 + \tau_3\right)\left(\tau_2 \mu + \tau_3\right) M_n' M_n \Delta t_n^3 + \frac{1}{6}\left(\tau_1 + \tau_2 + \tau_3\right)^3 M_n^3 \Delta t_n^3 \Bigg] \mathbf{u}_n + O\left(\Delta t_n^4\right). \tag{2.24}$$

This way, we arrive the following desirable form through rearrangement:

$$\begin{aligned}\mathbf{u}_{n+1} = \mathbf{u}_n + \Bigg[& \tau_1 M_n + \tau_2 \left(M_n + \mu \Delta t_n M_n' + \frac{(\mu \Delta t_n)^2}{2} M_n'' \right) \\ & + \tau_3 \left(M_n + \Delta t_n M_n' + \frac{\Delta t_n^2}{2} M_n'' \right) \\ & + \frac{1}{2} \left[(\tau_1 + \tau_2 + \tau_3) M_n + (\tau_2 + \tau_3 \mu) M_n' \Delta t_n + O\left(\Delta t_n^2\right) \right]^2 \Delta t_n^2 \\ & + \frac{1}{6} (\tau_1 + \tau_2 + \tau_3)^3 M_n^3 \Delta t_n^3 \Bigg] \mathbf{u}_n + O\left(\Delta t_n^4\right).\end{aligned} \tag{2.25}$$

Let

$$J_n = \tau_1 M_n + \tau_2 M_{n+\mu} + \tau_3 M_{n+1}, \tag{2.26}$$

where

$$\begin{aligned}\tau_2 &= -\frac{1}{6\mu(\mu - 1)}, \\ \tau_3 &= \frac{3\mu - 2}{6(\mu - 1)}.\end{aligned} \tag{2.27}$$

Then the previous equation implies

$$\mathbf{u}_{n+1} = \left[1 + J_n \Delta t_n + \frac{1}{2} (J_n \Delta t_n)^2 + \frac{1}{3!} (J_n \Delta t_n)^3 \right] \mathbf{u}_n + O\left(\Delta t_n^4\right). \tag{2.28}$$

The above result illustrates that the time-dependent three-stage Runge-Kutta method can be treated as a single-step method without losing the order of accuracy. In addition, it shares the same form with (2.5) if J_n is replaced by M. Next, we derive a similar argument for the four-stage Runge-Kutta method.

Derivation of Adaptive Optimal Time Step for the Four-Stage Runge-Kutta Method

Applying the four-stage Runge-Kutta method to (2.18), we get

$$\begin{aligned}k_1 &= M_n \mathbf{u}_n, \\ k_2 &= M_{n+\alpha_2} (\mathbf{u}_n + \beta_{21} \Delta t k_1), \\ k_3 &= M_{n+\alpha_3} (\mathbf{u}_n + \Delta t (\beta_{31} k_1 + \beta_{32} k_2)), \\ k_4 &= M_{n+\alpha_4} (\mathbf{u}_n + \Delta t (\beta_{41} k_1 + \beta_{42} k_2 + \beta_{43} k_3)), \\ \mathbf{u}_{n+1} &= \mathbf{u}_n + \Delta t (r_1 k_1 + r_2 k_2 + r_3 k_3 + r_4 k_4).\end{aligned} \tag{2.29}$$

Since $M_{n+\alpha_i} = M_n + \alpha_i \Delta t_n M_n' + ((\alpha_i \Delta t_n)^2/2!) M_n'' + ((\alpha_i \Delta t_n)^3/3!) M_n''' + O(\Delta t^4)$

$$
\begin{aligned}
k_2 &= \left[M_n + \left(\alpha_2 M_n' + \beta_{21} M_n^2 \right) \Delta t_n + \left(\frac{\alpha_2^2}{2} M_n'' + \alpha_2 \beta_{21} M_n M_n' \right) \Delta t_n^2 \right. \\
&\quad \left. + \left(\frac{\alpha_2^3}{3!} M_n''' + \frac{\alpha_2^2 \beta_{21}}{2} M_n'' M_n \right) \Delta t_n^3 \right] \mathbf{u}_n + O\left(\Delta t_n^4 \right), \\
k_3 &= \left[M_n + \alpha_3 M_n' \Delta t_n + (\beta_{31} + \beta_{32}) M_n^2 \Delta t_n + \frac{\alpha_3^2}{2} M_n'' \Delta t_n^2 \right. \\
&\quad + (\beta_{31}\alpha_3 + \beta_{32}(\alpha_2 + \alpha_3)) M_n' M_n \Delta t_n^2 + \beta_{32}\beta_{21} M_n^3 \Delta t_n^2 + \frac{\alpha_3^3}{3!} M_n''' \Delta t_n^3 \\
&\quad + \frac{1}{2} \left(\beta_{31}\alpha_3^2 + \beta_{32} \left(\alpha_2^2 + \alpha_3^2 \right) \right) M_n'' M_n \Delta t_n^3 + \beta_{32}\alpha_2\alpha_3 \left(M_n' \right)^2 \Delta t_n^3 \\
&\quad \left. + \beta_{32}\beta_{21}(\alpha_2 + \alpha_3) M_n' M_n^2 \Delta t_n^3 \right] \mathbf{u}_n + O\left(\Delta t_n^4 \right), \\
k_4 &= \left[M_n + \alpha_4 M_n' \Delta t_n + (\beta_{41} + \beta_{42} + \beta_{43}) M_n^2 \Delta t_n + \frac{1}{2} \alpha_4^2 M_n'' \Delta t_n^2 \right. \\
&\quad + (\beta_{41}\alpha_4 + \beta_{42}(\alpha_2 + \alpha_4) + \beta_{43}(\alpha_3 + \alpha_4)) M_n' M_n \Delta t_n^2 \\
&\quad + (\beta_{42}\beta_{21} + \beta_{43}(\beta_{31} + \beta_{32})) M_n^3 \Delta t_n^2 + \frac{1}{3!} \alpha_4^3 M_n''' \Delta t_n^3 \\
&\quad + \frac{1}{2} \left(\beta_{41}\alpha_4^2 + \beta_{42} \left(\alpha_2^2 + \alpha_4^2 \right) + \beta_{43} \left(\alpha_3^2 + \alpha_4^2 \right) \right) M_n'' M_n \Delta t_n^3 \\
&\quad + (\beta_{42}\beta_{21}(\alpha_2 + \alpha_4) + \beta_{43}\beta_{31}(\alpha_3 + \alpha_4) + \beta_{43}\beta_{32}(\alpha_2 + \alpha_3 + \alpha_4)) M_n' M_n^2 \Delta t_n^3 \\
&\quad \left. + (\beta_{42}\alpha_2\alpha_4 + \beta_{43}\alpha_3\alpha_4) \left(M_n' \right)^2 \Delta t_n^3 + \beta_{43}\beta_{32}\beta_{21} M_n^4 \Delta t_n^3 \right] \mathbf{u}_n + O\left(\Delta t_n^4 \right).
\end{aligned}
\tag{2.30}
$$

By consistency of the method,

$$
\begin{aligned}
\sum_{i=1}^{4} \gamma_i &= 1, \\
\alpha_q &= \sum_{j=1}^{q-1} \beta_{qj}, \quad q = 2, \ldots, 4, \\
\gamma_2\alpha_2 + \gamma_3\alpha_3 + \gamma_4\alpha_4 &= \frac{1}{2}, \\
\gamma_2\alpha_2^2 + \gamma_3\alpha_3^2 + \gamma_4\alpha_4^2 &= \frac{1}{3},
\end{aligned}
$$

$$\begin{aligned}
\gamma_2\alpha_2^3 + \gamma_3\alpha_3^3 + \gamma_4\alpha_4^3 &= \frac{1}{4},\\
\gamma_3\alpha_2\beta_{32} + \gamma_4\left(\alpha_2\beta_{42} + \beta_{43}\alpha_3\right) &= \frac{1}{6},\\
\gamma_3\beta_{32}\alpha_2\alpha_3 + \gamma_4\beta_{42}\alpha_2\alpha_4 + \gamma_4\beta_{43}\alpha_3\alpha_4 &= \frac{1}{8},\\
\gamma_3\alpha_2^2\beta_{32} + \gamma_4\alpha_2^2\beta_{42} + \gamma_4\alpha_3^2\beta_{43} &= \frac{1}{12},\\
\gamma_4\alpha_2\beta_{43}\beta_{32} &= \frac{1}{24}.
\end{aligned} \tag{2.31}$$

Thus,

$$\begin{aligned}
\mathbf{u}_{n+1} = \mathbf{u}_n + \Bigg[& M_n\Delta t_n + \frac{1}{2}M_n'\Delta t_n^2 + \frac{1}{6}M_n''\Delta t_n^3 + \frac{1}{24}M_n'''\Delta t_n^4\\
& + \frac{1}{2}M_n^2\Delta t_n^2 + \frac{1}{2}M_n'M_n\Delta t_n^3 + \frac{1}{6}M_n''M_n\Delta t_n^4 + \frac{1}{8}\left(M_n'\right)^2\Delta t_n^4\\
& + \frac{1}{6}M_n^3\Delta t_n^3 + \frac{1}{4}M_n'M_n^2\Delta t_n^4 + \frac{1}{24}M_n^4\Delta t_n^4\Bigg]\mathbf{u}_n + O\left(\Delta t_n^5\right).
\end{aligned} \tag{2.32}$$

We further assume

$$\begin{aligned}
\sum_{i=1}^{4}\tau_i &= 1,\\
\tau_2\mu_1 + \tau_3\mu_2 + \tau_4 &= \frac{1}{2},\\
\tau_2\mu_1^2 + \tau_3\mu_2^2 + \tau_4 &= \frac{1}{3},\\
\tau_2\mu_1^3 + \tau_3\mu_2^3 + \tau_4 &= \frac{1}{4}.
\end{aligned} \tag{2.33}$$

The previous equation hence can be written as

$$\begin{aligned}
\mathbf{u}_{n+1} = \mathbf{u}_n + \Bigg[& \left(\tau_1 + \tau_2 + \tau_3 + \tau_4\right)M_n\Delta t_n + \left(\tau_2\mu_1 + \tau_3\mu_2 + \tau_4\right)M_n'\Delta t_n^2\\
& + \frac{1}{2}\left(\tau_2\mu_1^2 + \tau_3\mu_2^2 + \tau_4\right)M_n''\Delta t_n^3 + \frac{1}{6}\left(\tau_2\mu_1^3 + \tau_3\mu_2^3 + \tau_4\right)M_n'''\Delta t_n^4\\
& + \frac{1}{2}\left(\tau_1 + \tau_2 + \tau_3 + \tau_4\right)^2M_n^2\Delta t_n^2 + \left(\tau_1 + \tau_2 + \tau_3 + \tau_4\right)\\
& * \left(\tau_2\mu_1 + \tau_3\mu_2 + \tau_4\right)M_n'M_n\Delta t_n^3\\
& + \frac{1}{2}\left(\tau_1 + \tau_2 + \tau_3 + \tau_4\right)\left(\tau_2\mu_1^2 + \tau_3\mu_2^2 + \tau_4\right)M_n''M_n\Delta t_n^4
\end{aligned}$$

$$+\frac{1}{2}\left(\tau_2\mu_1+\tau_3\mu_2+\tau_4\right)^2\left(M_n'\right)^2\Delta t_n^4+\frac{1}{6}\left(\tau_1+\tau_2+\tau_3+\tau_4\right)^3M_n^3\Delta t_n^3$$
$$+\frac{1}{2}\left(\tau_1+\tau_2+\tau_3+\tau_4\right)\left(\tau_2\mu_1+\tau_3\mu_2+\tau_4\right)M_n'M_n^2\Delta t_n^4$$
$$+\frac{1}{24}M_n^4\Delta t_n^4\Bigg]\mathbf{u}_n+O\left(\Delta t_n^5\right). \tag{2.34}$$

That is,

$$\mathbf{u}_{n+1}=\left[1+J_n\Delta t_n+\frac{1}{2}\left(J_n\Delta t_n\right)^2+\frac{1}{3!}\left(J_n\Delta t_n\right)^3+\frac{1}{4!}\left(J_n\Delta t_n\right)^4\right]\mathbf{u}_n+O\left(\Delta t_n^5\right), \tag{2.35}$$

where

$$\begin{aligned}
J_n&=\tau_1M_n+\tau_2M_{n+\mu_1}+\tau_3M_{n+\mu_2}+\tau_4M_{n+1},\\
\tau_2&=\frac{2\mu_2-1}{12\left(-\mu_2+\mu_1\right)\left(\mu_1-1\right)\mu_1},\\
\tau_3&=-\frac{-1+2\mu_1}{12\mu_2\left(\mu_1\mu_2+\mu_2-\mu_2^2-\mu_1\right)},\\
\tau_4&=\frac{6\mu_1\mu_2-4\mu_2+3-4\mu_1}{12\left(\mu_2-1\right)\left(\mu_1-1\right)}.
\end{aligned} \tag{2.36}$$

We now turn to examine the more general situation in which the reaction term is not zero, that is, $\mathbf{b}\neq 0$. In this case, we have

$$\mathbf{u}_{n+1}=\left(\sum_{i=0}^{m}\frac{\left(\Delta t_nJ_n\right)^i}{i!}\right)\mathbf{u}_n+\mathbf{F}\left(\mathbf{b}_n,\mathbf{b}_{n+\mu_1},\ldots,\mathbf{b}_{n+1}\right)+O\left(\Delta t_n^{i+1}\right). \tag{2.37}$$

Similar to our discussion in the previous section, the accumulation error for (2.37) is

$$\left|\mathbf{u}_{n+1}-\mathbf{v}_{n+1}\right|=\left|\sum_{i=0}^{m}\frac{\left(\Delta t_nJ_n\right)^i}{i!}\right|\times\left|\mathbf{u}_n-\mathbf{v}_n\right|+O\left(\Delta t_n^{i+1}\right). \tag{2.38}$$

We remark again that the amplification factor $\sum_{i=0}^{m}\left(\left(\Delta t_nJ_n\right)^i/i!\right)$ in (2.38) at the nth local step has the same form with (2.5) except M being replaced by J_n. Therefore, we can apply the strategy demonstrated in Theorems 2.5 and 2.6 to look for the optimal time steps for Runge-Kutta schemes. The present $a_{\max}$ and $a_{\min}$ appeared in the optimal step size formulas then, respectively, represent the greatest and smallest real parts of the eigenvalues of the matrix J_n. Notice that by the similar argument outlined in the previous proofs, the stability is preserved with this step size.

An Explicit Adaptive Optimal Time Stepping Scheme for Solving (2.18)

(1) Set up initial condition $\mathbf{u_0}$ and initial step size Δt_0.

(2) Set J_n in accordance with the stage number m, and apply m-stage Runge-Kutta schemes.

(3) Use the Gerschgorin theorem to estimate the interval, $[-a^n_{\max}, -a^n_{\min}]$ for negative real parts of the eigenvalues of J_n.

(4) Place Δt_{n+1},

(i) $m = 2$: $\Delta t_{n+1} = 2/(a^n_{\max} + a^n_{\min})$,

(ii) $m = 3$: $\Delta t_{n+1} = 2.512745327/a^n_{\max}$,

(iii) $m = 4$:

$$
\begin{aligned}
\Delta t_{n+1} = \frac{1}{3}\Bigg(& 172a^6_{\max} + 192a^5_{\max}a_{\min} + 276a^4_{\max}a^2_{\min} + 448a^3_{\max}a^3_{\min} \\
& + 276a^4_{\min}a^2_{\max} + 192a_{\max}a^5_{\min} + 172a^6_{\min} \\
& + 36\Big(29a^6_{\max} + 30a^5_{\max}a_{\min} + 51a^4_{\max}a^2_{\min} + 68a^3_{\max}a^3_{\min} + 51a^4_{\min}a^2_{\max} \\
& \qquad + 30a_{\max}a^5_{\min} + 29a^6_{\min}\Big)^{1/2} a^3_{\max} \\
& + 36\Big(29a^6_{\max} + 30a^5_{\max}a_{\min} + 51a^4_{\max}a^2_{\min} + 68a^3_{\max}a^3_{\min} + 51a^4_{\min}a^2_{\max} \\
& \qquad + 30a_{\max}a^5_{\min} + 29a^6_{\min}\Big)^{1/2} a_{\min}a^2_{\max} \\
& + 36\Big(29a^6_{\max} + 30a^5_{\max} + 51a^4_{\max}a^2_{\min} + 68a^3_{\max}a^3_{\min} + 51a^4_{\min}a^2_{\max} \\
& \qquad + 30a_{\max}a^5_{\min} + 29a^6_{\min}\Big)^{1/2} a_{\max}a^2_{\min} \\
& + 36\Big(29a^6_{\max} + 30a^5_{\max}a_{\min} + 51a^4_{\max}a^2_{\min} + 68a^3_{\max}a^3_{\min} + 51a^4_{\min}a^2_{\max} \\
& \qquad + 30a_{\max}a^5_{\min} + 29a^6_{\min}\Big)^{1/2} a^3_{\min}\Bigg)^{1/3} \Big/ \Big(a^3_{\max} + a_{\min}a^2_{\max} + a_{\max}a^2_{\min} + a^3_{\min}\Big) \\
& - \frac{4}{3}\Big(5a^4_{\max} + 10a^3_{\max}a_{\min} + 6a^2_{\max}a^2_{\min} + 10a_{\max}a^3_{\min} + 5a^4_{\min}\Big) \Big/ \\
& \quad \Bigg(\Big(a^3_{\max} + a_{\min}a^2_{\max} + a_{\max}a^2_{\min} + a^3_{\min}\Big) \\
& \qquad \times \Bigg(172a^6_{\max} + 192a^5_{\max}a_{\min} + 276a^4_{\max}a^2_{\min} + 448a^3_{\max}a^3_{\min}
\end{aligned}
$$

$$
\begin{aligned}
&+ 276a_{\min}^4 a_{\max}^2 + 192a_{\max}a_{\min}^5 + 172a_{\min}^6 \\
&+ 36\Big(29a_{\max}^6 + 30a_{\max}^5 a_{\min} + 51a_{\max}^4 a_{\min}^2 + 68a_{\max}^3 a_{\min}^3 + 51a_{\min}^4 a_{\max}^2 \\
&\qquad +30a_{\max}a_{\min}^5 + 29a_{\min}^6\Big)^{1/2} ar^3 \\
&+ 36\Big(29a_{\max}^6 + 30a_{\max}^5 a_{\min} + 51a_{\max}^4 a_{\min}^2 + 68a_{\max}^3 a_{\min}^3 + 51a_{\min}^4 a_{\max}^2 \\
&\qquad +30a_{\max}a_{\min}^5 + 29a_{\min}^6\Big)^{1/2} a_{\min}a_{\max}^2 \\
&+ 36\Big(29a_{\max}^6 + 30a_{\max}^5 a_{\min} + 51a_{\max}^4 a_{\min}^2 + 68a_{\max}^3 a_{\min}^3 + 51a_{\min}^4 a_{\max}^2 \\
&\qquad +30a_{\max}a_{\min}^5 + 29a_{\min}^6\Big)^{1/2} a_{\max}a_{\min}^2 \\
&+ 36\Big(29a_{\max}^6 + 30a_{\max}^5 a_{\min} + 51a_{\max}^4 a_{\min}^2 + 68a_{\max}^3 a_{\min}^3 + 51a_{\min}^4 a_{\max}^2 \\
&\qquad +30a_{\max}a_{\min}^5 + 29a_{\min}^6\Big)^{1/2} a_{\min}^3\Big)^{1/3}\Big) \\
&+ \frac{4}{3}\Big(a_{\max}^2 + a_{\max}a_{\min} + a_{\min}^2\Big)\Big/\Big(a_{\max}^3 + a_{\min}a_{\max}^2 + a_{\max}a_{\min}^2 + a_{\min}^3\Big),
\end{aligned}
\tag{2.39}
$$

and then let $t_{n+1} = t_n + \Delta t_{n+1}$. When an $a_{\max}^n$ is equal to or close to zero, simply choose a reasonable step size for Δt_{n+1}.

Note that the time step for $m = 4$ can be solved by mathematical software such as MAPLE from the following equation:

$$
\sum_{i=1}^{4} \frac{1}{i!}\Big(a_{\max}^i - a_{\min}^i\Big)\Delta t_{n+1}^{i-1} = 0. \tag{2.40}
$$

2.2.1. The "Best" Optimal Step Size and the Time-Dependent Homogeneous Systems

We point out that for those eigenvalues with negative real parts, one may also assume they are enclosed in an ellipse with one of the vertex lying at the origin, that is, $a_{\min}^n = 0$. In this way, only $a_{\max}^n$ are needed in forming optimal time step formulas and time steps Δt_{n+1} in step 4 are switched as

(i) $m = 2$: $\Delta t_{n+1} = 2/a_{\max}^n$,

(ii) $m = 3$: $\Delta t_{n+1} = 2.512745327/a_{\max}^n$,

(iii) $m = 4$: $\Delta t_{n+1} = 2.785293563/a_{\max}^n$,

where $a_{\max}^n$ is defined as before in step 2. We remark that when Δt_{n+1} is specified as above values, $p_m(a, \Delta t)$ is equal to one. The stability condition does not seem to be satisfied. However, this hidden problem is avoidable by requiring Gerschgorin theorem or other

equivalent theorems in step 3 as an estimation for the distribution of real part of eigenvalues. This is because the theorem provides an overestimation for the distribution of negative real part of eigenvalues. As a result, $p_m(a, \Delta t)$ is less than one. Hence, it is safe to use the above time step.

In particular, when the reaction vector is negligible, we can further write the m-stage Runge-kutta method as some equivalent m-stage formulas while the order of accuracy remains invariant. For example, $m = 3$, we have

$$\begin{aligned}
\mathbf{u}_n^{(0)} &= \mathbf{u}_n + \frac{\Delta t_n}{3} J_n \mathbf{u}_n, \\
\mathbf{u}_n^{(1)} &= \mathbf{u}_n + \frac{\Delta t_n}{2} J_n \mathbf{u}_n^{(0)}, \\
\mathbf{u}_{n+1} &= \mathbf{u}_n + \Delta t J_n \mathbf{u}_n^{(1)}.
\end{aligned} \tag{2.41}$$

For $m = 4$,

$$\begin{aligned}
\mathbf{u}_n^{(0)} &= \mathbf{u}_n + \frac{\Delta t_n}{4} J_n \mathbf{u}_n, \\
\mathbf{u}_n^{(1)} &= \mathbf{u}_n + \frac{\Delta t_n}{3} J_n \mathbf{u}_n^{(0)}, \\
\mathbf{u}_n^{(2)} &= \mathbf{u}_n + \frac{\Delta t_n}{2} J_n \mathbf{u}_n^{(1)}, \\
\mathbf{u}_{n+1} &= \mathbf{u}_n + \Delta t_n J_n \mathbf{u}_n^{(2)}.
\end{aligned} \tag{2.42}$$

Of course, J_n is defined according to their stage number.

3. Numerical Examples

3.1. Overview

In this section, we demonstrate the implementation and the efficiency of our optimal adaptive time stepping method by setting a one-dimension testing problem and simulating some problems from a series of real biological experiments. The 1D testing problem with the known analytic solution is used to show the implementation process of our scheme. It is also designed to show the rate of convergence as well as the computational cost. Those results are illustrated through comparison with standard m-stage Runge-Kutta methods and the Runge-Kutta-Fehlberg (RKF) method. To test our numerical methods on real biological experiments, we apply our optimal adaptive two-stage Runge-Kutta method to a two-dimensional reaction-diffusion-chemotaxis model for a series of biological experiments on bacterial chemotaxis reported in [9]. Some results will be shown here.

3.2. Testing Problems

Consider

$$u_t = u_{xx} - (txu)_x + f, \quad x \in (0, 2\pi),\ t > 0, \tag{3.1}$$

where $u = u(x,t)$ and $f = (tx-1)e^{-t}\cos(x-t) + te^{-t}\sin(x-t)$. The three terms on the right-hand side represent diffusion, chemotaxis, and reaction, respectively. Assume the periodic boundary condition: $u(o,t) = u(2\pi,t), t \geq 0$ and the initial condition: $u(x,0) = \sin x$. The analytic solution of (3.1) is

$$u(x,t) = e^{-t}\sin(x-t). \tag{3.2}$$

To apply MOL, we simply use the difference scheme for the spatial discretization. The standard second-order difference is applied to the diffusion term. The upwind scheme is employed in the chemotaxis for some stability consideration [17]. After the discretization, we then apply m-stage Runge-Kutta method with the adaptive optimal time stepping scheme as the time integration strategy. By denoting $h = 2\pi/N$, $x_i = ih$, $i = 0, 1, \ldots, N$, and the numerical solution as u_i, the resulting ODE system is

$$\frac{d\mathbf{u}}{dt} = M(t)\mathbf{u} + \mathbf{f}(\mathbf{t}), \tag{3.3}$$

where

$$\mathbf{u} = (u_0, u_1, \ldots, u_N)^T,$$

$$\mathbf{f}(\mathbf{t}) = \left(f(x_0,t), f(x_1,t), \ldots, f(x_N,t)\right)^T,$$

$$M(t_n) = \begin{pmatrix} \frac{-2}{h^2} - \frac{x_0 t_{n-1}}{h} & \frac{1}{h^2} & & & & \frac{1}{h^2} - t_{n-1} & 0 \\ \frac{1}{h^2} + \frac{x_0 t_{n-1}}{h} & \frac{-2}{h^2} - \frac{x_1 t_{n-1}}{h} & \frac{1}{h^2} & & & 0 & 0 \\ & \frac{1}{h^2} + \frac{x_1 t_{n-1}}{h} & \frac{-2}{h^2} - \frac{x_2 t_{n-1}}{h} & \frac{1}{h^2} & & 0 & 0 \\ & \ddots & \ddots & \ddots & & & \\ & & \ddots & \ddots & \ddots & & \\ & & & \ddots & \ddots & \ddots & \\ 0 & \frac{1}{h^2} & & & 0 & \frac{1}{h^2} + \frac{x_{N-1} t_{n-1}}{h} & \frac{-2}{h^2} - \frac{x_N t_{n-1}}{h} \end{pmatrix}. \tag{3.4}$$

Generally, the actual eigenvalues of the spatial matrix $M(t)$ are not available. One may use the power method and the inverse power method [20] to estimate the largest and smallest magnitude of eigenvalues. But these methods are usually time consuming. Moreover, only negative real parts of the eigenvalues are needed for our scheme. Therefore, we suggest using Gerschgorin theorem to estimate the distribution of eigenvalues. As we should show immediately, it is a simple and inexpensive way to find the range for real parts of the eigenvalues. It is therefore adequate for implementing our scheme. In fact, if a formula for the distribution of eigenvalues or actual eigenvalues can be found ahead of time, then it is not necessary to use the theorem to estimate the range at each time step. A simple version of the Gerschgorin theorem is stated as follows.

Theorem 3.1 (Gerschgorin). *The union of all discs*

$$K_i := \left\{ \mu \in \left| \mu - a_{ii} \right| \leq \sum_{k=1,\, k \neq i}^{n} |a_{ik}| \right\} \tag{3.5}$$

contains all eigenvalues of the $n \times n$ matrix $A = [a_{ik}]$.

The theorem states that if A is a real matrix, the range of the real parts of the eigenvalues can be easily detected by checking the intersection intervals of these discs with the real axis.

From Gerschgorin Theorem, we obtain

$$-a_{\max} \leq \mathrm{Re}(\lambda) < 0, \tag{3.6}$$

where

$$a_{\max} = \frac{4}{\Delta x^2} + t_n\left(\frac{4\pi}{\Delta x} + 1\right). \tag{3.7}$$

Thus, for m-stages, where $m = 2, \ldots, 4$, the optimal time steps at the current step are

$$\begin{aligned} m = 2\colon\ \Delta t_{\mathrm{opt}} &= \frac{2}{(4/\Delta x^2) + t_n((4\pi/\Delta x) + 1)}, \\ m = 3\colon\ \Delta t_{\mathrm{opt}} &= \frac{2.512745327}{(4/\Delta x^2) + t_n((4\pi/\Delta x) + 1)}, \\ m = 4\colon\ \Delta t_{\mathrm{opt}} &= \frac{2.785293563}{(4/\Delta x^2) + t_n((4\pi/\Delta x) + 1)}. \end{aligned} \tag{3.8}$$

Figure 3 shows the relative error between the numerical and the analytic solutions. Observe that the relative error for the standard two-stage Runge-Kutta method increases dramatically around $t = 5.2$, but the optimal time-stepping m-stage Runge-Kutta methods still converge to the analytic solution.

Tables 1, 2, and 3 demonstrate the number of iteration for our scheme (Optimal m-stage RK) with that of two other methods: standard m-stage Runge-Kutta method with fixed

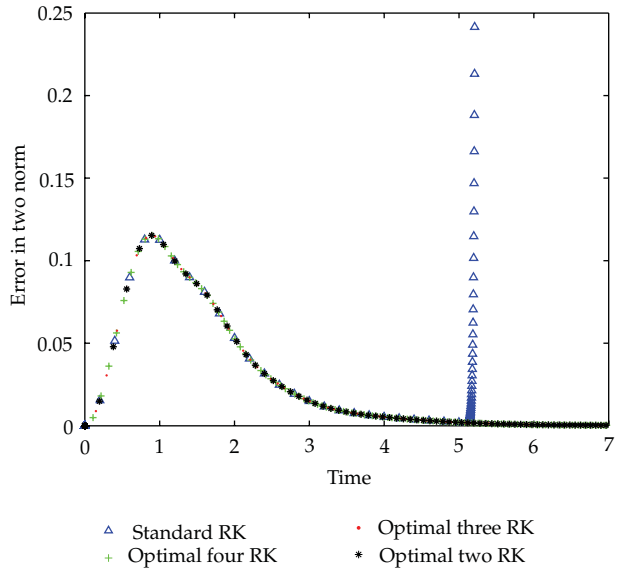

Figure 3: Relative error between numerical simulations and the analytic solution.

Table 1: Comparison for number of iterations among optimal two-stage RK, RKF 23, and standard two-stage RK. The optimal two-stage RK method is counted twice for the function evaluation per iteration, while the RKF 23 is counted four times per iteration. "Div" is the abbreviation for Divergent.

Method/Time	1	2	3	4	5
Optimal two-stage RK	638	1278	1918	2558	3200
RKF 23	1175	2765	4310	6075	8250
Std two-stage RK ($\Delta t = 0.0025$)	800	1600	2400	Div	Div

Table 2: Comparison for number of iterations among the optimal three-stage RK, RKF 34, and standard three-stage RK. The optimal three-stage RK method is counted three times for the function evaluation per iteration, while the RKF 34 is five times per iteration.

Method/Time	1	2	3	4	5
Optimal three-stage RK	678	1524	2535	3717	5067
RKF 34	3925	6325	7935	9655	11570
Std three-stage RK ($\Delta t = 0.003$)	1002	2001	3000	Div	Div

step size (Std m-stage RK) and the Runge-Kutta-Fehlberg methods (RKF). These tables basically indicate that while the optimal time stepping scheme always ensure convergence, the standard m-stage Runge-Kutta methods or other adaptive methods like RKF either diverge or converge slower since they require a larger number of iterations. Similar results can also be illustrated by calculating CPU time following from Tables 4, 5, and 6. The computations were done on Dell Latitude D620 2600.

Tables 4–6 illustrate the computational efficiency for our method with CPU time.

3.3. *Further Discussion on the Efficiency of the Optimal RK Method*

We continue our discussion about the computational efficiency for optimal RK methods with time steps mentioned in Sections 2.2. We are interested in measuring the efficiency difference

Table 3: Comparison for number of iterations among the optimal four-stage RK, RKF 45, and standard four-stage RK. The optimal four-stage RK method is counted four times for the function evaluation per iteration while the RKF 45 is six times per iteration.

Method/Time	1	2	3	4	5
Optimal four-stage RK	816	1832	3052	4472	6096
RKF 45	3480	5598	7152	8910	10866
Std four-stage RK ($\Delta t = 0.004$)	1000	2000	Div	Div	Div

Table 4: Comparison of CPU time among the optimal two-stage RK, RKF 23, and standard two-stage RK with $\Delta t = 0.001$.

CPU/Time	10	20	30	40	50
Optimal two-stage RK	0.5940	1.8430	3.7960	6.4690	9.7820
RKF 23	1.3910	3.9060	7.4530	12.0620	17.6090
Std two-stage RK	0.9840	3.5310	Div	Div	Div

Table 5: Comparison of CPU time among the optimal three-stage RK, RKF 34, and standard three-stage RK with $\Delta t = 0.0005$ and $\Delta t = 0.001$, respectively.

CPU/Time	10	20	30	40	50
Optimal three-stage RK	0.8910	2.8280	5.7970	9.7970	15.0000
RKF 34	1.7190	4.5150	8.5630	13.6880	20.0780
Std three-stage RK	3.1710	6.6410	11.0630	13.1250	19.2340
Std three-stage RK	1.6880	3.310	Div	Div	Div

Table 6: Comparison of CPU time among the optimal four-stage RK, RKF 45, and standard four-stage RK with $\Delta t = 0.001$.

CPU/Time	10	20	30	40	50
Optimal four-stage RK	1.0000	3.2030	6.5780	11.1560	16.9530
RKF 45	1.8750	5.0000	9.5000	15.3280	23.6410
Std four-stage RK	2.2660	4.6250	Div	Div	Div

between RKF and our method. To make one's point, we take the optimal four-stage RK method as an example. Let us start with the "best" optimal step size as in Section 2.2.1. Then the current time step for the optimal four-stage RK is

$$\Delta t = \frac{2.785293563}{a_{\max}}. \tag{3.9}$$

To get the "worst" case, set $a_{\max} = a_{\min}$. Then

$$\Delta t = \frac{1.596071638}{a_{\max}}. \tag{3.10}$$

Now, let us assign Δt to be the average of (3.9) and (3.10). We obtain

$$\Delta t = \frac{2.1906826005}{a_{\max}}. \tag{3.11}$$

Table 7: Comparison of CPU time between the optimal four-stage RK with the average time step of the "best" and the "worst" cases, and the RKF 45.

CPU/Time	10	20	30	40	50
Optimal four-stage RK	1.0000	3.2030	6.5780	11.1560	16.9530
Four-stage RK Δt = (3.11)	1.2660	4.0470	8.3600	14.2190	21.5160
RKF 45	1.8750	5.0000	9.5000	15.3280	23.6410

Table 7 shows that even with the "medium" optimal time step (3.11), our numerical scheme still performs better than the RKF 45. In addition, the computational efficiency of RKF 45 is approximately equal to the optimal four-stage RK when the time step is chosen as (3.11).

3.4. Computer Simulations of Chemotaxis in Bacteria

Our numerical experiment is based on the biological experiments reported in (2.28) and the corresponding mathematical model given in (2.28). Interesting patterns are developed when *Escherichia coli* or *Salmonella typhimurium* is incoulated on intermediates of the tricarboxylic acid (TCA) cycle. Bacteria form symmetrical rings of spots or strips if they are inoculated in semisolid agar on the intermediates of TCA cycle. When placed in a liquid medium and fed on intermediates of the TCA cycle, they secrete aspartate as a chemoattractant. Cells then arrange themselves into high density aggregates. In this case, aggregates form randomly as time evolves and fade in a time interval less than the bacteria generation. Here, attractant chemicals are excreted by the bacterial themselves instead of being added into the Petri dish artificially.

A nondimensionalized mathematical models were proposed in (2.28) for the liquid medium experiments in (2.28). The model is a classical chemotaxis system, which reads as

$$\begin{aligned} \frac{\partial u}{\partial t} &= \nabla \cdot \left(D_u \nabla u - \frac{\alpha u}{(1+v)^2} \nabla v \right), \\ \frac{\partial v}{\partial t} &= \Delta v + \omega \frac{u^2}{\mu + u^2}, \end{aligned} \tag{3.12}$$

where u, v, and ω represent cell density, concentration of chemotactic substance, and succinate, respectively. Simulations were done with zero flux boundary condition for both u and v. Initial conditions are set to be zero for v and the random perturbation at $u_0 = 1$ for the initial condition of u. The noise amplitude is of order 10^{-1}. They were created by the C^{++} random number generator. The initial, boundary conditions for u and v, and the noise amplitude are chosen to be the same as described in (2.28) except for the random numbers which may not be identical due to the use of different softwares.

Numerical simulations are showed in Figure 4. Simulations did capture the characteristics as described in (2.28) qualitatively. The aggregates first are divided into small regions and then cojoin with others.

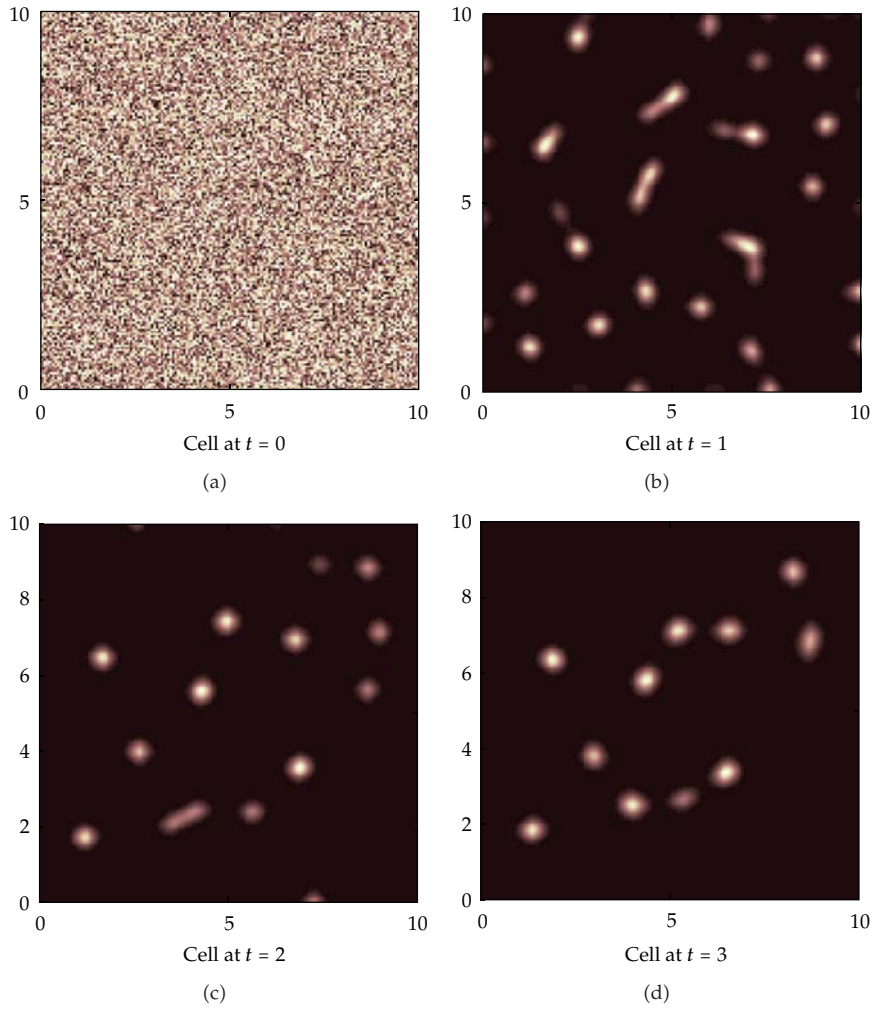

Figure 4: Numerical simulations for bacterial aggregates they exposed to TCA cycle: from left to right, top to bottom. The aggregates are separated into small regions and then cojoin other aggregates. The aggregates become fewer but larger.

4. Conclusions and Discussions

We investigate an optimal adaptive time stepping strategy for fully explicit m-stage Runge-Kutta methods to solve general reaction-diffusion-chemotaxis systems. It is designed specially for handling spatially nonhomogeneous pattern formations. The method is based on m-stage Runge-Kutta methods and simple estimation on the optimal step size at each iteration. With some optimization techniques, we efficiently discard the decay modes and only allow the growth modes to grow. In this way, we guarantee that the numerically generated patterns follow the primary model equations. The scheme is proven to be extremely robust and accurate by theoretical analysis, numerical experiments on the testing problem, and real pattern simulations on bacterial chemotaxis. The numerical experiments also show that our method is superior to RKF in solving reaction-diffusion-chemotaxis systems.

Acknowledgment

This work was supported by National Science Council under Grant no. NSC 97-2115-M-126-003 in Taiwan.

References

[1] E. Keller and L. Segel, "Model for chemotaxis," *Journal of Theoretical Biology*, vol. 30, pp. 225–234, 1971.
[2] D. Lauffenburger, C. Kennedy, and R. Aris, "Traveling bands of chemotactic bacteria in the context of population growth," *Bulletin of Mathematical Biology*, vol. 46, pp. 19–40, 1984.
[3] E. O. Budrene and H. C. Berg, "Complex patterns formed by motile cells of Escherichia Coli," *Nature*, vol. 349, no. 6310, pp. 603–633, 1991.
[4] C. Chiu and F. C. Hoppensteadt, "Mathematical models and simulations of bacterial growth and chemotaxis in a diffusion gradient chamber," *Journal of Mathematical Biology*, vol. 42, no. 2, pp. 120–144, 2001.
[5] C. Chiu and J. L. Yu, "An optimal adaptive time-stepping scheme for solving reaction-diffusion-chemotaxis systems," *Mathematical Biosciences and Engineering*, vol. 4, no. 2, pp. 187–203, 2007.
[6] E. Ben-Jacob, I. Cohen, I. Golding, and Y. Kozlovsky, "Modeling branching and chiral colonial patterning of lubricating bacteria," in *Mathematical Models for Biological Pattern Formation*, K. M. Philip and G. O. Hans, Eds., vol. 121 of *The IMA Volumes in Mathematics and Its Applications*, pp. 211–253, Springer, New York, NY, USA, 2001.
[7] R. Tyson, S. R. Lubkin, and J. D. Murray, "Model and analysis of chemotactic bacterial patterns in a liquid medium," *Journal of Mathematical Biology*, vol. 38, no. 4, pp. 359–375, 1999.
[8] J. Yu, *A fully explicit optimal two-stage numerical scheme for solving reaction-diffusion-chemotaxis systems*, Ph.D. thesis, Michigan State University, 2005.
[9] J. Adler, "Chemotaxis in bacteria," *Science, New Series*, vol. 153, no. 3737, pp. 708–716, 1966.
[10] E. O. Budriené, A. A. Polezhaev, and M. O. Ptitsyn, "Mathematical modelling of intercellular regulation causing the formation of spatial structures in bacterial colonies," *Journal of Theoretical Biology*, vol. 135, no. 3, pp. 323–341, 1988.
[11] J. D. Murray, *Mathematical Biology*, vol. 19 of *Biomathematics*, Springer, Berlin, Germany, 3rd edition, 1993.
[12] P. C. Fife, *Mathematical Aspects of Reacting and Diffusing Systems*, vol. 28 of *Lecture Notes in Biomathematics*, Springer, Berlin, Germany, 1979.
[13] J. Smoller, *Shock Waves and Reaction-Diffusion Equations*, vol. 258 of *Grundlehren der Mathematischen Wissenschaften*, Springer, New York, NY, USA, 1983.
[14] R. Tyson, L. G. Stern, and R. J. LeVeque, "Fractional step methods applied to a chemotaxis model," *Journal of Mathematical Biology*, vol. 41, no. 5, pp. 455–475, 2000.
[15] C. Chiu, F. C. Hoppensteadt, and W. Jäger, "Analysis and computer simulation of accretion patterns in bacterial cultures," *Journal of Mathematical Biology*, vol. 32, pp. 841–855, 1994.
[16] C. Chiu and N. Walkington, "An ADI method for hysteretic reaction-diffusion systems," *Society for Industrial and Applied Mathematics Journal on Numerical Analysis*, vol. 34, no. 3, pp. 1185–1206, 1997.
[17] J. C. Strikwerda, *Finite Difference Schemes and Partial Differential Equations*, Wadsworth & Brooks/Cole Advanced Books & Software, Pacific Grove, Calif, USA, 1989.
[18] G. W. Gear, *Numerical Initial Value Problems in Ordinary Differential Equations*, Prentice-Hall, Englewood Cliffs, NJ, USA, 1971.
[19] K. E. Atkinson, *An Introduction to Numerical Analysis*, John Wiley & Sons, New York, NY, USA, 2nd edition, 1989.
[20] J. Stoer and R. Bulirsch, *Introduction to Numerical Analysis*, Springer, New York, NY, USA, 2nd edition, 1992.

Hindawi Publishing Corporation
Journal of Applied Mathematics
Volume 2011, Article ID 970467, 23 pages
doi:10.1155/2011/970467

Research Article

Numerical Study of the Effect of a Power Plant Cooling Water Discharge in the Montevideo Bay

Mónica Fossati, Pablo Santoro, Santiago Urrestarazu, and Ismael Piedra-Cueva

Institute of Fluid Mechanics and Environmental Engineering, School of Engineering, Universidad de la Republica, J. Herrera y Reissig 565, Montevideo, Uruguay

Correspondence should be addressed to Mónica Fossati, mfossati@fing.edu.uy

Received 30 December 2010; Accepted 21 February 2011

Academic Editor: Jürgen Geiser

Copyright © 2011 Mónica Fossati et al. This is an open access article distributed under the Creative Commons Attribution License, which permits unrestricted use, distribution, and reproduction in any medium, provided the original work is properly cited.

The numerical simulation of the water temperature in the Río de la Plata River and Montevideo's Bay was done using the numerical model of finite elements RMA-10 in its 2D vertical integrated mode. Parameters involved in the formulations of thermal exchange with the atmosphere were adjusted using measurements of water temperature in several locations of the water body. After calibrating the model, it was used to represent the operation of a power plant located in Montevideo's Bay. This central takes water from the bay in order to cool its generators and also discharges high-temperature water into the bay. The correct representation of temperatures at the water intake and discharge of the plant reflects that the model is able to represent the operation of the central. Several analysis were made to study the thermal plume, the effects of the water discharge on the water intake of the power plant, and the effect on environmental variables of the study area like currents.

1. Introduction

The National Electric Power Company (UTE) has a thermal power plant in the city of Montevideo, located on the Montevideo Bay (Figure 1), called Central Batlle. This power plant takes water from the Montevideo Bay and discharges into the bay again after using it to cool the condensers of the plant. More precisely, the discharge point is located inside the Montevideo Port.

Currents in the Montevideo Bay are primarily induced by winds of various speeds and directions, which are highly variable in time, by tides, and, to a lesser degree, by the salinity wedge in the navigation channel.

The far-field water temperature is primarily affected by air temperature and solar radiation. Winds affect also its spatial variation. In the near-field, the thermal plume at the channel outlet is affected primarily by the exit water temperature and flow rate. The outlet

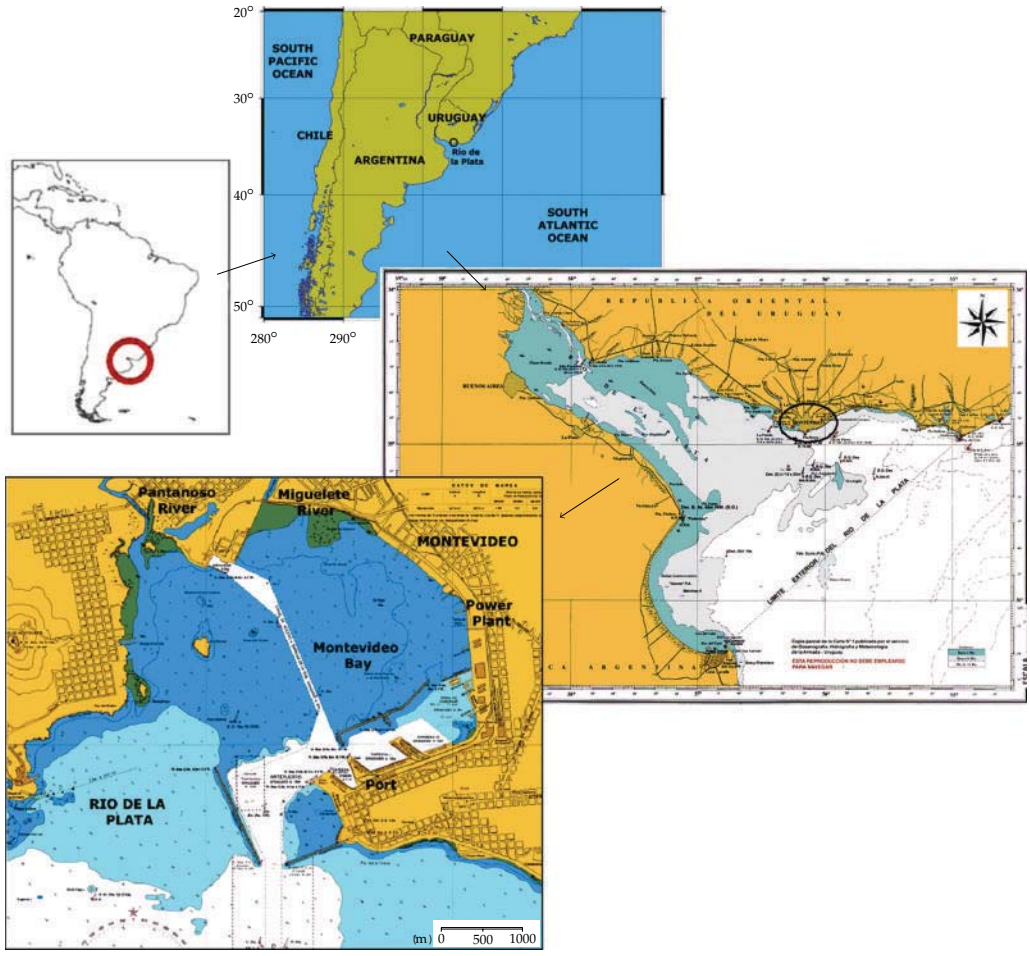

Figure 1: Study area location.

water has a temperature of 11°C–14°C above the far-field water temperature, depending on the season. Both the flow and temperature difference between the water intake and discharge of the power plant modify the flow pattern in both areas and, therefore, affect the currents and temperature fields.

Numerical models are simplified mathematical representations of physical systems and processes. A numerical model can be constructed as a one-, two-, or three-dimensional model in accordance with the dominant spatial directions of the physical processes [1–3]. In this study, a three-dimensional model for the entire water body would be computationally challenging. It was found that a two-dimensional model for the entire water body would resolve properly the horizontal variation of water temperature in the near and far field area.

A dynamic model is used to take into account antecedent conditions for currents and temperature. Both of these parameters are affected by long-term physical processes such as wind speed, direction, and heat input. The main mechanism for the formation of the temperature field around the heated effluents is its mixing with the ambient water or, in other words, dilution.

The research on discharge of cooling water from power plants into water bodies has been of interest for many years [4–7]. It is not only of great theoretical importance to the study of the transfer and movement of thermal discharge water, but also of great economic value. Without proper management methods, the thermal wastes would probably do great harm to the ecological health of the surrounding water regions.

Therefore, a numerical model has been developed for the Montevideo Bay to study the changes in the currents and temperature field due to the intake and discharge of cooling water and to identify if the temperature of the water intake is to some extend affected by the discharge of heated water in the harbor.

2. Study Area

Uruguay is located in the east coast of South America between Argentina and Brazil. It has an area of 176,215 km^2 and 3.46 million inhabitants. Most of its political limits are water bodies including rivers, estuaries, lakes, and the Atlantic Ocean. To the southwest, in the limit with Argentina, lies the Río de la Plata. This water body is located between 34° 00′–36° 10′ South latitude and 55° 00′–58° 10′ West longitude and has the second largest basin of South America (3.170.000 km^2) after the Amazonic one (Figure 1). The Paraná and Uruguay rivers provide more than 97% of the continental water inlet with an annual mean flow of 22.000 m^3/s. Other minor rivers and streams discharge along both coastal shores of the Rio de la Plata. The fresh water mixes with the oceanic water creating a zone of brackish waters in the Rio de la Plata that behaves as a microtidal estuary. The flow dynamic in the Rio de la Plata and the Maritime Front is very complex due to the topographic variation of the river and the influence of continental flows, astronomical and meteorological tides coming from the ocean, and the local winds. River level variations produced by astronomical tides are lower than those generated by the wind and oceanic waves.

Montevideo is located on the central zone of the Rio de la Plata, where the salinity shows significant fluctuations as a function of the seasons, fresh water flow, and tides. The coastal zone of Montevideo includes several beaches, hard points, a big bay (Montevideo's Bay), and navigation channels. Montevideo Bay is a big enclosed water body and covers an area of around 12 km^2. Water depth reaches 5 m in the outer part of the bay, but the average depth is between 1 m to 1.5 m in the inner part. Navigation channels are around 11 m deep. The bay receives municipal effluents and two polluted streams, Pantanoso and Miguelete, where multiple industries discharge. Moreover, a large thermoelectric power station and the major petroleum refinery are located next to the bay.

3. Existing Power Plant and Operation

Built in 1930, the power station consists of different units that are run according to energy demand. The first unit to go into operation is called sixth unit and can generate a maximum power of 125 MW. When this unit is not sufficient to meet the demand, the fifth unit, whose generating capacity reaches 80 MW, is turned on. Sometimes this sequence of operation is reversed; the 5th is dispatched first and then the 6th if necessary. Units 5 and 6 have been operational since 1970 and 1976, respectively.

A continuous flow of cooling fresh water is required to absorb heat from the steam turbine condenser. The flow intake and discharge of the power plant depends on the operating schedule, that is, units that are running. The 5th unit requires a cooling flow of 3.9 m^3/s,

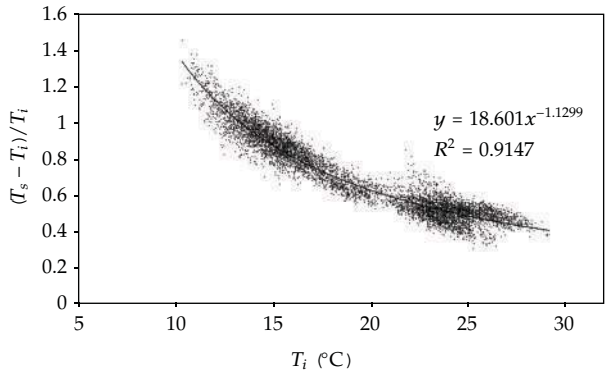

Figure 2: Input and output temperature fit equation for the units 5 and 6 working together from data between September 2003 and March 2007.

while the 6th unit has a higher flow rate, equal to 4.4 m^3/s. The discharge point is located about 600 m south from the water intake inside the dock of Montevideo Port.

Submerged multiport diffusers are generally thought to be the most effective means for handling the rapid initial dilution of thermal discharges, since heated water is discharged from many spaced ports at high velocity, forming a turbulent jet into the receiving water body (see, e.g., [4]). However, Central Batlle power station discharges in the Montevideo Port through a single open channel with low initial mixing. The water depth at the discharge point is about 6 m.

The power plant administration has been automatically monitoring the temperature of water in the intake and discharge zone continuously since 2003 with a time frequency of 30 minutes, including periods when the plant is turned off. The analysis of temperature data recorded at the intake and discharge of the power plant shows a behavior captured by (3.1). The higher the temperature of the cooling water, the greater the thermal output to the bay for a given flow rate. The rated thermal loading of the condenser unit represents the average heat output of the condenser unit

$$T_o - T_i = A \times T_i^B, \tag{3.1}$$

where T_o = output temperature of power plant, T_i = input temperature of power plant, and A and B are parameters.

Data from the period September 2003 to March 2007 were selected to adjust the tuning parameters of (3.1) for the different operation schemes of the plant.

For the case where the two units (5th and 6th) are dispatched together, (3.1) was adjusted considering as inlet and outlet temperature the average of each unit input and outlet temperature, respectively.

The result is a set of parameters A and B as a function of the diagram of operation of the plant, the 5th unit operating alone, the 6th unit operating alone, and both units working together, which are presented in Table 1 together with the R^2 parameter. Figure 2 shows an example of the adjustment of the temperature data for the diagram of operation of both units. Note the good quality of the fit obtained in all cases.

Table 1: Coefficients A and B for the inlet and outlet temperature power plan formulation for the three operating schemes.

Operating scheme	Coefficient A	Coefficient B	Fit (R^2)
5th Unit	14,9630	−0,0540	0,7223
6th Unit	6,5187	0,2171	0,7479
5th and 6th Unit	18,6010	−0,1299	0,9147

4. Materials and Methods

A good description of topographic variations and coastline is needed to simulate the hydrodynamic details of the Montevideo Bay. Moreover, due to the complex flow distribution along the bay mouth, the simulation of the flow around the Río de la Plata and Maritime front is also required to properly represent the hydrodynamic in the bay. Therefore, the domain of calculation covers from the mouths of major tributaries, the Paraná and Uruguay rivers in its western border, to the continental shelf in the Atlantic Ocean.

The finite element model RMA-10 [8], which was designed to analyze systems using the 3D shallow water equations, is applied. The model is capable of couple the spatial density variations induced by salinity and temperature gradients to the hydrodynamic calculations. This enables the model to simulate phenomena such as saline wedges and thermal plumes. RMA-10 has been previously applied to this kind of studies; see, for instance, Golder Associates, 2001 [9].

Because of the very shallow depth of the bay, no stratification can develop, and the system can be regarded as well mixed. RMA-10 was used in a vertical averaged mode but keeping the coupling between salinity and temperature gradients to the velocities in order to model the velocity and temperature fields. Considering the limitations implied by the depth averaging in the deeper part of the outer region of the Rio de la Plata, the results in that area must be analyzed carefully.

4.1. Model Description

The model resolves the set of equations derived from a combination of Reynolds form of the Navier-Stokes equations, the volume continuity equation, the advection diffusion equation for salinity or temperature transport, and an equation of state relating water density to salinity or temperature. In Cartesian coordinates, the governing equations are the following:

The momentum equations

$$\rho\cdot\left(\frac{\partial u}{\partial t}+u\frac{\partial u}{\partial x}+v\frac{\partial u}{\partial y}+w\frac{\partial u}{\partial z}\right)-\frac{\partial}{\partial x}\left(\varepsilon_{xx}\frac{\partial u}{\partial x}\right)-\frac{\partial}{\partial y}\left(\varepsilon_{xy}\frac{\partial u}{\partial y}\right)-\frac{\partial}{\partial z}\left(\varepsilon_{xz}\frac{\partial u}{\partial z}\right)+\frac{\partial p}{\partial x}-\Gamma_x=0,$$

$$\rho\cdot\left(\frac{\partial v}{\partial t}+u\frac{\partial v}{\partial x}+v\frac{\partial v}{\partial y}+w\frac{\partial v}{\partial z}\right)-\frac{\partial}{\partial x}\left(\varepsilon_{yx}\frac{\partial v}{\partial x}\right)-\frac{\partial}{\partial y}\left(\varepsilon_{yy}\frac{\partial v}{\partial y}\right)-\frac{\partial}{\partial z}\left(\varepsilon_{yz}\frac{\partial v}{\partial z}\right)+\frac{\partial p}{\partial y}-\Gamma_y=0,$$

$$\rho\cdot\left(\frac{\partial w}{\partial t}+u\frac{\partial w}{\partial x}+v\frac{\partial w}{\partial y}+w\frac{\partial w}{\partial z}\right)-\frac{\partial}{\partial x}\left(\varepsilon_{zx}\frac{\partial w}{\partial x}\right)-\frac{\partial}{\partial y}\left(\varepsilon_{zy}\frac{\partial w}{\partial y}\right)$$
$$-\frac{\partial}{\partial z}\left(\varepsilon_{zz}\frac{\partial w}{\partial z}\right)+\frac{\partial p}{\partial z}+\rho\cdot g-\Gamma_z=0, \tag{4.1}$$

the continuity equation

$$\frac{\partial u}{\partial x} + \frac{\partial v}{\partial y} + \frac{\partial w}{\partial z} = 0, \tag{4.2}$$

the advection diffusion equation

$$\begin{aligned}
&\frac{\partial s}{\partial t} + u\frac{\partial s}{\partial x} + v\frac{\partial s}{\partial y} + w\frac{\partial s}{\partial z} - \frac{\partial}{\partial x}\left(D_x\frac{\partial s}{\partial x}\right) - \frac{\partial}{\partial y}\left(D_y\frac{\partial s}{\partial y}\right) - \frac{\partial}{\partial z}\left(D_z\frac{\partial s}{\partial z}\right) - \theta_s = 0,\\
&\frac{\partial T}{\partial t} + u\frac{\partial T}{\partial x} + v\frac{\partial T}{\partial y} + w\frac{\partial T}{\partial z} - \frac{\partial}{\partial x}\left(D_x\frac{\partial T}{\partial x}\right) - \frac{\partial}{\partial y}\left(D_y\frac{\partial T}{\partial y}\right) - \frac{\partial}{\partial z}\left(D_z\frac{\partial T}{\partial z}\right) - \theta_T = 0,
\end{aligned} \tag{4.3}$$

and the equation of state

$$\rho = F(s, T), \tag{4.4}$$

where x, y, z = the Cartesian coordinate system, u, v, w = velocities in the Cartesian directions, t = time, p = water pressure, D_x, D_y, D_z = the eddy diffusion coefficients, $\varepsilon_{xx}, \varepsilon_{xy}, \varepsilon_{xz}, \varepsilon_{yx}, \varepsilon_{yy}, \varepsilon_{yz}, \varepsilon_{zx}, \varepsilon_{zy}, \varepsilon_{zz}$ = the turbulent eddy coefficients, g = the acceleration due to gravity, ρ = water density, $\Gamma_x, \Gamma_y, \Gamma_z$ = the external forces components, s = salinity, T = temperature, and θ_s, θ_T = the source/sink for salinity/temperature.

The basic equations, with appropriate boundary and initial conditions, are integrated numerically using the finite elements method. The vertical component of the momentum equation is simplified following the hydrostatic approximation, and thus its vertical integration determines the pressure field, and, in turn, the horizontal pressure gradients which are substituted in the horizontal components of the momentum equation. A horizontal turbulence-closure scheme is used to dynamically set eddy viscosity terms in the momentum equations and horizontal diffusion coefficients in the transport equations. The Smagorinsky method of describing horizontal eddy-viscosity and diffusivity coefficients uses mesh-element velocity gradients and areas in a generalization of a mixing-length representation for these terms. The model also maintains a heat budget for every element, which accounts for heat inputs and losses. This heat budget incorporates net short-wave input, long-wave radiation, long-wave back radiation, evaporation, and conduction with the atmosphere. A more detailed model description can be found in [10, 11].

To simulate the temperature distribution, it is necessary to consider heat exchange through the water surface. This exchange includes both radiation transfer and diffusive processes. The upper surface boundary condition is formulated in relation to the heat flux through it. RMA-10 states this condition according to the following formulation:

$$Q = K(T_s - T_{\text{eq}}), \tag{4.5}$$

where Q = heat flux (KJ/m^{2}hr), K = coefficient of heat transfer (KJ/m^{2}hr°C), T_s = water surface temperature (°C), and T_{eq} = equilibrium temperature (°C). The equilibrium

temperature and the coefficient of heat transfer (BTU/ft^{2}día°F) are given by the following expressions:

$$T_{\text{eqf}} = \frac{Q_{\text{sn}}}{23 + f(W) \times (\beta + 0.255)} + T_d,$$
$$K = 23 + (\beta_W + 0.255) \times 17 \times W_2, \tag{4.6}$$

where T_{eqf} = equilibrium temperature (°F), Q_{sn} = short wave net solar radiation (BTU/ft^{2}día), T_d = dew point temperature (°F), $f(W)$ = empirical function of wind velocity (BTU/ft^{2}day mmHg) ($f(W) = 17 \cdot W^2$), $W_2 = 2$ meter wind velocity, and β = function of temperature (mmHg/°F)

$$\beta = 0.255 - 0.0085T_m + 0.000204T_m^2,$$
$$T_m = 0.5 \times (T_s + T_d), \tag{4.7}$$
$$\beta_W = 0.255 - 0.0085T_s + 0.000204T_s^2.$$

4.2. Implementation of the Model

Figure 3(up-left) shows the horizontal configuration of the finite element mesh used, and Figure 3(up-right) shows a mesh detail in Montevideo Bay. It was structured on the basis of an east-west and north-south coordinate system. The figure shows the triangular finite elements mesh. Mesh size depends on the accuracy required in the different parts of the domain. In total, there are 7,462 elements and 15,526 nodes, with element side sizes ranging from 10 km in the ocean boundary up to 50 m within the bay.

The bathymetry of the domain was constructed from mapping information from nautical charts of the Rio de la Plata and the continental shelf. Figure 3(down) shows the detail of the bathymetry of the Montevideo Bay. It clearly shows the deepest parts corresponding to the Port, the La Teja channel, and the breakwaters.

Simulations were made considering the temporal variability of the river discharge, tides, and winds. Water surface elevation is prescribed at the open boundary condition. The input flow is separated in two sections, one for the discharge of both Uruguay and Paraná Guazú rivers and the second one for the discharge of Paraná-Las Palmas river. Daily data from the Argentine Water Institute (INA) was used as well as wind speed and wind direction recorded at Punta Brava station. A constant value of 35 ppt is specified for salinity at the ocean boundary, and a constant water temperature of 20°C was applied in both water boundaries, river and ocean. Flow contribution from the Miguelete and Pantanoso streams were also considered through the specification of the mean averaged values, 0.54 m^3/s for Pantanoso and 1.593 m^3/s for Miguelete.

In addition, the thermal modulus requires information on cooling water inlet and outlet canal flow rates which affect near-field flow circulation conditions: power plant cooling water temperatures in the outlet channel which, in conjunction with the flow rates, determines the amount of discharged heat and near field thermal dispersion, evaporation coefficients (A and B) for the entire water surface area to determine heat loss to the atmosphere, altitude of the cooling water body and cloud cover to compute solar heat input, and dry and wet bulb air temperatures for calculating the heat exchange between

the water surface and the atmosphere. Meteorological time series were obtained from the meteorological station of Punta Brava, operated by the oceanographic, hydrographic, and meteorological service of army (SOHMA).

4.3. Model Calibration

The approach used in this study to calibrate the RMA10 model was to match the simulated results and field measurements as closely as possible to observations by adjusting the parameters requiring calibration within acceptable ranges.

The model calibration procedure is summarized below.

(i) The first step was to adjust the Manning's n values to calibrate the hydrodynamic model together with dispersion coefficient (eddy viscosity) to calibrate the salinity transport.

(ii) The second step was to adjust some constants to calibrate the thermal module for water temperatures in the far field.

(iii) The third step was to calibrate the model of the power plant intake and discharge.

4.3.1. Hydrodynamic Calibration

Simulations were performed to determine water surface elevation, currents, and the salinity field resulting from the interaction of continental river discharge with the tide entering from the ocean, winds, and salinity gradients. The heat exchange with the atmosphere and the thermal field induced by the operation of the power plant were not included at this stage.

Salinity spin-up simulation was conducted from August 2003 to January 2004. The calibration period was February and March 2004, and the validation was done for April 2004. The hydrodynamic calibration was performed comparing model result with hydrodynamic data. For comparison of water surface elevation, hourly records of water surface level at stations of La Paloma, Montevideo, Colonia, and Buenos Aires were used. Comparison of currents was based on measurements of velocity performed at two points off the coast of Montevideo. They were obtained using acoustic current profiler (ADCP). There is no available salinity data during the simulation time. However, salinity was calibrated in former studies [11]. The location of the measuring stations is presented in Figure 4.

4.3.2. Thermal Calibration

The variability of water temperature in the domain was modeled including the interchange with the atmosphere. The following information is required at this step: evaporation coefficients (A and B) to determine heat loss to the atmosphere, cloud cover for calculating solar heat input to the bay, and dry and wet bulb air temperatures to compute the heat exchange with the atmosphere.

Thermal model calibration was performed by adjusting two parameters. One is an atmospheric attenuation factor that represents the atmosphere's capacity to intercept some of the solar radiation that passes through it, and the second parameter is a solar extinction coefficient representing the rate of decrease of the radiation absorbed by the water with increasing depth. These parameters were determined from the comparison of temperature

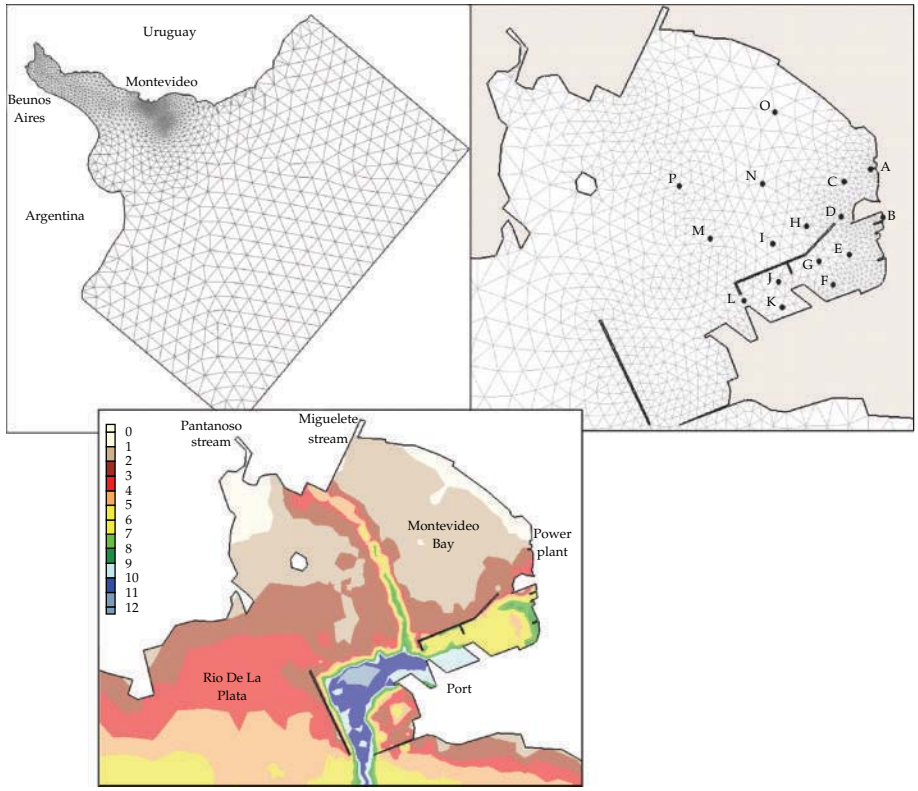

Figure 3: General and detail in Montevideo Bay of the finite element model grid and bathymetry detail in Montevideo Bay.

registered and calculated by the model in two control points, where measurements were available during the simulated period. One set of data corresponds to the data collected twice a day in the meteorological station of Punta Brava, and the second one corresponds to the data collected in the input channel of the power plant in Montevideo Bay. The simulation period, February 1st to March 15th 2004, was purposely selected during a time in which the power plant was not in operation (so that the measured temperature in the bay data is not affected by the power plant). The location of the stations is presented in Figure 4.

After the calibration, a period of 45 days during the winter of 2004 was simulated (July 20th to August 20th, 2004) to assess the ability of the model to represent the temperature field during a period much colder than the one used for calibration. An accurate representation of the observed temperature in the control points during the validation period allowed us to verify the adjustment of the simulated variables.

4.3.3. Power Plant Calibration

Finally, the model was calibrated regarding the power plant income and discharge. The existing conditions in the Montevideo Bay were simulated using actual flow data from the power plant. The flow rate depends on the condenser units and pumps in operation. As we mentioned above, the 5th units requires a flow of $3.9\,m^3/s$, the 6th unit $4.4\,m^3/s$, and both units together a total water flow of $8.3\,m^3/s$.

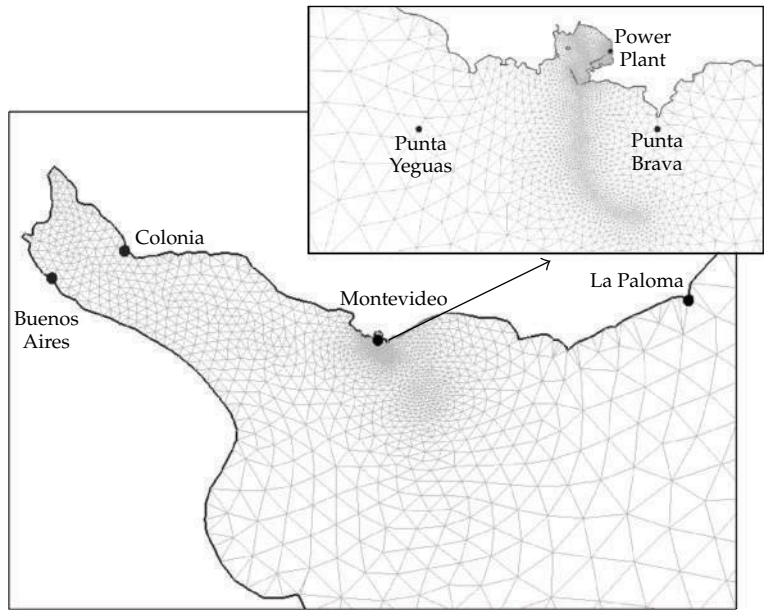

Figure 4: Location of the water surface elevation Rio de la Plata stations (Buenos Aires, Colonia, Montevideo, and La Paloma), ADCP stations (Punta Yeguas and Punta Brava), and temperature stations (Punta Brava and Power Plant).

The RMA-10 model can simulate the cooling water circulation used by a power plant. The model calculates the water temperature of the discharge according to the intake water, the flow, and power of the plant. Nevertheless, as we mentioned above, the data collected in the plant show that the heat exchange in the plant is dependent on the intake water flow and temperature. So, the formulation included in the RMA-10 was substituted by the formulation obtained from the data ((3.1) with parameters presented in Table 1).

The selected calibration period extended from March 19th to July 16th, 2004. During this period, the power plant operated almost continuously although with alternating schemes in terms of units dispatched.

The model was validated with the comparison of the water temperature modeled and measured in the power plant discharge zone. Due to the temperature variation of the bay between warm and cold seasons of the year, time periods representatives of both seasons were simulated.

4.4. Model Applications

Once the model was calibrated and validated, several analyses were made to study the thermal plume, the effects of the water discharge on the water intake of the power plant, and the effect on environmental variables of the study area like currents. The period between March 19th and July 16th, 2004, was simulated. During that period, the power plant worked almost without interruption although with different operating schemes.

In order to evaluate the effect of the power plant cooling water discharge on the environment, simulations were done twice: one with the power plant operating and a second one with the power plant off.

Temperature differences between the simulation with the plant turned on minus the one with the plant turned off (ΔT) were computed to determine the degree of affectation produced by the plant discharge on the temperature in the bay and at the plant water intake. Thus, the time frequency and spatial distribution of the temperature increase were analyzed.

Several control points were defined in the bay and port, including the intake and discharge of the plant, for further analyses of the results obtained by the model (Figure 3). Point A is located in the water intake of the plant, and point B represents the outflow of the power plant. Points E, F, G, K, J, and L are located inside the port area, C and D are located close to the intake of the power plant, H and I are located close to the port zone, and M, N, O and P are located far from the outflow of the power plant.

To analyze the effect of the intake and outflow generated by the power plant over the hydrodynamic field, the directional currents frequency distributions were calculated in both simulations, with the plant on and off. The directional analysis was done considering the 8 nautical directions. The mean and maximum velocity values for each simulation in the control points were also calculated.

5. Results

5.1. Model Calibration and Validation

5.1.1. Hydrodynamic Calibration

After the calibration process, it was found that the hydrodynamic model accurately represents the time variability of water level and currents. As an example, Figure 5(a) presents a comparison between measured and modeled surface water levels in four stations of the Río de la Plata. It is shown that the model results reproduce the temporal variation of recorded water surface elevation, especially in the Montevideo area. In addition, a comparison between modeled and observed velocities is presented in Figure 5(b). The results again show a good agreement.

5.1.2. Thermal Calibration

The comparison of the measured and modeled temperature for the period February to April 2004 at Punta Brava station is presented in Figure 6. It shows that the model reproduces both the general behavior and the major fluctuations of the observed temperature. For example, during the months of February and March, measurements generally range between 21°C and 25°C, and the model represents temperatures between 22°C and 24°C. It is further noted that during the month of March, temperatures decrease, and the model reproduces the behavior. Figure 7 shows the comparison of the measured and modeled temperature in the point of the power plant water intake. It shows that the model reproduces the temperature during the simulation period, also showing the daily cycle of water temperature. On some days, there are differences between the measured temperatures and that obtained from the model but generally not exceeding 4°C.

The obtained results during the validation stage of the thermal model (Figure 8) show that without changing model parameters, the quality of the temperature modeling was maintained, reproducing water temperature variations in the Río de la Plata coastal zone and in Montevideo Bay.

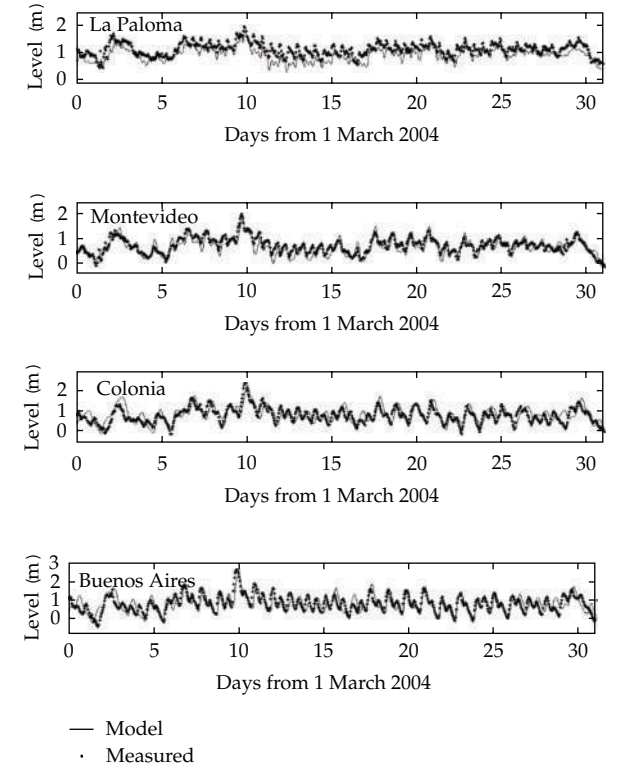

(a)

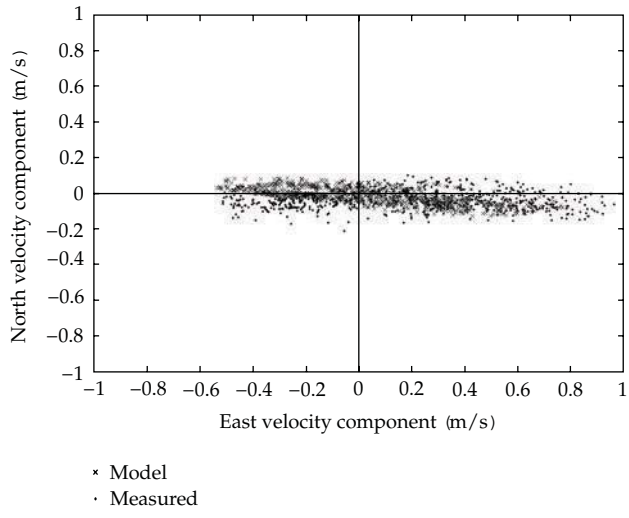

(b)

Figure 5: Temporal water level variation obtained with the model and measured in La Paloma, Montevideo, Colonia, and Buenos Aires during the calibration period March 2004 (a). Comparison of the spatial variation of the modeled and measured currents in Punta Brava during the days between 17 and 29 February 2004 (b).

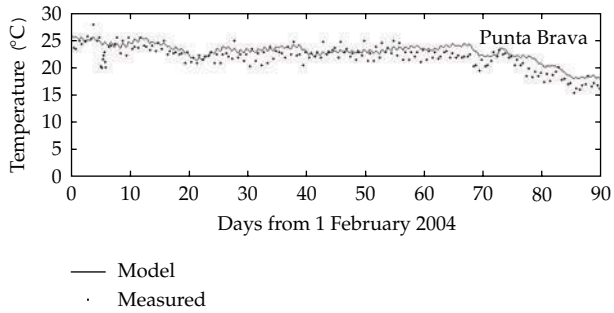

Figure 6: Comparison of the measured and modeled water temperature in Punta Brava station from February, March, and April 2004.

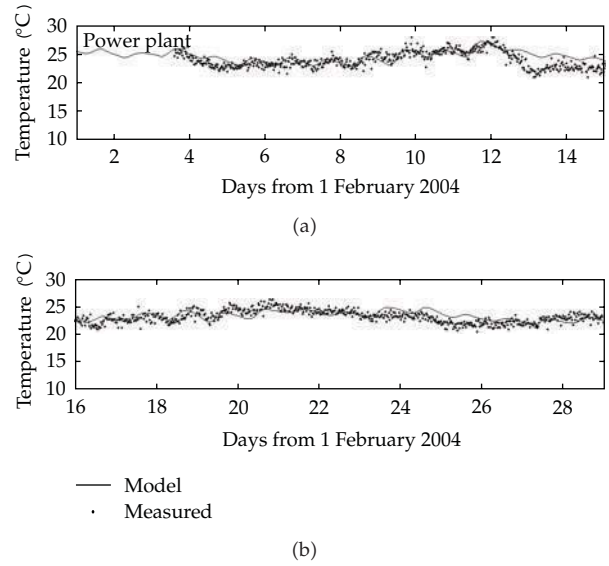

Figure 7: Comparison of the measured and modeled water temperature in power plant station from February 2004.

5.1.3. Hydrodynamic Validation

After the second calibration step, the model dynamically coupled with temperature was verified. The surface water levels and currents calculated with the model were compared with observed values. The results show (Figure 9) that the hydrodynamic model maintains the good agreement between observed and modeled data.

5.1.4. Power Plant Validation

Most of the time, the power station works with 5th and 6th units in operation simultaneously. Using the parameters for that operation scheme, a good representation of the power plant effect of temperature on the discharge was obtained with the model. For example, Figures 10 and 11 show the comparison of temperatures measured and modeled in two time periods

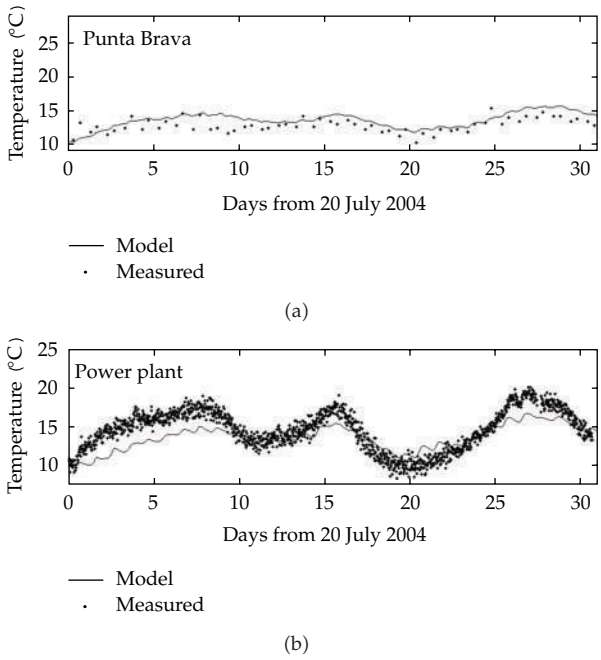

Figure 8: Comparison of the measured and modeled water temperature in Punta Brava and power plant station in July 2004.

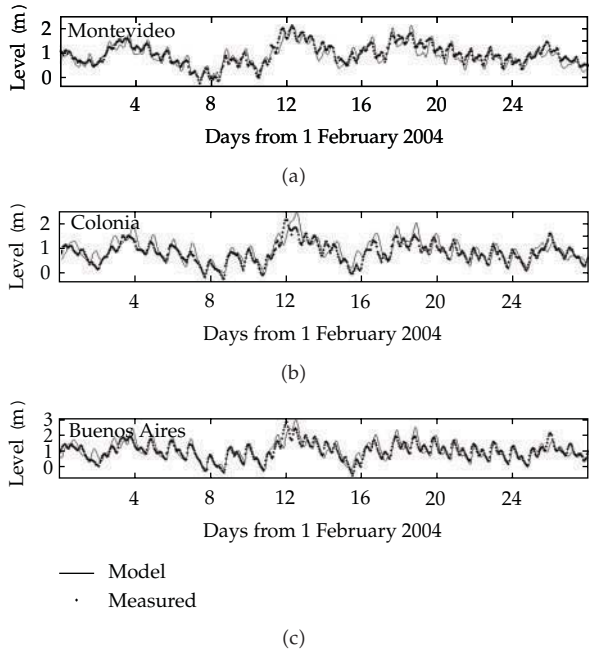

Figure 9: Comparison of water level measured and obtained with the model in three stations of the Rio de la Plata during February 2004.

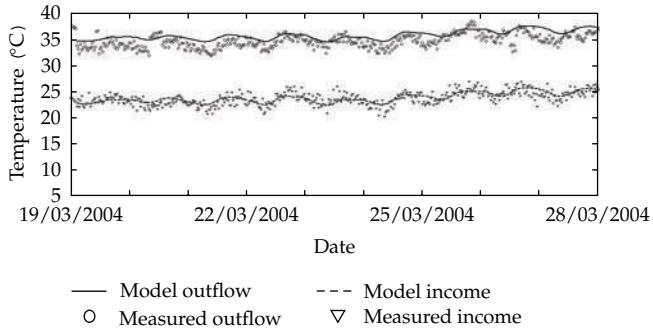

Figure 10: Comparison of the measured and modeled temperatures in the income and outflow of the power plant with the 5th and 6th units in operation for the days between 19 and 28 March 2004.

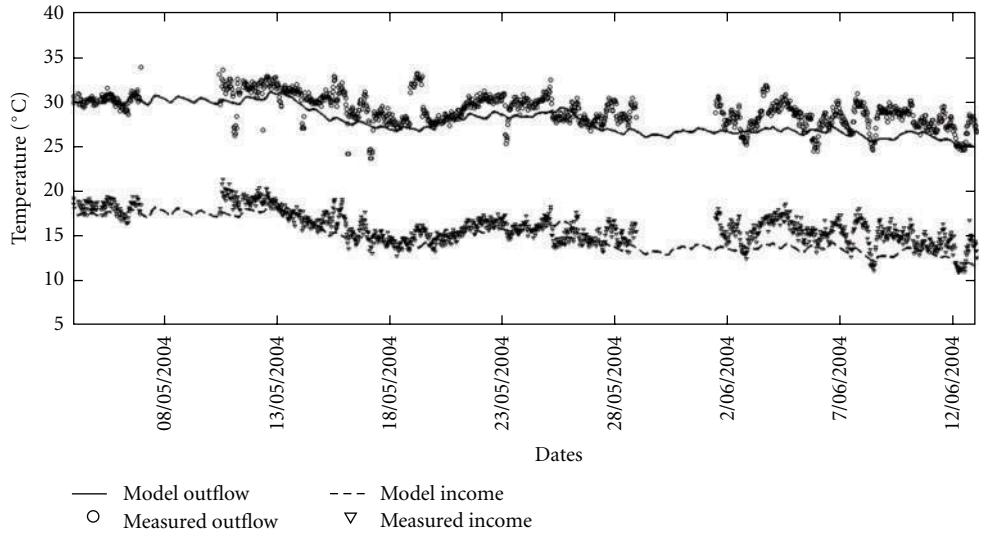

Figure 11: Comparison of the measured and modeled temperatures in the income and outflow of the power plant with the 5th and 6th units in operation for the days between 3 May and 15 June 2004.

in which both units were running. The model correctly reproduces the overall behavior of temperature at the water intake and in the discharge, both in warmer months where temperatures are between 20°C and 25°C, as in the cold months of June and July in which the temperature in the bay has an average value of 15°C.

Figure 12 shows the comparison between the measured and modeled temperatures in the water intake and outflow of the plant with only the 5th unit in operation, and Figure 13 shows the same comparison but for a case with the 6th unit in operation. Both cases show a good representation by the model of the water temperature in the zone associated with the plant.

The temperature plume nearby the zone of discharge and the currents generated for the intake and outflow of the plant are presented in Figures 14 and 15. These images show different time snaps corresponding to different seasons and power plant operation schemes. They clearly show the area of intake and discharge of water from the plant with higher water

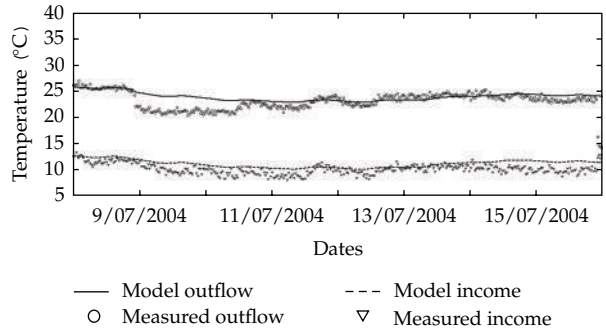

Figure 12: Comparison of the measured and modeled temperatures in the income and outflow of the power plant with the 5th units in operation for the days between 8 and 16 July 2004.

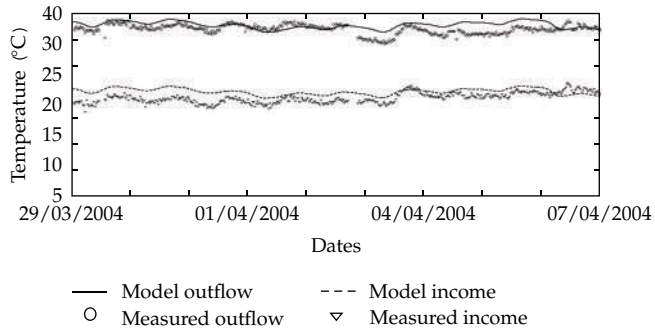

Figure 13: Comparison of the measured and modeled temperatures in the income and outflow of the power plant with the 6th units in operation for the days between 29 March and 7 April 2004.

temperatures and flow intensities in the discharge area and with a current going out of the port which is directed to the plant intake zone.

5.2. Power Plant Intake and Discharge Effects

5.2.1. Influence of the Discharge in the Intake Water Temperature

Figure 16 shows the temporal variation of water temperature in the intake of the power plant calculated with the plant turned on and turned off. It shows that the calculated values are different in both scenarios, meaning that temperature of water intake is affected by the power plant discharge. The frequency distribution of temperature difference corresponding to the control point located near the water intake shows that 26.5% of the time, the temperature increment is less than 0.2°C, 53.7% of time, it is less than 0.6°C, and 70.7% of the time, it is less than 1°C (only 29.3% of the time the temperature increment is higher than 1°C). This result is very important, since it could change the working point of the turbine, with the resulting loss of efficiency. The maximum value of temperature increase during the simulation period was 2.3°C.

The time evolution of water temperature with the power plant turned on and turned off and the histogram of ΔT in the points H and J are presented in Figures 17 and 18,

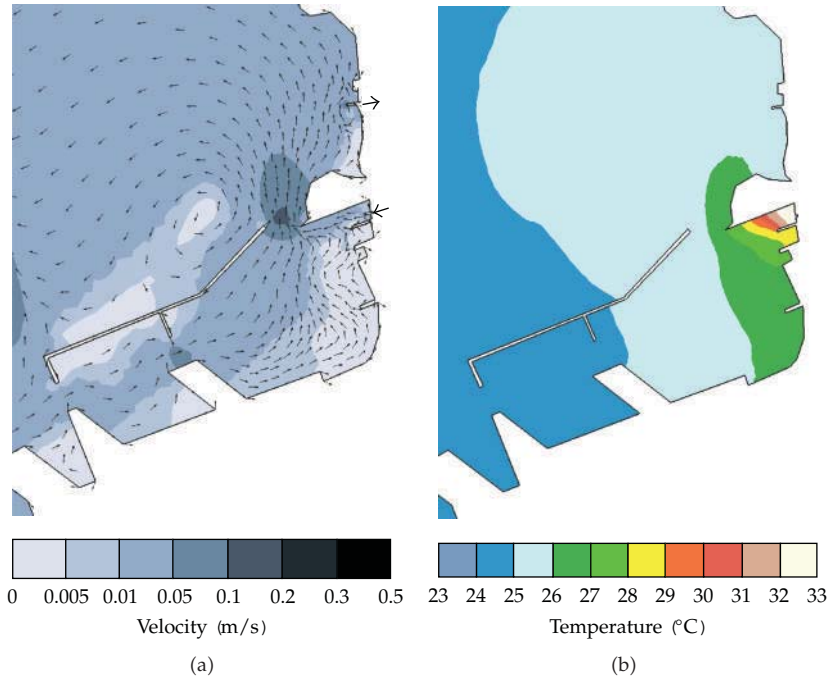

Figure 14: Velocity field and temperature field obtained with the model for the March 30th 14:00 hours with the 6th unit of the power plan in operation.

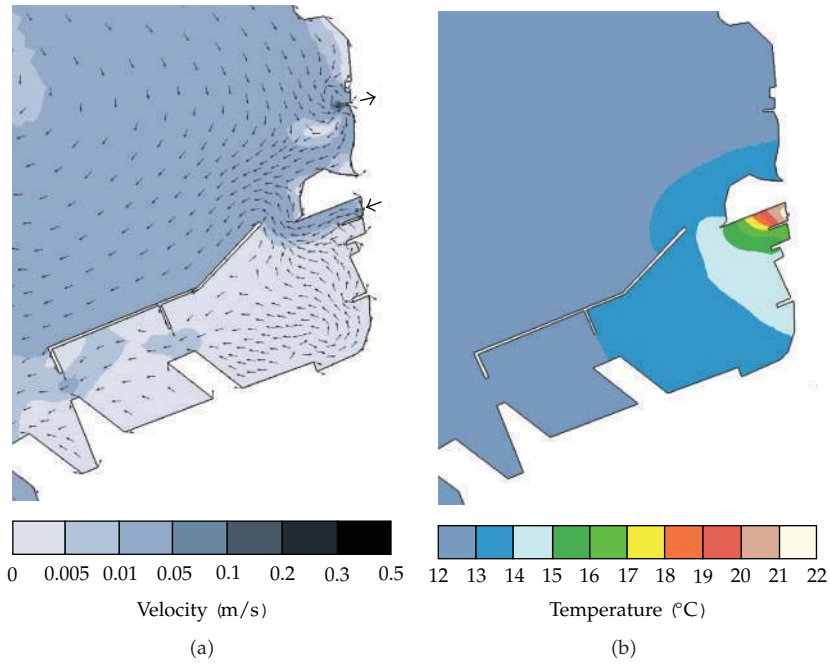

Figure 15: Velocity field and temperature field obtained with the model for the 17 June 18:30 hours with the 5th and 6th units of the Power Plan in operation.

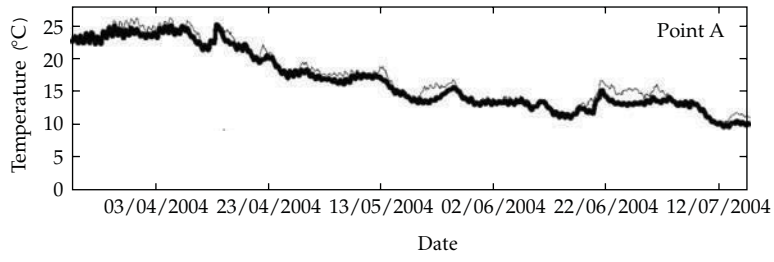

(a)

T	Frequency (%)
<0.2	26.9
<0.4	42.4
<0.6	53.7
<0.8	61.1
<1	70.7
<1.2	77.6
<1.4	84.7
<1.6	89.9
<1.8	92.6
<2	95.3
<2.2	98
<2.4	100

(b)

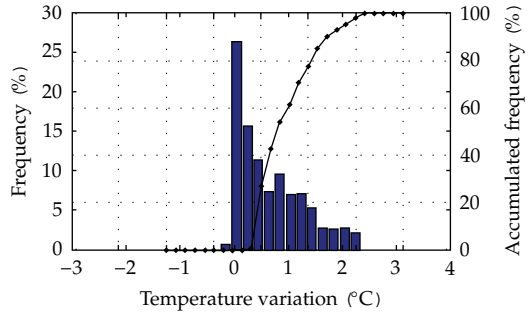

(c)

Figure 16: Time evolution of the water temperature calculated with the model in the income power plant (point A) with the power plant turned on and turned off. Histogram of the ΔT in point A.

respectively. It is noticeable that there is a greater impact on the water temperature in the port area represented by the point J than in the outside area represented by the point H.

Figure 19 presents the residual value of the temperature increment. It shows that the mean value of temperature increment near the power plant water intake is about 0.75°C.

5.2.2. Influence of the Cooling Flow Intake Outflow in the Bay Circulation

The influence of the power plant cooling water intake discharge on the circulation pattern can be obtained comparing the directional distribution of currents at the control points for both cases of power plant turned on and turned off. It was found that the power plant has greater effects in points C and D besides the intake and outflow points A and B. Figure 20 shows the results for point C and D with most frequent flow direction towards the south in the case of power plant turned off. But in the case of the power plant turned on, northern velocities increase their frequencies, inverting the direction of the residual flow. Results of residual flow presented in Figure 21 confirm this finding.

Regarding the flow intensity, the results also show an increase of velocity in the area related with points C and D. Table 2 presents the mean and maximum flow intensity obtained with the model in both simulations.

Finally, Figure 21 presents the residual flow distribution for both cases (power plant turned on and off). It shows that when the power plant is turned off, the flow directions is from the bay toward the port, but when the power plant is on, the flow direction is inverted, flowing from the port towards the bay.

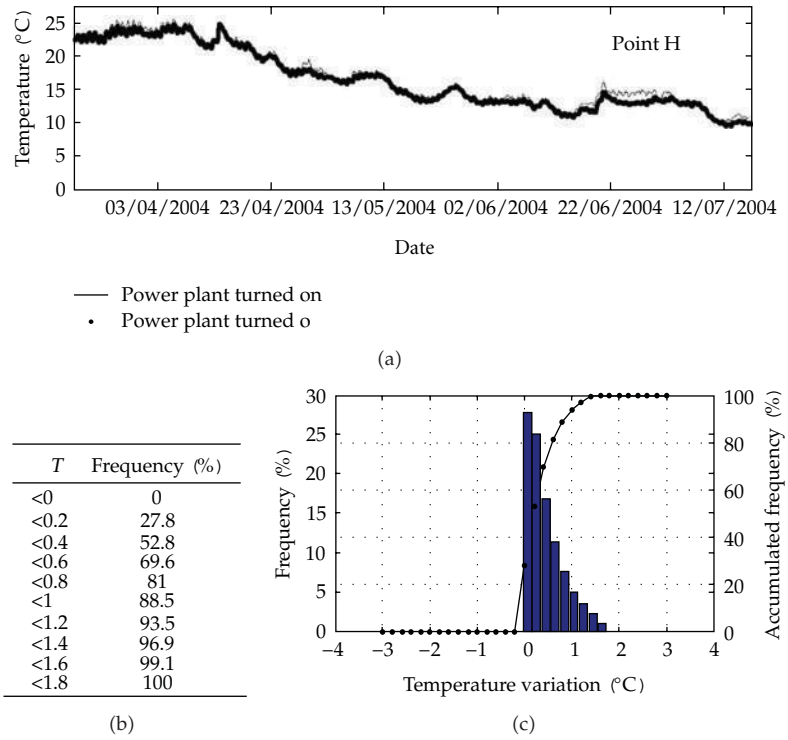

T	Frequency (%)
<0	0
<0.2	27.8
<0.4	52.8
<0.6	69.6
<0.8	81
<1	88.5
<1.2	93.5
<1.4	96.9
<1.6	99.1
<1.8	100

(b)

Figure 17: Time evolution of the water temperature calculated with the model in the zone outside the port (point H) with the power plant turned on and turned off. Histogram of the ΔT in point H.

Table 2: Mean and maximum velocity calculated for the model in different locations of the Montevideo Bay considering the power plant turned off and turned on.

Location	Mean velocity (cm/s)		Maximum velocity (cm/s)	
	Power plant turned off	Power plant turned on	Power plant turned off	Power plant turned on
A	0,69	19,13	4,54	34,06
B	0,00	11,32	0,00	15,56
C	3,29	3,22	16,67	17,31
D	5,62	5,47	27,85	29,08
E	0,96	1,00	6,11	6,03
F	0,57	0,60	3,86	3,80
G	1,37	1,32	6,27	6,10
H	3,01	3,01	14,67	14,41
I	3,92	3,91	17,46	17,35
J	1,39	1,39	6,37	6,45
K	0,53	0,52	3,30	3,36
L	3,72	3,72	17,95	17,73
M	5,34	5,36	18,67	18,72
N	3,31	3,30	13,91	14,18
O	4,31	4,29	20,62	20,74
P	4,91	4,92	20,71	21,08

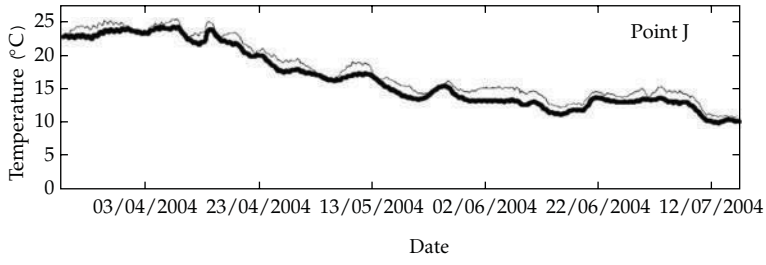

(a)

T	Frequency (%)
<0	0
<0.2	7.2
<0.4	13.3
<0.6	21.1
<0.8	29.9
<1	44.1
<1.2	56.7
<1.4	72.7
<1.6	88.6
<1.8	94.1
<2	99.5
<2.2	100

(b)

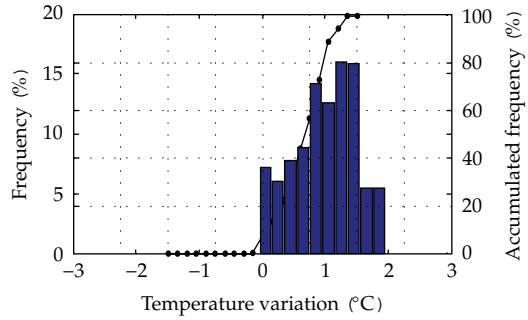

(c)

Figure 18: Time evolution of the water temperature calculated with the model in the zone inside the port (point J) with the power plant turned on and turned off. Histogram of the ΔT in point J.

6. Conclusions

A good representation of the temporal variations of temperature in the Montevideo Bay was obtained with the implementation, calibration, and validation of the finite element model RMA-10 in its vertically integrated two-dimensional mode.

The model can correctly represent the water temperature in the intake and in the discharge of the plant. Comparing the results of the model with the power plant turned on and off, it is possible to determine the effect of the power plant on the temperature field.

One of the objectives of this work was to determine the size and spatial distribution of the thermal plume resulting from the power plant discharge. The predictive computer model developed for this study shows the areas of the thermal plume (or mixing zone) in which the temperature decreases sufficiently to approach the far field values of temperature. Using this information, the study suggests a number of conclusions which are discussed below.

(i) Spatial distribution. Various simulations performed for the summer and winter of 2004 showed that the spatial distribution of the thermal plume is variable. On March 30th, the thermal plume extended in a northerly direction, reaching the plant water intake. On other occasions, such as June 17th (Figure 14), the plume extended in a narrower area of the port. However, at times, the plume also extended more than one kilometer beyond the discharge. The spatial distribution of the thermal plume is undoubtedly affected by wind patterns and other phenomenon such as tide effects (i.e., the naturally occurring back and forth movement of water resulting in constantly changing water levels and velocities).

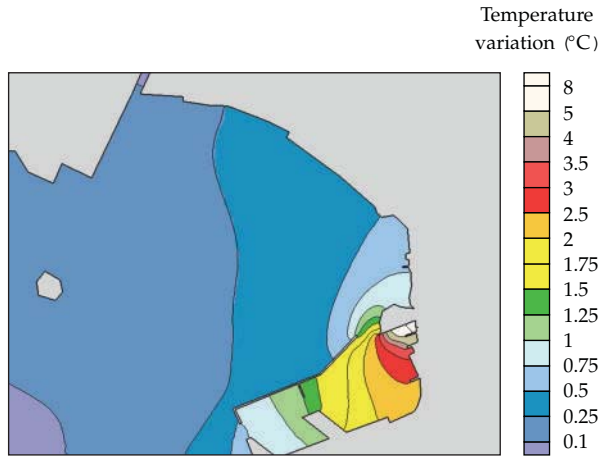

Figure 19: Spatial distribution of the mean increment water temperature generated by the outflow of power plant.

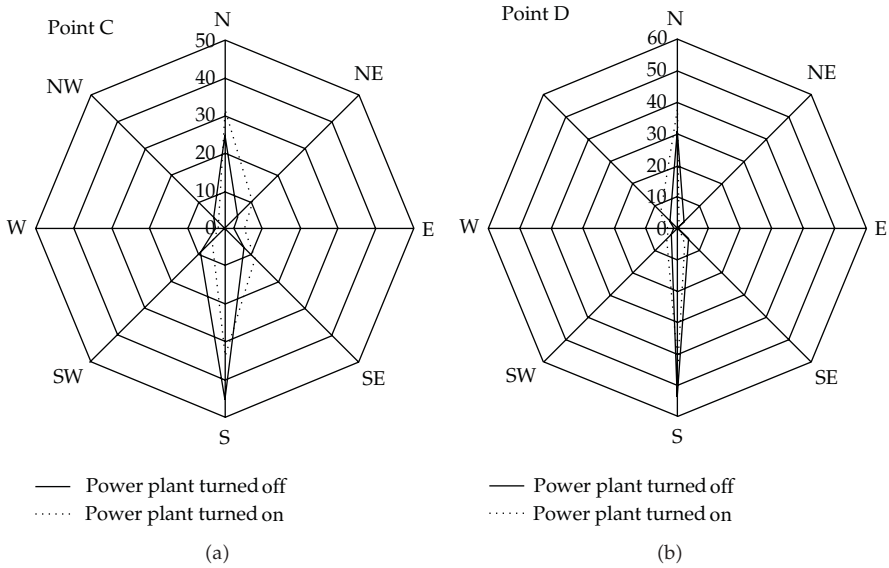

Figure 20: Directional frequency distribution in points C and D obtained in the simulation with the power plant and without the power plant.

(ii) Temperatures at the water intake. The study showed that during the period between March 19th and July 16th, 2004, 28.5% of the time, the temperature of water reaching the water intake increases by at least 1°C, while the maximum value of temperature increase during the simulation period was 2.3°C.

The model simulations provide valuable information regarding the size, spatial distribution, and location of the thermal mixing zone. As discussed previously, the size and spatial distribution of the mixing zone tend to vary considerably from one day to another. However, in general, the size of the thermal plume extends to the west, north, and south of the discharge

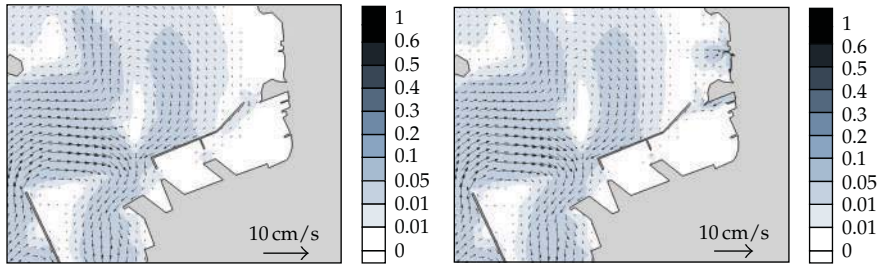

(a) (b)

Figure 21: Mean field currents in the simulation with power plant turned off (a) and power plant turned on (b). Velocities in cm/s.

point. Figure 19 shows the time average temperature field (from March 19th to July 16th, 2004) obtained averaging instantaneous differences between the thermal field obtained with the power plant on and off. Near the water intake, the mean value of temperature increase was 0.75°C.

Discharge-induced mixing is generally defined as the area where active mixing of the discharge plume and dilution of water is occurring. Beyond that area, the mixing becomes more passive or random, while the plume becomes much more disperse. Given these characterizations, model results suggest that discharge-induced mixing generally ceases just beyond the west end of the jetty located between the port and the bay, and so, this mixing zone is limited to a narrow zone near the discharge point.

In addition, it was observed that the modification of the circulation pattern induced by the intake discharge of cooling water is limited to the thermal plume area. However, it is found that residual currents produced when the power plant is operating show a very distinctive pattern. In that circumstance, the circulation pattern shows a predominant flow from the discharge zone to the bay and towards the power plant water intake. When the power plant is off, the circulation pattern reverses, that is, from the bay towards the port.

References

[1] M. Abbaspour, A. H. Javid, P. Moghimi, and K. Kayhan, "Modeling of thermal pollution in coastal area and its economical and environmental assessment," *International Journal of Environmental Science and Technology*, vol. 2, no. 1, pp. 13–26, 2005.

[2] S. A. Lowe, F. Schuepfer, and D. J. Dunning, "Case study: three-dimensional hydrodynamic model of a power plant thermal discharge," *Journal of Hydraulic Engineering*, vol. 135, no. 4, pp. 247–256, 2009.

[3] D. G. Kim and H. Y. Cho, "Modeling the buoyant flow of heated water discharged from surface and submerged side outfalls in shallow and deep water with a cross flow," *Environmental Fluid Mechanics*, vol. 6, no. 6, pp. 501–518, 2006.

[4] G. H. Jirka, "Multiport diffusers for heated disposal: a summary," *Journal of the Hydraulics Division*, vol. 108, no. 12, pp. 1425–1468, 1982.

[5] S. H. Chieh, "Two-dimensional numerical model of thermal discharges in coastal regions," *Journal of Hydraulic Engineering*, vol. 113, no. 8, pp. 1032–1040, 1987.

[6] J. M. Beckers and J. J. Van Ormelingen, "Thermohydrodynamical modelling of a power plant in the Zeebrugge Harbour," *Journal of Hydraulic Research*, vol. 33, no. 2, pp. 163–180, 1995.

[7] Y. Yunli, W. Deguan, W. Zhigang, and L. Xijun, "Numerical simulation of thermal discharge based on FVM method," *Journal of Ocean University of China*, vol. 5, no. 1, 2006.

[8] I. P. King, *RMA-10 A finite element model for three-dimensional density stratified flow*, Department of Civil and Environmental Engineering, University of California, Davis, Calif, USA, 1993.

[9] Golder Associates Ltd., "The modelling assessment of thermal effects of Genesee plant cooling water discharge," Report to EPCOR, Edmonton, Alberta, Canada, May 2001.
[10] I. Piedra-Cueva and M. Fossati, "Residual currents and corridor of flow in the Rio de la Plata," *Applied Mathematical Modelling*, vol. 31, no. 3, pp. 564–577, 2007.
[11] M. Fossati and I. Piedra-Cueva, "Numerical modelling of residual flow and salinity in the Río de la Plata," *Applied Mathematical Modelling*, vol. 32, no. 6, pp. 1066–1086, 2008.

Hindawi Publishing Corporation
Journal of Applied Mathematics
Volume 2011, Article ID 323485, 25 pages
doi:10.1155/2011/323485

Research Article

Numerical Analysis of Water Forced Convection in Channels with Differently Shaped Transverse Ribs

Oronzio Manca, Sergio Nardini, and Daniele Ricci

Dipartimento di Ingegneria Aerospaziale e Meccanica, Seconda Università degli Studi di Napoli, Real Casa dell'Annunziata, Via Roma, 29, 81031 Aversa, Italy

Correspondence should be addressed to Oronzio Manca, oronzio.manca@unina2.it

Received 15 January 2011; Accepted 14 March 2011

Academic Editor: Shuyu Sun

Copyright © 2011 Oronzio Manca et al. This is an open access article distributed under the Creative Commons Attribution License, which permits unrestricted use, distribution, and reproduction in any medium, provided the original work is properly cited.

Heat transfer enhancement technology has the aim of developing more efficient systems as demanded in many applications. An available passive method is represented by the employ of rough surfaces. Transversal turbulators enhance the heat transfer rate by reducing the thermal resistance near surfaces, because of the improved local turbulence; on the other hand, higher losses are expected. In this paper, a numerical investigation is carried out on turbulent water forced convection in a ribbed channel. Its external walls are heated by a constant heat flux. Several arrangements of ribs in terms of height, width, and shape are analyzed. The aim is to find the optimal configuration in terms of high heat transfer coefficients and low losses. The maximum average Nusselt numbers are evaluated for dimensionless pitches of 6, 8, and 10 according to the shape while the maximum friction factors are in the range of pitches from 8 to 10.

1. Introduction

Heat transfer enhancement technology plays an important role in the fields of engineering research and industry since every heat exchanger is virtually a potential candidate to be "enhanced". Several heat transfer augmentation techniques are developed in order to obtain size reductions, improve the thermodynamic process efficiency, or save costs. According to the thermal device and aims, different techniques are available. Their use is widely diffused in many applications as heat exchangers for refrigeration, automotive and aeronautic field, process industry, solar heaters, and so forth.

According to Bergles et al. [1] and Bergles [2], there are several enhancement techniques available. Thirteen different techniques are identified and grouped into "passive" and "active" ones, as pointed out by Webb and Kim [3]. Passive techniques employ special surface geometries, like coated surfaces, rough surfaces, extended surfaces or swirl flow

devices, and fluid additives to obtain the enhancement targets. The active techniques need the supply of external power sources, such as mechanical aids, electric or acoustic fields, and surface vibration.

One of the possible solutions to enhance passively the heat transfer is represented by the employ of integral roughness [4–8]. Considerable data exist for single-phase forced convection flow over rough surface for geometries like flat plates, circular tubes, noncircular channels, longitudinal flows in rod bundles, annuli and flow orthogonal to circular tubes. Internally roughened geometries represent a reliable and widely adopted technology in several commercial applications as in evaporators [4], condensers [5], steam condensers [6], gas turbine blades refrigeration [7], solar heaters [8], and so forth.

Several experimental studies in this area have been accomplished, as showed for example in [9, 10] but actually a growing number of numerical investigation is carried out by adopting suitable means in order to overcome computational limitations and correctly describe the complexity of flow patterns [11]. In this work, an attempt is made to predict numerically the details of both the velocity and temperature fields responsible for heat transfer enhancement in water forced convection and quantify the effective improvement in terms of heat transfer rate analyzing the consequent increase of losses.

The use of artificial roughness in the form of repeated ribs has been found to be as an efficient method to enhance the heat transfer rates in forced convection, as pointed out by several investigators [12–16]. The integral ribs are generated on the heat transferring surface and their role consists into break the laminar sublayer near the wall and create local turbulence. In this way, the goal of the heat transfer augmentation is achieved by reducing the thermal resistance. The enhancement, due to the improved local turbulence caused by ribs, is significantly higher than the part obtained by the fin effect linked to the presence of turbulators, as underlined by Lee and Abdel-Moneim [17].

On the other hand, the use of artificial roughness produces higher friction losses leading to important power requirements for the fluids flow through duct and channels. It is consequently advisable to promote a stronger turbulence only in the region very close to the heat transferring surface, such as in the viscous sublayer, in order to generate a minimum disturb into the core flow. This may be obtained by keeping the height of roughness elements to be small in comparison with the duct dimensions [1].

The study on rough ducts and ribbed tubes dates back to Nikuradse [18], Dipprey and Sabersky [19], who developed the friction similarity law for heat and momentum transfer analogy for fluid flow in rough pipes, and Webb et al. [20] developed heat transfer and friction factor correlations for turbulent flow in tubes having rectangular repeated rib roughness. Their investigations inspired many researchers, who applied different modern approaches and instruments. For example, Liou and Hwang [14, 15] used a real-time Laser Holographic Interferometry (LHI) to measure the local as well as average heat transfer coefficient and compared the performance of square triangular and semicircular ribs and showed that the square-ribs give best heat transfer performance among them. For developing and fully developed turbulent air flow, heat transfer and friction characteristics of ducts with rib turbulators on two opposite wall of the square and rectangular ducts have been extensively studied, from experimental point of view.

Also the numerical investigations are in a good number and their accuracy has grown with the improvement of calculator computational power and turbulence modelling. Several authors provided numerical studies on the effects of ribs in ducts and channels with air, considering different arrangements, in terms of height, shape and orientation of turbulators [21–26]. Although these approaches have adopted sophisticated turbulence closure models

that range from two-equation models to large eddy simulations (LES) for the velocity field, a rather simple heat transfer turbulence model based on the Reynolds analogy, that is, heat momentum transport similarity, via a turbulent Prandtl number, is used for the temperature field. Simulations indicated the importance of roughness geometry and pitches on the heat transfer mechanics, with optimal dimensionless spacing in the range 8–14, as underlined by Slanciauskas [27]. Liou et al. [28] performed a comparison between an experimental and a numerical investigation on the heat transfer and the air flow behaviour in a rectangular channel with streamwise periodic ribs mounted on one of the principal walls. They concluded that the flow acceleration and turbulence intensity are two major factors influencing the heat transfer coefficient and they found the optimum in terms of heat transfer coefficient enhancement for the pitch to rib height ratio equal to 10. Rau et al. [29] experimentally confirmed optimum pitch to rib height ratio equal to 9. Hence, their investigation reveal that not only the rib geometry but also its geometry arrangement play a vital role in enhancing the heat transfer coefficient, as pointed out by Wang and Sundén [30]. They underlined that the local heat transfer was strongly dependent on the rib shape, for example regarding the region just downstream the rib. However, their results are in contrast with the results provided by Ahn [31] who evaluated the best heat transfer performances for the triangular-shaped ribs studied, in fully developed regime. Several turbulence models and their improvements have been recently proposed. Ryu et al. [32, 33] solved the Reynolds-averaged Navier-Stokes equations, coupled with the k-ω turbulence model with near-wall treatment, by a finite-volume method. They studied both the thermal and fluid-dynamic behaviours of turbulent flows with two-dimensional ribs and three-dimensional blocks in the context of rough surfaces. Elements were square, triangular, semicircular and wavy wall-shaped ribs with a dimensionless height equal to 0.1, finding that the maximum resistance occurs at pitch to height ratio below 10. Chaube et al. [34] confirmed the good matching between the predictions by SST k-ω turbulent model and experimental results and they underlined the significant enhancement of the heat transfer in comparison to that for a smooth surface even for small Reynolds numbers.

This work extends the investigation carried out in [35] about a two-dimensional channel with differently shaped ribs. In particular, the working fluid is water instead of air because a few literature data has been carried out at this time. The ribs are obtained on the principal walls, heated by a constant uniform heat flux. The main aim of the present analysis is to analyze the flow and the heat transfer characteristics of the ribbed channel by means of Fluent code v6.3 [36]. The ribs are provided on the heated walls. A large amount of friction and heat transfer data, for different values of the dimensionless pitch and height with square, rectangular, trapezoidal and triangular shape ribs, has been generated for Reynolds numbers in the range between 20000 and 60000.

2. Governing Equations

A computational fluid-dynamic analysis of a two-dimensional channel model, provided with differently shaped ribs, as reported in Figure 1, is considered in order to evaluate its thermal and fluid-dynamic behaviours and study the temperature and velocity fields. A constant uniform heat flux is applied on the external channel walls. Different inlet velocities are considered in the ranges of turbulent regime and the working fluid is water with constant properties.

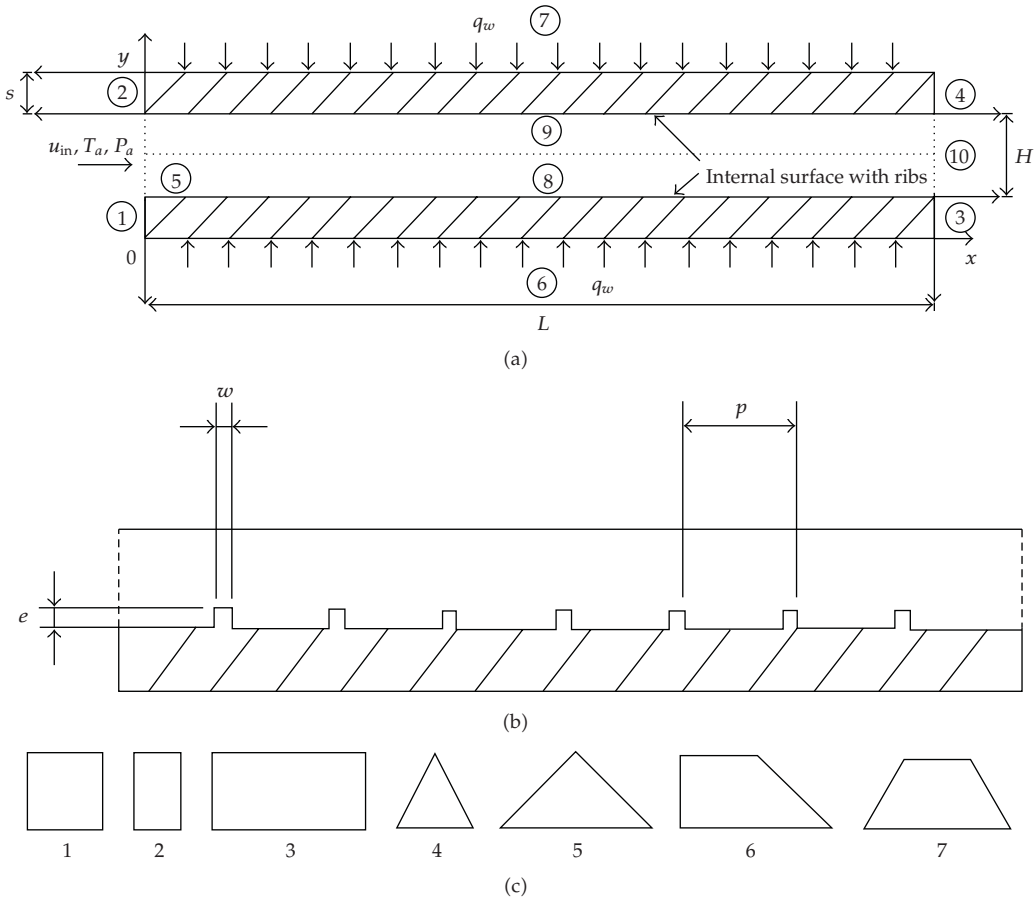

Figure 1: Sketch of the model: (a) geometrical model, (b) characteristic rib parameters, and (c) shapes of the considered ribs—(1) square-rib, (2) rectangular rib with $w/e = 0.5$, (3) rectangular rib with $w/e = 2.0$, (4) triangular rib with $w/e = 1.0$, (5) triangular rib with $w/e = 2.0$, (6) rectangular trapezoidal rib with $w/e = 2.0$, and (7) isosceles trapezoidal rib with $w/e = 2.0$.

Governing equations of continuity, momentum and energy are solved for a steady state turbulent flow in rectangular coordinates, under the hypotheses of steady state, two-dimensional, incompressible, turbulent, constant properties flow conditions:

$$\text{Continuity:} \quad \frac{\partial}{\partial x_i}(\rho u_i) = 0,$$

$$\text{Momentum:} \quad \frac{\partial}{\partial x_j}(\rho u_i u_j) = -\frac{\partial P}{\partial x_i} + \frac{\partial}{\partial x_j}\left[\mu\left(\frac{\partial u_i}{\partial x_j} + \frac{\partial u_j}{\partial x_i} - \frac{2}{3}\delta_{ij}\frac{\partial u_i}{\partial x_j}\right)\right] + \frac{\partial}{\partial x_j}\left(-\rho\overline{u_i' u_j'}\right), \quad (2.1)$$

$$\text{Energy:} \quad \frac{\partial}{\partial x_i}\left[u_i(\rho E + p)\right] = \frac{\partial}{\partial x_j}\left[\left(\lambda + \frac{c_p \mu_t}{Pr_t}\right)\frac{\partial T}{\partial x_j} + u_i(\tau_{ij})_{\text{eff}}\right],$$

where E is the total energy, $E = c_pT - p/\rho + u^2/2$, and $(\tau_{ij})_{\text{eff}}$ is the deviatoric stress tensor, defined as

$$(\tau_{ij})_{\text{eff}} = \mu_{\text{eff}}\left(\frac{\partial u_j}{\partial x_i} + \frac{\partial u_i}{\partial x_j}\right) - \frac{2}{3}\mu_{\text{eff}}\frac{\partial u_i}{\partial x_j}\delta_{ij}. \tag{2.2}$$

The Shear-Stress Transport (SST) k-ω turbulence model has been adopted and its equations are reported below in the form, developed by Menter [37]:

$$\begin{aligned}\frac{\partial}{\partial x_i}(\rho k u_i) &= \frac{\partial}{\partial x_j}\left(\Gamma_k\frac{\partial k}{\partial x_j}\right) + \widetilde{G}_k - Y_k + S_k,\\ \frac{\partial}{\partial x_i}(\rho\omega k u_i) &= \frac{\partial}{\partial x_j}\left(\Gamma_\omega\frac{\partial \omega}{\partial x_j}\right) + G_\omega - Y_\omega + D_w + S_\omega,\end{aligned} \tag{2.3}$$

where G_k is the production of turbulence kinetic energy due to mean velocity gradients, G_ω represents the generation of ω:

$$\widetilde{G}_k = \min(G_k, 10\beta^* k\omega) \tag{2.4}$$

with $G_k = -\rho\overline{u_i'u_j'}(\partial u_j/\partial x_i)$

$$G_\omega = \frac{\alpha}{\nu_t}G_k, \tag{2.5}$$

where ν_t is the kinematic turbulent viscosity and β^* a model constant; α is given by

$$\alpha = \alpha_\infty\frac{(\alpha_0^* + \text{Re}_t/\text{Re}_w)}{(1 + \text{Re}_t/\text{Re}_w)}, \tag{2.6}$$

where $R_\omega = 2.95$. $\beta_i = 0.072$ and α is represented by

$$\begin{aligned}\alpha_\infty &= F_1\alpha_{\infty,1} + (1 - F_1)\alpha_{\infty,2},\\ \alpha_{\infty,1} &= \frac{\beta_{i,1}}{\beta_\infty^*} - \frac{\kappa^2}{\sigma_{\omega,1}\sqrt{\beta_\infty^*}},\\ \alpha_{\infty,1} &= \frac{\beta_{i,2}}{\beta_\infty^*} - \frac{\kappa^2}{\sigma_{\omega,2}\sqrt{\beta_\infty^*}},\end{aligned} \tag{2.7}$$

where $\kappa = 0.41$. In the High-Reynolds number form, $\alpha = \alpha_\infty = 1.0$. Γ_k and Γ_ω represent the effective diffusivity of k and ω:

$$\begin{aligned} \Gamma_k &= \mu + \frac{\mu_t}{\sigma_k}, \\ \Gamma_\omega &= \mu + \frac{\mu_t}{\sigma_\omega}, \end{aligned} \tag{2.8}$$

where σ_k and σ_w are the turbulent Prandtl numbers for k and ω, respectively,

$$\begin{aligned} \sigma_k &= \frac{1}{F_1/\sigma_{k,1} + (1 - F_1)/\sigma_{k,2}}, \\ \sigma_w &= \frac{1}{F_1/\sigma_{w,1} + (1 - F_1)/\sigma_{w,2}}, \end{aligned} \tag{2.9}$$

and μ_t is the turbulent viscosity, computed from

$$\mu_t = \alpha^* \frac{\rho k}{\omega}. \tag{2.10}$$

The coefficient α^* dampens the turbulent viscosity. It is given by

$$\alpha^* = \alpha^*_\infty \frac{(\alpha^*_0 + \mathrm{Re}_t/\mathrm{Re}_k)}{(1 + \mathrm{Re}_t/\mathrm{Re}_k)}, \tag{2.11}$$

where $\mathrm{Re}_t = \rho k/\mu\omega$, $R_k = 6$, $\alpha^*_0 = \beta_i/3$, and $\beta_i = 0.072$. In the High-Reynolds number form $\alpha^* = \alpha^*_\infty = 1.0$. The blending equation F_1 is given by

$$\begin{aligned} F_1 &= \tan\left(\Phi_1^4\right), \\ \Phi_1 &= \min\left[\max\left(\frac{\sqrt{k}}{0.09\omega y}, \frac{500\mu}{\rho y^2 \omega}\right), \frac{4\rho k}{\sigma_{w,2} D_\omega{}^+ y^2}\right], \\ D^+_\omega &= \max\left[2\rho \frac{1}{\sigma_{\omega,2}} \frac{1}{\omega} \frac{\partial k}{\partial x_j} \frac{\partial w}{\partial x_j}, 10^{-10}\right], \end{aligned} \tag{2.12}$$

where y is the distance to the next surface and D^+_ω is the positive portion of the cross-diffusion term.

Y_k and Y_ω represent the dissipation of k and ω due to turbulence:

$$\begin{aligned} Y_k &= \rho\beta^* k\omega, \\ Y_\omega &= \rho\beta\omega^2, \end{aligned} \tag{2.13}$$

Table 1: Shear stress transport k-ω model constants.

$\sigma_{\kappa,1} = 1.176$	$\sigma_{\kappa,2} = 1.0$	$\sigma_{\omega,1} = 2.0$	$\sigma_{\omega,2} = 1.168$	$\alpha_1 = 0.31$	$\beta_{i,1} = 0.075$
$\beta_{i,2} = 0.0828$	$\alpha^*_\infty = 1.0$	$\alpha_\infty = 0.52$	$\beta^*_\infty = 0.09$	$\beta_i = 0.072$	$\alpha_0 = 1/9$
$R_\beta = 8.0$	$R_\kappa = 6.0$	$R_\omega = 2.95$	$\xi^* = 1.5$	$\sigma_\kappa = 2.0$	$\sigma_\omega = 2.0$

with β and β^* are model constants; moreover

$$\beta_i = F_1\beta_{i,1} + (1 - F_1)\beta_{i,2}. \tag{2.14}$$

D_ω represents the cross-diffusion term while S_k and S_ω are possible source terms. In particular, D_ω is given by

$$D_\omega = 2(1 - F_1)\rho\sigma_{\omega,2}\frac{1}{\omega}\frac{\partial k}{\partial x_j}\frac{\partial \omega}{\partial x_j}. \tag{2.15}$$

The model constants are summarized in Table 1. A two-dimensional conduction model in heated walls is employed and the equation in the steady-state regime is

$$\frac{\partial}{\partial x_j}\left(\lambda\frac{\partial T}{\partial x_j}\right) = 0. \tag{2.16}$$

The working fluid is water and the assigned boundary conditions are the following:

(i) inlet section: uniform velocity and temperature profile,

(ii) outlet section: outflow,

(iii) duct walls: velocity components equal to zero,

(iv) external duct walls: uniform heat flux.

3. Geometrical Configuration

The two-dimensional model, depicted in Figure 1, represents a channel with a length, L, equal to 250 mm while its height H is set equal to 10 mm and width W is 1000 mm; the hydraulic diameter is equal to 20.0 mm. The 3 mm thick wall is made up by aluminium and a constant heat flux equal to 10 kW/m^2 has been applied on the external surfaces. Square, rectangular, triangular and trapezoidal ribs are mounted on the internal principal walls and they are characterized by different geometry ratios as depicted in Figures 1(b) and 1(c). The roughness parameters are determined by the height (e), pitch (p) width (w) and shape of turbulators. These parameters identify the families of geometrically similar roughness and they can be expressed in the form of the following dimensionless parameters:

(i) relative roughness pitch, p/e,

(ii) relative roughness height, e/d,

(iii) relative roughness width, w/e.

Table 2: Properties of water.

ρ (kg/m^3)	997
c_p (J/kg K)	4177
μ (Pa s)	$845e-6$
λ (W/m K)	0.610

In this paper, square-ribs, rectangular ribs ($w/e = 0.5$ and 2.0), triangular ribs ($w/e = 1.0$ and 2.0) and trapezoidal ribs (isosceles and rectangular trapezium with $w/e = 2.0$) are considered. The range of dimensionless roughness parameters and Reynolds numbers employed in this investigation are given below:

(i) reynolds number, Re (from 20000 to 60000),

(ii) dimensionless roughness pitch, p/e (from 4 to 20),

(iii) dimensionless height, e/d (0.02 and 0.05).

The dimensionless parameters, here considered, are

$$\mathrm{Re} = \frac{u_{\mathrm{av}} d}{\nu}, \tag{3.1}$$

$$\mathrm{Nu}_{\mathrm{av}} = \frac{\dot{q} d}{(T_w - T_m)\lambda_f}, \tag{3.2}$$

where T_w and T_m represent the average wall temperature and the average bulk temperature, respectively.

$$f = 2\frac{\Delta P d}{L}\frac{1}{\rho u_{\mathrm{av}}^2}. \tag{3.3}$$

4. Numerical Model

The governing equations are solved by means of the finite volume method. The working fluid is water and its properties are considered constant. In Table 2 the values of density, specific heat, thermal conductivity and dynamic viscosity, obtained by Rohsenow et al. [38], are given. A steady-state solution and a segregrated method are chosen to solve the governing equations, which are linearized implicitly with respect to dependent variables of the equation. A second-order upwind scheme is chosen for energy and momentum equations. The SIMPLE coupling scheme is chosen to couple pressure and velocity. The convergence criteria of 10^{-5} and 10^{-8} are assumed for the residuals of the velocity components and energy, respectively. It is assumed that the incoming flow is turbulent at ambient temperature, $T_a = 293$ K, and pressure. Different inlet uniform velocities, u_{in}, equal to 0.85, 1.28, 1.70, 2.13 and 2.56 m/s, corresponding to Reynolds numbers ranging from 20000 to 60000, were considered. Furthermore, the inlet turbulence intensity value is set to 1%. Along the solid walls no slip condition is employed whereas a velocity inlet and outflow conditions are given for the inlet and outlet surfaces. The boundary conditions in the mathematical forms are given in Table 3 and the initial conditions for temperature and velocity are T_a and u_{in}, respectively.

Table 3: Boundary conditions.

Wall	u_i	u_j	T
1, 2, 3, 4			$\partial T_{\mathrm{sl}}/\partial x = 0$
5	$u_i = u_{in}$	$u_j = 0$	$T_f = T_a$
6			$-\lambda_{\mathrm{sl}}(\partial T_{\mathrm{sl}}/\partial y) = \dot{q_w}$
7			$\lambda_{\mathrm{sl}}(\partial T_{\mathrm{sl}}/\partial y) = \dot{q_w}$
8, 9	$u_i = 0$	$u_j = 0$	$T_f = T_{\mathrm{sl}}$ $\lambda_{\mathrm{sl}}(\partial T_{\mathrm{sl}}/\partial y) = \lambda_f(\partial T_f/\partial y)$
10	$\partial u_i/\partial x = 0$	$\partial u_j/\partial x = 0$	$\partial T_f/\partial x = 0$

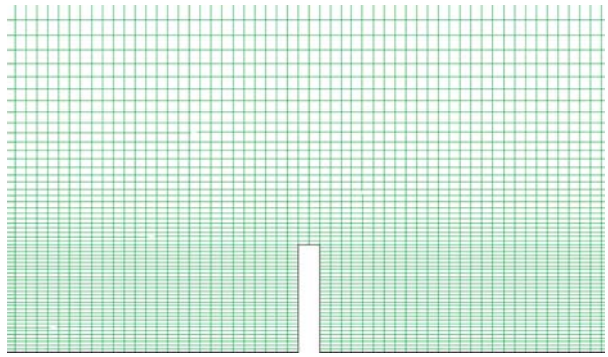

Figure 2: Scheme of the adopted mesh into the channel.

Four different grid distributions are tested, to ensure that the numerical results were grid independent for the channel with rectangular ribs, with $p/e = 20$, $e/d = 0.05$, and $w/e = 0.5$. They have 27000, 55400, 108100, 189900 and 385000 nodes, respectively. The grid mesh is structured in each case and optimized taking into account the grid adoption for $y^+ = 1$ at adjacent wall region. The sketch of the chosen grid distribution is reported in Figure 2. The third grid case has been adopted because it ensured a good compromise between the machine computational time and the accuracy requirements. In fact, comparing the third and fourth mesh configurations, in terms of wall average temperature, mass-weighted average outlet temperature, average outlet velocity and pressure drops, the corresponding percentage relative errors are 0.9%, 0.3% and 1.5%, respectively.

Results are validated by comparing the obtained numerical data with the literature ones in terms of average Nusselt numbers and friction coefficients, in the case of smooth channel and ribbed one [3, 22, 39]. For the smooth channel the following correlations are adopted and the comparison is depicted in Figure 3.

$$\textit{Dittus-Boelter}\ \text{correlation: } \mathrm{Nu}_s = 0.024\,\mathrm{Re}_d^{0.8}\,\mathrm{Pr}^{0.4} \tag{4.1}$$

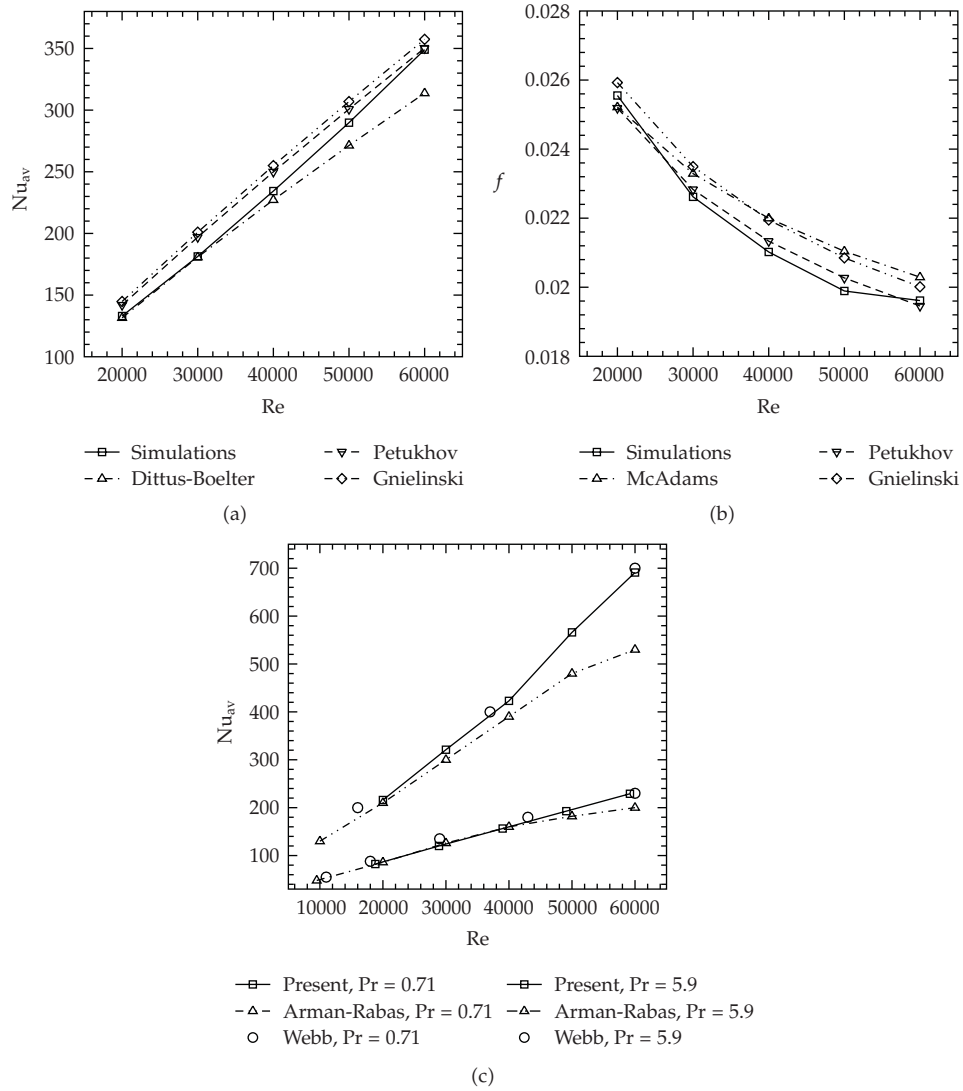

Figure 3: Validation of results: (a) average Nusselt number, smooth channel, (b) friction factor, smooth channel, and (c) average Nusselt number, ribbed channel (rectangular ribs, $w/e = 0.5$, $e/d = 0.02$, and $p/e = 20$).

for $0.5 < \mathrm{Pr} < 120$, $6.0 \times 10^3 < \mathrm{Re}_d < 1.0 \times 10^7$; $60 < (L/d)$

$$\textit{Petukhov} \text{ correlation: } \mathrm{Nu}_s = \frac{\mathrm{Re}_d \mathrm{Pr} f/8}{1.07 + 12.7(f/8)^{1/2}\left(\mathrm{Pr}^{2/3} - 1\right)} \tag{4.2}$$

with $f_s = (1.84 \log_{10}\mathrm{Re}_d - 1.64)^{-2}$ for $0.5 < \mathrm{Pr} < 200$, $1.0 \times 10^4 < \mathrm{Re}_d < 5.0 \times 10^6$;

$$\textit{Gnielinski} \text{ correlation: } \mathrm{Nu}_s = \frac{f/8(\mathrm{Re}_d - 1000)\mathrm{Pr}}{1 + 12.7(f/8)^{1/2}\left(\mathrm{Pr}^{2/3} - 1\right)} \tag{4.3}$$

with $f_s = (0.79 \log_{10}\mathrm{Re}_d - 1.64)^{-2}$ for $0.5 < \mathrm{Pr} < 200$, $1.0 \times 10^4 < \mathrm{Re}_d < 5.0 \times 10^6$;

$$McAdams \text{ correlation: } f_s = 0.184\,\mathrm{Re}_d^{-0.2} \tag{4.4}$$

for $2.0 \times 10^4 < \mathrm{Re}_d < 3.0 \times 10^5$.

There is a very good correspondence with the given correlations in terms of average Nusselt number, as reported in Figure 3(a) while Figure 3(b) shows the little percentage error in terms of friction factor and a good fitting with the experimental curves. A difference of 5% at most has been calculated by comparing results with ones for *Gnielinski* correlation. The comparison with experimental and numerical data available for water forced convection in a ribbed channel [3, 22] with rectangular turbulators ($e/d = 0.02$, $p/e = 20$, and $w/e = 0.5$) is reported. The present results, shown in Figure 3(c), fit very well with the experimental data and improve the accuracy in comparison with the previous numerical approach.

5. Results and Discussion

Results are presented in form of graphs depicting the average Nusselt number, friction factors and required pumping power at different dimensionless pitches, heights and ribs shapes, and Reynolds numbers, and also temperature fields and streamlines contours for some significant cases are given. Ribs are characterized by square, rectangular, trapezoidal and triangular shapes with different values of w/e ratio.

Figure 4 presents the profiles of the ratio $\mathrm{Nu_{av}}/\mathrm{Nu_{av,s}}$ in order to describe the heat transfer rate improvement of the ribbed configuration compared to the smooth channel. Results are reported as a function of p/e ratio for square, rectangular, triangular and trapezoidal ribs, with e/d equal to 0.05 at Re = 20000, 30000, and 60000. In Figure 4(a), it is observed that the profile for square-ribs increases from the lowest values of p/e, attaining the maximum value at the dimensionless pitch of 8; then, it decreases for further increases in the pitch values. This behaviour may be noticed for all the considered Reynolds numbers; moreover, $\mathrm{Nu_{av}}/\mathrm{Nu_{av,s}}$ ratio tends to increase as Re increases. In fact, $\mathrm{Nu_{av}}/\mathrm{Nu_{av,s}} = 1.97$, 2.03, 2.05 at $p/e = 8$ for Re = 20000, 30000, and 60000, respectively. Figure 4(b) is referred to the rectangular ribs and it shows that the shape with $w/e = 0.5$ is characterized by more significant thermal performances compared to the elements with $w/e = 2.0$. The maximum values are attained at $p/e = 10$. The triangular ribs exhibit the highest thermal performances. Maxima are observed for $p/e = 6$, where $\mathrm{Nu_{av}}/\mathrm{Nu_{av,s}} = 2.60$ and 2.58 at Re = 60000, for $w/e = 2.0$ and 1.0, respectively. Lower Nusselt number augmentation ratios are detected for the trapezoidal ribs, which show the maximum values at $p/e = 10$, like the rectangular ones but the thermal performances are slightly improved. For all the considered configurations, although the rib-surface area increases, the heat transfer rate does not grow in such evident way; this result suggests that the primary cause for the enhancement is the strong turbulent motion induced by the ribs.

$\mathrm{Nu_{av}}/\mathrm{Nu_{av,s}}$ ratio decreases by reducing the height of the rough elements, as reported in Figure 5. In fact, for $e/d = 0.02$, an average reduction of 20–25%, in terms of average Nusselt number, is observed at Re = 40000. Maxima are attained at the same values of dimensionless pitch, previously reported. For example, at $p/e = 10$ $\mathrm{Nu_{av}}/\mathrm{Nu_{av,s}} = 1.62$ and 2.07, for the *rect* trapezoidal turbulators, at $e/d = 0.02$ and 0.05, respectively.

The highest values of the average Nusselt number are exhibited for slightly lower pitches, in comparison with the results for air as working fluid, reported in [35] while the

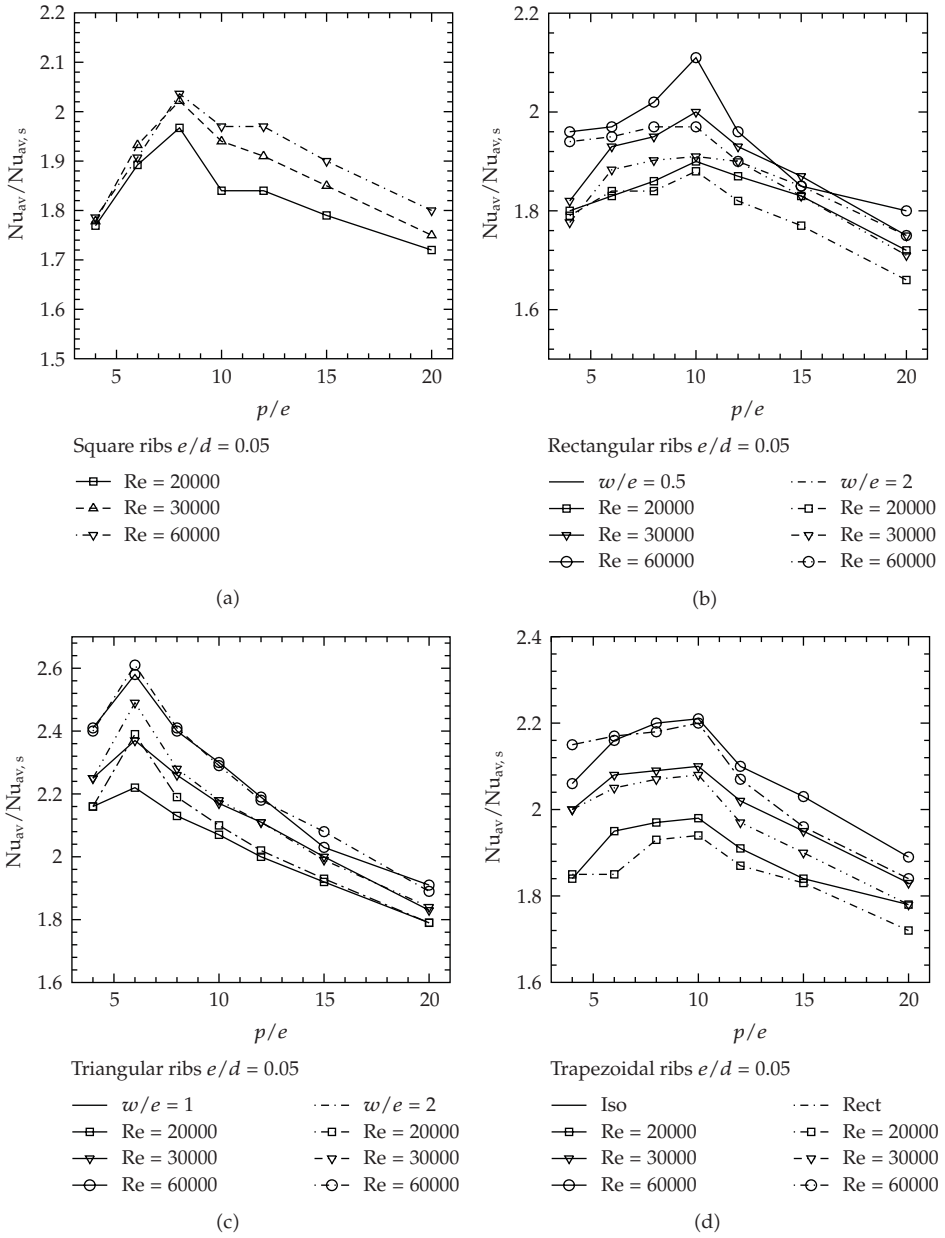

Figure 4: Average Nusselt number profiles, referred to the smooth channel results, as a function of p/e at Re = 20000, 30000, and 60000, for $e/d = 0.05$: (a) square-ribs, (b) rectangular ribs with $w/e = 0.5$ and 2.0, (c) triangular ribs with $w/e = 1.0$ and 2.0, and (d) isosceles and rectangular trapezoidal ribs with $w/e = 2.0$.

results in terms of friction factor are confirmed, as depicted in Figure 6, which shows the results in terms of friction factor as a function of p/e at Re = 20000, 30000, and 60000, and e/d equal to 0.05 for different shapes. The square turbulators show in Figure 6(a) that for $p/e < 10$ the friction coefficient ratio, referred to the smooth channel, increases rapidly as relative roughness pitch augments; f factor reaches for the maximum value at $p/e = 10$ and

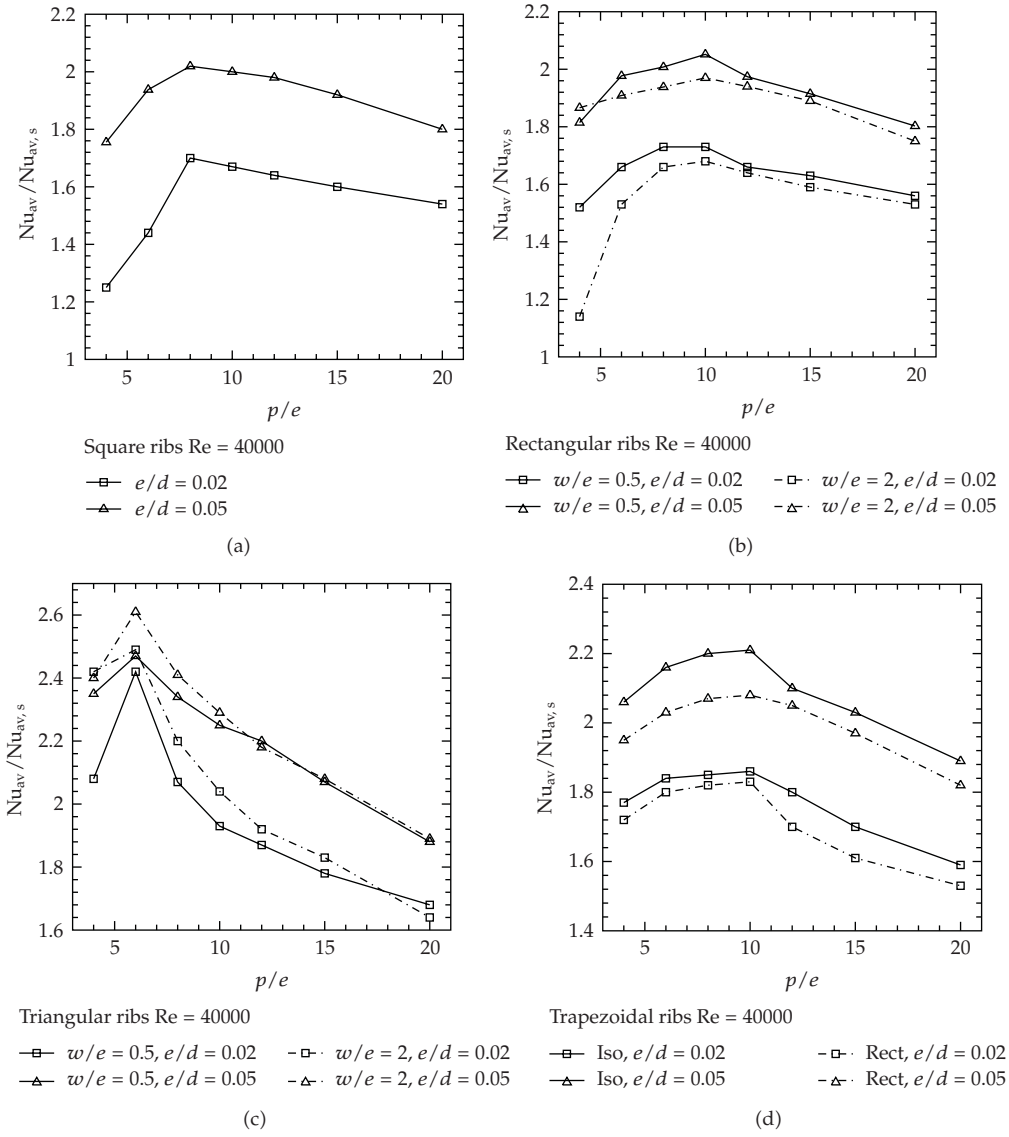

Figure 5: Average Nusselt number profiles, referred to the smooth channel results, as a function of p/e at Re = 40000, for $e/d = 0.02$ and 0.05: (a) square-ribs, (b) rectangular ribs with $w/e = 0.5$ and 2.0, (c) triangular ribs with $w/e = 1.0$ and 2.0, and (d) isosceles and rectangular trapezoidal ribs with $w/e = 2.0$.

a further increase of relative roughness pitch leads to a consequent decrease; this effect is similar to the one observed in rough ducts at high Reynolds numbers. The maximum values are observed for $p/e = 10$, for rectangular and trapezoidal ribs, and 8, for the triangular ones, for all the considered Reynolds numbers. The highest values are obtained for Re = 60000 in correspondence with the triangular turbulators with the aspect ratio $w/e = 1.0$, as depicted in Figure 6(c). In fact, at Re = 60000 $f/f_s = 12.8$, 11.7 and 11.8, for triangular turbulators with $w/e = 1.0$ and 2.0, and rectangular ones with $w/e = 0.5$, respectively. The lowest values of friction factor are obtained for the rectangular elements with $w/e = 2.0$ and for the trapezoidal ones, as described in Figures 6(b) and 6(d).

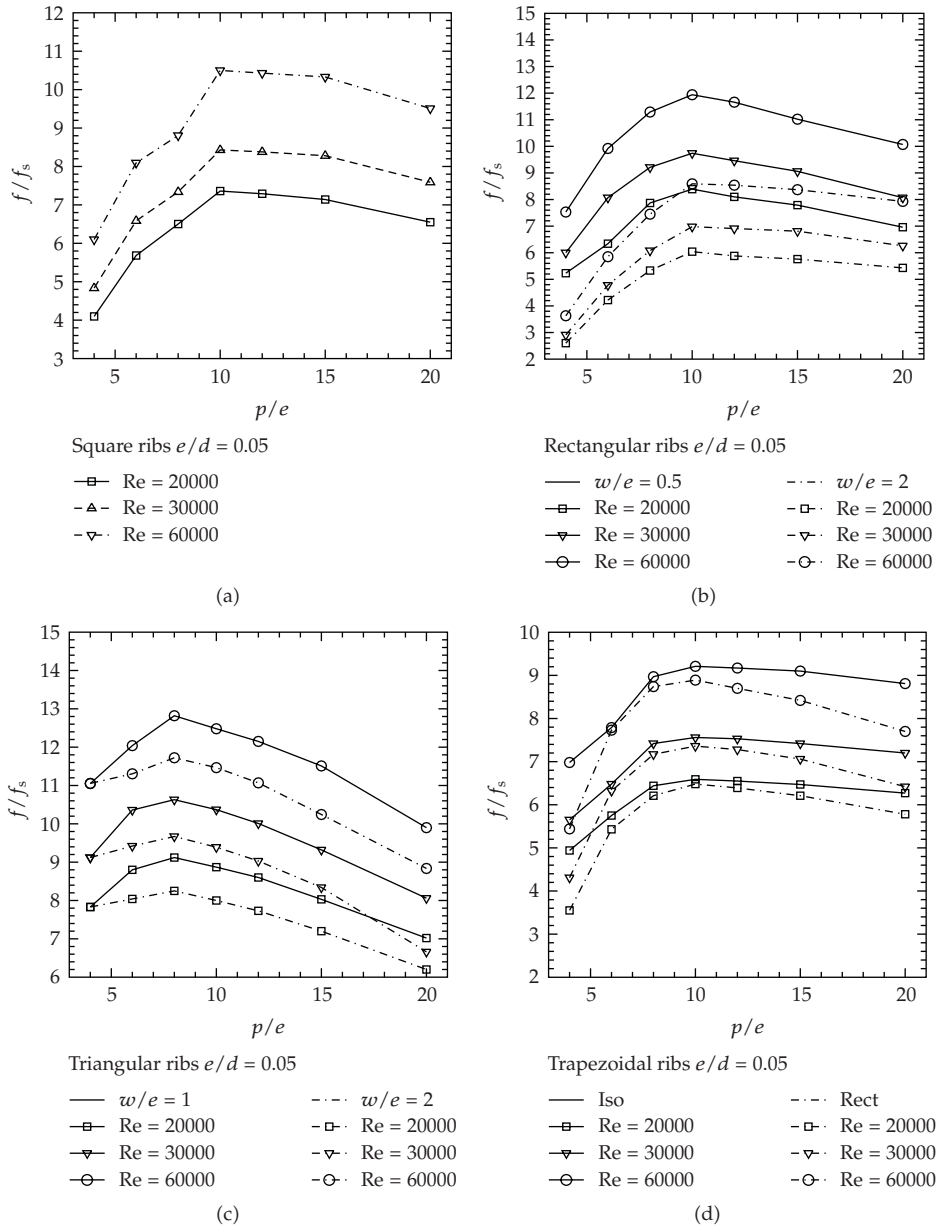

Figure 6: Friction factor profiles, referred to the smooth channel results, as a function of p/e at Re = 20000, 30000, and 60000, for $e/d = 0.05$: (a) square-ribs, (b) rectangular ribs with $w/e = 0.5$ and 2.0, (c) triangular ribs with $w/e = 1.0$ and 2.0, and (d) isosceles and rectangular trapezoidal ribs with $w/e = 2.0$.

Furthermore, the friction factor, f, decreases as dimensionless height reduces and, in fact, at $e/d = 0.02$, f values are 2-3 times lower than ones, obtained for ribs with e/d 0.05. This behaviour is described in Figure 7 which is referred to Re = 40000. The most significant differences are observed for the rectangular and trapezoidal ribs, as reported in Figures 7(b) and 7(d). For example, for the rectangular elements with $w/e = 0.5$, f/f_s is equal to 10.8 and 3.8 at most, at $e/d = 0.05$ and 0.02, respectively, while, for the *iso* trapezoidal ribs, the ratio values are 8.3 and 3.5 at $p/e = 10$.

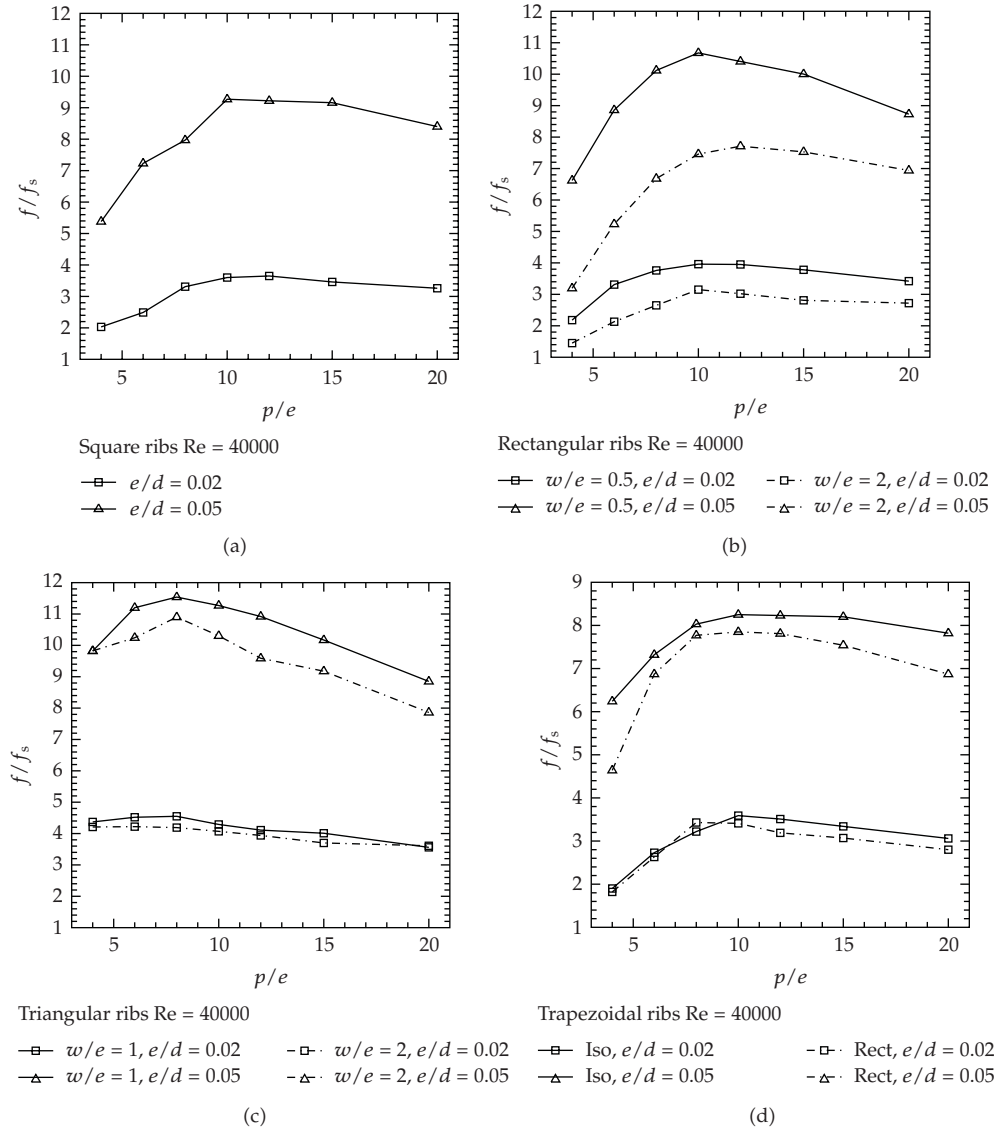

Figure 7: Friction factor profiles, referred to the smooth channel results, as a function of p/e at Re = 40000, for e/d = 0.02 and 0.05: (a) square-ribs, (b) rectangular ribs with w/e = 0.5 and 2.0, (c) triangular ribs with w/e = 1.0 and 2.0, and (d) isosceles and rectangular trapezoidal ribs with w/e = 2.0.

It is significant to underline that the maximum values of average Nusselt number and friction factor are attained at about the same value of p/e ratio for all the considered Reynolds numbers for each configuration. Moreover, the highest values of friction factor are observed near the values of pitch, where the highest Nusselt numbers are evaluated.

Figure 8 depicts the results in terms of the required pumping power, PP, defined as $u_{\text{av}}A\Delta P$, referred to the smooth channel, at Re = 40000, for e/d = 0.02 and 0.05 and for different shapes of turbulators. The profiles of PP/PP_s follow the ones, reported in terms of f/f_s. They confirm that the highest losses are detected for both the considered triangular elements and for the rectangular ones with the aspect ratio w/e = 0.5, as observed in Figures 8(c) and 8(b). Moreover, maxima are attained at the same values of pitch, evaluated for f/f_s.

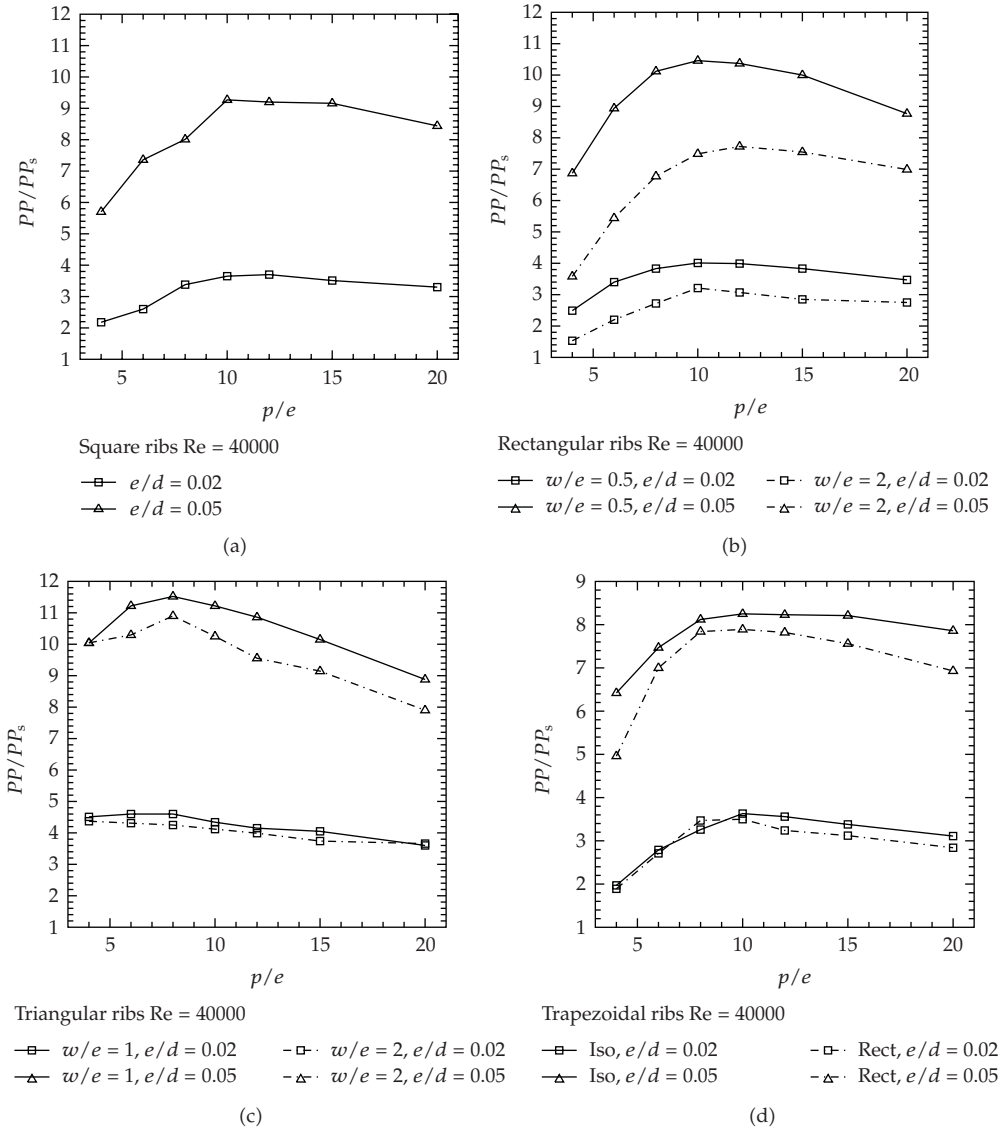

Figure 8: Required pumping power profiles, referred to the smooth channel results, as a function of p/e at Re = 40000, for $e/d = 0.02$ and 0.05: (a) square-ribs, (b) rectangular ribs with $w/e = 0.5$ and 2.0, (c) triangular ribs with $w/e = 1.0$ and 2.0, and (d) isosceles and rectangular trapezoidal ribs with $w/e = 2.0$.

PEC index is introduced in order to summarize the results and give a method to evaluate and compare the efficiency of different rough elements. As described in [3], it is defined as $\text{PEC} = (\text{Nu}_{\text{av}}/\text{Nu}_{\text{av},s})/(f/f_s)^{1/3}$. Results in terms of PEC index are reported in Figure 9, for Re = 40000, $e/d = 0.02$ and 0.05, and differently shaped turbulators. Profiles increase as Re decreases as well as e/d values. Maxima are attained near the pitches, where the maximum values of the average Nusselt number are observed, such as at $p/e = 6$ for the triangular turbulators and $p/e = 8$ for the other configurations. Although the triangular ribs exhibit the most significant losses, they show the highest values of PEC index as well. In fact, PEC is equal to 1.54 at $p/e = 6$ and $e/d = 0.02$ for the triangular ribs with $w/e = 2.0$ while the lowest values are detected for the rectangular ones with $w/e = 0.5$ (PEC = 1.04).

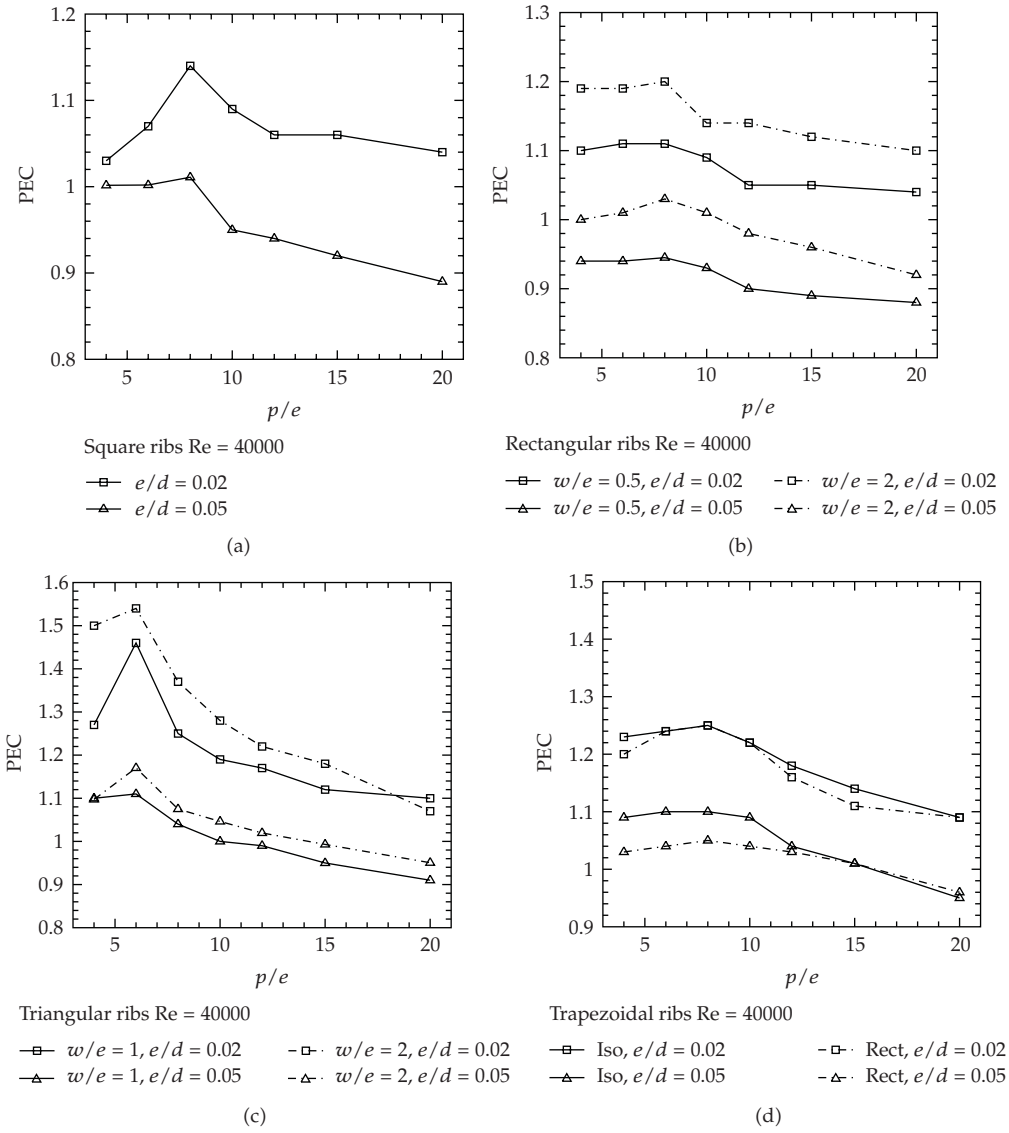

Figure 9: PEC index profiles as a function of p/e at Re = 40000, for $e/d = 0.02$ and 0.05: (a) square-ribs, (b) rectangular ribs with $w/e = 0.5$ and 2.0, (c) triangular ribs with $w/e = 1.0$ and 2.0, and (d) isosceles and rectangular trapezoidal ribs with $w/e = 2.0$.

The dependence on Reynolds number of average Nusselt number and friction factor is presented in Figure 10. Results are given at $e/d = 0.05$ in the range of Reynolds numbers from 20000 to 60000 in correspondence with significant p/e ratios. Average Nusselt number grows linearly as Reynolds number increases for all the considered configurations, as shown in Figure 10(a). The most significant thermal behavior is provided by the triangular ribbed channel with $w/e = 2.0$ while the lowest average Nusselt numbers are detected for the rectangular ribbed case with $w/e = 2.0$. At Re = 20000 average Nusselt number is at least 1.8 times greater than the value calculated for the smooth channel while, for the most improved configuration, a growth of about 2.6 times is calculated. In Figure 10(b) it is noticed that at

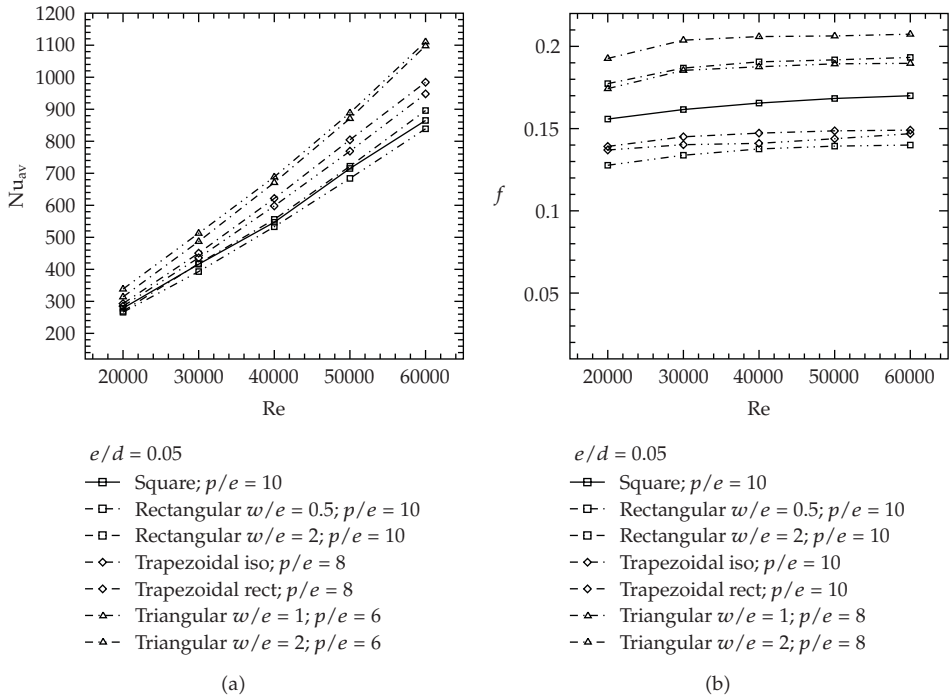

Figure 10: Profiles as a function of Reynolds numbers in the range 20000–60000 at $e/d = 0.05$ for different rib shapes and significant pitches: (a) average Nusselt number and (b) friction factor.

low velocities the friction factor coefficient tends to increase as Reynolds number increases rapidly until Re = 40000. From this value of Re, the profile seems to tend to an asymptotic, constant value, termed *fully rough condition*, which depends on the height of the roughness. The introduction of the ribbed elements in the channel yields to higher friction factor. The highest values are evaluated for the triangular shape with $w/e = 1.0$ while the lowest are detected for the rectangular shape with $w/e = 2.0$ and for trapezoidal ones. At Reynolds number equal to 60000 the friction factor is 7 times greater than the value referred to the smooth duct at least and 18 times at most.

The required pumping power increases more than linearly as Reynolds number increases as depicted in Figure 11(a); furthermore, it is equal to about 13 times greater than the smooth channel one at most and 8.5 times at least at Re = 60000, as shown in Figure 11(b).

Figures 12 and 13 depict the flow pattern in the interrib region at Re = 20000 and 60000 for different shapes, such as square, rectangular with $w/e = 0.5$, triangular with $w/e = 1.0$ and trapezoidal ones, in order to clearly show the eddy formation, adjacent to the rib when the flow is stabilized for small pitches. The stabilization happens after 4-5 ribs, such as when the vortex structures tend to repeat almost similarly from this zone. Figure 12(a) refers to the behavior at lower pitch ratio ($p/e < 6$) for a square-ribbed channel at Re = 20000 and 50000. It exhibits a *d-type* roughness behavior: a single eddy is trapped between adjacent ribs and hinders the heat transfer. As a result, the outer flow is relatively disturbed by the roughness elements. The letter d denotes the significant length scale, linked to the boundary layer thickness, channel hydraulic diameter or channel height. Pressure drops are relatively high and the heat transfer enhancement low. A similar behavior is detected for the other shapes ribs as shown in Figure 13(a) where it is clear that the flow difficultly penetrates into

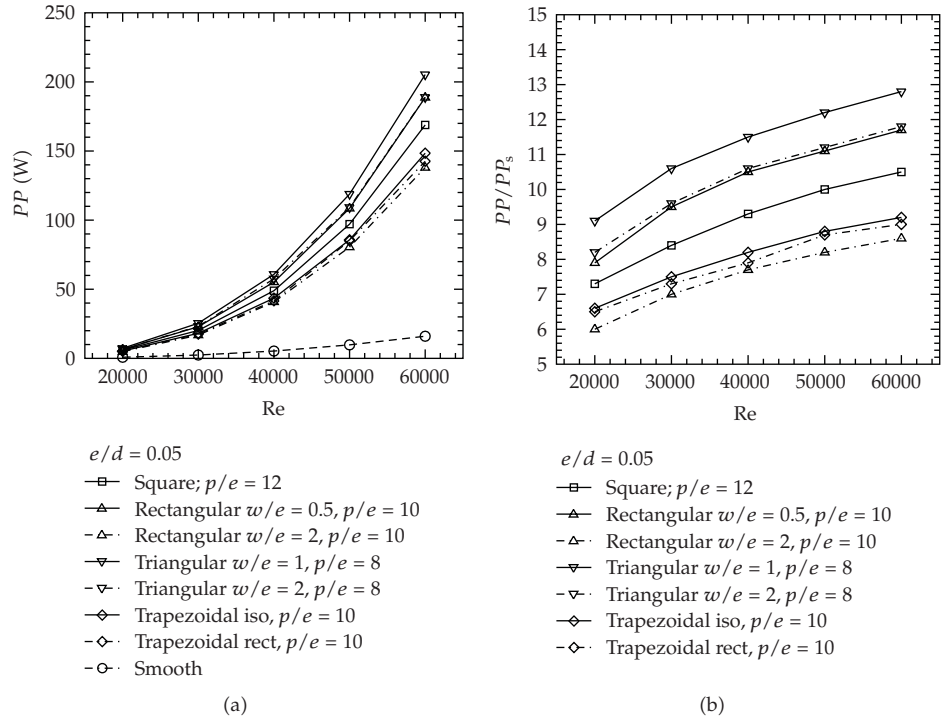

Figure 11: Profiles as a function of Reynolds numbers in the range 20000–60000 at $e/d = 0.05$ for different rib shapes and significant pitches: (a) required pumping power and (b) pumping power referred to the smooth channel results.

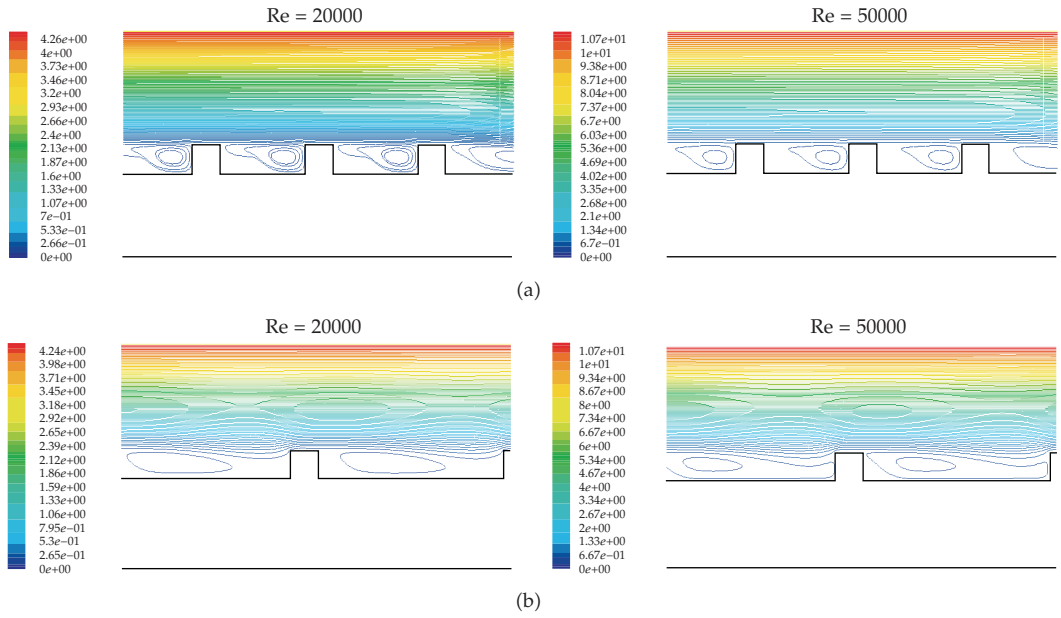

Figure 12: Stream function contours at Re = 20000 and 50000, for square-ribs, $e/d = 0.05$: (a) $p/e = 4$ and (b) $p/e = 8$.

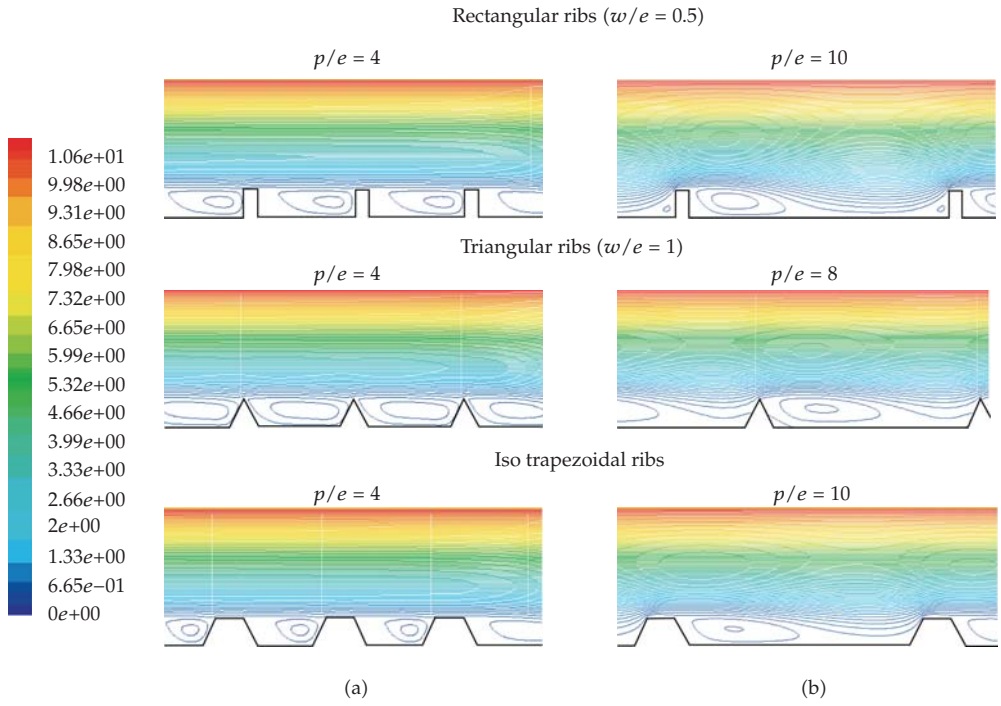

Figure 13: Stream function contours at Re = 50000 and different significant pitches, for square, rectangular ($w/e = 0.5$), triangular ($w/e = 1.0$) and *iso* trapezoidal ribs, $e/d = 0.05$: (a) *d-type* behavior and (b) *k-type* behaviour.

the cell between two adjacent ribs also for Re = 50000, except for the triangular elements in which the entrapment of fluid, due to the adjacent turbulators, is lower. Moreover, vortex intensity augments as Re and e/d ratio increase as described in Figures 12(a) and 12(b).

Figures 12(b) and 13(b) depict the stream function contours for square-ribs at Re = 20000 and 50000 and rectangular ($w/e = 0.5$), triangular ($w/e = 1.0$) and *iso* trapezoidal ones at Re = 50000, respectively, for $p/e > 6$. They clarifies the *k-type* roughness behavior: the value of p/e increases and the stream functions change; the y-velocity gradient reduces along the fluid direction and the flow separates then it reattaches after six-to-eight rib heights downstream from the turbulators. Near this point, the Nusselt number is expected to be maximum as well as the friction factor. The length scale for *k-type* is the roughness height and the eddies penetrate into the bulk flow toward boundary layer, promoting a more intense turbulent mixing.

Figure 14 reports the dimensionless temperature fields for significant pitches at Re = 50000 for the configuration with square, rectangular ($w/e = 0.5$), triangular ($w/e = 2.0$), *iso* and *rect* trapezoidal ribs, characterized by $e/d = 0.05$. Dimensionless temperature, T^*, is defined by the following relation:

$$T^* = \frac{(T - T_{m,\text{in}})}{(T_{m,\text{out}} - T_{m,\text{in}})}. \tag{5.1}$$

Figure 14 depicts the temperature field for square-ribs, typically observed for configurations, characterized by a *d-type* behaviour since the value of p/e is equal to 4, and *k-type* one for

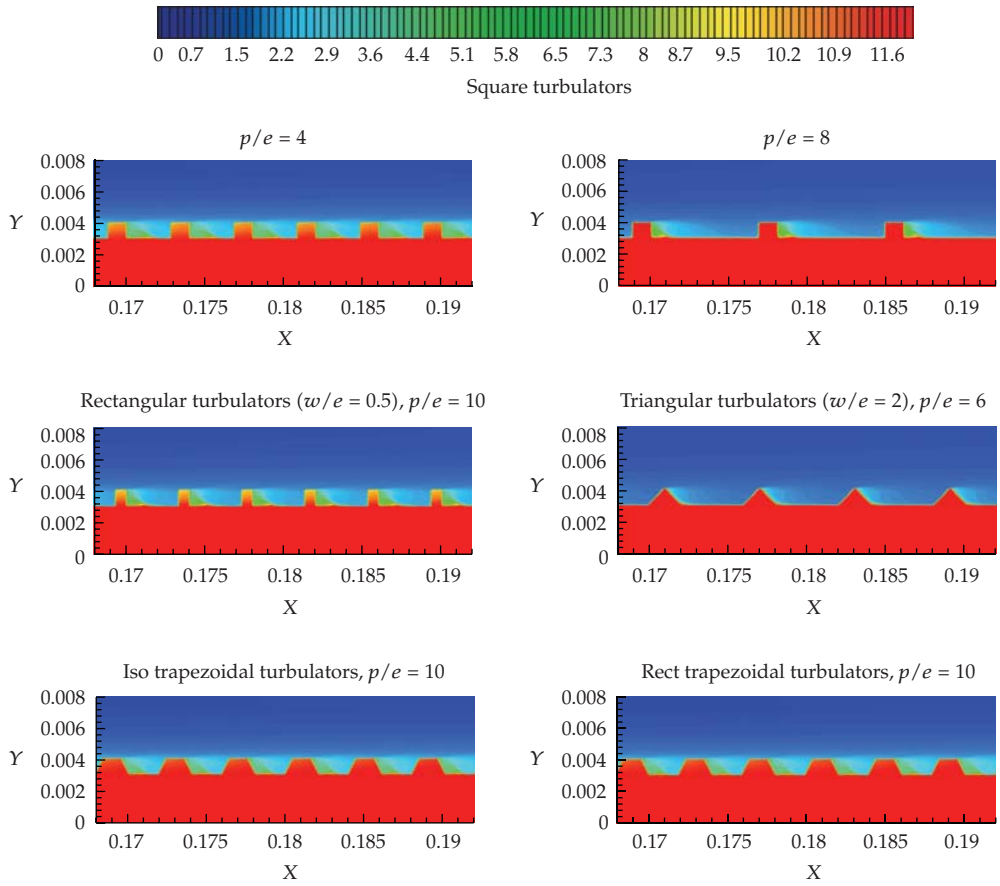

Figure 14: Temperature fields at Re = 50000 and different significant pitches, for square, rectangular (w/e = 0.5), triangular (w/e = 2.0) and trapezoidal ribs, e/d = 0.05.

p/e = 8. In the figure on the left, the fluid temperature is very high near the rib-wall juncture behind the turbulator but the fluid in the core region is poorly influenced, because of the recirculation entrapped into the interrib zone. For p/e = 8, such as for a configuration which exhibits a *k-type* behaviour, the mixing effects are stronger and the average temperature also in the core region is higher; as a result, the difference between the average temperature of fluid and wall decreases and the heat transfer mechanism becomes more efficient, as also described for the rectangular shape (w/e = 0.5) at p/e = 10, *iso* and *rect* trapezoidal turbulators at p/e = 10. The triangular elements show the best thermal performances also for low values of pitches in comparison with the other shapes, such as at p/e = 6; in fact, low values of p/e does not badly affect the heat transfer mechanism, because of water conductivity and rough element geometry, as noticed for the other shapes of turbulators. Moreover, figures show that the temperature is lowest on the windward face of the rib, and highest on the leeward face, while heat flux is highest on the front face and lowest on the back face.

6. Conclusions

In this paper, a ribbed channel with square, rectangular, triangular, and trapezoidal turbulators, characterized by different geometric ratios and heights has been analyzed by means

of FLUENT code. The external walls are heated by a constant heat flux and the flow regime is turbulent. The aim of the investigation consists into find out the optimal pitch of ribs at different Reynolds number, between 20000 and 60000, in order to ensure the maximum heat transfer rate and contain losses.

Simulations show that maximum average Nusselt numbers are detected in correspondence with p/e ratio equal to 6, 8, and 10, for triangular, square, rectangular and trapezoidal ribs, respectively. The average Nusselt number values increase as Reynolds number and e/d grow and they are at most equal to 2.6 times greater than the smooth channel results. Furthermore, the friction factor is the highest at $p/e = 10$ for the rectangular, trapezoidal and square-ribs while the triangular ones show the maximum values at $p/e = 8$; it increases as Re and e/d increases as well as the required pumping power. For Re > 40000 an asymptotic behavior is detected. The most significant thermal performances are provided by triangular ribs with $w/e = 2.0$, while the weakest ones are detected for the rectangular shape with $w/e = 2.0$, which present the lowest friction factor values, on the other hand. Finally, temperature fields and stream function contours are given in order to visualize the temperature distribution and flow pattern in presence of *d-type* and *k-type* roughness behavior also for triangular ribs.

Nomenclature

A: Cross section area (m^2)
a: Thermal diffusivity (m^2/s)
c_p: Specific heat (J/kgK)
e: Rib height (m)
f: Friction coefficient (Equation (3.3))
H: Channel height (m)
h: Heat transfer coefficient (W/m^2K)
L: Channel length (m)
Nu: Nusselt number (Equation (3.2))
P: Pressure (Pa)
p: Rib pitch (m)
PP: Pumping power (W)
Pr = ν/a: Prandtl number
q: Heat flux (W/m^2)
Re: Reynolds number (Equation (3.1))
s: Duct thickness (m)
T: Temperature (K)
u: Velocity component (m/s)
W: channel width (m)
w: Rib width (m)
x, y: Spatial coordinates (m).

Greek Symbols

λ: Thermal conductivity (W/mK)
μ: Dynamic viscosity (Pa s)
ρ: Density (kg/m^3)

d: Hydraulic diameter (m)
σ: Turbulent Prandtl number
τ: Wall shear stress (kg/m)
ν: kinematic viscosity (m^2/s).

Subscripts

a: Ambient
av: Average
f: Fluid
i, j: Components
in: Inlet section
m: Mass
out: Outlet section
s: Smooth
sl: Solid
t: Turbulent
w: Wall.

Acknowledgment

This work was supported by SUN with a 2008 Grant and by MIUR with Articolo D.M. 593/2000 Grandi Laboratori "EliosLab".

References

[1] A. E. Bergles, W. M. Rohsenow, J. P. Hartnett, and E. Ganie, *Techniques to Augment Heat Transfer, Handbook of Heat Transfer Application*, McGraw Hill, New York, NY, USA, 1985.

[2] A. E. Bergles, "Some perspective on enhanced heat transfer—second-generation heat transfer technology," *Journal of Heat Transfer*, vol. 110, no. 4, pp. 1082–1096, 1988.

[3] R. L. Webb and N. H. Kim, *Principles of Enhanced Heat Transfer*, Taylor & Francis, New York, NY, USA, 2nd edition, 2005.

[4] R. L. Webb, "Advances in shell side boiling of refrigerants," *Proceedings of the Institute of Refrigeration*, vol. 87, pp. 75–86, 1990.

[5] R. L. Webb and G. F. Robertson, "Shell-side evaporators and condensers used in the refrigeration industry," in *Heat Transfer Equipment Design*, R. K. Shah, E. C. Subbarao, and R. A. Mashelkar, Eds., pp. 559–570, Hemisphere Pub. Corp., Washington, DC, USA, 1988.

[6] H. M. Jaber, R. L. Webb, and P. Stryker, "Experimental investigation of enchanced tubes for steam condensers," in *National Heat Transfer Conference*, pp. 1–8, July 1991.

[7] B. Sunden and G. Xie, "Gas turbine blade tip heat transfer and cooling: a literature survey," *Heat Transfer Engineering*, vol. 31, no. 7, pp. 527–554, 2010.

[8] K. B. Muluwork, S. C. Solanky, and J. S. Saini, "Study of heat transfer and friction in solar air heaters roughened with staggered discete ribs," in *Proceedings of the 4th ISHMT-ASME Heat and Mass Transfer Conference*, pp. 391–398, Pune, India, 2000.

[9] R. Karwa, S. C. Solanki, and J. S. Saini, "Thermo-hydraulic performance of solar air heaters having integral chamfered rib roughness on absorber plates," *Energy*, vol. 26, no. 2, pp. 161–176, 2001.

[10] C. Thianpong, T. Chompookham, S. Skullong, and P. Promvonge, "Thermal characterization of turbulent flow in a channel with isosceles triangular ribs," *International Communications in Heat and Mass Transfer*, vol. 36, no. 7, pp. 712–717, 2009.

[11] R. Kamali and A. R. Binesh, "The importance of rib shape effects on the local heat transfer and flow friction characteristics of square ducts with ribbed internal surfaces," *International Communications in Heat and Mass Transfer*, vol. 35, no. 8, pp. 1032–1040, 2008.

[12] D. Giupta, *Investigations on fluid flow and heat transfer in solar air heaters with roughened absorbers*, Ph.D. thesis, University of Roorkee, India, 1993.

[13] R. Karwa, S. C. Solanki, and J. S. Saini, "Heat transfer coefficient and friction factor correlations for the transitional flow regime in rib-roughened rectangular ducts," *International Journal of Heat and Mass Transfer*, vol. 42, no. 9, pp. 1597–1615, 1999.

[14] T. M. Liou and J. J. Hwang, "Turbulent heat transfer augmentation and friction in periodic fully developed channel flows," *Journal of Heat Transfer*, vol. 114, no. 1, pp. 56–64, 1992.

[15] T.-M. Liou and J.-J. Hwang, "Effect of ridge shapes on turbulent heat transfer and friction in a rectangular channel," *International Journal of Heat and Mass Transfer*, vol. 36, no. 4, pp. 931–940, 1993.

[16] G. Tanda, "Heat transfer in rectangular channels with transverse and V-shaped broken ribs," *International Journal of Heat and Mass Transfer*, vol. 47, no. 2, pp. 229–243, 2004.

[17] C. K. Lee and S. A. Abdel-Moneim, "Computational analysis of the heat transfer in turbulent flow past a horizontal surface with two-dimensional ribs," *International Communications in Heat and Mass Transfer*, vol. 28, no. 2, pp. 161–170, 2001.

[18] J. Nikuradse, "Laws of Flow in Rough Pipes," National Advisory Committee for Aeronautics Technical Memorandum 1292, 1950.

[19] D. F. Dipprey and R. H. Sabersky, "Heat and momentum transfer in smooth and rough tubes at various prandtl numbers," *International Journal of Heat and Mass Transfer*, vol. 6, no. 5, pp. 329–353, 1963.

[20] R. L. Webb, E. R. G. Eckert, and R. J. Goldstein, "Heat transfer and friction in tubes with repeated-rib roughness," *International Journal of Heat and Mass Transfer*, vol. 14, no. 4, pp. 601–617, 1971.

[21] B. K. Lee, N. H. Cho, and Y. D. Choi, "Analysis of periodically fully developed turbulent flow and heat transfer by k-ε equation model in artificially roughened annulus," *International Journal of Heat and Mass Transfer*, vol. 31, no. 9, pp. 1797–1806, 1988.

[22] B. Arman and T. J. Rabas, "Disruption share effects on the performance of enhanced tubes with the separation and reattachment mechanism," in *Proceedings of the 28th National Heat Transfer Conference and Exhibition*, pp. 67–75, August 1992.

[23] S. Acharya, S. Dutta, T. A. Myrum, and R. S. Baker, "Periodically developed flow and heat transfer in a ribbed duct," *International Journal of Heat and Mass Transfer*, vol. 36, no. 8, pp. 2069–2082, 1993.

[24] R. Manceau, S. Parneix, and D. Laurence, "Turbulent heat transfer predictions using the $\overline{v^2}$-f model on unstructured meshes," *International Journal of Heat and Fluid Flow*, vol. 21, no. 3, pp. 320–328, 2000.

[25] G. Iaccarino, A. Ooi, P. A. Durbin, and M. Behnia, "Conjugate heat transfer predictions in two-dimensional ribbed passages," *International Journal of Heat and Fluid Flow*, vol. 23, no. 3, pp. 340–345, 2002.

[26] D. K. Tafti, "Evaluating the role of subgrid stress modeling in a ribbed duct for the internal cooling of turbine blades," *International Journal of Heat and Fluid Flow*, vol. 26, no. 1, pp. 92–104, 2005.

[27] A. Slanciauskas, "Two friendly rules for the turbulent heat transfer enhancement," *International Journal of Heat and Mass Transfer*, vol. 44, no. 11, pp. 2155–2161, 2001.

[28] T. M. Liou, J. J. Hwang, and S. H. Chen, "Simulation and measurement of enhanced turbulent heat transfer in a channel with periodic ribs on one principal wall," *International Journal of Heat and Mass Transfer*, vol. 36, no. 2, pp. 507–517, 1993.

[29] G. Rau, M. Çakan, D. Moeller, and T. Arts, "The effect of periodic ribs on the local aerodynamic and heat transfer performance of a straight cooling channel," *Journal of Turbomachinery*, vol. 120, no. 2, pp. 368–375, 1998.

[30] L. Wang and B. Sundén, "Experimental investigation of local heat transfer in a square duct with various-shaped ribs," *Heat and Mass Transfer/Waerme- und Stoffuebertragung*, vol. 43, no. 8, pp. 759–766, 2007.

[31] S. W. Ahn, "The effects of roughness types on friction factors and heat transfer in roughened rectangular duct," *International Communications in Heat and Mass Transfer*, vol. 28, no. 7, pp. 933–942, 2001.

[32] D. N. Ryu, D. H. Choi, and V. C. Patel, "Analysis of turbulent flow in channels roughened by two-dimensional ribs and three-dimensional blocks. Part I: resistance," *International Journal of Heat and Fluid Flow*, vol. 28, no. 5, pp. 1098–1111, 2007.

[33] D. N. Ryu, D. H. Choi, and V. C. Patel, "Analysis of turbulent flow in channels roughened by two-dimensional ribs and three-dimensional blocks. Part II: heat transfer," *International Journal of Heat and Fluid Flow*, vol. 28, no. 5, pp. 1112–1124, 2007.
[34] A. Chaube, P. K. Sahoo, and S. C. Solanki, "Analysis of heat transfer augmentation and flow characteristics due to rib roughness over absorber plate of a solar air heater," *Renewable Energy*, vol. 31, no. 3, pp. 317–331, 2006.
[35] O. Manca, S. Nardini, and D. Ricci, "Numerical investigation of air forced convection in channels with differently shaped transverse ribs," *International Journal of Numerical Methods for Heat and Fluid Flow*, vol. 21, no. 5, 2010.
[36] Fluent corporation, "Fluent v6.3 user guide," 2006.
[37] F. R. Menter, "Two-equation eddy-viscosity turbulence models for engineering applications," *AIAA journal*, vol. 32, no. 8, pp. 1598–1605, 1994.
[38] W. M. Rohsenow, J. P. Hartnett, and Y. I. Cho, *Handbook of Heat Transfer*, McGraw-Hill, New York, NY, USA, 3rd edition, 1998.
[39] F. P. Incropera, P. D. Witt, T. L. Bergman, and A. S. Lavine, *Fundamentals of Heat and Mass Transfer*, John Wiley & Sons, Hoboken, NJ, USA, 5th edition, 2007.

Hindawi Publishing Corporation
Journal of Applied Mathematics
Volume 2011, Article ID 190371, 8 pages
doi:10.1155/2011/190371

Research Article

Numerical Simulation of Solid Tumor Blood Perfusion and Drug Delivery during the "Vascular Normalization Window" with Antiangiogenic Therapy

Jie Lv,[1] Jin-feng Cao,[1] Yan Cai,[1] Yu Zhou,[1] Quan Long,[2] Wei Yao,[1] and Shi-xiong Xu[1]

[1] *Department of Mechanics and Engineering Science, Fudan University, Shanghai 200433, China*
[2] *Brunel Institute for Bioengineering, Brunel University, Middlesex, Uxbridge UB8 3PH, UK*

Correspondence should be addressed to Shi-xiong Xu, xusx@hotmail.com

Received 19 January 2011; Revised 1 March 2011; Accepted 31 March 2011

Academic Editor: Jürgen Geiser

Copyright © 2011 Jie Lv et al. This is an open access article distributed under the Creative Commons Attribution License, which permits unrestricted use, distribution, and reproduction in any medium, provided the original work is properly cited.

To investigate the influence of vascular normalization on solid tumor blood perfusion and drug delivery, we used the generated blood vessel network for simulations. Considering the hemodynamic parameters changing after antiangiogenic therapies, the results show that the interstitial fluid pressure (IFP) in tumor tissue domain decreases while the pressure gradient increases during the normalization window. The decreased IFP results in more efficient delivery of conventional drugs to the targeted cancer cells. The outcome of therapies will improve if the antiangiogenic therapies and conventional therapies are carefully scheduled.

1. Introduction

Angiogenesis, the growth of a network of blood vessels, plays a significant role in tumor's growth, invasion, and metastasis. Therefore, blocking angiogenesis could be a strategy for arresting tumor growth [1]. As the features of angiogenesis inhibitors are of low toxicity and have less acquired resistance, it comes to a new strategy to suppress tumor growth by restraining angiogenesis. The widely held view is that the antiangiogenic therapies can destroy the tumor vasculature, thereby depriving the tumor of oxygen and nutrients. When administered as single agents, antiangiogenic therapies have produced modest objective responses in clinical trials, but they have not obtained a long-term effect. However, several preclinical and clinical studies have shown that antiangiogenic therapies

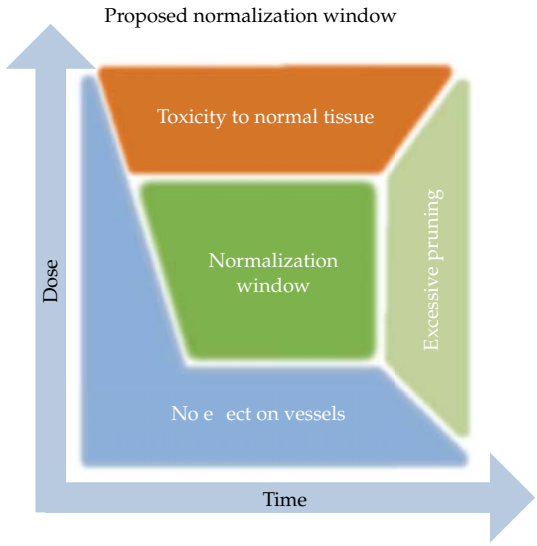

Figure 1: Proposed effect of drug dose and schedule on tumor vasculature normalization window [2].

improve the outcome of cytotoxic therapies. This is paradoxical. Based on that, Jain [2] proposed a new hypothesis that the antiangiogenic therapies can transiently "normalize" the abnormal structure and function of tumor vascular and microenvironment (Figure 1). There is a "vasculature normalization window" during antiangiogenic therapy. This view has been supported by clinical data.

The vasculature of solid tumors is structurally and functionally different from normal blood vessels [3]. They are leaky, tortuous, dilated, and saccular. Branches are irregular, and vessel diameters are uneven. In addition, the vessel wall has abnormal structure. The endothelial cells have aberrant morphology. They are loosely attached, and usually there are gaps. The basement membrane has diverse thickness with broken or missing pieces.

In normal tissues, interstitial fluid pressure (IFP) is close to zero; however, IFP is elevated in tumors in patients. The high IFP poses a strong barrier to the delivery of drugs into tumors and interstitium [4]. There are two other characteristics of the abnormal tumor microenvironment—hypoxia and acidosis [5–7]. One of the main functions of vasculature system is to provide cells with nutrition and oxygen and take away the waste of metabolism at the same time. However, tumor vasculature does not have the same function. Hypoxia renders tumor cells resistant to both radiation and cytotoxic drugs. Meanwhile, the low PH value hindered the efficacy of therapies.

Above all of these show that if we could find a way to fix the abnormal tumor vasculature and microenvironment, we would improve the treatment of cancer. Jain [8] showed that antiangiogenic therapy could cause a transient "vascular normalization window" and decrease IFP by changing the tumor sizes, vascular hydraulic permeability, and/or the surface area per unit tissue volume of tumor vessels. Normalization of tumor vasculature and microenvironment results in more efficient delivery of conventional drugs to the targeted cancer cells. The outcome of therapies will improve if the antiangiogenic therapies and conventional therapies are carefully scheduled.

In recent years, several mathematical models used different approaches to improve the understanding of tumor hemodynamics. McDougall et al. (2002) [9] built a two-dimensional

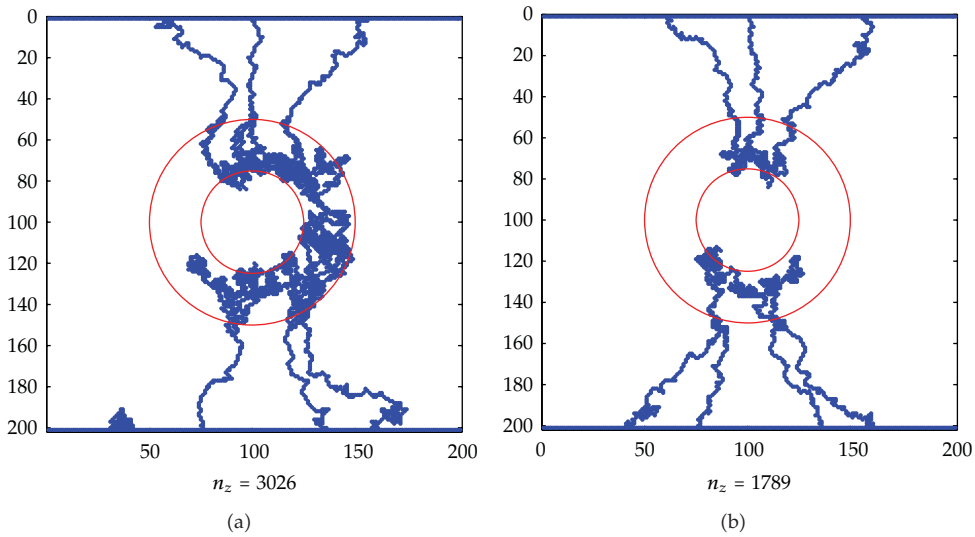

Figure 2: The vasculature for flow simulations; the blue lines on top and bottom of lattice represent the parent vessels, and the big red circle represents the tumor domain. (a) The tumor vasculature without antiangiogenesis therapy; (b) the tumor vasculature under antiangiogenesis therapy.

capillary network model to study nutrition, oxygen, and drugs transport to the tumor. Tee et al. (2004) [10] created a discrete model to simulate the drug delivery mode under endostatin and the effect on tumor angiogenesis caused by drug clearance. Our research group has done some related work. Gaiping et al. (2006) [11] built the network model under Endostatin using random discrete methods. Wu et al. (2009) [12] simulated tumor blood perfusion based on 3D angiogenic microvasculature. Here, we use 2D microvasculature built by the group before and simulate the blood perfusion and drug delivery during vasculature normalization.

2. Blood Perfusion during the "Vasculature Normalization Window"

We employ a mathematical model to show the effect of the kinetic parameters on tumor blood perfusion; detailed equations and numerical methods can be seen in [12].

In this paper, we used the vascular network generated by our group for the simulation, shown in Figure 2. The actual size is 4 mm × 4 mm, divided into 200 × 200 equally spaced grids. Tumor was located in the center of the region, with a radius of 1 mm. The surrounding is normal tissue, and two parent vessels are in the upper and lower bounds, respectively.

During the "vascular normalization window," several parameter values of microenvironment become close to normal tissues [13–16], such as L_p, K_P, S/V, $\sigma(\pi_v - \pi_i)$, and R. Here, L_p is the vascular wall permeability (cm/mmHgs), K_P is the interstitial hydraulic conductivity (cm^2/mmHgs), S/V is the surface area of vessel wall per unit volume of tissue (cm^{-1}), $\sigma(\pi_v - \pi_i)$ is oncotic pressure (mmHg), and R is the tumor radius. Our analysis suggests, however, that $\sigma(\pi_v - \pi_i)$ is much smaller than the value of normal tissues, even after antiangiogenic therapies. Consequently, oncotic pressure dose not significantly influence the tumor blood perfusion.

The simulation results are shown in Figure 3. We show here that vascular normalization can decrease tumor IFP in a number of ways. The maximum value of IFP dropped from 11.87 mmHg to 4.06 mmHg. Furthermore, the phenomenon of high interstitial pressure

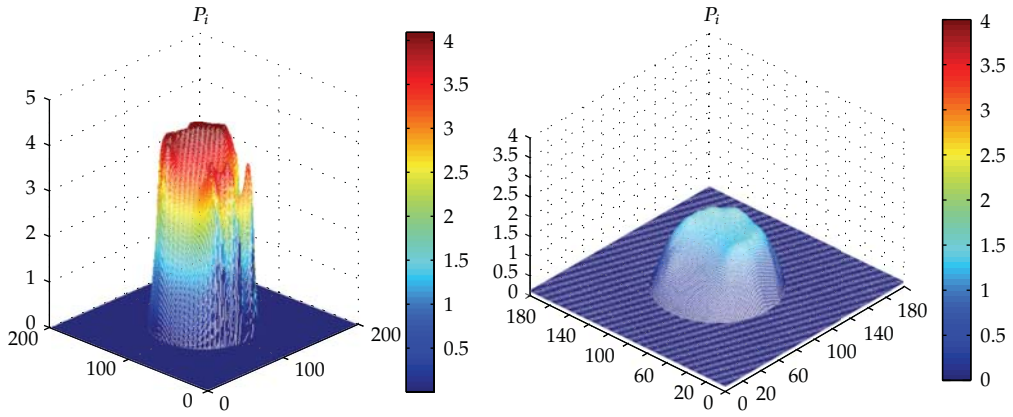

(a) before treatment (b) after treatment

Figure 3: The simulation results of blood perfusion. P_i is the interstitial fluid pressure (IFP).

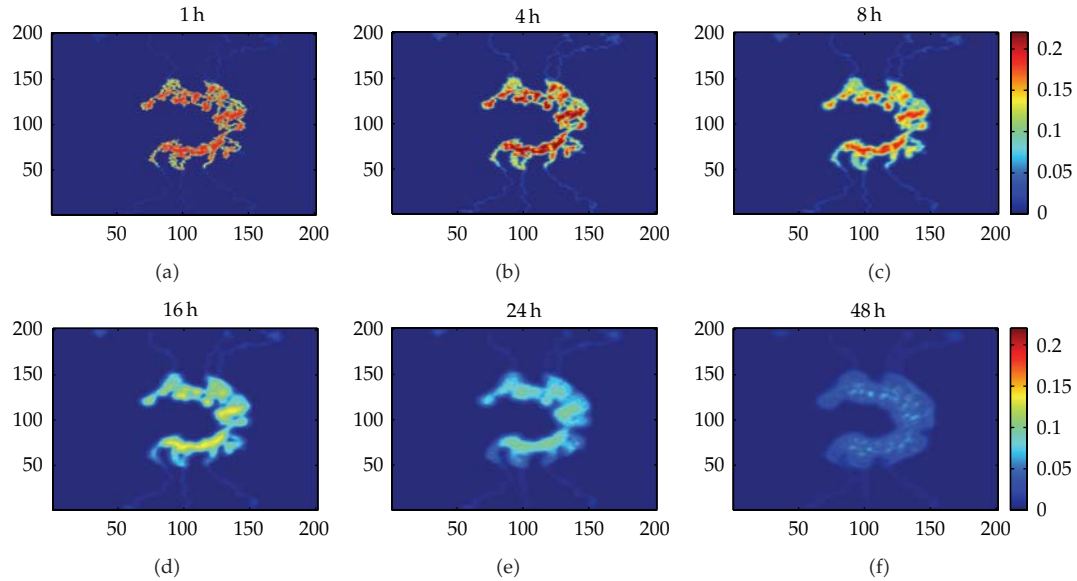

Figure 4: The simulation result of drug concentration before treatment.

gradient has been greatly improved, except that the boundary of the tumor still has a slightly higher pressure gradient. All of these will benefit the drug delivery and the outcome of conventional therapies.

3. Drug Delivery during Vascular Normalization

3.1. Mathematical Model

Drugs enter the circulatory system of human body and transport to the tumor microcirculation. To balance the plasma drug concentration is related to the systemic circulation.

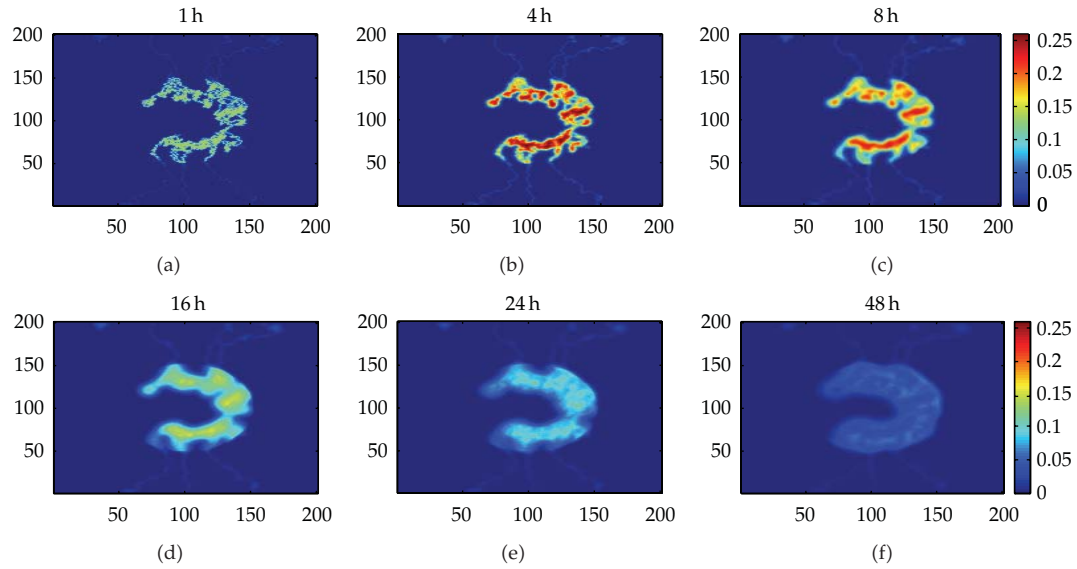

Figure 5: The simulation result of drug concentration after treatment.

Compared with the scale of the human body, the tumor is small. Therefore, the influence on plasma drug concentration reaching stable state can be neglected. In our model, drugs enter the interstitium through capillary walls. A part of the drugs in the interstitium are absorbed by lymphatic vessels as well as cleared by certain organs. The average drug concentrations in plasma (C_P) and in interstitium (C_e) are represented by the following equations:

$$\begin{aligned} \frac{dC_P(t)}{dt} &= -ke \cdot C_P(t) - K \cdot C_P + I(t), \\ \frac{dC_e(t)}{dt} &= K \cdot C_p(t) - L \cdot C_e(t). \end{aligned} \tag{3.1}$$

ke denotes drug clearance. K and L are transport coefficients from the plasma to the interstitium and from the interstitium to lymphatic vessels, respectively. $I(t)$ denotes the amount of drugs injected into plasma:

$$I(t) = \begin{cases} 1, t = 0, \\ 0, t > 0. \end{cases} \tag{3.2}$$

The initial conditions are given by

$$C_P(0) = 0, \qquad C_e(0) = 0. \tag{3.3}$$

After drugs enter the tumor, the interstitial flow influences the drug delivery as well as the diffusion effect. Here, we use the results of the blood perfusion descried before. Due to the

Table 1: Baseline parameter values used for drug delivery simulations [19–21]. Parameter values with superscripts "T," "N" represent the internal and external parameters of the tumor.

Parameter	Value	Parameter	Value
$ke(\mathrm{s}^{-1})$	1.33×10^{-4}	$P_{\mathrm{eff}}(10^{-6}\,\mathrm{cm/s})$	1.91^{N}
$K(10^{-10}\,\mathrm{cm}^3/\mathrm{s/M})$	1.566		14.9^{T}
$L(10^{-9}\,\mathrm{cm}^3/\mathrm{s/M})$	1.138	$D(10^{-8}\,\mathrm{cm}^2/\mathrm{s})$	1.2^{N}
β	0.1		4.4^{T}
$K_a(10^{-4}/\mathrm{M/s})$	0^{N}	K_d	0^{N}
	1.33^{T}		1.51^{T}

high IFP, the convection effect in the tumor can be ignored [17]. The concentration of drugs ($d(x,y,t)$) in the tumor satisfies the diffusion equation

$$\begin{aligned}
&\frac{\partial d(x,y,t)}{\partial t} + \nabla \cdot \left[R_f \vec{U}(x,y) d(x,y,t)\right] \\
&\quad = \nabla \cdot \left[D(x,y)\nabla d(x,y,t)\right] + \phi_s(x,y,t) - K_a \cdot d(x,y,t) \cdot \left[A_0 - d_B(x,y,t)\right] + K_d \cdot d_B(x,y,t) \\
&\frac{\partial d_B(x,y,t)}{\partial t} = K_a \cdot d(x,y,t) \cdot \left[A_0 - d_B(x,y,t)\right] - K_d \cdot d_B(x,y,t),
\end{aligned} \tag{3.4}$$

where R_f represents the relative velocity of drugs to the interstitial flow, $\vec{U}(x,y)$ is the velocity distribution of the flow and can be gotten from

$$\vec{U}(x,y) = -K_P \cdot \nabla P_i, \tag{3.5}$$

(see [12]). $D(x,y)$ denotes the diffusion coefficient of drugs, $d_B(x,y,t)$ is the concentration of antigen-binding drugs, K_a and K_d represent the association rate and dissociation rate with antigens, and $\phi_s(x,y,t)$ is the source term given by Kedem-Katchalsky equation [18]

$$\phi_s(x,y,t) = \Gamma(x,y) \cdot \left[C_p(t) - d(x,y,t)\right] \cdot A. \tag{3.6}$$

Here, A represents the generated vessel network, and $\Gamma(x,y)$ is the permeability across the capillary and is taken to be

$$\Gamma(x,y) = \beta \cdot P_{\mathrm{eff}} \cdot \frac{S}{V}, \tag{3.7}$$

where β is the corresponding coefficient and P_{eff} denotes the effective permeability coefficient.

To solve the mathematical model, we use the FTBS method. The boundary condition is set to be $d(x,y,t) = 0$ when the point (x,y) is not in the computational domain. The initial conditions are $d(x,y,0) = 0$ and $d_B(x,y,0) = 0$.

The parameter values for simulation are in Table 1.

4. Results and Discussion

In this paper, Figures 4 and 5 show the simulation results before and after antiangiogenic therapies. We choose six time points to see the drug distribution within two days after the injection. Figure 4 shows the uneven distribution of the concentration due to the blood vessel network. The concentration in the blood-vessel-rich region is higher. There are almost no vessels in the center, and the drug transports to this region only by diffusion. As a result, the concentration is relatively low. Without supplement, the concentration decreases as time goes. After four hours, the concentration gets smaller because of the drug clearance. Two days later, there are almost no drugs at all. The concentration of drug in solid tumor can be meliorated by normalization such as a lower IFP and a higher permeability. The drug delivery result in Figure 5 is much better, not only the maximum but also the area of drug distribution. Consequently it improves the outcome of chemotherapies.

In the paper, we ignore the change of the blood vessel network after antiangiogenic therapies. As a matter of fact, the structure, number, and distribution of the vasculature become different during the "vascular normalization window." In the further work, we will consider the factor. Besides, the sensitivity analysis of the parameters will be considered, so that we can elaborate on the effect of each parameter on the results. To do that, a quantitative measure should be defined to evaluate the effect of the antiangiogenic therapies, for example, the area covered by the drug.

The final goal of those combined therapies is to kill tumor cells, which makes it important to study how the tumor grows after therapies. Besides, studies have shown that antiangiogenesis-induced tumor cell starvation may enhance chemotherapeutic drug activity, despite a decrease in drug uptake. Balance can be found between them to improve the outcome of therapies if both are carefully scheduled.

Acknowledgment

The project was supported by the National Natural Science Foundation of China (10772751), Shanghai Leading Academic Discipline Project (B112).

References

[1] J. Folkman, "Therapeutic implications," *New England Journal of Medicine*, vol. 285, no. 21, pp. 1182–1186, 1971.

[2] R. K. Jain, "Normalization of tumor vasculature: an emerging concept in antiangiogenic therapy," *Science*, vol. 307, no. 5706, pp. 58–62, 2005.

[3] R. K. Jain, "Molecular regulation of vessel maturation," *Nature Medicine*, vol. 9, no. 6, pp. 685–693, 2003.

[4] R. K. Jain, "Barriers to drug delivery in solid tumors," *Scientific American*, vol. 271, no. 1, pp. 58–65, 1994.

[5] A. L. Harris, "Hypoxia: a key regulatory factor in tumor growth," *Nature Reviews Cancer*, vol. 2, no. 1, pp. 38–47, 2002.

[6] G. Helmlinger, F. Yuan, M. Dellian, and R. K. Jain, "Interstitial pH and pO_2 gradients in solid tumors in vivo: high-resolution measurements reveal a lack of correlation," *Nature Medicine*, vol. 3, no. 2, pp. 177–182, 1997.

[7] J. L. Tatum et al., "Hypoxia: importance in tumor bioglogy, noninvasive measurement by imaging, and value of its measurement in the management of cancer therapy," *International Journal of Radiation Biology*, vol. 82, no. 10, pp. 699–757, 2006.

[8] R. K. Jain, R. T. Tong, and L. L. Munn, "Effect of vascular normalization by antiangiogenic therapy on interstitial hypertension, peritumor edema, and lymphatic metastasis: insights from a mathematical model," *Cancer Research*, vol. 67, no. 6, pp. 2729–2735, 2007.

[9] S. R. McDougall, A. R. A. Anderson, M. A. J. Chaplain et al., "Mathematical modeling of flow through vascular network: implications for tumor-induced angiogenesis and chemotherapy strategies," *Bulletin of Mathematical Biology*, vol. 64, pp. 673–702, 2002.

[10] D. Tee and J. DiStefano III, "Simulation of tumor-induced angiogenesis and its response to anti-angiogenic drug treatment: mode of drug delivery and clearance rate dependencies," *Journal of Cancer Research and Clinical Oncology*, vol. 130, no. 1, pp. 15–24, 2004.

[11] Z. Gaiping, G. Hao, W. Jie et al., "2D numerical simulation of effect of antiangiogenic factors Angiostatin and Endostatin on tumor-induced angiogenesis," *Journal of Medical Biomechanics*, vol. 21, no. 4, pp. 272–279, 2006.

[12] J. Wu, Q. Long, S. Xu, and A. R. Oadhani, "Study of tumor blood perfusion and its variation due to vascular normalization by anti-angiogenic therapy based on 3D angiogenic microvasculature," *Journal of Biomechanics*, vol. 42, no. 6, pp. 712–721, 2009.

[13] B. Rippe and B. Haraldsson, "Capillary permeability in rat hindquaters as determined by estimations of capillary reflection coefficients," *Acta Physiologica Scandinavica*, vol. 127, no. 3, pp. 289–303, 1986.

[14] J. A. Tyrrell, V. Mahadevan, R. T. Tong, E. B. Brown, R. K. Jain, and B. Roysam, "A 2-D/3-D model-based method to quantify the complexity of microvasculature imaged by in vivo multiphoton microscopy," *Microvascular Research*, vol. 70, no. 3, pp. 165–178, 2005.

[15] R. T. Tong, Y. Boucher, S. V. Kozin et al., "Vascular normalization by vascular endothelial growth factor receptor 2 blockade induces a pressure gradient across the vasculature and improves drug penetration in tumors," *Cancer Research*, vol. 64, pp. 3731–3737, 2004.

[16] C. Jinfeng, L. Jie, Z. Hongyi et al., "Research on the effect of microenvironment of tumor blood perfusion under anti-angiogenesis therapy," *Progress in Biomedical Engineering*, vol. 3, pp. 125–130, 2010 (Chinese).

[17] R. K. Jain, "Determinants of tumor blood flow: a review," *Cancer Research*, vol. 48, no. 10, pp. 2641–2658, 1988.

[18] O. Kedem and A. Katchalsky, "Thermodynamic analysis of permeability of biological membranes to non-electrolytes," *Biochimica et Biophysica Acta*, vol. 27, no. C, pp. 229–246, 1958.

[19] L. T. Baxter and R. K. Jain, "Transport of fluid and macromolecules in tumors. I. Role of interstitial pressure and convection," *Microvascular Research*, vol. 37, no. 1, pp. 77–104, 1989.

[20] L. T. Baxter and R. K. Jain, "Transport of fluid and macromolecules in tumors. II. Role of heterogeneous perfusion and lymphatics," *Microvascular Research*, vol. 40, pp. 246–263, 1990.

[21] L. T. Baxter and R. K. Jain, "Transport of fluid and macromolecules in tumors. III. Role of binding and metabolism," *Microvascular Research*, vol. 41, no. 1, pp. 5–23, 1991.

Hindawi Publishing Corporation
Journal of Applied Mathematics
Volume 2011, Article ID 538637, 14 pages
doi:10.1155/2011/538637

Research Article

Simulation of Thermomagnetic Convection in a Cavity Using the Lattice Boltzmann Model

Mahshid Hadavand[1] and Antonio C. M. Sousa[1,2]

[1] *Department of Mechanical Engineering, University of New Brunswick, Fredericton, NB, Canada E3B 5A3*
[2] *Department of Mechanical Engineering, University of Aveiro, Aveiro 3810-193, Portugal*

Correspondence should be addressed to Antonio C. M. Sousa, asousa@unb.ca

Received 15 January 2011; Accepted 14 March 2011

Academic Editor: Shuyu Sun

Copyright © 2011 M. Hadavand and A. C. M. Sousa. This is an open access article distributed under the Creative Commons Attribution License, which permits unrestricted use, distribution, and reproduction in any medium, provided the original work is properly cited.

Thermomagnetic convection in a differentially heated square cavity with an infinitely long third dimension is numerically simulated using the single relaxation time lattice Boltzmann method (LBM). This problem is of considerable interest when dealing with cooling of microelectronic devices, in situations where natural convection does not meet the cooling requirements, and forced convection is not viable due to the difficulties associated with pumping a ferrofluid. Therefore, circulation is achieved by imposing a magnetic field, which is created and controlled by placing a dipole at the bottom of the enclosure. The magnitude of the magnetic force is controlled by changing the electrical current through the dipole. In this study, the effects of combined natural convection and magnetic convection, which is commonly known as "thermomagnetic convection," are analysed in terms of the flow modes and heat transfer characteristics of a magnetic fluid.

1. Introduction

Natural convection in enclosures is of interest in many engineering applications, such as the cooling of electronic equipment and solar energy collection, and it has been extensively studied experimentally and numerically by several researchers [1–4]. The enhancement of convective heat transfer in these devices is an active area of research. For small length-scale applications, such as the cooling of microelectronic devices, thermomagnetic convection has been identified as a viable approach for augmenting and controlling the convective heat transfer. This involves controlling the motion of colloidal suspensions containing magnetic nanoparticles, known as ferrofluids, using external magnetic fields [5, 6].

The study of flow and heat transfer characteristics of natural convection of a magnetic fluid has received considerable attention lately. Finlayson [7] in 1970 explained how an external magnetic field imposed on a ferrofluid with varying magnetic susceptibility, for

example, due to a temperature gradient, results in a nonuniform magnetic body force, which leads to thermomagnetic convection. This phenomenon is complex in nature, and so a thorough understanding of the relation between an applied magnetic field and the resulting heat transfer is necessary for the proper design and control of thermomagnetic devices [8].

The numerical studies of heat transfer with magnetic fluids reported in the literature are relatively scarce and invariably use as governing equations the Navier-Stokes and energy equations. In what follows, relevant work in the field is succinctly reviewed. Yamaguchi et al. [9] experimentally and numerically studied the heat transfer characteristics and flow behavior for natural convection of a magnetic fluid in a rectangular cavity under an imposed uniform vertical magnetic field. Al-Najem et al. [10] numerically calculated the flow and temperature fields under uniform magnetic field in a tilted square cavity with isothermal vertical walls and adiabatic horizontal walls at a low Prandtl number of 0.71 and demonstrated that the suppression effect of the magnetic field on convection currents and heat transfer is more significant for low inclination angles and high Rayleigh numbers. Krakov and Nikiforov [11] determined the influence of the angle between the direction of the temperature gradient and that of a uniform magnetic field on the convection structure and intensity of heat flux in a square cavity.

A few other researchers have considered spatially nonuniform magnetic fields for the experimental or numerical investigations but did not fully describe the variations in those fields [12–15]. For example, Sawada et al. [12] and Kikura et al. [13] experimentally investigated the influence of a varying magnetic field in a cubical enclosure and in concentric horizontal annuli, respectively, but the field gradient was only measured in a single direction. Moreover, the orientation of the magnetic field was not described. Hadavand et al. [16] simulated thermomagnetic convection in a cavity which was in close proximity to a line dipole. The imposed nonuniform magnetic field was considered only in one direction and the effect of temperature on the magnetic susceptibility was ignored. Ganguly et al. [8] performed a study to simulate thermomagnetic convection in a square enclosure by introducing a line dipole using a Navier-Stokes solver. The effect of temperature on the magnetic susceptibility was considered; because they used a very strong nonuniform magnetic field, the buoyancy was neglected in their simulation. They found that the average Nusselt number on the wall increases with increasing the magnetic dipole strength and temperature but decreases by increasing the fluid viscosity.

The magnetic control has enabled numerous developments dealing with technical and medical applications, and these suspensions are already being considered the next generation heat transfer fluids as they offer the possibility of achieving heat transfer rates much higher than those of conventional heat transfer fluids and fluids containing microsized metallic particles [17].

In the present work, the objective is to numerically study the effects of combined natural convection and magnetic convection in a square enclosure using the lattice Boltzmann method. The square enclosure is under the influence of an imposed nonuniform two-dimensional magnetic field that satisfies Maxwell's equations. The variation of the ferrofluid susceptibility with the temperature difference is considered in this study.

2. Physical Model

In the absence of an external magnetic field, the nanoparticles are oriented randomly in the ferrofluid; once the external magnetic field is applied, the nanoparticles align with the applied magnetic field. The generated force between the magnetic field and the homogenously

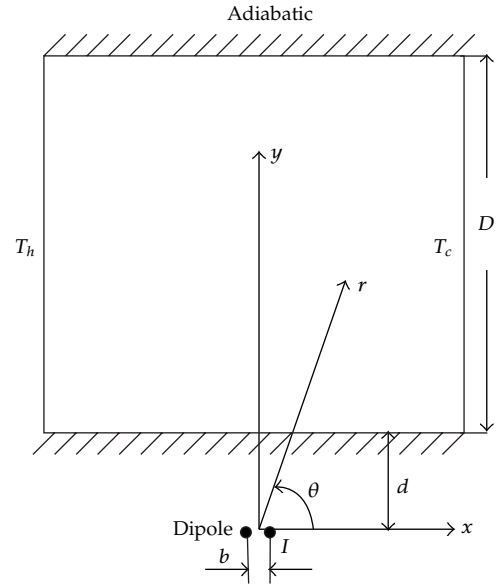

Figure 1: Schematic of the cavity and position of the line dipole magnet.

distributed magnetic nanoparticles enables the manipulation of the ferrofluid by adjusting the applied external magnetic field. This uniformly distributed magnetic force manifests itself as a body force analogous to the gravity field. These suspensions, in general, exhibit normal liquid behavior coupled with super paramagnetic properties. This leads to the possibility of controlling the properties and the flow of these liquids with relatively moderate magnetic field strengths. Each solid magnetic nanoparticle in the ferrofluid is covered with a dispersant material in order to keep the particles separated, and, in this way, preventing agglomeration of the particles due to gravity, coagulation, or an external magnetic field.

Figure 1 presents a schematic of the enclosure used for the numerical simulation, which has height D and its vertical walls are at constant, but different, temperatures. The third dimension is considered to be infinite; therefore, the flow in this configuration can be assumed to be two-dimensional. The left and right vertical walls are at constant high temperature, T_h, and constant low temperature, T_c, respectively. The upper and lower walls are adiabatic. A line dipole, which provides the external magnetic field, is placed adjacent to the lower adiabatic wall at a distance d. The magnetic field is governed by the Maxwell relations in static form [18], as follows:

$$\begin{aligned} \nabla \cdot B &= 0, \\ \nabla \times H &= 0, \end{aligned} \tag{2.1}$$

where B is the magnetic field inside the ferrofluid due to the line dipole which can be expressed as follows [8]:

$$B = \mu_0(1+\chi)m\left[\frac{\sin\theta}{r^2}e_r - \frac{\sin\theta}{r^2}e_\theta\right], \tag{2.2}$$

where H and B are related through the following equation:

$$H = \frac{1}{\mu_0(1+\chi)}B, \tag{2.3}$$

where μ_0 is the magnetic permeability of free space, $\mu_0 = 4\pi \times 10^{-7}(\mathrm{N/A^2})$; m denotes the magnetic dipole moment of the electromagnet coil (having two parallel counter-conductors separated by a distance b and carrying current I) per unit length ($m = Ib/2\pi$). The magnetic fluid susceptibility, χ, varies with temperature as follows:

$$\chi = \frac{\chi_0}{1+\beta(T-T_0)}, \tag{2.4}$$

where T_0 is the reference temperature and χ_0 is the magnetic field susceptibility at reference temperature.

The magnetization of the ferrofluid occurs when it becomes polarized in the presence of an external magnetic field. Consequently, attractive forces acting on each particle are produced due to the interaction of the ferrofluid polarization and the external magnetic field. The attractive force acting on the particles can then be treated as a body force acting on the ferrofluid, which is dealt with as a homogenous medium. The attractive force on the ferrofluid per unit volume is

$$F = (M \cdot \nabla)B, \tag{2.5}$$

where M is the magnetization vector and is related to H by $M = \chi H$. The magnetic field strength diminishes with increasing distance from the dipole. The Kelvin body force, see (2.5), can be written as follows:

$$F = \mu_0\chi(1+\chi)(H\cdot\nabla)H = \frac{1}{2}\mu_0\chi(1+\chi)\nabla(H\cdot H) + \mu_0\chi H(H\cdot\nabla\chi). \tag{2.6}$$

The first term on the right-hand side of (2.6) has a same nature as the pressure term in the momentum equation. The second term becomes important when there is a spatial gradient in the fluid susceptibility. In the absence of a temperature gradient, this term is zero. The Kelvin body force is simplified in another study [19] to the following format by defining an effective pressure as

$$P^* = P - \frac{\mu_0\chi_0}{2}H^2, \tag{2.7}$$

and it yields

$$F = \frac{1}{2}\mu_0\chi_0\left[1-\beta(T-T_0)\right]\nabla(H\cdot H) + \mu_0\chi_0^2\,\beta(H\cdot\nabla T)H. \tag{2.8}$$

In this work, the single relaxation time lattice Boltzmann method is used to simulate the thermomagnetic convection in a two-dimensional square enclosure.

3. Numerical Model

The lattice Boltzmann method (LBM) is a discrete particle-based mesoscopic approach for viscous fluid flow simulation. The LBM has been shown to be an efficient tool for flow simulation in complex geometries, when compared with conventional fluid dynamics approaches [20]. In this method, finite volumes of fluid are presented as discrete particles and the fluid dynamics is obtained based on a probability distribution function of the particles and a discrete set of prescribed velocities.

The thermal lattice Boltzmann model, which is employed in the present work, is a double-distribution-function thermal model. Two distinct distribution functions for the flow and temperature fields are f and g, respectively, where f is the density (or fluid particles) distribution function and g is the temperature distribution function. This present thermal lattice Boltzmann model uses the BGK approximation [21] and it is based on the work of He et al. [22] and Shi et al. [23]:

$$\begin{aligned} f_i(x + c_i\delta t, t + \delta t) - f_i(x,t) &= -\frac{\delta t}{\tau_v}\left[f_i(x,t) - f_i^{\mathrm{eq}}(x,t)\right] + f_g + F, \\ g_i(x + c_i\delta t, t + \delta t) - g_i(x,t) &= -\frac{\delta t}{\tau_c}\left[g_i(x,t) - g_i^{\mathrm{eq}}(x,t)\right], \end{aligned} \tag{3.1}$$

where δx and δt are the lattice grid spacing and the lattice time step, respectively. These two are related to each other through the streaming speed, c, as $c = \delta x/\delta t$. However, in most of the LBM simulations on a uniform lattice, including those of the present work, δx and δt for simplicity are considered to be equal to one, and f_g is the buoyant body force term, which is formulated by using the Boussinesq approximation [24], namely:

$$f_g = 3\omega_i\beta\rho g_y(T - T_{\mathrm{ave}})c_{iy}, \tag{3.2}$$

where β is the thermal expansion coefficient, g_y is the acceleration of gravity acting in the y-direction of the lattice links, and c_{iy} is the y-component of c_i. The terms ρ and T are the local density and temperature and are calculated at each lattice site. T_{ave} is the average temperature of hot and cold wall. The Kelvin body force, F, is the force that a magnetic fluid experiences in nonuniform magnetic field that can be calculated based on (2.5).

The most common two-dimensional lattice is the D2Q9 lattice, which is used in this study, where "2" denotes the number of space dimensions and "9" refers to the discrete set of nine velocities as proposed by Qian et al. [25]. The D2Q9 lattice and its labelling for the lattice directions are shown in Figure 2. For the D2Q9 lattice, the discrete velocity set is formulated as follows:

$$\begin{aligned} c_i &= c\left[\cos\left(\frac{(i-1)\pi}{2}\right), \sin\left(\frac{(i-1)\pi}{2}\right)\right], \quad i = 1,2,3,4, \\ c_i &= \sqrt{2}c\left[\cos\left(\frac{(2i-1)\pi}{4}\right), \sin\left(\frac{(2i-1)\pi}{4}\right)\right], \quad i = 5,6,7,8, \\ c_9 &= 0. \end{aligned} \tag{3.3}$$

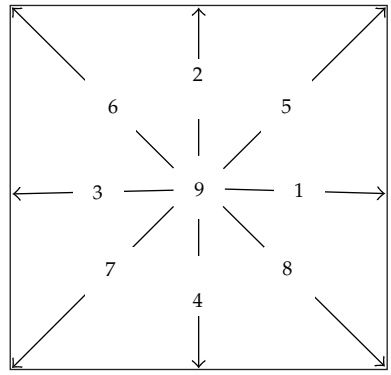

Figure 2: Topology of the D2Q9 lattice and labelling of the directions.

The corresponding equilibrium distribution functions for the density and temperature distribution functions are f_i^{eq} and g_i^{eq}, respectively. These two parameters are in the form of a second-order truncated expansion of the Maxwell-Boltzmann equilibrium function:

$$\begin{aligned} f_i^{\mathrm{eq}} &= \rho\omega_i\left[1+\frac{1}{c_s^2}c_i\cdot u+\frac{1}{2c_s^4}(c_i\cdot u)^2-\frac{1}{2c_s^2}u\cdot u\right], \\ g_i^{\mathrm{eq}} &= \omega_i T\left[1+\frac{1}{c_s^2}c_i\cdot u+\frac{1}{2c_s^4}(c_i\cdot u)^2-\frac{1}{2c_s^2}u\cdot u\right], \end{aligned} \tag{3.4}$$

where c_s is the lattice sound speed and is equal to $1/\sqrt{3}$ for a two-dimensional lattice with 9 velocities (D2Q9). ω_i is the weighting factor and is defined as follows for the D2Q9 lattice:

$$\omega_i=\begin{cases}\dfrac{4}{9}, & i=9,\\[2mm] \dfrac{1}{9}, & i=1,2,3,4,\\[2mm] \dfrac{1}{36}, & i=5,6,7,8.\end{cases} \tag{3.5}$$

The macroscopic density (ρ), pressure (P), velocity (u), and temperature (T) on each lattice site are calculated as follows:

$$\rho=\sum_i f_i,\qquad P=\rho c_s^2,\qquad \rho u_i=\sum_i c_i,\qquad T=\sum_i g_i. \tag{3.6}$$

The kinematic viscosity and the thermal diffusivity are given by

$$\begin{aligned} \nu &= \left(\tau_\nu-\frac{1}{2}\right)c_s^2, \\ \alpha &= \left(\tau_c-\frac{1}{2}\right)c_s^2. \end{aligned} \tag{3.7}$$

Table 1: Comparison of the predicted average Nusselt number for two different Rayleigh numbers against the values reported in [26].

Rayleigh number	Average Nusselt number	
10^4	Present work	2.247
	de Vahl Davis [26]	2.243
10^5	Present work	4.481
	de Vahl Davis [26]	4.519

The no-slip solid-wall boundary condition is set for the vertical and horizontal walls of the enclosure by using the bounce back method. As mentioned before, the top and bottom walls are adiabatic, and the vertical walls are isothermal, with the left wall at higher temperature than that of the right wall.

4. Results and Discussion

The physical domain considered in this study is a two-dimensional square cavity. The parameters D and d are depicted in Figure 1, where D is set to 2 mm and d is equal to $D/2$. The density and dynamic viscosity of the ferrofluid at 300 K were set equal to 1180 kg/m^3 and 1.0×10^{-3} kg/ms, respectively. The Prandtl number, Pr, and fluid compressibility, β, are taken as 5.5 and 5.6×10^{-4} K^{-1}, respectively.

A uniform lattice system is employed for the simulations. The numerical solution should be independent of the lattice size, and to this purpose, three different lattice sizes of 81×81, 101×101, and 121×121 were examined; results with a lattice density of 101×101 lattice units were found to be adequate to establish lattice-independent solutions for the range of the parameters used in the present study. In order to validate the thermal LBM predictions, laminar natural convection of air, Pr = 0.71, in a cavity was simulated for Rayleigh numbers of 10^4 and 10^5. The predicted natural convection results with the 101×101 grid system for Ra = 10^4 and 10^5, respectively, were in excellent agreement with the benchmark steady flow patterns and temperature fields reported by de Vahl Davis [26]. In Table 1, the predicted average Nusselt numbers on the hot wall are compared against the values reported by de Vahl Davis [26] for the same conditions and, as it can be observed, are in excellent agreement.

The average Nusselt number on the side walls is determined from the following relation:

$$\overline{\mathrm{Nu}} = -\frac{1}{\Delta T} \sum_{1}^{D} \frac{dT}{dx}. \tag{4.1}$$

The two dimensionless parameters which characterize the natural convective flow, Rayleigh number (Ra) and the Prandtl number (Pr), are defined as follows:

$$\mathrm{Ra} = \frac{g_y \beta \Delta T D^3}{\nu \alpha}, \qquad \mathrm{Pr} = \frac{\nu}{\alpha}, \tag{4.2}$$

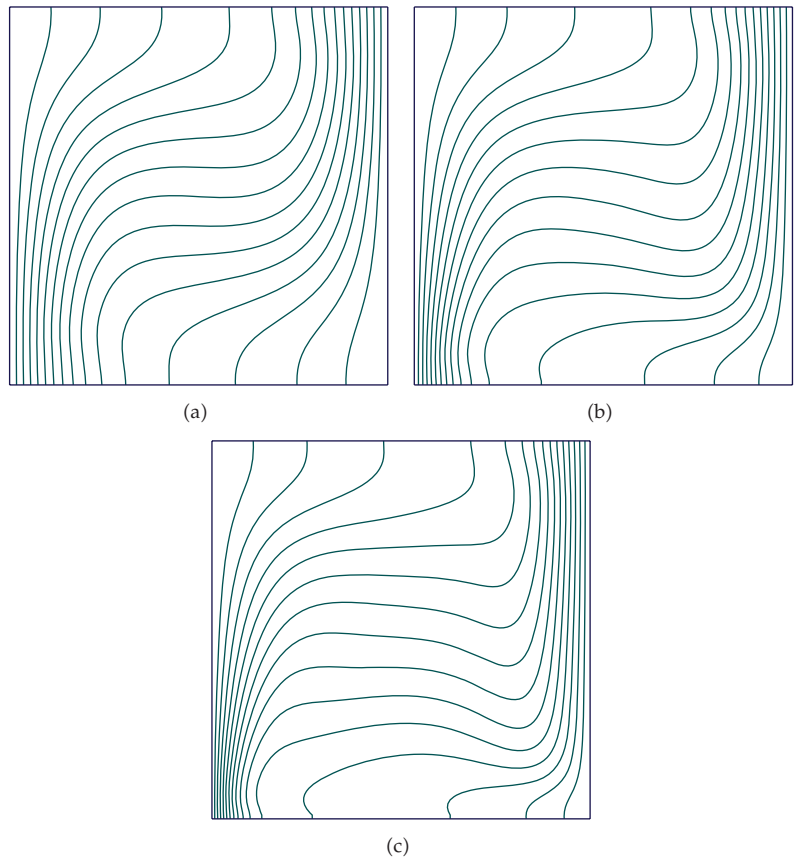

Figure 3: Isotherms for the thermomagnetic flow in a square cavity for $\Delta T = 30\,\text{K}$, $\text{Ra} = 10^4$: (a) $m = 0.0$, (b) $m = 0.05$, and (c) $m = 0.1\,\text{Am}$.

where g_y, β, ΔT, and D are the gravitational acceleration, working fluid thermal expansion coefficient, temperature difference between the two vertical walls, and the characteristic length (equal to the width of the cavity), respectively.

Presenting the magnetic dipole will disturb the flow motion in the cavity; consequently, the temperature distribution will be affected along with the heat transfer rate at the walls of the cavity. The isotherms for three different values of m equal to 0.0, 0.05, and 0.1 Am, are shown in Figures 3(a)–3(c) for $\Delta T = 30\,\text{K}$ ($\text{Ra} = 10^4$). The influence of the induced magnetic field on the temperature distributions is apparent. If the magnetic field magnitude is relatively weak, the buoyancy effect is dominant and the isotherms and streamlines are similar to those of pure natural convection in the absence of a magnetic field. For a stronger magnetic field the isotherm stratification in the core will change, as shown in Figure 3(c); this is due to the suppression of the free convective flow by the magnetic field. By increasing the magnetic field strength, the effect of the natural convection is eventually eliminated and the flow motion of the ferrofluid is governed by the strength of the magnetic field.

Figures 4(a)–4(c) report the isotherms at $\Delta T = 60\,\text{K}$ ($\text{Ra} = 2 \times 10^4$) for $m = 0.0$, 0.05, and 0.1 Am. From these figures, it can be observed that for large values of ΔT, the effect of increasing the magnetic strength on the temperature distribution in the enclosure

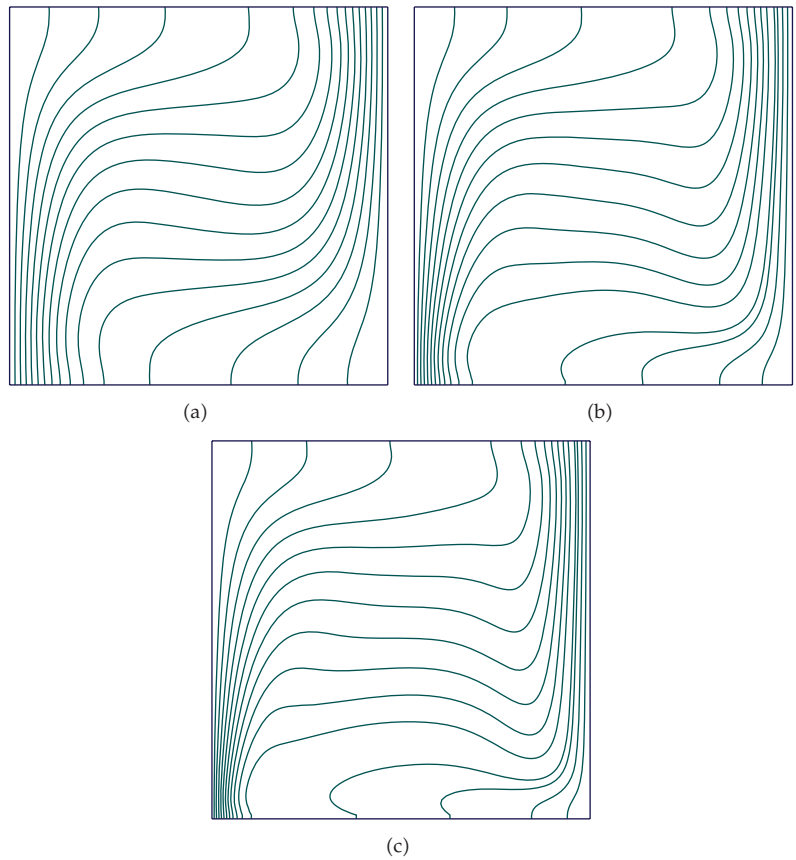

Figure 4: Isotherms for the thermomagnetic flow in a square cavity for $\Delta T = 60\,\text{K}$, $\text{Ra} = 2 \times 10^4$: (a) $m = 0.0$, (b) $m = 0.05$, and (c) $m = 0.1$ Am.

is more prominent compared to that in the case of a smaller ΔT ($\text{Ra} = 10^4$, Figure 3). This is because the magnetic susceptibility depends on temperature and influences the motion of the ferrofluid in the cavity. In these circumstances, the colder fluid close to the lower temperature wall moves down towards the region of larger field strength due to its higher magnetic susceptibility, while the warmer fluid with lower susceptibility is displaced away from the line dipole and is pushed upward along the hot wall.

For sufficiently large values of m, the natural convection is suppressed and the magnetic field effect is the dominant factor. As a result, the isotherms will be almost independent of Ra number for a relatively high magnetic field strength. The streamlines for the thermomagnetic flow in the square cavity for $\Delta T = 30\,\text{K}$ and $\Delta T = 60\,\text{K}$ and for different values of m, 0.0, 0.05, and 0.1 Am, are presented in Figures 5(a)–5(c) and 6(a)–6(c), respectively.

Figure 7 shows the predicted values of the average Nusselt number on the hot wall for a range of temperature difference, $15 \leq \Delta T \leq 90$, $5 \times 10^3 \leq \text{Ra} \leq 3 \times 10^4$, and $0 \leq m \leq 0.2$. It can be observed that the average Nusselt number increases with both magnetic field strength and temperature difference. The average Nusselt number increases more than double for $m = 0.2$ Am compared to the Nusselt number for free convection only.

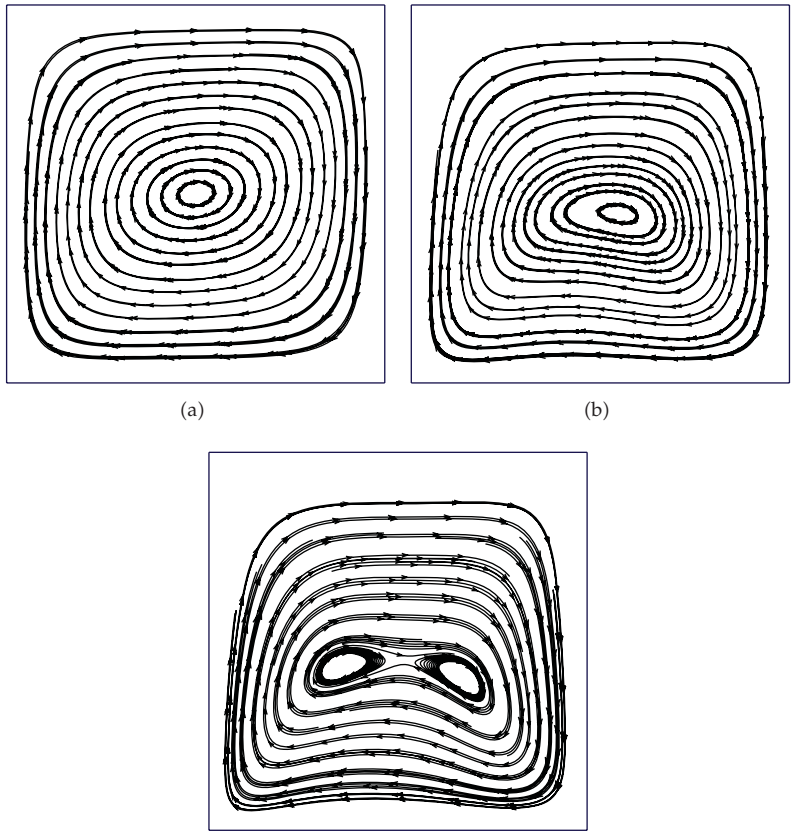

Figure 5: Streamlines for the thermomagnetic flow in a square cavity for $\Delta T = 30\,\text{K}$, $\text{Ra} = 10^4$: (a) $m = 0.0$, (b) $m = 0.05$, and (c) $m = 0.1\,\text{Am}$.

To show the effect of magnetic field strength on heat transfer enhancement, the buoyancy force was turned off and the average Nusselt numbers on the hot wall were compared with those from the combination of buoyancy and magnetic force. In Figure 8, the average Nusselt numbers are presented for different magnetic field strengths and a range of temperature difference. For magnetic field moment, m, lower than 0.1 Am the buoyancy force has a noticeable effect on the Nusselt number, but with increasing magnetic field strength the effect of the buoyancy force is reduced and the Nusselt number can be calculated by considering only the magnetic force for m larger than 0.15 Am.

5. Conclusion

Simulations for thermomagnetic convection were conducted for a range of Rayleigh numbers and magnetic field strengths in the laminar regime. The effects of these parameters on the heat transfer characteristics were analyzed; the numerical results showed that with the application of an external magnetic field, the temperature and velocity fields were significantly modified.

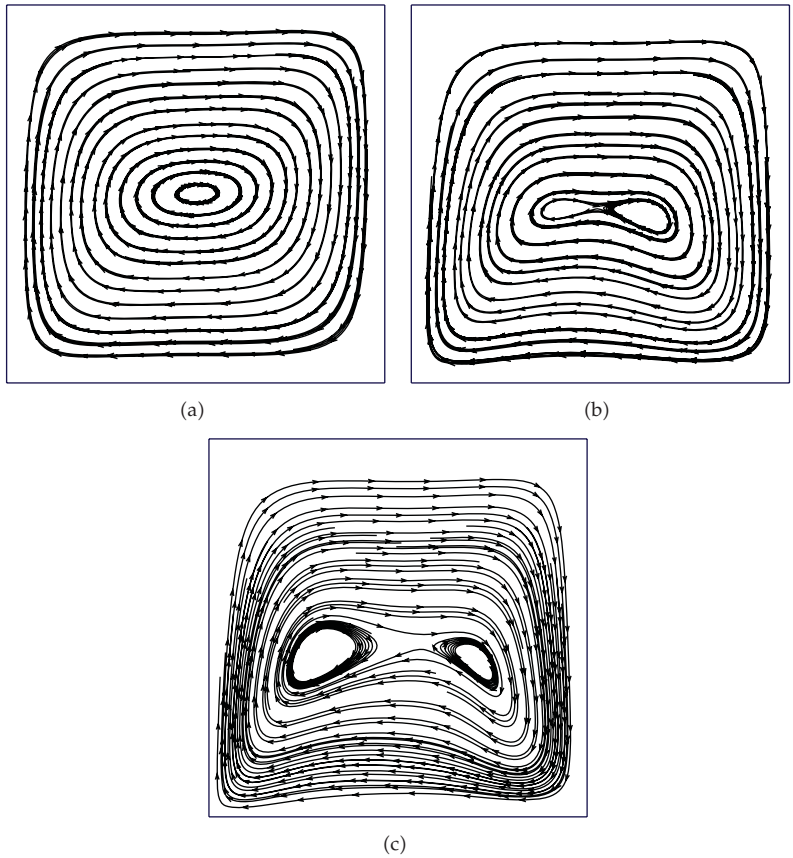

Figure 6: Streamlines for the thermomagnetic flow in a square cavity $\Delta T = 60\,\text{K}$, $\text{Ra} = 2 \times 10^4$: (a) $m = 0.0$, (b) $m = 0.05$, and (c) $m = 0.1\,\text{Am}$.

For weak magnetic fields, both buoyancy force and magnetic force have effects on the heat transfer. However, for sufficiently high magnetic field strength, the magnetic convection is suppressed for all the examined values of the Rayleigh number. This study shows that even for relatively weak magnetic fields, the increase in heat transfer for small scale devices is considerable.

Nomenclature

c_i: Particle discrete velocity set
c_s: Speed of sound
d: Distance between dipole and enclosure
D: Enclosure height
f: Distribution function for the flow field
g: Distribution function for the temperature field
g_y: Acceleration of gravity in the y-direction
H: Defined in (2.3)
m: Magnetic field moment

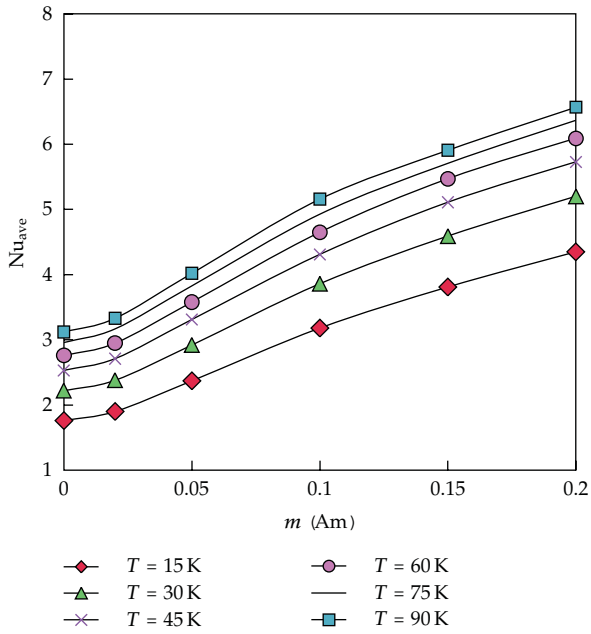

Figure 7: Average Nusslet number for different temperature difference and magnetic field strength.

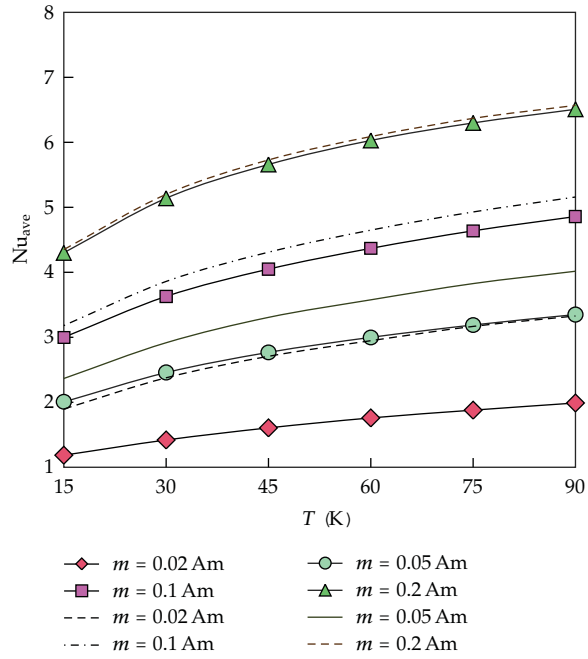

Figure 8: Average Nusslet number based on the magnetic force and combination of magnetic and buoyancy force. (The solid lines are the Nu_{ave} based on the combination of the magnetic and buoyancy force. The marked lines are calculated based on the magnetic force only.)

M: Magnetization
Nu: Nusselt number
Pr: Prandtl number
Ra: Rayleigh number
t: Time
T: Temperature
x, y: Cartesian coordinate
u: Velocity component.

Greek Letters

α: Thermal diffusivity
β: Fluid compressibility
χ: Magnetic susceptibility
μ: Viscosity
μ_0: Magnetic permeability
ρ: Density
τ: Lattice relaxation time
ν: Fluid kinematic viscosity
ω_i: Lattice weighting factor.

Acknowledgments

The authors acknowledge the support received from Natural Sciences and Engineering Research Council of Canada (NSERC) Discovery Grant 12875 (ACMS) and Foundation for Science and Technology-Portugal (FCT) Grant PTDC/EME-MFE/105031/2008 (ACMS). M. Hadavand would like to thank Dr. R. Ganguly for helpful discussions.

References

[1] A. E. Gill, "The boundary-layer regime for convection in a rectangular cavity," *Journal of Fluid Mechanics*, vol. 26, pp. 515–536, 1966.
[2] S. Ostrach, "Natural convection in enclosures," *Journal of Heat Transfer*, vol. 110, no. 4, pp. 1175–1190, 1988.
[3] V. Mariani and I. Moura Belo, "Numerical studies of natural convection in a square cavity," *Thermal Engineering*, vol. 5, pp. 68–72, 2006.
[4] X. Shi and J. M. Khodadadi, "Laminar natural convection heat transfer in a differentially heated square cavity due to a thin fin on the hot wall," *Journal of Heat Transfer*, vol. 125, no. 4, pp. 624–634, 2003.
[5] S. Odenbach, "Recent progress in magnetic fluid research," *Journal of Physics Condensed Matter*, vol. 16, no. 32, pp. R1135–R1150, 2004.
[6] K. Raj and R. Moskowitz, "Commercial applications of ferrofluids," *Journal of Magnetism and Magnetic Materials*, vol. 85, no. 1–3, pp. 233–245, 1990.
[7] B. A. Finlayson, "Convective instability of ferromagnetic fluids," *Journal of Fluid Mechanics*, vol. 40, no. 4, pp. 753–767, 1970.
[8] R. Ganguly, S. Sen, and I. K. Puri, "Thermomagnetic convection in a square enclosure using a line dipole," *Physics of Fluids*, vol. 16, no. 7, pp. 2228–2236, 2004.
[9] H. Yamaguchi, I. Kobori, Y. Uehata, and K. Shimada, "Natural convection of magnetic fluid in a rectangular box," *Journal of Magnetism and Magnetic Materials*, vol. 201, no. 1–3, pp. 264–267, 1999.

[10] N. M. Al-Najem, K. M. Khanafer, and M. M. El-Refaee, "Numerical study of laminar natural convection in tilted cavity with transverse magnetic field," *International Journal of Numerical Methods for Heat & Fluid Flow*, vol. 8, pp. 651–672, 1998.

[11] M. S. Krakov and I. V. Nikiforov, "To the influence of uniform magnetic field on thermomagnetic convection in square cavity," *Journal of Magnetism and Magnetic Materials*, vol. 252, no. 1–3, pp. 209–211, 2002.

[12] T. Sawada, H. Kikura, A. Saito, and T. Tanahashi, "Natural convection of a magnetic fluid in concentric horizontal annuli under nonuniform magnetic fields," *Experimental Thermal and Fluid Science*, vol. 7, no. 3, pp. 212–220, 1993.

[13] H. Kikura, T. Sawada, and T. Tanahashi, "Natural convection of a magnetic fluid in a cubic enclosure," *Journal of Magnetism and Magnetic Materials*, vol. 122, no. 1–3, pp. 315–318, 1993.

[14] K. Nakatsuka, B. Jeyadevan, S. Neveu, and H. Koganezawa, "The magnetic fluid for heat transfer applications," *Journal of Magnetism and Magnetic Materials*, vol. 252, no. 1–3, pp. 360–362, 2002.

[15] S. M. Snyder, T. Cader, and B. A. Finlayson, "Finite element model of magnetoconvection of a ferrofluid," *Journal of Magnetism and Magnetic Materials*, vol. 262, no. 2, pp. 269–279, 2003.

[16] M. Hadavand, A. Nabovati, and A. C. M. Sousa, "Numerical simulation of thermomagnetic convection in an enclosure using the Lattice Boltzmann Method," in *Proceedings of the 8th International Conference on Nanochannels, Micorchannels and Minichannels (FEDSM-ICNMM '10)*, Montreal, Canada, 2010.

[17] X. Q. Wang and A. S. Mujumdar, "Heat transfer characteristics of nanofluids: a review," *International Journal of Thermal Sciences*, vol. 46, no. 1, pp. 1–19, 2007.

[18] D. J. Griffiths, *Introduction to Electrodynamics*, Prentice Hall, 3rd edition, 2002.

[19] A. Mukhopadhyay, R. Ganguly, S. Sen, and I. K. Puri, "A scaling analysis to characterize thermomagnetic convection," *International Journal of Heat and Mass Transfer*, vol. 48, no. 17, pp. 3485–3492, 2005.

[20] A. Nabovati, *Pore level simulation of single and two phase flow in porous media using Lattice Boltzmann method*, Ph.D. dissertation, University of New Brunswick, New Brunswick, NJ, USA, 2009.

[21] P. L. Bhatnagar, E. P. Gross, and M. Krook, "A model for collision processes in gases. I. Small amplitude processes in charged and neutral one-component systems," *Physical Review*, vol. 94, no. 3, pp. 511–525, 1954.

[22] X. He, S. Chen, and G. D. Doolen, "A novel thermal model for the Lattice Boltzmann method in incompressible limit," *Journal of Computational Physics*, vol. 146, no. 1, pp. 282–300, 1998.

[23] Y. Shi, T. S. Zhao, and Z. L. Guo, "Thermal lattice Bhatnagar-Gross-Krook model for flows with viscous heat dissipation in the incompressible limit," *Physical Review E*, vol. 70, no. 6, Article ID 066310, 2004.

[24] P. H. Kao and R. J. Yang, "Simulating oscillatory flows in Raleigh-Bénard convection using the lattice Boltzmann method," *International Journal of Heat and Mass Transfer*, vol. 50, pp. 3315–3328, 2008.

[25] Y. H. Qian, D. d'Humieres, and P. Lallemand, "Lattice BGK model for Navier-Stokes equation," *Europhysics Letters*, vol. 17, no. 6, pp. 479–484, 1992.

[26] G. de Vahl Davis, "Natural convection of air in a square cavity: a benchmark numerical solution," *International Journal for Numerical Methods in Fluids*, vol. 3, no. 3, pp. 249–264, 1983.

Hindawi Publishing Corporation
Journal of Applied Mathematics
Volume 2011, Article ID 535484, 19 pages
doi:10.1155/2011/535484

Research Article

A Parallel Stochastic Framework for Reservoir Characterization and History Matching

Sunil G. Thomas,[1,2] Hector M. Klie,[1,3] Adolfo A. Rodriguez,[1,3] and Mary F. Wheeler[4,5]

[1] *Institute for Computational Engineering and Sciences, The University of Texas at Austin, Austin, TX 78712, USA*
[2] *Chevron ETC, San Ramon, CA 94583, USA*
[3] *ConocoPhillips, Houston, TX 77252, USA*
[4] *Institute for Computational Engineering and Sciences, Department of Aerospace Engineering and Engineering Mechanics, The University of Texas at Austin, Austin, TX 78712, USA*
[5] *Department of Petroleum and Geosystems Engineering, The University of Texas at Austin, Austin, TX 78712, USA*

Correspondence should be addressed to Sunil G. Thomas, sunil.g.thomas@gmail.com

Received 15 December 2010; Accepted 1 February 2011

Academic Editor: Shuyu Sun

Copyright © 2011 Sunil G. Thomas et al. This is an open access article distributed under the Creative Commons Attribution License, which permits unrestricted use, distribution, and reproduction in any medium, provided the original work is properly cited.

The spatial distribution of parameters that characterize the subsurface is never known to any reasonable level of accuracy required to solve the governing PDEs of multiphase flow or species transport through porous media. This paper presents a numerically cheap, yet efficient, accurate and parallel framework to estimate reservoir parameters, for example, medium permeability, using sensor information from measurements of the solution variables such as phase pressures, phase concentrations, fluxes, and seismic and well log data. Numerical results are presented to demonstrate the method.

1. Introduction

Uncertainties associated with the measurement of subsurface medium properties such as rock permeability and porosity are widely known. Deterministic models of multiphase flow and transport through porous media require accurate estimate of such properties, since these affect the estimation and location of recoverable reserves, in addition to revealing true subsurface flow characteristics under various injection scenarios. Modern drilling instruments routinely have sensors installed at strategic locations in a reservoir. Specialized sensors are capable of measuring at a high local resolution, fluid, and rock properties [1, 2]. These advances together with 4d time-lapse seismic studies are revealing enormous potential in reducing uncertainty associated with reservoir characterization. Meanwhile new stochastic

optimization and statistical learning methods are emerging as promising tools to determining nontrivial correlations between data measurements and responses in addition to developing optimal reservoir exploration plans [3]. In this work, the existence of a number of prior realizations of the unknown data (i.e., estimates, e.g., from seismic studies) is assumed. The estimation and sampling is then performed at a fixed resolution using a parallel version of the SPSA [4] (simultaneous perturbation, stochastic approximation) algorithm. A multilevel approach, coupled to neural-network engines that enhance the solution by calculating sensitivities in the vicinity of the most promising solution was presented in [5, 6].

Suppose that a set of N realizations, $\mathbf{x}_i$, $i = 1, \ldots, N$ is given of a reservoir property (e.g., permeability) where each $\mathbf{x}_i \in \mathbb{R}^M$, M being the number of grid elements. Using methods such as wavelet analysis [7] or the principle component analysis (PCA) method [8, 9], it is possible to determine a reduced set of basis functions that characterize a majority of the variability. In this work, the PCA method is adopted. Then, let the set of realizations be denoted by the matrix $\mathbf{X}$, given by

$$\mathbf{X} = \{\mathbf{x}_1, \mathbf{x}_2, \ldots, \mathbf{x}_N\}. \tag{1.1}$$

Further, let the empirical mean be given by

$$\overline{\mathbf{x}} = \frac{1}{N}\sum_{i=1}^{N}\mathbf{x}_i. \tag{1.2}$$

Next, let $\mathbf{Y}$ denote the deviation of the data from the mean, given by

$$\mathbf{Y} = \mathbf{X} - \{\overline{\mathbf{x}}, \overline{\mathbf{x}}, \ldots, \overline{\mathbf{x}}\}. \tag{1.3}$$

In the PCA method, the covariance matrix $\mathbf{C}$ is required of the deviation of the data from the mean. The covariance matrix is given by

$$\mathbf{C} = E\left(\mathbf{Y}\mathbf{Y}^T\right). \tag{1.4}$$

Since each of the N realizations is in general equally likely, in (1.4), it is possible to further reduce the expression for covariance as $\mathbf{C} = E(\mathbf{Y}\mathbf{Y}^T) = (1/N)\mathbf{Y}\mathbf{Y}^T$. Thus, the covariance matrix $\mathbf{C}$ is symmetric and positive definite. Hence, it is possible to compute the eigen decomposition of $\mathbf{C}$ and the associated eigen values as follows

$$\mathbf{C} = \mathbf{V}\mathbf{D}\mathbf{V}^{-1} \quad \text{with } \mathbf{D} = \operatorname{diag}\left(\{\lambda_i\}_{i=1}^{M}\right). \tag{1.5}$$

In (1.5), $\mathbf{V} = \{\mathbf{v}_i\}_{i=1}^{M}$, the matrix of eigen vectors of $\mathbf{C}$ and λ_i are the corresponding eigen values. Let λ_i be arranged in descending order $\lambda_1 > \lambda_2 > \cdots > \lambda_M$. Then each realization can be expressed to a desired level of accuracy as a linear combination of the first P eigen value/vector pairs ($P < M$). Infact, since $\mathbf{C}$ is symmetric in addition to being positive definite, the eigen vectors of $\mathbf{V}$ are orthogonal and thus, (1.5) can be expressed in terms of orthormal eigen vectors. In such a case, the eigen values coincide with the singular values.

Then, a well known result can be drawn upon from linear algebra, restated here for this special case without proof.

Theorem 1.1. *Suppose* $\mathbf{C}$ *is an* $M \times M$ *matrix with singular values* $\lambda_1 > \lambda_2 > \cdots > \lambda_M > 0$. *Then for any* $P < M$, *the matrix given by* $\widetilde{\mathbf{C}} \equiv \sum_{i=1}^{P} \lambda_i \mathbf{v}_i \mathbf{v}_i^T$ *is the best "rank-P" approximation of* $\mathbf{C}$ *in the sense of the Frobenius norm, that is,* $\widetilde{\mathbf{C}}$ *is the minimizer of* $\|\mathbf{C} - \mathbf{Z}\|_{\mathcal{F}}$ *where* $\mathbf{Z} \in \mathbb{R}^{M \times M}$.

In Theorem 1.1, recall that the Frobenius norm (which is an operator norm) of the matrix $\mathbf{C}$ is given by $\|\mathbf{C}\|_{\mathcal{F}} \equiv \sqrt{\sum_{i=1}^{M} \lambda_i^2}$. Also, note that $\mathbf{v}_i \mathbf{v}_i^T$ denotes the outer product (sometimes referred to as the "tensor product") of the vectors $\mathbf{v}_i$ and $\mathbf{v}_i^T$. Therefore, the theorem serves to guarantee that the reduced basis corresponding to the subspace spanned by the first P eigen vectors is the best possible "rank-P" choice. In other words, it suffices to determine coefficients α_j, such that the "true" property sought can be expressed as $\mathbf{x} \approx \overline{\mathbf{x}} + \sum_{i=1}^{P} \alpha_j \mathbf{v}_j$ in the subspace, $\operatorname{span}\{\mathbf{v}_j\}_{j=1}^{P}$. Hence, the dimension of the system is greatly reduced. The coefficients α_j are actually determined by minimizing an objective function, using the SPSA method, described in the following section.

2. Simultaneous Perturbation, Stochastic Approximation (SPSA)

Consider the problem of finding the root, θ^*, of the problem $\mathbf{g}(\theta) \equiv \nabla L(\theta) = 0$, where $L : \mathbb{R}^P \to \mathbb{R}$ is assumed to be a differentiable loss function that measures a weighted, time- and space-integrated error between observed measurements (of the phase pressures, concentrations, fluxes, seismic travel-times and well-log data) and computed solutions in some suitable norm. In this work, the expression for L takes the form

$$L(\theta) \equiv \sum_{\mathbf{f} \in \mathcal{D}} \sum_{i=1}^{N_T - 1} \left[0.5 \left(\left\| w_{\mathbf{f},i} \left(\mathbf{f}_i^d - \mathbf{f}_i \right) \right\|_2^2 + \left\| w_{\mathbf{f},i+1} \left(\mathbf{f}_{i+1}^d - \mathbf{f}_{i+1} \right) \right\|_2^2 \right) \Delta t_i \right]. \tag{2.1}$$

Several terms in (2.1) which is written in concise terms, deserve mention. The functions $\mathbf{f} \in \mathcal{D}$ denote any property of interest in the calculations, $\mathbf{f}(\theta)$ which is a function of θ. The set of all such properties is denoted by $\mathcal{D}$. In this work, for the case of two-phase flow (and specifically the oil water model) $\mathcal{D} \equiv \{\mathbf{p}, \mathbf{N}, \mathbf{u}, \mathbf{q}, \tau\}$, where $\mathbf{p}$ denotes the (oil)phase pressures, $\mathbf{N}$ denotes the (oil)phase concentration, $\mathbf{q}$ denotes the well-data (includes well-rates, bottom-hole pressures, and oil water ratios depending on the kind of well), $\mathbf{u}$ denotes the phase fluxes and τ denotes seismic travel-times. Thus it can be seen that the right-hand side of (2.1) is a function of θ. The superscript d denotes measure data, while terms without the superscript denote computed solution. The index i denotes the time instant at which measurements are recorded and $w_{\mathbf{f},i}$ is a space- and time-dependent weight function on the property $\mathbf{f}$, assigned based on priority and relevance at a given time instant and location in space. Finally, N_T is the number of time instants in $[0, T]$ when data measurements are recorded and Δt_i denotes the time interval between such measurements.

In this problem, $\theta \equiv \{\alpha_1, \alpha_2, \ldots, \alpha_P\}$ with α_i the coefficients in the expansion of the unknown (permeability) vector $\mathbf{x}$, as described in Section 1. Let θ_k denote the estimate for θ at the kth iterate. Then, the SPSA algorithm has the form

$$\theta_{k+1} = \theta_k - a_k \mathbf{g}_k(\theta_k), \tag{2.2}$$

where $\mathbf{g}_k(\theta_k)$ is a simultaneous perturbation, stochastic approximation of the gradient $\mathbf{g}(\theta_k)$ defined as follows. Let $\Delta_k \in \mathbb{R}^P$ be a vector consisting of $\{\pm 1\}$ values that are randomly generated using a Bernoulli distribution, that is, satisfying $E(\Delta_{k,i}) = 0$, $i = 1, 2, \ldots, P$. Then $\mathbf{g}_k(\theta_k)$ is defined by the central-differences equation (component wise)

$$g_{k,i}(\theta_k) = \frac{L(\theta_{k,i} + c_k\Delta_{k,i}) - L(\theta_{k,i} - c_k\Delta_{k,i})}{2c_k\Delta_{k,i}}, \quad i = 1, 2, \ldots, P. \tag{2.3}$$

From (2.3), it is evident the method is very cheap because it only involves two relatively inexpensive forward realizations (or simulations) for every iteration to update the estimated property. Here a_k, c_k are monotonically, decreasing sequences of positive scalars chosen according to the method prescribed in [4]. The relevant formulae are given by

$$a_k = \frac{a}{(A + k + 1)^{\alpha}}, \qquad c_k = \frac{c}{(k + 1)^{\gamma}}, \tag{2.4}$$

where a, c, α, A, and γ are positive real numbers satisfying

$$0 < \alpha \leq 1, \quad \alpha = \gamma > 0.5, \quad \alpha > 2\gamma. \tag{2.5}$$

This ensures that some technical conditions are satisfied [4] which are in turn required for the convergence of the stochastic gradient to the steepest descent gradient. The choice of a, c, α, A and γ is to some extent case dependent and may require some experimentation. It is known that $\alpha = 1$ and $\gamma = 1/6$ are asymptotically optimum values but choosing smaller values, for example, $\alpha = 0.602$ and $\gamma = 0.101$ are found to be effective in practise. A common recommendation [4] is to set A equal to 5 to 10 percent of the maximum number of iterations allowed.

Spall [4] has shown that the method converges and can be regarded as stochastic analogue of the steepest descent method with similar rates of convergence. Therein, proofs of convergence of the method in a "stochastic sense" (i.e., in the sense of expectations) are presented. Similar proofs can also be found in [10]. For completeness, the basic steps of a proof are presented here to show that the expectation of the stochastic gradient $\mathbf{g}_k(\theta_k)$ equals the actual gradient $\mathbf{g}(\theta_k)$. Thus, it can be expected that the method will converge at a rate equal to the steepest descent method.

Theorem 2.1. *The expectation of the stochastic gradient $\mathbf{g}_k(\theta_k)$ of the SPSA method equals the true gradient $\mathbf{g}(\theta_k)$.*

Proof. A standard Taylor-series expansion yields that

$$L(\theta_k + c_k\Delta_k) = L(\theta_k) + c_k\sum_{j=1}^{P}\Delta_{k,j}\frac{\partial L(\theta_k)}{\partial\theta_{k,j}} + \mathcal{O}\left(c_k^2\|\Delta_k\|^2\right), \tag{2.6}$$

and likewise

$$L(\theta_k - c_k\Delta_k) = L(\theta_k) - c_k\sum_{j=1}^{P}\Delta_{k,j}\frac{\partial L(\theta_k)}{\partial\theta_{k,j}} + \mathcal{O}\left(c_k^2\|\Delta_k\|^2\right). \tag{2.7}$$

Subtracting (2.7) from (2.6), then rearranging the resulting terms and neglecting the higher-order terms, $\mathcal{O}(c_k^2\|\Delta_k\|^2)$ yields

$$\frac{L(\theta_k + c_k\Delta_k) - L(\theta_k - c_k\Delta_k)}{2c_k} = \sum_{j=1}^{P}\Delta_{k,j}\frac{\partial L(\theta_k)}{\partial\theta_{k,j}} = \Delta_k^T\nabla L(\theta_k). \tag{2.8}$$

Next, define the inverse of Δ_k as

$$\Delta_k^{-1} = \left[\Delta_{k,1}^{-1}, \Delta_{k,2}^{-1}, \ldots, \Delta_{k,P}^{-1}\right]. \tag{2.9}$$

Then, from $\Delta_{k,i}^{-1} = \Delta_{k,i}$ (recall that $\Delta_{k,i} = \pm 1$), it follows that

$$\Delta_k^{-1} = \Delta_k. \tag{2.10}$$

From (2.10), it follows that the stochastic gradient in (2.3) can be written as

$$\mathbf{g}_k(\theta_k) = \frac{L(\theta_k + c_k\Delta_k) - L(\theta_k - c_k\Delta_k)}{2c_k}\Delta_k = \Delta_k\frac{L(\theta_k + c_k\Delta_k) - L(\theta_k - c_k\Delta_k)}{2c_k}. \tag{2.11}$$

Then, using (2.8) in (2.11) yields

$$\mathbf{g}_k(\theta_k) = \Delta_k\Delta_k^T\nabla L(\theta_k). \tag{2.12}$$

The expectation of the stochastic gradient is then given by

$$E[\mathbf{g}_k(\theta_k)] = E\left[\Delta_k\Delta_k^T\right]\nabla L(\theta_k). \tag{2.13}$$

Observe that the form of the matrix $\Delta_k\Delta_k^T$ on the right-hand side of (2.13) is given by

$$\Delta_k\Delta_k^T = \begin{bmatrix} \Delta_{k,1}^2 & \Delta_{k,2}\Delta_{k,1} & \cdots & \Delta_{k,P}\Delta_{k,1} \\ \Delta_{k,1}\Delta_{k,2} & \Delta_{k,2}^2 & \cdots & \Delta_{k,P}\Delta_{k,2} \\ \vdots & \vdots & \ddots & \vdots \\ \Delta_{k,1}\Delta_{k,P} & \Delta_{k,2}\Delta_{k,P} & \cdots & \Delta_{k,P}^2 \end{bmatrix}. \tag{2.14}$$

In (2.14), note that for any $j = 1, 2, \ldots, P$, the only value that $\Delta_{k,j}^2$ can take is 1. Hence,

$$E\left[\Delta_{k,j}^2\right] = 1. \tag{2.15}$$

Further, because $\Delta_{k,i}$ and $\Delta_{k,j}$ are independent random variables (when $i \neq j$), it follows that

$$E\left[\Delta_{k,i}\Delta_{k,j}\right] = E[\Delta_{k,i}]E\left[\Delta_{k,j}\right] = 0, \quad \forall i \neq j. \tag{2.16}$$

From this, it follows also that

$$E\left[\Delta_k \Delta_k^T\right] = \mathbf{I}, \tag{2.17}$$

where $\mathbf{I}$ denotes the $P \times P$ identity matrix. Applying (2.14)–(2.16) to (2.13) yields

$$E[\mathbf{g}_k(\theta_k)] = \nabla L(\theta_k) \equiv \mathbf{g}(\theta_k), \tag{2.18}$$

which is the desired result. □

3. A Parallel SPSA Algorithm

In this section, a parallel SPSA algorithm is described that runs several instances of the basic SPSA algorithm, one on each processor. This helps improve the convergence by widening the search space. Numerical tests were performed on various challenging problems on upto 256 processors. Sometimes, convergence is obtained in as few as 2 or 3 iterations. Each processor has its own copy of the vector θ_k, (i.e., the coefficients of the natural logarithm of permeability field), represented by say, θ_k^{id}. The random vectors Δ_k are generated on each processor and are not the same as those on other processors. This is easily achieved by using a different seed on each processor for the Bernoulli random number generator program that can be found, for example, in [11]. Thus each processor also has a copy of the stochastic gradient and updates θ_k according to (2.3).

Figure 1 shows the flow chart of the parallel SPSA algorithm for a single SPSA iteration step. Most of the steps in the figure are self-explanatory. The superscript id in θ_k^{id} represents the processor ID and np is the total number of processors. The main step that needs to be described is the box "All Gather mean/min". Two approaches are implemented to gather θ_k^{id} from each processor and step to $\theta_{k+1}^{\mathrm{id}}$—the "mean" and "min" approaches. In the "mean" method, as the name indicates, the updated vector, θ_{k+1} broadcast to all processors for the next iteration is simply the mean of the processor updates, $\theta_{k+1}^{\mathrm{id}}$, that is,

$$\theta_{k+1} = \frac{1}{\mathrm{np}} \sum_{i=1}^{\mathrm{np}} \theta_{k+1}^{\mathrm{id}}. \tag{3.1}$$

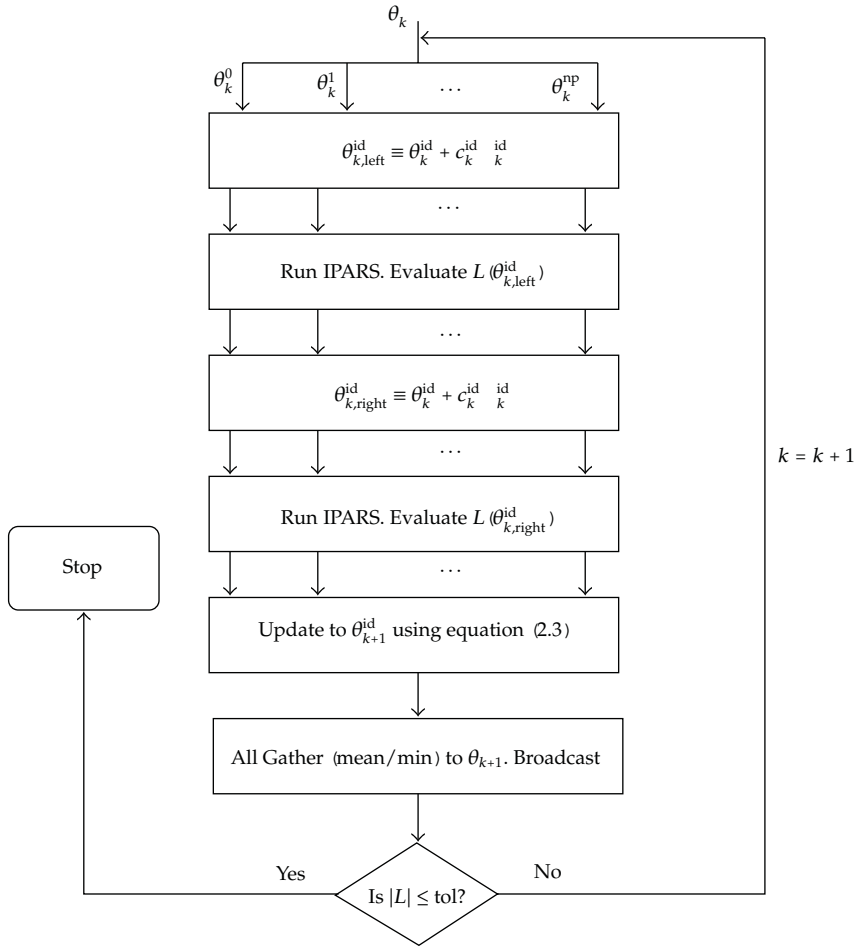

Figure 1: A parallel SPSA algorithm.

In the "min" method, again as the name indicates, first the processor with the least objective is identified. In other words, the index of that processor, $\mathrm{id}^{\min}$ say, is defined first as

$$\mathrm{id}^{\min} \equiv \min_{1 \leq \mathrm{id} \leq \mathrm{np}} L\left(\theta_{k+1}^{\mathrm{id}}\right). \tag{3.2}$$

Then the value of the vector $\theta_{k+1}^{\mathrm{id}^{\min}}$ on the processor $\mathrm{id}^{\min}$ is broadcast to all others for the next iteration

$$\theta_{k+1} = \theta_{k+1}^{\mathrm{id}^{\min}}. \tag{3.3}$$

The mean method was observed to be more stable and robust in general while the min method, although faster, sometimes exhibited the tendency to get trapped in local minima. Each box with text "Run IPARS.." in the flow chart of Figure 1 is a forward run of the reservoir simulator IPARS [12] with the value of permeability being calculated from the

current perturbation of the value of vector, θ_k^{id} (i.e., left or right perturbation). It is also noted that in practise, the implementation takes the components of θ_k on each processor to be the coefficients of $\ln \mathbf{x}$ in place of $\mathbf{x}$. (i.e., natural log of permeability instead of permeability), since the permeabilities can vary by several orders of magnitude in most real-world problems. The permeability $\mathbf{x}$ can then be easily calculated from $\ln \mathbf{x}$ using an exponential transormation.

4. Numerical Results

Two examples are presented in this section. In the first example, a 2d heterogeneous permeability field derived from the 10th SPE project [13] is used to test the parallel parameter estimation and history matching implementation. The second example likewise determines the heterogeneous permeability field and performs history matching for an upscaled version of the synthetic "Brugge" field [14] test case.

For both tests, basis functions are first generated using sample realizations (see Section 1). A total of 8 basis functions are used in the expansion of permeability for the first example where an isotropic permeability field is assumed. A total of 10 basis functions for each direction (i.e., K_{xx}, K_{yy}, and K_{zz}) is assumed for the second example (this is a nonisotropic case). Both examples use the two-phase hydrology (oil and water), model as the base model in IPARS to perform history matching and parameter estimation. It is noted however that IPARS can handle general multiphase and compositional flow problems using various discretization methods. The reason for the choice here is that the inverse modeling framework is currently only supported with the single-phase and two-phase models of IPARS. Both problems presented here were tested on various parallel platforms including the Bevo2 and Ranger linux cluster at The University of Texas at Austin and Blue Gene cluster, IBM.

4.1. Example 1: Sensor Tests

In this example, the goal was to perform history matching and estimate the permeability field (assuming a known "true" permeability field). Knowledge of the "true" permeability field only serves to validate the final answer and is not required (and is in fact not known) in practise. Without this assumption, the parallel SPSA implementation can guarantee that the objective function is minimized, but that does not necessarily mean that the minimizer is the (unique) real permeability field. In practise, the objective functions can have several local minima, hence it is important to ensure that the algorithm not only minimized the objective function, but that it is also converging to the "true" permeability field.

In this example, different objective function combinations based on different sensor combinations were tested (by activating or deactivating the weight functions $w_{\mathbf{f},i}$ in (2.1)). The problem simulates an oil gas immiscible model using the hydrology model in IPARS. This is achieved by treating in the input, oil phase as the actual "gas-phase" and assigning the properties of gas to it. Likewise, the water-phase is treated in the input as the actual "oil phase". Then the oil phase (actually "gas") is injected to produce water (actually "oil"). While this may sound confusing, it is quite common in reservoir simulation to reuse existing two- or three-phase codes to solve problems in contexts they may not have been designed for. The full set of properties $\mathcal{D}$, is available for use in the objective function but as mentioned, some may be "turned-off" by setting the weights to zero. It is also noted that only the production well was included in the objective calculations. Table 1 summarizes the problem data describing this example.

Table 1: Parameter estimation: data for example 1, (based on 10th SPE permeability set).

Property	Value
Simulation end-time, days	1000.0
Grid dimensions	$100 \times 1 \times 20$
Physical dimensions, m^3	$2500 \times 25 \times 50$
Flowing phases modeled	Gas, oil
Reference gas density, lb/ft^3	0.06
Gas viscosity, cp	0.01
Reference oil density, lb/ft^3	43.68
Oil viscosity, cp	1.0
Gas compressibility, 1/psi	2.0×10^{-4}
Oil compressibility, 1/psi	1.0×10^{-6}
Initial (residual) gas pressure, psi	1000
Initial (residual) gas conc., lb/ft^3	0.006
Medium porosity	0.2
Number of wells	2 (gas-inj. and oil prod.)
Gas injection rate, lb/day	43.84
BHP of oil prod. well, psi	995.0

Since the "true" θ^*, that is, the coefficients corresponding to the actual permeability field are known, the problem is first run using the true permeability and the true solution ($\mathbf{p}^*$, $\mathbf{N}^*$, $\mathbf{q}^*$, $\mathbf{u}^*$, and τ^*) are recorded at discrete time instants and at all the grid elements (or faces in case of fluxes). Seismic travel times are recorded as the set of times it takes for seismic waves to travel from one end of the reservoir (from each element face on the "source" end) to the other end (each element face on the "target" end). These are then recorded as data. The SPSA iterations are then performed starting with an initial guess θ_0 that is obtained by randomly perturbing the "true" θ^*. A total of 1000 SPSA iterations were computed for this test, although the permeability field converged in very few (early) iterations.

Figure 2 shows the history matching versus time in days, of the oil phase (actually, "gas") pressures in units of psi shown across a section through the middepth of the 2d reservoir. In this figure, it is noted that Figure 2(a) presents the match obtained when all sensors were active (i.e., the weights $w_{\mathbf{f},i} \equiv 1$ at all element locations and time instants). Figure 2(b) presents the match obtained when only the production well-sensor and the solution sensors (i.e., $w_{\mathbf{p},i}$, $w_{\mathbf{u},i}$, and $w_{\mathbf{N},i}$) at the midsection were active (i.e., at the location $x = 1250$ m and for all time instants). Figure 2(c) presents the match obtained when only the production well-sensor was active. The seismic sensor result was not included here because it was found to influence the history match in very insignicant amounts.

From the Figure 2, it is clear that sensors are not required at every grid element (and potentially not at every time instant as well) which is reassuring since installing such costly equipment as sensors at high areal densities can be very expensive and impractical. Figure 3 shows a similar match for the oil phase (actually "gas") concentration in units of lb/cu-ft across a section passing through the middepth of the reservoir. Once again a fairly good match is obtained with fewer measurements. As a demonstration of the flux matches, Figure 4 shows the history match obtained for oil phase fluxes (actually "gas") at the same section as the previous cases.

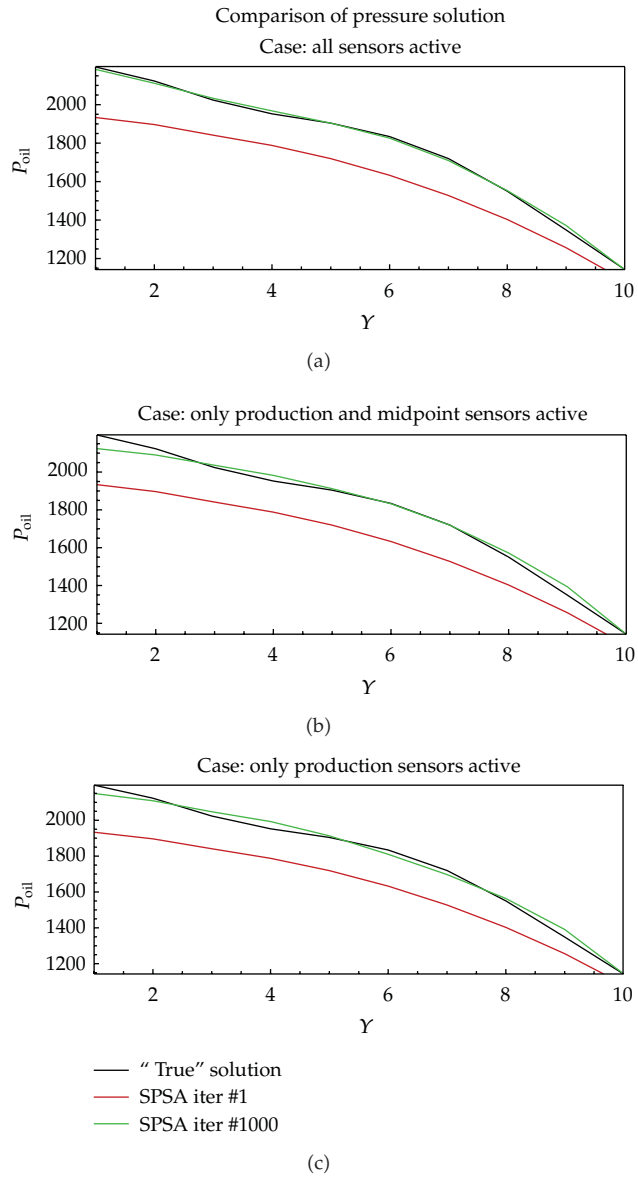

Figure 2: Example 1: history matching of oil phase pressures based on sensor choices.

It is observed that flux match is poorer when fewer sensors are used (as opposed to the quality of the pressure and concentration history matches). Finally, the production well-data history matches versus time in days of oil production (actually "gas") in mscf/day and oil gas (actually "water-gas") ratio and permeability estimation (for the case when only the midsection and production well sensors are active) is shown in the Figures 5, 6, and 7, respectively. For the permeability estimate, it is pointed out that the legend spans 50 to 900 mD to allow consistent comparison. From these graphs, the convergence of the parallel SPSA method can be seen to be very effective.

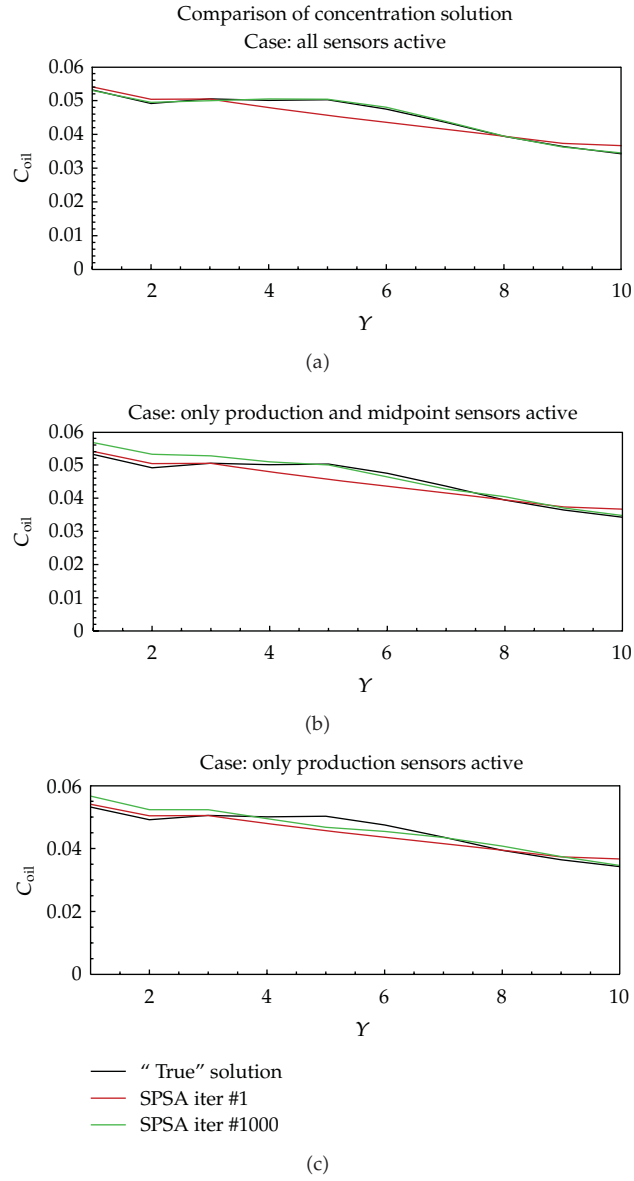

Figure 3: Example 1: history matching of oil phase concentrations based on sensor choices.

4.2. Example 2: Brugge Field Test

In this example, a synthetic reservoir referred to as the Brugge field is used for the purpose of history matching and permeability estimation. This synthetic field was constructed by the Norwegian research center, TNO in February 2008 for a comparative case study on history matching and reservoir characterization. It consisted of 104 upscaled realizations of a 3-D geological model with well-log data from 30 wells with fixed spatial positions; first 10 years production history; inverted time-lapse seismic data in terms of pressures and saturations as well as economic parameters for oil, water and discount rates. A more detailed description

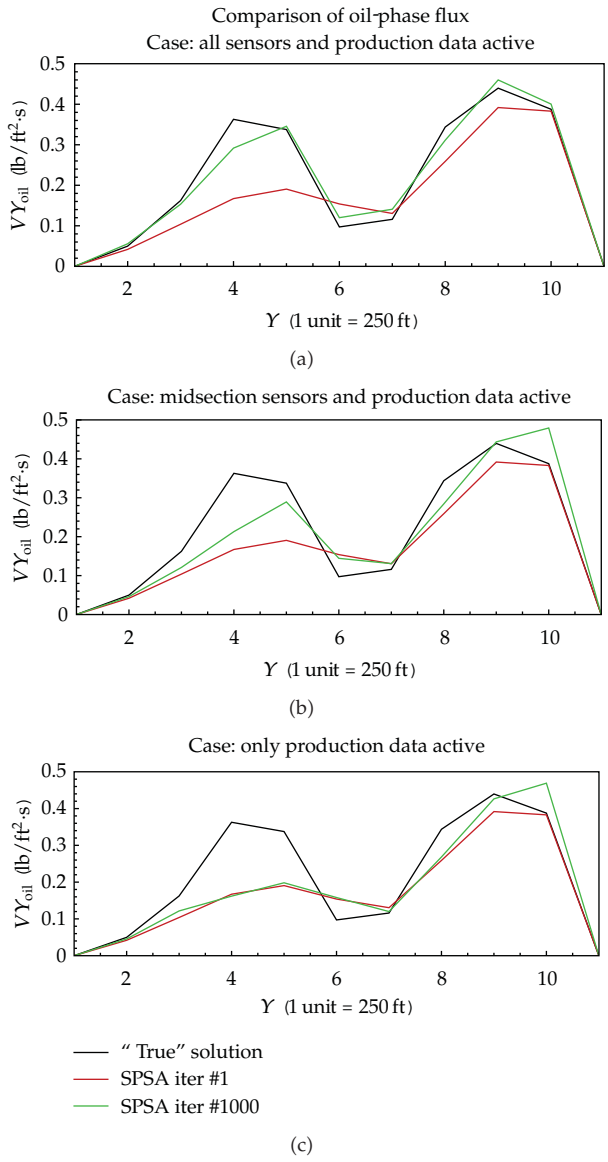

Figure 4: Example 1: history matching of oil phase fluxes based on sensor choices.

as well as the data from the field can be found at [14]. This problem is very challenging for several reasons.

The computational domain is a full 3d domain, it is irregular in geometry with a geologic fault as shown in Figure 8. The permeability field is anisotropic and very heterogeneous and hence, many more unknowns have to be estimated in this case. Finally, there are 30 wells driving the flow in this oil water problem (actually oil water!). There are 10 water injection wells and 20 oil production wells that can be shut-in based on rate or bottom-hole constraints. All these combine to make this a fairly challenging problem. Table 2 summarizes the data that describe the problem that was solved. It is noted that well #19

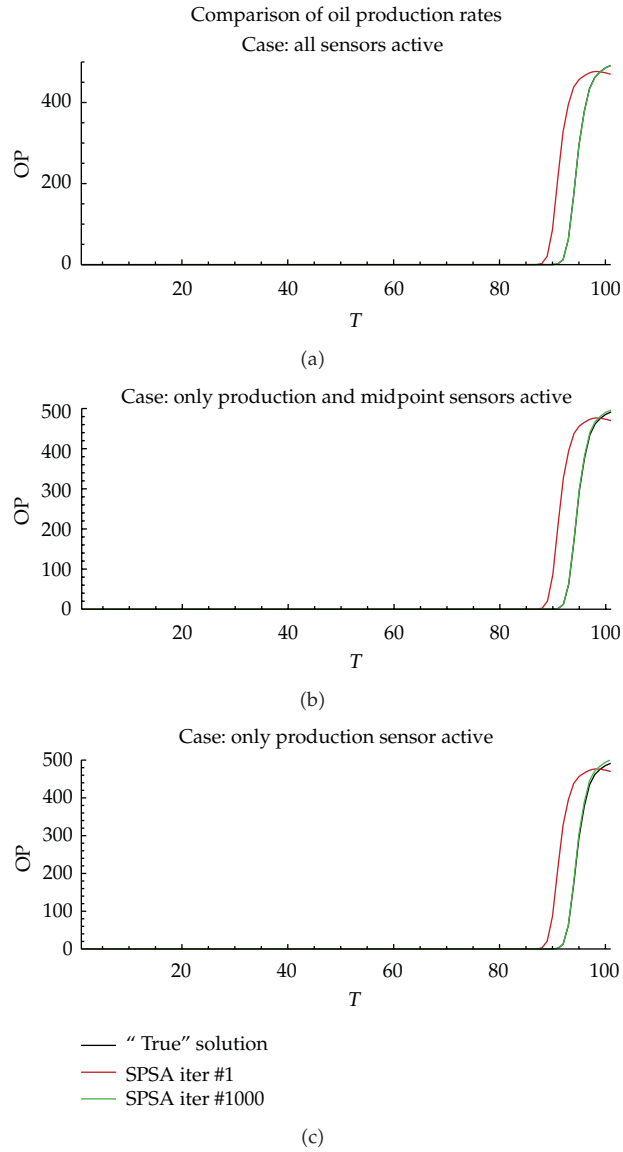

Figure 5: Example 1: history matching of well-data based on sensor choices.

(a production well) was the only bottom-hole pressure specified well without any constraint. All other wells were rate specified with a bottom-hole pressure constraint for shut-in. It is also noted that different injectors start injecting water at different times (earliest at $t = 600$ days) while the producers start producing as early as $t = 0$ days.

The first challenge with this problem was in accurately modeling the geometry of the domain with the faults. A stair-stepped approximation was once again employed to treat the geometry in keeping with the stencil resulting from mixed FEM [15]. A bounding box grid of $35 \times 21 \times 57$ was used and suitably interpolated to get values of the properties at corners of the box that intersect with the actual domain. For all other points, negative values are

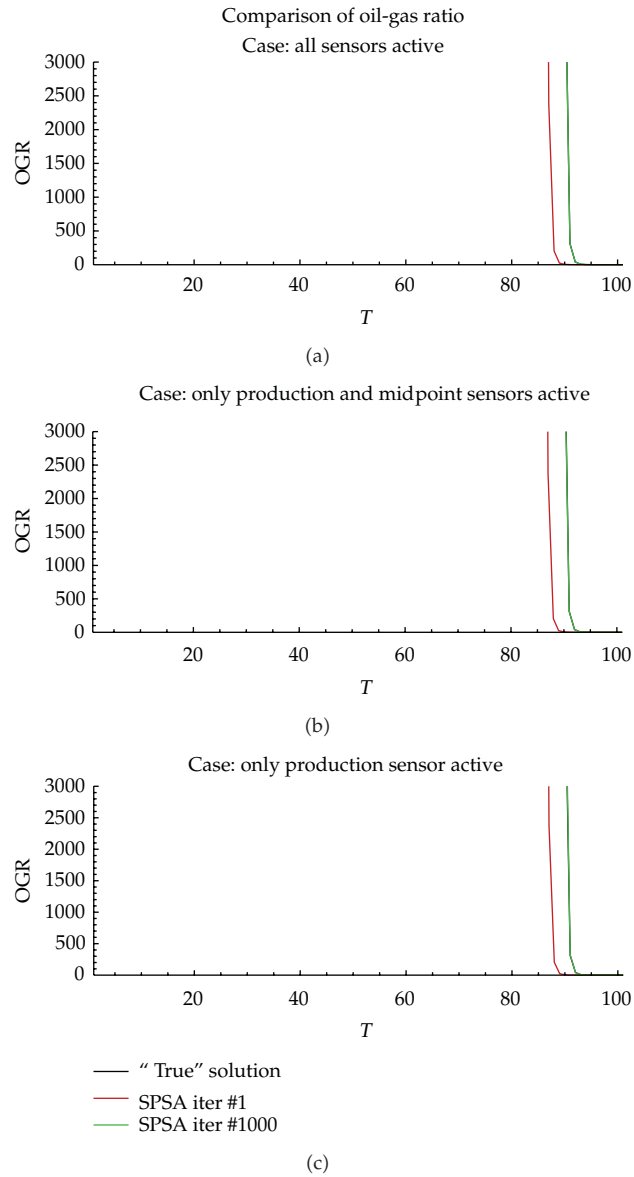

Figure 6: Example 1: history matching of well-data based on sensor choices.

assigned and these are used to keyout the elements that are actually inactive in the bounding box (i.e., for the corners that do not intersect the actual domain). Figure 8 shows the true and approximated geometries with the initial water saturation and mesh superimposed. The well locations are indicated by colored spheres, black for injectors and orange for producers.

A parallel SPSA history matching simulation was performed on the Brugge field for $P = 10$ unknowns in each direction of anisotropy (i.e., a total of 30 unknowns) and a subset ($M = 16$) of the realizations. For proof of concept, the mean permeability was assumed to be the true permeability and data (measurements) derived from the solution corresponding to the mean at prescribed intervals of time at all grid elements. Again, it is noted that this

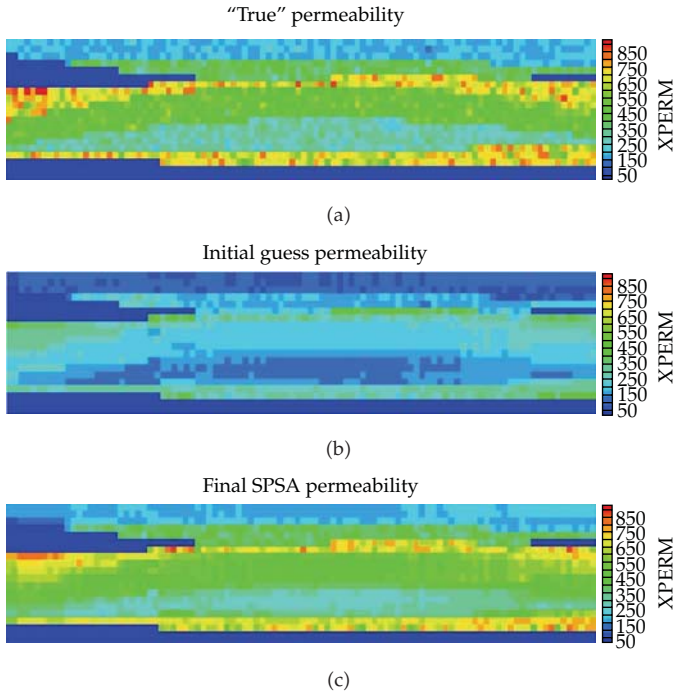

Figure 7: Example 1: permeability estimation using SPSA.

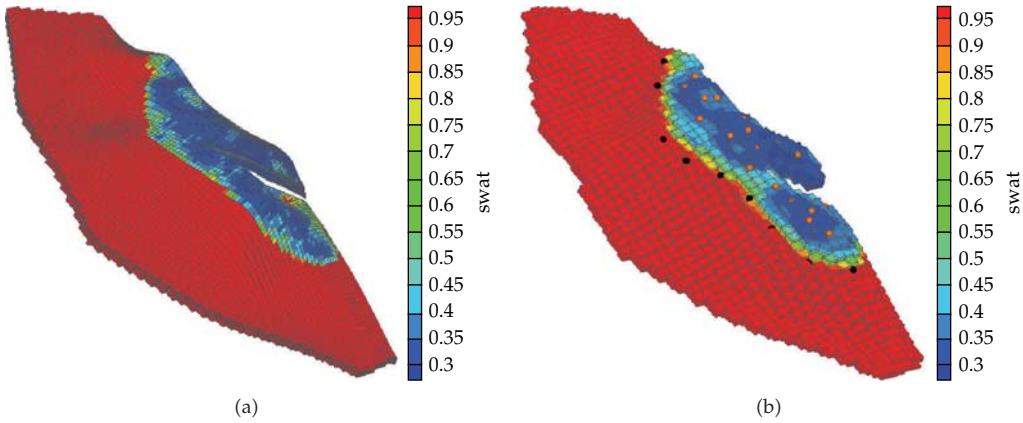

Figure 8: Example 2 (Brugge field): true (a), approximate (b) geometry with initial water saturation and grid superimposed.

is strictly not a required step, since ideally history matching is the only goal in such studies while estimated permeability is a by-product. But assuming a "true" permeability, allows one to test the effectiveness of the applied algorithm. Also, it is assumed that the history matching is performed for 20-year simulation period. Figure 10 shows the permeability estimate when the production data and solution (pressures and concentrations) measured at intervals of 5 grid elements in either areal direction are included in the loss function. The legend again spans 50 to 900 mD for all iterations for ease of comparison.

Table 2: Parameter estimation: data for example 2 (Brugge field test).

Property	Value
Simulation end-time, years	20.0
Grid dimensions	$21 \times 57 \times 35$
Physical dimensions, ft^3	$21000 \times 57000 \times 1750$
Flowing phases modeled	Oil, water
Reference oil density, lb/ft^3	56.0
Oil viscosity, cp	1.29
Reference water density, lb/ft^3	62.6
Water viscosity, cp	0.32
Oil compressibility, 1/psi	9.26×10^{-6}
Water compressibility, 1/psi	3.0×10^{-6}
Initial oil pressure, psi	≈2500
Initial oil conc., lb/ft^3	Residual-water (0.2)
Medium porosity	≈0.2
Number of wells	30 (10 water-inj. and 20 oil prod.)
Water injection rate, lb/day	4000.0
Oil-prod rate, lb/day	2000.0

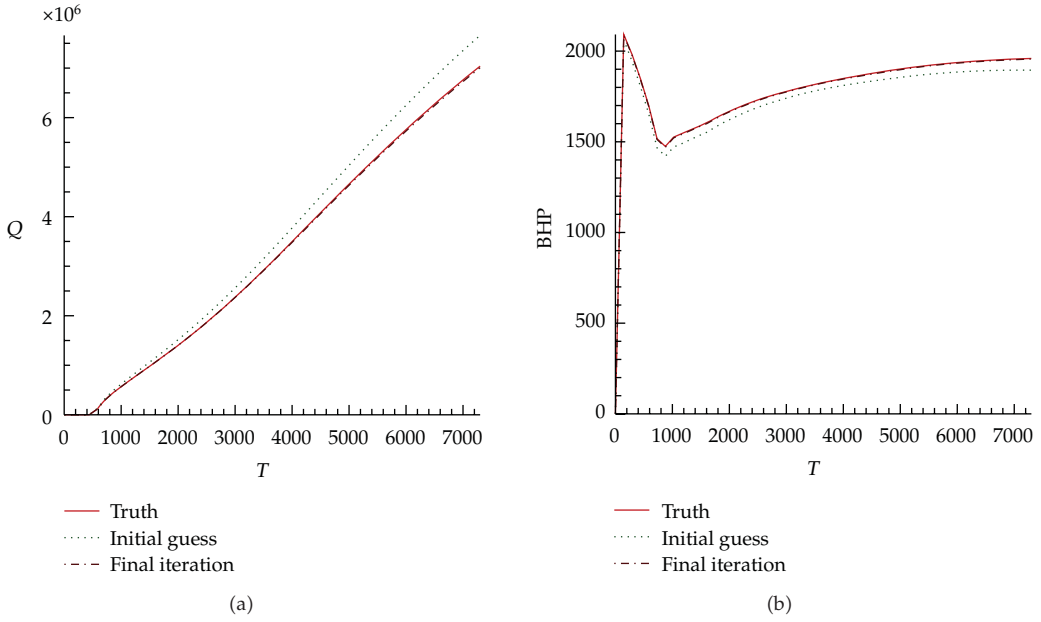

Figure 9: Example 2 (Brugge field test): well 19 (a) production curves and well 21 (b) BHP history match.

Since the physical dimensions of the Brugge formation was huge, this was a reasonable areal density (about 1 sensor every 4 square km) for sensor locations. It is observed that even though the initial guess was very far from the "target" or "true" permeability, the algorithm "coverges" in as few as 5–10 iterations. To fix ideas, it is noted that the initial permeability error is more than 60% (measured in an l_2-norm) and the normalized objective function value is 0.84 approximately. At the end of 10 iterations the permeability error is reduced to 25% and

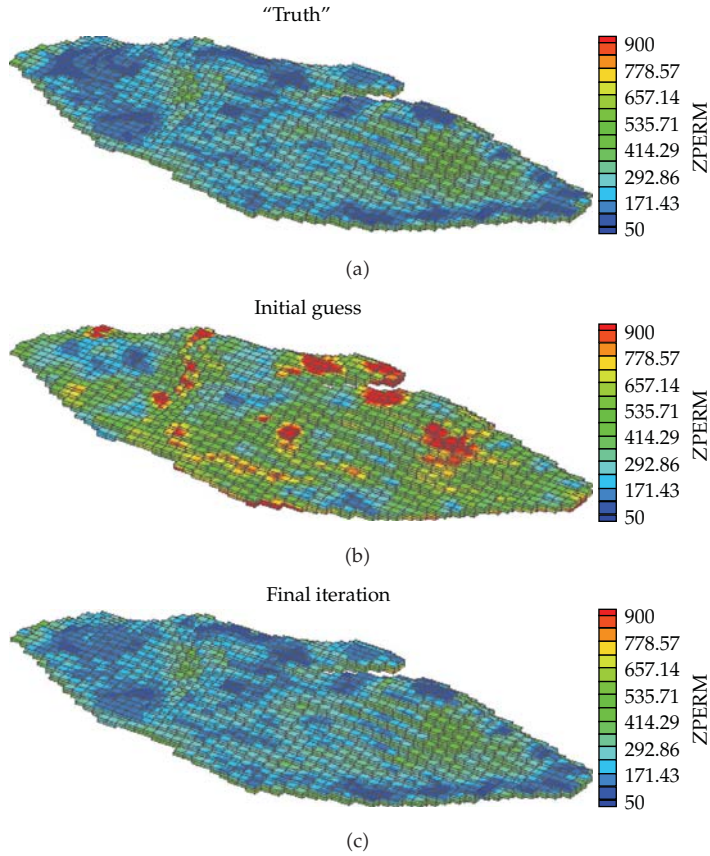

Figure 10: Example 2 (Brugge field test): estimate of permeability with SPSA iteration number.

the objective function to 0.076! At the end of 50 iterations, the permeability error is reduced to 13% and the objective to 0.016. Finally, at the end of 200 iterations, the permeability error is reduced to 3.5% while the objective is reduced to 0.001! These numbers are very encouraging given the problem at hand.

Figure 9 shows the history match versus time in days obtained with respect to bottom-hole pressures (in psi, shown for rate specified producing well #21) and cumulative production rate (in lb/day, shown for bottom-hole pressure specified producing well #19). The matches obtained for all wells were equally good. These parallel runs were performed on up to 64 processors on the Bevo2 cluster at ICES as well as on the Ranger cluster (at TACC, The University of Texas at Austin) on up to 512 processors.

4.3. Conclusions

This paper presents a robust and efficient parallel stochastic framework for subsurface reservoir characterization and history matching problems using sensor measurements of data from general multiphase flow scenarios. The parallel algorithm involves triggering multiple SPSA (simultaneous perturbation, stochastic approximation) instances, one on each processor which uses its own realization of the estimated property based on its own seed. At the end of each iteration, two options are available to compute the starting value of the

estimated property for the ensuing iteration; one based on the minimum objective across all processors and the other based on the mean of the properties across all processors. It is generally observed that a very accurate history match is obtained in as few as 5 to 10 iterations even for fairly general and complex problems. If a "true" permeability is assumed, a very accurate permeability match is also attained in as few iterations. The algorithm itself is shown to converge at a rate equivalent to that of the steepest descent method in the sense of expectations. A natural extension of this work would be to support parallel domain decomposition in each SPSA "instance" of the algorithm, so that the method not only takes advantage of a wider search space but also utilizes a divide and conquer strategy within each search path. This is perhaps the optimal strategy for such problems and may form the subject of a future work.

Acknowledgments

A portion of this paper was supported by the United States Department of Energy (DoE) through the Office of Basic Energy Sciences, Office of Science. The Center for Frontiers of Subsurface Energy Security (CFSES) is a DOE Energy Frontier Research Center, set up under contract no. DE-SC0001114. The authors gratefully acknowledge the financial support provided by the NSF-CDI under Contract no DMS 0835745 and DOE Grant no. DE-FGO2-04ER25617. Finally, the first author thanks Dr. G. Pencheva and Dr. T. Wildey for their help with input data used in the second numerical example.

References

[1] R. Versteeg, M. Ankeny, J. Harbour et al., "A structured approach to the use of near-surface geophysics in long-term monitoring," *Leading Edge*, vol. 23, no. 7, pp. 700–703, 2004.

[2] D. E. Lumley and M. J. Blunt, "Time-lapse seismic reservoir management," *Geophysics*, vol. 66, pp. 50–53, 2001.

[3] H. Kile, W. Bangerth, M. F. Wheeler, M. Parashar, and V. Matossian, "Parallel well-location optimization using stochastic algorithms on the grid computational framework," in *Proceedings of the 9th European Conference on the Mathematics of Oil Recovery (ECMOR '04)*, Cannes, France, 2004.

[4] J. C. Spall, *Introduction to Stochastic Search and Optimization: Estimation, Simulation and Control*, Wiley-Interscience Series in Discrete Mathematics and Optimization, Wiley-Interscience, Hoboken, NJ, USA, 2003.

[5] R. E. Banchs, H. Klie, A. Rodriguez, S. G. Thomas, and M. F. Wheeler, "A neural stochastic multiscale optimization framework for sensor-based parameter estimation," *Integrated Computer-Aided Engineering*, vol. 14, no. 3, pp. 213–223, 2007.

[6] H. Klie, A. Rodriguez, S. G. Thomas, M. F. Wheeler, and R. Banchs, "Assessing the value of sensor information in 4-D seismic history matching," *SEG Technical Program Expanded Abstracts*, vol. 25, no. 1, pp. 3245–3249, 2006.

[7] P. Lu, *Reservoir parameter estimation using wavelet analysis*, Ph.D. thesis, Stanford University, Palo Alto, Calif, USA, 2001.

[8] K. Pearson, "On lines and planes of closest fit to systems of points in space," *Physical Magazine*, vol. 2, no. 6, pp. 559–572, 1901.

[9] I. T. Jolliffe, *Principal Component Analysis*, Springer Series in Statistics, Springer, New York, NY, USA, 2nd edition, 2002.

[10] A. C. Reynolds, G. Gao, and G. Li, "A stochastic optimization algorithm for automatic history matching," in *Proceedings of the SPE Annual Technical Conference and Exhibition*, Houston, Tex, USA, September 2004.

[11] W. H. Press, S. A. Teukolsky, W. T. Vetterling, and B. P. Flannery, *Numerical Recipes in Fortran 77: The Art of Scientific Computing*, Cambridge University Press, Cambridge, UK, 2nd edition, 1992.

[12] J. Wheeler et al., "Integrated parallel and accurate reservoir simulator," Tech. Rep. TICAM01-25, Institute of Computational Engineering and Sciences, The University of Texas at Austin, Austin, Tex, USA, 2001.

[13] M. A. Christie and M. J. Blunt, "Tenth SPE comparative solution project: a comparison of upscaling techniques," *SPE Reservoir Evaluation and Engineering*, vol. 4, no. 4, pp. 308–316, 2001.

[14] E. Peters, R. J. Arts, G. K. Brouwer et al., "Results of the brugge benchmark study for flooding optimization and history matching," *SPE Reservoir Evaluation and Engineering*, vol. 13, no. 3, pp. 391–405, 2010.

[15] F. Brezzi and M. Fortin, *Mixed and Hybrid Finite Element Methods*, vol. 15 of *Springer Series in Computational Mathematics*, Springer, New York, NY, USA, 1991.

Hindawi Publishing Corporation
Journal of Applied Mathematics
Volume 2011, Article ID 193781, 27 pages
doi:10.1155/2011/193781

Research Article

Computing Exponential for Iterative Splitting Methods: Algorithms and Applications

Jürgen Geiser

Humboldt-Univeristät zu Berlin, 10099 Berlin, Germany

Correspondence should be addressed to Jürgen Geiser, geiser@mathematik.hu-berlin.de

Received 29 November 2010; Accepted 27 January 2011

Academic Editor: Shuyu Sun

Copyright © 2011 Jürgen Geiser. This is an open access article distributed under the Creative Commons Attribution License, which permits unrestricted use, distribution, and reproduction in any medium, provided the original work is properly cited.

Iterative splitting methods have a huge amount to compute matrix exponential. Here, the acceleration and recovering of higher-order schemes can be achieved. From a theoretical point of view, iterative splitting methods are at least alternating Picards fix-point iteration schemes. For practical applications, it is important to compute very fast matrix exponentials. In this paper, we concentrate on developing fast algorithms to solve the iterative splitting scheme. First, we reformulate the iterative splitting scheme into an integral notation of matrix exponential. In this notation, we consider fast approximation schemes to the integral formulations, also known as ϕ-functions. Second, the error analysis is explained and applied to the integral formulations. The novelty is to compute cheaply the decoupled exp-matrices and apply only cheap matrix-vector multiplications for the higher-order terms. In general, we discuss an elegant way of embedding recently survey on methods for computing matrix exponential with respect to iterative splitting schemes. We present numerical benchmark examples, that compared standard splitting schemes with the higher-order iterative schemes. A real-life application in contaminant transport as a two phase model is discussed and the fast computations of the operator splitting method is explained.

1. Introduction

We are motivated to solving multiple phase problems that arose of transport problem in porous media. In the last years, the interest in numerical simulations with multiphase problems, that can be used to model potential damage events has significantly increased in the area of final repositories for chemical or radioactive waste.

Here, the modeling of the underlying porous media, which is the geosphere, spooled with water, is important, and we apply mobile and immobile pores as a two-phase problem in the media. With such a model, we achieve more realistic scenarios of the transported species, see [1]. The transport is structured in a convection and a diffusion portion. The convection portion is determined by the velocity vector $\mathbf{v}$ and indicates the spatial direction

of the concentrations with the velocity. The diffusion portion is the spatial diffusion process of the concentrations, see [1].

The sorption allegorizes the exchange between the solute (mobile) pollutant and at the surface sorbed (immobile) pollutants and appears in the temporal term as well as in the reaction term. The reaction is reversible. The equilibrium-sorption therefore can be declared as a coefficient in the specific terms.

We concentrate on simplified models and taken into account all real conditions for achieving statements of such realistic simulations of potential damage event. Here we have the delicate problem of coupled partial and ordinary differential equations and their underlying multiscale problems. While we deal with splitting methods and decomposing such scale problems, we can overcome such scaling problems, see [2].

Moreover the computational part is important, while we dealing with large matrices and standard splitting schemes are expensive with respect to compute the exponential matrices. We solve the computational problem with a novel iterative splitting scheme, that concentrate on developing fast algorithms to solve an integral formulation of matrix exponentials. In such a scheme, we consider fast approximation schemes to the integral formulations, also known as ϕ-functions, see [3]. The novelty is to compute cheaply the decoupled exp matrices and apply only cheap matrix-vector multiplications for the higher-order terms. In general, we discuss an elegant way of embedding recent survey on methods for computing matrix exponential with respect to iterative splitting schemes.

In the following, we describe our model problem. The model equation for the multiple phase equations are given as coupled partial and ordinary differential equations:

$$\begin{aligned}\phi\partial_t c_i + \nabla\cdot\mathbf{F}_i &= g(-c_i + c_{i,\mathrm{im}}) + k_\alpha(-c_i + c_{i,\mathrm{ad}})\\ &\quad -\lambda_{i,i}\phi c_i + \sum_{k=k(i)}\lambda_{i,k}\phi c_k + \widetilde{Q}_i, \quad \text{in } \Omega\times[0,t],\end{aligned} \tag{1.1}$$

$$\mathbf{F}_i = \mathbf{v}c_i - D^{e(i)}\nabla c_i + \eta\mathbf{E}c_i, \tag{1.2}$$

$$\begin{aligned}\phi\partial_t c_{i,\mathrm{im}} &= g(c_i - c_{i,\mathrm{im}}) + k_\alpha(c_{i,\mathrm{im,ad}} - c_{i,\mathrm{im}})\\ &\quad -\lambda_{i,i}\phi c_{i,\mathrm{im}} + \sum_{k=k(i)}\lambda_{i,k}\phi c_{k,\mathrm{im}} + \widetilde{Q}_{i,\mathrm{im}}, \quad \text{in } \Omega\times[0,t],\end{aligned} \tag{1.3}$$

$$\phi\partial_t c_{i,\mathrm{ad}} = k_\alpha(c_i - c_{i,\mathrm{ad}}) - \lambda_{i,i}\phi c_{i,\mathrm{ad}} + \sum_{k=k(i)}\lambda_{i,k}\phi c_{k,\mathrm{ad}} + \widetilde{Q}_{i,\mathrm{ad}}, \quad \text{in } \Omega\times[0,t], \tag{1.4}$$

$$\begin{aligned}\phi\partial_t c_{i,\mathrm{im,ad}} &= k_\alpha(c_{i,\mathrm{im}} - c_{i,\mathrm{im,ad}}) - \lambda_{i,i}\phi c_{i,\mathrm{im,ad}}\\ &\quad + \sum_{k=k(i)}\lambda_{i,k}\phi c_{k,\mathrm{im,ad}} + \widetilde{Q}_{i,\mathrm{im,ad}}, \quad \text{in } \Omega\times[0,t],\end{aligned} \tag{1.5}$$

$$c_i(\mathbf{x},t) = c_{i,0}(\mathbf{x}), \quad c_{i,\mathrm{ad}}(\mathbf{x},t) = 0, \quad c_{i,\mathrm{im}}(\mathbf{x},t) = 0, \quad c_{i,\mathrm{im,ad}}(\mathbf{x},t) = 0, \quad \text{on } \Omega, \tag{1.6}$$

$$c_i(\mathbf{x},t) = c_{i,1}(\mathbf{x},t), \quad c_{i,\mathrm{ad}}(\mathbf{x},t) = 0, \quad c_{i,\mathrm{im}}(\mathbf{x},t) = 0, \quad c_{i,\mathrm{im,ad}}(\mathbf{x},t) = 0, \quad \text{on } \partial\Omega\times[0,t], \tag{1.7}$$

where the initial value is given as $c_{i,0}$ and we assume Dirichlet boundary conditions with the function $c_{i,1}(x,t)$ sufficiently smooth, all other initial and boundary conditions of the other phases zero.

ϕ: effective porosity $(-)$,

c_i: concentration of the ith gaseous species in the plasma chamber phase $(\mathrm{mol/cm^3})$,

$c_{i,\mathrm{im}}$: concentration of the ith gaseous species in the immobile zones of the plasma chamber phase $(\mathrm{mol/cm^3})$,

$c_{i,\mathrm{ad}}$: concentration of the ith gaseous species in the mobile adsorbed zones of the plasma chamber phase $(\mathrm{mol/cm^3})$,

$c_{i,\mathrm{im,ad}}$: concentration of the ith gaseous species in the immobile adsorbed zones of the plasma chamber phase $(\mathrm{mol/cm^3})$,

$\mathbf{v}$: velocity through the chamber and porous substrate [4] (cm/nsec),

$D^{e(i)}$: element-specific diffusions-dispersions tensor $(\mathrm{cm^2/nsec})$,

$\lambda_{i,i}$: decay constant of the ith species (1/nsec),

$\widetilde{Q}_i$: source term of the ith species $(\mathrm{mol/(cm^3 nsec)})$,

g: exchange rate between the mobile and immobile concentration (1/nsec),

k_α: exchange rate between the mobile and adsorbed concentration or immobile and immobile adsorbed concentration (kinetic controlled sorption) (1/nsec),

$\mathbf{E}$: stationary electric field in the apparatus (V/cm),

η: the mobility rate in the electric field, see [5] $(\mathrm{cm^2/nsec})$.

with $i = 1, \ldots, M$ and M denotes the number of components.

The parameters in (1.1) are further described, see also [1].

The effective porosity is denoted by ϕ and declares the portion of the porosities of the aquifer, that is filled with plasma, and we assume a nearly fluid phase. The transport term is indicated by the Darcy velocity $\mathbf{v}$, that presents the flow-direction and the absolute value of the plasma flux. The velocity field is divergence-free. The decay constant of the ith species is denoted by λ_i. Thereby does $k(i)$ denote the indices of the other species.

In this paper we concentrate on solving linear evolution equations, such as the differential equation,

$$\partial_t u = Au, \qquad u(0) = u_0, \tag{1.8}$$

where A can be an unbounded operator. We assume to achieve large-scale differential equation, which are delicate to solve with standard solvers.

Our main focus will be to consider and contrast higher-order algorithms derived from standard schemes as for example Strang-splitting schemes.

We propose iterative splitting schemes as a solver scheme which is simple to implement and parallelisible.

A rewriting to integral formulation, allows to reduce the computation to numerical approximation schemes. While standard schemes has the disadvantage to compute commutators to achieve higher-order schemes, we could speed up our schemes by recursive algorithms. Iterative schemes can be seen as Successive approximations, which are based on recursive integral formulations in which an iterative method is enforce the time dependency.

The paper is outlined as follows. In Section 2, we present the underlying splitting methods. The algorithms for the exponentials are given in Section 3. Numerical verifications are given in Section 4. In Section 5, we briefly summarize our results.

2. Iterative Splitting Method

The following algorithm is based on the iteration with fixed-splitting discretization step-size τ, namely, on the time interval $[t^n, t^{n+1}]$ we solve the following subproblems consecutively for $i = 0, 2, \ldots, 2m$. (cf. [6, 7]):

$$\begin{aligned} \frac{\partial c_i(t)}{\partial t} &= Ac_i(t) + Bc_{i-1}(t), \quad \text{with } c_i(t^n) = c^n,\ c_0(t^n) = c^n,\ c_{-1} = 0.0, \\ \frac{\partial c_{i+1}(t)}{\partial t} &= Ac_i(t) + Bc_{i+1}(t), \quad \text{with } c_{i+1}(t^n) = c^n, \end{aligned} \tag{2.1}$$

where c^n is the known split approximation at the time level $t = t^n$. The split approximation at the time level $t = t^{n+1}$ is defined as $c^{n+1} = c_{2m+1}(t^{n+1})$, (clearly, the function $c_{i+1}(t)$ depends on the interval $[t^n, t^{n+1}]$, too, but, for the sake of simplicity, in our notation we omit the dependence on n).

In the following we will analyze the convergence and the rate of convergence of the method (2.1) for m tends to infinity for the linear operators $A, B : \mathbf{X} \to \mathbf{X}$, where we assume that these operators and their sum are generators of the C_0 semigroups. We emphasize that these operators are not necessarily bounded, so the convergence is examined in a general Banach space setting.

The novelty of the convergence results are the reformulation in integral-notation. Based on this, we can assume to have bounded integral operators which can be estimated and given in a recursive form. Such formulations are known in the work of [8, 9] and estimations of the kernel part with the exponential operators are sufficient to estimate the recursive formulations.

2.1. Error Analysis

We present the results of the consistency of our iterative method. We assume for the system of operator the generator of a C_0 semigroup based on their underlying graph norms.

Theorem 2.1. *Let one consider the abstract Cauchy problem in a Hilbert space* $\mathbf{X}$

$$\begin{aligned} \partial_t c(x,t) &= Ac(x,t) + Bc(x,t), \quad 0 < t \le T,\ x \in \Omega, \\ c(x,0) &= c_0(x), \quad x \in \Omega, \\ c(x,t) &= c_1(x,t), \quad x \in \partial\Omega \times [0,T], \end{aligned} \tag{2.2}$$

where $A, B : D(\mathbf{X}) \to \mathbf{X}$ are given linear operators which are generators of the C_0-semigroup and $c_0 \in \mathbf{X}$ is a given element. We assume A, B are unbounded. Further, we assume the estimations of the unbounded operator B with sufficient smooth initial conditions (see [8]):

$$\left\| B \exp((A+B)\tau) u_0 \right\| \leq \kappa. \tag{2.3}$$

Further we assume the estimation of the partial integration of the unbounded operator B (see [8]):

$$\left\| B \int_0^\tau \exp(Bs) s ds \right\| \leq \tau C. \tag{2.4}$$

Then, we can bound our iterative operator splitting method as

$$\left\| \left(S_i - \exp((A+B)\tau) \right) \right\| \leq C\tau^i, \tag{2.5}$$

where S_i is the approximated solution for the ith iterative step and C is a constant that can be chosen uniformly on bounded time intervals.

Proof. Let us consider the iteration (2.1) on the subinterval $[t^n, t^{n+1}]$.

For the first iterations, we have

$$\partial_t c_1(t) = A c_1(t), \quad t \in \left(t^n, t^{n+1}\right], \tag{2.6}$$

and for the second iteration we have:

$$\partial_t c_2(t) = A c_1(t) + B c_2(t), \quad t \in \left(t^n, t^{n+1}\right]. \tag{2.7}$$

In general, we have:

(i) for the odd iterations, $i = 2m + 1$ for $m = 0, 1, 2, \ldots$

$$\partial_t c_i(t) = A c_i(t) + B c_{i-1}(t), \quad t \in \left(t^n, t^{n+1}\right], \tag{2.8}$$

where for $c_0(t) \equiv 0$,

(ii) for the even iterations, $i = 2m$ for $m = 1, 2, \ldots$

$$\partial_t c_i(t) = A c_{i-1}(t) + B c_i(t), \quad t \in \left(t^n, t^{n+1}\right]. \tag{2.9}$$

We have the following solutions for the iterative scheme: the solutions for the first two equations are given by the variation of constants:

$$\begin{aligned} c_1(t) &= \exp\Big(A\Big(t^{n+1}-t\Big)\Big)c(t^n), \quad t \in \Big(t^n, t^{n+1}\Big], \\ c_2(t) &= \exp(Bt)c(t^n) + \int_{t^n}^{t^{n+1}} \exp\Big(B\Big(t^{n+1}-s\Big)\Big)Ac_1(s)ds, \quad t \in \Big(t^n, t^{n+1}\Big]. \end{aligned} \tag{2.10}$$

For the recurrence relations with even and odd iterations, we have the solutions: for the odd iterations: $i = 2m+1$, for $m = 0, 1, 2, \ldots$,

$$c_i(t) = \exp(A(t-t^n))c(t^n) + \int_{t^n}^{t} \exp\Big(\Big(t^{n+1}-s\Big)A\Big)Bc_{i-1}(s)ds, \quad t \in \Big(t^n, t^{n+1}\Big]. \tag{2.11}$$

For the even iterations, $i = 2m$, for $m = 1, 2, \ldots$

$$c_i(t) = \exp(B(t-t^n))c(t^n) + \int_{t^n}^{t} \exp\Big(\Big(t^{n+1}-s\Big)B\Big)Ac_{i-1}(s)ds, \quad t \in \Big(t^n, t^{n+1}\Big]. \tag{2.12}$$

The consistency is given as the following.

For e_1, we have

$$\begin{aligned} c_1(\tau) &= \exp(A\tau)c(t^n), \\ c(\tau) &= \exp((A+B)\tau)c(t^n) = \exp(A\tau)c(t^n) \\ &\quad + \int_{t^n}^{t^{n+1}} \exp\Big(A\Big(t^{n+1}-s\Big)\Big)B\exp(s(A+B))c(t^n)ds. \end{aligned} \tag{2.13}$$

We obtain

$$\|e_1\| = \|c - c_1\| \le \left\|\exp((A+B)\tau)c(t^n) - \exp(A\tau)c(t^n)\right\| \le C_1\tau c(t^n). \tag{2.14}$$

For e_2 we have (alternating)

$$\begin{aligned} c_2(\tau) &= \exp(B\tau)c(t^n) + \int_{t^n}^{t^{n+1}} \exp\Big(B\Big(t^{n+1}-s\Big)\Big)A\exp(sA)c(t^n)ds, \\ c(\tau) &= \exp(B\tau)c(t^n) + \int_{t^n}^{t^{n+1}} \exp\Big(B\Big(t^{n+1}-s\Big)\Big)A\exp(sA)c(t^n)ds \\ &\quad + \int_{t^n}^{t^{n+1}} \exp(Bs)A\int_{t^n}^{t^{n+1}-s} \exp\Big(A\Big(t^{n+1}-s-\rho\Big)\Big)B\exp\big(\rho(A+B)\big)c(t^n)d\rho ds. \end{aligned} \tag{2.15}$$

We obtain

$$\|e_2\| \leq \left\|\exp((A+B)\tau)c(t^n) - c_2\right\| \leq C_2\tau^2 c(t^n). \tag{2.16}$$

For odd and even iterations, the recursive proof is given in the following. For the odd iterations (only iterations over A), $i = 2m+1$ for $m = 0, 1, 2, \ldots$, for e_i, we have:

$$\begin{aligned}
c_i(\tau) &= \exp(A\tau)c(t^n) \\
&+ \int_{t^n}^{t^{n+1}} \exp\Big(A\Big(t^{n+1}-s\Big)\Big)B\exp(sA)c(t^n)ds \\
&+ \int_{t^n}^{t^{n+1}} \exp\Big(A\Big(t^{n+1}-s_1\Big)\Big)B\int_{t^n}^{t^{n+1}-s_1} \exp\Big(\Big(t^{n+1}-s_1-s_2\Big)A\Big)B\exp(s_2A)c(t^n)ds_2ds_1 \\
&+ \cdots \\
&+ \int_{t^n}^{t^{n+1}} \exp\Big(A\Big(t^{n+1}-s_1\Big)\Big)B\int_{t^n}^{t^{n+1}-s_1} \exp\Big(\Big(t^{n+1}-s_1-s_2\Big)A\Big)B\exp(s_2A)c(t^n)ds_2ds_1 + \cdots \\
&+ \int_{t^n}^{t^{n+1}} \exp\Big(A\Big(t^{n+1}-s_1\Big)\Big)B\cdots\int_{t^n}^{t^{n+1}-\sum_{j=1}^{i-2}s_j} \exp\left(\left(t^{n+1}-\sum_{j=1}^{i-1}s_j\right)A\right)B \\
&\qquad \times \exp(s_iA)c(t^n)\,ds_{i-1}\cdots ds_2ds_1, \\
c(\tau) &= \exp(A\tau)c(t^n) \\
&+ \int_{t^n}^{t^{n+1}} \exp\Big(A\Big(t^{n+1}-s\Big)\Big)B\exp(sA)c(t^n)ds \\
&+ \int_{t^n}^{t^{n+1}} \exp\Big(A\Big(t^{n+1}-s_1\Big)\Big)B\int_{t^n}^{t^{n+1}-s_1} \exp\Big(\Big(t^{n+1}-s_1-s_2\Big)A\Big)B\exp(s_2A)c(t^n)ds_2ds_1 \\
&+ \cdots \\
&+ \int_{t^n}^{t^{n+1}} \exp\Big(A\Big(t^{n+1}-s_1\Big)\Big)B\int_{t^n}^{t^{n+1}-s_1} \exp\Big(\Big(t^{n+1}-s_1-s_2\Big)A\Big)B\exp(s_2A)c(t^n)ds_2ds_1 + \cdots \\
&+ \int_{t^n}^{t^{n+1}} \exp\Big(A\Big(t^{n+1}-s_1\Big)\Big)B\cdots\int_{t^n}^{t^{n+1}-\sum_{j=1}^{i-2}s_j} \exp\left(\left(t^{n+1}-\sum_{j=1}^{i}s_j\right)A\right)B \\
&\qquad \times \exp(s_iA)c(t^n)\,ds_i\cdots ds_2ds_1.
\end{aligned} \tag{2.17}$$

We obtain

$$\|e_i\| \leq \left\|\exp((A+B)\tau)c(t^n) - c_i\right\| \leq C\tau^i c(t^n), \tag{2.18}$$

where i is the number of iterative steps.

The same idea can be applied to the even iterative scheme and also for alternating A and B. □

Remark 2.2. The same idea can be applied to $A = \nabla D \nabla$ $B = -\mathbf{v}\cdot\nabla$, so that one operator is less unbounded, but we reduce the convergence order

$$\begin{aligned} &\|e_1\| = K\|B\|\tau^{\alpha_1}\|e_0\| + \mathcal{O}\left(\tau^{1+\alpha_1}\right), \\ &\text{and hence,} \\ &\|e_2\| = K\|B\|\|e_0\|\tau^{1+\alpha_1+\alpha_2} + \mathcal{O}\left(\tau^{1+\alpha_1+\alpha}\right), \end{aligned} \tag{2.19}$$

where $0 \leq \alpha_1, \alpha_2 < 1$.

Remark 2.3. If we assume the consistency of $\mathcal{O}(\tau^m)$ for the initial value $e_1(t^n)$ and $e_2(t^n)$, we can redo the proof and obtain at least a global error of the splitting methods of $\mathcal{O}(\tau^{m-1})$.

2.2. Splitting Method to Couple Mobile, Immobile, and Adsorbed Parts

The motivation of the splitting method are based on the following observations.

(i) The mobile phase is semidiscretized with fast finite volume methods and can be stored into a stiffness-matrix. We achieve large time steps, if we consider implicit Runge-Kutta methods of lower order (e.g., implicit Euler) as a time discretization method.

(ii) The immobile, adsorbed and immobile-adsorbed phases are purely ordinary differential equations and each of them is cheap to solve with explicit Runge-Kutta schemes.

(iii) The ODEs can be seen as perturbations and can be solved all explicit in a fast iterative scheme.

For the full equation we consider the following matrix notation:

$$\begin{aligned} \partial_t \mathbf{c} &= A_1\mathbf{c} + A_2\mathbf{c} + B_1(\mathbf{c} - \mathbf{c}_{\text{im}}) + B_2(\mathbf{c} - \mathbf{c}_{\text{ad}}) + \mathbf{Q}, \\ \partial_t \mathbf{c}_{\text{im}} &= A_2\mathbf{c}_{\text{im}} + B_1(\mathbf{c}_{\text{im}} - \mathbf{c}) + B_2(\mathbf{c}_{\text{im}} - \mathbf{c}_{\text{im,ad}}) + \mathbf{Q}_{\text{im}}, \\ \partial_t \mathbf{c}_{\text{ad}} &= A_2\mathbf{c}_{\text{ad}} + B_2(\mathbf{c}_{\text{ad}} - \mathbf{c}) + \mathbf{Q}_{\text{ad}}, \\ \partial_t \mathbf{c}_{\text{im,ad}} &= A_2\mathbf{c}_{\text{im,ad}} + B_2(\mathbf{c}_{\text{im,ad}} - \mathbf{c}_{\text{im}}) + \mathbf{Q}_{\text{im,ad}}, \end{aligned} \tag{2.20}$$

where $\mathbf{c} = (c_1, \ldots, c_m)^T$ is the spatial discretized concentration in the mobile phase, see (1.1), $\mathbf{c}_{\text{im}} = (c_{1,\text{im}}, \ldots, c_{m,\text{im}})^T$ is the concentration in the immobile phase, the some also for the other phase concentrations. A_1 is the stiffness matrix of (1.1), A_2 is the reaction matrix of the right-hand side of (1.1), B_1 and B_2 are diagonal matrices with the exchange of the immobile and kinetic parameters, see (1.4) and (1.5).

Further, $\mathbf{Q}, \ldots, \mathbf{Q}_{\text{im,ad}}$ are the spatial discretized sources vectors.

Now, we have the following ordinary differential equation:

$$\partial_t \mathbf{C} = \begin{pmatrix} A_1 + A_2 + B_1 + B_2 & -B_1 & -B_2 & 0 \\ -B_1 & A_2 + B_1 + B_2 & 0 & -B_2 \\ -B_2 & 0 & A_2 + B_2 & 0 \\ 0 & -B_2 & 0 & A_2 + B_2 \end{pmatrix} \mathbf{C} + \tilde{\mathbf{Q}}, \tag{2.21}$$

where $\mathbf{C} = (\mathbf{c}, \mathbf{c}_{\text{im}}, \mathbf{c}_{\text{ad}}, \mathbf{c}_{\text{im,ad}})^T$ and the right-hand side is given as $\tilde{\mathbf{Q}} = (\mathbf{Q}, \mathbf{Q}_{\text{im}}, \mathbf{Q}_{\text{ad}}, \mathbf{Q}_{\text{im,ad}})^T$.

For such an equation, we apply the decomposition of the matrices:

$$\begin{aligned} \partial_t \mathbf{C} &= \tilde{A}\mathbf{C} + \tilde{\mathbf{Q}}, \\ \partial_t \mathbf{C} &= \tilde{A}_1 \mathbf{C} + \tilde{A}_2 \mathbf{C} + \tilde{\mathbf{Q}}, \end{aligned} \tag{2.22}$$

where

$$\tilde{A}_1 = \begin{pmatrix} A_1 + A_2 & 0 & 0 & 0 \\ 0 & A_2 & 0 & 0 \\ 0 & 0 & A_2 & 0 \\ 0 & 0 & 0 & A_2 \end{pmatrix}, \qquad \tilde{A}_2 = \begin{pmatrix} B_1 + B_2 & -B_1 & -B_2 & 0 \\ -B_1 & B_1 + B_2 & 0 & -B_2 \\ -B_2 & 0 & B_2 & 0 \\ 0 & -B_2 & 0 & B_2 \end{pmatrix}. \tag{2.23}$$

The equation system is numerically solved by an iterative scheme.

Algorithm 2.4. We divide our time interval $[0, T]$ into subintervals $[t^n, t^{n+1}]$, where $n = 0, 1, \ldots N$, $t^0 = 0$, and $t^N = T$.

We start with $n = 0$.

(1) The initial conditions are given with $\mathbf{C}_0(t^{n+1}) = \mathbf{C}(t^n)$. We start with $k = 0$.

(2) Compute the fix-point iteration scheme given as

$$\partial_t \mathbf{C}^k = \tilde{A}_1 \mathbf{C}^k + \tilde{A}_2 \mathbf{C}^{k-1} + \tilde{\mathbf{Q}}, \tag{2.24}$$

where k is the iteration index, see [10]. For the time integration, we apply Runge-Kutta methods as ODE solvers, see [11, 12].

(3) The stop criterion for the time interval $[t^n, t^{n+1}]$ is given as

$$\left\| \mathbf{C}^k\left(t^{n+1}\right) - \mathbf{C}^{k-1}\left(t^{n+1}\right) \right\| \leq \text{err}, \tag{2.25}$$

where $\|\cdot\|$ is the maximum norm over all components of the solution vector. err is a given error bound, for example, err $= 10^{-4}$.

If (2.25) is fulfilled, we have the result

$$\mathbf{C}\left(t^{n+1}\right) = \mathbf{C}^k\left(t^{n+1}\right). \tag{2.26}$$

If $n = N$ then we stop and are done.

If (2.25) is not fulfilled, we do $k = k + 1$ and go to (2).

The error analysis of the schemes are given in the following Theorem.

Theorem 2.5. *Let $A, B \in \mathcal{L}(\mathbf{X})$ be given linear bounded operators in a Banach space $\mathcal{L}(\mathbf{X})$. We consider the abstract Cauchy problem:*

$$\begin{aligned} \partial_t \mathbf{C}(t) &= \widetilde{A}\mathbf{C}(t) + \widetilde{B}\mathbf{C}(t), \quad t_n \leq t \leq t_{n+1}, \\ \mathbf{C}(t_n) &= \mathbf{C}_n, \quad \textit{for } n = 1, \ldots, N, \end{aligned} \tag{2.27}$$

where $t_1 = 0$ and the final time is $t_N = T \in \mathbb{R}^+$. Then problem (2.27) has a unique solution. For a finite steps with time size $\tau_n = t^{n+1} - t^n$, the iteration (2.24) for $k = 1, 2, \ldots, q$ is consistent with an order of consistency $\mathcal{O}(\tau_n^q)$.

Proof. The outline of the proof is given in [2]. □

In the next section we describe the computation of the integral formulation with exp-functions.

3. Exponentials to Compute Iterative Schemes

The theoretical ideas can be discussed in the following formulation:

$$\begin{aligned} D_A(B,t)^{[0]} &= \exp(tB), \\ D_A(B,t)^{[k]} &= k \int_0^t \exp((t-s)B) A D_A(B,s)^{[k-1]} ds, \end{aligned} \tag{3.1}$$

and the matrix formulation of our two-step scheme is given as

$$\widetilde{A} = \begin{pmatrix} A & 0 & \cdots & \cdots \\ A & B & 0 & \cdots \\ 0 & B & A & \cdots \\ \vdots & \ddots & \ddots & \ddots \\ 0 & \cdots & B & A \end{pmatrix}, \tag{3.2}$$

the computation of the exp-Matrix can be expressed as:

$$\exp\left(\widetilde{A}t\right) := \begin{pmatrix} \exp(At) & 0 & \cdots & \cdots \\ D_A(B) & \exp(Bt) & 0 & \cdots \\ \dfrac{D_B(A)^{[2]}}{2!} & \dfrac{D_B(A)^{[1]}}{1!} & \exp(At) & \cdots \\ \vdots & \ddots & \ddots & \ddots \\ \dfrac{D_B(A)^{[n]}}{n!} & \cdots & \dfrac{D_B(A)^{[1]}}{1!} & \exp(At) \end{pmatrix}. \tag{3.3}$$

Here, we have to compute the right-hand side as time dependent term, means we evaluate $\exp(At)$ and $\exp(Bt)$ as a Taylor expansion. Then the integral formulation can be done with polynomials and we derive the expansion of such integral operators with the ϕ-function.

The ϕ-functions are defined as the integration of the exp-functions. We can analytically derive ϕ-functions with respect to the integral-formulation of a matrix exp-function.

In the following we reduce to a approximation of the fixed right-hand side (means we assume $D_A(B,s)^{[k-1]} \approx D_A(B,0)^{[k-01]}$).

Later we also follow with more extended schemes.

Computing ϕ-Functions:

$$\begin{aligned} \phi_0(x) &= e^x, \\ \phi_{k+1}(x) &= \frac{\phi_k(x) - 1/k!}{x}, \quad k \geq 0. \end{aligned} \tag{3.4}$$

So the matrix formulation of our scheme is given as

$$Y(t) = \exp\left(\widetilde{A}t\right) Y(0), \tag{3.5}$$

where $\widetilde{A}$ is given as,

$$\widetilde{A} = \begin{pmatrix} A & 0 & \cdots & \cdots \\ A & B & 0 & \cdots \\ 0 & A & B & \cdots \\ \vdots & \ddots & \ddots & \ddots \\ 0 & \cdots & B & A \end{pmatrix}, \tag{3.6}$$

the computation of the exp-Matrix can be expressed in a first-order scheme and with the assumption of commutations is given as:

$$\exp\left(\widetilde{A}t\right) := \begin{pmatrix} \exp(At) & 0 & \cdots & \cdots & \cdots \\ \phi_1(Bt)A\ t & \exp(Bt) & 0 & \cdots & \cdots \\ \phi_2(At)B(B+A)t^2 & \phi_1(At)Bt & \exp(At) & \cdots & \cdots \\ \vdots & \ddots & \ddots & \ddots & \vdots \\ \phi_i(At)B(A+B)^{i-1}\ t^i & \cdots & \phi_1(At)Bt & & \exp(At) \end{pmatrix}, \tag{3.7}$$

where we assume $u_i(s) = u(t^n)$, mean we approximate the right-hand side term.

For higher-orders we should also include the full derivations of $c_1, c_2, \ldots$.

3.1. Derivation of the Formula

Consider the equation

$$\dot{x} = Ax + a, \quad x(0) = 0, \tag{3.8}$$

the solution of this equation in terms of the $\phi_k, k = 0, 1$, is given as

$$x = t\phi_1(tA)a. \tag{3.9}$$

Similarly, the equation

$$\dot{x} = Ax + bt, \quad x(0) = 0, \tag{3.10}$$

has a solution of the form

$$x = t^2\phi_2(tA)b. \tag{3.11}$$

In general, the solution of the equation

$$\dot{x} = Ax + a + bt + c\frac{t^2}{2!} + \cdots, \quad x(0) = 0, \tag{3.12}$$

admits the form

$$x = t\phi_1(tA)a + t^2\phi_2(tA)b + t^3\phi_3(tA)c + \cdots. \tag{3.13}$$

In this section, we use the formula (3.21) for iterative schemes given as

$$\begin{aligned} \dot{u}_1 &= Au_1, \\ \dot{u}_2 &= Au_1 + Bu_2, \\ \dot{u}_3 &= Au_3 + Bu_2, \\ \dot{u}_4 &= \cdots. \end{aligned} \tag{3.14}$$

The solution of the first iteration given by

$$u_1 = e^{At}u_0. \tag{3.15}$$

Inserting this into (3.26) and expanding e^{At} up to the order 1, we have 2nd order approximation of the exact solution which has a form

$$u_2 = e^{Bt}u_0 + \phi_1(tA)Atu_0. \tag{3.16}$$

Similarly, inserting (3.16) into (3.27) and expanding $\phi_1(tA)$, we have a third order approximation of the exact solution

$$u_3 = e^{Bt}u_0 + \phi_1(tB)Btu_0 + \phi_2(tB)B(B + A)t^2u_0. \tag{3.17}$$

In general for $i = 0, 2, 4, \ldots$, we have the $p = i + 1$-th order approximation of the exact solution in terms of the ϕ_i function as follows:

$$u_i = e^{At}u_0 + \phi_1(tA)Atu_0 + \phi_2(tA)A(B + A)t^2u_0 + \cdots + \phi_i(tA)A(A + B)^{i-1}u_0. \tag{3.18}$$

For $i = 1, 3, 5, \ldots$, we have

$$u_i = e^{Bt}u_0 + \phi_1(tB)B\ tu_0 + \phi_2(tB)B(B + A)t^2u_0 + \cdots + \phi_i(tB)B(B + A)^{i-1}t^iu_0. \tag{3.19}$$

3.2. Algorithms

In the following, we discuss the one- and two-side algorithms.

3.3. Two-Side Scheme

For the implementation of the integral formulation, we have to deal with parallel ideas, which means we select independent parts of the formulation.

Step 1. Determine the order of the method by fixed iteration number.

Step 2. Consider the time interval $[t_0, T]$, divide it into N subintervals so that time step is $h = (T - t_0)/N$.

Step 3. On each subinterval, $[t_n, t_n+h]$, $n = 0, 1, \ldots, N$, use the algorithm by considering initial conditions for each step as $u(t_0) = u_0$, $u_i(t_n) = u_{i-1}(t_n) = u(t_n)$,

$$\begin{aligned}
u_2(t_n + h) &= \left(\phi_0(Bt) + \phi_1(Bt)At\right)u(t_n)\\
u_3(t_n + h) &= \left(\phi_0(At) + \phi_1(At)Bt + \phi_2(At)B(B + A)\ t^2\right)u(t_n)\\
&\vdots\\
u_{2i}(t_n + h) &= \left(\phi_0(Bt) + \phi_1(Bt)At + \cdots + \phi_{2i-1}(Bt)A(A + B)^{2i-1}\ t^{2i}\right)u_{2i-1}(t_n)\\
u_{2i+1}(t_n + h) &= \left(\phi_0(At) + \phi_1(At)Bt + \cdots + \phi_{2i}(At)B(B + A)^{2i}t^{2i+1}\right)u_{2i}(t_n).
\end{aligned} \tag{3.20}$$

Step 4. $u_i(t_n + h) \rightarrow u(t_n + h)$.

Step 5. Repeat this procedure for next interval until the desired time T is reached.

3.4. One-Side Scheme (Alternative Notation with Commutators)

For the one-side scheme, we taken into account of the following commutator relation.

Definition 3.1. The following relation is given:

$$\exp(-tA)B\exp(tA) = \left[B, \exp(tA)\right], \tag{3.21}$$

where $[\cdot, \cdot]$ is the matrix commutator.

The integration is given as

$$\int_0^t \exp(-sA)B\exp(sA)ds = \left[B, \phi_1(tA)\right], \tag{3.22}$$

the representation is given in [13].

Further, we have the recursive integration

$$\left[B, \phi_i(tA)t^i\right] = \int_0^t \left[B, \phi_{i-1}(sA)\right] ds, \tag{3.23}$$

where ϕ_i given defined as

$$\begin{aligned} \phi_0(At) &= \exp(At), \\ \phi_i(At) &= \int_0^t \phi_{i-1}(As)ds, \\ \phi_i(At) &= \frac{\phi_{i-1}(At) - I\left(t^{i-1}/(i-1)!\right)}{A}. \end{aligned} \tag{3.24}$$

The iterative scheme with the equations

$$\dot{u}_1 = Au_1, \tag{3.25}$$

$$\dot{u}_2 = Au_2 + Bu_1, \tag{3.26}$$

$$\dot{u}_3 = Au_3 + Bu_2, \tag{3.27}$$

$$\dot{u}_4 = \cdots, \tag{3.28}$$

is solved as

$$\begin{aligned} c_1(t) &= \exp(At)c(t^{\mathrm{n}}), \\ c_2(t) &= c_1(t) + c_1(t)\int_0^t \left[B, \exp(sA)\right] ds, \\ c_2(t) &= c_1(t) + c_1(t)\left[B, \phi_1(tA)\right], \\ c_3(t) &= c_2(t) + c_1(t)\int_0^t \left[B, \exp(sA), B, \phi_1(sA)\right] ds, \\ c_3(t) &= c_2(t) + c_1(t)\left(\left[B, \exp(tA), B, \phi_2(tA)\right] + \left[B, A\exp(tA), B, \phi_3(tA)\right]\right) + O\left(t^3\right), \\ &\cdots \end{aligned} \tag{3.29}$$

The recursion is given as

$$c_i(t) = c_{i-1}(t) + c_1(t)\int_0^t \left[B, \exp(sA)\right] \int_0^{s_1} \left[B, \exp(s_1A)\right] \int_0^{s_2} \cdots \int_0^{s_{i-2}} \left[B, \exp(s_{i-1}A)\right] ds_{i-1} \cdots ds_1 dt. \tag{3.30}$$

Remark 3.2. For the novel notation, we have embedded the commutator to the computational scheme. For such a scheme we could save to compute additional the commutators.

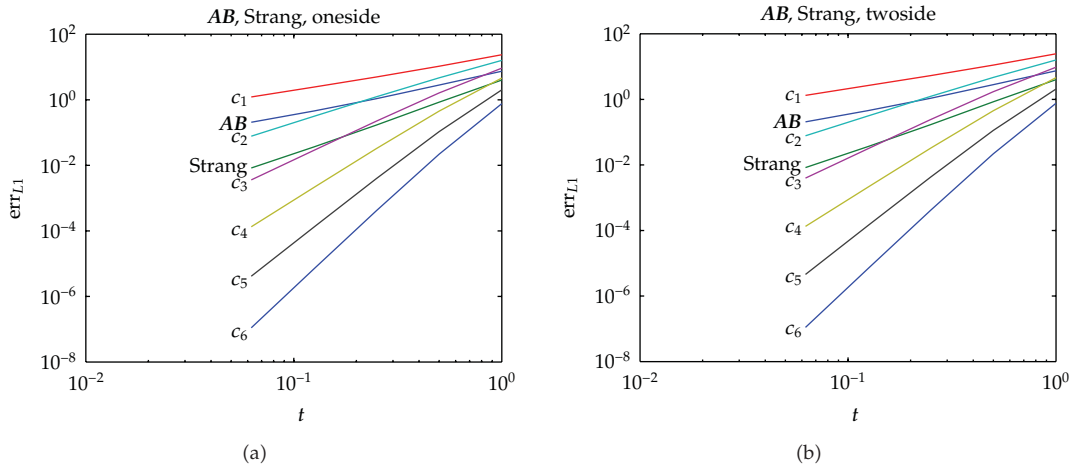

Figure 1: Numerical errors of the standard splitting scheme (a) and the iterative schemes (b) with $1, \ldots, 6$ iterative steps.

4. Numerical Examples

In the following, we deal with numerical example to verify the theoretical results.

4.1. First Example: Matrix Problem

For another example, consider the matrix equation

$$u'(t) = \begin{bmatrix} 1 & 2 \\ 3 & 0 \end{bmatrix} u, \qquad u(0) = u_0 = \begin{pmatrix} 0 \\ 1 \end{pmatrix}, \tag{4.1}$$

the exact solution is

$$u(t) = \frac{2\left(e^{3t} - e^{-2t}\right)}{5}. \tag{4.2}$$

We split the matrix as

$$\begin{bmatrix} 1 & 2 \\ 3 & 0 \end{bmatrix} = \begin{bmatrix} 1 & 1 \\ 1 & 0 \end{bmatrix} + \begin{bmatrix} 0 & 1 \\ 2 & 0 \end{bmatrix}. \tag{4.3}$$

The Figure 1 presents the numerical errors between the exact and the numerical solution.

The Figure 2 presents the CPU time of the standard and the iterative splitting schemes.

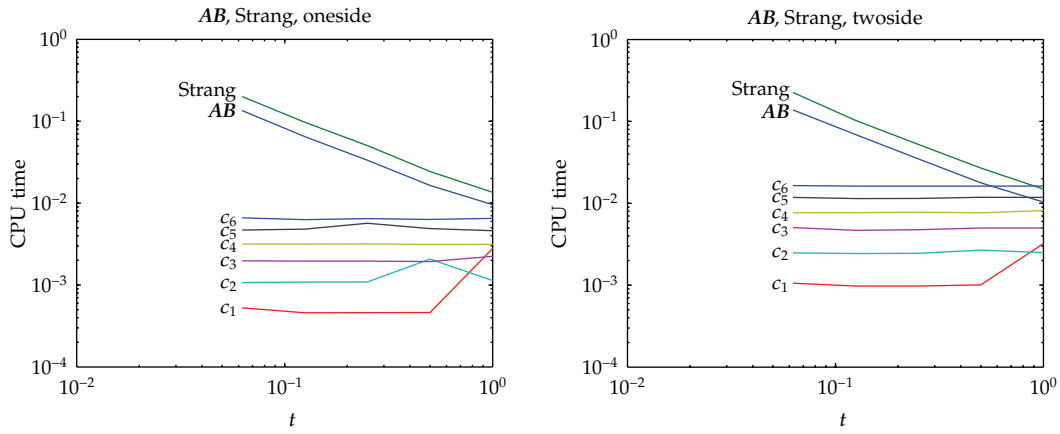

Figure 2: CPU time of the standard splitting scheme (a) and the iterative schemes (b) with $1, \ldots, 6$ iterative steps.

4.2. *Second Experiment:* 10×10 *Matrix*

We deal in the first with an ODE and separate the complex operator in two simpler operators.

We deal with the 10×10 ODE system:

$$\partial_t u_1 = -\lambda_{1,1} u_1 + \lambda_{2,1} u_2 + \cdots + \lambda_{10,1} u_{10}, \tag{4.4}$$

$$\partial_t u_2 = \lambda_{1,2} u_1 - \lambda_{2,2}(t) u_2 + \cdots + \lambda_{10,2} u_{10}, \tag{4.5}$$

$$\vdots \tag{4.6}$$

$$\partial_t u_{10} = \lambda_{1,10} u_1 + \lambda_{2,10}(t) u_2 + \cdots - \lambda_{10,10} u_{10}, \tag{4.7}$$

$$u_1(0) = u_{1,0}, \ldots, \; u_{10}(0) = u_{10,0} \quad \text{(initial conditions)}, \tag{4.8}$$

where $\lambda_1(t) \in \mathbb{R}^+$ and $\lambda_2(t) \in \mathbb{R}^+$ are the decay factors and $u_{1,0}, \ldots, u_{10,0} \in \mathbb{R}^+$. We have the time interval $t \in [0, T]$.

We rewrite (4.4) in operator notation, we concentrate us to the following equations:

$$\partial_t u = A(t)u + B(t)u, \tag{4.9}$$

where $u_1(0) = u_{10} = 1.0$, $u_2(0) = u_{20} = 1.0$ are the initial conditions, where we have $\lambda_1(t) = t$ and $\lambda_2(t) = t^2$.

The operators are splitted in the following way, while operator A, see (4.10), covers the upper diagonal entries and operator B, see (4.11), covers the lower diagonal entries of

the ODE system (4.4)–(4.7). Such a decomposition allows to reduce the computation of the matrix exponential to a upper or lower matrix and speedup the solver process

$$A = \begin{pmatrix} -0.01 & 0.01 & 0 & \cdots & & & & & & \\ 0.01 & -0.01 & 0 & \cdots & & & & & & \\ 0.01 & 0.01 & -0.02 & 0 & \cdots & & & & & \\ 0.01 & 0.01 & 0.01 & -0.03 & 0 & \cdots & & & & \\ \vdots & & & & & & & & & \\ 0.01 & 0.01 & 0.01 & 0.01 & 0.01 & 0.01 & 0.01 & 0.01 & -0.08 & 0 \\ 0.01 & 0.01 & 0.01 & 0.01 & 0.01 & 0.01 & 0.01 & 0.01 & 0 & -0.08 \end{pmatrix}, \tag{4.10}$$

$$B = \begin{pmatrix} -0.08 & 0 & 0.01 & 0.01 & 0.01 & 0.01 & 0.01 & 0.01 & 0.01 & 0.01 \\ 0 & -0.08 & 0.01 & 0.01 & 0.01 & 0.01 & 0.01 & 0.01 & 0.01 & 0.01 \\ \vdots & & & & & & & & & \\ 0 & 0 & 0 & 0 & 0 & 0 & 0 & -0.02 & 0.01 & 0.01 \\ 0 & 0 & 0 & 0 & 0 & 0 & 0 & 0 & -0.01 & 0.01 \\ 0 & 0 & 0 & 0 & 0 & 0 & 0 & 0 & 0.01 & -0.01 \end{pmatrix}. \tag{4.11}$$

The Figure 3 present the numerical errors between the exact and the numerical solution. Here we have the best approximation to the exact solution with a sixth-order iterative scheme (6 iterative steps), but no additionally more computational time for finer time step.

The Figure 4 present the CPU time of the standard and the iterative splitting schemes. Compared to standard splitting schemes, the iterative schemes are cheaper to compute and higher in accuracy. We can also choose smaller time steps to obtain more accurate results and use nearly the same computational resource.

Remark 4.1. The computational results show the benefit of the iterative schemes. We save computational time and achieve higher-order accuracy. The one-side and two-side schemes have the same results.

4.3. Third Example: Commutator Problem

We assume to have a large norm of the commutator $[A, B]$ and deal with the matrix equation

$$u'(t) = \begin{bmatrix} 10 & 1 \\ 1 & 10 \end{bmatrix} u, \qquad u(0) = u_0 = \begin{pmatrix} 1 \\ 1 \end{pmatrix}. \tag{4.12}$$

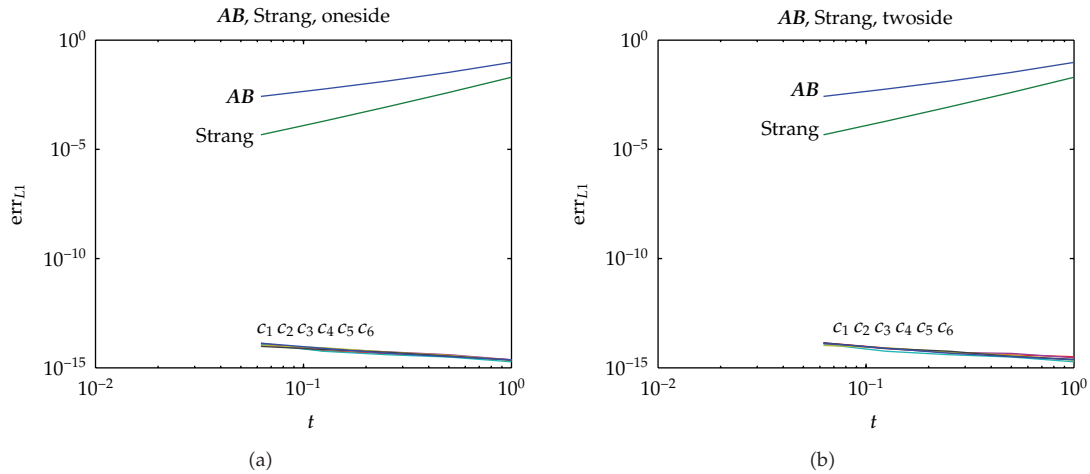

Figure 3: Numerical errors of the standard splitting scheme (a) and the iterative schemes (b) with $1, \ldots, 6$ iterative steps.

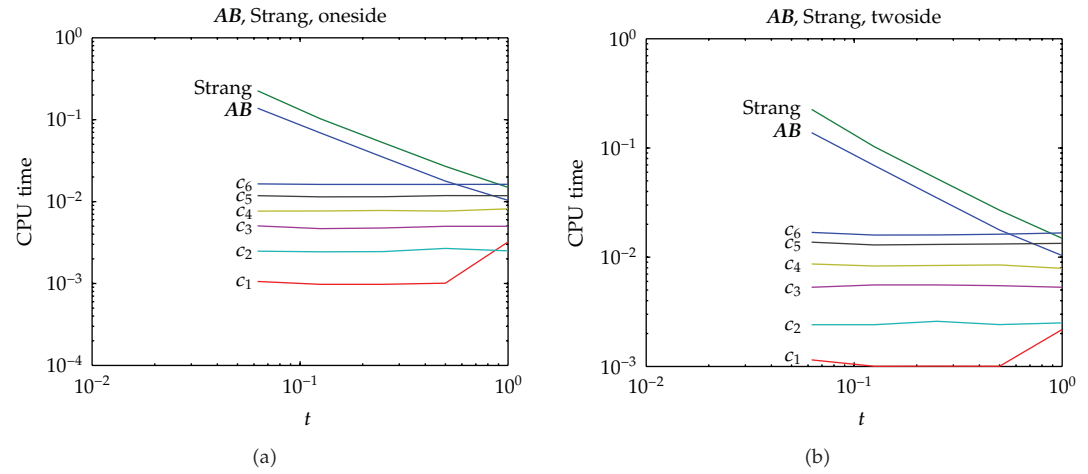

Figure 4: CPU time of the standard splitting scheme (a) and the iterative schemes (b) with $1, \ldots, 6$ iterative steps.

In the following, we discuss different splitting ideas.

Version 1

We split the matrix as

$$\begin{bmatrix} 10 & 1 \\ 1 & 10 \end{bmatrix} = \begin{bmatrix} 9 & 0 \\ 1 & 1 \end{bmatrix} + \begin{bmatrix} 1 & 1 \\ 0 & 9 \end{bmatrix}, \tag{4.13}$$

while $\|[A, B]\| \geq \max\{\|A\|, \|B\|\}$.

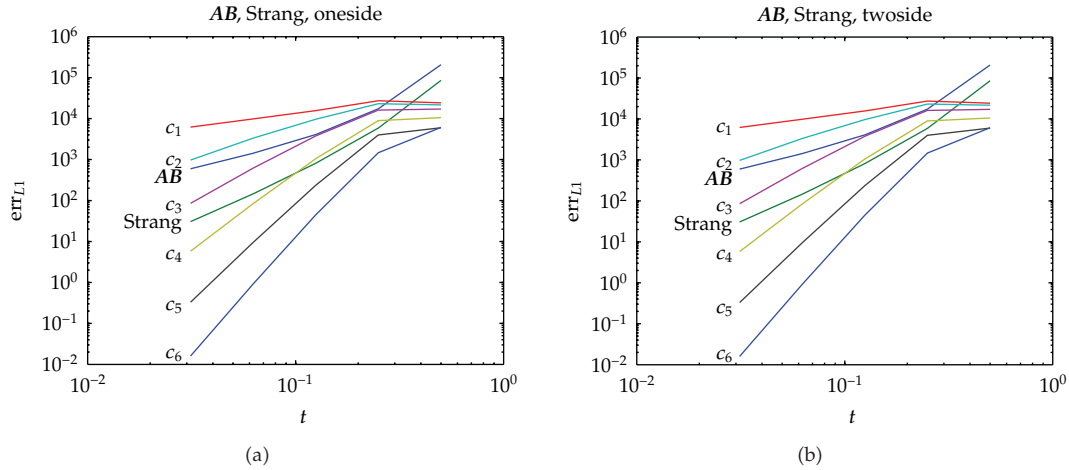

Figure 5: Numerical errors of the standard splitting scheme (a) and the iterative schemes (b) with $1, \ldots, 6$ iterative steps.

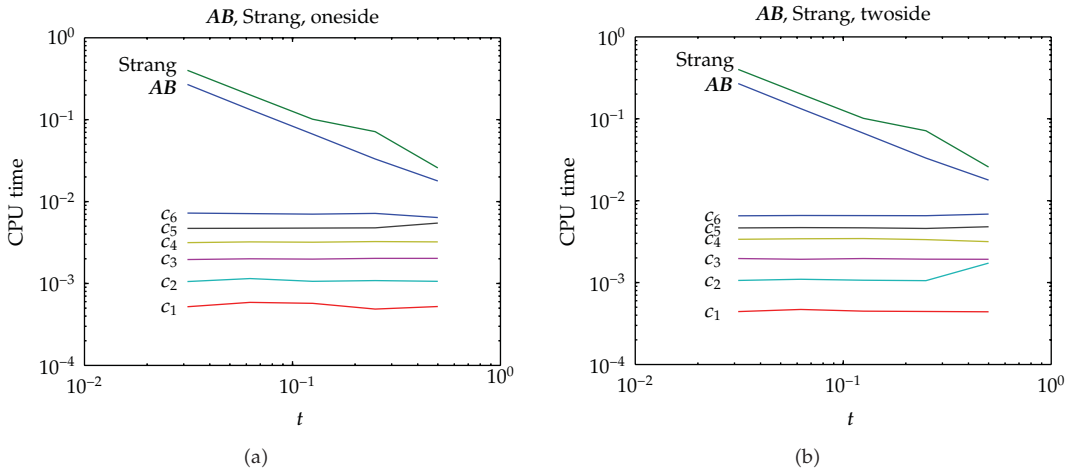

Figure 6: CPU time of the standard splitting scheme (a) and the iterative schemes (b) with $1, \ldots, 6$ iterative steps.

Here we have to deal with highly noncommutative operators and the computational speedup is given in the iterative schemes, while the commutator is not needed to obtain more accurate results, while the standard splitting schemes deal with such commutators for the error reduction.

The Figure 5 present the numerical errors between the exact and the numerical solution.

The Figure 6 present the CPU time of the standard and the iterative splitting schemes.

Further for the one-side,we obtain more improved results for the following splitting.

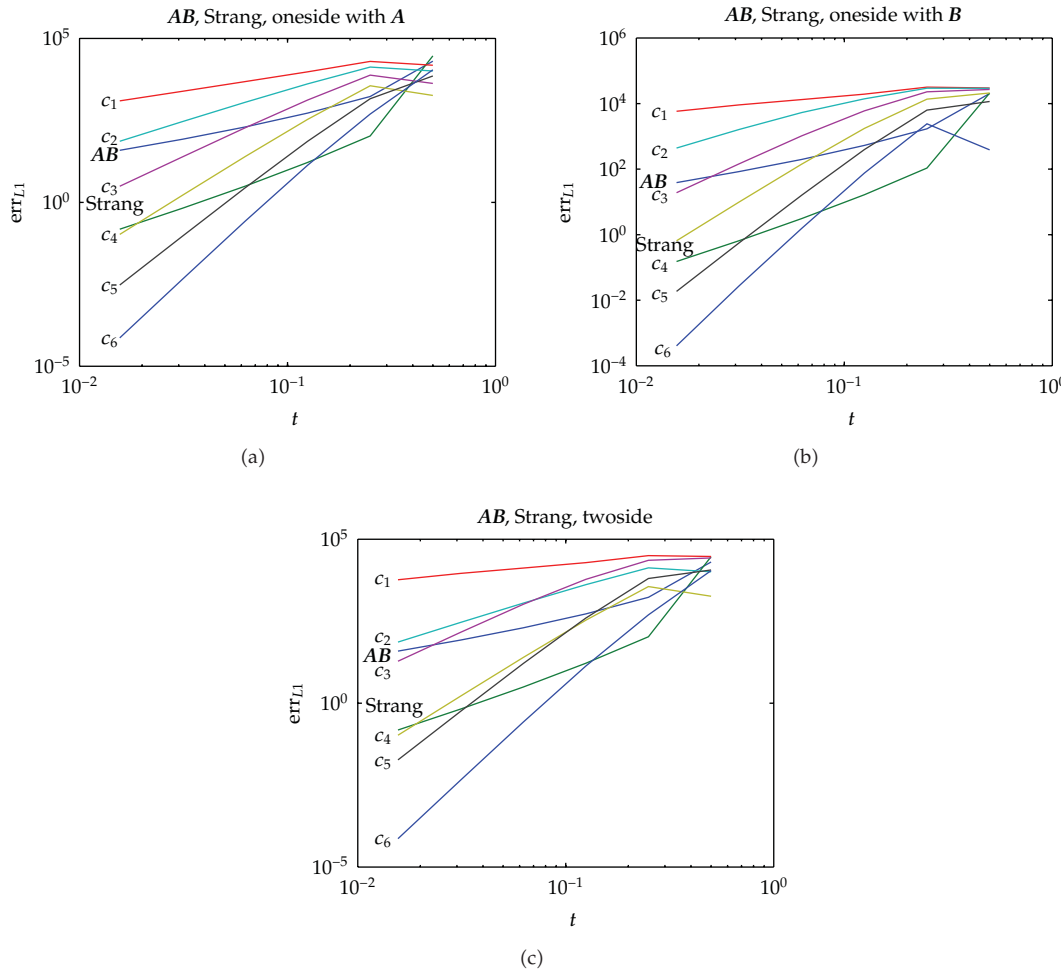

Figure 7: Numerical errors of the standard splitting scheme (a) and the iterative schemes based on one-side to operator A or B (b) and two-side scheme (c).

Version 2

In this version, we have

$$\begin{bmatrix} 10 & 1 \\ 1 & 10 \end{bmatrix} = \begin{bmatrix} 9 & 0 \\ 1 & 9 \end{bmatrix} + \begin{bmatrix} 1 & 1 \\ 0 & 1 \end{bmatrix}. \tag{4.14}$$

The Figure 7 presents the numerical errors between the exact and the numerical solution.

A more delicate problem is given for the stiff matrices.

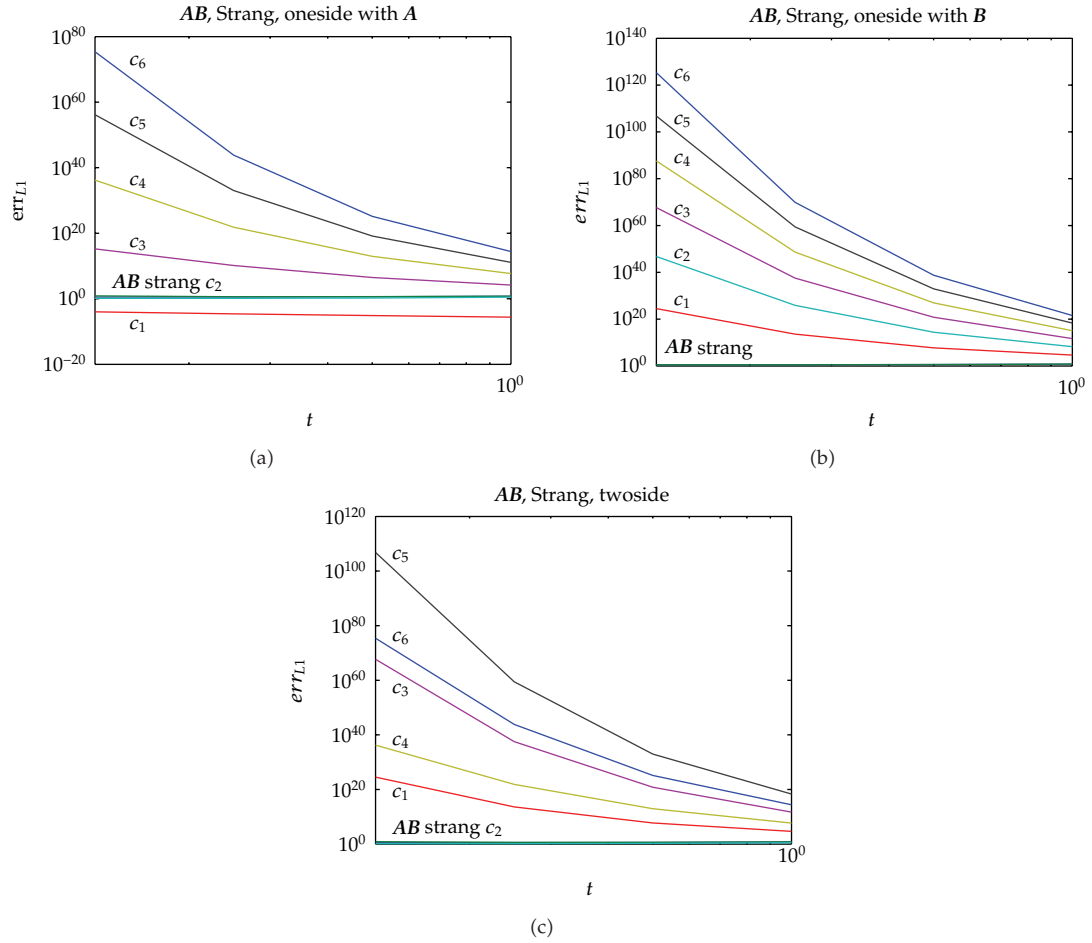

Figure 8: Numerical errors of the one-side splitting scheme with A (a), the one-side splitting scheme with B (b) and the iterative schemes with $1, \ldots, 6$ iterative steps (c).

Version 3

In this version, we have

$$\begin{bmatrix} 10^4 & 1 \\ 1 & 10^4 \end{bmatrix} = \begin{bmatrix} 10^4 - 1 & 0 \\ 1 & 10^4 - 1 \end{bmatrix} + \begin{bmatrix} 1 & 1 \\ 0 & 1 \end{bmatrix}. \tag{4.15}$$

The Figure 8 present the numerical errors between the exact and the numerical solution.

The Figure 9 present the CPU time of the standard and the iterative splitting schemes.

Remark 4.2. The iterative schemes with fast computations of the exponential matrices have a speedup. The constant CPU time of the iterative schemes shows that it benefit instead of the expensive standard schemes. Also for stiff problems with multi iterative steps, we reach the same results of the standard A-B or Strang-Splitting schemes, while we are independent of the commutator estimation.

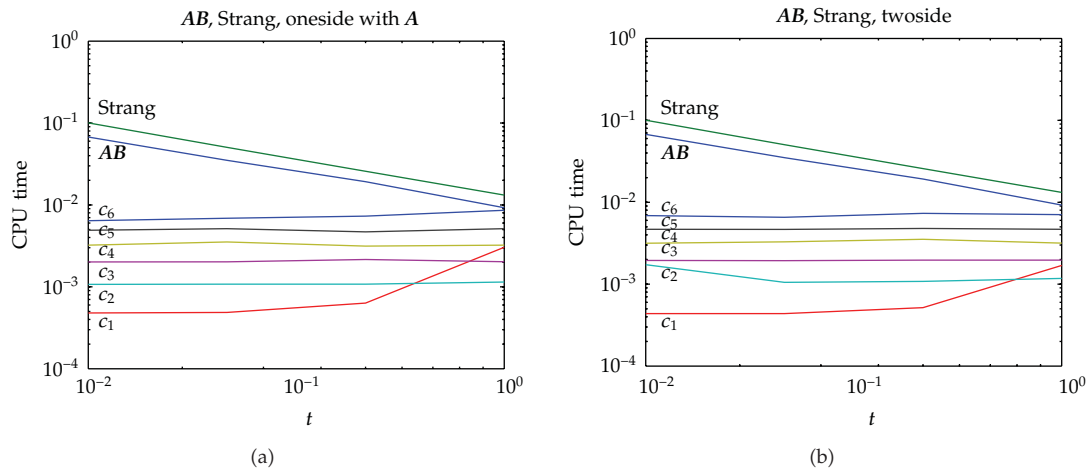

Figure 9: CPU time of the one-side splitting scheme with A (a) and the iterative schemes with $1,\ldots,6$ iterative steps (b).

4.4. Two-Phase Example

The next example is a simplified real-life problem for a multiphase transport-reaction equation. We deal with mobile and immobile pores in the porous media, such simulations are given for waste scenarios.

We concentrate on the computational benefits of a fast computation of the iterative scheme, given with matrix exponentials.

The equation is given as:

$$\begin{aligned}
\partial_t c_1 + \nabla \cdot \mathbf{F} c_1 &= g(-c_1 + c_{1,\mathrm{im}}) - \lambda_1 c_1, \quad \text{in } \Omega \times [0,t],\\
\partial_t c_2 + \nabla \cdot \mathbf{F} c_2 &= g(-c_2 + c_{2,\mathrm{im}}) + \lambda_1 c_1 - \lambda_2 c_2, \quad \text{in } \Omega \times [0,t],\\
\mathbf{F} &= \mathbf{v} - D\nabla,\\
\partial_t c_{1,\mathrm{im}} &= g(c_1 - c_{1,\mathrm{im}}) - \lambda_1 c_{1,\mathrm{im}}, \quad \text{in } \Omega \times [0,t],\\
\partial_t c_{2,\mathrm{im}} &= g(c_2 - c_{2,\mathrm{im}}) + \lambda_1 c_{1,\mathrm{im}} - \lambda_2 c_{2,\mathrm{im}}, \quad \text{in } \Omega \times [0,t],\\
c_1(\mathbf{x},t) &= c_{1,0}(\mathbf{x}), \quad c_2(\mathbf{x},t) = c_{2,0}(\mathbf{x}), \quad \text{on } \Omega,\\
c_1(\mathbf{x},t) &= c_{1,1}(\mathbf{x},t), \quad c_2(\mathbf{x},t) = c_{2,1}(\mathbf{x},t), \quad \text{on } \partial\Omega \times [0,t],\\
c_{1,\mathrm{im}}(\mathbf{x},t) &= 0, \quad c_{2,\mathrm{im}}(\mathbf{x},t) = 0, \quad \text{on } \Omega,\\
c_{1,\mathrm{im}}(\mathbf{x},t) &= 0, \quad c_{2,\mathrm{im}}(\mathbf{x},t) = 0, \quad \text{on } \partial\Omega \times [0,t].
\end{aligned} \tag{4.16}$$

In the following, we deal with the semidiscretized equation given with the matrices:

$$\partial_t \mathbf{C} = \begin{pmatrix} A - \Lambda_1 - G & 0 & G & 0 \\ \Lambda_1 & A - \Lambda_2 - G & 0 & G \\ G & 0 & -\Lambda_1 - G & 0 \\ 0 & G & \Lambda_1 & -\Lambda_2 - G \end{pmatrix} \mathbf{C}, \tag{4.17}$$

where $\mathbf{C} = (\mathbf{c}_1, \mathbf{c}_2, \mathbf{c}_{1\mathrm{im}}, \mathbf{c}_{2\mathrm{im}})^T$, while $\mathbf{c}_1 = (\mathbf{c}_{1,1}, \ldots, \mathbf{c}_{1,I})$ is the solution of the first species in the mobile phase in each spatial discretization point ($i = 1, \ldots, I$), the same is also for the other solution vectors.

We have the following two operators for the splitting method

$$A = \frac{D}{\Delta x^2} \cdot \begin{pmatrix} -2 & 1 & & & \\ 1 & -2 & 1 & & \\ & \ddots & \ddots & \ddots & \\ & & 1 & -2 & 1 \\ & & & 1 & -2 \end{pmatrix} + \frac{v}{\Delta x} \cdot \begin{pmatrix} 1 & & & & \\ -1 & 1 & & & \\ & \ddots & \ddots & & \\ & & -1 & 1 & \\ & & & -1 & 1 \end{pmatrix} \in \mathbb{R}^{I \times I}, \tag{4.18}$$

where I is the number of spatial points.

$$\Lambda_1 = \begin{pmatrix} \lambda_1 & 0 & & & \\ 0 & \lambda_1 & 0 & & \\ & \ddots & \ddots & \ddots & \\ & & 0 & \lambda_1 & 0 \\ & & & 0 & \lambda_1 \end{pmatrix} \in \mathbb{R}^{I \times I},$$

$$\Lambda_2 = \begin{pmatrix} \lambda_2 & 0 & & & \\ 0 & \lambda_2 & 0 & & \\ & \ddots & \ddots & \ddots & \\ & & 0 & \lambda_2 & 0 \\ & & & 0 & \lambda_2 \end{pmatrix} \in \mathbb{R}^{I\times I},$$

$$G = \begin{pmatrix} g & 0 & & & \\ 0 & g & 0 & & \\ & \ddots & \ddots & \ddots & \\ & & 0 & g & 0 \\ & & & 0 & g \end{pmatrix} \in \mathbb{R}^{I\times I}. \tag{4.19}$$

We decouple into the following matrices:

$$A_1 = \begin{pmatrix} A & 0 & 0 & 0 \\ 0 & A & 0 & 0 \\ 0 & 0 & 0 & 0 \\ 0 & 0 & 0 & 0 \end{pmatrix} \in \mathbb{R}^{4I\times 4I},$$

$$\tilde{A}_2 = \begin{pmatrix} -\Lambda_1 & 0 & 0 & 0 \\ \Lambda_1 & -\Lambda_2 & 0 & 0 \\ 0 & 0 & -\Lambda_1 & 0 \\ 0 & 0 & \Lambda_1 & -\Lambda_2 \end{pmatrix} \in \mathbb{R}^{4I\times 4I}, \tag{4.20}$$

$$\tilde{A}_3 = \begin{pmatrix} -G & 0 & G & 0 \\ 0 & -G & 0 & G \\ G & 0 & -G & 0 \\ 0 & G & 0 & -G \end{pmatrix} \in \mathbb{R}^{4I\times 4I}.$$

For the operator A_1 and $A_2 = \tilde{A}_2 + \tilde{A}_3$, we apply the iterative splitting method.

Based on the decomposition, operator A_1 is only tridiagonal and operator A_2 is block diagonal. Such matrix structure reduce the computation of the exponential operators.

The Figure 10 present the numerical errors between the exact and the numerical solution. Here we obtain optimal results for one-side iterative schemes on operator B, means we iterate with respect to B and use A as right-hand side.

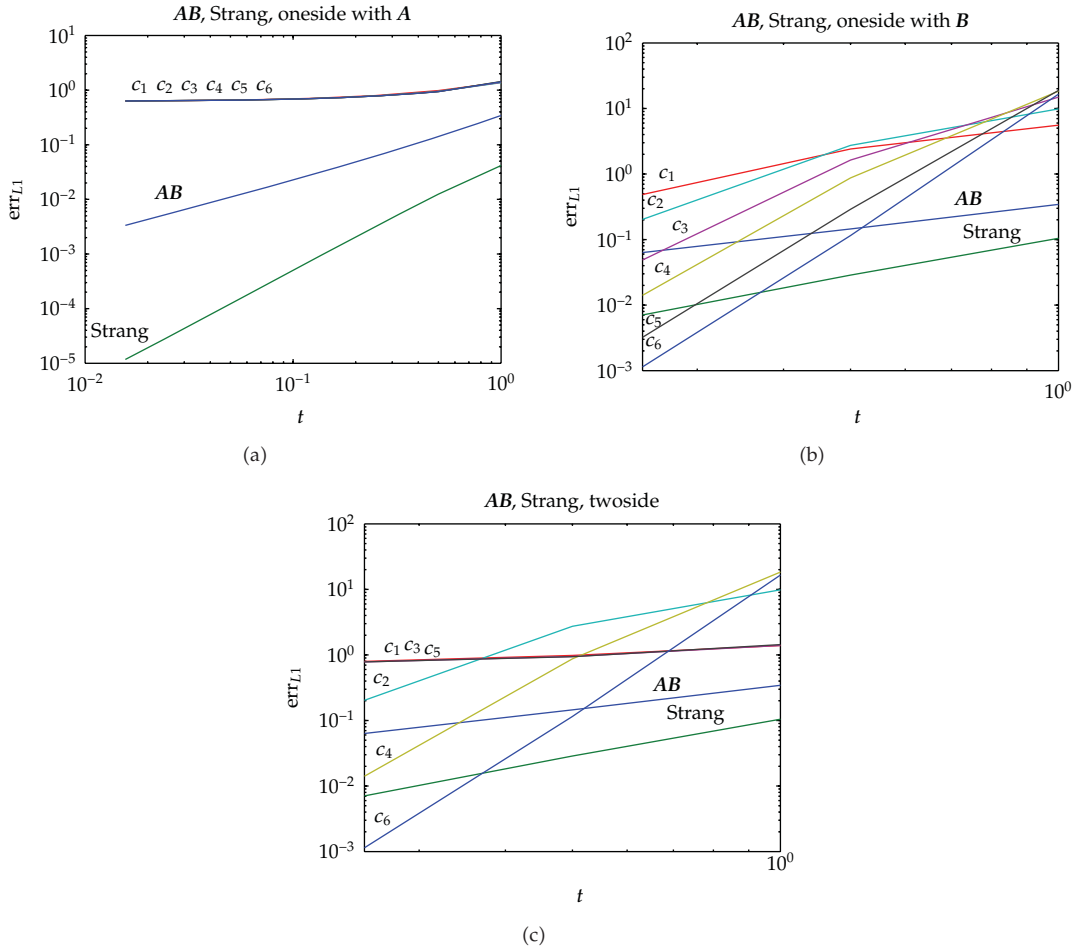

Figure 10: Numerical errors of the one-side splitting scheme with A (a), the one-side splitting scheme with B (b) and the iterative schemes with $1, \ldots, 6$ iterative steps (c).

Remark 4.3. For all iterative schemes, we can reach faster results as for the The iterative schemes with fast computations of the exponential matrices standard schemes. With 4-5 iterative steps we obtain more accurate results as we did for the expensive standard schemes. With one-side iterative schemes we reach the best convergence results.

5. Conclusions and Discussions

In this work, we have presented a very economical and practical method by successive approximations. Here the idea to decouple the expensive computation of matrix exponential via iterative splitting schemes has the benefit of less computational time. While the error analysis present stable methods and higher-order schemes, the applications show the speedup with the iterative schemes. In, future, we concentrate on matrix dependent scheme, based on iterative splitting algorithms.

References

[1] J. Geiser, *Discretisation methods for systems of convective-diffusive dispersive-reactive equations and applications*, Ph.D. thesis, Universität Heidelberg, Heidelberg, Germany, 2004.

[2] J. Geiser, "Decomposition methods for partial differential equations: theory and applications in multiphysics problems," in *Numerical Analysis and Scientific Computing Series*, Magoules and Lai, Eds., CRC Press, Boca Raton, Fla, USA, 2009.

[3] M. Hochbruck and A. Ostermann, "Explicit exponential Runge-Kutta methods for semilinear parabolic problems," *SIAM Journal on Numerical Analysis*, vol. 43, no. 3, pp. 1069–1090, 2005.

[4] H. Rouch, "MOCVD research reactor simulation," in *Proceedings of the COMSOL Users Conference*, Paris, France, 2006.

[5] L. Rudniak, "Numerical simulation of chemical vapour deposition process in electric field," *Computers and Chemical Engineering*, vol. 22, no. 1, supplement, pp. S755–S758, 1998.

[6] R. Glowinski, "Numerical methods for fluids," in *Handbook of Numerical Analysis*, P. G. Ciarlet and J. Lions, Eds., vol. 9, North-Holland, Amsterdam, The Netherlands, 2003.

[7] J. F. Kanney, C. T. Miller, and C. T. Kelley, "Convergence of iterative split-operator approaches for approximating nonlinear reactive problems," *Advances in Water Resources*, vol. 26, no. 3, pp. 247–261, 2003.

[8] E. Hansen and A. Ostermann, "Exponential splitting for unbounded operators," *Mathematics of Computation*, vol. 78, no. 267, pp. 1485–1496, 2009.

[9] T. Jahnke and C. Lubich, "Error bounds for exponential operator splittings," *BIT Numerical Mathematics*, vol. 40, no. 4, pp. 735–744, 2000.

[10] I. Faragó and J. Geiser, "Iterative operator-splitting methods for linear problems," *International Journal of Computational Science and Engineering*, vol. 3, no. 4, pp. 255–263, 2007.

[11] E. Hairer, S. P. Nørsett, and G. Wanner, *Solving ordinary differential equations. I*, vol. 8 of *Springer Series in Computational Mathematics*, Springer, Berlin, 1987, Nonstiff problem.

[12] E. Hairer and G. Wanner, *Solving Ordinary Differential Equations. II*, vol. 14 of *Springer Series in Computational Mathematics*, Springer, Berlin, Germany, 2nd edition, 1996.

[13] W. Magnus, "On the exponential solution of differential equations for a linear operator," *Communications on Pure and Applied Mathematics*, vol. 7, pp. 649–673, 1954.

Hindawi Publishing Corporation
Journal of Applied Mathematics
Volume 2011, Article ID 498098, 41 pages
doi:10.1155/2011/498098

Research Article

Numerical Simulation of Pollutant Transport in Fractured Vuggy Porous Karstic Aquifers

Xiaolin Fan,[1] Shuyu Sun,[2] Wei Wei,[1] and Jisheng Kou[2]

[1] *Department of Mathematics, College of Science, Guizhou University, Huaxi, Guiyang 550025, China*
[2] *Computational Transport Phenomena Laboratory (CPTL), Division of Physical Sciences and Engineering (PSE), King Abdullah University of Science and Technology (KAUST), Thuwal 23955-6900, Saudi Arabia*

Correspondence should be addressed to Shuyu Sun, shuyu.sun@kaust.edu.sa

Received 15 December 2010; Accepted 8 January 2011

Academic Editor: Zhangxin Chen

Copyright © 2011 Xiaolin Fan et al. This is an open access article distributed under the Creative Commons Attribution License, which permits unrestricted use, distribution, and reproduction in any medium, provided the original work is properly cited.

This paper begins with presenting a mathematical model for contaminant transport in the fractured vuggy porous media of a species of contaminant (PCP). Two phases are numerically simulated for a process of contaminant and clean water infiltrated in the fractured vuggy porous media by coupling mixed finite element (MFE) method and finite volume method (FVM), both of which are locally conservative, to approximate the model. A hybrid mixed finite element (HMFE) method is applied to approximate the velocity field for the model. The convection and diffusion terms are approached by FVM and the standard MFE, respectively. The pressure distribution and temporary evolution of the concentration profiles are obtained for two phases. The average effluent concentration on the outflow boundary is obtained at different time and shows some different features from the matrix porous media. The temporal multiscale phenomena of the effluent concentration on the outlet are observed. The results show how the different distribution of the vugs and the fractures impacts on the contaminant transport and the effluent concentration on the outlet. This paper sheds light on certain features of karstic groundwater are obtained.

1. Introduction

As is well known, Karst topography is characterized by subterranean limestone caverns, which are carved by groundwater flow. A schematic presentation of a karstic area is showed in Figure 1.

Karstic area is significantly rich in water resource, the percentage of which for human drinking is up to about 25 and is to be increasing to 50 in the future in the world [1, 2]. Karst formations are cavernous and therefore have very high permeability, resulting in some different features in comparison with non-karstic aquifers. The fluid flow and transport of

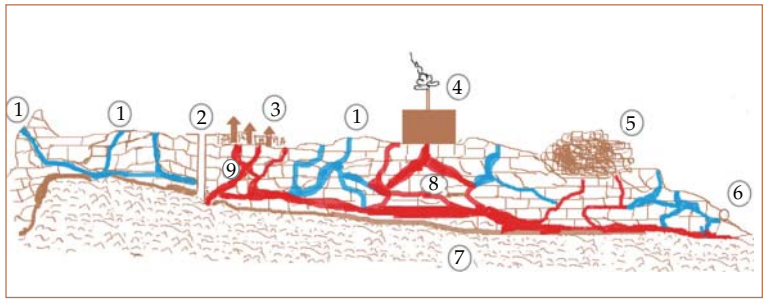

Figure 1: A schematic presentation of water supply and waste disposal in a karstic area (1) ponor (swallow hole), (2) water well, (3) disposal of municipal waste water into karst aquifer, (4) disposal of industrial waste water into a ponor, (5) solid waste disposal into a karstic depression, (6) karst spring (with limited watershed area), (7) base of karstification (impervious basement), (8) industrial waste water into karst aquifers, (9) municipal waste water into karst aquifers.

pollutants occurring in a karstic region have some different features from those in non-karstic areas. With rapid development of local economics and increasing population in the Karst region, numerous pollutants are occurring in some Karst region mainly comprising the following four aspects grouped as municipal, industrial, agricultural, and farraginous. The groundwater in the karst area is seriously affected by human activities on the quality and quantity. Consequently, transport of a contaminant in the Karst topography is an important aspect to be investigated. Although groundwater flow in the Karst terrane has been studied many years in some specific, there are still a number of topics to be researched because of its importance and complexity. One of the most important aspects is the simulation of fluid flow and the pollutant transport in the karstic field.

A large number of models have been created to predict water levels and spring discharge, which can reflect some properties of the groundwater flow in the Karst aquifers. Black box model is the simplest one in which no spatial information is included, but can predict spring discharge or other aquifer properties. Time moment analysis is used to relate a time series of inputs (recharge) to a series of outputs [3]. Zaltsberg applied the simple regression models to predict water levels in Karst aquifers [4]. Lack of predictive power is the obvious limitation of these types of models [5, 6].

Some deterministic models [5, 6] for groundwater flow are physically derived, and both distributed and lumped parameters are contained therein. The spatial dimension is not contained in lumped models [7] so that they need to solve the only ordinary linear differential equations. Therefore fewer data requirements for parameterization and calibration are provided to simulate a given lumped system than that of distributed counterparts. Quinn et al. [5] and Barrett and Charbeneau [6] ,for example, developed a system including lumped parameters in groundwater applications generally with single-cell models. Yurtsever and Payne [8] employed a series of linear reservoirs to model Karst aquifers. Normally many researchers apply distributed parameter models to increase the accuracy of predictions or to achieve a high degree of spatial resolution. Also some distributed parameter models using a single equivalent porous medium have been created for the San Antonio portion of Edwards [9] although none performs better than the nine-cell model developed by Wannakule and Robert Anaya. One of the most sophisticated distributed parameter models was created by Kuniansky and Holligan [10] at the US Geological Survey, which is a finite element

model of the Edwards/Trinity aquifer system, in which over 7000 elements were included. Though the high degree of spatial resolution is achieved, difficulties in generating input parameters have limited its use.

Some researchers have also developed dual porosity distributed parameter models for Karst system [11]. Conduit and diffuse flow were generally described as separate systems linked by a transfer function in these models. They have the advantage of being able to represent the fast transit and slow depletion often exhibited by Karst aquifers, but at the cost of more than doubling the number of parameters required for calibration.

These models demonstrate the evolution in model complexity associated with attempts to increase the accuracy of predictions. The general tendency of the research is to increase the number of cells in the $x - y$ plane while neglecting improvement of which might be achieved by incorporating variation in the vertical direction. This approach has not been consistently successful. The spatially detailed models have been difficult to calibrate and verify. In addition, input data must be developed for each cell; consequently, these models are not used to any great extent by regulatory agencies or other groups. A model developed by Barrett and Charbeneau [12] is simple to calibrate and use and yet achieves a high degree of accuracy. His modeling effort differs from preceding studies by retaining a simple spatial description of the aquifer, but allowing vertical variations in aquifer properties such as specific yield within cells.

Many other numerical models of groundwater flow use finite-difference methods to discretize and solve the governing PDEs [13, 14]. These models often require a highly refined finite-difference mesh to achieve accurate solutions in the areas of interest where gradients vary rapidly in space. Use of a fine mesh over the entire domain can be computationally intensive, and in some cases intractable, while using a variably spaced mesh can lead to cells with a large aspect ratio and refinement in areas where such detail is not needed. In addition, a fine discretization is often needed within models that have already been constructed, and redesigning the entire grid is not feasible. One solution to these predicaments is to use local grid refinement in which the mesh is only refined locally in the area of interest [15, 16]. Mehl and Hill [15, 16] proposed a new method for locally refining block-centered finite-difference grids using iteratively coupled shared nodes (a new method of interpolation) in the context of groundwater flow modeling. His method couples the grids by sharing nodes and iteratively updating the right-hand side of the matrix equations to ensure that heads and fluxes are consistent between both grids. The iterative method presented in their work is a compromise between the accuracy of a variably spaced grid [17, 18] and the speed of the traditional grid refinement methods. In the methods presented in their work, they made use of the Darcy-weighted interpolation to deal with the interface between parent grids and child grids. Two years later [15, 16], they extended the methods to three dimensions mainly by proposing a new 3D interpolation scheme.

The selection of the appropriate model to achieve the goals of simulating the groundwater flow in a Karst system is a major task [19]. An appropriate conceptual model should be sufficiently simple so as to be amenable to mathematical treatment, but it should not be too simple so as to exclude those features which are of interest to the investigation at hand. The information should be available for calibrating the model, and the model should be the most economic one for solving the problem at hand.

Modeling a system requires a very detailed knowledge of the physical properties and the processes governing water movement. The virtue of a model rests in its ability to predict a general system from incomplete or partial data [20]. The parsimonious model simplifies the representation of the physical structure or of the processes involved [6].

This is especially appropriate in the light of the extraordinary heterogeneity exhibited by Karst aquifers.

Recent studies on vuggy fractured porous media simulation are closer to our research. Fard and Firoozabadi [21] did some comprehensive study of immiscible fluid flow in fractured vuggy porous media. Hoteit and Firoozabadi [22] showed that multi-component compressible flow in discrete fractured vuggy media can be modeled. Sonnenthal et al. [23] made use of the TOUGHREACT reactive transport software to model the coupled heat transfer and reactive transport processes in porous media. A Crank-Nicolson-Galerkin finite element model is presented in Hossain's research to simulate nonlinearly the macrophase contaminant transport combined with microphase contaminant transport [24]. Alajmi and Grader [25] gave the relationship between fractured vuggy matrix environment with multiphase flow. Sun and Geiser [26] and Sun and Wheeler [27] employed multiscale discontinuous Galerkin and operator-splitting methods to model subsurface flow and transport with anisotropic and dynamic mesh. Sun et al. [28–30] also used the compatible algorithms for coupled flow and transport to simulate the groundwater flow and contaminant transport. Among these approaches the researchers assumed the pressure in a fracture or vuggy element was equal to the pressure in the ambient matrix elements, by using the cross-flow equilibrium.

Vugs and fractures are the most important factors in the fluid flow and contaminant transport in the karstic aquifers. We calculate the contaminant transport through the vuggy fractured matrix by using a bulk material property by the distribution coefficient K_d, which describes the distribution of contaminant between the liquid and solid phases. In this paper, the adsorption term is considered to be linear with concentration of the contaminant in the matrix media.

In this paper, a karstic aquifers of some size $(0, 0.80) \times (0, 0.80)$ are considered in which the groundwater is clean at first. At some time, a species of contaminant (PCP, i.e., pentachlorophenol) is abruptly infiltrated into the inflow boundary, which lasted T_1 hours, and then the clean water is infiltrated into the aquifers again. Among the three phases, the same models of fluid flow and contaminant transport are presented with different boundary conditions and initial conditions which will be described in the sequent sections in this paper. We apply a discrete-fracture model and a discrete-vug model to describe flow and transport processes in fractured porous media and vuggy porous media, respectively. Other than classical discrete fracture or discrete vug model where the cracks or large caves are presented by $(n-1)$ dimensional elements, the discrete fracture or vug model in this paper still uses physically sense n dimensional elements. An adaptive mesh is generated based on this type of model. Then we employ the mixed finite element (MFE) method to approach the second-order partial derivative terms of the flow and transport equations, and an upwind finite volume method (FVM) is used to approximate the convection term in the transport.

This paper is organized as follows. First, we mainly give the mathematical models approximately describing the fluid flow and the contaminant diffusion and transport in the fractured vuggy porous media for karst aquifers. Secondly, the numerical algorithms for the mathematical models are discussed. We describe in detail the MFE method for the flow equation, the MFE-FVM method for the reactive transport system in the models together with the numerical discretization in time. Then we give some cases in vuggy porous media with vug being differently distributed. For each case, we provide and discuss simulated concentration profiles at different time, as well as velocity and pressure fields. At last, we numerically give the different time scale for concentration in

order to analyze the influence on the concentration, pressure, and velocity by vugs and fractures.

2. Mathematical Model

Two coupled differential systems are made up of the model equations for the transport of contaminant through the vuggy fractured porous media, that is, the flow equation of the fluid and the transport equations of the contaminant.

2.1. Flow Equation

We here consider the flow in vuggy fractured porous media in two-dimension steady flow of single phase, the flow equation of which is obtained from the conservation of total fluid volume and Darcy's law mathematically given by

$$\begin{aligned} &\mathbf{u} + K\nabla p = \mathbf{0}, \\ &\nabla \cdot \mathbf{u} = q, \end{aligned} \qquad \mathbf{x} \in \Omega. \tag{2.1}$$

Here K denotes the hydraulic conductivity (i.e., the proportionality constant for the flow of water through a porous media, m/s) as follows:

$$K = \frac{\kappa \cdot g}{\nu} = \frac{\kappa \cdot g \cdot \rho}{\eta}. \tag{2.2}$$

In the two equations above, g is the gravity acceleration, ν and η are the kinematic (s/m^2) and dynamic viscosities of the fluid (kg/(m·s)), respectively; ρ and κ are the density of the fluid (kg/m^3) and the (absolute) permeability (m^2) of the porous media, respectively. The unknowns are p (the pressure head of the fluid mixture (N/m^2) and $\mathbf{u}$ (the Darcy velocity of the mixture, i.e., the discharge of fluid flowing per unit area, with units of length per time, m/s). We assume that K is uniformly symmetric positive definite and bounded. For simplicity of computation, the computational domain of interest Ω is assumed to be polygonal and bounded in R^2 with boundary $\Gamma = \partial\Omega = \Gamma_D \cup \Gamma_N$ (Γ_D, Γ_N stand for the Dirichlet boundary and Neumann boundary, resp.). We take the boundary conditions as follows:

$$\begin{aligned} p &= p_B, \quad \mathbf{x} \in \Gamma_D, \\ \mathbf{u} \cdot \mathbf{n} &= u_B, \quad \mathbf{x} \in \Gamma_N, \end{aligned} \tag{2.3}$$

where p_B and u_B are the given pressure on Γ_D and the normal velocity component on Γ_N (p_B and u_B can be measured in practice in some points on boundary), respectively, and $\mathbf{n}$ is the outward norm vector towards $\mathbf{u}$.

2.2. Transport System

The concentration of a contaminant species of interest in the fluid and in the solid together with their relation is described by the following system, which is obtained from the mass conservation of the considered contaminant species:

$$\begin{aligned} &\frac{\partial(\phi c_f)}{\partial t} + \nabla \cdot \left(\mathbf{u} c_f - D(\mathbf{u}) \nabla c_f\right) = r(c_f, c_s), \\ &\frac{\partial(\phi c_s)}{\partial t} = -r(c_f, c_s), \quad \mathbf{x} \in \Omega,\ t \in (0, T], \\ &c_s = K_d c_f. \end{aligned} \tag{2.4}$$

In the system (2.4), ϕ and T stand for the effective porosity and the final simulation time, respectively; ϕ is assumed to be time dependent and uniformly bounded above and below by positive numbers. K_d represents a parameter of the distribution coefficient of the considered contaminant species between the matrix and fluid. $D(\mathbf{u})$, the dispersion-diffusion tensor, contributes from molecular diffusion and mechanical dispersion, and it can be computed by

$$D(\mathbf{u}) = \phi\{d_m \mathbf{I} + |\mathbf{u}|[d_l \mathbf{E}(\mathbf{u}) + d_t(\mathbf{I} - \mathbf{E}(\mathbf{u}))]\}, \tag{2.5}$$

where $\mathbf{E}(\mathbf{u})$ denotes the projected tensor onto the $\mathbf{u}$ direction, which is calculated by

$$\mathbf{E}(\mathbf{u}) = \frac{1}{\left(u_1^2 + u_2^2\right)^{1/2}} \begin{bmatrix} u_1^2 & u_1 u_2 \\ u_2 u_1 & u_2^2 \end{bmatrix}, \tag{2.6}$$

where $|\mathbf{u}| = (u_1^2 + u_2^2)^{1/2}$ represents the Euclidean norm of $\mathbf{u} = (u_1, u_2) \in R^2$; d_m (strictly positive) is the molecular diffusivity, d_t and d_l are the transverse dispersivity and the longitudinal dispersivity, respectively, and both are nonnegative. The unknowns c_f as well as c_s are the concentrations of the species considered within the fluid and solid, respectively.

By summing of the first two equations using the third equation in (2.4), we can obtain

$$\frac{\partial(\phi^e c_f)}{\partial t} + \nabla \cdot \left(\mathbf{u} c_f - D(\mathbf{u}) \nabla c_f\right) = 0, \tag{2.7}$$

where $\phi^e = \phi + \rho K_d$ is calculated for the matrix and for the vugs, respectively, as follows:

-in the vugs and/or fractures: $\phi = 1$, $K_d = 0$, $\phi^e = \phi = 1.0$,

-in the matrix: $\phi = \phi_m$, $\phi^e = \phi + \rho K_d$.

The boundary conditions for transport system are given by

$$\begin{aligned} &\left(\mathbf{u} c - D(\mathbf{u}) \nabla c_f\right) \cdot \mathbf{n} = c_B \mathbf{u} \cdot \mathbf{n}, \quad \mathbf{x} \in \Gamma_{\text{inflow}}, \\ &D(\mathbf{u}) \nabla c_f \cdot \mathbf{n} = 0, \quad \mathbf{x} \in \Gamma_{\text{outflow}}, \end{aligned} \tag{2.8}$$

where c_B is the prescribed given concentration on the boundary; Γ_{inflow} denotes the inflow boundary, and Γ_{outflow} denotes the outflow boundary, defined by

$$\begin{aligned} \Gamma_{\text{inflow}} &= \{\mathbf{x} \in \partial\Omega : \mathbf{u} \cdot \mathbf{n}_{\partial\Omega} \leq 0\}, \\ \Gamma_{\text{outflow}} &= \{\mathbf{x} \in \partial\Omega : \mathbf{u} \cdot \mathbf{n}_{\partial\Omega} > 0\}. \end{aligned} \tag{2.9}$$

The initial condition is taken as

$$c_f(\mathbf{x}, 0) = c_0(\mathbf{x}), \quad \mathbf{x} \in \Omega, \tag{2.10}$$

where $c_0(\mathbf{x})$ is a prescribed given function for the concentration at $t = 0$, which can be measured for some points in the considered domain in practice.

3. Numerical Algorithms

In this paper, the system is made up of two parts: the flow equations including the Darcy velocity and the pressure, and the contaminant species transport equations for presenting the evolution of concentration. A triangular mesh for spatial partitioning is employed for accurately approaching the velocity and the concentration around the vugs and fractures. Vugs and fractures are initially characterized by ellipses of different sizes and rectangles of different sizes, respectively. A mixed finite method (FEM) is used to solve the flow equation, based on the triangular mesh; then we solve the transport system by combining the finite volume method (FVM) and MFE method semi-implicitly (implicitly for diffusion and adsorption and explicitly for convection) in time, getting ODEs for concentration over time.

3.1. Triangular Mesh Generation for Vuggy Fractured Porous Media

Similar to any other numerical modeling, the first step of our algorithm is creating a mesh. The vugs and fractures may be distributed randomly in the domain, so a triangular mesh is required to fit the vuggy fractured porous media much better than a rectangular mesh (though it is easier to generate). A large number of triangular mesh programs are available. Three of them (including DISTMESH, MESHGEN, and TRIANGLE) have much higher mesh quality than any other one in generating adaptive triangular mesh [31]. In this paper, we apply the MESHGEN [32] to generate an adaptive triangular mesh. The fractures are presented in rectangles distributed randomly in the domain considered, and the vugs are described in ellipses distributed randomly.

3.2. Mixed Finite Element Method

We employ a mixed finite element (MFE) method for the treatment of the flow equation. MFE method [33] is based on the variational principle that expresses an equilibrium that can be satisfied locally on each finite element. The MFE formulation for the flow equation contains solution for both the scalar variable (pressure) and flux vector (total velocity). Choosing MFE

method to approach spaces can satisfy three important properties: local mass conservation, flux continuity, and the same order of convergence (and in some cases super convergence) for both the scalar variable and the flux [33]. MFE method can directly accommodate full permeability tensors and it is more accurate in flux calculation than the conventional finite volume and finite element methods.

We first give some symbol notations. Let $(\cdot,\cdot)$ represent the $L^2(\Omega)$ inner product over a domain $\Omega \in R^2$ for scalar functions, and $(L^2(\Omega))^2$ denotes inner product for vector functions. Some necessary spaces are given by

$$\begin{gathered} V = L^2(\Omega), \\ \mathbf{W} = H(\mathrm{div};\Omega) = \left\{ \mathbf{w} \in \left(L^2(\Omega)\right)^2 : \nabla \cdot \mathbf{w} \in L^2(\Omega) \right\}, \\ \mathbf{W}^0 = \{\mathbf{w} \in H(\mathrm{div};\Omega) : \mathbf{w} \cdot \mathbf{n} = \mathbf{0} \text{ on } \partial\Omega\}, \\ \mathbf{W}_N^0 = \{\mathbf{w} \in H(\mathrm{div};\Omega) : \mathbf{w} \cdot \mathbf{n} = \mathbf{0} \text{ on } \Gamma_N\}. \end{gathered} \tag{3.1}$$

Based on these spaces, we give the weak formulations for flow equation and reactive equation as follows, respectively.

3.3. MFE for Flow Equation

3.3.1. Weak Formulation

For the flow equation, the weak formulation is to find $p \in V$ and $\mathbf{u} \in \mathbf{W}_N^0 + \mathbf{E}(\mathbf{u}_B)$ such that

$$\begin{gathered} \left(K^{-1}\mathbf{u}, \mathbf{w}\right) - (\nabla \cdot \mathbf{w}, p) = -\int_\Gamma p_B \mathbf{w} \cdot \mathbf{n}\, ds, \quad \forall \mathbf{w} \in \mathbf{W}_N^0,\ t \in (0,T], \\ (\nabla \cdot \mathbf{u},\ v) = (q, v), \quad \forall v \in V,\ t \in (0,T], \end{gathered} \tag{3.2}$$

where $\mathbf{E}(\mathbf{u}_B)$ denotes the velocity extension which lets its component agrees with $\mathbf{u}_B$ on Γ_N. There is the derivation of (3.2) in Appendix A.

3.3.2. MFE Scheme

We apply the RT (Raviart-Thomas) finite element space [34] to approximate the Darcy velocity. As is well known, the rth order RT space for the two-dimensional triangular element is given by

$$V_h(K) = P_r(K), W_h(K) = (x_1, P_r(K)x_2 P_r(K)) \oplus (P_r(K))^2, \tag{3.3}$$

where $\oplus$ represents the direct sum. We employ the case $r = 0$ in this paper. Therefore, $W_h(K)$ has the form

$$W_h(K) = \{\mathbf{w} : \mathbf{w} = (a_K + b_K x_1, c_K + b_K x_2),\ a_K, b_K, c_K \in R\}. \tag{3.4}$$

Restricted to the element, $P_r(K)$ is the polynomial space of degree less than or equal to r. We apply RT_0 space in our coming numerical examples. So our MFE method for approaching the weak formulation for the flow equation is to find $p_h(\cdot,\cdot) \in V_h$ and $\mathbf{u}_h(\cdot,\cdot) \in \mathbf{W}_N^0 = \mathbf{W^0} \cap \mathbf{W}_h + \mathbf{E}_h(\mathbf{u}_B)$ such that

$$\begin{gathered}\left(K^{-1}\mathbf{u}_h, \mathbf{w}\right) - \left(\nabla \cdot \mathbf{w}, p_h\right) = -\int_\Gamma p_B \mathbf{w} \cdot \mathbf{n}\, ds, \quad \forall \mathbf{w} \in \mathbf{W}_h, t \in (0,T], \\ \left(\nabla \cdot \mathbf{u}_h, v\right) = (0, v), \quad \forall v \in V_h,\ t \in (0,T].\end{gathered} \tag{3.5}$$

Because the MFE formulation leads to a saddle point problem for the elliptic equations, we need to use the Mixed-Hybrid algorithms [32] for the pressure equation. Those algorithms mainly use adding unknowns denoting the edge pressure averages, such that the reduced linear system we will solve contains a positive and symmetric definite matrix, and therefore we take the advantages in iterative linear solvers.

Based on the RT_0 space, (3.5) can be expressed as an algebraic linear system with the unknowns P_E (the pressure edge averages)

$$A_T P_E = J. \tag{3.6}$$

The derivation of (3.6) is presented in Appendix B.

3.4. FVM and FME for Reactive Transport System

3.4.1. Weak Formulation

The weak formulation for the reactive transport system is to find the concentration solution $c \in V$ and the diffusive flux solution $\mathbf{w} \in W^0$ such that

$$\begin{gathered}\left(\frac{\partial(\phi^e c_f)}{\partial t}, v\right) + (\nabla \cdot \mathbf{w}, v) + \sum_K \int_{\partial K} v \mathbf{u} c_f^* \cdot \mathbf{n}\, ds - \sum_K \left(c_f^* \mathbf{u}, \nabla v\right) = 0, \quad \forall v \in V,\ t \in (0,T], \\ \left(-D^{-1}\mathbf{w}, \widehat{\mathbf{w}}\right) + \left(c_f, \nabla \cdot \mathbf{w}\right) = 0, \quad \forall \mathbf{w} \in \mathbf{W^0}, t \in (0,T], \\ \left(c_f, v\right) = \left(c_{f,0}, v\right), \quad \forall v \in V,\ t = 0,\end{gathered} \tag{3.7}$$

where c_f^* represents the upwind value of the concentration on an edge. There is the derivation of (3.7) in Appendix C.

3.4.2. MFE Scheme

On the basis of the weak formulation (3.7), the continuous-in-time MFE method to approach the reactive transport system is to find $c_{fh} \in V_h$ and $\mathbf{w}_h \in W_h^0$ such that

$$\begin{aligned}
&\left(\frac{\partial(\phi^e c_{fh})}{\partial t}, v\right) + (\nabla \cdot \mathbf{w}_h, v) + \sum_K \int_{\partial K} v\mathbf{u}c_f^* \cdot \mathbf{n}\, ds - \sum_K \left(c_{fh}^* \mathbf{u}, \nabla v\right) = 0, \quad \forall v \in V_h,\ t \in (0,T], \\
&\left(-D^{-1}\mathbf{w}_h, \widehat{\mathbf{w}}\right) + \left(c_{fh}, \nabla \cdot \mathbf{w}\right) = 0, \quad \forall \widehat{\mathbf{w}} \in \mathbf{W}_h^0,\ t \in (0,T], \\
&\left(c_f, v\right) = \left(c_{f0}, v\right), \quad v \in V_h,\ t = 0.
\end{aligned} \tag{3.8}$$

Then we specify a fully discretized algorithm for the transport. We discretize the simulation time $[0,T]$ into n subintervals: $0 = t_0 < t_1 < \cdots < t_{n-1} < t_n = T$. Let $\Delta t_l = t_l - t_{l-1}$, $\Delta t = \max_l \Delta t_l$. Provided that there exists a constant $C > 0$ such that $\Delta t \le C \min_l \Delta t_l$, and the transport equation can be solved by semi-implicit Euler method in time together with the combined FVM-MFE method in space.

Therefore the fully discretized approximation is to find $c_{fh,l} \in V_h$, $\mathbf{w}_{h,k} \in W_h^0$ ($l = 0, 1, \ldots, n$) such that

$$\begin{aligned}
&\left(\frac{\phi^e\left(c_{fh,l} - c_{fh,l-1}\right)}{\Delta t_l}, v\right) + (\nabla \cdot \mathbf{w}_{h,l}, v) + \sum_K \int_{\partial K} v\mathbf{u}c_{fh,l-1}^* \cdot \mathbf{n}\, ds - \sum_K \left(c_{fh,l-1}^* \mathbf{u}, \nabla v\right) \\
&\quad = 0,\ \forall v \in V_h, \\
&\left(-D^{-1}\mathbf{w}_{h,l}, \widehat{\mathbf{w}}\right) + \left(c_{fh,l}, \nabla \cdot \widehat{\mathbf{w}}\right) = 0, \quad \forall \mathbf{w} \in \mathbf{W}_h^0, \\
&\left(c_{fh,0}, v\right) = \left(c_{f0}, v\right), \quad \forall v \in V_h.
\end{aligned} \tag{3.9}$$

We employ the standard MFE algorithm to solve reactive transport equation (3.7). We here also use RT_0 on the reactive transport system, and thus the linear system (2.4) can be specified as the following algebraic linear ordinary differential equation system

$$L\frac{dX}{dt} + \left(\widehat{R} + \widehat{R}\right)X = b. \tag{3.10}$$

Ordinary differential equations (3.10) are solved by backward Euler method in this paper. The derivation of (3.10) is presented in Appendix D.

Table 1: Standard parameters for the mathematical model in practice.

Saturated hydraulic conductivity, K_s (cm/s)	Saturated effective diffusion coefficient, D_e (cm^2/s)	Effective porosity	Distribution coefficient K_d
$1.0e{-}12$	$5.0e{-}11$	0.184	0.395

4. Numerical Results

4.1. Simulation Cases

We mainly simulate two sequential phases for an infiltration process with different initial and boundary conditions: at first, the clean water infiltration process, with initial concentration $c_1(\mathbf{x}, 0) = 0$ and boundary condition in the inflow boundary $c_1(\mathbf{x}, t) = 0, \mathbf{x} \in \Gamma_{\text{inflow}}$. In the first phase, the polluted water infiltration process, with initial concentration in the whole region $c_2(\mathbf{x}, 0) = 0.0$ and boundary condition in the inflow boundary$c_1(\mathbf{x}, t) = 1.0, \mathbf{x} \in \Gamma_{\text{inflow}}$. In the second phase, again the clean water infiltration process, with initial concentration in the whole region $c_3(\mathbf{x}, 0) = c_1(\mathbf{x}, T_1)$ and boundary condition in the inflow boundary $c_3(\mathbf{x}, t) = 0$, $\mathbf{x} \in \Gamma_{\text{inflow}}$, where $c_1(\mathbf{x}, T_1)$ is the concentration distribution at T_1 in the first phase. The domain considered for all cases in this paper is a bounded rectangular domain $\Omega \subset R^2$ of $(0, 0.80\,\text{m}) \times (0, 0.80\,\text{m})$ with randomly generated vugs and fractures into an adaptive triangular mesh. The mesh is fixed for all time during the simulation. The region around the fractures and/or vugs is deeply refined because of dramatically changing of some parameters for the models. For all cases in the paper, a series of standard parameters applied in practice are listed in Table 1 as follows [1].

Case 0 as a base case describes the porous media without vugs and fractures to be compared with the other cases, that is, the fractured vuggy porous media with vugs and fractures distributed differently. In Case 1, in the fractured vuggy porous media, the vugs are located on the inflow boundary connected with the fractures, and the fracture does not elongate to the outflow boundary. In Case 2, the vugs are still located on the inflow boundary connected with the fracture, but the fractures extend to the outflow boundary. In Case 3, the vugs connected with fracture are located within the region, and both the vugs and the fractures do not elongate to any boundary. In Cases 5 and 6, the vugs lie on the outflow boundary connected with fracture, but in Case 5 the fractures are connected with the inflow boundary and the fractures are not in Case 6. The vugs in Case 7 are connected with fractures, and the fractures are connected with inflow boundary and outflow boundary. In the last case, the fractures are located within the region connecting the vugs that lie on the inflow boundary and the outflow boundary. The no-flow boundaries in all cases are taken as the top ($y = 0.80\,\text{m}$) and the bottom boundaries ($y = 0.80\,\text{m}$). The inflow boundary and outflow boundary are taken as the left boundary ($x = 0.0\,\text{m}$) and the right boundary ($x = 0.80\,\text{m}$) of the domain, respectively. A constant pressure of 0 (the gauge pressure against a reference pressure) is specified on the outflow boundary ($x = 0.80\,\text{m}$). In the first phase of the simulation, the polluted water is continuously injected on the left boundary ($x = 0\,\text{m}$), that is, the inflow boundary, and the region is initially full of clean water. In the second phase of the simulation, the clean water is continuously injected at the final of the first phase. We simulate up to 35,000 years and 35,000 for the first phase and the second phase for all cases, respectively. The injection on the inflow boundary for the two phases is showed in Figure 2.

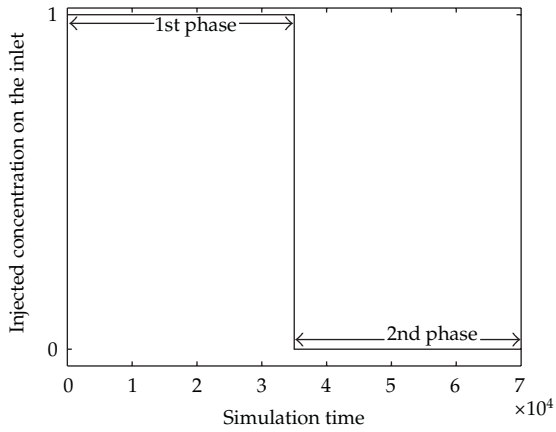

Figure 2: Injection on the inflow boundary for the two phases of the simulation.

4.2. Simulation Results

Case 0: Matrix Porous Media

In this situation, the area is matrix porous media as a base case to be compared with 8 other cases. In the first phase the polluted water is constantly injected into the inflow boundary at the time interval $(0, T_1]$. The conductivity distribution is showed in Figure 3. An adaptive triangular mesh for this domain is generated (Figure 3). We approximate the Darcy equation and transport equation using RT_0 − MFE and semi-implicit FVM-MFE presented before, respectively, with a uniform time step of 350 years. The pressure field and the streamlines field (Figure 4) are obtained. Figure 5 demonstrates the results of simulated profiles at different time. The results show that the polluted water is uniformly diffusing from the inflow boundary through the domain to the outflow boundary in the first phase. In the second phase, the clean water is being injected on the inflow boundary. Figure 6 shows the results of the simulated profiles at different time for the second phase. The results demonstrate that the polluted water is uniformly ejected out from the outflow boundary. The effluent concentration on the outlet is obtained for the two phases to be compared with the other cases.

Case 1: Vugs on the Inflow Boundary Connected with Fractures inside the Domain

In this case, vugs are located on the inflow boundary of the considered domain connected with fractures not touching the outflow boundary, which is depicted in Figure 7. The pressure distribution and the streamlines field are shown in Figure 8. From Figure 8, it is obviously demonstrated that the vugs and fractures affect the pressure distribution compared with the base case. The vugs and fractures have corresponding locally irregular pressure, and the pressure around vugs and fractures is higher than other regions in the domain. Therefore the quantity of velocity in the vugs and fractures is much larger than that in the matrix media. Furthermore, we can observe that the streamlines are inclined to converging into the vugs and the fractures near the inflow part but diverge from the fractures on the right part, which show that the vugs and fractures are the main pathways for contaminant transport by convection. Results of simulated concentration sections are shown in Figure 9 at different time.

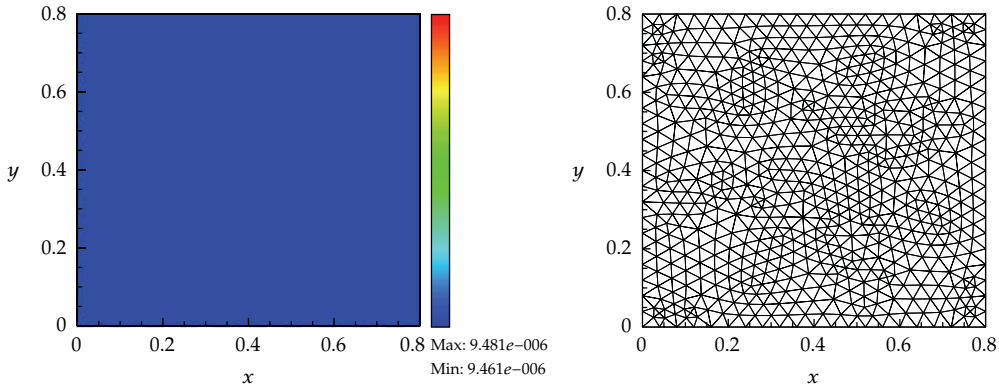

(a) Conductivity distribution (b) Adaptive triangular mesh

Figure 3: Conductivity distribution and adaptive triangular mesh for Case 0.

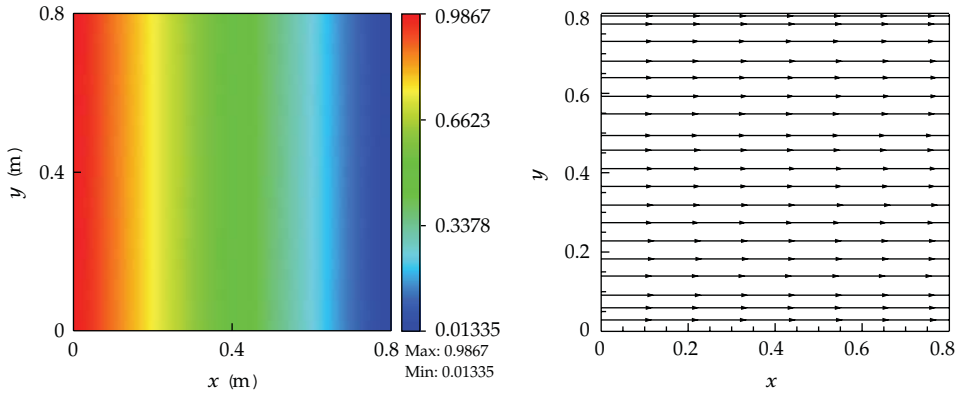

(a) Pressure distribution (b) Streamlines field

Figure 4: Pressure distribution and streamlines field for base case.

The results show that the contaminant transports essentially via convection in the domain of vugs and fractures from the first year to the 3500th year. After the 14000th year, convection and diffusion through the matrix area also begin to take obvious effect on the contaminant transport behavior. During the second phase of the simulation, from the 35001th to 38500th year the vuggy and fractured region is first getting much cleaner than that in the matrix, which is showed in Figure 10. After the 49000th year, the clean water begins to infiltrate into the matrix porous media displayed in Figure 10.

Case 2: Vugs on the Inflow Boundary Connected with Fractures Extending to the Outflow Boundary

Compared with Case 1, the fractures in this case are extending to the outflow boundary, the conductivity and the adaptive triangular mesh of which are shown in Figure 11. The pressure

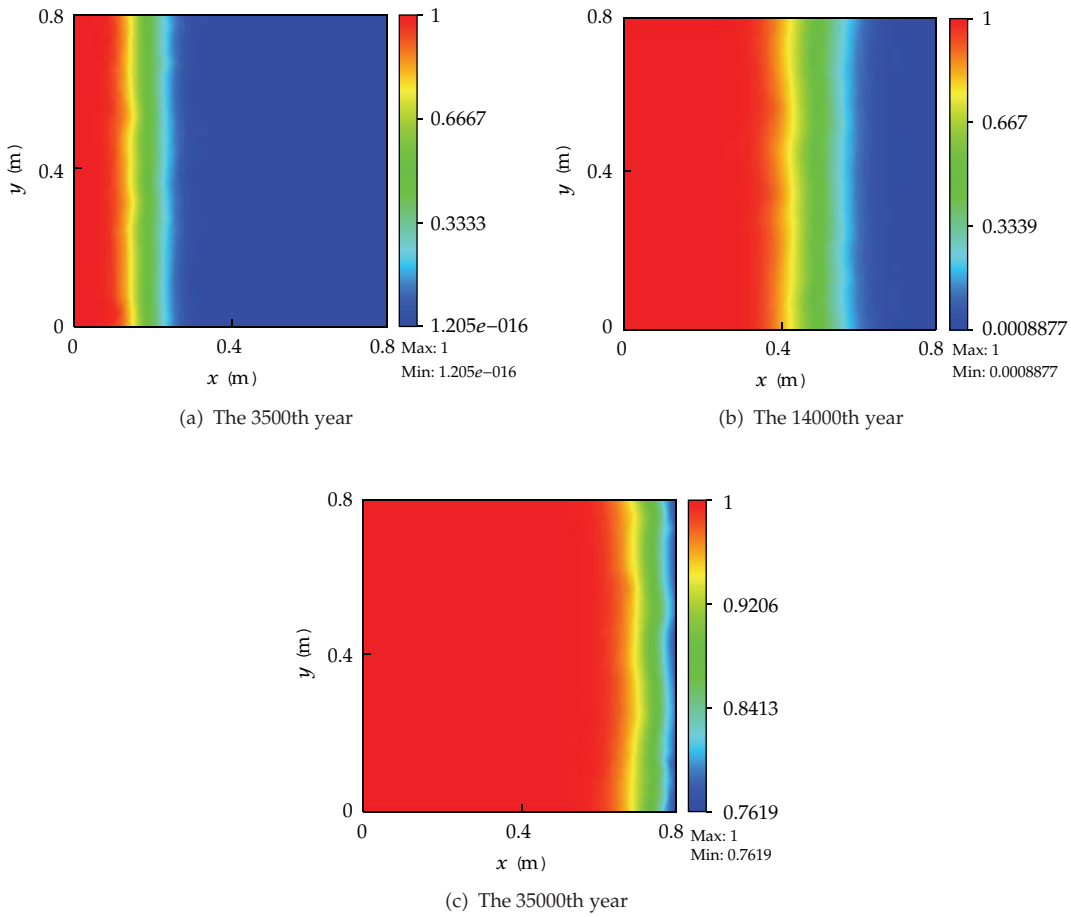

(a) The 3500th year

(b) The 14000th year

(c) The 35000th year

Figure 5: Concentration distribution at different time for the first phase for base case.

distribution and the streamlines field are shown in Figure 12. Similar to Case 1, the vugs and fractures affect the pressure distribution compared with the base case, and the vugs and fractures have corresponding locally irregular pressure. But different from Case 1, the streamlines are inclined to converging into the vugs and the fractures from the inlet to the outlet, which show that the vugs and fractures are still the main pathways for transporting contaminant by convection. Results of simulated concentration profiles are shown in Figure 13 at different time for the first phase. From the first year to the 14000th year, the contaminant transports mainly through the vugs and the fractures because of the much faster velocity in the vugs and the fractures than that in matrix. And the pollutant quickly passes through fractures to the outflow boundary. From the 14001th year to the 35000th year, the matrix begins to become a significant role in contaminant transport, as is shown in Figure 13. During the second phase of the simulation, the clean water quickly passes through the vugs and fractures to the outlet from the 35001th year to the 38500th year demonstrated in Figure 14, and the matrix near the inflow boundary begins getting clean from the 38501th year, which is shown in Figure 14.

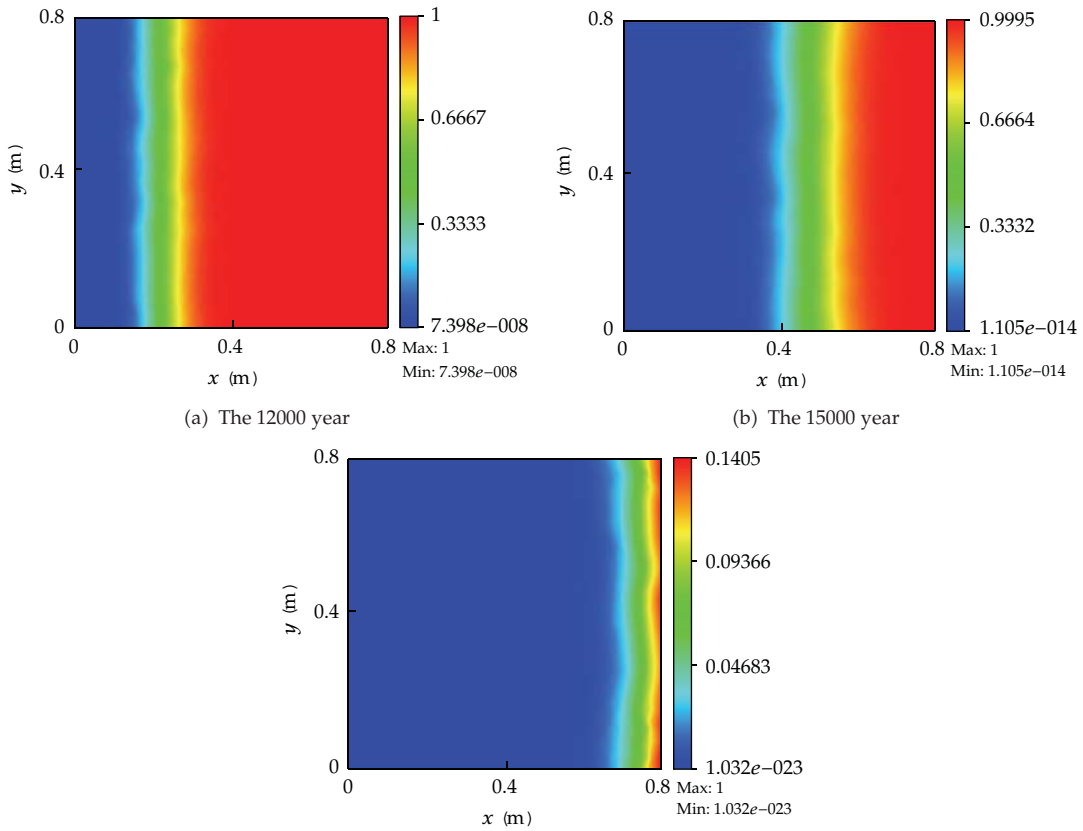

(a) The 12000 year

(b) The 15000 year

(c) The 20000 year

Figure 6: Concentration distribution at different time for the second phase for base case.

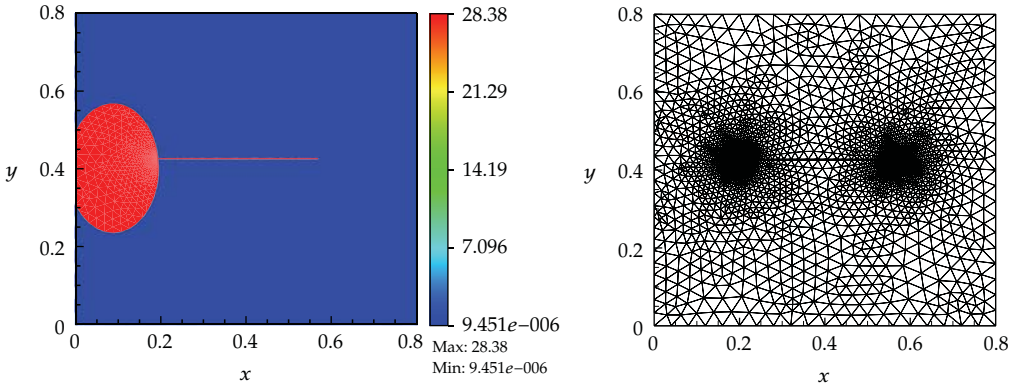

(a) Conductivity distribution

(b) Adaptive triangular mesh

Figure 7: Conductivity distribution and adaptive triangular mesh for Case 1.

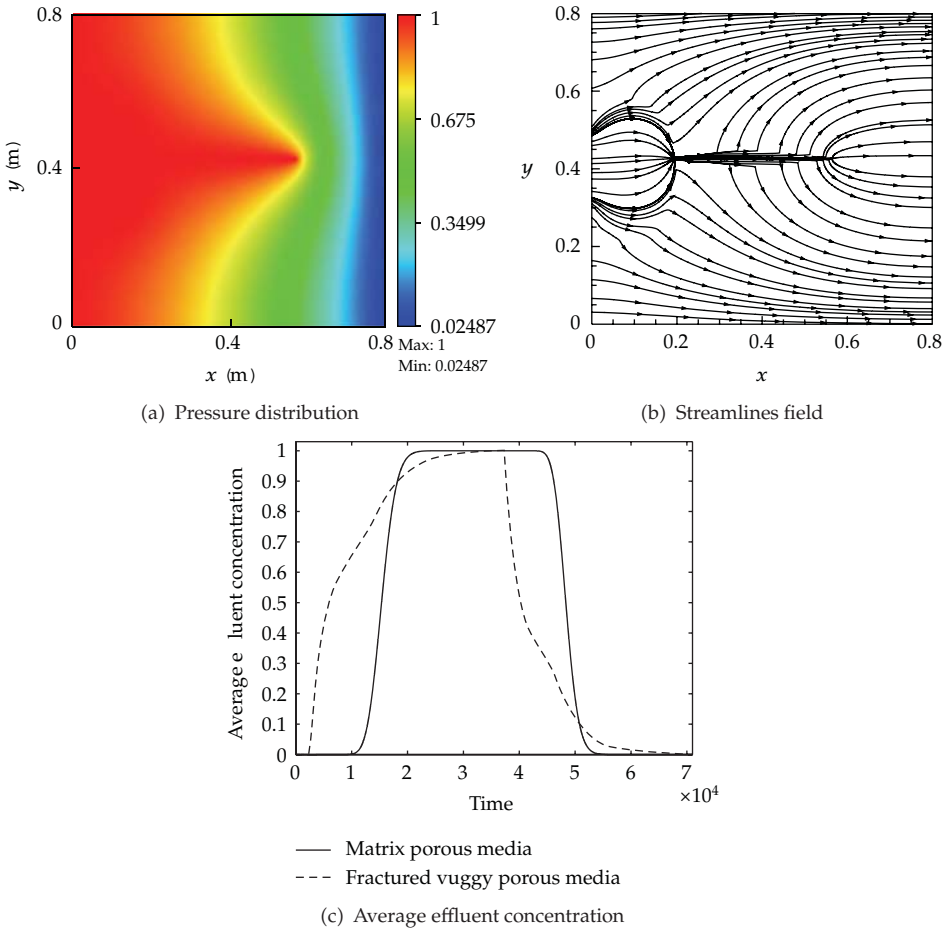

Figure 8: Pressure distribution, streamlines field, and average effluent concentration for Case 1.

Case 3: Vugs Connected with Fractures inside the Domain

In this case, none of the vugs and fractures touches the boundary, the conductivity and adaptive triangular mesh of which are displayed in Figure 15. We can observe that the vugs observably affect the pressure distribution from the pressure field in Figure 16. On the contrary, the fractures do not affect the pressure distribution so obviously as the vugs. From the streamlines field in Figure 16, we also find out that the streamlines converge into the vugs and fractures for the inflow boundary and diverge from the endpoint of the fractures. For the first phase of the simulation, the results of simulated concentration profiles are shown in Figure 17. From the initial situation to 1400th year, the contaminant mainly transports in the matrix porous media via convection and diffusion. From the 1401th year to the 3500th year, the contaminant mainly infiltrates into the vugs and fractures (Figure 17). From the 3501th year, the matrix starts to significantly take effect on the transport through diffusion and convection. When injecting clean water in the second phase, from the 35001th year the porous matrix media are firstly getting cleaner than that in matrix, and from the 38500th year the clean water quickly infiltrate into the vugs and fractures with the contaminant remained

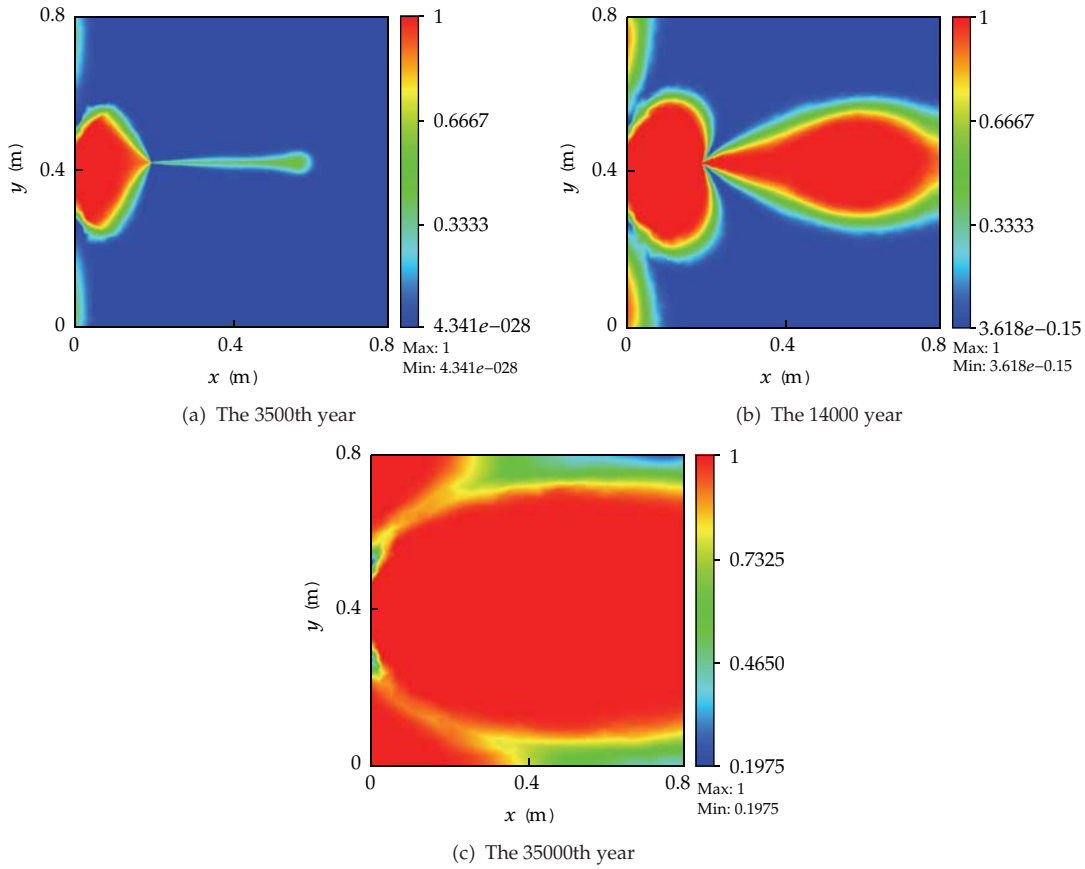

(a) The 3500th year

(b) The 14000 year

(c) The 35000th year

Figure 9: Concentration distribution at different time for the first phase for Case 1.

in the matrix media. From 49000th year the clean water starts to infiltrate the matrix (Figure 18).

Case 4: Vugs on the Outflow Boundary Connected with Fractures inside the Domain

Now we consider the vugs on the outlet connected with fractures no touching the inlet. The conductivity distribution and adaptive triangular mesh of the case are displayed in Figure 19. It is observed that the pressure field (Figure 20) is not affected by vugs so significantly as that in Case 3. This is because we take the pressure a 0 on the outflow boundary. From the streamlines field (Figure 20), we can find out that the streamlines converge into the fractures from the inflow boundary and diverge at the end of the fractures. From the results of the simulated concentration sections (Figure 21). We can observe that from first year to the 3500th year, the contaminant transports mainly through the matrix via diffusion and convection. From the 3501th year to the 5000th year, the fractures and vugs begin to influence the transport of contaminant via convection (Figure 21). From the 5001th year to the 35000th year the contaminant transports through the whole fractured vuggy porous media (Figure 21). In the second phase of the simulation, the clean water almost uniformly flows through the matrix from the 35001th year to the 38500th year (Figure 22), and from the 3900th year to

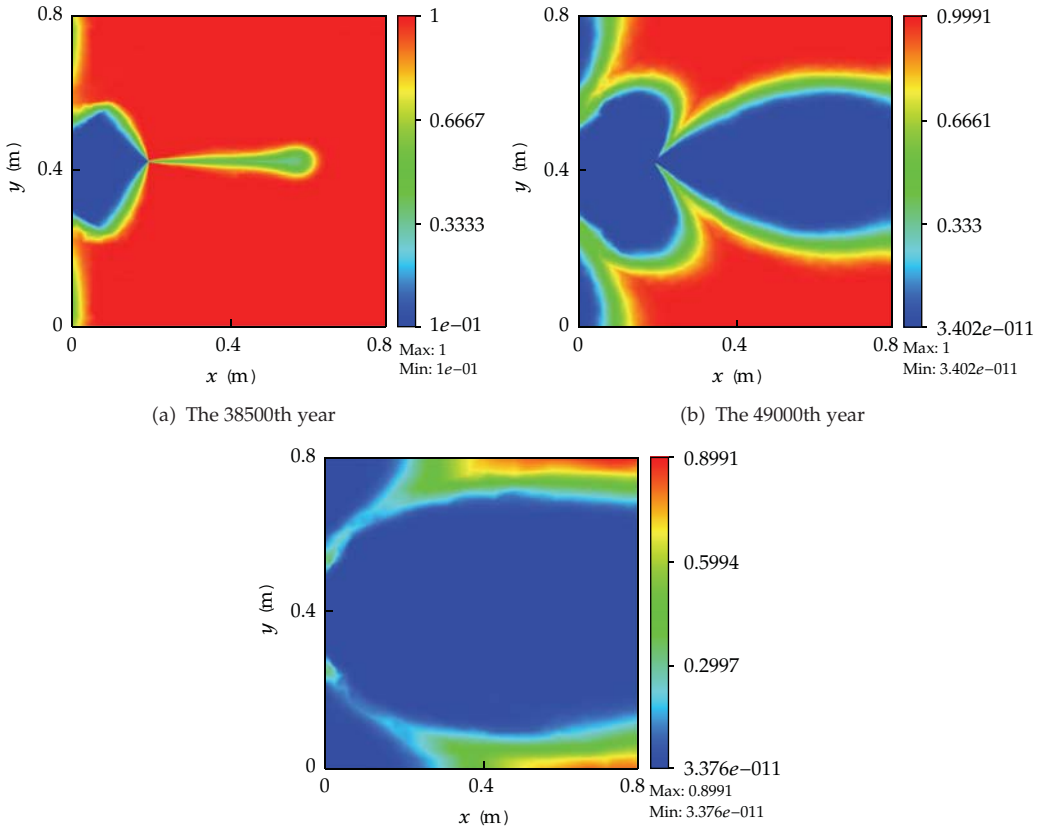

(a) The 38500th year

(b) The 49000th year

(c) The 70000th year

Figure 10: Concentration distribution at different time for the second phase for Case 1.

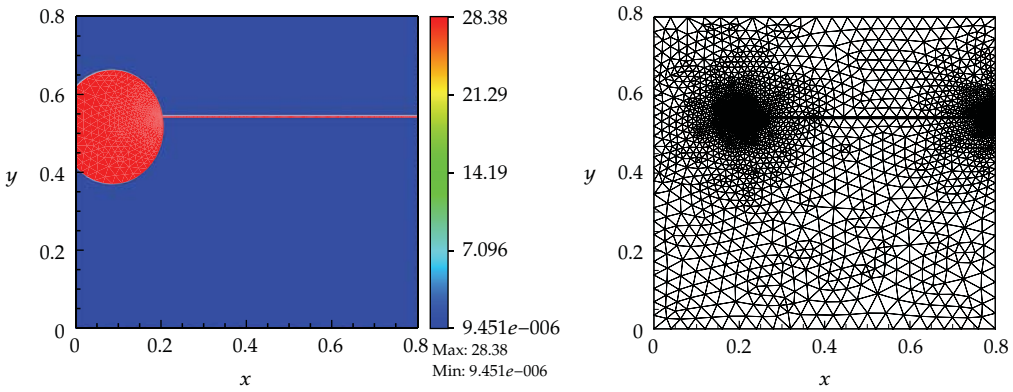

(a) Conductivity distribution

(b) Adaptive triangular mesh

Figure 11: Conductivity distribution and adaptive triangular mesh for Case 2.

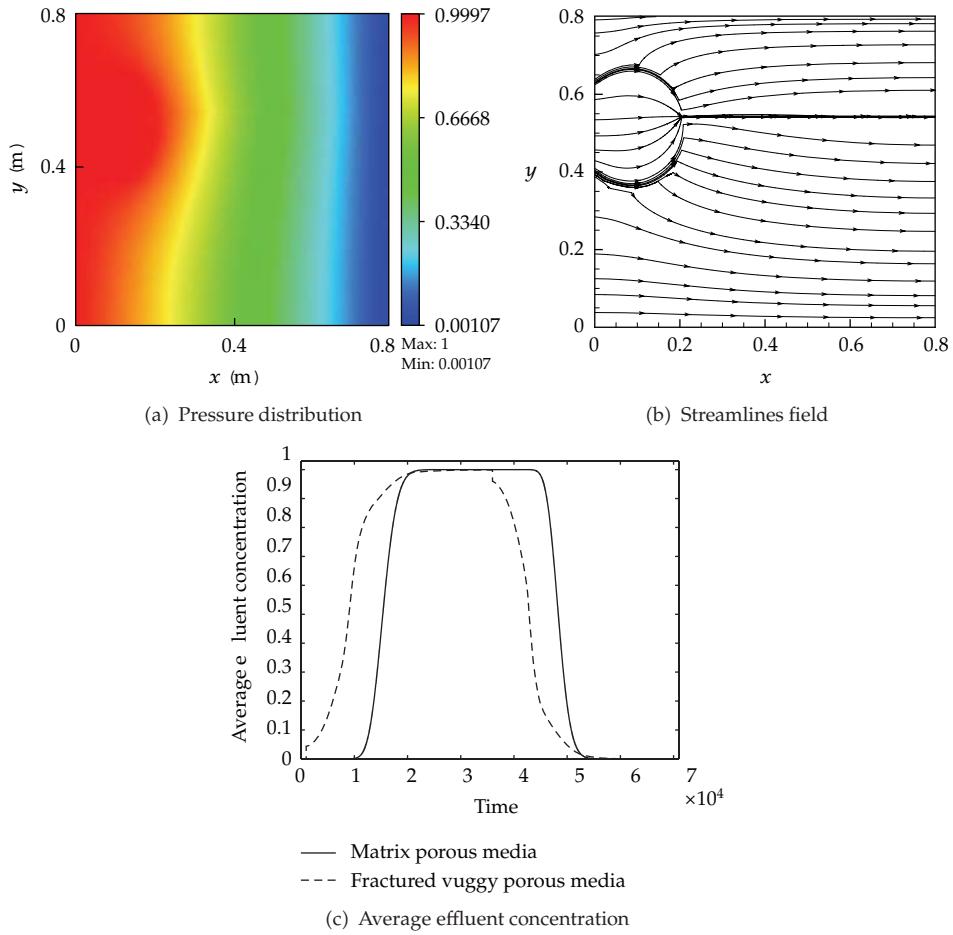

(a) Pressure distribution

(b) Streamlines field

(c) Average effluent concentration

Figure 12: Pressure distribution, streamlines field, and average effluent concentration for Case 2.

the 44000th year, the clean water mainly passes through the vugs and fractures (Figure 22). From the 44001th year to 70000th year, clean water begins to pass the whole fractured vuggy porous media (Figure 22).

Case 5: Vugs on the Outflow Boundary Connected with Fractures Extending to the Inflow Boundary

Similar to Case 4, but the fractures are now extending to the inflow boundary. The conductivity distribution and adaptive triangular mesh of this situation are given in Figure 23. The pressure and streamlines fields are displayed in Figure 24. The pressure field shows that the fractures and vugs do not affect the pressure distribution. But the fractures significantly affect the streamlines distribution (Figure 24). From the results of the simulated concentration, different from Case 4, the contaminant transport mainly passes through vugs and fractures via convection from year 1 to year 3500 in the first phase, and the contaminant quickly passes through vugs and fractures to the outlet (Figure 25). From the 3501th year the contaminant starts to infiltrate into the matrix media (Figure 25).

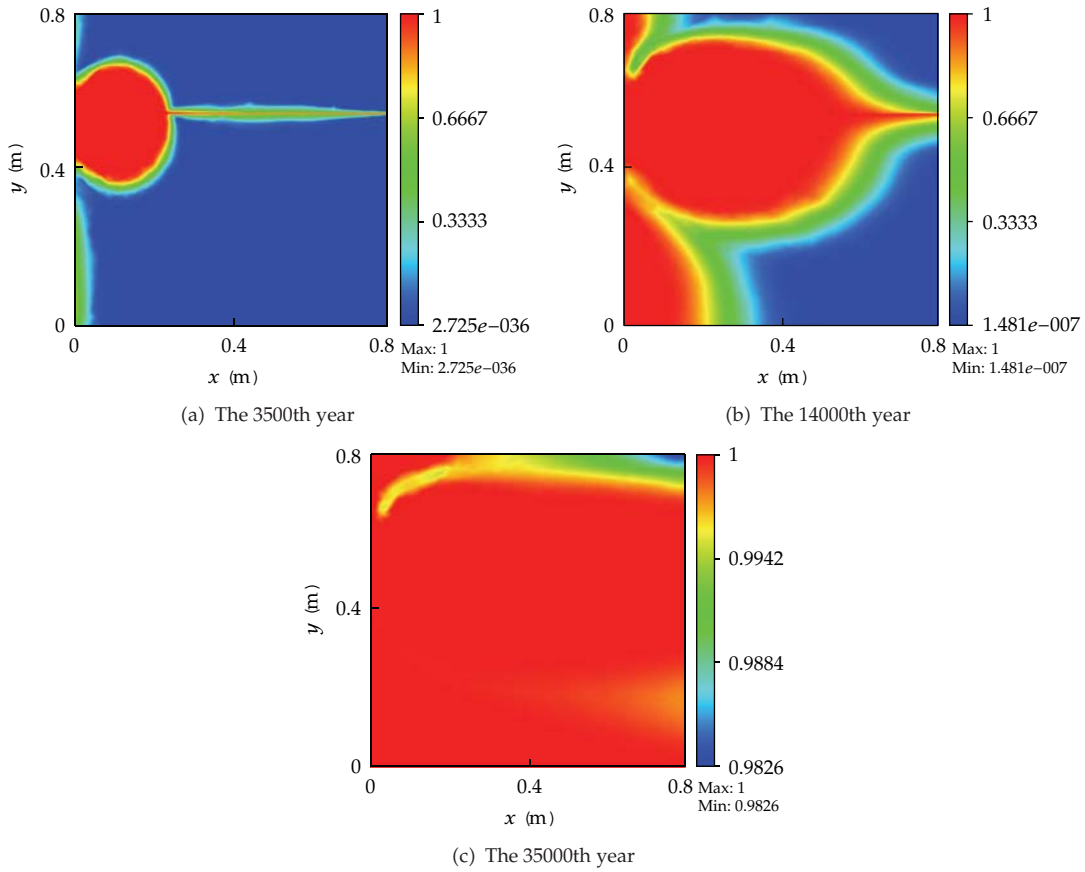

Figure 13: Concentration distribution at different time for the first phase for Case 2.

In the second phase, the clean water firstly passes through the fractures and vugs (Figure 26).

Case 6: Vugs inside the Domain Connected with Fractures Extending Both Inflow and Outflow Boundaries

Now the vugs are located inside the domain connected with fractures extending to the inlet and outlet. The conductivity distribution and adaptive triangular mesh are displayed in Figure 27. The pressure field and streamlines field are demonstrated in Figure 28. The pressure field suggests that the fractures near the inflow boundary and vugs significantly affect the pressure distribution while the fractures near the outflow boundary not. The streamlines field shows that the streamlines converge into the fractures and the vugs. The results of the simulated concentration are showed in Figure 29. From Figure 29, we can observe that the contaminant quickly passes through the vugs and fractures to the outlet via convection during year 1 to year 3500, after that the contaminant starts to pass through the matrix. In the second phase, the clean water behaves as the contaminant in the first phase as shown in Figure 30.

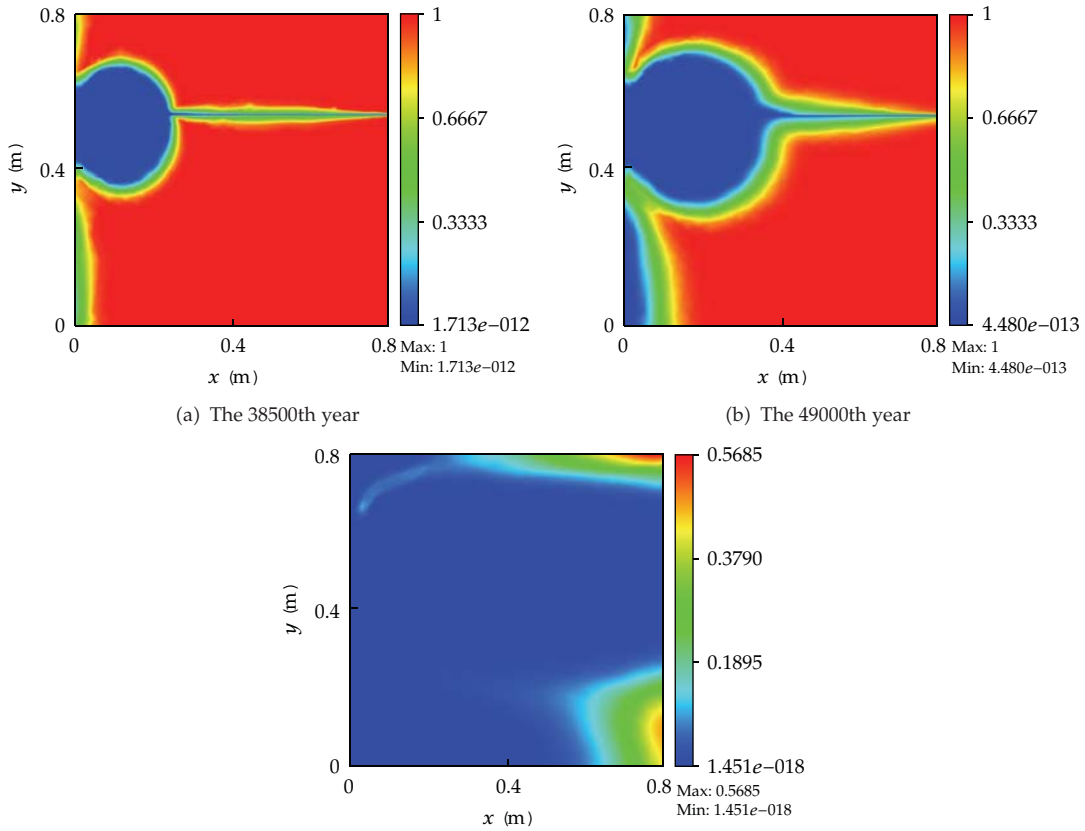

(a) The 38500th year

(b) The 49000th year

(c) The 70000th year

Figure 14: Concentration distribution at different time for the second phase for Case 2.

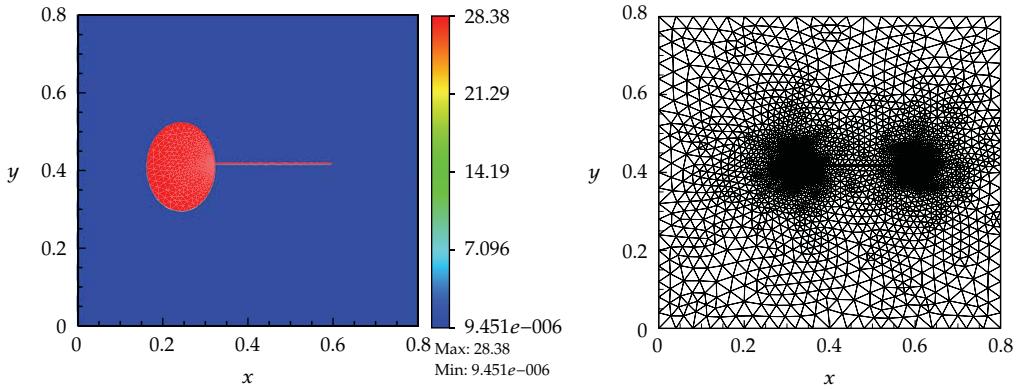

(a) Conductivity distribution

(b) Adaptive triangular mesh

Figure 15: Conductivity distribution and adaptive triangular mesh for Case 3.

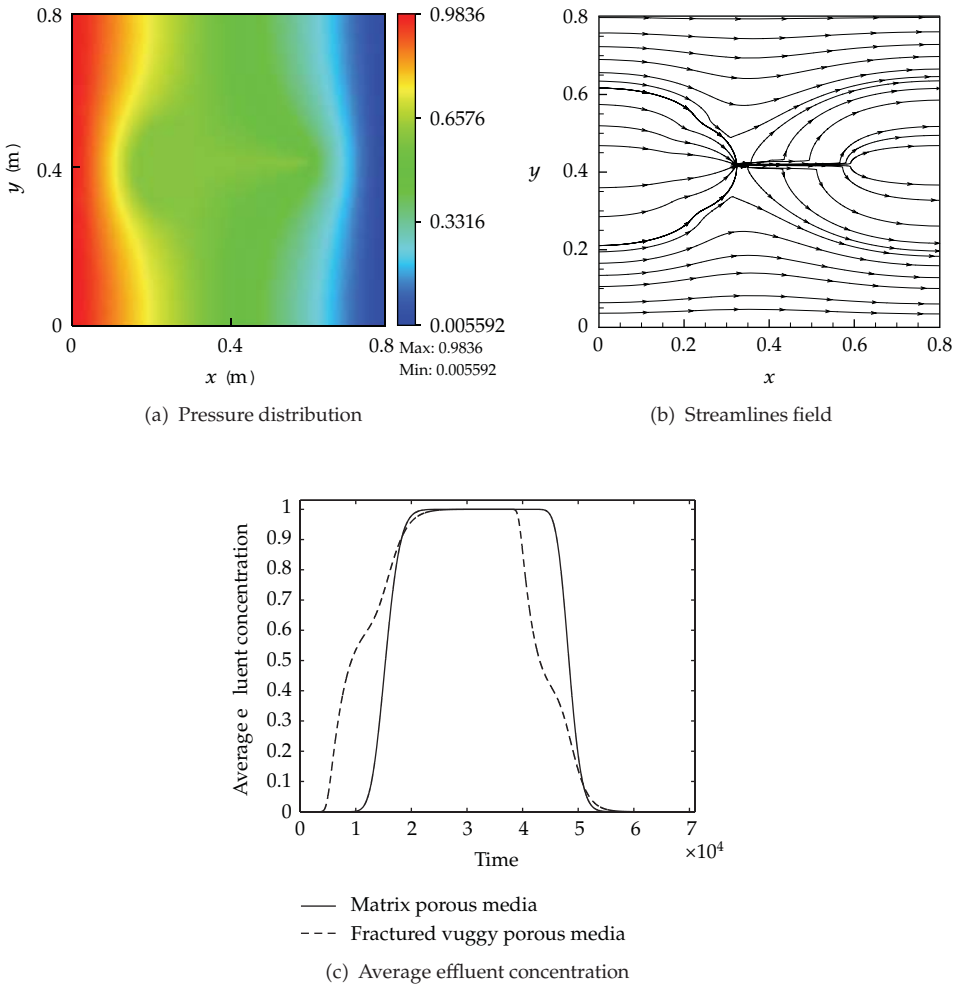

(a) Pressure distribution

(b) Streamlines field

(c) Average effluent concentration

Figure 16: Pressure distribution, streamlines field, and average effluent concentration for Case 3.

Case 7: Vugs on the Inflow Boundary and Outflow Boundary Connected with Fractures through the Domain

In this case, the vugs are located on the inlet and outlet connected with fractures, the conductivity distribution and adaptive triangular mesh of which are displayed in Figure 31. The pressure and streamlines fields are showed in Figure 32. From Figure 32 we can observe that the vugs near the inflow boundary obviously affect the pressure distribution while the fractures and the vugs near the outflow boundary not. From year 1 to year 3500, the contaminant transports mainly through the vugs and fractures via convection (Figure 33). From the 3501th year, the contaminant starts to infiltrate into the matrix porous media (Figure 33). In the second phase, the clean water quickly passes through the vugs and fractures to the outlet during year 35001 and the 38500th year. After that the clean water starts to infiltrate into the whole domain (Figure 34).

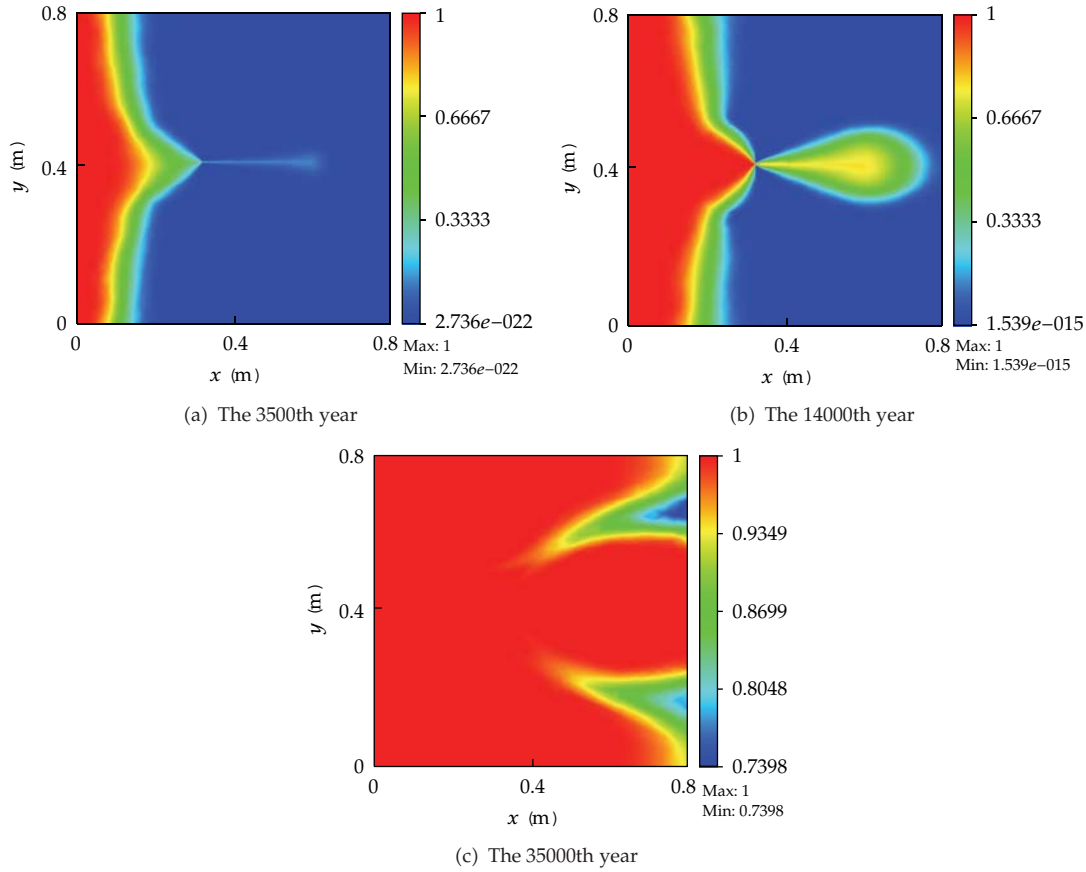

(a) The 3500th year

(b) The 14000th year

(c) The 35000th year

Figure 17: Concentration distribution at different time for the first phase for Case 3.

4.3. Analysis of the Concentration on the Outflow Boundary at Different Time

We get the effluent concentration on the outlet for every case at different time (Figures 8, 12, 16, 20, 24, 28, and 32). For Case 1 to Case 7, they have a common feature that the effluent concentration quickly becomes higher in shorter time than that in the base case during the first phase, and then the concentration increases gradually until it gets to the highest (1.0). This suggests that there are time multiscale phenomena in the contaminant transport in karstic aquifers. A main reason may be that the vugs and fractures have much higher porosity than that in matrix porous media, and the velocity in the vugs and fractures is also higher than that in matrix porous media. Once the clean water is injected into the inlet, the fractured vuggy porous media, the effluent concentration becomes lower in shorter time than that in the base case except for the Case 4. It is easily to understand that the vugs and fractures are the main pathways for contaminant transport. But it takes longer time for the vuggy fractured porous media to get the lowest concentration than that in base case (Figures 8, 12, 16, 20, 24, 28, and 32). It may be because when the clean water is injected into the inlet, it firstly infiltrates into the vugs and fractures, but there remains much contaminant in the matrix porous media by adsorption. So we can conclude that karst groundwater becomes polluted more easily and

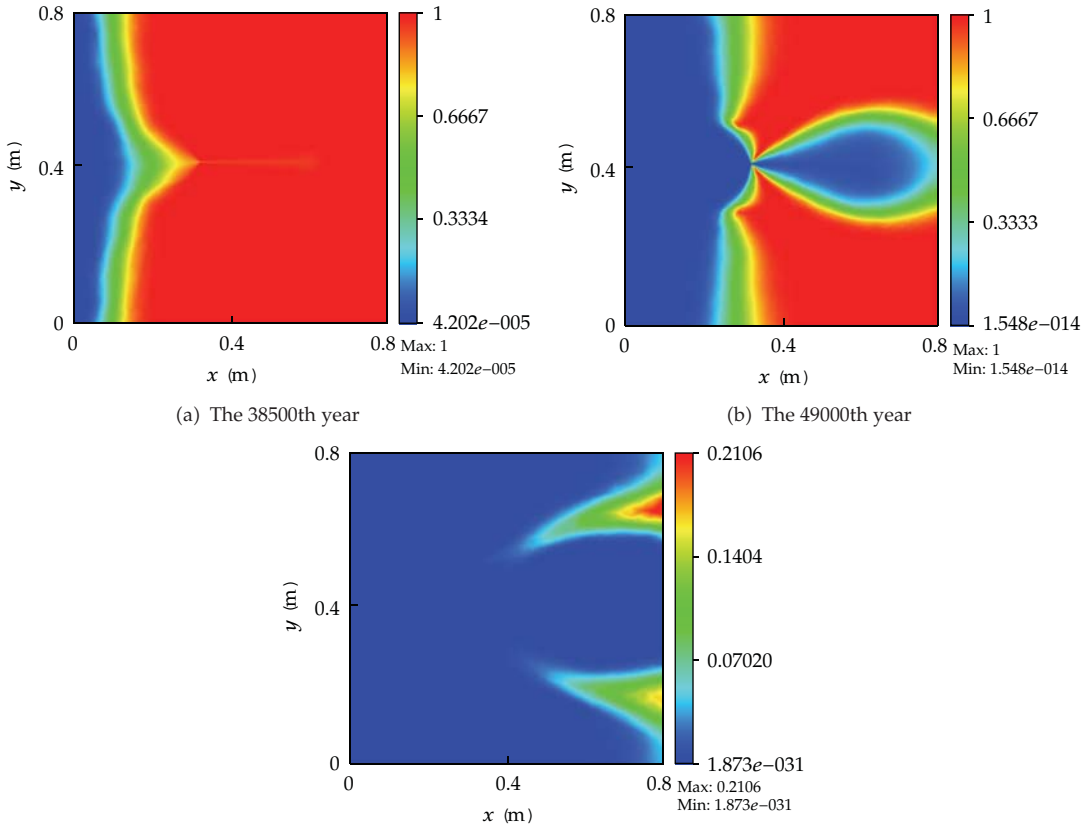

(a) The 38500th year

(b) The 49000th year

(c) The 70000th year

Figure 18: Concentration distribution at different time for the second phase for Case 3.

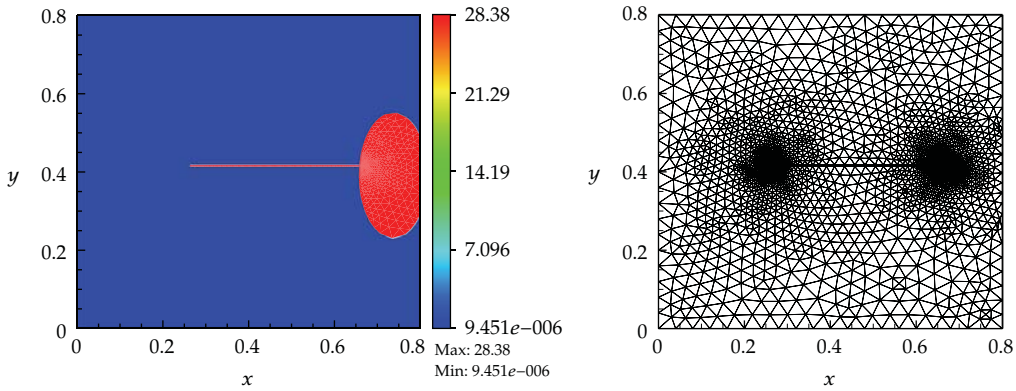

(a) Conductivity distribution

(b) Adaptive triangular mesh

Figure 19: Conductivity distribution and adaptive triangular mesh for Case 4.

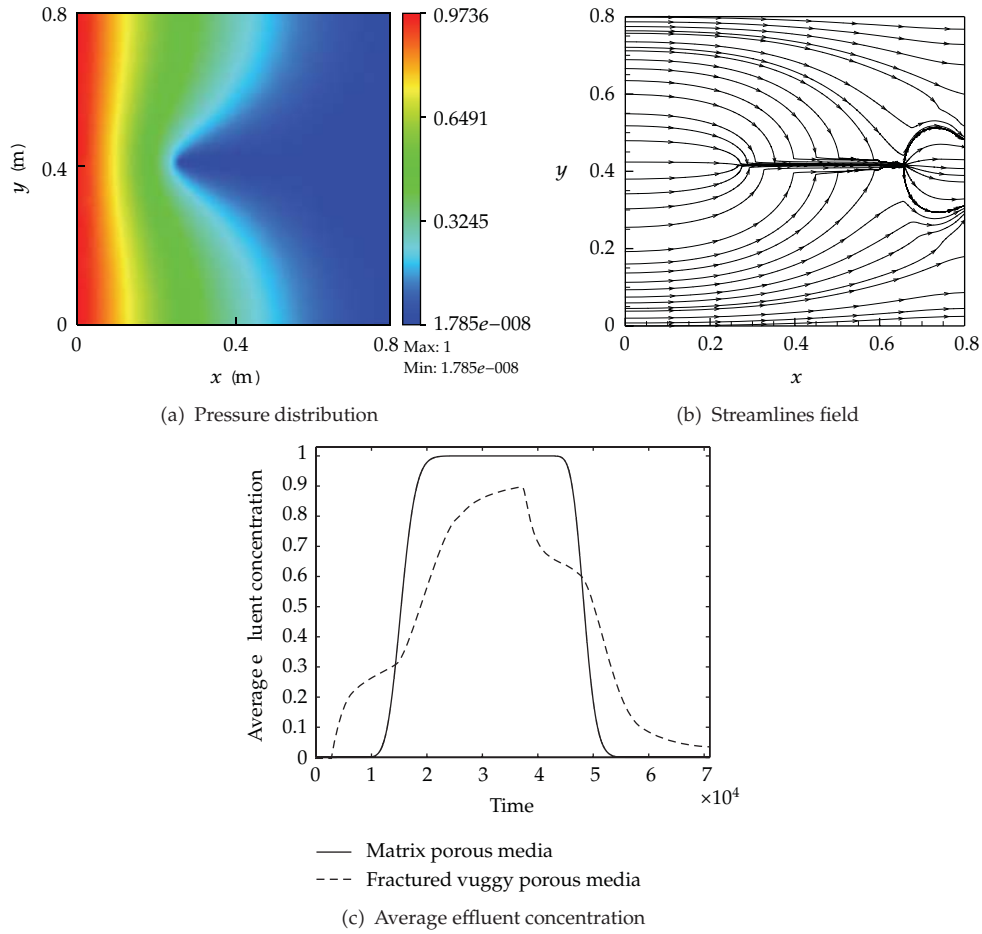

Figure 20: Pressure distribution, streamlines field, and average effluent concentration for Case 4.

in shorter time periods than that in non-karstic aquifers. Even though the aquifers are injected clean water which has been polluted by some contaminants, it will take a much longer time to render the groundwater to be clean again than that in non-karstic areas, because of the significant difference of adsorption between the vugs, fractures, and matrix porous media.

5. Conclusions

This paper begins with presenting a mathematical model for some contaminant transport in the fractured vuggy porous media. Two phases are numerically simulated for a process of contaminant and clean water infiltrated in the fractured vuggy porous media by coupling mixed finite element (MFE) method and finite volume method (FVM), both of which are locally conservative, to approximate the model. A hybrid mixed finite element (HMFE) method is applied to approximate the velocity field for the model. The convection and diffusion terms are approached by FVM and the standard MFE, respectively. The pressure distribution and temporary evolution of the concentration profiles are obtained for two phases. The average effluent concentration on the outflow boundary is obtained at different

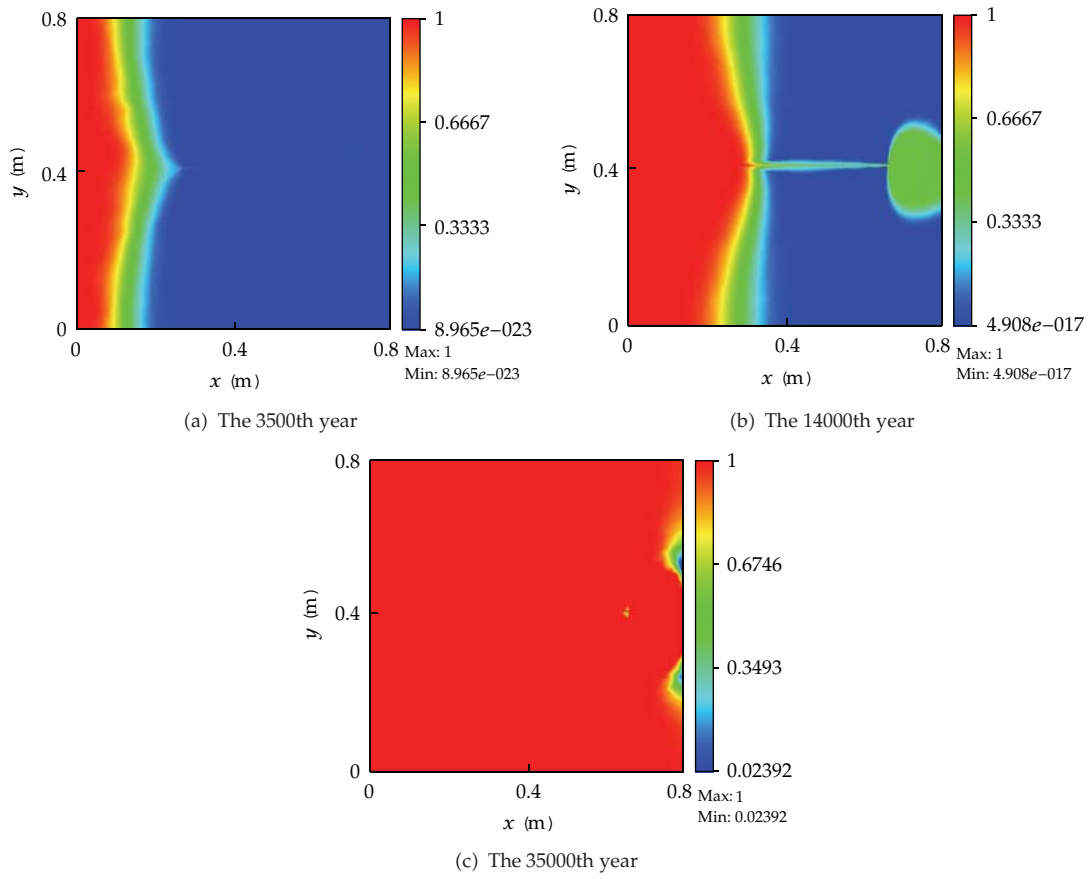

(a) The 3500th year

(b) The 14000th year

(c) The 35000th year

Figure 21: Concentration distribution at different time for the first phase for Case 4.

time that shows some obviously different features from the matrix porous media, and the time multi-scale of the effluent concentration on the outlet is observed. The results show how the different distribution of the vugs and the fractures impact the contaminant transport and the effluent concentration on the outlet.

Appendices

A. Weak Formulation of Flow Equation

We represent the derivation of the weak formulation of the flow equation here.

We at first denote the inner product notation by the following formulation

$$(u, v) = \int_{\Omega} uvd\Omega, \tag{A.1}$$

where Ω is a plane area, u and v are scalar functions or vector functions, which depends on the physical meaning of the quantities u and v. And the boundary of Ω is denoted by

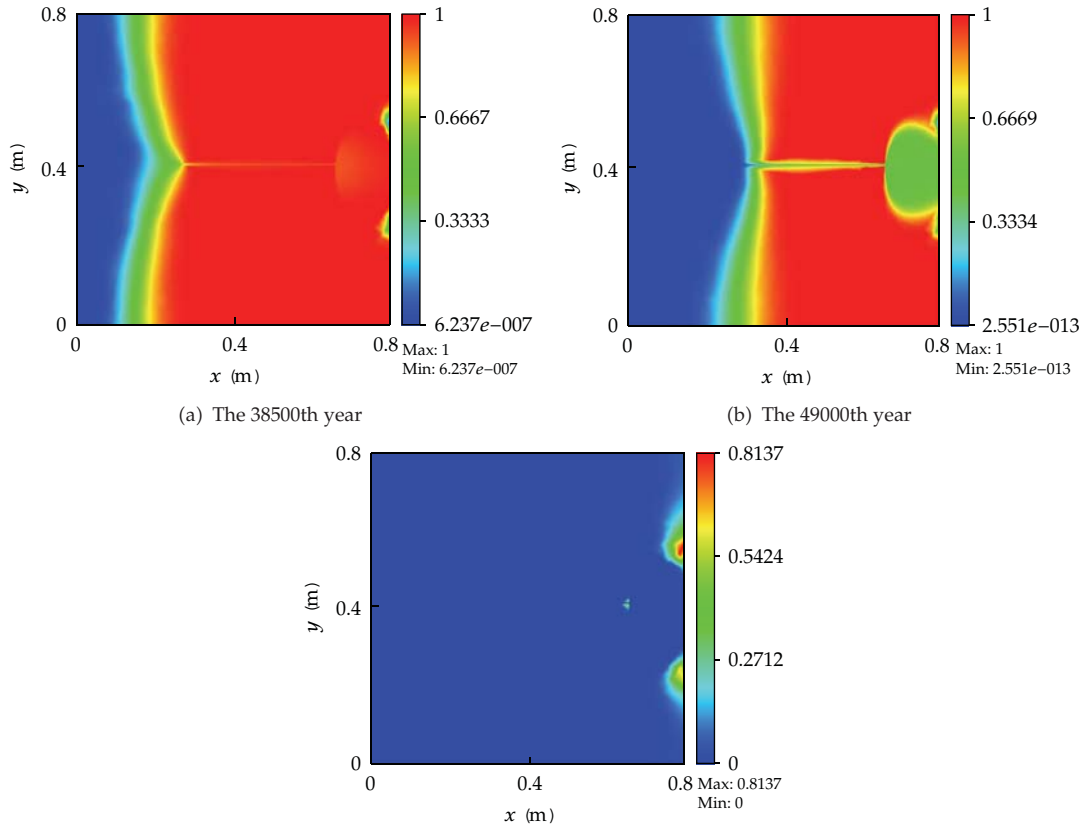

(a) The 38500th year

(b) The 49000th year

(c) The 70000th year

Figure 22: Concentration distribution at different time for the second phase for Case 4.

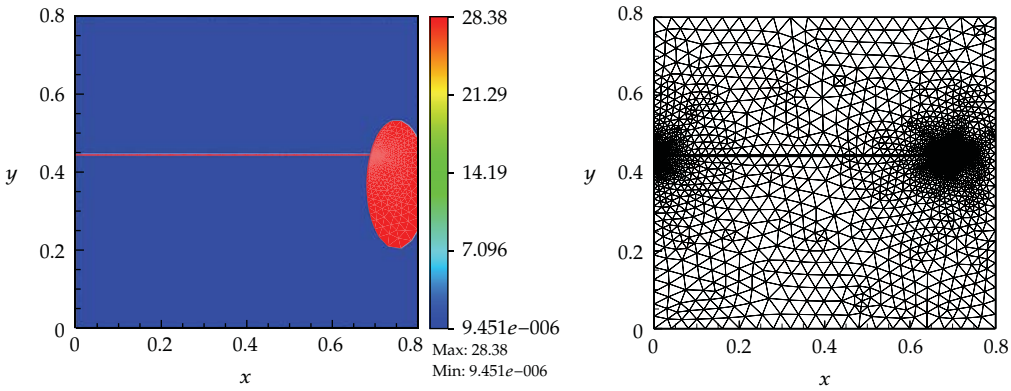

(a) Conductivity distribution

(b) Adaptive triangular mesh

Figure 23: Conductivity distribution and adaptive triangular mesh for Case 5.

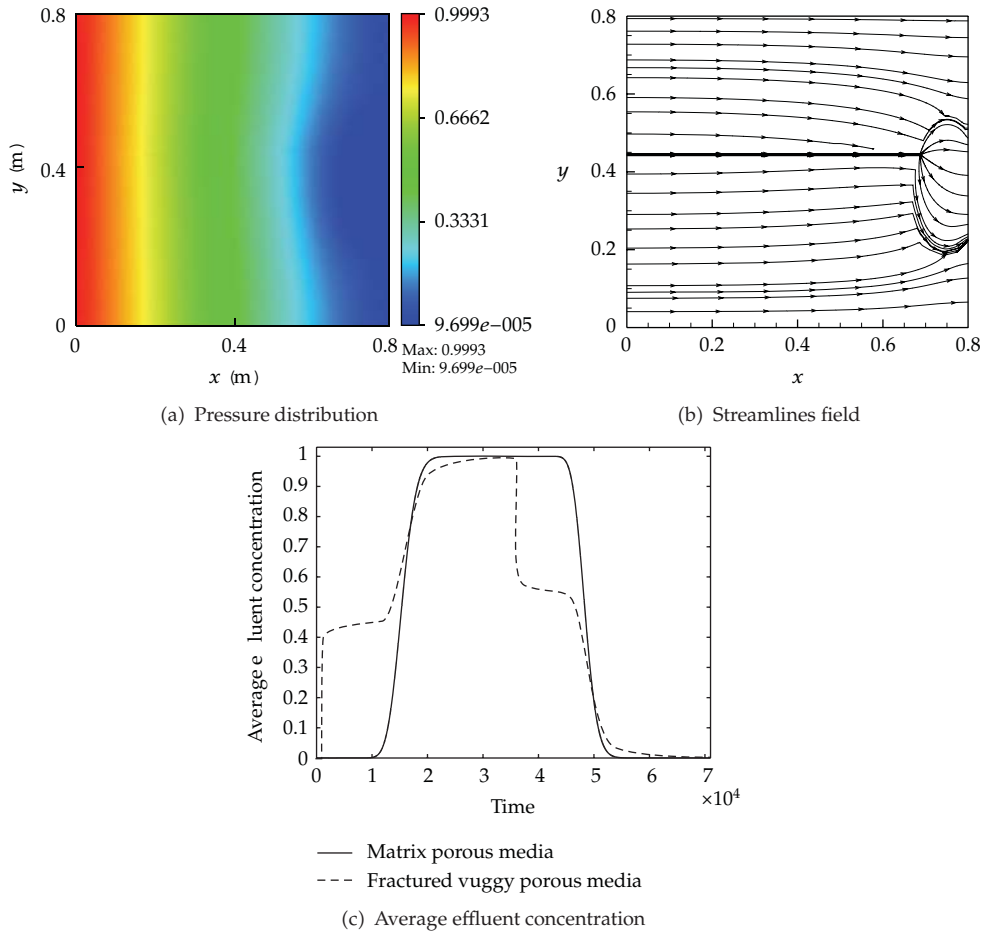

(a) Pressure distribution

(b) Streamlines field

(c) Average effluent concentration

Figure 24: Pressure distribution, streamlines field, and average effluent concentration for Case 5.

$\Gamma = \Gamma_D \cup \Gamma_N$, Γ_D representing the Dirichlet boundary, Γ_N representing the Neumann boundary. And the divergence theorem is given by

$$\int_{\Omega} \nabla \cdot \mathbf{w} d\Omega = \int_{\Gamma} \mathbf{w} \cdot \mathbf{n}\, ds, \tag{A.2}$$

where $\mathbf{n}$ is the outward unit normal vector towards Γ.

The flow equation considered in this paper here is the same

$$\begin{aligned} \mathbf{u} + K\nabla p &= 0, \\ \nabla \cdot \mathbf{u} &= q, \end{aligned} \tag{A.3}$$

where $\mathbf{u} \in \mathbf{W}_N^0 + \mathbf{E}(\mathbf{u}_B)$, $p \in V$, $\mathbf{W}_N^0 = \{\mathbf{w} \in H(\mathrm{div}; \Omega) : \mathbf{w} \cdot \mathbf{n} = \mathbf{0} \text{ on } \Gamma_N\}$, $V = L^2(\Omega)$ and $\mathbf{E}(\mathbf{u}_B)$ is the velocity extension that make the normal component of $\mathbf{u}$ agreeing with $\mathbf{u}_B$ on Γ_N, where $\mathbf{u}_B$ is the prescribed given normal component on Γ_N.

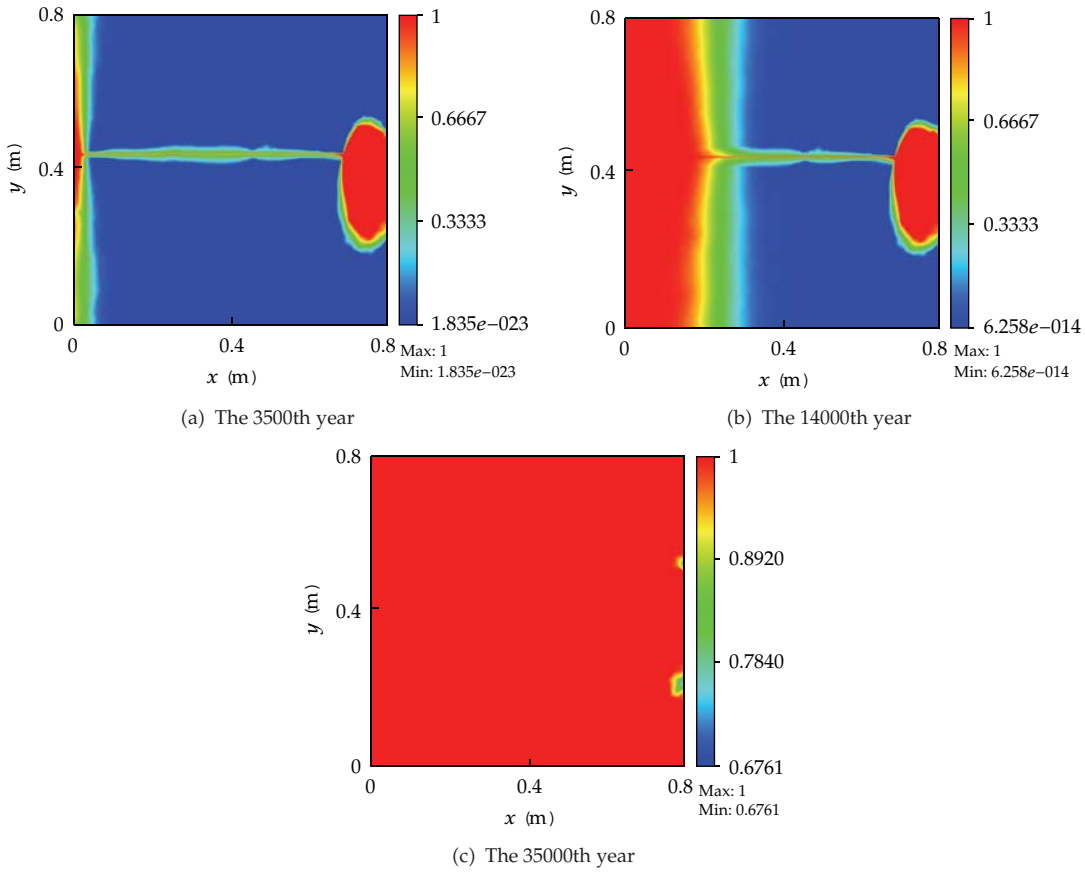

(a) The 3500th year

(b) The 14000th year

(c) The 35000th year

Figure 25: Concentration distribution at different time for the first phase for Case 5.

We begin with rewriting the first equation in (A.2) as the following one:

$$K^{-1}\mathbf{u} = -\nabla p. \tag{A.4}$$

Multiplying (A.3) by $\forall \mathbf{w} \in \mathbf{W}_N^0$ and integrating over Ω, we have

$$\int_\Omega K^{-1}\mathbf{u}\mathbf{w}\, d\Omega = -\int_\Omega \nabla p\mathbf{w}\, d\Omega. \tag{A.5}$$

For (A.5), by the divergence theorem and the definition of $\mathbf{w}$, we can obtain

$$\int_\Omega K^{-1}\mathbf{u}\mathbf{w}\, d\Omega = -\int_\Omega \nabla p\mathbf{w}\, d\Omega. \tag{A.6}$$

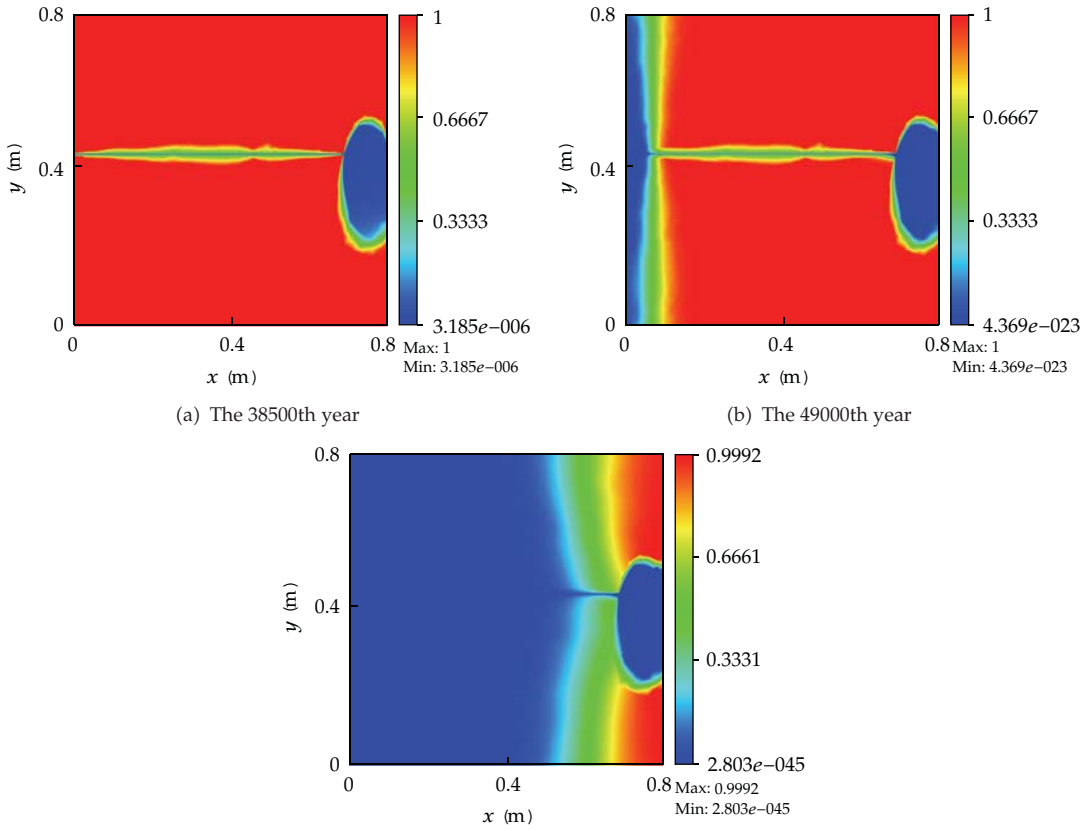

(a) The 38500th year

(b) The 49000th year

(c) The 70000 year

Figure 26: Concentration distribution at different time for the second phase for Case 5.

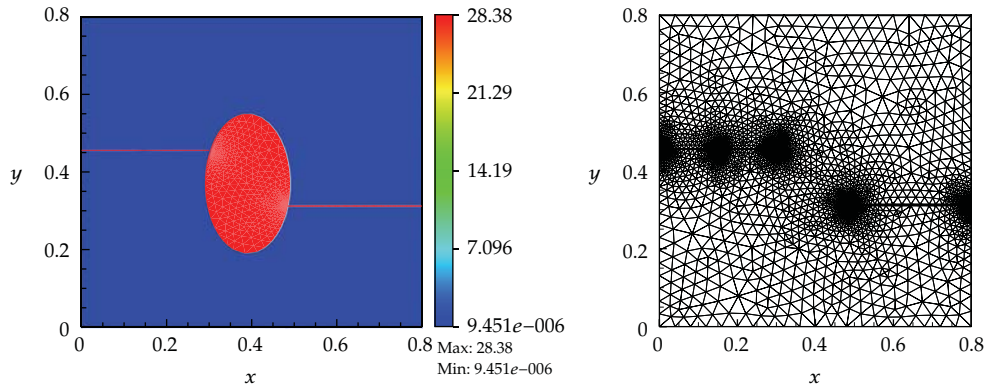

(a) Conductivity distribution

(b) Adaptive triangular mesh

Figure 27: Conductivity distribution and adaptive triangular mesh for Case 6.

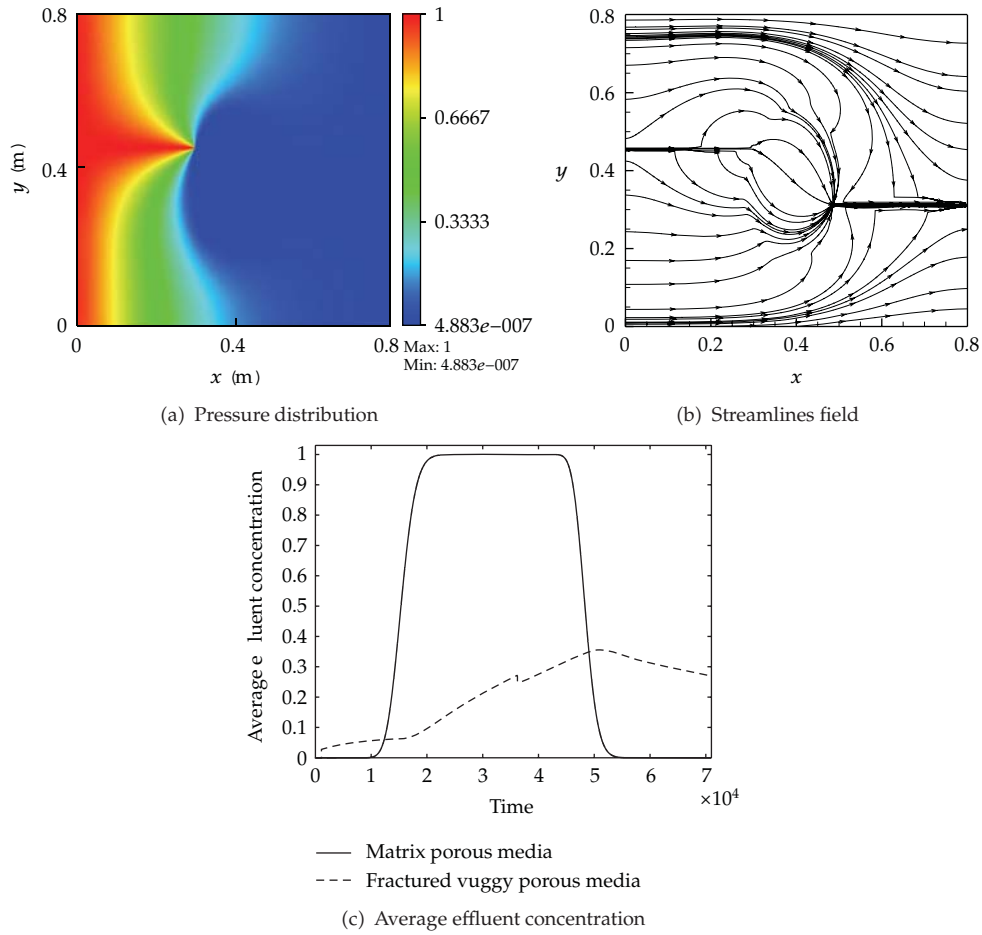

Figure 28: Pressure distribution, streamlines field, and average effluent concentration for Case 6.

By the definition of inner product, we can get

$$\int_{\Omega} K^{-1}\mathbf{u}\mathbf{w}\, d\Omega = -\int_{\Gamma} p_B \mathbf{w}\cdot\mathbf{n}\, ds + \int_{\Omega} \nabla\cdot\mathbf{w} p\, d\Omega, \tag{A.7}$$

where p_B is the value of p on Γ.

We rewrite (A.7) with the notation of inner product as follows:

$$\left(K^{-1}\mathbf{u},\mathbf{w}\right) = (\nabla\cdot\mathbf{w},p) - \int_{\Gamma} p_B\mathbf{w}\cdot\mathbf{n}\, ds. \tag{A.8}$$

Because $\mathbf{w}\in\mathbf{W}_N^0$, we can get

$$\left(K^{-1}\mathbf{u},\mathbf{w}\right) = (\nabla\cdot\mathbf{w},p) - \int_{\Gamma_D} p_B\mathbf{w}\cdot\mathbf{n}\, ds. \tag{A.9}$$

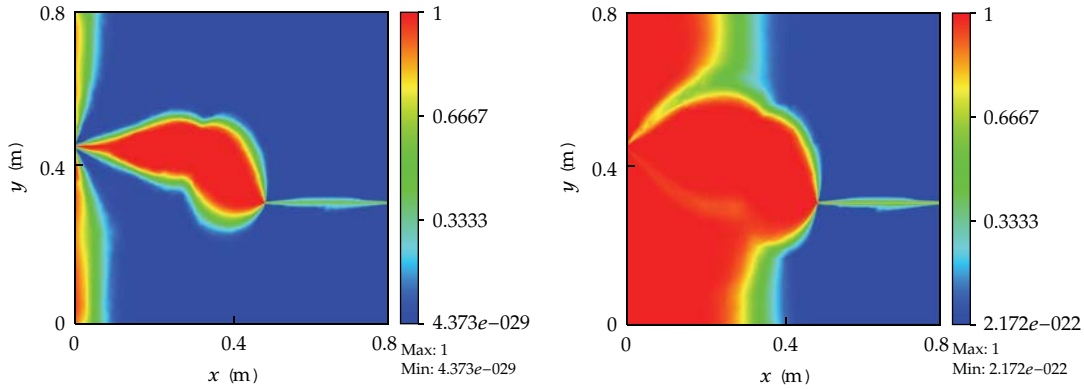

(a) The 3500th year

(b) The 14000th year

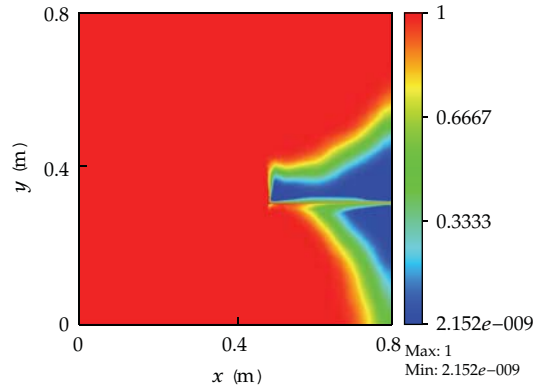

(c) The 35000th year

Figure 29: Concentration distribution at different time for the first phase for Case 6.

Multiplying the second one in the flow equation by $v \in V$, similarly, we can obtain

$$(\nabla \cdot \mathbf{u}, v) = (q, v). \tag{A.10}$$

Combining (A.9) and (A.10), we get the weak formulation of the flow equation

$$\begin{aligned} \left(K^{-1}\mathbf{u}, \mathbf{w}\right) &= (\nabla \cdot \mathbf{w}, p) - \int_{\Gamma_D} p_B \mathbf{w} \cdot \mathbf{n}\, ds, \\ (\nabla \cdot \mathbf{u}, v) &= (q, v). \end{aligned} \tag{A.11}$$

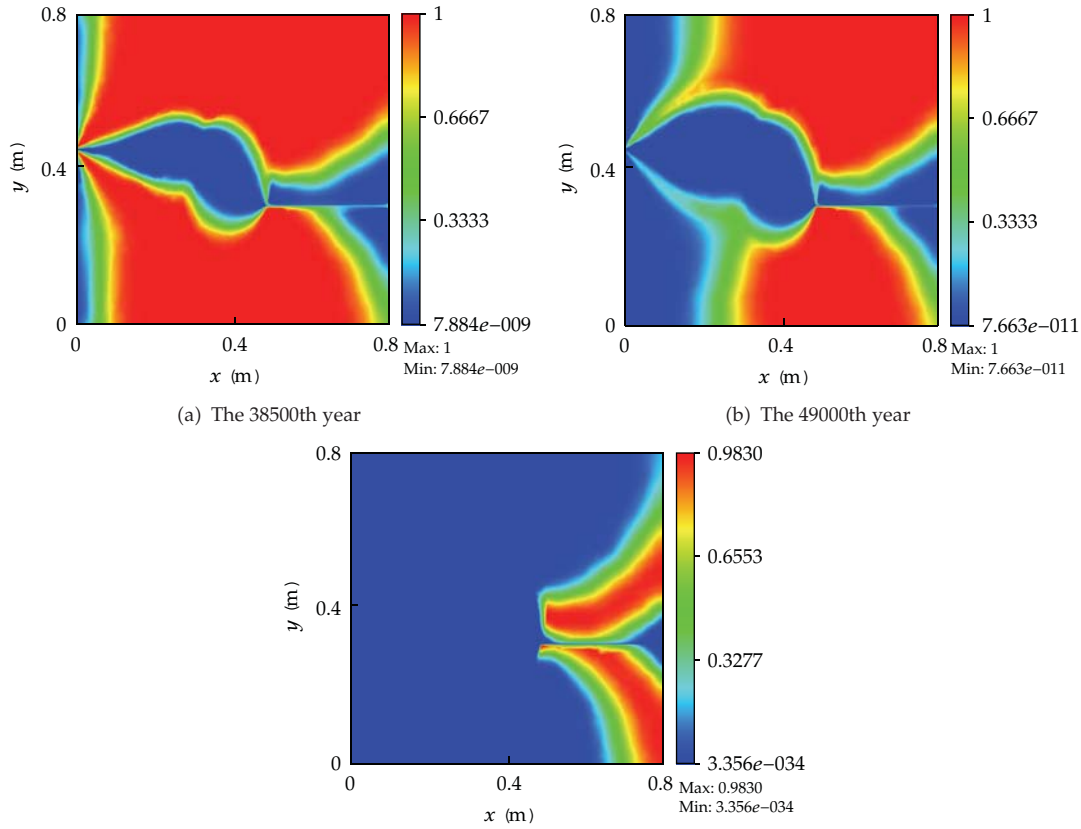

(a) The 38500th year (b) The 49000th year

(c) The 70000th year

Figure 30: Concentration distribution at different time for the second phase for Case 6.

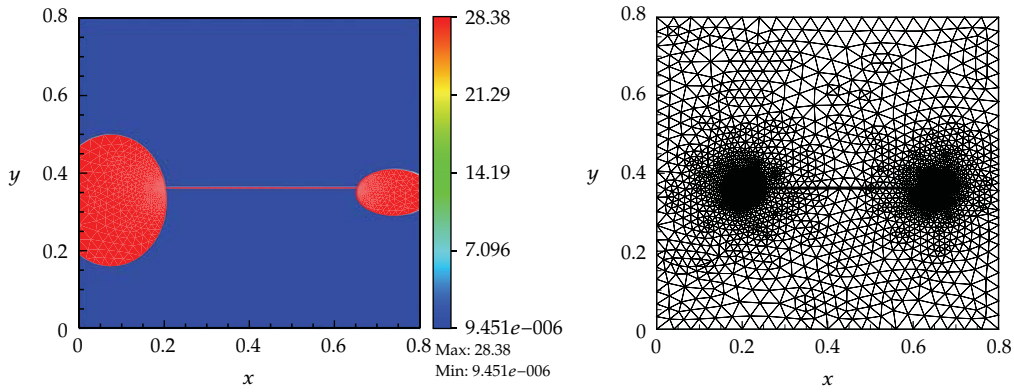

(a) Conductivity distribution (b) Adaptive triangular mesh

Figure 31: Conductivity distribution and adaptive triangular mesh for Case 7.

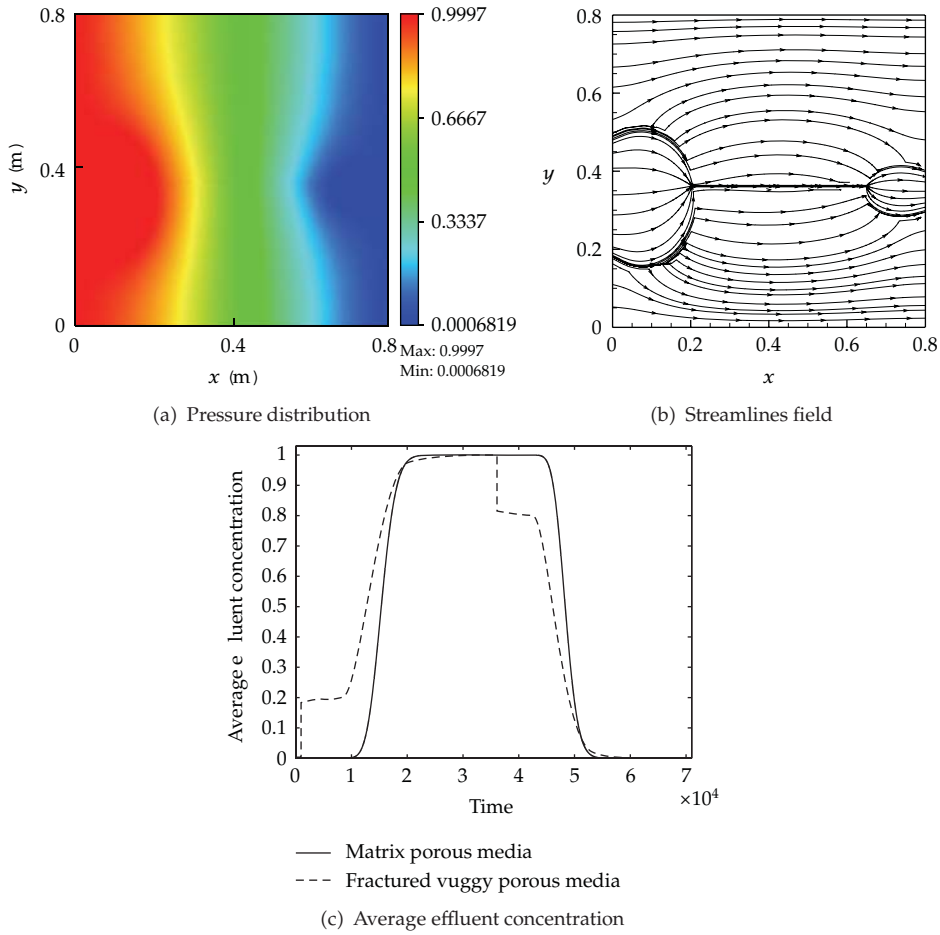

(a) Pressure distribution

(b) Streamlines field

(c) Average effluent concentration

Figure 32: Pressure distribution, streamlines field, and Average effluent concentration for Case 7.

B. Matrix Formulation of Flow Equation

We derive the matrix formulation of the flow equation. We begin with a single triangular element K. By RT_0 space, $\mathbf{u}_h$ in (3.5) can be written as

$$\mathbf{u}_h = \sum_{E \in \partial K} u_{K,E} w_{K,E} \,, \tag{B.1}$$

where $w_{K,E}$ is a shape function of the RT_0 space and $u_{K,E}$ represents the total flux across an edge E of element K. Taking $w_{K,E}$ as the test function $\mathbf{w}$, the total flux is given by

$$A_K U_K = p_K e - P_{KE}. \tag{B.2}$$

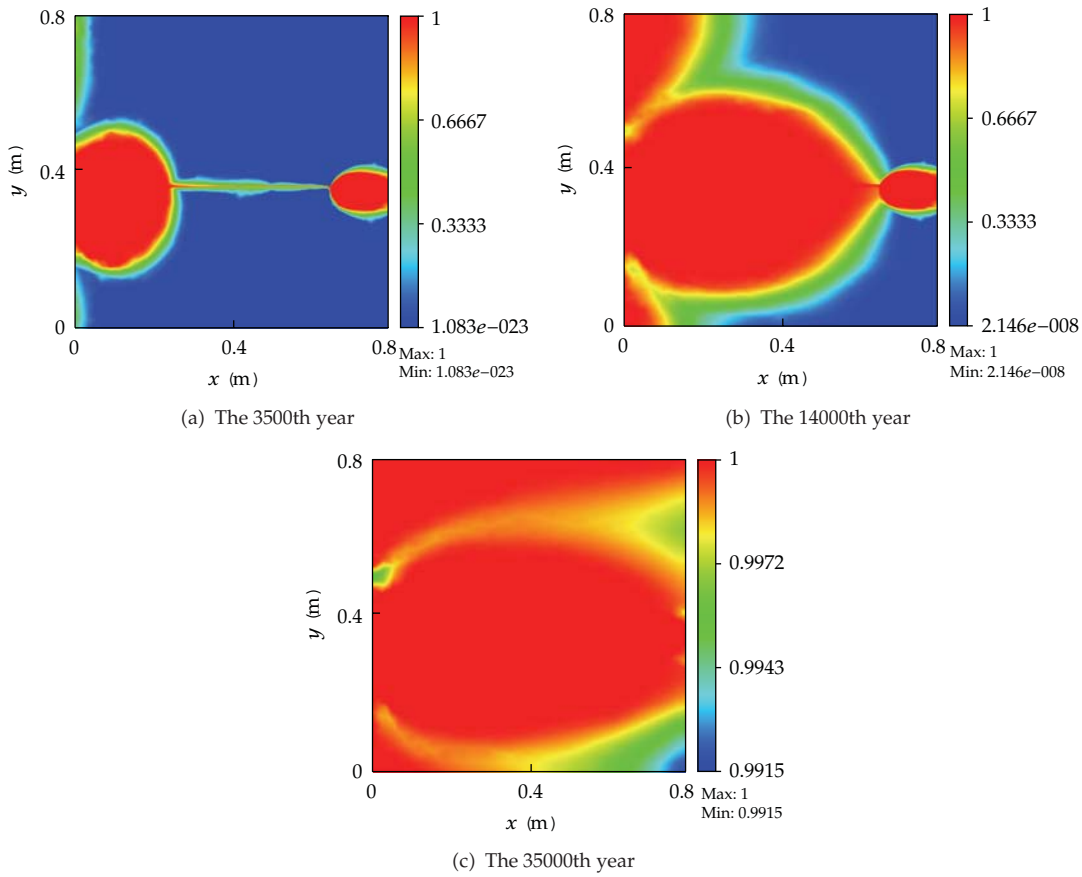

(a) The 3500th year

(b) The 14000th year

(c) The 35000th year

Figure 33: Concentration distribution at different time for the first phase for Case 7.

By (B.2), we have

$$U_K = A_K^{-1}(p_K e - P_{KE}), \tag{B.3}$$

where $A_K = [(A_K)_{E,E'\in\partial K}]$, $(A_K)_{E,E'} = \int_K w_{K,E} K^{-1} w_{K,E'} dK$, $U_K = [(U_K)_{E\in\partial K}]$, $e = [1]_{E\in\partial K}$, $P_{K,E} = [\overline{p}_{K,E}]_{E\in\partial K}$. As a result, the flow $u_{K,E}$ in (B.2) passing through each edge is given by a function of the cell pressure average p_K and edge pressure average $\overline{p}_{K,E}$. For simplicity, we rewrite the equation as

$$u_{K,E} = a_{K,E} p_K - \sum_{E\in\partial K} b_{K,E,E'} \overline{p}_{K,E}, \tag{B.4}$$

where $a_{K,E} = \sum_{E\in\partial K} (A_K^{-1})_{E,E'}$, $b_{K,E,E'} = (A_K^{-1})_{E,E'}$.

For the second one in (3.5), $v \in V_h(K) = P_0(K)$ combining (B.1), we can obtain

$$B_K U_K = 0, \tag{B.5}$$

where $B_K = (B_K)_{K,E}$, $(B_K)_{K,E} = \int_K (\nabla \cdot w_{K,E}) dK$ $(w_K = 1)$.

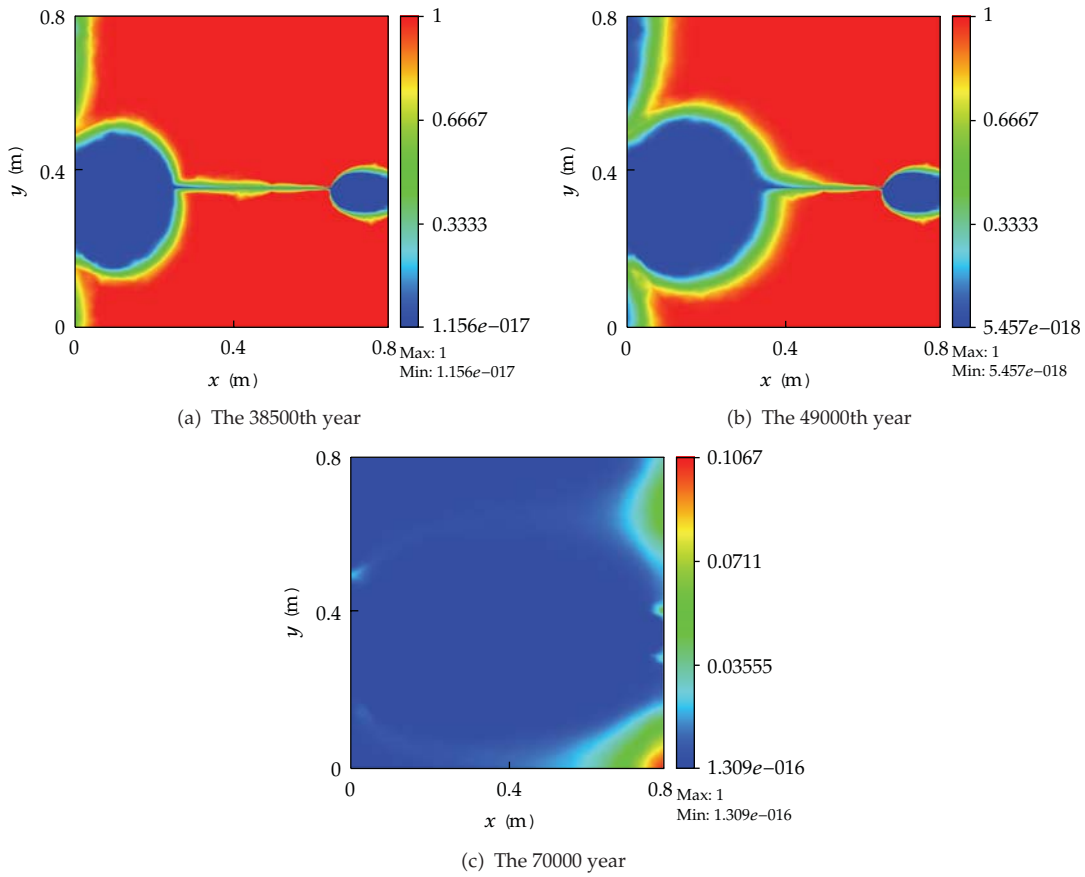

Figure 34: Concentration distribution at different time for the second phase for Case 7.

Substituting (B.3) into (B.5) we can get

$$B_K A_K^{-1} p_K e - B_K A_K^{-1} P_{KE} = 0. \tag{B.6}$$

Hence

$$p_K = \left(B_K A_K^{-1} e\right)^{-1} B_K A_K^{-1} P_{KE}, \tag{B.7}$$

by the continuity of the flux across the interelement boundaries, then $u_{K,E}$ is given by

$$u_{K,E} = \begin{cases} u_E^N, & E = K \cap K', \\ -u_{K,E'}, & E \in \Gamma_N. \end{cases} \tag{B.8}$$

Thus by (B.2), (B.7), and (B.8), we can obtain the algebraic linear system of P_E (the pressure average) as follows:

$$A_T P_E = J, \tag{B.9}$$

where $A_T = D^T F - G$, $D = [a_{K,E}]_{N_K,N_E}$, $E \in \partial K$, $F = [(B_K A_K^{-1} e)^{-1} B_K A_K^{-1}]_{N_K}$, $G = [\sum_{E,E\subset\partial K} b_{K,E,E'}]_{N_E,N_{E'}}$, $E \notin \Gamma_D$. N_K and N_E stand for the number of elements and the number of edges not belonging to Γ_D in the mesh, respectively. J represents a vector of size N_E denoting the boundary conditions.

C. Weak Formulation of the Transport Equation

We derive the weak formulation of the transport equation in this appendix. We let

$$\mathbf{w} = -D(\mathbf{u})\nabla c, \tag{C.1}$$

by MFE method in (2.7), and we rewrite (C.1) to get

$$\nabla c = -D^{-1}(\mathbf{u})\mathbf{w}. \tag{C.2}$$

Now we can get

$$\begin{aligned}
&\frac{\partial(\phi^e c_f)}{\partial t} + \nabla\cdot(\mathbf{u}c_f + \mathbf{w}) = 0,\\
&\nabla c = -D^{-1}(\mathbf{u})\mathbf{w},\\
&(\mathbf{u}c + \mathbf{w})\cdot\mathbf{n} = c_B\mathbf{u}\cdot\mathbf{n}, \quad \mathbf{x}\in\Gamma_{\text{inflow}},\\
&-\mathbf{w}\cdot\mathbf{n} = 0, \quad \mathbf{x}\in\Gamma_{\text{outflow}},\\
&c_f(\mathbf{x},0) = c_0(\mathbf{x}), \quad \mathbf{x}\in\Omega.
\end{aligned} \tag{C.3}$$

Multiplying the first equation in (C.3) by w, the second by $\hat{\mathbf{v}}$, and the last by w, we can obtain

$$\begin{aligned}
&\left(\frac{\partial(\phi^e c_f)}{\partial t}, v\right) + \left(\nabla\cdot(\mathbf{u}c_f + \mathbf{w}), v\right) = (0, v), \quad v\in V,\ t\in(0,T],\\
&(\nabla c, \hat{\mathbf{w}}) = \left(-D^{-1}(\mathbf{u})\mathbf{w}, \hat{\mathbf{w}}\right), \quad \mathbf{w}\in\mathbf{W^0},\\
&\left(c_f(\mathbf{x},\ 0), v\right) = (c_0(\mathbf{x}), v), \quad v\in V,\ t=0,\\
&(\mathbf{u}c + \mathbf{w})\cdot\mathbf{n} = c_B\mathbf{u}\cdot\mathbf{n}, \quad \mathbf{x}\in\Gamma_{\text{inflow}},\\
&-\mathbf{w}\cdot\mathbf{n} = 0, \quad \mathbf{x}\in\Gamma_{\text{outflow}}.
\end{aligned} \tag{C.4}$$

Using the upwind value of the concentration, the boundary condition, and the initial condition, we now get the weak formulation

$$\begin{gathered}\left(\frac{\partial\left(\phi^e c_f^*\right)}{\partial t}, v\right) + (\nabla\cdot\mathbf{w}, v) + \sum_K \int_{\partial K} v\mathbf{u}c_f^*\cdot\mathbf{n}\,ds - \sum_K \left(c_f^*\mathbf{u}, \nabla v\right) = 0, \qquad \forall v\in V, t\in(0,T],\\ \left(-D^{-1}\mathbf{w}, \widehat{\mathbf{w}}\right) + \left(c_f, \nabla\cdot\mathbf{w}\right) = 0, \quad \forall \mathbf{w}\in\mathbf{W^0}, t\in(0,T],\\ \left(c_f, v\right) = \left(c_{f,0}, v\right), \quad \forall v\in V, t=0.\end{gathered} \tag{C.5}$$

D. MFE Method to Solve the Transport System

We apply the standard MFE method to solve the transport system (3.8). We handle the second one in the system similarly to handling flow equation. Based on RT_0 space, the $\mathbf{w}_h$ in (3.8) can written as

$$\mathbf{w}_h = \sum_{E\in\partial K} \widehat{W}_{K,E}\widehat{w}_{K,E}, \tag{D.1}$$

where $\widehat{w}_{K,E}$ is a basis function of RT_0 space, $\widehat{w}_{K,E}$ is the total diffusive flux across the edge E. We take the test function $\widehat{\mathbf{w}}$ as $\widehat{w}_{K,E}$ and integrate over Ω, using the Green formulation, and therefore the total diffusive flux is given by

$$A_K^{\mathrm{con}}\widehat{W}_K = c_K B_K^{\mathrm{con}}, \tag{D.2}$$

where $A_K^{\mathrm{con}} = [\int_K \widehat{w}_{K,E}D^{-1}w_{K,E}]_{E,E'\in\partial K}$, $\widehat{W}_K = [\widehat{W}_{K,E}]_{E\in\partial K}$, and $A_K^{\mathrm{con}} = [\int_K(\nabla\cdot\widehat{w}_{K,E})w_K dK]_{E,E'\in\partial K} = [\int_K(\nabla\cdot\widehat{w}_{K,E})dK]_{E,E'\in\partial K}(w_K = 1)$. So the diffusion term in the first equation in (3.8)

$$\left(\frac{\partial\left(\phi^e c_h\right)}{\partial t}, v\right) + (\nabla\cdot\mathbf{w}_h, v) = 0 \tag{D.3}$$

and we can get

$$M_K^{\mathrm{con}}\frac{dc_K}{dt} + \left(B_K^{\mathrm{con}}\right)^T\widehat{W}_K = 0, \tag{D.4}$$

where $M_K^{\mathrm{con}} = [\int_K \phi^e v_K\cdot v_K] = [\int_K \phi^e dK](v_K = 1)$.

By (D.2) and (D.4), we have the ordinary differential equations of the concentration cell averages C and the diffusive flux $\widehat{W}_K$ as follows:

$$\begin{pmatrix} 0 & 0 \\ 0 & \operatorname{diag}\left(M_K^{\mathrm{con}}\right)_{N_K} \end{pmatrix} \begin{pmatrix} \dfrac{d\widehat{W}}{dt} \\ \dfrac{dC}{dt} \end{pmatrix} + \begin{pmatrix} \operatorname{diag}\left(A_K^{\mathrm{con}}\right)_{N_K} & -\left(B_K^{\mathrm{con}}\right)_{N_K} \\ \left(B_K^{\mathrm{con}}\right)_{N_K} & 0 \end{pmatrix} \begin{pmatrix} \widehat{W} \\ C \end{pmatrix} = 0. \tag{D.5}$$

For the advection component in system (3.8),

$$\left(\frac{\partial \phi^e c}{\partial t}, v\right) + \sum_K \int_{\partial K} v\mathbf{u}c^* \cdot \mathbf{n}\, dl - \sum_K (c^*\mathbf{u}, \nabla v) = 0. \tag{D.6}$$

Because v is a function of RT_0 space, $\nabla v = 0$. The given equation above is written as

$$\left(\frac{\partial \phi^e c}{\partial t}, v\right) + \sum_K \int_{\partial K} v\mathbf{u}c^* \cdot \mathbf{n}\, dl = 0. \tag{D.7}$$

Denote the velocity across each edge by $\mathbf{u}_i$, and then give

$$u_{iE}^{\perp} = \mathbf{u}_i \cdot \mathbf{n}_i, \quad i = 1, 2, \ldots, N_E, \tag{D.8}$$

where $\mathbf{n}_i$ is the outward unit normal vector to each edge. Denote the edge-element signed adjacency matrices by F^+ the entry of which equals to 1 if $u_{iE}^{\perp} > 0$ for each edge, and the entry of F^- equals to -1 if $u_{iE}^{\perp} < 0$. And therefore the upwind concentration is given by F^+C or F^-C. Let $\mathbf{u}^{\perp} = [u_{iE}^{\perp}]_{N_E}$, $\mathbf{u}_+^{\perp} = \max(0, \mathbf{u}^{\perp})$, and $\mathbf{u}_-^{\perp} = \min(0, \mathbf{u}^{\perp})$, using the boundary condition, and then we can obtain the flux across the edges as follows:

$$q = \operatorname{diag}\left(\mathbf{u}_+^{\perp}\right) F^+ C + \operatorname{diag}\left(\mathbf{u}_-^{\perp}\right)\left(F^- C + BC_B\right), \tag{D.9}$$

where B and C_B represent the edge-boundary adjacency matrix and the concentration on the inflow boundary, respectively. We denote edge-adjacency matrix by $F = F^+ + F^-$. And then the total divergence amount is given by

$$Q = F^T q = F^T\left(\operatorname{diag}\left(\mathbf{u}_+^{\perp}\right) F^+ + \operatorname{diag}\left(\mathbf{u}_-^{\perp}\right) F^-\right) C + F^T \operatorname{diag}\left(\mathbf{u}_-^{\perp}\right) BC_B. \tag{D.10}$$

Equation (D.10) gives an ordinary differential equations as follows:

$$\left[\operatorname{diag}\left(M_K^{\mathrm{con}}\right)_{N_K}\right] \frac{dC}{dt} + \left[F^T\left(\operatorname{diag}\left(\mathbf{u}_+^{\perp}\right) F^+ + \operatorname{diag}\left(\mathbf{u}_-^{\perp}\right) F^-\right)\right] C = -F^T \operatorname{diag}\left(\mathbf{u}_-^{\perp}\right) BC_B. \tag{D.11}$$

Now we finally can obtain the ordinary differential equations by (D.4) and (D.11) for the transport system

$$L\frac{dX}{dt} + \left(\widehat{R} + \widehat{\widehat{R}}\right)X = b, \tag{D.12}$$

where $L = \begin{pmatrix} 0 & 0 \\ 0 & \operatorname{diag}(M_K^{\mathrm{con}})_{N_K} \end{pmatrix}$, $\widehat{R} = \begin{pmatrix} 0 & 0 \\ 0 & F^T(\operatorname{diag}(\mathbf{u}_+^{\perp})F^+ + \operatorname{diag}(\mathbf{u}_-^{\perp})F^-) \end{pmatrix}$, $\widehat{\widehat{R}} = \begin{pmatrix} \operatorname{diag}(A_K^{\mathrm{con}})_{N_K} & -[B_K^{\mathrm{con}}]_{N_K} \\ ([B_K^{\mathrm{con}}]_{N_K})^T & 0 \end{pmatrix}$, $b = \begin{pmatrix} 0 \\ -F^T \operatorname{diag}(\mathbf{u}_-^{\perp})BC_B \end{pmatrix}$.

Acknowledgments

This paper is supported by the Foundation for Young Talents of Guizhou Province under Grant Z073245. The authors thank its support. The authors also take this opportunity to thank the Computational Transport Phenomena Laboratory (CPTL), Division of Physical Sciences and Engineering (PSE), King Abdullah University of Science and Technology (KAUST) for supporting this paper.

References

[1] F. K. lu, "Review of groundwater pollution and protection in karst areas," *Water, Air, and Soil Pollution*, vol. 113, no. 1–4, pp. 337–356, 1999.

[2] C. M. Weedon, "Compact vertical flow constructed wetland systems—first two years' performance," *Water Science and Technology*, vol. 48, no. 5, pp. 15–23, 2003.

[3] M. E. Reid and S. J. Dreiss, "Modeling the effects of unsaturated, stratified sediments on groundwater recharge from intermittent streams," *Journal of Hydrology*, vol. 114, no. 1-2, pp. 149–174, 1990.

[4] E. A. Zaltsberg, "Forecast of karst water levels, hydrogeology of karstic terraines," in *International Contributions to Hydrogeology*, pp. 40–42, Heise, Hannover, Germany, 1984.

[5] J. J. Quinn, D. Tomasko, and J. A. Kuiper, "Modeling complex flow in a karst aquifer," *Sedimentary Geology*, vol. 184, no. 3-4, pp. 343–351, 2006.

[6] M. E. Barrett and R. J. Charbeneau, "A parsimonious model for simulating flow in a karst aquifer," *Journal of Hydrology*, vol. 196, no. 1–4, pp. 47–65, 1997.

[7] N. Wanakule and P. E. Robert Anaya, *Lumped parameter model for the Edwards aquifer*, Ph.D. thesis, 1994.

[8] Y. Yurtsever and B. R. Payne, "Time-variant linear compartmental model approach to study flow dynamics of a karstic groundwater system by the aid of environmental tritium (a case study of south-eastern karst area in Turkey)," in *Proceedings of the Ankara-Antalya Symposium, Karst Water Resources*, G. A. Gultekin and I. Johnson, Eds., pp. 545–561, 1985.

[9] D. Thorkildson and P. McElhaney, "Model refinement and applications for the Edwards aquifer (Balcones Fault Zone) in the San Antonio region," Tech. Rep. 340, Texas Water Development Board, Tex, USA, 1992.

[10] E. L. Kuniansky and K. Q. Holligan, "Simulations of flow in the Edwards-trinity aquifer system and contiguous hydraulically connected units, west-central," Tech. Rep. 93-4039, US Geological Survey Water-Resources Investigations, Tex, USA, 1994.

[11] G. Teutsch and M. Sauter, "Groundwater modeling in karst terranes: scale effects, data acquisition, and field validation," in *Proceedings of the 3rd Conference on Hydrogeology, Ecology, Monitoring, and Management of Ground Water in Karst Terranes*, pp. 17–34, Nashville, Tenn, USA, 1991.

[12] M. E. Barrett and R. J. Charbeneau, "A parsimonious model for simulation of flow and transport in a karst aquifer," Tech. Rep. 269, Center for Research in Water Resources, The University of Texas at Austin, 1996.

[13] D. Y. Kwak, H. J. Kwon, and S. Lee, "Multigrid algorithm for cell centered finite difference on triangular meshes," *Applied Mathematics and Computation*, vol. 105, no. 1, pp. 77–85, 1999.

[14] A. J. Long and R. G. Derickson, "Linear systems analysis in a karst aquifer," *Journal of Hydrology*, vol. 219, no. 3-4, pp. 206–217, 1999.
[15] S. Mehl and M. C. Hill, "Three-dimensional local grid refinement for block-centered finite-difference groundwater models using iteratively coupled shared nodes: a new method of interpolation and analysis of errors," *Advances in Water Resources*, vol. 27, no. 9, pp. 899–912, 2004.
[16] S. Mehl and M. C. Hill, "Development and evaluation of a local grid refinement method for block-centered finite-difference groundwater models using shared nodes," *Advances in Water Resources*, vol. 25, no. 5, pp. 497–511, 2002.
[17] P. A. Forsyth, Jr. and P. H. Sammon, "Quadratic convergence for cell-centered grids," *Applied Numerical Mathematics*, vol. 4, no. 5, pp. 377–394, 1988.
[18] J. Koclas, "Comparisons of the different approximations leading to mesh centered finite differences starting from the Analytic Nodal Method," *Annals of Nuclear Energy*, vol. 25, no. 11, pp. 821–838, 1998.
[19] D. Y. Kwak, H. J. Kwon, and S. Lee, "Multigrid algorithm for cell centered finite difference on triangular meshes," *Applied Mathematics and Computation*, vol. 105, no. 1, pp. 77–85, 1999.
[20] P.-H. Maire, "A high-order cell-centered Lagrangian scheme for compressible fluid flows in two-dimensional cylindrical geometry," *Journal of Computational Physics*, vol. 228, no. 18, pp. 6882–6915, 2009.
[21] K. Fard and A. Firoozabadi, "Numerical simulation of water injection in 2-D fractured media using discrete-fracture model," *SPE Reservoir Evaluation and Engineering*, vol. 4, pp. 117–126, 2003.
[22] H. Hoteit and A. Firoozabadi, "Multicomponent fluid flow by discontinuous Galerkin and mixed methods in unfractured and fractured media," *Water Resources Research*, vol. 41, no. 11, Article ID W11412, pp. 1–15, 2005.
[23] E. L. Sonnenthal, N. Spycher, and S. Mukhopadhyay, "Modeling of coupled heat transfer and reactive transport processes in porous media: application to seepage studies at Yucca mountain, Nevada," *Journal of Porous Media*, vol. 12, no. 8, pp. 725–748, 2009.
[24] A. M. Mayenna and M. A. Hossain, "Crank-nicolson galerkin model for nonlinearly coupled macrophase and microphase transport in the subsurface," *Journal of Porous Media*, vol. 12, no. 9, pp. 835–845, 2009.
[25] A. F. Alajmi and A. Grader, "Influence of fracture tip on fluid flow displacements," *Journal of Porous Media*, vol. 12, no. 5, pp. 435–447, 2009.
[26] S. Sun and J. Geiser, "Multiscale discontinuous Galerkin and operator-splitting methods for modeling subsurface flow and transport," *International Journal for Multiscale Computational Engineering*, vol. 6, no. 1, pp. 87–101, 2008.
[27] S. Sun and M. F. Wheeler, "Anisotropic and dynamic mesh adaptation for discontinuous Galerkin methods applied to reactive transport," *Computer Methods in Applied Mechanics and Engineering*, vol. 195, no. 25–28, pp. 3382–3405, 2006.
[28] S. Sun and M. F. Wheeler, "Projections of velocity data for the compatibility with transport," *Computer Methods in Applied Mechanics and Engineering*, vol. 195, no. 7-8, pp. 653–673, 2006.
[29] C. Dawson, S. Sun, and M. F. Wheeler, "Compatible algorithms for coupled flow and transport," *Computer Methods in Applied Mechanics and Engineering*, vol. 193, no. 23–26, pp. 2565–2580, 2004.
[30] S. Sun and M. F. Wheeler, "A posteriori error estimation and dynamic adaptivity for symmetric discontinuous Galerkin approximations of reactive transport problems," *Computer Methods in Applied Mechanics and Engineering*, vol. 195, no. 7-8, pp. 632–652, 2006.
[31] L. Ju, "Conforming centroidal Voronoi Delaunay triangulation for quality mesh generation," *International Journal of Numerical Analysis and Modeling*, vol. 4, no. 3-4, pp. 531–547, 2007.
[32] S. Lalitha, S. Chattopadhyay, and R. N. Ghosh, "Development of software on finite element mesh generation (MESHGEN) for metallurgical applications," *Engineering Fracture Mechanics*, vol. 36, no. 3, pp. 527–530, 1990.
[33] F. Brezzi and M. Fortin, *Mixed and Hybrid Finite Element Methods*, vol. 15 of *Springer Series in Computational Mathematics*, Springer, New York, NY, USA, 1991.
[34] P.-A. Raviart and J. M. Thomas, "A mixed finite element method for 2nd order elliptic problems," in *Mathematical Aspects of Finite Element Methods*, vol. 606 of *Lecture Notes in Mathematics*, pp. 292–315, Springer, Berlin, Germany, 1977.

Hindawi Publishing Corporation
Journal of Applied Mathematics
Volume 2011, Article ID 861905, 24 pages
doi:10.1155/2011/861905

Research Article

Multiscale Time-Splitting Strategy for Multiscale Multiphysics Processes of Two-Phase Flow in Fractured Media

Jisheng Kou,[1] Shuyu Sun,[1] and Bo Yu[2]

[1] *Computational Transport Phenomena Laboratory, Division of Physical Science and Engineering, King Abdullah University of Science and Technology, Thuwal 23955-6900, Saudi Arabia*
[2] *Beijing Key Laboratory of Urban Oil and Gas Distribution Technology, China University of Petroleum, Beijing 102249, China*

Correspondence should be addressed to Shuyu Sun, shuyu.sun@kaust.edu.sa

Received 15 December 2010; Accepted 8 January 2011

Academic Editor: Zhangxin Chen

Copyright © 2011 Jisheng Kou et al. This is an open access article distributed under the Creative Commons Attribution License, which permits unrestricted use, distribution, and reproduction in any medium, provided the original work is properly cited.

The temporal discretization scheme is one important ingredient of efficient simulator for two-phase flow in the fractured porous media. The application of single-scale temporal scheme is restricted by the rapid changes of the pressure and saturation in the fractured system with capillarity. In this paper, we propose a multi-scale time splitting strategy to simulate multi-scale multi-physics processes of two-phase flow in fractured porous media. We use the multi-scale time schemes for both the pressure and saturation equations; that is, a large time-step size is employed for the matrix domain, along with a small time-step size being applied in the fractures. The total time interval is partitioned into four temporal levels: the first level is used for the pressure in the entire domain, the second level matching rapid changes of the pressure in the fractures, the third level treating the response gap between the pressure and the saturation, and the fourth level applied for the saturation in the fractures. This method can reduce the computational cost arisen from the implicit solution of the pressure equation. Numerical examples are provided to demonstrate the efficiency of the proposed method.

1. Introduction

The fractured porous media is composed of two distinct pore spaces: the fracture and the matrix. The fracture spaces have higher permeability than the matrix, but possess very small volume compared with the matrix. Numerical simulation of multiphase flow in fractured porous media is of importance in the subsurface flow, environmental problems and petroleum reservoir engineering. In this paper, we focus on two-phase fluid flow in

fractured porous media with capillarity. In the displacement of the nonwetting phase by the wetting phase, the injected fluid flows rapidly across the fracture network if the effect of capillarity is neglected; however, when the capillarity is taken into account, the capillary contrast between the matrix and the fracture may have a significant influence on flow paths. In the fractured porous media, the different capillary pressure functions are employed within the fracture and the matrix blocks because of their different permeability types; that is, the capillary pressure functions are not continuous on the matrix-fracture interfaces. Therefore, the discontinuity of the saturation is predicted because of the continuity of capillary pressure [1].

To simulate the multiphase flow in fractured porous media, several conceptual models have been developed [2–16], such as the single-porosity model, the dual-porosity/dual-permeability model, and the discrete-fracture model. In the single-porosity model, the fractures are treated similarly to the matrix. This model requires the excessive gridcells because of the contrast of geometrical scales between the matrix and the fracture. The dual-porosity/dual-permeability model [3, 8–10, 13, 15, 16] envisions the matrix blocks and the fractures as two separate parts, which are interconnected by fluid mass transfer across their interfaces. The discrete fracture model [2, 11, 12] is based on the conception that the fracture aperture is very small compared to the matrix blocks, and as a result, we can simplify the fracture as the lower dimensional domain to reduce the contrast of geometric scales occurring in the single-porosity model. The discrete fracture model is shown to be is numerically superior to the single-porosity model and the dual-porosity models [6, 7]. This model will be used in this paper.

The implicit pressure explicit saturation (IMPES) method [17–24] is a popular time-stepping approach employed in multiphase flow simulation. Based on the property of multiphysics processes, the IMPES method splits the coupled system into one pressure equation and one saturation equation. The saturation and capillary pressure in the pressure equation are treated explicitly to eliminate its nonlinearity. These treatments result in the decoupling between the pressure equation and the saturation equation, and the instability of the IMPES method [21], especially for the case with capillarity in the heterogeneous media. In order to improve the stability of IMPES, we present an implicit treatment of capillarity in [25], which will be described in Section 3. The iterative version of this method is presented in [26]. Based on the previous works, we will discuss this approach being applied in the fractured media. For the fluid flow in porous media, the pressure changes less rapidly than the saturation with the time, and hence we can take a larger time-step for the pressure than the one for saturation. This approach is an improvement of IMPES originally proposed in [17, 24, 27]. It is also demonstrated that this technique is very efficient for the method proposed in [25]. Relevant work in coupled flow and transport simulation can be found in, for example, [28–35]. In this paper, we will describe a multiscale time strategy for multiphysics processes of two-phase flow in fractured media.

For fractured media, the pressure and saturation in the fracture network change more rapidly than the ones in the matrix blocks. The explicit treatment of saturation in the pressure equation may be instable, and thus the small time-step size is required if the same time scale is employed in the entire spatial domain. The explicit scheme used for updating the saturation suffers from Courant number stability constraints, and as a result, we should use the smallest time-step size to match the rapid changes in the fracture network if using the single-scale time-stepping. To resolve this problem, we should use the multiscale time-stepping for the pressure and the saturation in the fracture and the matrix.

Multiscale time splitting strategy has been studied in the literature, for example, [36–45]. An explicit subtiming scheme is proposed in [41, 42]. The computational domain is divided into separate coarse and fine-grid locations. We fist carry out the computations for all coarse grid-blocks by using a time-step size that satisfies the coarse grid-block stability constraint. Once the solutions in a coarsely discretized region are obtained, the unknowns within the fine grids are solved by using a smaller time-step size that matches the fine grid stability constraints. In the subtiming methodology for implicit-type time-stepping schemes proposed in [39], the fully implicit schemes with multiple time-step sizes are utilized to the different portions of a domain, which have different accuracy requirements. This technique has been applied to the time-dependent flow and transport simulations in fractured porous media [40], which uses the implicit subtime-stepping in the locations within and near the fractures. It is demonstrated that the implicit multiple time-stepping is capable to significantly improve the accuracy and efficiency of numerical simulation. The hybrid implicit-explicit approach [46] treats implicitly the portions of the domain with the particular stability requirements, along with the explicit time-stepping applied to the remainder of the domain. The advantage of this approach is that it can reduce the size of the problems being solved implicitly at each time-step.

In this paper, we present a multiscale time splitting strategy for two-phase flow in fractured porous media. Taking account into the different physical properties of the matrix blocks and the fracture network, and the multiphysics processes of two-phase flow, we apply multiple time scales for the pressure and saturation equations. The pressure equation is formed from the conception proposed in [25]; that is, the capillary pressure is treated implicitly in the pressure equation. For the pressure, we employ a large time-step size in the matrix domain, along with a small time-step size being applied in the fracture system. The time-step for the pressure in the fractures is further partitioned to a few subtime-steps, in which the saturation will be updated explicitly. The updating process of the saturation employs two-scale time-stepping; a coarse time-stepping is applied in the matrix blocks, along with a fine one in the fracture system.

The rest of this paper is organized as follows. In Section 2, we review the two-phase incompressible flow model, along with the discrete-fracture model. In Section 3, we describe our multiscale time splitting strategy. Here, the cell-centered finite difference (CCFD) method [47] is employed for spatial discretization, but it can be extended to the other discretization schemes. In Section 4, some numerical examples are given to demonstrate the advantage of the proposed method. Finally, we summarize this work.

2. Mathematical Model of Two-Phase Incompressible Flow

2.1. Governing Equations of Two-Phase Flow

We now describe two-phase incompressible and immiscible fluid flow in porous media, and denote the wetting phase by a subscript w and the nonwetting phase by n. The mass conservation equation of each phase is given by

$$\phi \frac{\partial S_\alpha}{\partial t} + \nabla \cdot \mathbf{u}_\alpha = q_\alpha, \quad \alpha = w, n, \tag{2.1}$$

where ϕ is the porosity of the medium, S_α is the saturation of phase α, and q_α is the external mass flow rate. In (2.1), Darcy's velocity $\mathbf{u}_\alpha$ of each phase α is given by

$$\mathbf{u}_\alpha = -\frac{k_{r\alpha}}{\mu_\alpha}\mathbf{K}\left(\nabla p_\alpha + \rho_\alpha g \nabla z\right), \quad \alpha = w, n, \tag{2.2}$$

where $\mathbf{K}$ is the absolute permeability tensor in the porous medium, g is the gravity acceleration, z is the depth, and $k_{r\alpha}$, μ_α, p_α, and ρ_α are the relative permeability, viscosity, pressure and density of each phase, respectively.

In addition, the saturations of two phases are subject to the following constraint

$$S_w + S_n = 1. \tag{2.3}$$

The difference between the nonwetting phase and wetting phase pressures is described by the capillary pressure

$$p_c(S_w) = p_n - p_w. \tag{2.4}$$

In this paper, we use the two-phase flow formulation [1, 7, 48] given by

$$\nabla \cdot (\mathbf{u}_a + \mathbf{u}_c) \equiv -\nabla \cdot \lambda_t \mathbf{K} \nabla \Phi_w - \nabla \cdot \lambda_n \mathbf{K} \nabla \Phi_c = q_t, \tag{2.5}$$

$$\phi \frac{\partial S_w}{\partial t} - q_w = -\nabla \cdot \left(f_w \mathbf{u}_a\right) \equiv \nabla \cdot \lambda_w \mathbf{K} \nabla \Phi_w, \tag{2.6}$$

where $q_t = q_w + q_n$, $\lambda_\alpha = k_{r\alpha}/\mu_\alpha$, $\lambda_t = \lambda_w + \lambda_n$, $f_w = \lambda_w/\lambda_t$, $\Phi_\alpha = p_\alpha + \rho g z$, $\Phi_c = p_c + (\rho_n - \rho_w) g z$, $\mathbf{u}_a = -\lambda_t \mathbf{K} \nabla \Phi_w$, and $\mathbf{u}_c = -\lambda_n \mathbf{K} \nabla \Phi_c$. From the above definitions, the wetting-phase velocity is expressed as

$$\mathbf{u}_w = f_w \mathbf{u}_a. \tag{2.7}$$

Finally, we consider the boundary and initial conditions. We divide the boundary $\partial\Omega$ of the computational domain Ω into the two nonoverlapping parts: the Dirichelt part Γ^D and Newmann part Γ^N, where $\partial\Omega = \Gamma^D \cup \Gamma^N$. The pressure equation (2.5) is subject to the following boundary conditions

$$\begin{aligned} p_w (\text{or } p_n) &= p^D \quad \text{on } \Gamma^D, \\ (\mathbf{u}_a + \mathbf{u}_c) \cdot \mathbf{n} &= \mathbf{u}^N \quad \text{on } \Gamma^N, \end{aligned} \tag{2.8}$$

where p^D is the pressure on Γ^D, $\mathbf{n}$ is the outward unit normal vector to $\partial\Omega$ and $\mathbf{u}^N$ is the imposed inflow rate on Γ^N. The boundary conditions for the saturations are given by

$$S_w (\text{or } S_n) = S^N \quad \text{on } \Gamma^N. \tag{2.9}$$

The initial saturation of the wetting phase is given by

$$S_w = S_w^0 \quad \text{in } \Omega. \tag{2.10}$$

2.2. Discrete-Fracture Model

Here, we employ the discrete-fracture model [6, 7] to explicitly describe the fractures in fractured porous media. In this model, different geometrical dimensions are taken for the matrix and fracture grid cells; that is, for n-dimensional domain, the matrix gridcells are n-dimensional, but the fracture gridcells are simplified as the matrix gridcell interfaces that are $(n-1)$-dimensional. This treatment is capable to considerably improve the computational efficiency since it can remove the length-scale contrast resulting from the explicit representation of the fracture aperture as in the single-porosity model. The entire domain is decomposed into two parts: the matrix Ω_m (n-dimensional) and fracture Ω_f ($(n-1)$-dimensional), and the fractures are surrounded by the matrix blocks. The pressure equation in the matrix domain is given by

$$-\nabla \cdot \lambda_{t,m}\mathbf{K}_m\nabla\Phi_{w,m} - \nabla \cdot \lambda_{n,m}\mathbf{K}_m\nabla\Phi_{c,m} = q_{t,m}, \tag{2.11}$$

where the subscript m represents the matrix domain. Equation (2.11) is subject to the matrix-fracture interface condition

$$\Phi_{w,m} = \Phi_{w,f}, \Phi_{c,m} = \Phi_{c,f}, \quad \text{on } \partial\Omega_m \cap \Omega_f. \tag{2.12}$$

The fracture width is denoted by ε. In the fracture system, we assume the potentials and saturations are constant along the fracture width, and then by integrating the equation, obtain the pressure equation in the fracture (represented by the subscript f) as

$$-\nabla \cdot \lambda_{t,f}\mathbf{K}_f\nabla\Phi_{w,f} - \nabla \cdot \lambda_{n,f}\mathbf{K}_f\nabla\Phi_{c,f} = q_{t,f} + Q_{t,f}, \tag{2.13}$$

where $Q_{t,f}$ is the mass transfer across the matrix-fracture interfaces. Similarly, we can express the saturation equation in the matrix domain as

$$\phi_m\frac{\partial S_{w,m}}{\partial t} - \nabla \cdot \lambda_{w,m}\mathbf{K}_m\nabla\Phi_{w,m} = q_{w,m}, \tag{2.14}$$

with the interface condition

$$S_{w,m} = S_{w,f}, \quad \text{on } \partial\Omega_m \cap \Omega_f. \tag{2.15}$$

In accordance, the saturation equation in the fracture system is given by

$$\phi_f\frac{\partial S_{w,f}}{\partial t} - \nabla \cdot \lambda_{w,f}\mathbf{K}_f\nabla\Phi_{w,f} = q_{w,f} + Q_{w,f}, \tag{2.16}$$

where $Q_{w,f}$ represents the mass transfer across the matrix-fracture interfaces. This form of saturation equation will be used to rebuild the coupling relationship between the pressure and saturation. The other form of saturation equation is used to compute the saturation, which is expressed as in the matrix domain

$$\phi_m \frac{\partial S_{w,m}}{\partial t} + \nabla \cdot \left(f_{w,m} \mathbf{u}_{a,m} \right) = q_{w,m}, \tag{2.17}$$

and in the fractures

$$\phi_f \frac{\partial S_{w,f}}{\partial t} + \nabla \cdot \left(f_{w,f} \mathbf{u}_{a,f} \right) = q_{w,f} + \widehat{Q}_{w,f}, \tag{2.18}$$

where $\widehat{Q}_{w,f}$ is the same to $Q_{w,f}$, but with different expressions in the spatial discretization.

3. Multi-Scale Time Splitting Strategy

In this paper, we use the cell-centered finite difference (CCFD) method for the spatial discretization, but apparently, our approach can be also extended to the other spatial discretization schemes. In this paper, we focus on the case of two-dimensional space. The extension to three-dimensional case is straightforward. We assume that the porous media are isotropic and the absolute permeability is a scalar function.

3.1. Multi-Scale Time Splitting Approach for the Pressure Equation with Implicit Capillary Pressure

We firstly divide the total time interval $[0, T]$ into $N_{p,m}$ time-steps as $0 = t^0 < t^1 < \cdots < t^{N_{p,m}} = T$. This time division is used for the pressure in the matrix domain. Define the time-step length $\Delta t^i = t^{i+1} - t^i$. Since the pressure in the fractures varies more rapidly than the matrix domain, we use a smaller time-step size for the pressure in the fractures; that is, we partition each subinterval $(t^i, t^{i+1}]$ into $N_{p,f}$ subsubintervals as $(t^i, t^{i+1}] = \bigcup_{j=0}^{N_{p,f}-1} (t^{i,j}, t^{i,j+1}]$, where $t^{i,0} = t^i$ and $t^{i,N_{p,f}} = t^{i+1}$, and denote the subsubinterval length by $\Delta t^{i,j} = t^{i,j+1} - t^{i,j}$. We denote the value of a variable v on the t^i time point by v^i and the one on $t^{i,j}$ by $v^{i,j}$.

We consider the grid system with rectangular cells for the matrix domain. The fracture that is one-dimensional can be partitioned into many spatial subintervals. The classical IMPES method is instable because each cell capillary potential Φ_c is explicitly calculated by using the cell saturations from the previous time-step and the capillary pressure functions. In this paper, we employ the implicit approach to handle capillary pressure proposed in [25]. This method treats the variables λ_w, λ_n, and λ_t in the pressure equation as IMPES, but the capillary potentials Φ_c will be treated implicitly. From this, we obtain the mass conservation equation in the matrix domain

$$-\nabla \cdot \lambda_t \left(S_{w,m}^i \right) \mathbf{K}_m \nabla \Phi_{w,m}^{i+1} - \nabla \cdot \lambda_n \left(S_{w,m}^i \right) \mathbf{K}_m \nabla \left((1-\omega) \Phi_{c,m}^i + \omega \Phi_{c,m}^{i+1} \right) = q_{t,m}^{i+1}, \tag{3.1}$$

where the superscript i represents the time-step and ω is the temporal discretization parameter. Apparently, it becomes the form of IMPES if $\omega = 0$. Here, we always take $\omega \geq 1/2$;

that is, the capillarity is implicitly treated. It is similar to obtain the form in the fracture (referred to by the subscript f) as

$$-\nabla\cdot\lambda_t\left(S^i_{w,f}\right)\mathbf{K}_f\nabla\Phi^{i+1}_{w,f}-\nabla\cdot\lambda_n\left(S^i_{w,f}\right)\mathbf{K}_f\nabla\left((1-\omega)\Phi^i_{c,f}+\omega\Phi^{i+1}_{c,f}\right)=q^{i+1}_{t,f}+Q^{i+1}_{t,f}. \tag{3.2}$$

Let e indicate the boundary of the matrix gridcells. We use the CCFD scheme applied to (3.1) and obtain

$$\sum_{e\in\partial K}F^{i+1}_{a,m,e}+\sum_{e\in\partial K}\left((1-\omega)F^i_{c,m,e}+\omega F^{i+1}_{c,m,e}\right)=q^{i+1}_{t,m,K}|K|, \tag{3.3}$$

where $|K|$ indicates the area of the cell K, and F indicates the flux across the boundary e of the gridcell K. Here, we assume that e is also a gridcell of the fractures if $e\in\Omega_f$. On each interface $e\in\partial K\cap\partial K'$, $\mathbf{n}_e$ is the unit normal vector pointing from K to K'. If $e\in\partial K\cap\partial K'$ and $e\not\subseteq\Omega_f$, the fluxes in (3.3) are given by

$$\begin{aligned}
F^{i+1}_{a,m,e}&=-|e|\beta^i_{t,e}\frac{\Phi^{i+1}_{w,m,K'}-\Phi^{i+1}_{w,m,K}}{d_{K,K'}},\\
F^i_{c,m,e}&=-|e|\beta^i_{n,e}\frac{\Phi^i_{c,m,K'}-\Phi^i_{c,m,K}}{d_{K,K'}},\\
F^{i+1}_{c,m,e}&=-|e|\beta^i_{n,e}\frac{\Phi^{i+1}_{c,m,K'}-\Phi^{i+1}_{c,m,K}}{d_{K,K'}},
\end{aligned} \tag{3.4}$$

where $|e|$ is the length of e and $d_{K,K'}$ stands for the Euclidean distance between the central points of the cells K and K'. In (3.4), the terms $\beta^i_{t,e}$ and $\beta^i_{n,e}$ are given by

$$\begin{aligned}
\beta^i_{t,e}&=\frac{d_{K,K'}\lambda^i_{t,m,K}\lambda^i_{t,m,K'}\mathbf{K}_{m,K}\mathbf{K}_{m,K'}}{d_{K,e}\lambda^i_{t,m,K'}\mathbf{K}_{m,K'}+d_{K',e}\lambda^i_{t,m,K}\mathbf{K}_{m,K}},\\
\beta^i_{n,e}&=\frac{d_{K,K'}\lambda^i_{n,m,K}\lambda^i_{n,m,K'}\mathbf{K}_{m,K}\mathbf{K}_{m,K'}}{d_{K,e}\lambda^i_{n,m,K'}\mathbf{K}_{m,K'}+d_{K',e}\lambda^i_{n,m,K}\mathbf{K}_{m,K}},
\end{aligned} \tag{3.5}$$

where $d_{K,e}$ stands for the Euclidean distance from the central points of the cell K and the cell boundary e. If $e\in\Omega_f\cap\partial K\cap\partial K'$ and e is a gridcell of the fracture system, we have

$$F^{i+1}_{a,m,e}\equiv F^{i+1}_{a,m,e,K}=-|e|\beta^i_{t,mf,e}\frac{\Phi^{i+1}_{w,f,e}-\Phi^{i+1}_{w,m,K}}{d_{K,e}+\varepsilon/2}, \tag{3.6}$$

$$F^i_{c,m,e}\equiv F^i_{c,m,e,K}=-|e|\beta^i_{n,mf,e}\frac{\Phi^i_{c,f,e}-\Phi^i_{c,m,K}}{d_{K,e}+\varepsilon/2}, \tag{3.7}$$

$$F^{i+1}_{c,m,e}\equiv F^{i+1}_{c,m,e,K}=-|e|\beta^i_{n,mf,e}\frac{\Phi^{i+1}_{c,f,e}-\Phi^{i+1}_{c,m,K}}{d_{K,e}+\varepsilon/2}, \tag{3.8}$$

where $\beta^i_{t,mf,e}$ and $\beta^i_{n,mf,e}$ are given by

$$\beta^i_{t,mf,e} = \frac{(d_{K,e} + \varepsilon/2)\lambda^i_{t,f,K}\lambda^i_{t,m,K}\mathbf{K}_{f,K}\mathbf{K}_{m,K}}{(\varepsilon/2)\lambda^i_{t,m,K}\mathbf{K}_{m,K} + d_{K,e}\lambda^i_{t,f,K}\mathbf{K}_{f,K}},$$
$$\beta^i_{n,mf,e} = \frac{(d_{K,e} + \varepsilon/2)\lambda^i_{n,f,K}\lambda^i_{n,m,K}\mathbf{K}_{f,K}\mathbf{K}_{m,K}}{(\varepsilon/2)\lambda^i_{n,m,K}\mathbf{K}_{m,K} + d_{K,e}\lambda^i_{n,f,K}\mathbf{K}_{f,K}}. \tag{3.9}$$

For the case e locating on the entire domain boundary, the pressure potential is provided by Dirichelt boundary conditions if $e \in \Gamma^D$, otherwise the fluxes are determined by the Newmann conditions if $e \in \partial\Omega^N$.

The above processes of deriving (3.3)–(3.9) can also be carried out for the reduced-dimensional fracture system. Let e be a gridcell of the fracture network. The CCFD scheme is applied to (3.2), and then we have

$$\sum_{\gamma\in\partial e} F^{i+1}_{a,f,\gamma} + \sum_{\gamma\in\partial e}\left((1-\omega)F^i_{c,f,\gamma} + \omega F^{i+1}_{c,f,\gamma}\right) = q^{i+1}_{t,f,e}|e| + Q^{i+1}_{t,f,e}|e|, \tag{3.10}$$

where γ indicates the face of the gridcell e in the fracture system and F indicates the flux across the boundary γ of the fracture gridcell e. Different from (3.3), no potential of the matrix domain is required for computing the fracture-fracture fluxes in (3.10), but the matrix-fracture transfer needs to be treated as a source term in the fracture system. We consider a gridcell e of the fracture network where $e \in \partial K \cap \partial K'$ and K and K' are the gridcells of the matrix domain. The fracture width is denoted by ε. The volumetric transfer across the matrix-fracture interface e is given by

$$Q^{i+1}_{t,f,e} = -\frac{\left(Q^{i+1}_{t,f,e,K} + Q^{i+1}_{t,f,e,K'}\right)}{\varepsilon},$$
$$Q^{i+1}_{t,f,e,K} = F^{i+1}_{a,m,e,K} + (1-\omega)F^i_{c,m,e,K} + \omega F^{i+1}_{c,m,e,K},$$
$$Q^{i+1}_{t,f,e,K'} = F^{i+1}_{a,m,e,K'} + (1-\omega)F^i_{c,m,e,K'} + \omega F^{i+1}_{c,m,e,K'}, \tag{3.11}$$

where $F^{i+1}_{a,m,e}$, $F^i_{c,m,e}$, and $F^{i+1}_{c,m,e}$ are defined by (3.6)–(3.8), respectively. We now consider the treatment of the interface connecting multiple fractures. Let Λ_γ be the set composed of the fracture grid cells that are jointed by γ. The discretization of the mass conservation equation is given by

$$\sum_{e\in\Lambda_\gamma}\left(F^{i+1}_{a,f,\gamma,e} + (1-\omega)F^i_{c,f,\gamma,e} + \omega F^{i+1}_{c,f,\gamma,e}\right) = 0, \tag{3.12}$$

where $F_{a,f,\gamma,e} = F_{a,f,\gamma}|_{\gamma\in e}$ and $F_{c,f,\gamma,e} = F_{c,f,\gamma}|_{\gamma\in e}$.

Combining the formulations in the matrix domain and fracture network, we obtain the discretization of total mass conservation equation given by

$$\begin{bmatrix} \mathbf{A}^i_{a,m,m} & \mathbf{A}^i_{a,m,f} \\ \mathbf{A}^i_{a,f,m} & \mathbf{A}^i_{a,f,f} \end{bmatrix} \begin{bmatrix} \Phi^{i+1}_{w,m} \\ \Phi^{i+1}_{w,f} \end{bmatrix} + \begin{bmatrix} \mathbf{A}^i_{c,m,m} & \mathbf{A}^i_{c,m,f} \\ \mathbf{A}^i_{c,f,m} & \mathbf{A}^i_{c,f,f} \end{bmatrix} \times \left\{ (1-\omega) \begin{bmatrix} \Phi^i_{c,m} \\ \Phi^i_{c,f} \end{bmatrix} + \omega \begin{bmatrix} \Phi^{i+1}_{c,m} \\ \Phi^{i+1}_{c,f} \end{bmatrix} \right\} = \begin{bmatrix} \mathbf{Q}^{i+1}_{ac,m} \\ \mathbf{Q}^{i+1}_{ac,f} \end{bmatrix}. \tag{3.13}$$

The terms $\mathbf{A}^i_{a,m,f}$, $\mathbf{A}^i_{a,f,m}$, $\mathbf{A}^i_{c,m,f}$, and $\mathbf{A}^i_{c,f,m}$ of (3.13) arise from the interconnections of the matrix blocks and fracture system. Since $\omega > 0$ and $\mathbf{S}^{i+1}_w$ is unknown, the above equation can not be solved immediately because of its nonlinearity. In order to eliminate the nonlinearity, we approximate the capillary pressure $\Phi_c(\mathbf{S}^{i+1}_w)$ at $\mathbf{S}^i_w$ by

$$\Phi_c\left(\mathbf{S}^{i+1}_w\right) \simeq \Phi_c\left(\mathbf{S}^i_w\right) + \Phi'_c\left(\mathbf{S}^i_w\right)\left(\mathbf{S}^{i+1}_w - \mathbf{S}^i_w\right). \tag{3.14}$$

Furthermore, we employ the backward Euler time discretization for the saturation equation both in the matrix domain

$$\phi_m \frac{S^{i+1}_{w,m} - S^i_{w,m}}{\Delta t^i} - \nabla \cdot \lambda_w\left(S^i_{w,m}\right)\mathbf{K}_m \nabla \Phi^{i+1}_{w,m} = q^{i+1}_{w,m}, \tag{3.15}$$

and in the fracture network

$$\phi_f \frac{S^{i+1}_{w,f} - S^i_{w,f}}{\Delta t^i} - \nabla \cdot \lambda_w\left(S^i_{w,f}\right)\mathbf{K}_f \nabla \Phi^{i+1}_{w,f} = q^{i+1}_{w,f} + Q^{i+1}_{w,f}. \tag{3.16}$$

It is analogous to the derivation of the pressure equation (3.13), and we approximate (3.15) and (3.16) by the CCFD method as

$$\frac{1}{\Delta t^i} \begin{bmatrix} \mathbf{M}_m & \\ & \mathbf{M}_f \end{bmatrix} \begin{bmatrix} \mathbf{S}^{i+1}_{w,m} - \mathbf{S}^i_{w,m} \\ \mathbf{S}^{i+1}_{w,f} - \mathbf{S}^i_{w,f} \end{bmatrix} + \begin{bmatrix} \mathbf{A}^i_{w,m,m} & \mathbf{A}^i_{w,m,f} \\ \mathbf{A}^i_{w,f,m} & \mathbf{A}^i_{w,f,f} \end{bmatrix} \begin{bmatrix} \Phi^{i+1}_{w,m} \\ \Phi^{i+1}_{w,f} \end{bmatrix} = \begin{bmatrix} \mathbf{Q}^{i+1}_{w,m} \\ \mathbf{Q}^{i+1}_{w,f} \end{bmatrix}. \tag{3.17}$$

Substituting (3.14) and (3.17) into (3.13), we obtain the coupled pressure equation

$$\mathbf{A}^i_t \begin{bmatrix} \Phi^{i+1}_{w,m} \\ \Phi^{i+1}_{w,f} \end{bmatrix} = \mathbf{Q}^i_t, \tag{3.18}$$

where

$$\begin{aligned}
\mathbf{A}_t^i &= \begin{bmatrix} \mathbf{A}_{a,m,m}^i & \mathbf{A}_{a,m,f}^i \\ \mathbf{A}_{a,f,m}^i & \mathbf{A}_{a,f,f}^i \end{bmatrix} - \omega \Delta t^i \begin{bmatrix} \mathbf{A}_{c,m,m}^i & \mathbf{A}_{c,m,f}^i \\ \mathbf{A}_{c,f,m}^i & \mathbf{A}_{c,f,f}^i \end{bmatrix} \begin{bmatrix} \Phi_c'(\mathbf{S}_{w,m}^i) & \\ & \Phi_c'\left(\mathbf{S}_{w,f}^i\right) \end{bmatrix} \\
&\quad \times \begin{bmatrix} \mathbf{M}_m^{-1} & \\ & \mathbf{M}_f^{-1} \end{bmatrix} \begin{bmatrix} \mathbf{A}_{w,m,m}^i & \mathbf{A}_{w,m,f}^i \\ \mathbf{A}_{w,f,m}^i & \mathbf{A}_{w,f,f}^i \end{bmatrix}, \\
\mathbf{Q}_t^i &= \begin{bmatrix} \mathbf{Q}_{ac,m}^{i+1} \\ \mathbf{Q}_{ac,f}^{i+1} \end{bmatrix} - \begin{bmatrix} \mathbf{A}_{c,m,m}^i & \mathbf{A}_{c,m,f}^i \\ \mathbf{A}_{c,f,m}^i & \mathbf{A}_{c,f,f}^i \end{bmatrix} \begin{bmatrix} \Phi_c(\mathbf{S}_{w,m}^i) \\ \Phi_c\left(\mathbf{S}_{w,f}^i\right) \end{bmatrix} - \omega \Delta t^i \begin{bmatrix} \mathbf{A}_{c,m,m}^i & \mathbf{A}_{c,m,f}^i \\ \mathbf{A}_{c,f,m}^i & \mathbf{A}_{c,f,f}^i \end{bmatrix} \\
&\quad \times \begin{bmatrix} \Phi_c'(\mathbf{S}_{w,m}^i) & \\ & \Phi_c'\left(\mathbf{S}_{w,f}^i\right) \end{bmatrix} \begin{bmatrix} \mathbf{M}_m^{-1} & \\ & \mathbf{M}_f^{-1} \end{bmatrix} \begin{bmatrix} \mathbf{Q}_{w,m}^{i+1} \\ \mathbf{Q}_{w,f}^{i+1} \end{bmatrix}.
\end{aligned} \tag{3.19}$$

Equation (3.18), along with (3.19), is utilized to compute the matrix pressure in a large time-step. In order to match the rapid changes of the pressure in the fracture network, we use a small time-step size in the fracture system. For each time substep, we consider the pressure equation in the fractures as

$$-\nabla \cdot \lambda_t\left(S_{w,f}^{i,j}\right)\mathbf{K}_f \nabla \Phi_{w,f}^{i,j+1} - \nabla \cdot \lambda_n\left(S_{w,f}^{i,j}\right)\mathbf{K}_f \nabla\left((1-\omega)\Phi_{c,f}^{i,j} + \omega \Phi_{c,f}^{i,j+1}\right) = q_{t,f}^{i,j+1} + Q_{t,f}^{i,j+1}. \tag{3.20}$$

It is obtained by using the CCFD scheme to (3.20) that

$$\sum_{\gamma \in \partial e} F_{a,f,\gamma}^{i,j+1} + \sum_{\gamma \in \partial e}\left((1-\omega)F_{c,f,\gamma}^{i,j} + \omega F_{c,f,\gamma}^{i,j+1}\right) = q_{t,f,e}^{i,j+1}|e| + Q_{t,f,e}^{i,j+1}|e|, \tag{3.21}$$

where γ is the face of the gridcell e in the fracture system and F represents the flux across the boundary γ of the fracture gridcell e. Let K and K' are the matrix gridcells and $e \in \partial K \cap K'$, then in (3.21), the matrix-fracture transfer is given by

$$\begin{aligned}
Q_{t,f,e}^{i,j+1} &= -\frac{\left(Q_{t,f,e,K}^{i,j+1} + Q_{t,f,e,K'}^{i,j+1}\right)}{\varepsilon}, \\
Q_{t,f,e,K}^{i,j+1} &= F_{a,m,e,K}^{i,j+1} + (1-\omega)F_{c,m,e,K}^{i,j} + \omega F_{c,m,e,K}^{i,j+1}, \\
Q_{t,f,e,K'}^{i,j+1} &= F_{a,m,e,K'}^{i,j+1} + (1-\omega)F_{c,m,e,K'}^{i,j} + \omega F_{c,m,e,K'}^{i,j+1},
\end{aligned} \tag{3.22}$$

where

$$F^{i,j+1}_{a,m,e,K} \equiv F^{i,j+1}_{a,m,e} = -|e|\beta^{i,j}_{t,mf,e}\frac{\Phi^{i,j+1}_{w,f,e} - \Phi^{i+1}_{w,m,K}}{d_{K,e} + \varepsilon/2}, \tag{3.23}$$

$$\begin{aligned} F^{i,j}_{c,m,e,K} &\equiv F^{i,j}_{c,m,e} = -|e|\beta^{i,j}_{c,mf,e}\frac{\Phi^{i,j}_{c,f,e} - \Phi^{i,j}_{c,m,K}}{d_{K,e} + \varepsilon/2}, \\ F^{i,j+1}_{c,m,e,K} &\equiv F^{i,j+1}_{c,m,e} = -|e|\beta^{i,j}_{c,mf,e}\frac{\Phi^{i,j+1}_{c,f,e} - \Phi^{i,j+1}_{c,m,K}}{d_{K,e} + \varepsilon/2}, \end{aligned} \tag{3.24}$$

along with

$$\begin{aligned} \beta^{i,j}_{t,mf,e} &= \frac{(d_{K,e} + \varepsilon/2)\lambda^{i,j}_{t,f,K}\lambda^{i,j}_{t,m,K}\mathbf{K}_{f,K}\mathbf{K}_{m,K}}{(\varepsilon/2)\lambda^{i,j}_{t,m,K}\mathbf{K}_{m,K} + d_{K,e}\lambda^{i,j}_{t,f,K}\mathbf{K}_{f,K}}, \\ \beta^{i,j}_{c,mf,e} &= \frac{(d_{K,e} + \varepsilon/2)\lambda^{i,j}_{c,f,K}\lambda^{i,j}_{c,m,K}\mathbf{K}_{f,K}\mathbf{K}_{m,K}}{(\varepsilon/2)\lambda^{i,j}_{c,m,K}\mathbf{K}_{m,K} + d_{K,e}\lambda^{i,j}_{c,f,K}\mathbf{K}_{f,K}}. \end{aligned} \tag{3.25}$$

The treatment of the interface connecting multiple fractures is similar to (3.12). Therefore, in the time-step used for the pressure in the fractures, we solve the following pressure equation

$$\mathbf{A}^{i,j}_{t,f}\Phi^{i,j+1}_{w,f} = \mathbf{Q}^{i,j}_{t,f}, \tag{3.26}$$

where

$$\begin{aligned} \mathbf{A}^{i,j}_{t,f} &= \mathbf{A}^{i,j}_{a,f,f} - \omega\Delta t^{i,j}\left(\mathbf{A}^{i,j}_{c,f,f}\Phi'_c\left(\mathbf{S}^{i,j}_{w,f}\right)\mathbf{M}_f^{-1}\mathbf{A}^{i,j}_{w,f,f} + \mathbf{A}^{i,j}_{c,f,m}\Phi'_c\left(\mathbf{S}^{i,j}_{w,m}\right)\mathbf{M}_m^{-1}\mathbf{A}^{i,j}_{w,m,f}\right), \\ \mathbf{Q}^{i,j}_{t,f} &= \mathbf{Q}^{i,j+1}_{ac,f} - \mathbf{A}^{i,j}_{a,f,m}\Phi^{i+1}_{w,m} \\ &\quad + \omega\Delta t^{i,j}\left(\mathbf{A}^{i,j}_{c,f,m}\Phi'_c\left(\mathbf{S}^{i,j}_{w,m}\right)\mathbf{M}_m^{-1}\mathbf{A}^{i,j}_{w,m,m} + \mathbf{A}^{i,j}_{c,f,f}\Phi'_c\left(\mathbf{S}^{i,j}_{w,f}\right)\mathbf{M}_f^{-1}\mathbf{A}^{i,j}_{w,f,m}\right)\Phi^{i+1}_{w,m} \\ &\quad - \mathbf{A}^{i,j}_{c,f,m}\Phi_c\left(\mathbf{S}^{i,j}_{w,m}\right) - \mathbf{A}^{i,j}_{c,f,f}\Phi_c\left(\mathbf{S}^{i,j}_{w,f}\right) \\ &\quad - \omega\Delta t^{i,j}\left(\mathbf{A}^{i,j}_{c,f,m}\Phi'_c\left(\mathbf{S}^{i,j}_{w,m}\right)\mathbf{M}_m^{-1}\mathbf{Q}^{i+1}_{w,m} + \mathbf{A}^{i,j}_{c,f,f}\Phi'_c\left(\mathbf{S}^{i,j}_{w,f}\right)\mathbf{M}_f^{-1}\mathbf{Q}^{i+1}_{w,f}\right). \end{aligned} \tag{3.27}$$

In the above equations, the inverse of $\mathbf{M}_m$ and $\mathbf{M}_f$ is not expensive as they are diagonal. In the time-step (t^i, t^{i+1}), we solve the linear system (3.18) implicitly to obtain the pressure $\Phi^{i+1}_{w,m}$, and then in the time substep $(t^{i,j}, t^{i,j+1})$ compute $\Phi^{i,j+1}_{w,f}$ by solving (3.26).

Once the pressures $\Phi_{w,m}^{i+1}$ and $\Phi_{w,f}^{i,j+1}$ is obtained, the fluxes can be evaluated as described below. For a boundary e of matrix gridcell K, $\mathbf{n}_e$ is the unit normal vector pointing towards outside K. If $e \in \partial K \cap \partial K'$ and $e \not\subset \Omega_f$,

$$F_{a,m,e}^{i,j+1} = -|e|\beta_{t,e}^{i,j} \frac{\Phi_{w,m,K'}^{i+1} - \Phi_{w,m,K}^{i+1}}{d_{K,K'}}, \tag{3.28}$$

where

$$\beta_{t,e}^{i,j} = \frac{d_{K,K'}\lambda_{t,m,K}^{i,j}\lambda_{t,m,K'}^{i,j}\mathbf{K}_{m,K}\mathbf{K}_{m,K'}}{d_{K,e}\lambda_{t,m,K'}^{i,j}\mathbf{K}_{m,K'} + d_{K',e}\lambda_{t,m,K}^{i,j}\mathbf{K}_{m,K}}. \tag{3.29}$$

If $e \in \Omega_f \cap \partial K \cap \partial K'$ and e is a fracture gridcell, the fluxes are computed by (3.23). The fluxes on the domain boundary $\partial\Omega^N$ are obtain by the boundary conditions as discussed above.

3.2. Multi-Scale Explicit Time-Stepping for the Saturation Equation

As the pressure computed by the above-described method has coupled with the saturation, the forward Euler time discretization is used for computing the saturation equation of the wetting phase in each time-step used for the pressure in the fracture. According to the concept proposed in [17, 24, 27], the time-step size for the pressure can be taken larger than the one for saturation, which is also demonstrated to be efficient for the method proposed in [25]. We divide the time-step $(t^{i,j}, t^{i,j+1}]$ for the pressure in the fracture network into $N_{s,m}$ time-steps as $(t^{i,j}, t^{i,j+1}] = \bigcup_{k=0}^{N_{s,m}-1}(t^{i,j,k}, t^{i,j,k+1}]$, where $t^{i,j,0} = t^{i,j}$ and $t^{i,j,N_{s,m}} = t^{i,j+1}$. This time division is used for the saturation in the matrix domain. Because of the permeability contrast between the matrix and the fracture, the saturation in the fractures changes more rapidly than that in the matrix domain. Therefore, a smaller time-step size is required for the saturation in the fracture system; that is, we partition $(t^{i,j,k}, t^{i,j,k+1}]$ into $N_{s,f}$ time substeps as $(t^{i,j,k}, t^{i,j,k+1}] = \bigcup_{l=0}^{N_{s,f}-1}(t^{i,j,k,l}, t^{i,j,k,l+1}]$, where $t^{i,j,k,0} = t^{i,j,k}$ and $t^{i,j,k,N_{s,f}} = t^{i,j,k+1}$. Denote $\Delta t^{i,j,k} = t^{i,j,k+1} - t^{i,j,k}$ and $\Delta t^{i,j,k,l} = t^{i,j,k,l+1} - t^{i,j,k,l}$. The explicit scheme is employed for the saturation equation both in the matrix domain

$$\phi_m \frac{S_{w,m}^{i,j,k+1} - S_{w,m}^{i,j,k}}{\Delta t^{i,j,k}} + \nabla \cdot \left(f_{w,m}^{i,j,k}\mathbf{u}_{a,m}^{i,j+1}\right) = q_{w,m}^{i,j,k}, \tag{3.30}$$

and in the fracture network

$$\phi_f \frac{S_{w,f}^{i,j,k,l+1} - S_{w,f}^{i,j,k,l}}{\Delta t^{i,j,k,l}} + \nabla \cdot \left(f_{w,f}^{i,j,k,l}\mathbf{u}_{a,f}^{i,j+1}\right) = q_{w,f}^{i,j,k,l} + Q_{w,f}^{i,j,k}. \tag{3.31}$$

We use the upwind CCFD method to discretize the saturation equation (3.30)

$$|K|\phi_{m,K} \frac{S_{w,m,K}^{i,j,k+1} - S_{w,m,K}^{i,j,k}}{\Delta t^{i,j,k}} + \sum_{e\in\partial K} f_{w,e}^{i,j,k} F_{a,m,e}^{i,j+1} = q_{w,m,K}^{i,j,k}|K|. \tag{3.32}$$

Let e be the interface between the matrix gridcells K and K'; that is, $e = \partial K \cap \partial K'$. If $e \not\subseteq \Omega_f$, the term $f_{w,e}$ in (3.32) is determined by

$$f_{w,e}^{i,j,k} = \begin{cases} f_{w,m,K}^{i,j,k}, & F_{a,m,e}^{i,j+1} > 0, \\ f_{w,m,K'}^{i,j,k}, & F_{a,m,e}^{i,j+1} < 0. \end{cases} \tag{3.33}$$

If $e \subseteq \Omega_f$ is a gridcell of the fracture network, the term $f_{w,e}$ in (3.32) is determined by

$$f_{w,e}^{i,j,k} = \begin{cases} f_{w,m,K}^{i,j,k}, & F_{a,m,e}^{i,j+1} > 0, \\ \widehat{f}_{w,f,e}^{i,j,k}, & F_{a,m,e}^{i,j+1} < 0, \end{cases} \tag{3.34}$$

where

$$\widehat{f}_{w,f,e}^{i,j,k} = \frac{1}{N_{s,f}} \sum_{l=0}^{N_{s,f}-1} \frac{f_{w,f,e}^{i,j,k,l+1} + f_{w,f,e}^{i,j,k,l}}{2}. \tag{3.35}$$

It is analogous to discretize the saturation equation in the fracture system as

$$|e|\phi_{f,e} \frac{S_{w,f,e}^{i,j,k,l+1} - S_{w,f,e}^{i,j,k,l}}{\Delta t^{i,j,k,l}} + \sum_{\gamma \in \partial e} f_{w,\gamma}^{i,j,k,l} F_{a,f,\gamma}^{i,j+1} = q_{w,f,\gamma}^{i,j,k,l} |e| + Q_{w,f,e}^{i,j,k,l} |e|, \tag{3.36}$$

where e is a gridcell of the fracture network. Let $\gamma = \partial e \cap \partial e'$ where e and e' are the fracture gridcells, then we have

$$f_{w,\gamma}^{i,j,k,l} = \begin{cases} f_{w,f,e}^{i,j,k,l}, & F_{a,f,\gamma}^{i,j+1} > 0, \\ f_{w,f,e'}^{i,j,k,l}, & F_{a,f,\gamma}^{i,j+1} < 0. \end{cases} \tag{3.37}$$

The volumetric transfer across the matrix-fracture interface e is given by

$$Q_{w,f,e}^{i,j,k,l} = -\frac{\left(F_{a,m,e,K}^{i,j+1} f_{w,e,K}^{i,j,k,l} + F_{a,m,e,K'}^{i,j+1} f_{w,e,K'}^{i,j,k,l}\right)}{\varepsilon}, \tag{3.38}$$

where

$$f_{w,e,K}^{i,j,k,l} = \begin{cases} f_{w,m,K}^{i,j,k}, & F_{a,m,e,K}^{i,j+1} > 0, \\ f_{w,f,e}^{i,j,k,l}, & F_{a,m,e,K}^{i,j+1} < 0. \end{cases} \tag{3.39}$$

In the above equations, the fluxes are obtained after solving the pressure equation.

To explicitly update of the saturation in the fractures, we use the previous matrix saturation in the matrix-fracture interfaces, and then obtain the matrix-vector form of (3.36)

$$\frac{1}{\Delta t^{i,j,k,l}}\mathbf{M}_f\left(\mathbf{S}_{w,f}^{i,j,k,l+1}-\mathbf{S}_{w,f}^{i,j,k,l}\right)+\mathbf{A}_{s,f,f}^{i,j+1}\mathbf{f}_{w,f}^{i,j,k,l}+\mathbf{A}_{s,f,m}^{i,j+1}\mathbf{f}_{w,m}^{i,j,k}=\mathbf{Q}_{s,f}^{i,j,k,l}. \tag{3.40}$$

After $N_{s,f}$ smaller time-steps, we update the saturation in the matrix domain by employing the following matrix-vector form of (3.32) as

$$\frac{1}{\Delta t^{i,j,k}}\mathbf{M}_m\left(\mathbf{S}_{w,m}^{i,j,k+1}-\mathbf{S}_{w,m}^{i,j,k}\right)+\mathbf{A}_{s,m,m}^{i,j+1}\mathbf{f}_{w,m}^{i,j,k}+\mathbf{A}_{s,m,f}^{i,j+1}\widehat{\mathbf{f}}_{w,f}^{i,j,k}=\mathbf{Q}_{s,m}^{i,j,k}. \tag{3.41}$$

In (3.40) and (3.41), $\mathbf{A}_{s,m,f}^{i,j+1}$ and $\mathbf{A}_{s,f,m}^{i,j+1}$ indicate the interconnections of the saturation in the matrix blocks and fracture system.

4. Numerical Tests

Four numerical examples are provided to demonstrate the efficiency of the multiscale time splitting strategy proposed in this work. We compare it with a conventional method that takes the larger time-step for the pressure than the saturation. The conventional method is referred to the method proposed in [25] when the capillarity is taken into account, while it becomes the classical IMPES method for the case without the effect of capillarity. The two methods use the same relaxation factor for each designated example with the capillarity.

4.1. Physical and Computational Data Used in Numerical Tests

The normalized saturation S_e is given by

$$S_e=\frac{S_w-S_{rw}}{1-S_{rw}-S_{rn}}, \tag{4.1}$$

where S_{rw} and S_{rn} are the residual saturations of the wetting and nonwetting phases, respectively. The capillary pressure function [1] is given by

$$p_c(S_w)=-B_c\log(S_e), \tag{4.2}$$

where B_c is a positive parameter related to the absolute permeability. The relative permeabilities of two phases are given by

$$\begin{aligned} k_{rw}&=S_e^d,\\ k_{rn}&=(1-S_e)^d, \end{aligned} \tag{4.3}$$

where d is a positive integer number.

Table 1: Relevant data for Examples 1–4.

Parameter	Example 1	Example 2	Examples 3 and 4
Domain dimensions	10 m × 10 m × 1 m	10 m × 10 m × 1 m	20 m × 15 m × 1 m
Fracture aperture	0.01 m	0.01 m	0.01 m
ϕ_m	0.2	0.2	0.15
ϕ_f	1	1	1
$\mathbf{K}_m$ (md)	1	1	50
$\mathbf{K}_f$ (md)	10^5	10^6	10^6
μ_w (cP)	1	1	1
μ_n (cP)	0.5	0.65	0.6
d	3	3	2
$B_{c,m}$ (bar)	0.15	0.1	0.003 (Example 3)
$B_{c,f}$ (bar)	10^{-3}	10^{-4}	10^{-4} (Example 3)
S_{rw}	0	0	0
S_{rn}	0	0	0
Injection rate	0.2 PV/year	0.15 PV/year	0.2 PV/year
ω	1	1	0.5

In Examples 1 and 2, we consider the horizontal layers with the same domain dimensions 10 m × 10 m × 1 m, but containing the different networks composed of two fractures. The domain of Examples 3 and 4 is a horizontal porous medium of 20 m × 15 m × 1 m with multiple interconnected fractures. With media being horizontal, it is reasonable to neglect the effect of gravity in all examples. We simulate the displacement process of oil by water; that is, we inject the water at the left end of the medium, which void is initially fully saturated with oil, to produce the oil at the right-hand side. The fluxes towards outsides of the other boundaries vanish. There is no other injection and no extraction to the interior of the domain.

The physical an computational data is provided in Table 1, in which the subscripts "m" and "f" of some raw titles represent the matrix domain and the fracture system, respectively. In Tables 2–5, the title for column Δt represents the time-step size used for the pressure in the matrix domain if the proposed method is applied, and the other column titles are defined as in Section 3.

4.2. Example 1

In Example 1, the fracture distribution in the tested medium is provided in Figure 1. The permeabilities in the matrix blocks and the fractures are 1 md and 10^5 md, respectively. The viscosities of the water and oil are 1 cP and 0.5 cP, respectively. The injection rate is 0.2 PV/year. We use the cubic relative permeabilities. The total number of matrix and fracture gridcells is 2704 in this example. The residual saturations of water and oil are zero. The other data used in this example is provided in Table 1.

We simulate the displacement process of oil by water the saturation until 0.35 pore volume injection (PVI). Displayed in Table 2 are the time-step sizes and multiple subtiming strategy required for obtaining the stable solutions by the proposed multiscale time strategy and the conventional temporal approach. In Figures 2 and 3, we show the water saturation profiles at 0.35 PVI computed by the two methods.

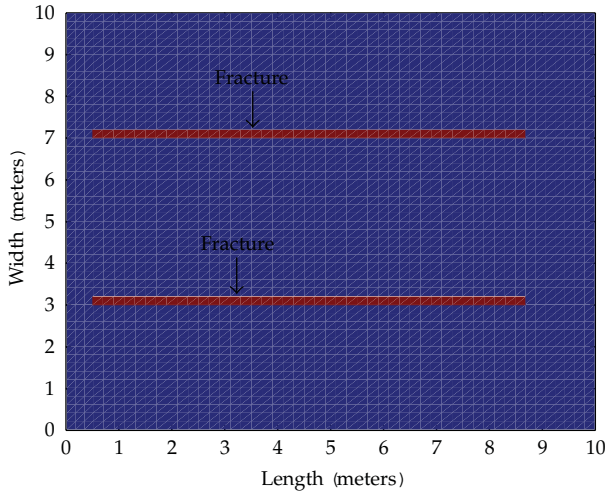

Figure 1: Distribution of fractures: Example 1.

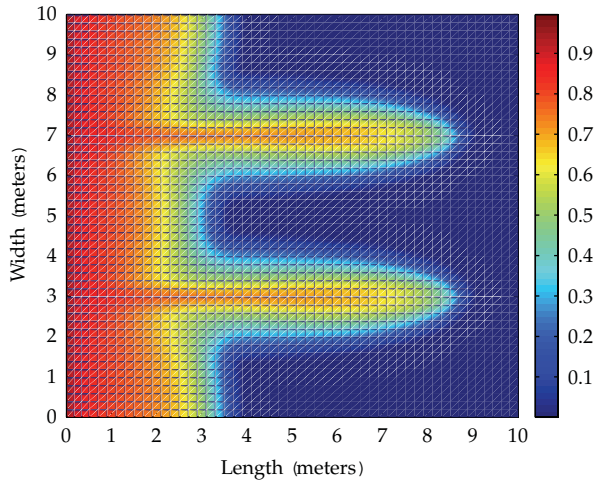

Figure 2: Water saturation profile at 0.35 PVI by the proposed method: Example 1.

In this example, the two-scale time splitting strategy is used only for the pressure equation, but with the single-scale time-stepping for the saturation equation. The two methods have the same subtiming between the pressure and the saturation, that is, $N_{s,m} = 6$. In order to achieve stable solutions, with two-scale strategy for the pressure equation, the proposed method can take the time-step size 0.9827 days, which is twice as many over the maximum time-step size 0.4121 days required by the conventional method. It is evident that the size of the pressure equation in the fine-scale time-steps is less than that in the coarse scale. Hence, this example demonstrates the efficiency of the proposed two-scale implicit treatment for the pressure equation.

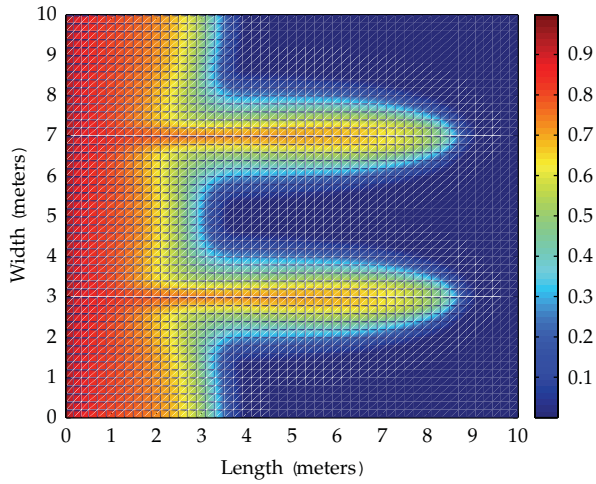

Figure 3: Water saturation profile at 0.35 PVI by the conventional method: Example 1.

Table 2: Comparison of Example 1.

Method	Δt (days)	$N_{p,f}$	$N_{s,m}$	$N_{s,f}$
New	0.9827	2	6	1
Conventional	0.4121	1	6	1

4.3. Example 2

In this example, we consider a fractured porous medium with two interconnected fractures, which is shown in Figure 4. The permeability in the fractures is 10^6 md. The viscosity of the oil is 0.65 cP. In this example, the total number of matrix and fracture gridcells is 2704. The other data used in this example is provided in Table 1. The displacement of oil by water is simulated until 0.45 PVI.

In this example, the proposed method takes the two-scale time splitting strategy for both the pressure and the saturation. The same subtiming between the pressure and the saturation are also employed in the two methods. The details are displayed in Table 3. The water saturation profiles at 0.45 PVI computed by the two methods are shown in Figures 5 and 6, respectively.

As shown in Table 3, in order to achieve stable solutions, the proposed method, with two-scale subtiming, can take a very large time-step size 1.6846 days, while the conventional method requires a very small time-step size, which is less than a tenth part of the proposed method. This example demonstrates that the two-scale time splitting strategy is efficient not only for the pressure equation, but also for the saturation equation.

4.4. Example 3

In this example, we consider a porous medium with a network composed of multiple interconnected fractures, which is shown in Figure 7. In Example 3, the total number of matrix and fracture gridcells is 3300. The commotional data used in this example is provided in Table 1. We simulate the displacement of oil by water until 0.5 PVI.

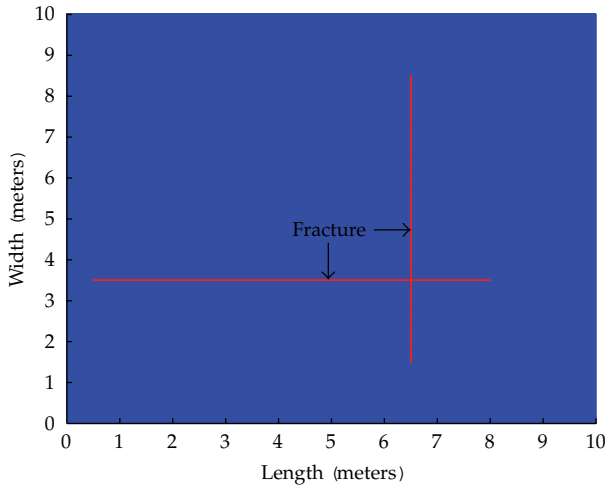

Figure 4: Distribution of fractures: Example 2.

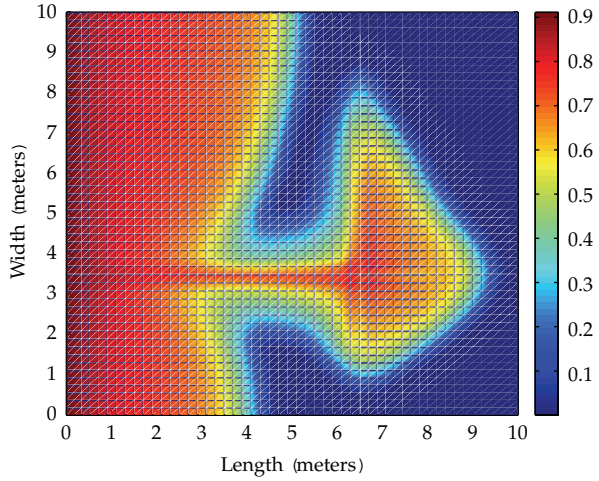

Figure 5: Water saturation profile at 0.45 PVI by the proposed method: Example 2.

Table 3: Comparison of Example 2.

Method	Δt (days)	$N_{p,f}$	$N_{s,m}$	$N_{s,f}$
New	1.6846	3	5	3
Conventional	0.1654	1	5	1

Table 4: Comparison of Example 3.

Method	Δt (days)	$N_{p,f}$	$N_{s,m}$	$N_{s,f}$
New	1.9010	8	5	2
Conventional	0.0895	1	5	1

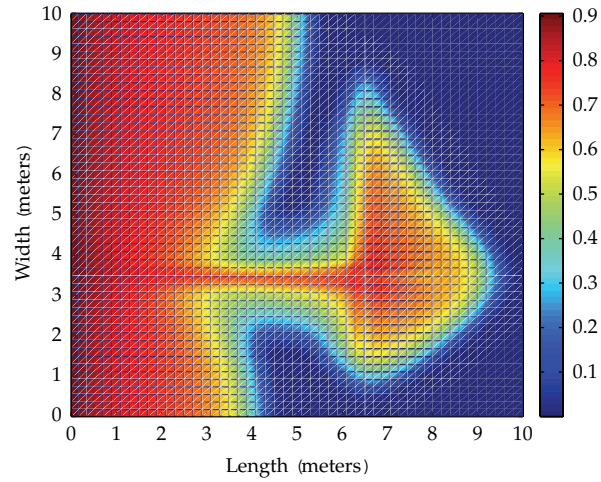

Figure 6: Water saturation profile at 0.45 PVI by the conventional method: Example 2.

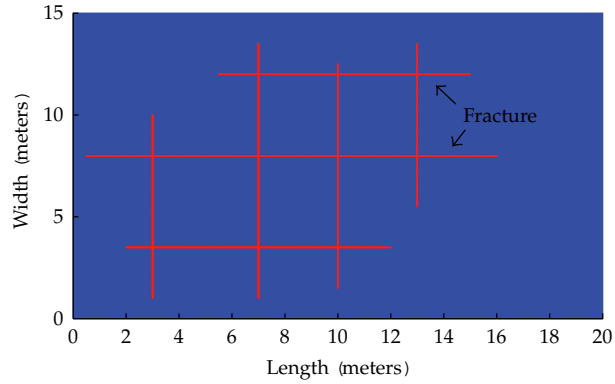

Figure 7: Distribution of fractures: Example 3.

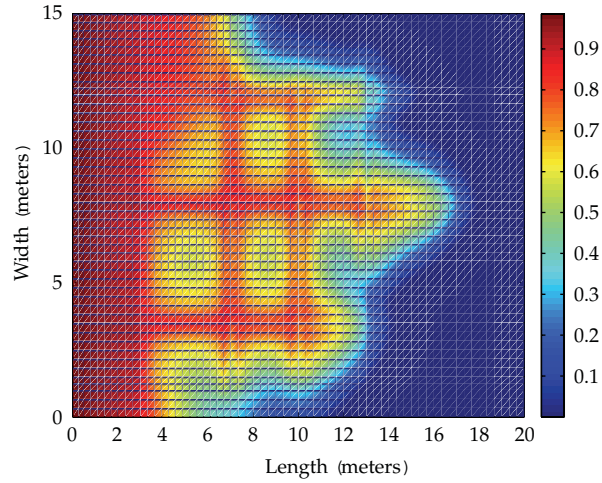

Figure 8: Water saturation profile at 0.5 PVI by the proposed method: Example 3.

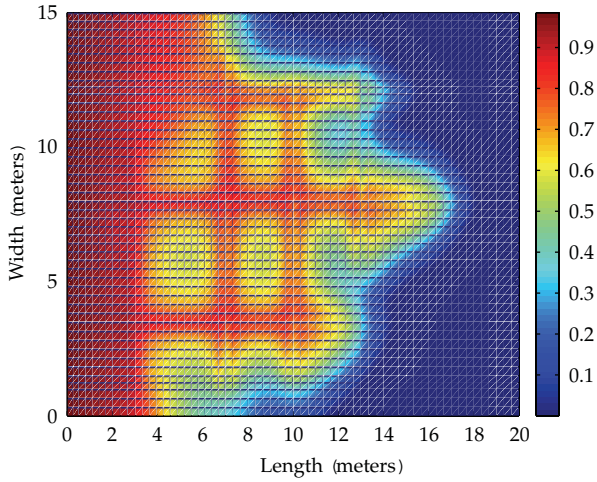

Figure 9: Water saturation profile at 0.5 PVI by the conventional method: Example 3.

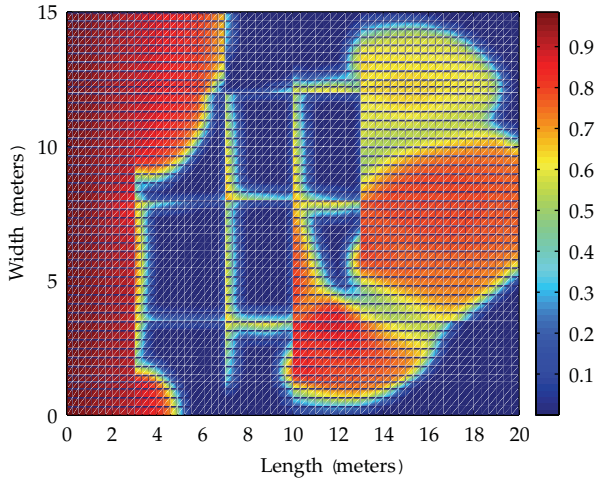

Figure 10: Water saturation profile at 0.5 PVI by the proposed method: Example 4.

In this example, we use the proposed method with two-scale time splitting strategy for both the pressure and the saturation, along with the subtiming approach between the pressure and the saturation that is also employed in the conventional method. The details are provided in Table 4. Figures 8 and 9 show the water saturation profiles at 0.5 PVI computed by the two methods, respectively.

From Table 4, we can see that the multiscale time splitting technique is capable of taking a very large time-step size 1.9010 days to achieve stable solutions. The conventional method, however, requires a very small time-step size, that is, 0.0895 days, which is the maximum time-step size for its stability with $N_{s,m} = 5$. Apparently, the multiscale time splitting strategy is superior to the conventional method for the multiple-fractured media.

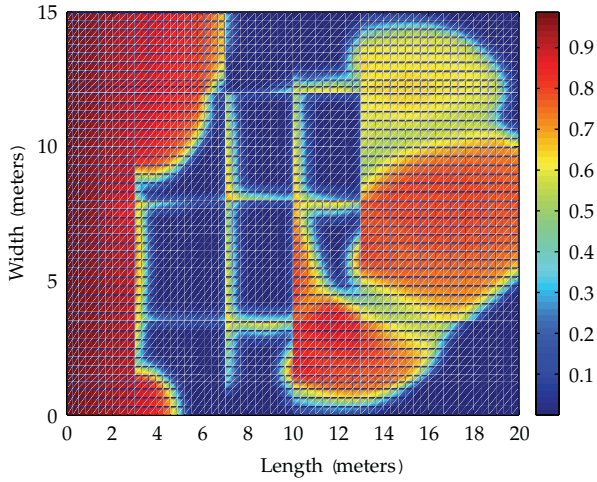

Figure 11: Water saturation profile at 0.5 PVI by the conventional method: Example 4.

Table 5: Comparison of Example 4.

Method	Δt (days)	$N_{p,f}$	$N_{s,m}$	$N_{s,f}$
New	4.5625	9	5	2
Conventional	0.1967	1	5	1

4.5. Example 4

In this example, we attempt to provide the performance of the proposed method for the case neglecting the capillarity. The domain, fluid and computational parameters of this example are the same to Example 3, but the capillarity is absent in this example. The displacement of oil by water is also simulated until 0.5 PVI.

Displayed in Table 5 is the comparison of the proposed multiscale time splitting strategy and the conventional method. Figures 10 and 11 are the water saturation profiles at 0.5 PVI computed by the two methods, respectively. From Figures 10 and 11, we can see that without the effect of capillary pressure contrast at the matrix-fracture interfaces, the water flows very quickly through the fractures. The results in Table 5 indicate that the proposed multiscale time splitting method is still efficient.

5. Conclusions

A multiscale time splitting strategy is introduced for simulating two-phase flow in fractured porous media. In the fractured porous media, the fracture system is high permeable, but with the very small storage. With different capillary pressure functions being imposed in the matrix blocks and the fracture network, the discontinuity of the saturation on the matrix-fracture interface results from the continuity of capillary pressure. As a result, the conventional single-scale temporal schemes have shortage to handle the complexity of the multiphysics processes of two-phase flow. In this paper, we use multiscale time schemes for both the pressure and saturation equations. Based on the conception proposed in [25], the capillary pressure is treated implicitly in the pressure equation, but the saturation

is yet explicitly updated. Our multiscale time splitting approach divides the total time interval into four temporal levels; the first level is used for the pressure in the entire domain, the second level matches the rapid changes of the pressure in the fractures, the third level is used to treat the response gap between the pressure and saturation, and the fourth level is used to match the fast changes of the saturation in the fracture system.

Numerical (Examples 1–3) demonstrate that when the effect of capillarity is considered, the multiscale time splitting approach can take a very large time-step size to achieve stable solutions, but a very small time-step size is required by the conventional method. The computational efficiency can be improved as it can reduce the cost of implicit solution of the pressure equation. Example 4 indicates that the proposed method is also efficient for the case without capillarity.

Acknowledgment

The authors cheerfully appreciate the generous support of the university research fund to the Computational Transport Phenomena Laboratory at KAUST.

References

[1] H. Hoteit and A. Firoozabadi, "Numerical modeling of two-phase flow in heterogeneous permeable media with different capillarity pressures," *Advances in Water Resources*, vol. 31, no. 1, pp. 56–73, 2008.

[2] R. G. Baca, R. C. Arnett, and D. W. Langford, "Modelling fluid flow in fractured-porous rock masses by finite-element techniques," *International Journal for Numerical Methods in Fluids*, vol. 4, no. 4, pp. 337–348, 1984.

[3] G. Barenblatt, Y. Zheltov, and I. Kochina, "Basic concepts in the theory of seepage of homogeneous fluids in fissurized rocks," *Journal of Applied Mathematics and Mechanics*, vol. 24, no. 5, pp. 1286–1303, 1983.

[4] Z. Chen, G. Huan, and Y. Ma, *Computational Methods for Multiphase Flows in Porous Media*, Computational Science & Engineering, SIAM, Philadelphia, Pa, USA, 2006.

[5] K. Ghorayeb and A. Firoozabadi, "Numerical study of natural convection and diffusion in fractured porous media," *SPE Journal*, vol. 5, no. 1, pp. 12–20, 2000.

[6] H. Hoteit and A. Firoozabadi, "Multicomponent fluid flow by discontinuous Galerkin and mixed methods in unfractured and fractured media," *Water Resources Research*, vol. 41, no. 11, pp. 1–15, 2005.

[7] H. Hoteit and A. Firoozabadi, "An efficient numerical model for incompressible two-phase flow in fractured media," *Advances in Water Resources*, vol. 31, no. 6, pp. 891–905, 2008.

[8] H. Kazemi, "Pressure transient analysis of naturally fractured reservoirs with uniform fracture distribution," *Society of Petroleum Engineers Journal*, vol. 9, no. 4, pp. 451–462, 1969.

[9] H. Kazeml, J. R. Gilman, and A. M. Elsharkawy, "Analytical and numerical solution of oil recovery from fractured reservoirs with empirical transfer functions," *SPE Reservoir Engineering (Society of Petroleum Engineers)*, vol. 7, no. 2, pp. 219–227, 1992.

[10] H. Kazemi and L. S. Merrill, "Numerical simulation of water imbibition in fractured cores," *Old SPE Journal*, vol. 19, no. 3, pp. 175–182, 1979.

[11] S. H. Lee, C. L. Jensen, and M. F. Lough, "Efficient finite-difference model for flow in a reservoir with multiple length-scale fractures," *SPE Journal*, vol. 5, no. 3, pp. 268–275, 2000.

[12] J. Noorishad and M. Mehran, "An upstream finite element method for solution of transient transport equation in fractured porous media," *Water Resources Research*, vol. 18, no. 3, pp. 588–596, 1982.

[13] K. Pruess and T. N. Narasimhan, "A practical method for modeling fluid and heat flow in fractured porous media," *Society of Petroleum Engineers journal*, vol. 25, no. 1, pp. 14–26, 1985.

[14] S. Sarkar, M. N. Toksoz, and D. R. Burns, "Fluid flow simulation in fractured reservoirs," in *Report of the Annual Consortium Meeting*, 2002.

[15] L. K. Thomas, T. N. Dixon, and R. G. Pierson, "Fractured reservoir simulation," *Society of Petroleum Engineers Journal*, vol. 23, no. 1, pp. 42–54, 1983.

[16] J. E. Warren and P.J. Root, "The behavior of naturally fractured reservoirs," *Old SPE Journal*, vol. 3, no. 3, pp. 245–255, 1963.
[17] Z. Chen, G. Huan, and B. Li, "An improved IMPES method for two-phase flow in porous media," *Transport in Porous Media*, vol. 54, no. 3, pp. 361–376, 2004.
[18] K. H. Coats, "Reservoir simulation: state-of-the-art," *Society of Petroleum Engineers. American Institute of Mining, Metall. and Petroleum Engineers Papers*, 1982.
[19] K. H. Coats, "Note on Impes and some Impes-based simulation models," in *Proceedings of the 15th SPE Reservoir Simulation Symposium*, pp. 21–39, February 1999.
[20] K. H. Coats, "IMPES stability: the CFL limit," in *Proceedings of the SPE Reservoir Simulation Symposium*, 2001.
[21] K. H. Coats, "IMPES stability: selection of stable timesteps," *SPE Journal*, vol. 8, no. 2, pp. 181–187, 2003.
[22] R. G. Fagin and S. CH, "A new approach to the two-dimensional multiphase reservoir simulator," *Old SPE Journal*, vol. 6, no. 2, pp. 175–182, 1966.
[23] J. W. Sheldon, B. Zondek, and W. T. Cardwell, "One-dimensional, incompressible, noncapillary, two-phase fluid flow in a porous medium," *Transactions of the American Institute of Mining and Metallurgical Engineers*, vol. 216, pp. 290–296, 1959.
[24] L. C. Young and R. E. Stephenson, "A generalized compositional approach for reservoir simulation," *Old SPE Journal*, vol. 23, no. 5, pp. 727–742, 1983.
[25] J. Kou and S. Sun, "A new treatment of capillarity to improve the stability of IMPES two-phase flow formulation," *Computers and Fluids*, vol. 39, no. 10, pp. 1923–1931, 2010.
[26] J. Kou and S. Sun, "On iterative IMPES formulation for two phase flow with capillarity in heterogeneous porous media," *International Journal of Numerical Analysis and Modeling. Series B*, vol. 1, no. 1, pp. 20–40, 2010.
[27] Q. Lu, *A parallel multiblock/multiphysics approach for multiphase flow in porous media*, Ph.D. thesis, The University of Texas at Austin, 2000.
[28] C. Dawson, S. Sun, and M. F. Wheeler, "Compatible algorithms for coupled flow and transport," *Computer Methods in Applied Mechanics and Engineering*, vol. 193, no. 23-26, pp. 2565–2580, 2004.
[29] V. J. Ervin, E. W. Jenkins, and S. Sun, "Coupled generalized nonlinear Stokes flow with flow through a porous medium," *SIAM Journal on Numerical Analysis*, vol. 47, no. 2, pp. 929–952, 2009.
[30] S. Sun and J. Liu, "A locally conservative finite element method based on piecewise constant enrichment of the continuous Galerkin method," *SIAM Journal on Scientific Computing*, vol. 31, no. 4, pp. 2528–2548, 2009.
[31] S. Sun and M. F. Wheeler, "A posteriori error estimation and dynamic adaptivity for symmetric discontinuous Galerkin approximations of reactive transport problems," *Computer Methods in Applied Mechanics and Engineering*, vol. 195, no. 7-8, pp. 632–652, 2006.
[32] S. Sun and M. F. Wheeler, "Anisotropic and dynamic mesh adaptation for discontinuous Galerkin methods applied to reactive transport," *Computer Methods in Applied Mechanics and Engineering*, vol. 195, no. 25-28, pp. 3382–3405, 2006.
[33] S. Sun and M. F. Wheeler, "Projections of velocity data for the compatibility with transport," *Computer Methods in Applied Mechanics and Engineering*, vol. 195, no. 7-8, pp. 653–673, 2006.
[34] S. Sun and M. F. Wheeler, "Symmetric and nonsymmetric discontinuous Galerkin methods for reactive transport in porous media," *SIAM Journal on Numerical Analysis*, vol. 43, no. 1, pp. 195–219, 2005.
[35] Y. Zhang, H. Wang, and T. Tang, "Simulating two-phase viscoelastic flows using moving finite element methods," *Communications in Computational Physics*, vol. 7, no. 2, pp. 333–349, 2010.
[36] T. Belytschko and Y. Y. Lu, "Convergence and stability analyses of multi-time step algorithm for parabolic systems," *Computer Methods in Applied Mechanics and Engineering*, vol. 102, no. 2, pp. 179–198, 1993.
[37] A. Gravouil and A. Combescure, "Multi-time-step explicit—implicit method for non-linear structural dynamics," *International Journal for Numerical Methods in Engineering*, vol. 50, no. 1, pp. 199–225, 2000.
[38] M. Klisinski, "Inconsistency errors of constant velocity multi-time step integration algorithms," *Computer Assisted Mechanics and Engineering Sciences*, vol. 8, no. 1, pp. 121–139, 2001.
[39] S. M. Bhallamudi, S. Panday, and P. S. Huyakorn, "Sub-timing in fluid flow and transport simulations," *Advances in Water Resources*, vol. 26, no. 5, pp. 477–489, 2003.
[40] Y. J. Park, E. A. Sudicky, S. Panday, J. F. Sykes, and V. Guvanasen, "Application of implicit sub-time stepping to simulate flow and transport in fractured porous media," *Advances in Water Resources*, vol. 31, no. 7, pp. 995–1003, 2008.

[41] V. Singh and S. M. Bhallamudi, "Complete hydrodynamic border-strip irrigation model," *Journal of Irrigation and Drainage Engineering*, vol. 122, no. 4, pp. 189–197, 1996.

[42] V. Singh and S. M. Bhallamudi, "Hydrodynamic modeling of basin irrigation," *Journal of Irrigation and Drainage Engineering*, vol. 123, no. 6, pp. 407–414, 1997.

[43] P. Smolinski, T. Belytschko, and M. Neal, "Multi-time-step integration using nodal partitioning," *International Journal for Numerical Methods in Engineering*, vol. 26, no. 2, pp. 349–359, 1988.

[44] P. Smolinski, S. Sleith, and T. Belytschko, "Stability of an explicit multi-time step integration algorithm for linear structural dynamics equations," *Computational Mechanics. Solids, Fluids, Engineered Materials, Aging Infrastructure, Molecular Dynamics, Heat Transfer, Manufacturing Processes, Optimization, Fracture & Integrity*, vol. 18, no. 3, pp. 236–243, 1996.

[45] S. Sun and J. Geiser, "Multiscale discontinuous Galerkin and operator-splitting methods for modeling subsurface flow and transport," *International Journal for Multiscale Computational Engineering*, vol. 6, no. 1, pp. 87–101, 2008.

[46] J. E. VanderKwaak, *Numerical simulation of flow and chemical transport in integrated surface-subsurface hydrologic systems*, Ph.D. thesis, University of Waterloo, 1999.

[47] P. A. Forsyth, Jr. and P. H. Sammon, "Quadratic convergence for cell-centered grids," *Applied Numerical Mathematics*, vol. 4, no. 5, pp. 377–394, 1988.

[48] J. E. P. Monteagudo and A. Firoozabadi, "Control-volume method for numerical simulation of two-phase immiscible flow in two- and three-dimensional discrete-fractured media," *Water Resources Research*, vol. 40, no. 7, pp. W074051–W0740520, 2004.

Hindawi Publishing Corporation
Journal of Applied Mathematics
Volume 2011, Article ID 941481, 9 pages
doi:10.1155/2011/941481

Research Article

Implementing Estimation of Capacity for Freeway Sections

Chang-qiao Shao

Beijing Key Lab of Transportation Engineering, Beijing University of Technology, Beijing 100124, China

Correspondence should be addressed to Chang-qiao Shao, shaocq@bjut.edu.cn

Received 3 December 2010; Accepted 19 January 2011

Academic Editor: Shuyu Sun

Copyright © 2011 Chang-qiao Shao. This is an open access article distributed under the Creative Commons Attribution License, which permits unrestricted use, distribution, and reproduction in any medium, provided the original work is properly cited.

Based on the stochastic concept for freeway capacity, the procedure of capacity estimation is developed. Due to the fact that it is impossible to observe the value of the capacity and to obtain the probability distribution of the capacity, the product-limit method is used in this paper to estimate the capacity. In order to implement estimation of capacity using this technology, the lifetime table based on statistical methods for lifetime data analysis is introduced and the corresponding procedure is developed. Simulated data based on freeway sections in Beijing, China, were analyzed and the results indicate that the methodology and procedure are applicable and validated.

1. Introduction

In the last decades, the capacity of a freeway section is most taken as a constant value. For example, in the currently published Highway Capacity Manual (HCM2000) [1], it was still defined as the maximum hourly rate at which vehicles reasonably can be expected to traverse a point or a uniform section of a lane or roadway during a given time period under prevailing roadway, traffic, and control conditions. However, more and more investigations [2–11] showed that the traditional definition of capacity cannot explain the traffic phenomena such as traffic breakdown occurring at various flow rate levels. And it is shown that the freeway capacity is not a deterministic but a stochastic phenomenon.

Despite the fact that traditional definition of capacity has played an important role in traffic planning, design, and operational analysis, it was challenged due to the inadequacy and impracticality. As a result, a stochastic concept for freeway capacity was defined and new methods were suggested [6–8]. But how to estimate capacity based on the new concept and methods was not discussed in detail.

The aim of this paper is to develop a procedure for estimating the capacity of a freeway section based on the stochastic concept for freeway capacity. To fulfill this purpose, the traffic flow rate is divided into several intervals according to the surveyed data and requirement of capacity estimation precision. Based on the data, the distribution of traffic breakdown flow was estimated using maximum likelihood estimation. Then, the definition of capacity based on the probability of breakdown was used and the capacity compute model was developed. In order to illustrate how to use the method and traffic breakdown data to estimate the capacity of a freeway section, the simulation result was provided.

2. Literature Review

In order to understand the freeway capacity, researchers have made great efforts to model and describe stochastic nature of freeway capacity and breakdown phenomenon. Polus and Pollatschek [2] studied the stochastic nature of freeway capacity and used Gamma distribution to describe the capacity. But the definition of capacity is still based on the maximum flow rates. Lorenz and Elefteriadou [6, 7] examined the process of breakdown in detail and noted that the current HCM freeway capacity definition does not accurately reflect the relationship between breakdown and flow rate. They also suggested that freeway capacity should be described by incorporating a probability of breakdown component in the definition. Brilon et al. [8] introduced a new understanding of freeway capacity as the traffic flow below which traffic still flows and above which the traffic breaks down. In their study, a traffic breakdown is regarded as a failure event and the Product Limit Method for lifetime data analysis was used to estimate the capacity. Elefteriadou et al. [9] studied the breakdown flow rates. It was found that breakdown may occur at flows lower than the capacity and that breakdown is a probabilistic event. A linear model for describing the process of breakdown at ramp-freeway junction was developed. Elefteriadou and Ponlathep [10] examined the breakdown flow, prebreakdown flow, and maximum discharge flow to determine which one would be more appropriate for use in defining the "capacity" of a freeway. It was recommended that the breakdown flow be used. But they also pointed out that the numerical value of each of these three parameters varies and their range is relatively large, in the order of several hundred veh/h/lanes. Ozbay and Ozguven [11] provided the parameter estimating method for capacity probability distribution. It was concluded that including random component in the model results in better representation of observed data and thus improves understanding of real-life situation.

From the efforts of these researches, it is concluded that there is variability in the maximum flow rates and that the breakdown flows vary greatly. The breakdown phenomenon and breakdown flow rate should be considered in the model. So, the traditional definition of freeway capacity is not proper, and the definition based on probability distribution should be the better one.

3. Methodology

According to the definition of traffic breakdown, when the traffic flow exceeds the capacity, the traffic will break down. Hence, the capacity cannot be observed directly. The breakdown flow rate which is defined as the flow rate [7] (expressed as a per-lane, equivalent hourly rate) observed immediately prior to breakdown is used to estimate the capacity. Due to the fact that the breakdown flow rate is not the real observed value of capacity, the lifetime analysis method was used to model the capacity distribution and based on it a procedure is suggested to estimate the capacity.

3.1. The Theory of Lifetime Data Analysis and Product Limit Method

In order to capture the real-life situation of the freeway capacity, a lifetime analysis application was proposed by Brilon et al. [8]. The capacity was regarded as a random variable C having its distribution as

$$F_c(q) = P(C < q), \tag{3.1}$$

where $F_c(q)$ is the probability function of capacity C, C is the freeway capacity, and q is the flow rate.

According to the definition of breakdown, when the traffic flow rate q reaches the capacity C, breakdown will occur. Therefore, the $F_c(q)$ is also the probability that the breakdown occurs at the flow rate q.

Analogically, the capacity survival function was defined to describe the probability that when traffic flow is above capacity, the traffic breakdown does not occur:

$$S_c(q) = P(C > q), \tag{3.2}$$

where $S_c(q)$ is the survival function.

In addition, the "product-limit method" [8] can be used to estimate the capacity survival function and capacity distribution function as

$$\begin{aligned} \widehat{S}_c(q) &= \prod_{i:q_i \le q} \frac{n_i - d_i}{n_i}, \\ \widehat{F}_c(q) &= 1 - \prod_{i:q_i \le q} \frac{n_i - d_i}{n_i}, \end{aligned} \tag{3.3}$$

where $\widehat{S}_c(q)$ is the estimate of survival function, q is the flow rate, q_i is the traffic flow rate in interval i, n_i is the number of intervals with traffic flow rate $q \le q_i$ and breakdown does not occur, $i = 1, \ldots, k+1$, d_i is the observed number of breakdown at a flow rate of q_i, $i = 1, \ldots, k+1$, and $\widehat{F}_c(q)$ is the estimated probability function of capacity C.

Equation (3.3) is the basis of estimating freeway capacity distribution, and it is directly transplanted from the lifetime data analysis. However, there is some difference between traffic data and lifetime data. First, to the lifetime data, the real individual death time can be observed in theory, but to the traffic flow, breakdown often lags traffic flow rate (traffic breakdown does not occur immediately after traffic flow overruns the capacity), and the observed time interval has a great effect on the analysis result. Second, there are "censored" observations which are used to explain that some individuals' explicit lifetimes are not observed in the lifetime data. In this sense, all traffic flow rates are "censored" data due to the reason that the capacity is not deterministic and it cannot be observed directly. If all the flow rates are taken into account, the capacity will be underestimated because that breakdown only occurred at few time intervals and it even can be taken as a small probability event. For example, for some days, the breakdown only occurred during morning and afternoon peak hours. If the time interval is 5 minutes, the probability of breakdown is only 1/144. Thereby, it is not appropriate to use observed traffic flow rate for all time intervals to estimate the capacity. In other words, only breakdown flow rates should be used.

3.2. Estimation of the Freeway Capacity Distribution

Based on the above analysis, only the breakdown flow rates are used to estimate the capacity. A procedure is developed as follows by using lifetime table method and theory in survival analysis [12].

Step 1. The breakdown traffic flow rates are divided into $k+1$ intervals and the jth interval is noted as $I_j = [a_{j-1}, a_j)$, $(j = 1, \ldots, k+1)$, where a_0 can be determined by $a_0 = \min\{q_i,\ i = 1, \ldots, N\} - q_0$, where q_i is the observed traffic breakdown flow rate at which the ith traffic breakdown occurs, N is the number of observed traffic breakdowns, q_0 is a constant greater than 0; $a_j = a_0 + h \times j,\ j = 1, \ldots, k$, where h is the interval length (h can be determined according to the requirement of estimation precision), $a_{k+1} = +\infty$.

Step 2. Calculate the statistics. Let N_j be the number of traffic breakdowns with a traffic flow rate $q > a_{j-1}$, d_j the number of traffic breakdowns with a traffic flow at the interval of $I_j = [a_{j-1}, a_j)$, $P(j)$ the probability that traffic breakdown does not occur with traffic flow rate $q < a_j$, p_j the probability that traffic breakdown does not occur with flow rate of $q < a_j$ while on the condition that traffic breakdown does not occur with flow rate of $q < a_{j-1}$, and $q(j)$ the probability that traffic breakdown occurs with a traffic volume at the interval of $I_j = [a_{j-1}, a_j)$ while on the condition that traffic breakdown does not occur with flow rate of $q < a_{j-1}$.

Then the following results can be obtained:

$$P(0) = 1, \tag{3.4}$$

$$P(k+1) = 0, \tag{3.5}$$

$$N_j = N_{j-1} - d_{j-1}, \tag{3.6}$$

$$p_j = \frac{P(j)}{P(j-1)}, \tag{3.7}$$

$$q(j) = 1 - p_j, \tag{3.8}$$

$$P(j) = p_1 p_2 \cdots p_j. \tag{3.9}$$

Step 3. Estimate the distribution of freeway capacity.

According to the knowledge of the probability theory [12], the number of traffic breakdowns $d_1, d_2, \ldots, d_k$ which are observed on the volume interval $I_1, I_2, \ldots, I_k$ has a multinomial distribution

$$P(d_1, d_2, \ldots, d_k) = \frac{N!}{d_1! \cdots d_k!} \prod_{i=1}^{k+1} \left(P_{j-1} - P_j\right)^{d_i}. \tag{3.10}$$

Inputing (3.7) and (3.8) into (3.10), it is derived that

$$P(d_1, d_2, \ldots, d_k) = \frac{N!}{d_1! \cdots d_k!} \prod_{i=1}^{k+1} q(j)^{d_j} \left[1 - q(j)\right]^{N_j - d_j}, \tag{3.11}$$

Table 1: Lifetime table for capacity analysis.

$I_j = [a_{j-1}, a_j)$	d_j traffic breakdown occurred in I_j	$N_j = n - d_1 - \cdots - d_{j-1}$	$\hat{q}(j) = d_j/N_j$	$\hat{P}_j = 1 - \hat{q}(j)$	$\hat{P}(j)$
$[a_0, a_1)$	d_1	N_1	$\hat{q}(1)$	$\hat{P}_1$	$\hat{P}(1)$
$[a_1, a_2)$	d_2	N_2	$\hat{q}(2)$	$\hat{P}_2$	$\hat{P}(2)$
$\vdots$	$\vdots$	$\vdots$	$\vdots$	$\vdots$	$\vdots$

where $N_j = n - d_1 - \cdots - d_{j-1}$. Using the maximum likelihood estimation (MLE) method, the MLE of $q(j)$ and $P(j)$ can be obtained:

$$\hat{q}(j) = \frac{d_j}{N_j}, \tag{3.12}$$

$$\hat{P}(j) = \hat{p}_1 \hat{p}_2 \cdots \hat{p}_j, \tag{3.13}$$

where $\hat{p}_j = 1 - \hat{q}(j)$. And freeway capacity can be estimated by (3.13).

In order to use the procedure simply, the "lifetime table" for capacity can be made referring to lifetime table methods used in the survival analysis [12]. Table 1 provides the lifetime table for capacity analysis, and the distribution of capacity can be estimated using it.

3.3. The Capacity Definition and Calculation Based on Traffic Breakdown Probability

According to the definition of freeway capacity based on the breakdown probability, "the rate of flow along a uniform freeway segment corresponding to the expected probability of breakdown was deemed acceptable under prevailing traffic and roadway conditions in a specified direction" [6]. The principle and method of estimating the freeway capacity can be illustrated as follows for the given acceptable breakdown probability $\alpha (0 < \alpha < 1)$, there exists a value of "j" and flow rate "q" which satisfies $\hat{P}_j < 1 - \alpha \leq \hat{P}_{j-1}$, and $a_{j-1} \leq q < a_j$ ($\hat{P}(j) = \hat{p}_1 \hat{p}_2 \cdots \hat{p}_j$ can be derived from formula (3.13) or Table 1. Then the value of "q" is one of the estimates of capacity C and it can be computed as follows.

(1) If $1 - \alpha = \hat{P}_j$, the capacity C can be estimated by

$$\hat{C} = \frac{[a_j + a_{j-1}]}{2}. \tag{3.14}$$

(2) If $\hat{P}_j < 1 - \alpha < \hat{P}_{j-1}$, the capacity C can be estimated as

$$\hat{C} = a_{j-1}. \tag{3.15}$$

Applying (3.14) or (3.15) to estimate capacity, the accuracy is closely related to the division of interval $I_j = [a_{j-1}, a_j)$ $(j = 1, \ldots, k)$. In order to improve the accuracy, one way is to divide more intervals.

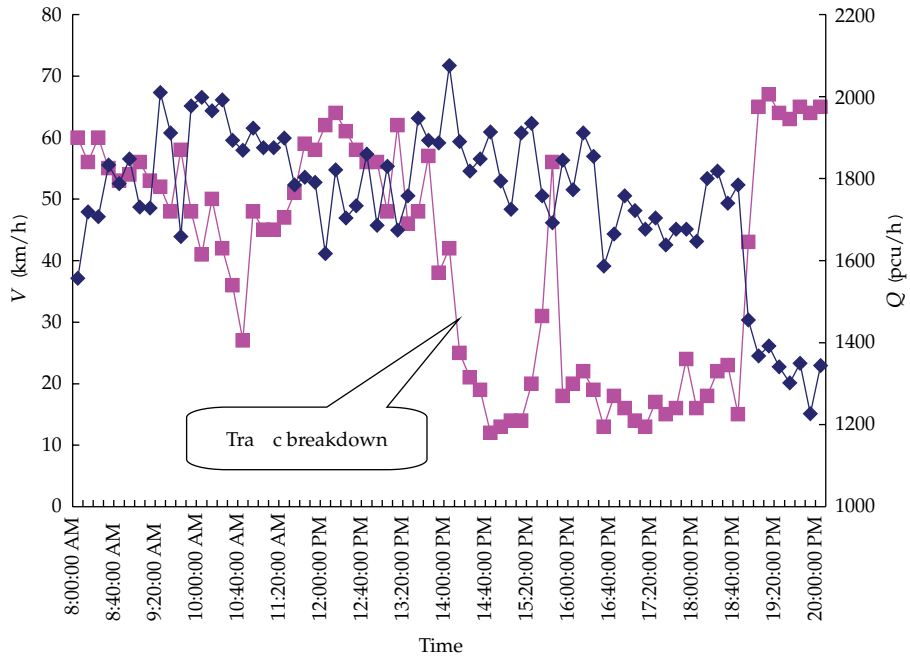

Figure 1: Time serial of traffic flow rates and speed.

Table 2: The statistical result of speed before breakdown.

Lane location	25% percentile	Median (km/h)	Mean (km/h)	75% percentile	Std. deviation	Minimum (km/h)	Maximum (km/h)
First lane inside	46.5	53.0	51.7	56.0	5.39	44.0	61.0
First lane outside	46.0	54.0	52.4	57.0	6.45	41.0	61.0

4. Empirical Analysis

4.1. Field Data Collection and Data Analysis

The field data were collected on the 3rd ring in Beijing City, China, by using microwave detectors. The posted speed limit on the 3rd ring is 80 km/h. Traffic volume is generally heavy and breakdowns are typical during morning and afternoon peak periods. One-month-period data are used in this paper for both traffic directions.

Figure 1 illustrates volume and speed changes on time-series plot. It is found from the figure that when traffic breakdown occurs, the speed of traffic flow will drop suddenly and the average speed will be less than a given threshold. Tables 2 and 3 represent the statistical results of the speed before and after breakdown in 10-minute analysis intervals. According to the analysis results, it is found that the speed value is lower than 35 km/h after breakdown and that the average speed is higher than 40 km/h.

Tables 4 and 5 are the statistical results of the flow rates before and after breakdown in 10-minute analysis intervals. It can be found that the average of flow rates after breakdown is higher than the one before breakdown and that the flow rates after breakdown are more stable then breakdown flow rates.

Table 3: The statistical result of speed after breakdown.

Lane location	25% percentile	Median (km/h)	Mean (km/h)	75% percentile	Std. deviation	Minimum (km/h)	Maximum (km/h)
First lane inside	20.5	27.0	25.5	30.0	5.35	18.0	33.0
First lane outside	21.3	24.0	24.0	28.0	4.50	17.0	31

Table 4: The statistics of flow rate before breakdown.

Lane location	25% percentile	Median (pcu/h/lane)	Mean (pcu/h/lane)	75% percentile	Std. deviation	Minimum (pcu/h/lane)	Maximum (pcu/h/lane)
First lane inside	1716	1878	1822	1966	190	1453	2067
First lane outside	1754	1857	1770	1943	279	1053	2052

Table 5: The statistics of flow rate after breakdown.

Lane location	25% percentile	Median (pcu/h/lane)	Mean (pcu/h/lane)	75% percentile	Std. deviation	Minimum (pcu/h/lane)	Maximum (pcu/h/lane)
First lane inside	1834	1863	1875	1987	132	1611	2085
First lane outside	1832	1893	1879	1992	139	1611	2085

4.2. Simulation Analysis Based on Field Data

Based on data collection and data analysis, the traffic flow is simulated by Monte-Carlo method and simulated data were used to validate the method and to demonstrate how to estimate the freeway capacity using the procedure. Tables 6, 7, and 8 list the estimated distributions of the freeway capacity for the inside lane, median lane, and shoulder lane, respectively.

If the acceptable breakdown probability is taken as $\alpha = 20\%$, then the estimated capacity is 1950 veh/h/lane, 1870 veh/h/lane, and 1850 veh/h/lane, respectively, for the three lanes. Also, the capacities for the three lanes are calculated using speed-volume relationship and the results are 2060 veh/h/lane, 2040 veh/h/lane, and 1990 veh/h/lane (The probability that breakdown occurs with the flow rates 2060 veh/h/lane, 2040 veh/h/lane, and 1990 veh/h/lane is also obtained as 0.63, 0.77, and 0.64), which is more than the expectation values of the breakdown flow rates. Therefore, the capacity based on the breakdown probability is more moderate than the traditional defined capacity comparatively.

5. Conclusion and Future Research

Based on the exiting research, the breakdown flow rate is determined to be used to study the capacity of the freeway sections in this paper. Due to the fact that, when the traffic flow approaches the level of capacity, breakdown will occur, it is impossible to observe the value of the capacity. The product-limit method is suggested to estimate the capacity. In order to complete this method, the lifetime table method and the estimate procedure are suggested. The results indicate that the lifetime table method and the suggested procedure are feasible and reasonable.

Table 6: Estimation result of the capacity distribution for the inside lane.

$I_j = [a_{j-1}, a_j)$	d_j	N_j	$\hat{q}(j)$	$\hat{p}_j = 1 - \hat{q}(j)$	$\hat{P}(j)$
[1740, 1790)	2	200	0.010	0.990	0.990
[1790, 1840)	1	198	0.005	0.995	0.985
[1840, 1890)	9	197	0.046	0.954	0.940
[1890, 1940)	11	188	0.059	0.941	0.885
[1940, 1990)	22	177	0.124	0.876	0.775
[1990, 2040)	38	155	0.245	0.755	0.585
[2040, 2090)	43	117	0.368	0.632	0.370
[2090, 2140)	28	74	0.378	0.622	0.230
[2140, 2190)	22	46	0.478	0.522	0.120
[2190, 2240)	15	24	0.625	0.375	0.045
[2240, 2290)	5	9	0.556	0.444	0.020
[2290, 2340)	3	4	0.750	0.250	0.005
[2340, 2390)	1	1	1.000	0.000	0.000
>2390		0			

Table 7: Estimation result of the capacity distribution for the median lane.

$I_j = [a_{j-1}, a_j)$	d_j	N_j	$\hat{q}(j)$	$\hat{p}_j = 1 - \hat{q}(j)$	$\hat{P}(j)$
[1720, 1770)	1	203	0.005	0.995	0.995
[1700, 1750)	3	202	0.015	0.985	0.980
[1750, 1800)	7	199	0.035	0.965	0.946
[1800, 1850)	11	192	0.057	0.943	0.891
[1850, 1900)	24	181	0.133	0.867	0.773
[1900, 1950)	39	157	0.248	0.752	0.581
[1950, 2000)	41	118	0.347	0.653	0.379
[2000, 2050)	30	77	0.390	0.610	0.232
[2050, 2100)	29	47	0.617	0.383	0.089
[2100, 2150)	8	18	0.444	0.556	0.049
[2150, 2200)	3	10	0.300	0.700	0.034
[2200, 2250)	6	7	0.857	0.1423	0.005
[2250, 2300)	1	1	1.000	0.000	0.000
>2300	0	0			

Table 8: Estimation result of the capacity distribution for the shoulder lane.

$I_j = [a_{j-1}, a_j)$	d_j	N_j	$\hat{q}(j)$	$\hat{p}_j = 1 - \hat{q}(j)$	$\hat{P}(j)$
[1700, 1840)	11	198	0.056	0.944	0.944
[1840, 1890)	28	187	0.150	0.850	0.803
[1890, 1940)	28	159	0.176	0.824	0.662
[1940, 1990)	59	131	0.450	0.550	0.364
[1990, 2040)	59	72	0.819	0.181	0.066
[2040, 2090)	9	13	0.692	0.308	0.020
[2090, 2140)	4	4	1.000	0.000	0.000
>2140		0			

However, there are still some problems to be solved in the future.

(1) The effect of geometric characteristics and traffic condition on the breakdown probability should be studied. Only by this, the research result may be applied generally.

(2) An acceptable breakdown probability value should be determined. This value reflects the balance between risk of breakdown and higher traffic volume. So, it is determined by the operating agency and questionnaires should be conducted.

(3) The definition of breakdown flow rate should be studied. Although, in this paper, the breakdown flow rate is defined as the flow rate observed immediately prior to breakdown, there are still some questions need to be answered, such as should the traffic flow be obtained for 5-minute, 10-minute, or 15-minute time interval prior to breakdown?

References

[1] Transportation Research Board, *Highway Capacity Manual*, National Research Council, Washington, DC, USA, 2000.

[2] A. Polus and M. A. Pollatschek, "Stochastic nature of freeway capacity and its estimation," *Canadian Journal of Civil Engineering*, vol. 29, no. 6, pp. 842–852, 2002.

[3] L. Zhang and L. David, "Some properties of flows at freeway bottlenecks," in *Proceedings of the 83rd Transportation Research Board's Annual Meeting*, National Research Council, Washington, DC, USA, 2004.

[4] Z. Tian, M. Kyte, and R. Bertini, "New perspectives on the two-capacity phenomenon in freeway operations," in *Proceedings of the 84th Transportation Research Board's Annual Meeting*, National Research Council, Washington, DC, USA, 2005.

[5] F. L. Hall and K. Agyemang-Duah, "Freeway capacity drop and the definition of capacity," *Transportation Research Record*, vol. 1320, pp. 91–97, 1991.

[6] M. R. Lorenz and L. Elefteriadou, "Defining freeway capacity as function of breakdown probability," *Transportation Research Record*, no. 1776, pp. 43–51, 2001.

[7] M. Lorenz and L. Elefteriadou, "A probabilistic approach to define freeway capacity and breakdown," in *Proceedings of the 4th International Symposium on Highway Capacity*, 2000.

[8] W. Brilon, J. Geistefeldt, and M. Regler, "Reliability of freeway traffic flow: a stochastic concept of capacity," in *Proceedings of the 4th International Symposium on Highway Capacity*, pp. 84–95, 2000.

[9] L. Elefteriadou, R. P. Roess, and W. R. McShane, "Probabilistic nature of breakdown at freeway merge junctions," *Transportation Research Record*, no. 1484, pp. 80–89, 1995.

[10] L. Elefteriadou and L. Ponlathep, "Defining, measuring and estimating freeway capacity," in *Proceedings of the 82nd Transportation Research Board's Annual Meeting*, National Research Council, Washington, DC, USA, 2003.

[11] K. Ozbay and E. E. Ozguven, "A comparative methodology for estimating the capacity of a freeway section," in *Proceedings of the 10th International IEEE Conference on Intelligent Transportation Systems (ITSC '07)*, pp. 1034–1039, October 2007.

[12] J. F. lawless, *Statistical Models and Methods for Lifetime Data*, China Statistics Press, Beijing, China, 2001.

Hindawi Publishing Corporation
Journal of Applied Mathematics
Volume 2011, Article ID 641920, 25 pages
doi:10.1155/2011/641920

Research Article

Modeling and Simulation of a Chemical Vapor Deposition

J. Geiser and M. Arab

Department of Mathematics, Humboldt University of Berlin, Unter den Linden 6, D-10099 Berlin, Germany

Correspondence should be addressed to J. Geiser, geiser@mathematik.hu-berlin.de

Received 29 November 2010; Accepted 17 January 2011

Academic Editor: Shuyu Sun

Copyright © 2011 J. Geiser and M. Arab. This is an open access article distributed under the Creative Commons Attribution License, which permits unrestricted use, distribution, and reproduction in any medium, provided the original work is properly cited.

We are motivated to model PE-CVD (plasma enhanced chemical vapor deposition) processes for metallic bipolar plates, and their optimization for depositing a heterogeneous layer on the metallic plate. Moreover a constraint to the deposition process is a very low pressure (nearly a vacuum) and a low temperature (about 400 K). The contribution of this paper is to derive a multiphysics system of multiple physics problems that includes some assumptions to simplify the complicate process and allows of deriving a computable mathematical model without neglecting the real-life processes. To model the gaseous transport in the apparatus we employ mobile gas phase streams, immobile and mobile phases in a chamber that is filled with porous medium (plasma layers). Numerical methods are discussed to solve such multi-scale and multi phase models and to obtain qualitative results for the delicate multiphysical processes in the chamber. We discuss a splitting analysis to couple such multiphysical problems. The verification of such a complicated model is done with real-life experiments for single species. Such numerical simulations help to economize on expensive physical experiments and obtain control mechanisms for the delicate deposition process.

1. Introduction

We motivate our research on producing high-temperature films by low-pressure deposition processes. Such deposition can only be achieved with plasma-enhanced processes; see [1]. In standard applications based on depositing binary systems such as TiN and TiC, new material classes arose. More delicate to deposit are nanolayered ternary metal-carbide or metal-nitride materials, including MAX-phase materials, while we have to control three species in the deposition process see [2].

To understand the growth of a thin film done by PE-CVD (plasma-enhanced chemical vapor deposition) processes, we have to model a complicated multiphysical process; see [3, 4].

Based on the process constraints, which are very low-pressure (nearly vacuum) and a low temperature (about 400 K), we can simplify the complicated model.

The delicate modeling part is to model the plasma, in which the deposition species, given as precursor gases, are transported; see [5]. We concentrate on plasma as an ionized medium, known as "cold" plasma or glow discharges; see [6, 7]. To model the gaseous transport of our deposition process in the cold plasma, a porous medium model with different permeable layers is an attractive simulation model; see [4]. In the chamber filled with an ionized plasma that is given as a porous medium, the gaseous transport involves several phases: mobile gas phase streams, and both immobile and adsorbed phases. For such processes, we present a multiphase and multispecies model; see [3, 8]. The species of the gaseous transport are MAX-phase materials; see [9–11], and we concentrate on Ti_3 Si C_2 molecules, so we have Ti, Si, and C in the gas phases.

Further a porous medium model with permeable layers is an attractive simulation model also for the electric field in the chamber that is used to control the gaseous transport to the deposition area. Here the expertise of similar simulation models are used; see [12].

So the transport, chemical and sorption processes in a heterogeneous medium can be used to simulate species transport in a plasma-enhanced environment, controlled by pressure, temperature and by additional electric fields. Such modeling methods have been developed in recent years and are focused on producing high-temperature films; see [4].

Fundamental models of CVD processes employ detailed descriptions of fluid flow, mass transfer, heat transfer and chemical kinetics; see [13, 14].

While having a powerful deposition process in low-temperature and low-pressure regimes, we have also taken into account some drawbacks of such a process, which is driven with ionized plasma. Here, we deal with multicomponent problems with heavier and lighter species. Such conditions have consequences in slower (strongly adsorbed) or faster traveling (weakly adsorbed) species.

The contributions of this paper are to couple numerical methods that are developed to solve such multiscale and multiphase models and to obtain qualitative results on the delicate multiphysical processes in the chamber. Here splitting schemes are applied as an attractive tool to decouple delicate processes; see [15]. We apply and analyze splitting schemes, in a way that combines discretization methods for partial differential and ordinary differential equations; see [12, 15].

The immobile, adsorbed and reaction terms can be treated with fast Runge-Kutta solvers, whereas the mobile terms are convection-diffusion equations and are solved with splitting semi-implicit finite volume methods and characteristic methods, [16].

Such a sequential treatment of the partial differential equations and ordinary differential equations allow of saving computational time, while expensive implicit Runge-Kutta methods are reduced to the partial operators and fast explicit Runge-Kutta methods are for the ordinary operators of the multiphase model.

With various source terms we control the required concentration at the final deposition area.

Different kinetic parameters allow of simulating the different time scales of the heavier and lighter gaseous species.

The numerical results are verified with physical experiments and we discuss the applications to the production of so-called metallic bipolar plates.

This paper is outlined as follows. In Section 2, we present our mathematical model based on the multiphases. In Section 3, we present the underlying physical experiments for the model equations. In Section 4, we discuss discretization and solver methods with respect to their efficiency and accuracy. The numerical experiments are given in Section 5. In Section 6, we briefly summarize our results.

2. Mathematical Modeling

In the model we have included the following multiple physical processes, related to the deposition process:

(i) flow field of the ionized plasma: Navier-Stokes equation; see [17],

(ii) transport system of the species: mobile and immobile gaseous phases with Kinetically controlled adsorption (heavier and lighter species); see [4],

(iii) electric field: Poisson equation; see [13, 18].

In the following we discuss the three models separately and combine all the models into a multiple physical model. We assume a two-dimensional domain of the apparatus with isotropic flow fields; see [17].

2.1. Flow Field

The conservation of momentum is given by (flow field: Navier-Stokes equation)

$$\begin{aligned} \frac{\partial}{\partial t}\mathbf{v} + \mathbf{v}\cdot\nabla\mathbf{v} &= -\nabla p, \quad \text{in } \Omega\times[0,t], \\ \mathbf{v}(\mathbf{x},t) &= \mathbf{v}_0(\mathbf{x}), \quad \text{on } \Omega, \\ \mathbf{v}(\mathbf{x},t) &= \mathbf{v}_1(\mathbf{x},t), \quad \text{on } \partial\Omega\times[0,t], \end{aligned} \tag{2.1}$$

where $\mathbf{v}$ is the velocity field, p the pressure, $\mathbf{v}_0$ the initial velocity field and the position vector $\mathbf{x} = (x_1, x_2)^t \in \Omega \subset \mathbb{R}^{2,+}$. Furthermore, we assume that the flow is divergence free and the pressure is predefined.

2.2. Transport Systems (Multiphase Equations)

We model the ionized plasma as an underlying medium in the chamber with mobile and immobile phases. Here transport in the plasma with gaseous species contain of mobile and immobile concentrations, [3]. For such a heterogenous plasma, we applied our expertise in modeling multiphase transport through a porous medium; see [2].

To amplify the modeling of the gaseous flow to the chamber which is filled with ionized plasma, we deal with the so-called far-field model based on a porous medium. Here the plasma can be modeled as a continuous flow [17], that has mobile and immobile phases; see [8].

We assume nearly a vacuum and a diffusion-dominated process, derived from the Knudsen diffusion, [19]. In such viscous flow regimes, we deal with small Knudsen numbers and a pressure of nearly zero. We discuss a modified model, including new system parameter spaces such as porosity and permeability, which describe the plasma flow through the reactor.

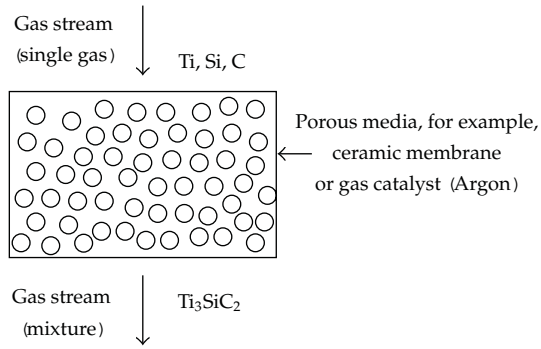

Figure 1: Chamber of the CVD apparatus.

In Figure 1, the chamber of the CVD apparatus is shown. It is modeled as a porous medium, where the porosity is given as the ratio between the void space and the total volume of the ceramic or bulk material:

$$\phi = \frac{V_v}{V_b}, \tag{2.2}$$

where V_v is the void space and V_b is the volume of the ceramic or bulk material.

For the one-phase model, the velocity v of the underlying fluid is calculated by Darcy's law and given by:

$$v = \frac{-\kappa}{\mu} \frac{\nabla p}{\phi}, \tag{2.3}$$

where κ is the permeability, ∇p is the pressure gradient, ϕ is the porosity and μ the dynamic viscosity.

To model a retarded gas concentration in the porous medium, we have to consider multiphases of the underlying fluid. The new model includes immobile and adsorbed phases, where the velocity of the fluid is zero and impermeable layers are given.

In the model, we consider both absorption and adsorption taking place simultaneously and with given exchange rates. Therefore we consider the effect of the gas concentrations' being incorporated into the porous medium.

We extend the model to two more phases:

(i) immobile phase,

(ii) adsorbed phase.

In Figure 2, the mobile and immobile phases of the gas concentration are shown in the macroscopic scale of the porous medium. Here the exchange rate between the mobile gas concentration and the immobile gas concentration control the flux to the medium.

In Figure 3, the mobile and adsorbed phases of the gas concentration are shown in the macroscopic scale of the porous medium. To be more detailed in the mobile and immobile phases, where the gas concentrations can be adsorbed or absorbed, we consider a further phase. Here the adsorption in the mobile and immobile phase is treated as a retardation and given by a permeability in such layers.

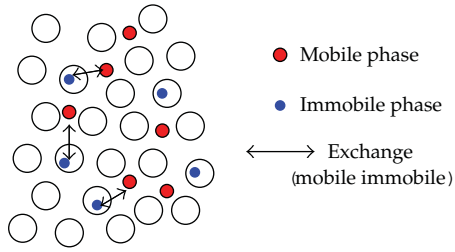

Figure 2: Mobile and immobile phase.

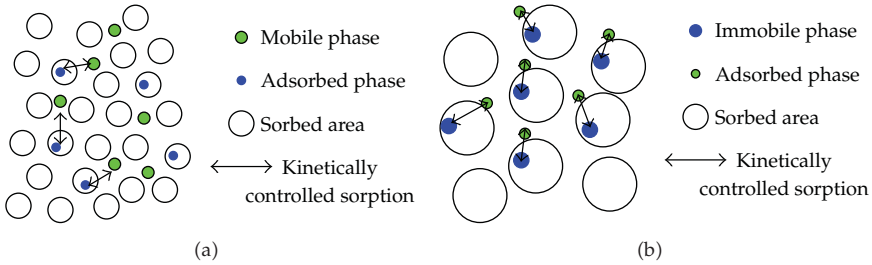

Figure 3: Mobile-adsorbed phase and immobile-adsorbed phase.

The model equations for the multiple phase equations are

$$\phi\partial_t c_i + \nabla\cdot\mathbf{F}_i = g(-c_i + c_{i,im}) + k_\alpha(-c_i + c_{i,ad}) - \lambda_{i,i}\phi c_i + \sum_{k=k(i)} \lambda_{i,k}\phi c_k + \tilde{Q}_i, \quad \text{in } \Omega\times[0,t], \tag{2.4}$$

$$\mathbf{F}_i = \mathbf{v}c_i - D^{e(i)}\nabla c_i + \eta\mathbf{E}c_i, \tag{2.5}$$

$$\phi\partial_t c_{i,im} = g(c_i - c_{i,im}) + k_\alpha(c_{i,im,ad} - c_{i,im}) - \lambda_{i,i}\phi c_{i,im} + \sum_{k=k(i)} \lambda_{i,k}\phi c_{k,im} + \tilde{Q}_{i,im}, \quad \text{in } \Omega\times[0,t], \tag{2.6}$$

$$\phi\partial_t c_{i,ad} = k_\alpha(c_i - c_{i,ad}) - \lambda_{i,i}\phi c_{i,ad} + \sum_{k=k(i)} \lambda_{i,k}\phi c_{k,ad} + \tilde{Q}_{i,ad}, \quad \text{in } \Omega\times[0,t], \tag{2.7}$$

$$\phi\partial_t c_{i,im,ad} = k_\alpha(c_{i,im} - c_{i,im,ad}) - \lambda_{i,i}\phi c_{i,im,ad} + \sum_{k=k(i)} \lambda_{i,k}\phi c_{k,im,ad} + \tilde{Q}_{i,im,ad}, \quad \text{in } \Omega\times[0,t], \tag{2.8}$$

$$c_i(\mathbf{x},t) = c_{i,0}(\mathbf{x}), \quad c_{i,ad}(\mathbf{x},t) = 0, \quad c_{i,im}(\mathbf{x},t) = 0, \quad c_{i,im,ad}(\mathbf{x},t) = 0, \quad \text{on } \Omega, \tag{2.9}$$

$$c_i(\mathbf{x},t) = c_{i,1}(\mathbf{x},t), \quad c_{i,ad}(\mathbf{x},t) = 0, \quad c_{i,im}(\mathbf{x},t) = 0, \quad c_{i,im,ad}(\mathbf{x},t) = 0, \quad \text{on } \partial\Omega\times[0,t], \tag{2.10}$$

where the initial value is given as $c_{i,0}$ and we assume a Dirichlet boundary conditions with the function $c_{i,1}(\mathbf{x},t)$ sufficiently smooth, all other initial and boundary conditions of the other phases are zero.

The parameters are given as:

ϕ: effective porosity [−],

c_i: concentration of the ith gaseous species in the plasma chamber,

$c_{i,im}$: concentration of the ith gaseous species in the immobile zones of the plasma chamber phase [mol/cm^3],

$\mathbf{v}$: velocity through the chamber and porous substrate [20] [cm/nsec],

$D^{e(i)}$: element-specific diffusions-dispersions tensor [cm^2/nsec],

$\lambda_{i,i}$: decay constant of the ith species [1/nsec],

$\tilde{Q}_i$: source term of the ith species [mol/(cm^{3}nsec)],

g: exchange rate between the mobile and immobile concentration [1/nsec],

k_a: exchange rate between the mobile and adsorbed concentration or immobile and immobile adsorbed concentration (kinetic controlled sorption) [1/nsec],

$\mathbf{E}$: stationary electricfield in the apparatus [V/cm],

η: the mobility rate in the electricfield; see [13] [cm^2/nsec],

with $i = 1, \ldots, M$ and M denotes the number of components.

The parameters in (2.4) are further described; see also [12].

The four phases are treated in the full domain, such that we have a full coupling in time and space.

The effective porosity is denoted by ϕ and declares the portion of the porosities of the aquifer that is filled with plasma, and we assume a nearly fluid phase. The transport term is indicated by the Darcy velocity $\mathbf{v}$, that presents the flow direction and the absolute value of the plasma flux. The velocity field is divergence free. The decay constant of the ith species is denoted by λ_i. Thereby, $k(i)$ denotes the indices of the other species which react with species i.

2.3. Electric Field (Distribution)

In addition, in order to find the distribution of the electric field, it is necessary to solve the Poisson equation which relates the divergence of the local electric fields to the charge density [13], and is given by

$$\nabla \cdot \mathbf{E} = \frac{e}{\epsilon_0} \sum_{i=1}^{n} Z_i c_i, \tag{2.11}$$

where e is the charge of the electron, ϵ_0 the permittivity of the gas mixture, c_i the particle density of species i and Z_i the relative charge of species i; see [21].

A general model for PECVD reactors is very complicated and we therefore simplify the model with some assumptions to obtain tractable problems.

(i) Predefined electric field $\mathbf{E}$ respecting different predefined areas Ω_j, we apply:

$$\nabla \cdot \mathbf{E} \approx \frac{e}{\epsilon_0} \sum_{i=1}^{n} Z_i \, c_{\text{const},i}|_{\Omega_j}, \tag{2.12}$$

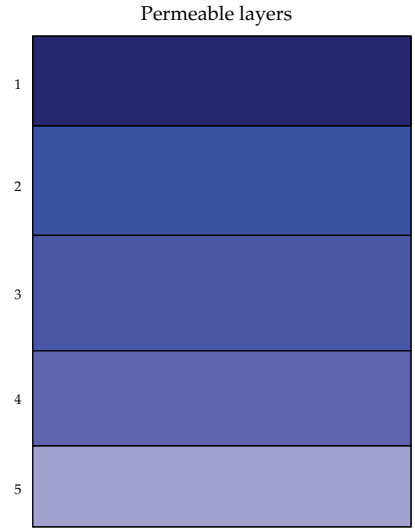

Figure 4: Electrical sectors in the domain of the apparatus.

where we assume that $c_i \approx c_{\text{const},i}$ for Ω_j is a constant particle density of species i in domain Ω_j with $j \in 1, \ldots, m$ and m is the number of domains.

(ii) The plasma chemistry in the reactor is neglected.

2.4. Multiphysics Model

We derive the multiphysics model based on the multiphase and electric field model.

We start by developing the multiphysics model in the following steps:

(i) transport system (multiphase model),

(ii) electrical field is approximated by a permeable layer (field model),

(iii) multiphysics model with multiphase transport and embedded electrical field.

We assume that the number of gas particles in the plasma atmosphere Ar (Argon) is low and the density of the particles can be treated as nearly constant.

Therefore, we can derive a constant field in each sector of the apparatus

$$\mathbf{E} \approx \mathbf{E}_{\Omega_j}, \tag{2.13}$$

where $\mathbf{E}_{\Omega_j}$ is constant and $\Omega_j \subset \Omega$ are sectors in the domain.

Such an electric field, see Figure 4, can be assumed in near-field experiments to be nearly homogeneous, where the field intensity is decreasing and can be assumed to be constant in small areas; see [4].

Next the idea is to embed the electric field into a porous medium model. A simplified model can be derived with given domain-dependent parameters and a retardation factor that includes the influence of the electric field.

First, the mobile phase equation (2.4) can be reformulated with retardation factor given by:

$$R_i \frac{\partial}{\partial t} c_i + \nabla \widetilde{F}_i - R_i R_{g,i} = 0, \quad \text{in } \Omega \times [0,t], \tag{2.14}$$

$$\widetilde{F}_i = \mathbf{v} c_i - D^{e(i)} \nabla c_i,$$

$$c_i(x,t) = c_{i,0}(x), \quad \text{on } \Omega, \tag{2.15}$$

$$c_i(x,t) = c_{i,1}(x,t), \quad \text{on } \partial\Omega \times [0,t],$$

where c_i is the particle density and $\widetilde{F}_i$ the flux of species i. $R_{g,i}$ is the reaction term of species i, meaning the right-hand side of (2.4), all other parameters as in (2.4)–(2.8). R_i is defined as a specific and constant Henry isotherm, called the retardation factor; see [22]. Such factors are known as sorption coefficients and model the rate between the mobile and immobile concentration, they are derived from experiments; see [23].

In a second step, we calculate the retardation factor, which is based on the influence of the electric field.

We subtract (2.4) from (2.14) and obtain

$$\nabla F_i = \frac{\nabla \widetilde{F}_i}{R_i}. \tag{2.16}$$

We include the assumption of the electric field dependence of the domain parts and consider

$$\left(\frac{1}{R_i} - 1\right) \nabla \left(\mathbf{v} - D^{e(i)} \nabla\right) c_i \approx \frac{e}{\epsilon_0} \sum_{k=1}^{n} Z_k \, c_{\text{const},k}|_{\Omega_j}, \quad \text{for } j = 1, \ldots, m, \tag{2.17}$$

so we obtain the derivation of R_i for a specific domain $\Omega_j \subset \Omega$ and we have:

$$R_i = \left(\frac{e}{\epsilon_0} \sum_{k=1}^{n} Z_k \, c_{\text{const},k}|_{\Omega_j} \frac{1}{\nabla (\mathbf{v} - D^{e(i)} \nabla) c_i} + 1 \right)^{-1}, \quad \text{for } \Omega_j. \tag{2.18}$$

In the third step we add the equations (2.6)–(2.8) to the modified mobile phase equation (2.14) and we obtain the full coupled system.

Here the novel contribution is to derive a full coupled system of a multiphase and multiflow problem to include all the physical processes in the chamber. Such ideas have been developed and considered in fluid dynamical models for many years [24].

Remark 2.1. For the flow through the chamber, for which we assume a homogeneous medium and nonreactive plasma, we have considered a constant flow [1]. A further simplification is given by the very small porous substrate, for which we can assume the underlying velocity to a first approximation as constant [4].

Remark 2.2. For an in-stationary medium and reactive or ionized plasma, we have to take into account the relations of the electrons in thermal equilibrium. Such spatial variation can be considered by modeling the electron drift. Such modeling of the ionized plasma is done with Boltzmanns relation, [3].

3. Physical Experiments

The base of the experimental setup is the plasma reactor chamber of a NIST *GEC reference cell*. The spiral antenna of a hybrid ICP/CCP-RF plasma source was replaced by a double spiral antenna [25]. This reduces the asymmetry of the magnetic field due to the superposition of the induced fields of both antennas. Also, the power coupling to the plasma increases and enhances the efficiency of the source. A set of MKS mass flow controllers allows any defined mixture of gaseous precursors. Even the flows of liquid precursors with high vapour pressure is controlled by this system. All other liquid and all solid precursors will be directly transported to the chamber by a controlled carrier gas flow. Besides the precursor flow, the density can also be changed by varying the pressure inside the recipient. Controlling the pressure is achieved with a valve between the recipient and vacuum pumps. In addition, a heated and insulated substrate holder was mounted. Thus, a temperature up to 800°C and a bias voltage can be applied to the substrate. While the pressure and RF power determine the undirected particle energy (plasma temperature), the bias voltage adds, only to the charged particles, energy directed at the substrate. Apart from the pressure and RF power control, the degree of ionization and number as well as the size of the molecular fractions can be controlled.

Altogether, this setup provides as free process parameters:

(i) pressure (typically 10^{-1}–10^{-2} mbar),

(ii) precursor composition (TMS, TMS + H_2, TMS + O_2),

(iii) precursor flow rate (ranging from SCCM to SLM),

(iv) RF Power (up to 1100 W),

(v) substrate temperature (RT—800°C),

(vi) bias voltage (DC, unipolar and bipolar pulsed, floating).

During all experiments, the process was observed by optical emission spectroscopy (OES) and mass spectroscopy (MS). The stoichiometry of the deposited films was analyzed *ex situ* in a scanning electron microscope (SEM) by energy dispersive X-ray analysis (EDX).

3.1. Realization of Physical Experiments

The following parameters were used for the physical experiments. Such a reduction allows of concentrating on the important flow and transport processes in the gas phase. Further, we apply the underlying mathematical model (far-field model, see Section 2.2) so that we can switch between physical and mathematical parameters (see Table 1).

(1) Precursor: Tetramethylsilan (TMS).

(2) Substrate: VA-Steel.

(3) Film at substrate: SiC_x.

Table 1: The physical experiments with the real-life apparatus.

Test	P_R (mbar)	ϑ_S (C)	P_{plasma} (W)	ϕ (TMS) (SCCM)	$\phi(H_2)$ (SCCM)	Ratio (C : Si)	Mass (growth) (g)	Time (min)
080701-01-VA	$9.7E-2$	400	900	10.23	0	0.97811	0.00012	120
080718-01-VA	$1.1E-1$	400	900	10.00	0	1.00174	0.00050	130
080718-02-VA	$4.5E-2$	400	900	10.00	0	1.24811	0.00070	110
080618-01-VA	$4.3E-2$	400	500	10.23	0	1.32078	—	127
080716-01-VA	$1.1E-1$	400	500	10.00	0	1.42544	0.00250	120
080715-02-VA	$1.1E-1$	400	100	10.00	0	1.58872	0.00337	122
080804-01-VA	$4.5E-2$	400	100	10.00	0	2.91545	0.00356	129
080630-01-VA	$9.9E-2$	800	900	10.23	0	1.09116	0.00102	120
080807-01-VA	$4.5E-2$	800	900	10.00	0	1.18078	0.00118	120
080625-01-VA	$3.9E-2$	800	500	10.23	0	1.06373	—	120
080626-01-VA	$9.3E-2$	800	500	10.23	0	1.12818	0.00174	130
080806-01-VA	$4.8E-2$	800	100	10.00	0	1.73913	0.00219	121
080715-01-VA	$1.1E-1$	800	100	10.00	0	1.62467	0.00234	120
081016-01-VA	$1.0E-1$	600	300	10.00	0	1.72898	0.00321	123
081020-01-VA	$1.1E-1$	600	300	10.00	50	1.49075	0.00249	114
081028-01-VA	$1.1E-1$	600	300	10.00	15	1.53549	0.00273	120
081023-01-VA	$1.1E-1$	600	300	10.00	10	1.54278	0.00312	127
081027-01-VA	$1.1E-1$	600	300	10.00	5.5	1.55818	0.00277	126
081024-01-VA	$1.1E-1$	600	300	10.00	3.5	1.64367	0.00299	120
081022-01-VA	$1.0E-1$	600	300	10.00	2.5	1.69589	0.00318	127

We apply the parameters in Table 2 for interpolation of the substrate temperature.

For the substrate temperature and plasma power, we use the parameters in Table 3.

Remark 3.1. In the process, the temperature and power of the plasma is important and experiments show that these are significant parameters. Based on these parameters, we initialize the mathematical model and interpolate the flux and reaction parts.

4. Discretization and Solver Methods

We distinguish between the mobile and immobile phases. Here the mobile phases are parabolic partial differential equations and the immobile phases are ordinary differential equations. So for the space-discretization of the PDE's we apply finite volume methods as mass-conserved discretization schemes and for the time-discretization of the PDE's and ODE's we apply Runge-Kutta methods.

So first we discretize in space, while we then apply a splitting method, taking into account the different matrices.

Table 2

Temperature (C)	Ratio (SiC : C)
400	2.4 : 1
600	1.5 : 1
700	1.211 : 1
800	1.1 : 1

Table 3

Temperature (C)	Power (W)	Ratio (SiC : C)
400	900	1 : 0.97
400	500	1.3 : 1
800	900	1.18 : 1

4.1. Spatial Discretization

We deal with the transport part of the mobile phase, see (2.14):

$$R_i \frac{\partial}{\partial t} c_i + \nabla \widetilde{F}_i = 0, \quad \text{in } \Omega \times [0,t], \qquad \widetilde{F}_i = \mathbf{v} c_i - D^{e(i)} \nabla c_i, \tag{4.1}$$

$$c_i(x,t) = c_{i,0}(x), \quad \text{on } \Omega, \qquad c_i(x,t) = c_{i,1}(x,t), \quad \text{on } \partial\Omega \times [0,t], \tag{4.2}$$

For the convection part, we use a piecewise constant finite volume method with upwind discretization; see [26]. For the diffusion-dispersion part, we also apply a finite volume method and we assume the boundary values are denoted by $\mathbf{n} \cdot D^{e(i)} \nabla c_i(x,t) = 0$, where $x \in \Gamma$ is the boundary $\Gamma = \partial\Omega$; compare with [27]. The initial conditions are given by $c_i(x,0) = c_{i,0}(x)$.

We integrate (4.1) over space and obtain

$$\int_{\Omega_j} R_i \frac{\partial}{\partial t} c_i \, dx = \int_{\Omega_j} \nabla \cdot \left(-\mathbf{v} c_i + D^{e(i)} \nabla c_i \right) dx. \tag{4.3}$$

The time integration is done later in the decomposition method with implicit-explicit Runge-Kutta methods. Further the diffusion-dispersion term is lumped; compare with [12]. Equation (4.3) is discretized over space using Green's formula

$$V_j R_i \frac{\partial}{\partial t} c_i \, dx = \int_{\Gamma_j} \mathbf{n} \cdot \left(-\mathbf{v} c_i + D^{e(i)} \nabla c_i \right) d\gamma, \tag{4.4}$$

where Γ_j is the boundary of the finite volume cell Ω_j and $V_u j$ is the volume of the cell j. We use the approximation in space; see [12].

The spatial integration for the diffusion part (4.4) is done by the mid-point rule over its finite boundaries and the convection part is done with a flux limiter and we obtain:

$$V_j R_i \frac{\partial}{\partial t} c_{i,j} = \sum_{e \in \Lambda_j} \mathbf{n}^e \nabla \mathbf{v} c_i^e d\gamma + \sum_{e \in \Lambda_j} \sum_{k \in \Lambda_j^e} \left| \Gamma_{jk}^e \right| \mathbf{n}_{jk}^e \cdot D_{jk}^e \nabla c_{i,jk}^e, \tag{4.5}$$

where $|\Gamma_{jk}^e|$ is the length of the boundary element Γ_{jk}^e. The gradients are calculated with the piecewise finite-element function ϕ_l.

We decide to discretize the ux with an up-winding scheme and obtain the following discretization for the convection part:

$$F_{j,e} = \begin{cases} \mathbf{v}_{j,e} c_{i,j}, & \text{if } v_{j,e} \geq 0, \\ \mathbf{v}_{j,e} c_{i,k}, & \text{if } v_{j,e} < 0, \end{cases} \tag{4.6}$$

where $v_{j,e} = \int_e \mathbf{v} \cdot \mathbf{n}_{j,e} ds$.

We obtain for the diffusion part:

$$\nabla c_{jk}^e = \sum_{l \in \Lambda^e} c_l \nabla \phi_l \left(\mathbf{x}_{jk}^e \right). \tag{4.7}$$

We get, using difference notation for the neighbour points j and l; compare with [28], the full semi-discretization:

$$V_j R_i \frac{\partial}{\partial t} c_{i,j} = \sum_{e \in \Lambda_j} F_{j,e} + \sum_{e \in \Lambda_j} \sum_{l \in \Lambda^e \setminus \{j\}} \left(\sum_{k \in \Lambda_j^e} \left| \Gamma_{jk}^e \right| \mathbf{n}_{jk}^e \cdot D_{jk}^e \nabla \phi_l \left(\mathbf{x}_{jk}^e \right) \right) (c_j - c_l), \tag{4.8}$$

where $j = 1, \ldots, m$.

Remark 4.1. For higher-order discretization of the convection equation, we apply a reconstruction which is based on Godunov's method. We apply a limiter function that fulfills the local min-max property. The method is explained in [26]. The linear polynomials are reconstructed by the element-wise gradient and are given by

$$\begin{aligned} u(x_j) &= c_j, \\ \nabla u|_{V_j} &= \frac{1}{V_j} \sum_{e=1}^{E} \int_{T^e \cap \Omega_j} \nabla c \, dx, \quad \text{with } j = 1, \ldots, I. \end{aligned} \tag{4.9}$$

The piecewise linear functions are denoted by

$$u_{jk} = c_j + \varphi_j \nabla u|_{V_j} (x_{jk} - x_j), \quad \text{with } j = 1, \ldots, I, \tag{4.10}$$

where $\varphi_j \in (0, 1)$ is the limiter function and it fulfills the discrete minimum-maximum property, as described in [26].

4.2. Splitting Method to Couple Mobile, Immobile, and Adsorbed Parts

The motivation of the splitting method is the following observations.

(i) The mobile phase is semidiscretized with fast finite volume methods and can be stored in a stiffness matrix. We achieve large time steps, if we consider implicit Runge-Kutta methods of lower order (e.g., implicit Euler) as a time discretization method.

(ii) The immobile, adsorpted, and immobile-adsorpted phases are pure ordinary differential equations and each is cheap to solve with explicit Runge-Kutta schemes.

(iii) The ODEs can be seen as perturbations and are solved explicitly in the iterative scheme.

For the full equation we use the following matrix notation:

$$\begin{aligned}
\partial_t \mathbf{c} &= A_1\mathbf{c} + A_2\mathbf{c} + B_1(\mathbf{c} - \mathbf{c}_{im}) + B_2(\mathbf{c} - \mathbf{c}_{ad}) + \mathbf{Q},\\
\partial_t \mathbf{c}_{im} &= A_2\mathbf{c}_{im} + B_1(\mathbf{c}_{im} - \mathbf{c}) + B_2(\mathbf{c}_{im} - \mathbf{c}_{im,ad}) + \mathbf{Q}_{im},\\
\partial_t \mathbf{c}_{ad} &= A_2\mathbf{c}_{ad} + B_2(\mathbf{c}_{ad} - \mathbf{c}) + \mathbf{Q}_{ad},\\
\partial_t \mathbf{c}_{im,ad} &= A_2\mathbf{c}_{im,ad} + B_2(\mathbf{c}_{im,ad} - \mathbf{c}_{im}) + \mathbf{Q}_{im,ad},
\end{aligned} \tag{4.11}$$

where $\mathbf{c} = (c_1, \ldots, c_m)^T$ is the spatial discretized concentration in the mobile phase, see (2.4), and $\mathbf{c}_{im} = (c_{1,im}, \ldots, c_{m,im})^T$ is the concentration in the immobile phase, and similarly for the other phase concentrations. A_1 is the stiffness matrix of (2.4), A_2 is the reaction matrix of the right-hand side of (2.4), B_1 and B_2 are diagonal matrices with entries the immobile and kinetic parameters, see (2.7) and (2.8).

Furthermore $\mathbf{Q}, \ldots, \mathbf{Q}_{im,ad}$ are the spatially discretized source vectors.

Now we have the following ordinary differential equation:

$$\partial_t \mathbf{C} = \begin{pmatrix} A_1 + A_2 + B_1 + B_2 & -B_1 & -B_2 & 0 \\ -B_1 & A_2 + B_1 + B_2 & 0 & -B_2 \\ -B_2 & 0 & A_2 + B_2 & 0 \\ 0 & -B_2 & 0 & A_2 + B_2 \end{pmatrix} \mathbf{C} + \tilde{\mathbf{Q}}, \tag{4.12}$$

where $\mathbf{C} = (\mathbf{c}, \mathbf{c}_{im}, \mathbf{c}_{ad}, \mathbf{c}_{im,ad})^T$ and the right-hand side is $\tilde{\mathbf{Q}} = (\mathbf{Q}, \mathbf{Q}_{im}, \mathbf{Q}_{ad}, \mathbf{Q}_{im,ad})^T$.

For such an equation we apply the decomposition of the matrices

$$\begin{aligned}
\partial_t \mathbf{C} &= \tilde{A}\mathbf{C} + \tilde{\mathbf{Q}},\\
\partial_t \mathbf{C} &= \tilde{A}_1\mathbf{C} + \tilde{A}_2\mathbf{C} + \tilde{\mathbf{Q}},
\end{aligned} \tag{4.13}$$

where

$$\widetilde{A}_1 = \begin{pmatrix} A_1 + A_2 & 0 & 0 & 0 \\ 0 & A_2 & 0 & 0 \\ 0 & 0 & A_2 & 0 \\ 0 & 0 & 0 & A_2 \end{pmatrix}, \qquad \widetilde{A}_2 = \begin{pmatrix} B_1 + B_2 & -B_1 & -B_2 & 0 \\ -B_1 & B_1 + B_2 & 0 & -B_2 \\ -B_2 & 0 & B_2 & 0 \\ 0 & -B_2 & 0 & B_2 \end{pmatrix}. \tag{4.14}$$

This system of equations is numerically solved by an iterative scheme.

Algorithm 4.2. We divide our time interval $[0,T]$ into subintervals $[t^n, t^{n+1}]$, where $n = 0,1,\ldots N$, $t^0 = 0$ and $t^N = T$.

We start with $n = 0$.

(1) The initial conditions are given by $\mathbf{C}_0(t^{n+1}) = \mathbf{C}(t^n)$. We start with $k = 0$.

(2) Compute the fixed-point iteration scheme given by

$$\partial_t \mathbf{C}^k = \widetilde{A}_1 \mathbf{C}^k + \widetilde{A}_2 \mathbf{C}^{k-1} + \widetilde{\mathbf{Q}}, \tag{4.15}$$

where k is the iteration index; see [29]. For the time integration, we apply Runge-Kutta methods as ODE solvers; see [30, 31].

(3) The stop criterion for the time interval t^n, t^{n+1} is given by

$$\left\| \mathbf{C}^k\left(t^{n+1}\right) - \mathbf{C}^{k-1}\left(t^{n+1}\right) \right\| \leq \text{err}, \tag{4.16}$$

where $\|\cdot\|$ is the maximum norm over all components of the solution vector. err is a given error tolerance, for example, err $= 10^{-4}$.

If (4.16) is fulfilled, we have the result

$$\mathbf{C}\left(t^{n+1}\right) = \mathbf{C}^k\left(t^{n+1}\right). \tag{4.17}$$

If $n = N$ (which means we reach the maximum iterative steps), then we stop and are done.

If (4.16) is not fulfilled, we do $k = k + 1$ and go to (2).

The error analysis of the schemes is given in the following theorem.

Theorem 4.3. *Let $A, B \in \mathcal{L}(\mathbf{X})$ be given linear bounded operators in a Banach space $\mathcal{L}(\mathbf{X})$. We consider the abstract Cauchy problem*

$$\begin{aligned} \partial_t \mathbf{C}(t) &= \widetilde{A}\mathbf{C}(t) + \widetilde{B}\mathbf{C}(t), \quad t_n \leq t \leq t_{n+1}, \\ \mathbf{C}(t_n) &= \mathbf{C}_n, \quad \textit{for } n = 1,\ldots,N, \end{aligned} \tag{4.18}$$

where $t_1 = 0$ and the final time is $t_N = T \in \mathbb{R}^+$. Then problem (4.18) has a unique solution. For finite steps with time size $\tau_n = t^{n+1} - t^n$, the iteration (4.15) for $k = 1,2,\ldots,q$ is consistent with an order of consistency $\mathcal{O}(\tau_n^q)$.

Proof. The outline of the proof is given in [15]. □

5. Experiments for the Multiple Phase Model

In the following subsections, we present our experiments based on the mobile, immobile and adsorbed gaseous phases.

We contribute ideas to obtain an optimal layer deposition, which is based on the PE-CVD process, while different additional phases are considered, for example, plasma and precursor media.

The main contributions are an optimal collection of point sources, line sources or moving sources to cover the deposition area, with respect to the remainder concentration in the immobile and adsorbed phases.

We simulate the deposition process with our boundary value solver algorithms and could deal with many different conditions that might be impossible for physical experiments. Such simulation results may benefit the physical experiment and give new ideas to optimize such deposition problems of a complicated physical process.

5.1. Verification of the Code with Analytical Solutions

In the verification of our software code UG; see [32], we apply the multiphase model (2.4) and (2.6) with the following parameters.

We use ascending parameters for the retardation factors. The retardation factors are given by $R_1 = 16$, $R_2 = 8$, $R_3 = 4$, R_4. The reaction factors are given by $\lambda_1 = 0.4$, $\lambda_2 = 0.3$, $\lambda_3 = 0.2$, $\lambda_0 \cdot 0$.

The initial conditions for the mobile phase are given by

$$c_i(x,0) = \begin{cases} a_i x + b_i, & x \in (x_1, x_2), \\ 0, & \text{otherwise}, \end{cases} \tag{5.1}$$

where the parameters are given by $x_1 = 0.0$, $x_2 = 1.0$, $a_1 = 1.0$, $b_1 = 1.0$, $a_2 = -1.0$, $b_2 = 1.0$, $a_3 = 1.0$, $b_3 = 0.0$, $a_4 = 2.0$, $b_4 = 1.0$.

The mobile-immobile exchange rate is $g = 0.5$.

The initial conditions for the immobile concentrations are $c_{im}(0) = (1,1,1,1)^t$.

For the time integration method we apply a fourth-order Runge-Kutta method and we apply $k = 1,\ldots,4$ iterative steps for the solver scheme.

The errors are given by

$$\text{err}_{i,j} = \sum_{k=1}^{N} \left| u_{i,\,\text{coupled},\,j-1}(x_k,t) - u_{i,\,\text{coupled},\,j}(x_k,t) \right|, \tag{5.2}$$

where $x_k = (k-1)\Delta x$, $k = 0,\ldots,N$, $\Delta x = 0.01$, $N = 1000$, and $j = 2,3,4,5$.

The solutions of the species are given in Figures 5 and 6.

Remark 5.1. The iterative scheme reduced the amount of numerical work to couple the mobile and immoble equations. We obtain more accurate results by using 3-4 iterative steps. Such schemes help the flexibility in coupling model equations by reducing the amount of recoding needed. More accuracy can be simply achieved with more iterative steps.

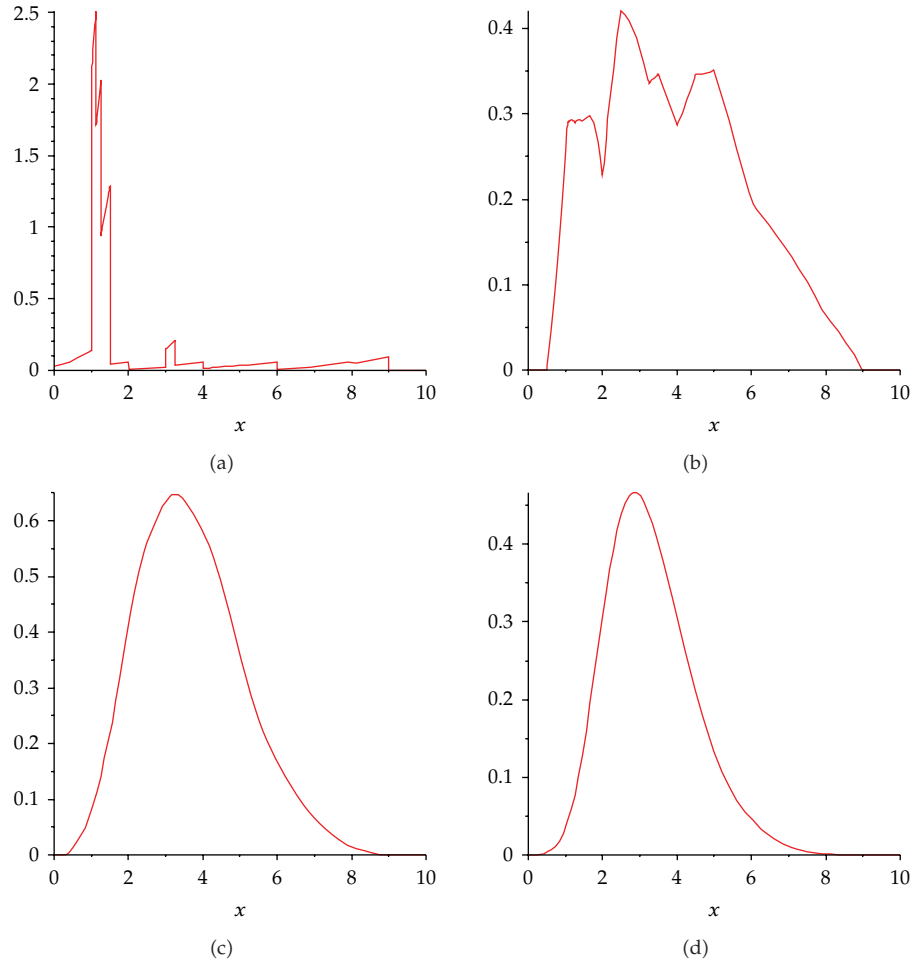

Figure 5: Experiment with the coupled model for the mobile solutions c_{im}, with $j = 2$ and $j = 4$ iteration steps at time point $t = 8$.

Table 4: Physical and mathematical parameters.

Physical parameter	Mathematical parameter
Temperature, pressure, power	Velocity, diffusion, reaction
T, p, W	V, D, λ

5.2. Verification of the Model with Physical Experiments

For the next experiments, we have the following parameters of the model, discretization, and solver methods.

We apply interpolation and regression methods to couple the physical parameters that were discussed in Section 3, to the mathematical parameters, see Figure 7 and Table 4.

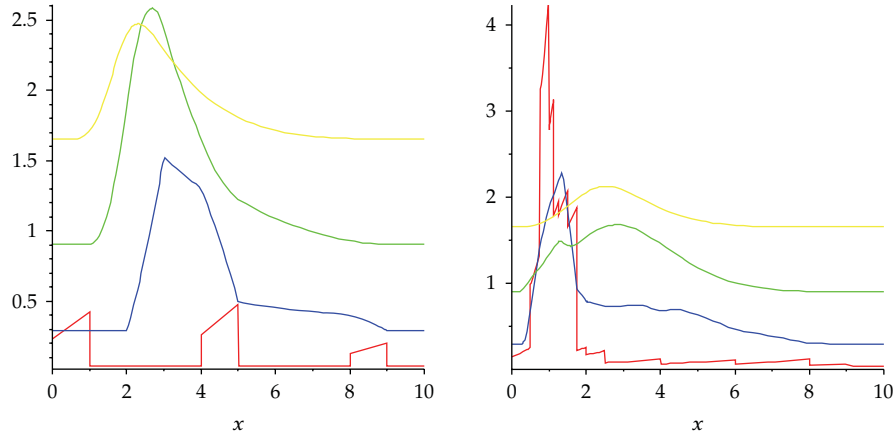

Figure 6: Experiment with the coupled model for the immobile solutions c_{im}, with $j = 2$ and $j = 4$ iteration steps at time point $t = 8$.

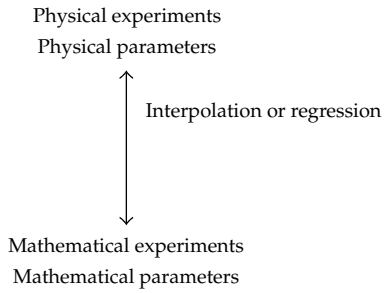

Figure 7: Coupling of physical and mathematical parameter space.

Parameters of (2.4)–(2.8)

In Table 8, we list the parameters for our simulation tool UG; see [32]. The software toolbox has a flexible user interface to allow a large number of numerical experiments and approximations using the known physical parameters.

Discretization Method

Finite-volume method of 2nd order is shown in Table 9.

Time Discretization Method

Crank-Nicolson method (2nd order).

Solver Method

In Tables 10 and 11, we deal with test examples which are approximations of physical experiments.

Table 5: Computed and experimental fitted parameters from UG simulations.

T	λ (fitted)	λ (interpolated)	Ratio (SiC : C) (computed with UG)
400	$1/2 \cdot 10^{-8}$	—	2.4 : 1
500	—	$0.35 \cdot 10^{-8}$	1.85 : 1
600	$1/4 \cdot 10^{-8}$	—	1.5 : 1
700	—	$0.171 \cdot 10^{-8}$	1.211 : 1
800	$1/8 \cdot 10^{-8}$	—	1.1 : 1

Table 6: Parameters of source concentration.

Point source at position	$(x, y) = (50, 20)$
Starting point of source concentration	$t_{\text{start}} = 0.0$
End point of source concentration	$t_{\text{end}} = 110^8$
Amount of permanent source concentration	$c_{\text{source}} = 1.0$
Number of time steps	25

Table 7: Rate of concentration.

Rate
$\text{SiC}_{\text{source, max}} : \text{SiC}_{\text{target, max}}\ 9 \cdot 10^6 : 6.5 \cdot 10^6 = 1.38$

Numerical Experiment

In the test example, we deal with the following reaction:

$$2\text{SiC} + 4\text{H} \longrightarrow_{\lambda} \text{SiC} + \text{CH4} + \text{Si}. \tag{5.3}$$

Here, we have physical experiments and approximate temperature parameters $T = 400, 600, 800$.

We compute the SiC : C ratio at a given temperature $T = 400, 600, 800$ with the UG program and fit to the parameter λ.

We use a Lagrangian formula to compute λ for the new temperatures $T = 500, 700$ and apply the ratio of the simulated new parameters (Table 5). These numerical results are used to initialise the physical experiments in Table 12.

One Source

See Table 6.

In Figure 8, we present the concentration of one point source at $(50, 20)$ with number of time steps equal to 25.

In Figure 9, we show the deposition rates of one point source at $(50, 20)$, with number of time steps equal to 25.

Remark 5.2. In the numerical experiments, we could approximate the physical experiments and obtain the same deposition rates for the Si: C deposition. Therefore, the model allows of making predictions about future deposition rates with various parameters. Such numerical experiments can replace expensive physical experiments and allow of restricting them to more special cases.

Table 8: Model parameters.

Density	$\rho = 1.0$
Mobile porosity	$\phi = 0.333$
Immobile porosity	0.333
Diffusion	$D = 0.0$
Longitudinal dispersion	$\alpha_L = 0.0$
Transversal dispersion	$\alpha_T = 0.00$
Retardation factor	$R = 100e - 4$ (Henry rate)
Velocity field	$\mathbf{v} = (0.0, -4.0 \cdot 10^{-8})^t$
Decay rate of species of 1st EX	$\lambda_{AB} = 1 \cdot 10^{-68}$
Decay rate of species of 2nd EX	$\lambda_{AB} = 2 \cdot 10^{-8}$, $\lambda_{BNN} = 1 \cdot ¡10^{-68}$
Decay rate of species of 3rd EX	$\lambda_{AB} = 0.25 \cdot 10^{-8}$, $\lambda_{CB} = 0.5 \cdot 10^{-8}$
Geometry (2D domain)	$\Omega = [0, 100] \times [0, 100]$
Boundary	Neumann boundary at top, left, and right boundaries Outflow boundary at bottom boundary

Table 9: Spatial discretization parameters.

Spatial step size	$\Delta x_{\min} = 1.56$, $\Delta x_{\max} = 2.21$
Refined levels	6
Limiter	Slope limiter
Test functions	Linear test function reconstructed with neighbour gradients

Table 10: Spatial discretization parameters.

Initial time step	$\Delta t_{\text{init}} = 5 \cdot 10^7$
Controlled time step	$\Delta t_{\max} = 1.298 \cdot 10^7$, $\Delta t_{\min} = 1.158 \cdot 10^7$
Number of time steps time step control	100, 80, 30, 25 time steps are controlled with the Courant number $\text{CFL}_{\max} = 1$

Table 11: Solver methods and their parameters.

Solver	BiCGstab (Bi conjugate gradient method)
Preconditioner	Geometric multigrid method
Smoother	Gauss-Seidel method as smoothers for the multigrid method
Basic level	0
Initial grid	Uniform grid with 2 elements
Maximum level	6
Finest grid	Uniform grid with 8192 elements

Table 12: L_2-norm of the solution with refinements and CPU time.

Max ·level	$L_2 \cdot$ norm	Max ·norm	Elements	CPU · time	Time steps
6	1.6232 + 09	7.5026 + 07	8192	1.1 min	19
7	1.6222 + 09	7.7068 + 07	32768	3.55 min	19
8	1.6155 + 09	7.6753 + 07	131072	15.7 min	19
9	1.6137 + 09	7.6267 + 07	524288	59.55 min	19

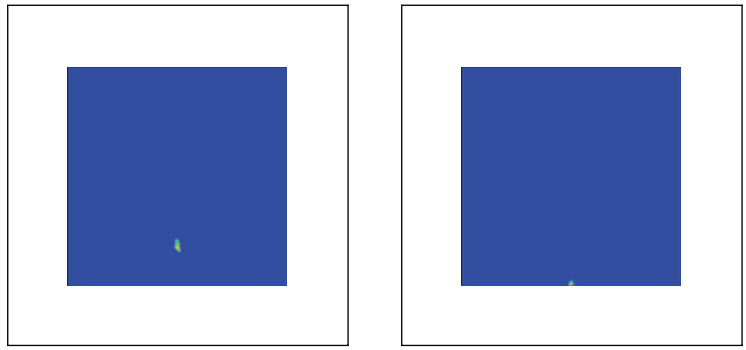

(a) (b)

Figure 8: One point source at $(50, 20)$ with 25 time steps, full concentration is given in red and zero concentration with blue.

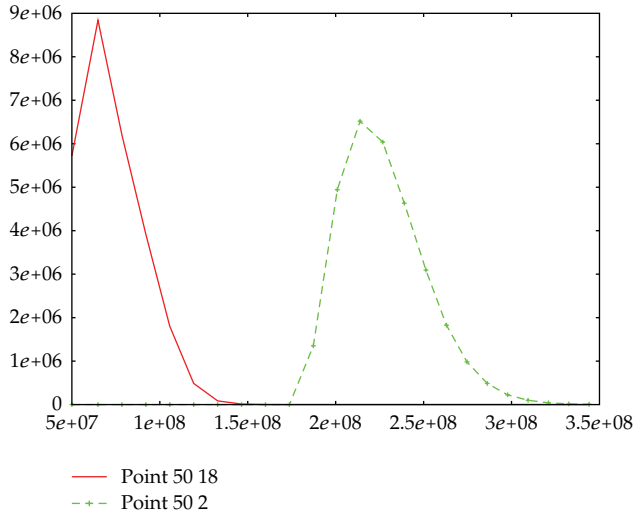

Figure 9: Deposition rates for one point source at $(50, 20)$, with 25 time steps (x-axis: time scale in (nsec), y-axis: deposition rate in (mol/nsec)).

5.3. *Experiments with Full Model* ($\alpha = 4 \cdot 10^{-14}$ *and Immobile Rate* $g = 8 \cdot 10^{-14}$)

In this experiment, we have taken into account the full model and verify with the previous simpler model equations that are verified by physial experiments.

Such novel experiments allow of giving prognoses of which direction of model modification can be important for future diagnostics of physical experiments.

We have the following outline of the experiment.

The exchange in the following experiments of the carbon (C) species between the mobile and immobile concentrations is very low, it is about $g = 8 \cdot 10^{-14}$, we assume less activities in the plasma environment. Further the exchange between the mobile and adsorbed mobile concentrations is also very low, it is about $\alpha = 4 \cdot 10^{-14}$, also the exchange rates between the immobile and adsorbed immobile concentration is the same as in the mobile and adsorbed mobile phases.

In previous experiments; see [33], we obtained optimal deposition results by combining multiple point sources which can be moved in the spatial directions (moving sources). Further we could approximate the physical results, while using mobile and immobile phase models.

In this experiment we increase the model to four phases in order to predict the delicate adsorped regions. Physicists called such regions lost deposition areas, where the deposition material vanishes into the apparatus; see [25].

We taken into account 11 point sources at the positions $Y = 20, 21, 22, 23, 24, 25, 26, 27, 28, 29, 30$, and these sources are moving in the X direction in equal spatial steps with 15.

The concentration of each source in each step is equal to 1. The starting movement of X is given with $50 \to 35 \to 20 \to 35 \to 50 \to 65 \to 80 \to 65 \to 50$.

In Figure 10, we present the experiment with 11 moving sources at the positions in four phases. We obtain high depositions in the mobile phase, while we have only marginal depositions in the immobile and adsorbed phases.

Here the important observations to give a measurement of the deposition are the various deposition rates in the different phases.

In Figure 11, we present the deposition rate of mobile concentration of 11 moving sources moving in the X-direction in steps of 15: X moves from $50 \to 35 \to 20 \to 35 \to 50 \to 65 \to 80 \to 65 \to 50$, with the number of time steps equal to 25.

In see Table 12, we discuss the CPU time for the spatial refinements. We consider the L_2-norm of the solution and obtain convergent results of the solutions.

Remark 5.3. With moving sources we gain improved deposition rates, this was also observed in [33]. Nevertheless the remaining concentration in the immobile and adsorbed phases are important for seeing the lost areas. In Figure 11, the maximum deposition rate of carbon in the mobile phase is $1.2 \cdot 10^8$ [mol], while the maximum lost deposition rate in the other phases are at least 18000 [mol]. So in the immobile and adsorbed phases we lost only 0.00018 percent concentration of the deposition material. This may seem to be neglectable, but we have considered only 1 [sec] deposition time, while a full cycle of deposition could be 1000 [sec]. Therefore we lost about 10% of the concentration in the apparatus, which is immense. Due to this fact, such models are important for foreseeing the percentage of lost concentration. One of the simulation results is the usage of higher amount of depositon material, that is, the higher amount of the underlying precursor gases are used to overcome the lost of concentrations in the apparatus. The second result is to consider more detailed models to predict the influence of the multiphases of the underlying gaseous species.

6. Conclusions and Discussions

We have presented a continuous model for the multiple phases, we assumed gaseous behaviour with exchange rates to adsorbed and immobile phases at very low-pressure and low temperature while dealing with catalyst processes, for example, plasma environment and precursor gases. We have to take into acount the remaining gas concentrations in each processes. Such detailed modelling allows of seeing the delicate retardation and sorption processes of the underlying plasma medium. From the methodology side of the numerical simulations, the contributions were to decouple the multiphase problem into single-phase problems, where each single problem can be solved with more accuracy. The iterative schemes allows of coupling the simpler equations and for each additional iterative step, we could reduce the splitting error. Such iterative methods allow of accelerating the solver process of multiphase problems.

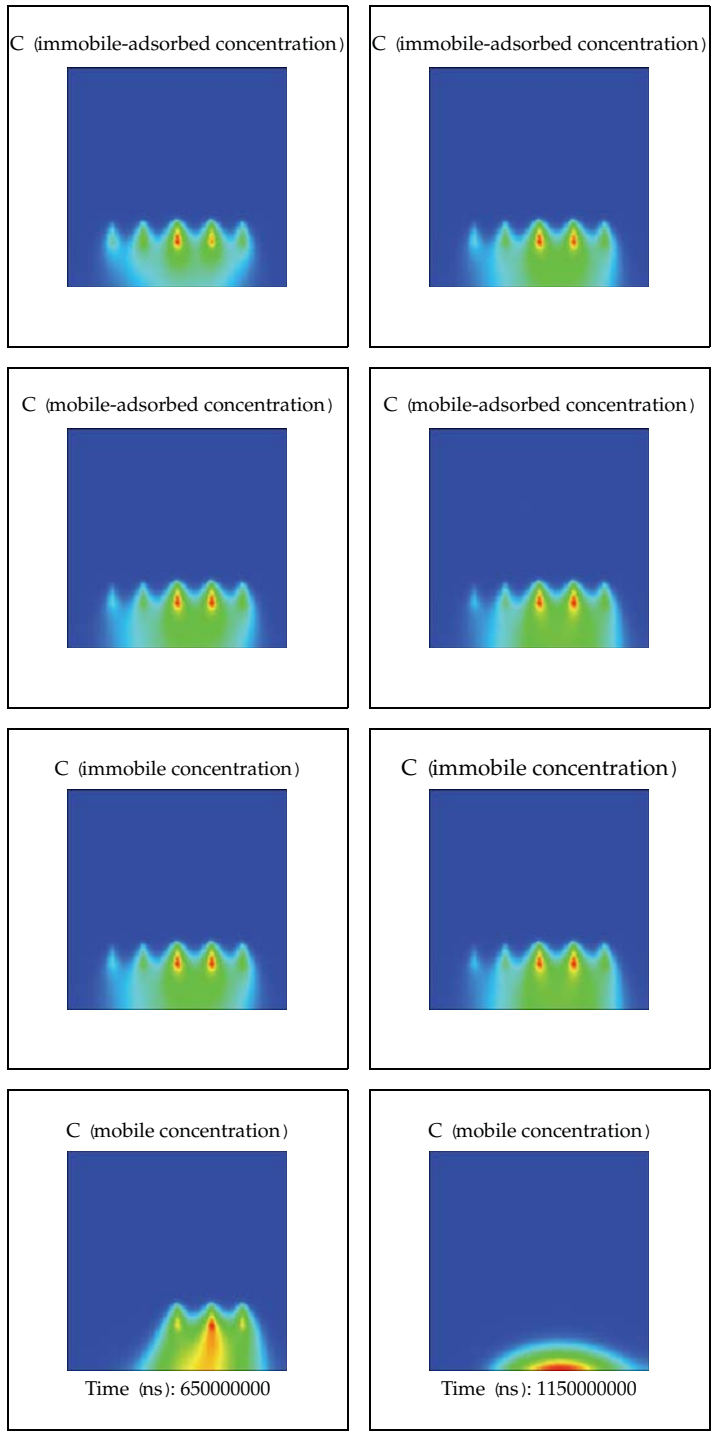

Figure 10: mobile (lowermost), immobile (lower-middle), mobile-adsorbed (upper-middle) and immobile-adsorbed (uppermost) case of 11 moving sources moving with number of time step equal to 15 (left figures) and 25 (right figures), where full concentration is given in red and zero concentration in blue.

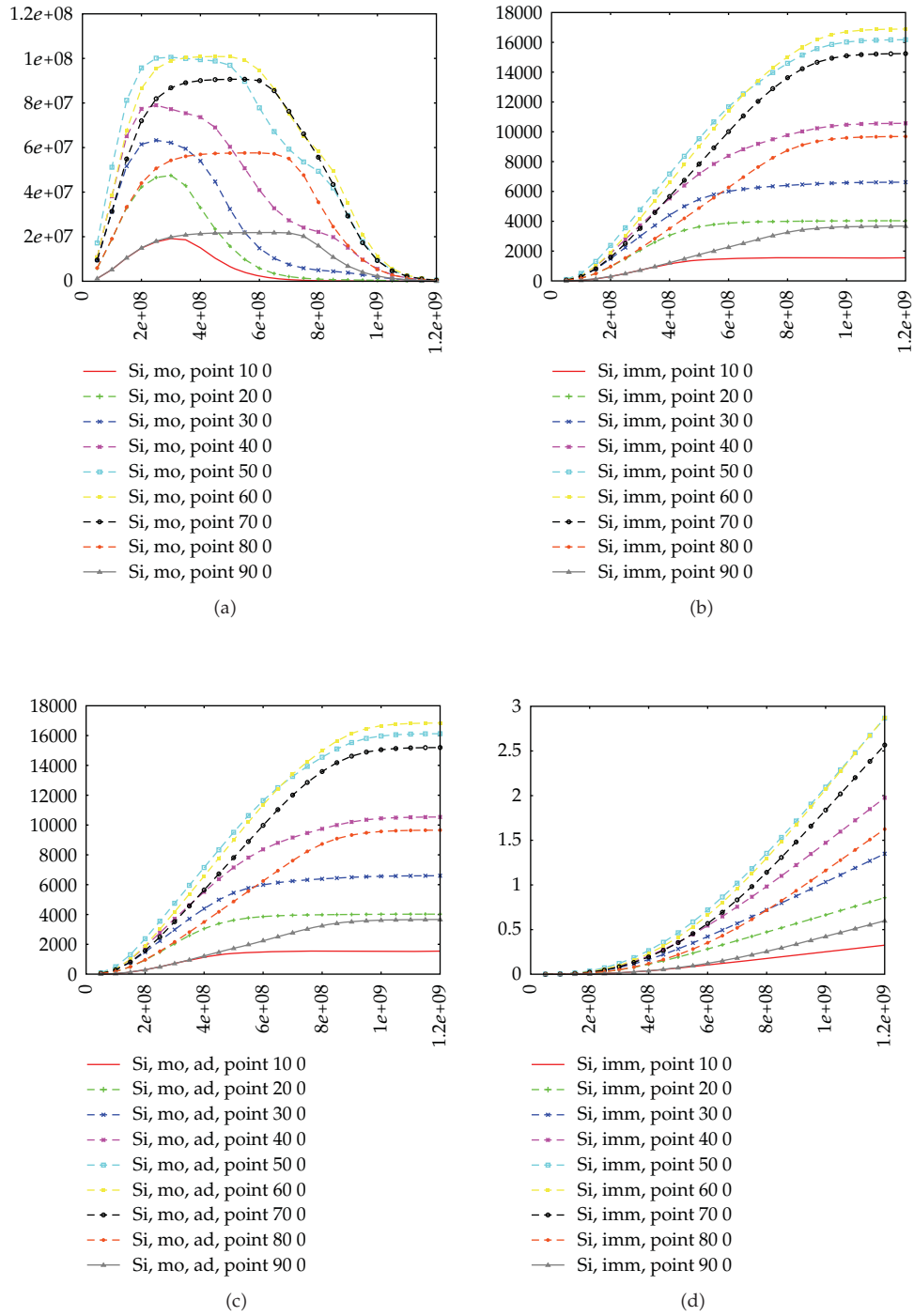

Figure 11: Deposition rates in four phases: mobile (a), immobile (b), mobile-adsorbed (c), immobile-adsorbed (d) concentration of 11 moving sources moving, (x-axis: time scale in (nsec), y-axis: deposition rate in (mol/nsec)).

We can see in the numerical experiments a loss of the deposition concentration, which means that we have to consider a higher inflow rate of the species. Further, we could verify the underlying model with physical experiments. In the numerical experiments, we presented various ideas to control an optimal deposition process. While numerical experiments are cheap and all possible parameter variations of the model can be done in less than a few weeks, the help in reducing the need for expensive physical experiments is enormous. Such simulations reduce the need for physical experiments and allow of foreseeing new directions of helpful optimizations.

In the future we are interested on analysing such fast processes due to very small time scales, for example, in a nanoscaled models (molecular dynamics model).

References

[1] V. Hlavacek, J. Thiart, and D. Orlicki, "Morphology and film growth in cvd reactions," *Journal de Physique IV France*, vol. 5, pp. 3–44, 1995.

[2] J. Geiser and M. Arab, "Simulation of a chemical vapor deposition: mobile and immobile zones and homogeneous layers," *Journal of Porous Media*, vol. 1, no. 2, 2010.

[3] M. A. Lieberman and A. J. Lichtenberg, *Principle of Plasma Discharges and Materials Processing*, Wiley-Interscience; John Wiley & Sons, New York, NY, USA, 2nd edition, 2005.

[4] M. Ohring, *Materials Science of Thin Films*, Academic Press, San Diego, Calif, USA, 2nd edition, 2002.

[5] L. Sansonnens, J. Bondkowski, S. Mousel, J. P. M. Schmitt, and V. Cassagne, "Development of a numerical simulation tool to study uniformity of large area PECVD film processing," *Thin Solid Films*, vol. 427, no. 1-2, pp. 21–26, 2003.

[6] B. Chapman, *Glow Discharge Processes. Sputering and Plasma Etching*, John Wiley & Sons, New York, NY, USA, 1st edition, 1980.

[7] N. Morosoff, *Plasma Deposition, Treatment and Etching of Polymers*, Academic Press, New York, NY, USA, 1st edition, 1990, R. d'Agostino, Ed.

[8] P. Favia, E. Sardella, R. Gristina, A. Milella, and R. D'Agostino, "Functionalization of biomedical polymers by means of plasma processes: plasma treated polymers with limited hydrophobic recovery and PE-CVD of -COOH functional coatings," *Journal of Photopolymer Science and Technology*, vol. 15, no. 2, pp. 341–350, 2002.

[9] M. W. Barsoum and T. El-Raghy, "Synthesis and characterization of a remarkable ceramic: ti_3sic_2," *Journal of the American Ceramic Society*, vol. 79, no. 7, pp. 1953–1956, 1996.

[10] Y. Du, J. C. Schuster, H. J. Seifert, and F. Aldinger, "Experimental investigation and thermodynamic calculation of the titanium-silicon-carbon system," *Journal of the American Ceramic Society*, vol. 83, no. 1, pp. 197–203, 2000.

[11] C. Lange, M. W. Barsoum, and P. Schaaf, "Towards the synthesis of MAX-phase functional coatings by pulsed laser deposition," *Applied Surface Science*, vol. 254, no. 4, pp. 1232–1235, 2007.

[12] J. Geiser, *Gekoppelte Diskretisierungsverfahren für Systeme von Konvektions-Dispersions-Diffusions-Reaktionsgleichungen*, Ph.D. thesis, Universität Heidelberg, 2003.

[13] L. Rudniak, "Numerical simulation of chemical vapour deposition process in electric field," *Computers and Chemical Engineering*, vol. 22, no. 1, pp. S755–S758, 1998.

[14] N. H. Tai and T. W. Chou, "Modeling of an improved chemical vapor infiltration process for ceramic composites fabrication," *Journal of the American Ceramic Society*, vol. 73, no. 6, pp. 1489–1498, 1990.

[15] J. Geiser, *Decomposition Methods for Differential Equations*, Chapman & Hall/CRC Numerical Analysis and Scientific Computing Series, CRC Press, Boca Raton, Fla, USA, 1st edition, 2009, Magoules and Lai, Ed.

[16] J. Geiser, "Discretization methods with embedded analytical solutions for convection-diffusion dispersion-reaction equations and applications," *Journal of Engineering Mathematics*, vol. 57, no. 1, pp. 79–98, 2007.

[17] M. K. Gobbert and C. A. Ringhofer, "An asymptotic analysis for a model of chemical vapor deposition on a microstructured surface," *SIAM Journal on Applied Mathematics*, vol. 58, no. 3, pp. 737–752, 1998.

[18] J. Geiser and M. Arab, "Porous media based modeling of pe-cvd apparatus: electrical fields and deposition geometries," *Special Topics and Reviews in Porous Media*, vol. 1, no. 3, pp. 215–229, 2010.

[19] G. Z. Cao, H. W. Brinkman, J. Meijerink, K. J. De Vries, and A. J. Burggraaf, "Kinetic study of the modified chemical vapour deposition process in porous media," *Journal of Materials Chemistry*, vol. 3, no. 12, pp. 1307–1311, 1993.

[20] H. Rouch, "Mocvd research reactor simulation," in *Proceedings of the COMSOL Users Conference*, Paris, France, 2006.

[21] T. K. Senega and R. P. Brinkmann, "A multi-component transport model for non-equilibrium low-temperature low-pressure plasmas," *Journal of Physics D*, vol. 39, no. 8, pp. 1606–1618, 2006.

[22] J. Bear, *Dynamics of Fluids in Porous Media*, American Elsevier, New York, NY, USA, 1st edition, 1972.

[23] E. Fein, "Software package r^3t," Tech. Rep., 2004.

[24] S. Farooq and D. M. Ruthven, "Dynamics of kinetically controlled binary adsorption in a fixed bed," *AIChE Journal*, vol. 37, no. 2, pp. 299–301, 1991.

[25] V. A. Kadetov, *Diagnostics and modeling of an inductively coupled radio frequency discharge in hydrogen*, Ph.D. thesis, Ruhr Universität Bochum, 2004.

[26] P. Frolkovič and J. Geiser, "Discretization methods with discrete minimum and maximum property for convection dominated transport in porous media," in *Numerical Methods and Applications*, I. Dimov, I. Lirkov, S. Margenov, and Z. Zlatev, Eds., pp. 445–453, Springer, Berlin, Germany, 2003.

[27] P. Frolkovič, "Flux-based method of characteristics for contaminant transport in flowing groundwater," *Computing and Visualization in Science*, vol. 5, no. 2, pp. 73–83, 2002.

[28] P. Frolkovič and H. De Schepper, "Numerical modelling of convection dominated transport coupled with density driven flow in porous media," *Advances in Water Resources*, vol. 24, no. 1, pp. 63–72, 2000.

[29] I. Farago and J. Geiser, "Iterative operator-splitting methods for linear problems," Tech. Rep. 1043, Weierstrass Institute for Applied Analysis and Stochastics, Berlin, Germany, Mohrenstrasse, Berlin, Germany, 2005.

[30] E. Hairer, S. P. Nørsett, and G. Wanner, *Solving Ordinary Differential Equations. I*, vol. 8 of *Springer Series in Computational Mathematics*, Springer, Berlin, Germany, 2nd edition, 1992.

[31] E. Hairer and G. Wanner, *Solving Ordinary Differential Equations. II*, vol. 14 of *Springer Series in Computational Mathematics*, Springer, Berlin, Germany, 2nd edition, 1996.

[32] P. Bastian, K. Birken, K. Eckstein et al., "Ug-a flexible software toolbox for solving partial differential equations," *Computing and Visualization in Science*, vol. 1, no. 1, pp. 27–40, 1997.

[33] J. Geiser and M. Arab, "Modelling, optimzation and simulation for a chemical vapor deposition," *Journal of Porous Media*, vol. 12, no. 9, pp. 847–867, 2009.

Hindawi Publishing Corporation
Journal of Applied Mathematics
Volume 2011, Article ID 124590, 10 pages
doi:10.1155/2011/124590

Research Article

Radiative Mixed Convection over an Isothermal Cone Embedded in a Porous Medium with Variable Permeability

M. F. El-Amin,[1,2] N. A. Ebrahiem,[2] Amgad Salama,[1] and Shuyu Sun[1]

[1] *Computational Transport Phenomena Laboratory (CTPL), Division of Physical Sciences and Engineering (PSE), King Abdullah University of Science and Technology (KAUST), Thuwal 23955-6900, Saudi Arabia*
[2] *Mathematics Department, Aswan Faculty of Science, South Valley University, Aswan 81258, Egypt*

Correspondence should be addressed to M. F. El-Amin, mohamed.elamin@kaust.edu.sa

Received 15 December 2010; Accepted 7 January 2011

Academic Editor: Zhangxin Chen

Copyright © 2011 M. F. El-Amin et al. This is an open access article distributed under the Creative Commons Attribution License, which permits unrestricted use, distribution, and reproduction in any medium, provided the original work is properly cited.

The interaction of mixed convection with thermal radiation of an optical dense viscous fluid adjacent to an isothermal cone imbedded in a porous medium with Rosseland diffusion approximation incorporating the variation of permeability and thermal conductivity is numerically investigated. The transformed conservation laws are solved numerically for the case of variable surface temperature conditions. Numerical results are given for the dimensionless temperature profiles and the local Nusselt number for various values of the mixed convection parameter χ, the cone angle parameter m, the radiation-conduction parameter R_d, and the surface temperature parameter H.

1. Introduction

The problem of convective heat transfer in porous medium has attracted researchers because of the several applications it incorporates. Examples include enhanced oil recovery, nuclear waste disposal, geothermal reservoirs, and ceramic processing. This topic has been extensively covered in literatures in connection with different geometries, boundary conditions, and media. While most of the cases concern with convection along semi-infinite vertical walls impeded in porous media (e.g., [1–5] and many others) several other geometries were also considered including cylinders (e.g., [6, 7]), wedges (e.g., [8]), spheres (e.g., [9], Huang et al., 1986), cones (e.g., [10]). The presence of thermal radiation was also investigated for the case of truncated cone by Yih [11] and for the case of vertical wall by Abbas et al. [12]. All these studies consider the permeability and conductivity of the medium

as constant. However, porosity measurements by Schwartz and smith [13], Tierney et al. [14], and Benenati and Brosilow [15] showed that the porosity in the vicinity of solid objects is not usually constant. In other words, it varies from the wall to the interior of the porous medium which results in variations in the permeability as well as the equivalent thermal conductivity across the medium. Chandrasekhara et al. [16–18], and have incorporated variable permeability when studying convection in porous media and reported its significant impact on the velocity field and heat transfer.

The present paper considers the case of mixed convection and radiation about a cone immersed in a porous medium. It is assumed that the immersion of the cone has caused disturbances to the host porous medium domain resulting in the porosity, the permeability, and the effective thermal conductivity of the neighboring region to vary. This scenario may result during the underground disposal of the high-level nuclear waste contained in canisters of conical shape. That is, the reprocessing of depleted nuclear reactor fuel elements usually results in the formation of considerable quantities of high-level, long-lived radioactive waste. These wastes are usually adopted and cast in metallic cylinders and are stored in canisters which may lately be burred underground. The decay heat generated from the spent nuclear fuel may last for decades and therefore might result in the temperature to be high enough so as to make it important to include radiation heat transfer into consideration.

On the other hand, the inclusion of thermal radiation into the energy equation requires that some care be taken. That is, unlike heat transfer by conduction and convection, thermal radiation is a more complex process because of its spectral and directional dependence in addition to the difficulty of determining accurate physical property values of the medium. Since the energy equation describes a local balance of energy arriving by all modes of energy transfer, internal energy stored, energy generated by sources, and energy leaving by all modes of transfer, the net energy associated with radiative effects can be viewed in the energy equation as a local energy source [19], that is,

$$\rho c_p \frac{DT}{D\tau} = \beta T \frac{DP}{D\tau} + \nabla \cdot \left(k\nabla T - q_r\right) + q''' + \Phi_d, \tag{1.1}$$

where $D/D\tau$ is the substantial derivative, β is the thermal coefficient of volume expansion of the fluid, q_r is the radiant flux vector, q''' is some sort of volumetric energy source, and Φ_d is the energy production by viscous dissipation. Hence an expression for $\nabla \cdot q_r$ is needed in terms of the temperature distribution.The Radiative Transfer Equation (RTE) describes the variation of the spectral radiative intensity for an absorbing-emitting-scattering medium in a given direction, s, in the solid angle $d\omega$ about the s direction as

$$\frac{dI_\lambda(s)}{ds} = -a_\lambda(s)I_\lambda(s) + a_\lambda(s)I_{\lambda b}(s) - \sigma_{s\lambda}(s)I_\lambda(s) + \int_{\omega'=0}^{4\pi} I_\lambda\left(s,\omega'\right)\xi_\lambda\left(\omega,\omega'\right)d\omega', \tag{1.2}$$

where $I_\lambda(s)$ is the spectral intensity of the radiation, $I_{\lambda b}$ is the blackbody intensity, s is the optical coordinate, and $\xi_\lambda(\omega,\omega')$ is the scattering phase function which represents the distribution of energy after it is scattered. The first term in the right hand side of the above equation represents the loss in spectral radiation intensity by absorption (includes induced emission), the second term represents the gain by spontaneous emission, the third term represents scattering loss, and the last term represents the gain by scattering into s direction. It is apparent that solutions to the above-given system of equations may not be possible,

however, certain simplification may be imposed that makes this system amenable to solution. One of these simplifications may be the assumption of optically thick medium in which radiation travels only a short distance before being scattered or absorbed. In this case the local radiation intensity at a point is assumed to only emerge within the neighborhood of that point. For this situation, it is possible to transform the relation of radiative energy into a diffusion-like relationship [19].

2. Analysis

Consider the radiative mixed convection along the surface of a cone immersed in a fluid-saturated porous medium whose properties are assumed to be functions of space (following [16]). Figure 1 describes the physical domain and the coordinate system. The governing equations for this problem may be given as

$$\frac{\partial ru}{\partial x} + \frac{\partial rv}{\partial y} = 0, \tag{2.1}$$

$$u = -\frac{K}{\mu}\left(\frac{\partial p}{\partial \overline{x}} + \rho g_x\right), \tag{2.2}$$

$$v = -\frac{K}{\mu}\left(\frac{\partial p}{\partial \overline{y}} + \rho g_y\right), \tag{2.3}$$

$$u\frac{\partial T}{\partial x} + v\frac{\partial T}{\partial y} = \frac{\partial}{\partial x}\left(\alpha_x \frac{\partial T}{\partial x}\right) + \frac{\partial}{\partial y}\left(\alpha_{\overline{y}} \frac{\partial T}{\partial y}\right) - \frac{1}{\left(\rho_\infty C_p\right)_f}\frac{\partial q^r}{\partial y}, \tag{2.4}$$

$$\rho = \rho_\infty\left[1 - \beta(T - T_\infty)\right], \tag{2.5}$$

$$K = K_o\left(1 + \zeta e^{-y/Y}\right), \tag{2.6}$$

$$\varepsilon = \varepsilon_o\left(1 + \zeta^* e^{-y/Y}\right), \tag{2.7}$$

$$\text{Subject to} \quad \begin{array}{lll} y = 0: & v = 0, & T = T_w, \\ y \longrightarrow \infty, & u = u_\infty, & T = T_\infty, \end{array} \tag{2.8}$$

where u and v are the velocity components in the x and y-directions, respectively, T, T_∞, and T_w are the temperatures of the fluid, the ambient medium, and the cone surface, respectively, $(\rho_\infty C_p)_f$ is the product of density and specific heat of the fluid, p is the pressure, K_0 and ε_0 are the permeability and porosity at the edge of the boundary layer, respectively, ζ and ζ^* are some constants whose values are taken as 3.0 and 1.5, respectively, (see [16]), β, μ, and ρ are the thermal expansion coefficient, the viscosity, and the density of the fluid, respectively, and g is the acceleration due to gravity, $\alpha_{\overline{x}}$, $\alpha_{\overline{y}}$ are the components of the thermal diffusivity in x and y directions, respectively. The quantity q^r in the right hand side of (2.4) represents the radiative heat flux in the y-direction. The radiative heat flux term is simplified by the Rosseland approximation (cf. [20]) and is taken as follows:

$$q^r = -\frac{4\sigma}{3\omega}\frac{\partial T^4}{\partial \overline{y}}, \tag{2.9}$$

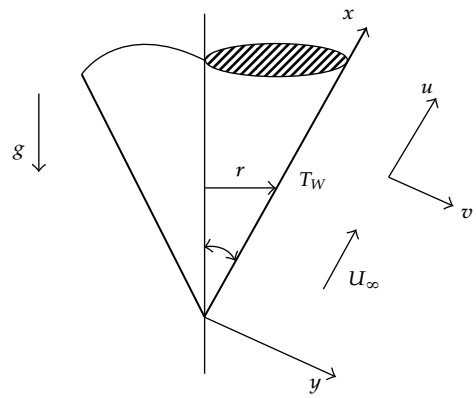

Figure 1: Schematic diagram of the problem.

where σ and ω are the Stefan-Boltzmann constant and the mean absorption coefficient. The radiative heat flux in the x-direction is considered negligible in comparison with that in the y-direction [20]. The normal component of the velocity near the boundary is small compared with the other component of the velocity, and the derivatives of any quantity in the normal direction are large compared with derivatives of the quantity in direction of the wall. Under these assumptions, and by cross differentiation of (2.2) and (2.3) and subtracting, the above system of equations reduces to

$$\frac{\partial ru}{\partial x} + \frac{\partial rv}{\partial y} = 0, \tag{2.10}$$

$$\frac{\partial u}{\partial y} = \frac{\rho_\infty g\beta \cos\gamma}{\mu} k(y) \frac{\partial T}{\partial y} + \frac{gK_o \cos\gamma}{\mu} \frac{\zeta}{\Upsilon} e^{-y/\Upsilon} \rho(y), \tag{2.11}$$

$$u\frac{\partial T}{\partial x} + v\frac{\partial T}{\partial y} = \frac{\partial}{\partial y}\alpha(y)\frac{\partial T}{\partial y} + \frac{16\sigma}{3\omega(\rho_\infty C_p)_f}\frac{\partial}{\partial y}\left(T^3\frac{\partial T}{\partial y}\right). \tag{2.12}$$

Noting that the thermal diffusivity term is defined by $\alpha(y) = \lambda_m(y)/(\rho_\infty C_p)_f$, where λ_m is the effective thermal conductivity of the saturated porous medium. Likewise, $\alpha(y)$ also varies in the y-direction since it is related to the effective thermal conductivity of the saturated porous medium $\lambda_m(y)$, which is defined as $\lambda_m = \lambda_f\varepsilon + (1-\varepsilon)\lambda_s$, where $\lambda_f(y)$ and $\lambda_s(y)$ are the thermal conductivity of the fluid and solid, respectively. Therefore, $\alpha(y)$ may be defined as

$$\alpha(y) = \alpha_0\left[\varepsilon_0\left(1 + \zeta^* e^{-y/\Upsilon}\right) + \sigma^*\left\{1 - \varepsilon_0\left(1 + \zeta^* e^{-y/\Upsilon}\right)\right\}\right], \tag{2.13}$$

where, $\alpha_0 = \lambda_f/(\rho_0 C_p)_f$ is the value of diffusivity at the edge of the boundary layer and $\sigma^* = \lambda_s/\lambda_f$ is the ratio of the thermal conductivity of the solid to the conductivity of the fluid. The term $16\sigma/3\omega(\rho_0 C_P)_f$ can be considered as the radiative conductivity.

Introducing the stream function, ψ, such that $ru = \partial\psi/\partial y$ and $rv = -\partial\psi/\partial x$, the continuity equation is automatically satisfied. Following Yih [10], we define the following transformations:

$$\eta = \left(\frac{y}{x}\right)\mathrm{Pe}_x^{1/2}\chi^{-1}, \qquad \chi^{-1} = 1 + \left(\frac{\mathrm{Ra}_x}{\mathrm{Pe}_x}\right)^{1/2}, \qquad \psi = \alpha_0 r \mathrm{Pe}_x^{1/2}\chi^{-1} f(\chi,\eta),$$
$$\theta = \frac{(T - T_\infty)}{(T_w - T_\infty)}, \qquad \mathrm{Pe}_x = \frac{u_\infty x}{\alpha_0}, \qquad \mathrm{Ra}_x = \frac{\rho_0 K_0 g\beta(T_w - T_\infty)x\cos\gamma}{\alpha_0\mu}. \tag{2.14}$$

Moreover, it is assumed that $u_\infty = Bx^m$ defines the velocity of the potential cone flow outside the boundary layer, where $m = \gamma(\pi - \gamma)$ is the cone angle parameter, γ is half the cone angle, and B is constant. The tabulated values of γ and m are given by Hess and Faulkner [21]. The cone angle of 15, 30, 45, 60, and 75^0 are discussed in this paper, therefore, m is 0.0316314, 0.1156458, 0.2450773, 0.4241237, and 0.6667277, respectively. Furthermore, we choose $Y = x\mathrm{Pe}_x^{-1/2}\chi$ such that $K(y)$ and $\alpha(y)$ are purely functions of η only. Substituting into (2.10) to (2.12), we obtain the following transformed governing equations:

$$f'' = (1-\chi)^2(1 + \zeta e^{-\eta})\theta' - (1-\chi)^2\zeta e^{-\eta}\theta + (1-\chi)^2\zeta N e^{-\eta}, \tag{2.15}$$

$$\alpha^*(\eta)\theta'' + \frac{1}{2}((1+m\chi))f\theta' + \frac{4R_d}{3}\left\{\theta'((H-1)\theta+1)^3\right\}' = -\left(\frac{\partial}{\partial\eta}\alpha^*(\eta)\right)\theta' - \frac{m}{2}\chi(1-\chi)\left(\theta'\frac{\partial f}{\partial\chi} - f'\frac{\partial\theta}{\partial\chi}\right), \tag{2.16}$$

where $N = 1/\beta(T_W - T_\infty)$, $\alpha^*(\eta) = \{\varepsilon_0 + \sigma^*(1-\varepsilon_0) + \varepsilon_0\zeta^* e^{-\eta}(1-\sigma^*)\}$, $R_d = 4\sigma T_\infty^3/(k\omega)$ is the radiation parameter, and $H = T_w/T_\infty$ is the surface temperature parameter.

The boundary conditions become

$$(1+m\chi)f(\chi,0) + m\chi(1-\chi)\frac{\partial f}{\partial\chi}(\chi,0) = 0, \quad \text{or } f = 0,\ \theta = 1,$$
$$f'(\chi,\infty) = \chi^2, \qquad \theta(\chi,\infty) = 0. \tag{2.17}$$

The Darcian velocity components may be defined as

$$u = u_\infty\chi^{-2}f(\chi,\eta),$$
$$v = -\frac{\alpha_0\mathrm{Pe}_x^{1/2}}{x}\chi^{-1}\left\{\left(\frac{m\chi+1}{2}\right)f - \left(\frac{1-m\chi}{2}\right)\eta f' + \frac{m}{2}\chi(1-\chi)\left(\frac{\partial f}{\partial\chi}\right)\right\}. \tag{2.18}$$

We note that $\chi = 0$ and 1 correspond to pure free and forced convection cases, respectively. Between these limits, it represents combined free and forced convection cases. The heat flux q_w at the surface of the cone is

$$q_w = -\left(\left[k + \frac{16\sigma T^3}{3(a_r + \sigma_s)}\right]\frac{\partial T}{\partial y}\right)_{y=0}. \tag{2.19}$$

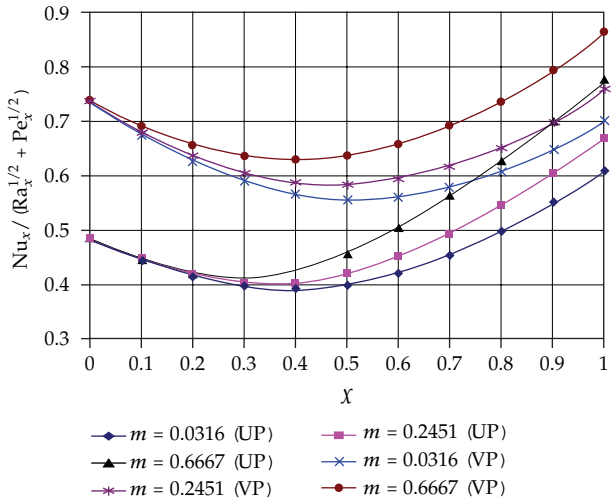

Figure 2: Comparison of values $\mathrm{Nu}_x/(\mathrm{Ra}_x^{1/2}+\mathrm{Pe}_x^{1/2})$ for m and χ with $R_d = 0.1$ and $H = 1.1$ for both UP and VP cases.

For practical applications, it is usually the local Nusselt number that is of interest. This can be expressed as

$$\mathrm{Nu}_x = \frac{hx}{k} = \frac{q_w x}{k(T_w - T_\infty)}, \tag{2.20}$$

where h denotes the local heat transfer coefficient and k represents the thermal conductivity. Substituting (2.6), and (2.19) into (2.20), we obtain

$$\frac{\mathrm{Nu}_x}{\mathrm{Ra}_x^{1/2}+\mathrm{Pe}_x^{1/2}} = -\left(1+\frac{4R_dH^3}{3}\right)\theta'(\chi,0). \tag{2.21}$$

Primes in the above equations denote differentiation with respect to η, $f_\chi = \partial f/\partial\chi$ and $\theta_\chi = \partial\theta/\partial\chi$.

3. Results and Discussion

Numerical results for the governing (2.8)-(2.9) and the boundary conditions (2.10) are nonlinear partial differential equations depending on the mixed convection parameter χ, the radiation-condition parameter R_d, and the surface temperature parameter H for both UP and VP cases. Numerical results are presented for the mixed convection parameter χ ranging from 0 to 1.0, the cone angle parameter m ranging from 0.03163 to 0.66672, the radiation parameter R_d ranging from 0 to 1, and the surface temperature parameter H from 1.1 to 3.0 for both uniform permeability (UP), that is, $d = d^* = 0$ and variable permeability (VP), that is, d, $d^* \neq 0$ cases. For the purpose of numerical integration we have assumed that $d = 3$, $d^* = 1.5$ and $\varepsilon_0 = 0.4$ (Christopher and Middleman [22]).

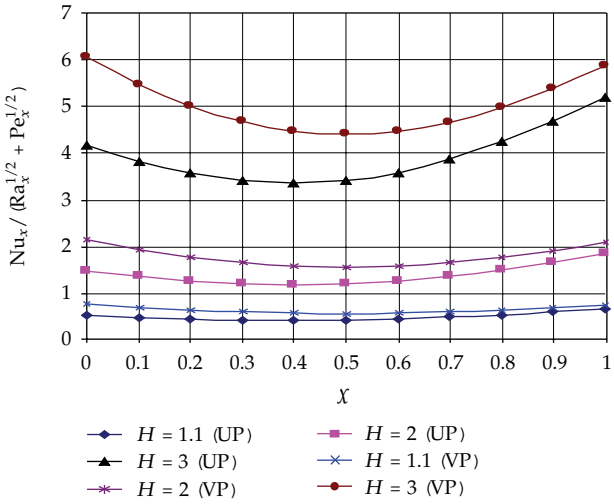

Figure 3: Comparison of values $\mathrm{Nu}_x/(\mathrm{Ra}_x^{1/2}+\mathrm{Pe}_x^{1/2})$ for H and χ with $m = 0.0316$ and $R_d = 0.3$ for both UP and VP cases.

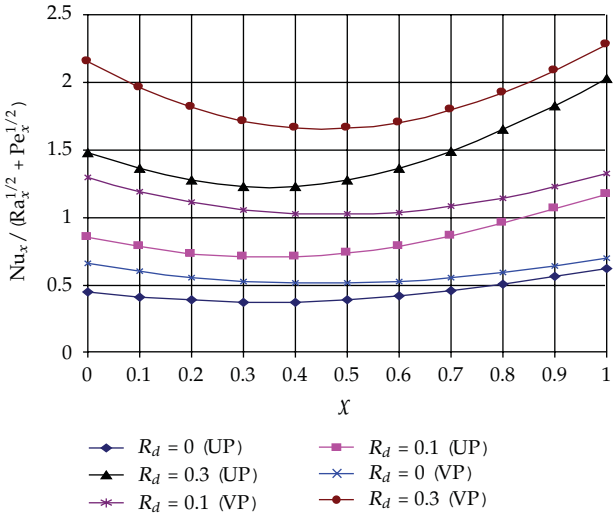

Figure 4: Comparison of values $\mathrm{Nu}_x/(\mathrm{Ra}_x^{1/2}+\mathrm{Pe}_x^{1/2})$ for R and χ with $m = 0.2451$ and $H = 2.0$ for both UP and VP cases.

Figures 2–4 display results for the Nusselt number for various values of m, R_d, χ and H for two cases UP and VP cases. From Figure 2, it is noteworthy that for pure free convection ($\chi = 0$), there is no effect of the parameter m on the heat transfer rate on the surface, while for the pure forced convection ($\chi = 1$), the parameter m enhances the heat transfer rate at the surface. It is observed from Figure 3 that the parameter H enhances the heat transfer rate, and Figure 4 shows that the parameter R_d enhances the heat transfer rate too. From Figures 2–4, it is interesting to note that the heat transfer rate at χ tends to 0 or 1 (i.e., at pure free and pure forced convection) and has the highest values.

Nomenclature

a_r: Rosseland mean extinction coefficient
B: Constant
C_p: Specific heat at constant pressure
d: Constant defined in(2.5)
d^*: Constant defined in(2.5)
f: Nondimensionless stream function
g: Acceleration due to gravity
h: Heat transfer coefficient
$K(y)$: Permeability of the porous medium
k_r: Thermal conductivity
K_0: Permeability at the edge of the boundary layer
m: Cone angle parameter
Nu_x: Local Nusselt number
Pe_x: Local Peclet number
q_r: The rate of heat transfer
q_w: Surface heat flux
r: Local radius of the cone
Ra_x: Local Rayleigh number
R_d: Radiation parameter
T: Fluid temperature
T_w: Wall temperature
T_∞: Free stream temperature
u, v: Darcian velocity in the x and y directions
u_∞: Free stream velocity
x, y: Coordinate axes along and perpendicular to the plate
$\alpha(y)$: Thermal diffusivity
α^*: Ratio of viscosities
α_0: Thermal diffusivity at the edge of the boundary layer
β: Volumetric coefficient of thermal expansion
γ: Half angle of the cone
$\varepsilon(y)$: Porosity of the saturated porous medium
ε_0: Porosity at the edge of the boundary layer
η: Dimensionless distance
θ: Dimensionless temperature
λ: Constant in(2.2)
λ_m: Effective thermal conductivity of the porous medium
μ: Viscosity of porous medium
ν: Kinematics viscosity of the fluid
ψ: Stream function
ρ: Density of fluid
χ: Mixed convection parameter
σ^*: Ratio of thermal conductivity of the solid to the liquid
σ: Permeability parameter

Subscripts

w: Surface conditions

∞: Condition far away from surface.

References

[1] J. C. Hsieh, T. S. Chen, and B. F. Armaly, "Nonsimilarity solutions for mixed convection from vertical surfaces in porous media: variable surface temperature or heat flux," *International Journal of Heat and Mass Transfer*, vol. 36, no. 6, pp. 1485–1493, 1993.

[2] A. A. Mohammadien and M. F. El-Amin, "Thermal dispersion-radiation effects on non-darcy natural convection in a fluid saturated porous medium," *Transport in Porous Media*, vol. 40, no. 2, pp. 153–163, 2000.

[3] M. A. El-Hakiem and M. F. El-Amin, "Thermal radiation effect on non-Darcy natural convection with lateral mass transfer," *Heat and Mass Transfer*, vol. 37, no. 2-3, pp. 161–165, 2001.

[4] P. Cheng, "Similarity solutions for mixed convection from horizontal impermeable surfaces in a saturated porous medium," *International Journal of Heat and Mass Transfer*, vol. 20, no. 9, pp. 893–898, 1977.

[5] Y. Josh and B. Gebhart, "Mixed convection in porous media adjacent to a vertical uniform heat flux surface," *International Journal of Heat and Mass Transfer*, vol. 28, pp. 1783–1786, 1985.

[6] J. H. Merkin and I. Pop, "Mixed convection boundary-layer on a vertical cylinder embedded in a saturated porous medium," *Acta Mechanica*, vol. 66, no. 1-4, pp. 251–262, 1987.

[7] W. B. Hooper, T. S. Chen, and B. F. Armaly, "Mixed convection along an isothermal vertical cylinder in porous media," *Journal of Thermophysics and Heat Transfer*, vol. 8, no. 1, pp. 92–99, 1994.

[8] M. Kumari and R. S. R. Gorla, "Combined convection along a non-isothermal wedge in a porous medium," *Heat and Mass Transfer*, vol. 32, no. 5, pp. 393–398, 1997.

[9] W. J. Minkowycz, P. Cheng, and C. H. Chang, "Mixed convection about a nonisothermal cylinder and sphere in a porous medium," *Number Heat Transfer*, vol. 8, no. 3, pp. 349–395, 1985.

[10] K. A. Yih, "Effect of radiation on natural convection about a truncated cone," *International Journal of Heat and Mass Transfer*, vol. 42, no. 23, pp. 4299–4305, 1999.

[11] K. A. Yih, "Mixed convection about a cone in a porous medium: the entire regime," *International Communications in Heat and Mass Transfer*, vol. 26, no. 7, pp. 1041–1050, 1999.

[12] I. Abbas, M. F. El-Amin, and S. Amgad, "Combined effect of thermal dispersion and radiation on free convection in a fluid saturated, optically thick porous medium," *Engineering Research*, vol. 72, no. 3, pp. 135–144, 2008.

[13] C. E. Schwartz and J. M. Smith, "Flow distribution in packed beds," *Industrial & Engineering Chemistry*, vol. 45, pp. 1209–1218, 1953.

[14] J. W. Tierney, L. H. S. Roblee, and R. M. Barid, "Redial porosity variation in packed beds," *AIChE Journal*, vol. 4, pp. 460–464, 1958.

[15] R. F. Benenati and C. B. Brosilow, "Void fraction distribution in beds of spheres," *AIChE Journal*, vol. 8, pp. 359–361, 1962.

[16] B. C. Chandrasekhara, A. R. Hanumanthappa, and S. Chandranna, "Mixed convection in the presence of horizontal impermeable surfaces in saturated porous media with variable permeability," in *Proceedings of the 12th National Conference Fluid Dynamics Fluid Power*, I.I.T. Delhi, India, December 1983.

[17] B. C. Chandrasekhara, P. M. S. Namboodiri, and A. R. Hanumanthappa, "Similarity solutions for buoyancy induced flows in a saturated porous medium adjacent to impermeable horizontal surfaces," *Wärme- und Stoffubertragung*, vol. 18, no. 1, pp. 17–23, 1984.

[18] B. C. Chandrasekhara and P. M. S. Namboodiri, "Influence of variable permeability on combined free and forced convection about inclined surfaces in porous media," *International Journal of Heat and Mass Transfer*, vol. 28, no. 1, pp. 199–206, 1985.

[19] R. Howell and J. R. Siegel, *Thermal Radiation Heat Transfer*, Taylor & Francis INC, Pa, USA, Sol edition edition, 2002.

[20] E. M. Sparrow and R. D. Cess, *Radiation Heat Transfer*, Hemisphere Publ Crop., DC, USA, Augmented Edition edition, 1978.

[21] J. L. Hess and S. Faulkner, "Accurate values of the exponent governing potential flow about semi-infinite cone," *AIAA Journal*, vol. 3, pp. 767–774, 1965.

[22] R. H. Christopher and S. Middleman, "Power-law flow through a paced tube," *Industrial & Engineering Chemistry Fundamentals*, vol. 4, pp. 422–426, 1983.

Hindawi Publishing Corporation
Journal of Applied Mathematics
Volume 2011, Article ID 793653, 16 pages
doi:10.1155/2011/793653

Research Article

Development of a Particle Interaction Kernel Function in MPS Method for Simulating Incompressible Free Surface Flow

Tony W. H. Sheu,[1,2,3] Chenpeng Chiao,[1] and Chinlong Huang[1]

[1] *Department of Engineering Science and Ocean Engineering, National Taiwan University, Taipei, 10617, Taiwan*
[2] *Taida Institute of Mathematical Science (TIMS), National Taiwan University, Taipei, 10617, Taiwan*
[3] *Center for Quantum Science and Engineering (CQSE), National Taiwan University, Taipei, 10617, Taiwan*

Correspondence should be addressed to Tony W. H. Sheu, twhsheu@ntu.edu.tw

Received 3 December 2010; Accepted 2 January 2011

Academic Editor: Zhangxin Chen

Copyright © 2011 Tony W. H. Sheu et al. This is an open access article distributed under the Creative Commons Attribution License, which permits unrestricted use, distribution, and reproduction in any medium, provided the original work is properly cited.

We aimed to derive a kernel function that accounts for the interaction among moving particles within the framework of particle method. To predict a computationally more accurate moving particle solution for the Navier-Stokes equations, kernel function is a key to success in the development of interaction model. Since the smoothed quantity of a scalar or a vector at a spatial location is mathematically identical to its collocated value provided that the kernel function is chosen to be the Dirac delta function, our guideline is to derive the kernel function that is closer to the delta function as much as possible. The proposed particle interaction model using the newly developed kernel function will be validated through the two investigated Navier-Stokes problems which have either the semianalytical or the benchmark solutions.

1. Introduction

Numerical methods that are now available for performing flow simulations can be divided into the Eulerian and Lagrangian two classes. In the Eulerian method, flow equations are solved at a fixed mesh system. On the contrary, in the Lagrangian method, which can be subdivided into the mesh-based and meshfree two subgroups, either meshes or particles, on the other hand, are advected with the fluid flow. The consequence is that in the transport equations we no longer have a need to approximate the convection terms. Avoidance of the approximation of convective terms is now known as one of the apparent advantages of employing the Lagrangian approach. Numerical errors of the cross-wind diffusion type can, as a result, be well eliminated. There exists another mathematically rigorous arbitrary Lagrangian-Eulerian (ALE) method [1] which involves the use of Lagrangian and Eulerian solution steps in the course of moving mesh.

In the literature, several well-known grid-based methods, such as the marker-and-cell (MAC) [2], volume-of-fluid (VOF) [3], and level-set [4] methods, have been developed to predict free surface flows. There existed also a major class of meshfree methods, which are known as the particle methods. Particle methods deal with the prescribed particles moving in the Lagrangian sense. As a result, the convection terms can be directly calculated without incurring any numerical diffusion error. Particle methods can be also separated into the Eulerian particle method, such as the particle-in-cell (PIC) method [5] and the Lagrangian particle methods, which include the smoothed particle hydrodynamics (SPHs) and moving particle semi-implicit (MPS) two classes of meshless methods. SPH method, introduced firstly by Lucy [6] and Gingold and Monaghan [7] in 1977, was developed mainly for the simulation of compressible fluid flows based on the interpolation theory through the introduced kernel function (or smoothing kernel). SPH method was later extended to simulate also the incompressible free surface flow [8].

Another gridless particle method, called the MPS, was more recently developed to simulate the incompressible Navier-Stokes fluid flows [9]. The motion of each particle in this method is calculated through the interaction of its neighboring particles by means of the kernel (or weight) function. This means that all the spatial derivatives can be calculated by the deterministic particle interaction without the need of generating meshes in the flow. This explains why MPS method is gradually becoming effective for use in simulating many practical problems involving the complicated geometry and complex physics. For the flow problems with an inflow or an outflow boundary, this method was however found to have difficulty of tracing a particle easily. In addition, MPS method requires an extra CPU time to search for all its neighboring points.

The rest of this paper will be organized as follows. In Section 2 we present the Navier-Stokes and the passive scalar equations, which involve convection and diffusion flux terms. This is followed by presenting the particle interaction models used for the approximation of the gradient and Laplacian differential operators. In Section 4 emphasis will be placed on subject to free surfaces the kernel function used in the particle method. In Section 5, we will validate the proposed particle model by solving two Navier-Stokes problems. In Section 6, conclusions will be drawn based on the predicted results.

2. Working Equations

In this study the following Navier-Stokes equations for the motion of an incompressible fluid flow will be considered in a simply connected domain Ω:

$$\frac{D\underline{u}}{Dt} = -\frac{1}{\rho}\nabla p + \nu\nabla^2\underline{u} + \underline{f}, \tag{2.1}$$

$$\frac{1}{\rho}\frac{D\rho}{Dt} = -\nabla\cdot\underline{u}, \tag{2.2}$$

where $D\underline{u}/Dt = \partial\underline{u}/\partial t + (\underline{u}\cdot\nabla)\underline{u}$. In (2.1), which is the momentum equation, ρ stands for the density of the investigated flow, ν the kinematic viscosity, and $\underline{f}$ the gravitational acceleration vector.

The following model equation will be considered in the development of kernel function since it is the key equation in the simulation of momentum equations for the incompressible fluid flow:

$$u\frac{\partial \phi}{\partial x} + v\frac{\partial \phi}{\partial y} = \mu\left(\frac{\partial^2 \phi}{\partial x^2} + \frac{\partial^2 \phi}{\partial y^2}\right). \tag{2.3}$$

Both of the velocity components u and v and the fluid viscosity μ in (2.3) are assumed to be the constant values to facilitate the development of the proposed kernel function in Section 4.

3. Particle Interaction Models for Two Differential Operators

Due to the difficulties of applying the grid-based methods to simulate complex flow physics, particle-based methods become gradually popular in the simulation of incompressible Navier-Stokes equations subject either to a free surface or an interface. In particle methods, the differential operators for the mass and momentum conservation equations need to be replaced by their corresponding particle interaction operators. In other words, partial differential equations (2.1)-(2.2) written in the continuous context will be transformed to their corresponding discrete particle interaction equations so that the transport equations under investigation can be approximated by the chosen moving particles and their interaction. The degree of success depends on the kernel (or weighting) function for the particles that are distanced from each other by the user's prescribed finite length for the approximation of velocity vectors and pressure in the incompressible fluid flows around these particles.

Consider a particle at which a physical quantity f_i is defined at a position $\underline{r}_i$. One can represent f_i approximately at each location as follows by virtue of the following kernel function $w(\underline{r})$

$$\langle f(\underline{r})\rangle \cdot \sum_i w(|\underline{r}_i - \underline{r}|) = \sum_i f_i w(|\underline{r}_i - \underline{r}|). \tag{3.1}$$

It is important to note that the smoothed quantity $\langle f\rangle_i$ for f at $\underline{r}_i$ turns out to be exactly identical to the local value of f_i if the kernel function in (3.1) is the Dirac delta function. This implies that the chosen kernel function $w(\underline{r})$, which should be constrained by the integral constraint equation $\int_V w(r)dV = 1$ shown in (3.1), determines the prediction quality of the particle methods. One can find different kernel functions in [10].

For a scalar ϕ at a location $\underline{r}_j$, its value can be expanded in Taylor series with respect to the value of ϕ at $\underline{r}_i$ as follows:

$$\phi_j = \phi_i + \nabla\phi|_{ij} \cdot \left(\underline{r}_j - \underline{r}_i\right) + H.O.T. \tag{3.2}$$

By dropping the higher-order terms shown above, we are led to get the first-order approximated equation $\phi_j - \phi_i = \nabla\phi|_{ij} \cdot (\underline{r}_j - \underline{r}_i)$. By multiplying the term $(\underline{r}_j - \underline{r}_i)^{-1}$ on both hand

sides of the resulting simplified equation, we can get

$$\nabla\phi|_{ij} = \frac{(\phi_j - \phi_i)\left(\underline{r}_j - \underline{r}_i\right)}{\left|\underline{r}_j - \underline{r}_i\right|\left|\underline{r}_j - \underline{r}_i\right|}. \tag{3.3}$$

Let $\nabla\phi|_{ij}$ be f. We then substitute it into (3.1) to get the following smoothed representation of $\nabla\phi$, which is denoted by $\langle\nabla\phi\rangle$ at the node ij, in a domain with d dimensions

$$\langle\nabla\phi\rangle|_{ij} = \frac{d}{n^0}\sum_{j\neq i}\frac{\phi_j - \phi_i}{\left|\underline{r}_j - \underline{r}_i\right|}\left(\underline{r}_j - \underline{r}_i\right)w\left(\underline{r}_j - \underline{r}_i\right). \tag{3.4}$$

In the above, n^0 denotes the particle number density and it is defined as $\sum_{j\neq i} w(|\underline{r}_j - \underline{r}_i|)$. Note that $n_i = n^0$ is true only under the incompressible flow condition.

One can similarly derive the Laplacian operator for a scalar ϕ, which has been derived in [9] as follows

$$\left\langle\nabla^2\phi\right\rangle|_i = \frac{2d}{\lambda n^0}\sum_{j\neq i}(\phi_j - \phi_i)w\left(\left|\underline{r}_j - \underline{r}_i\right|\right), \tag{3.5}$$

where

$$\lambda = \frac{\int_{V'}\left|\underline{r}_j - \underline{r}_i\right|^2 w\left(\left|\underline{r}_j - \underline{r}_i\right|\right)dV}{\int_{V'} w\left(\left|\underline{r}_j - \underline{r}_i\right|\right)dV}. \tag{3.6}$$

Note that V' shown above denotes the volume excluding of a small interval that contains the point at i. One can also employ the Laplacian operator given below [11]

$$\left\langle\nabla^2\phi\right\rangle|_{ij} = \frac{2d}{n^0}\sum_{j\neq i}\frac{\phi_j - \phi_i}{\left|\underline{r}_j - \underline{r}_i\right|}w\left(\left|\underline{r}_j - \underline{r}_i\right|\right). \tag{3.7}$$

The advantage of employing particle methods becomes clear in that all the spatial derivatives can be calculated from the chosen kernel function without the need of generating meshes in the physical domain. Much of the computational effort in the generation of a good quality mesh for performing an accurate numerical simulation in a domain with moving boundaries is therefore avoided.

Unlike the SPH particle method, calculations of the values for $\nabla\phi$ and $\nabla^2\phi$ in (3.4), (3.5), and (3.7) involve only the kernel function $w(\underline{r})$. Since the derivative of kernel function needs not to be calculated in the approximation of differential operators ∇ and ∇^2, numerical oscillations, which may be generated in the fixed grid Eulerian approach for the cases with high solution gradients, can be completely avoided. As a result, one has the flexibility to choose the kernel function that has a slope as steep as the Dirac delta function.

4. Development of the Kernel Functions

In view of (3.4) and (3.5)–(3.7), we know that the quality of approximating the operators $\langle \nabla \phi \rangle_{ij}$ and $\langle \nabla^2 \phi \rangle_i$ depends entirely on the chosen kernel function $w(\underline{r})$ and the number of the prescribed particles. Moreover, the chosen particle locations and the employed kernel function will determine the subsequent particle location in moving particle methods. For this reason, the chosen kernel function will be derived below in detail.

In the light of (3.1), we know that the Dirac delta function $\delta(\underline{r})$, which is constrained by $\int_{-\infty}^{\infty} \delta(\underline{r})dr = 1$, is an ideal kernel function. Such a function is, unfortunately, not implementable in computational practice. We have therefore to resort to its corresponding smoothed delta function when carrying out the simulations based on the particle method. The smoothed function is sometimes called as the nascent delta function $\delta_\varepsilon(\underline{r})$, which is defined as $\lim_{\varepsilon \to 0} \delta_\varepsilon(\underline{r}) = \delta(\underline{r})$. In the literature, one can find other nascent delta functions such as the Gaussian function, Lorentz line function, impulse function, and sinc function. There exists also the other class of kernel functions which were developed irrelevantly to the nascent delta functions. Typical examples include the exponential, cubic spline, and quadratic spline functions proposed by Belytschko et al. [12] and the kernel functions proposed by Koshizuka and Oka in 1996 [13] and Koshizuka et al. in 1998 [11].

4.1. Development of Kernel Function for the Pure Diffusion Equation

In this study a new kernel function will be rigorously developed and it will be used to simulate the incompressible Navier-Stokes equations using the particle methods. The guidelines of developing the proposed kernel function will be given below. The kernel function $w(\underline{r})$ under current development falls into the category of nascent delta function. This implies $\lim_{r_e \to 0} w(\underline{r}, r_e) = \delta(\underline{r})$,, where r_e is the radius of a small circle. The weight between two particles that have a distance r apart will be diminished as $r \geq r_e$. For the sake of accuracy, the kernel function will be developed to retain the following constraint condition in the Dirac delta function

$$\int_{-\infty}^{\infty} w(\underline{r}, r_e) d\underline{r} = 1. \tag{4.1}$$

Development of the current kernel function starts with representing it in terms of r/r_e as

$$w(r) = \begin{cases} \dfrac{a}{r_e} + \dfrac{b}{r_e}\left(\dfrac{r}{r_e}\right) + \dfrac{c}{r_e}\left(\dfrac{r}{r_e}\right)^2 + \dfrac{d}{r_e}\left(\dfrac{r}{r_e}\right)^3 + \dfrac{e}{r_e}\left(\dfrac{r}{r_e}\right)^4; & 0 \leq r \leq r_e, \\ 0; & r_e < r. \end{cases} \tag{4.2}$$

Derivation of $w(\underline{r})$ is followed by imposing the four constraint conditions given by $w(r = r_e) = (\partial w/\partial r)|_{r=r_e} = (\partial w/\partial r)|_{r=0} = 0$ and $\int_0^{r/r_e=1} w(r)dr = 1/2$. These imposed conditions

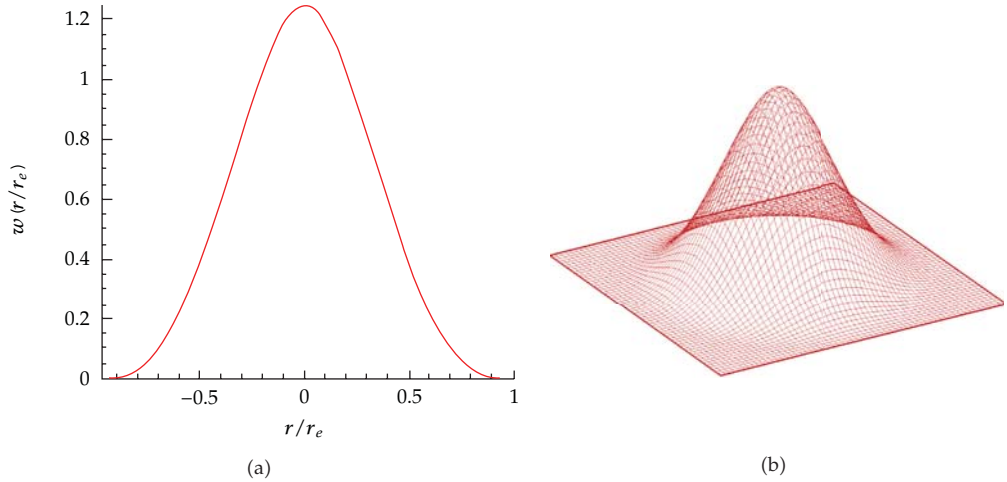

Figure 1: Plot of the developed kernel function. (a) cast in r/r_e coordinate; (b) plotted in xy plane.

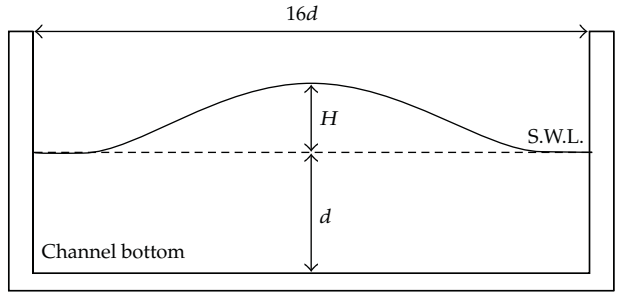

Figure 2: Schematic of the solitary wave propagation problem.

enable us to derive the algebraic equations given below

$$\begin{aligned} a + b + c + d + e &= 0, \\ b + 2c + 3d + 4e &= 0, \\ a + \frac{b}{2} + \frac{c}{3} + \frac{d}{4} + \frac{e}{5} &= \frac{1}{2}, \\ b &= 0. \end{aligned} \tag{4.3}$$

Given the above four equations, one can then easily express a, b, c, d in terms of e as $a = 1 - (1/15)e$, $b = 0$, $c = -3 + (6/5)e$, $d = 2 - (32/15)e$.

By substituting the resulting kernel function into (3.7) for $\nabla^2\phi$, one can get the corresponding discrete equation for the Laplace equation $\partial^2\phi/\partial x^2 + \partial^2\phi/\partial y^2 = 0$ based on

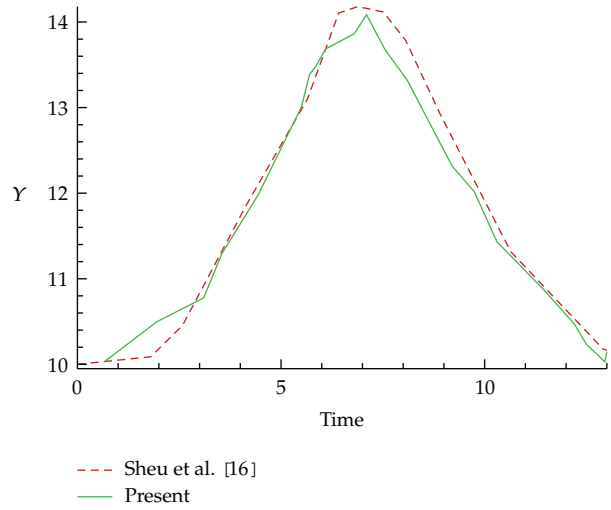

Figure 3: Comparison of the predicted run-up heights of the solitary wave on the right wall.

the particle method

$$\frac{1}{\left[w(h)+2w\left(\sqrt{2}h\right)\right]h^2}\left\{\left(\phi_{i+1,j}+\phi_{i-1,j}+\phi_{i,j+1}+\phi_{i,j-1}-4\phi_i\right)w(h)\right.$$
$$\left.+\left(\phi_{i+1,j+1}+\phi_{i-1,j+1}+\phi_{i+1,j-1}+\phi_{i-1,j-1}-4\phi_i\right)w\left(\sqrt{2}h\right)\right\}=0. \tag{4.4}$$

By performing the modified equation analysis on (4.4), we are led to get the following modified equation:

$$\frac{\partial^2\phi}{\partial x^2}+\frac{\partial^2\phi}{\partial y^2}=-\left[\frac{w\left(\sqrt{2}h\right)}{w(h)+2w\left(\sqrt{2}h\right)}\frac{\partial^4\phi}{\partial x^2\partial y^2}+\frac{1}{12}\frac{\partial^4\phi}{\partial x^4}+\frac{1}{12}\frac{\partial^4\phi}{\partial y^4}\right]h^2$$
$$-\left[\frac{w\left(\sqrt{2}h\right)}{12\left(w(h)+2w\left(\sqrt{2}h\right)\right)}\left(\frac{\partial^6\phi}{\partial x^4\partial y^2}+\frac{\partial^6\phi}{\partial x^2\partial y^4}\right)+\frac{1}{360}\frac{\partial^6\phi}{\partial x^6}+\frac{1}{360}\frac{\partial^6\phi}{\partial y^6}\right]h^4+\cdots. \tag{4.5}$$

Let $w(\sqrt{2}h)=(1/4)w(h)$ the first term on the right hand side of (4.5) turns out to be zero due to $\partial^2\phi/\partial x^2+\partial^2\phi/\partial y^2=0$.

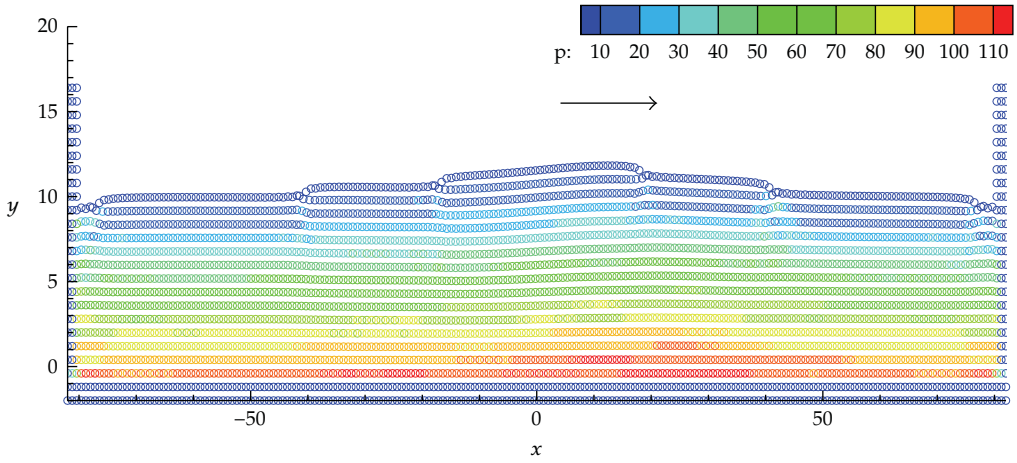

(a)

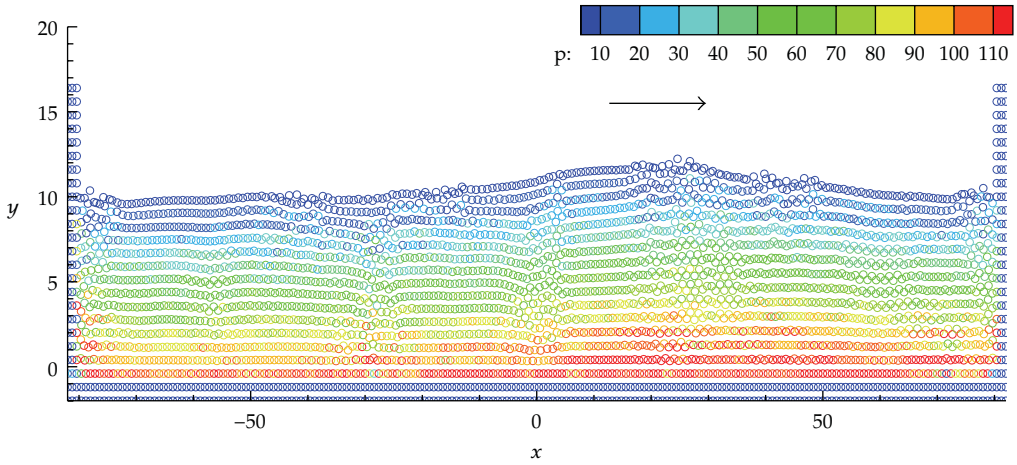

(b)

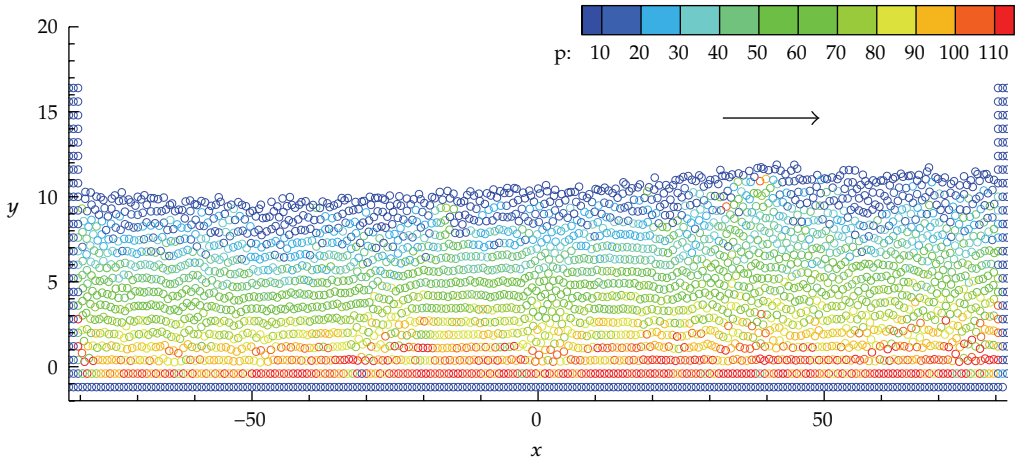

(c)

Figure 4: Continued.

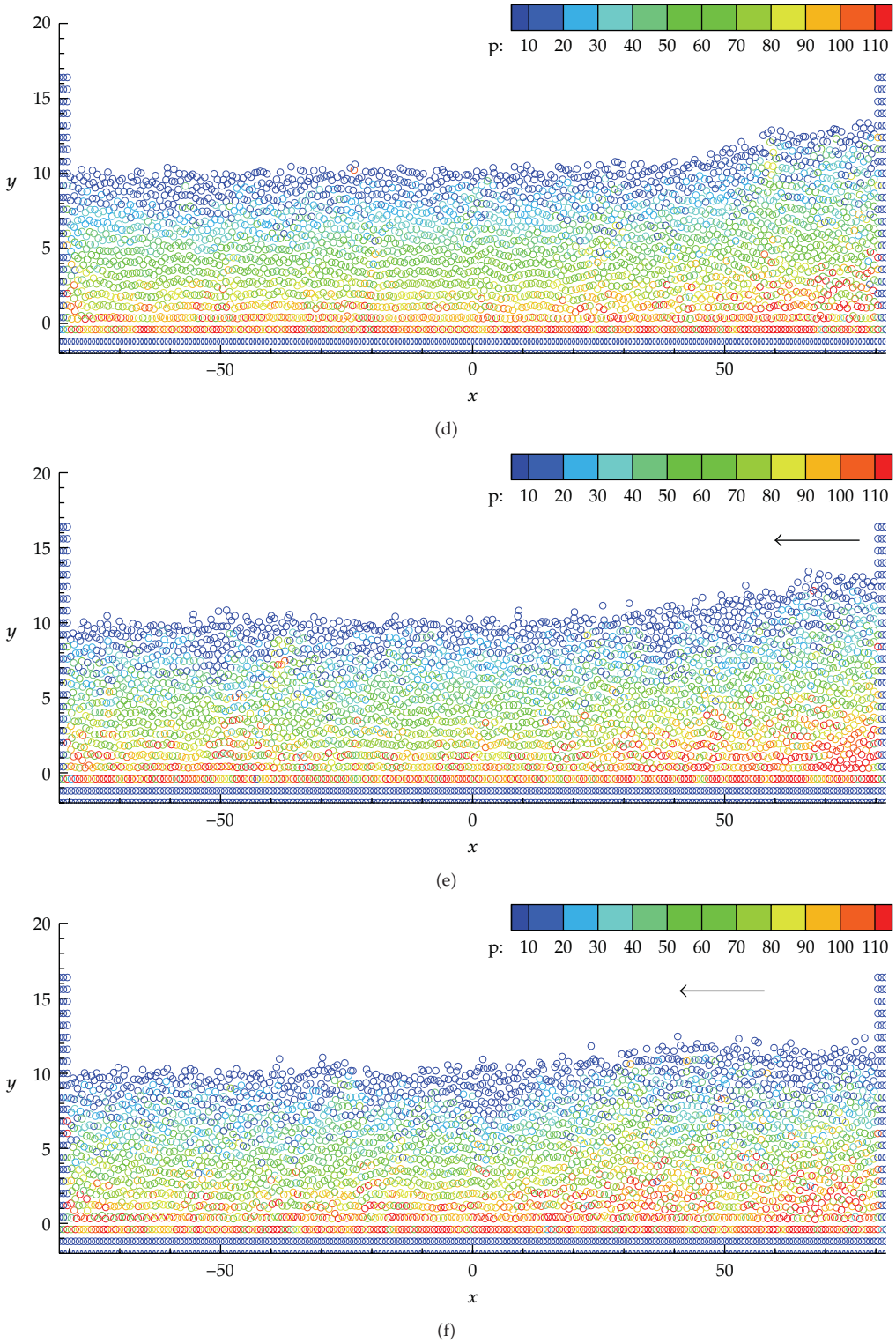

Figure 4: The predicted free surfaces and pressures at different times. (a) $t = 0.5$; (b) $t = 2.0$; (c) $t = 4.0$; (d) $t = 6.0$; (e) $t = 8.0$; (f) $t = 10.0$.

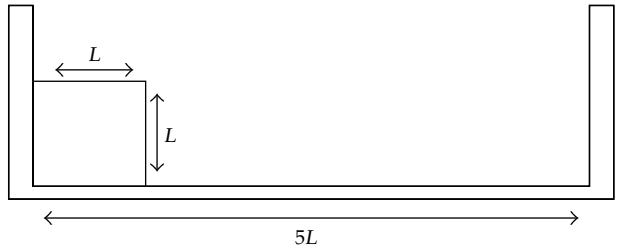

Figure 5: Schematic of the dam break problem.

Provided that $r_e = 2h$, where h denotes the grid size, we can easily know from the following nine-point equation that the resulting approximated equation for (2.3) investigated at the condition of $\mu = \infty$ has accuracy of the fourth order.

$$\frac{\phi_{i+1,j+1} + \phi_{i-1,j+1} + \phi_{i-1,j+1} + \phi_{i+1,j-1} + 4\phi_{i+1,j} + 4\phi_{i-1,j} + 4\phi_{i,j+1} + 4\phi_{i,j-1} - 20\phi_{i,j}}{6h^2} + O\left(h^4\right) = 0. \tag{4.6}$$

Note that (4.6) is derived under the condition of

$$3a + \left(2\sqrt{2} - \frac{1}{2}\right)b + \left(2 - \frac{1}{4}\right)c + \left(\sqrt{2} - \frac{1}{8}\right)d + \left(1 - \frac{1}{16}\right)e = 0. \tag{4.7}$$

The resulting five free parameters can then be uniquely determined from (4.3)–(17) and (4.7) as $a = (480\sqrt{2} - 705)/(512\sqrt{2} - 745)$, $b = 0$, $c = (-960\sqrt{2} + 1515)/(512\sqrt{2} - 745)$, $d = -210/(512\sqrt{2} - 745)$, $e = 480(\sqrt{2} - 600)/(512\sqrt{2} - 745)$.

In summary, the kernel function developed for simulating the pure diffusion equation in this study is given as follows:

$$w(r) = \begin{cases} \dfrac{480\sqrt{2} - 705}{512\sqrt{2} - 745}\dfrac{1}{r_e} + \dfrac{-960\sqrt{2} + 1515}{512\sqrt{2} - 745}\dfrac{1}{r_e}\left(\dfrac{r}{r_e}\right)^2 + \dfrac{-210}{512\sqrt{2} - 745}\dfrac{1}{r_e}\left(\dfrac{r}{r_e}\right)^3 \\ \qquad + \dfrac{480\sqrt{2} - 600}{512\sqrt{2} - 745}\dfrac{1}{r_e}\left(\dfrac{r}{r_e}\right)^4; & 0 \le r \le r_e, \\ 0; & r_e < r \end{cases} \tag{4.8}$$

under the condition given below

$$w\left(\sqrt{2}h\right) = \frac{1}{4}w(h). \tag{4.9}$$

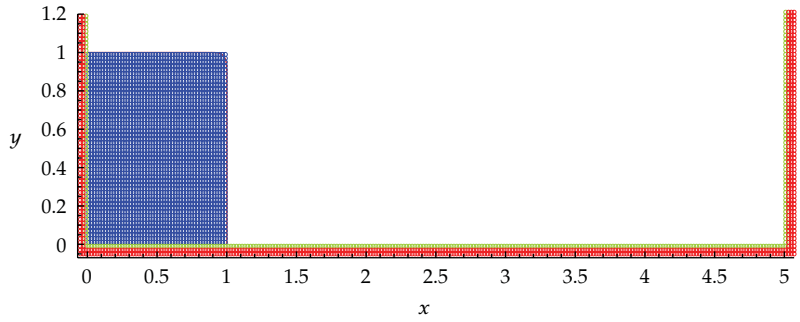

(a)

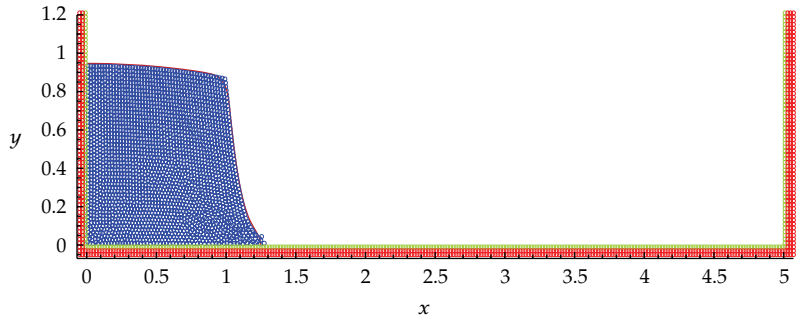

(b)

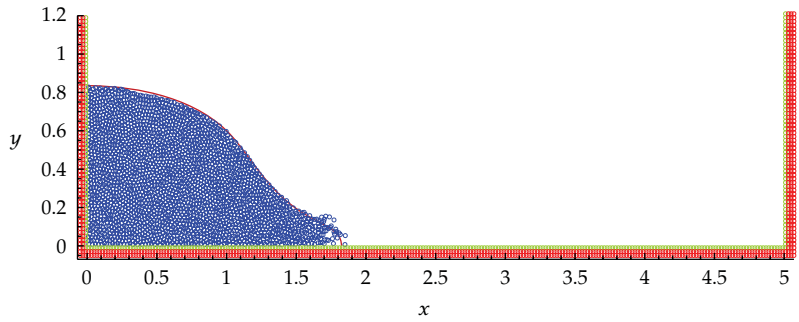

(c)

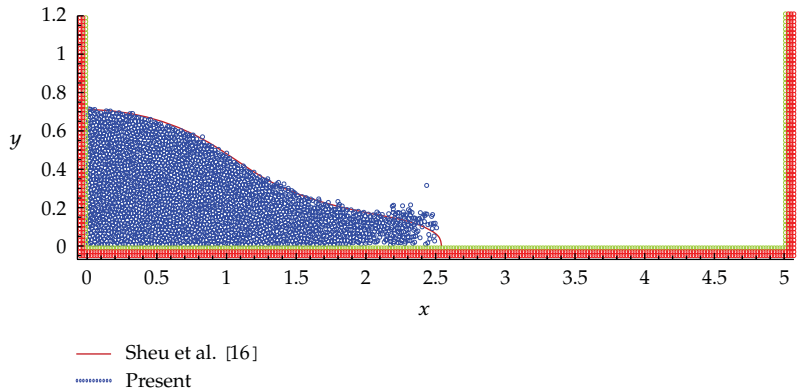

(d)

Figure 6: Continued.

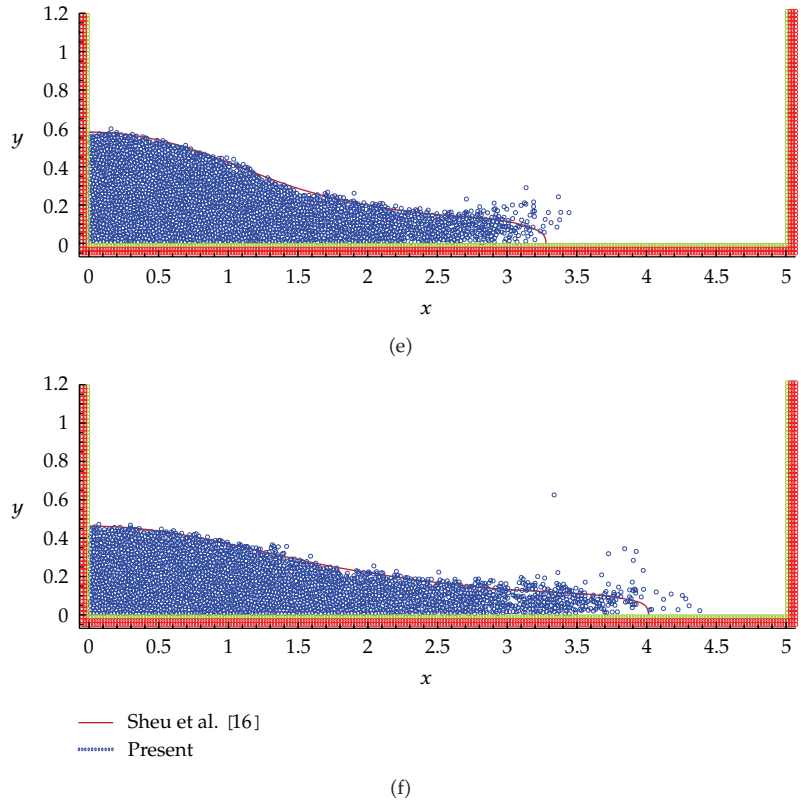

Figure 6: Comparison of the predicted free surfaces by the MPS and the level set methods at different times for the case with Re = 500. (a) $t = 0.0$; (b) $t = 0.5$; (c) $t = 1.0$; (d) $t = 1.5$; (e) $t = 2.0$; (f) $t = 2.5$.

Note that the kernel function $w(r) = r_e/r - 1$ given in [13] has an infinitely large magnitude as the value of r approaches zero. The newly developed kernel function shown in Figure 1, on the other hand, has its local maximum value at $r = 0$. It is also worthy to mention that the currently developed kernel function applied to predict the pure diffusion equation satisfies the following constraint condition, which is also embedded in the delta function

$$\int_{r/r_e=-1}^{r/r_e=1} w(r)dr = 1. \tag{4.10}$$

5. Numerical Results

5.1. Solitary Wave Propagation

Study of the solitary wave propagation in a rectangular channel has received a considerable attention since the resulting analysis can provide engineers with useful information about the wave loading on the structures [14]. The problem under consideration is schematic in

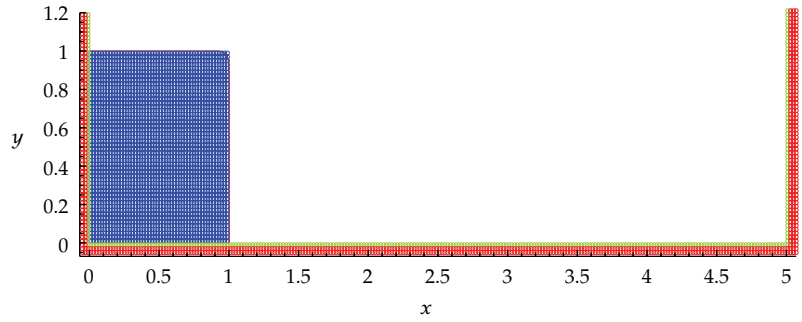

(a)

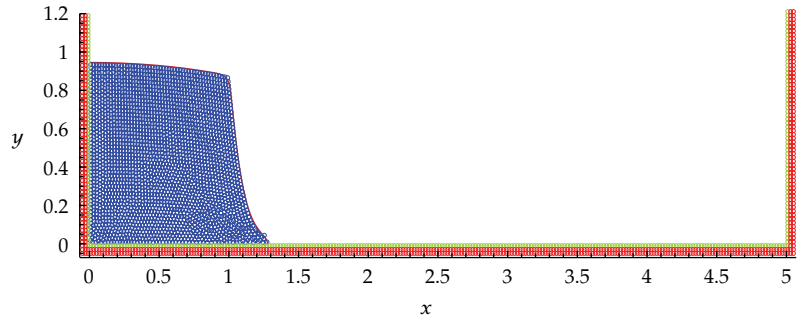

(b)

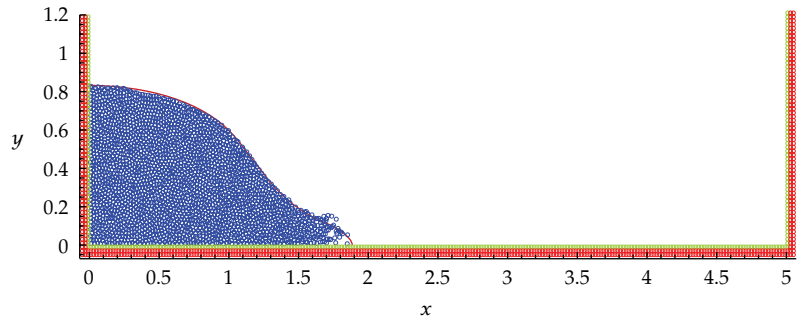

(c)

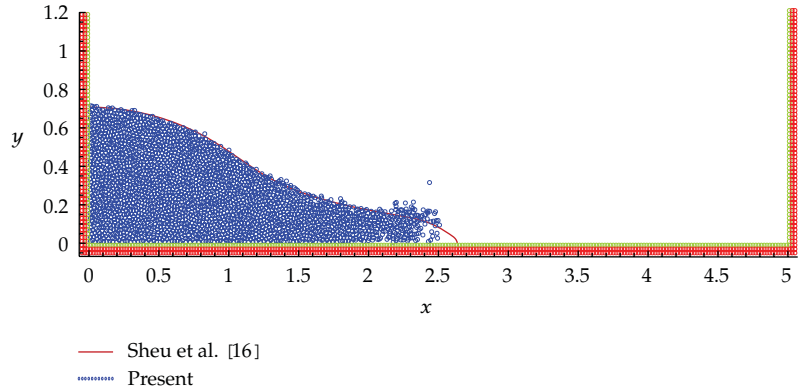

(d)

Figure 7: Continued.

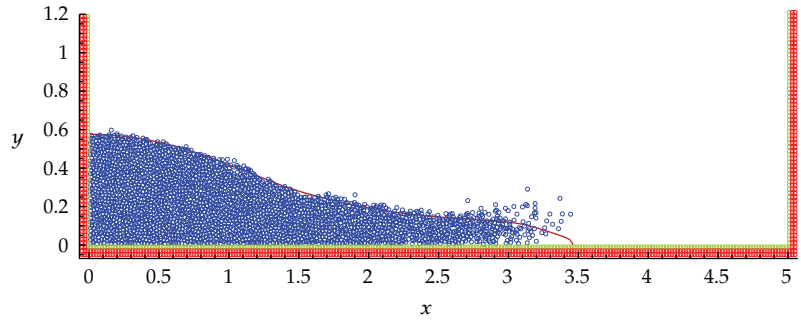

(e)

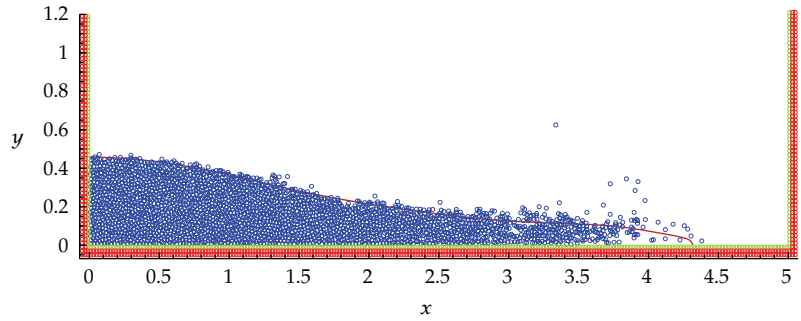

(f)

Figure 7: Comparison of the predicted free surfaces by the MPS and the level set methods at different times for the case with Re = 500. (a) $t = 0.0$; (b) $t = 0.5$; (c) $t = 1.0$; (d) $t = 1.5$; (e) $t = 2.0$; (lf) $t = 2.5$.

Figure 2 where the undisturbed water height is d and the channel width is $16d$. Above the undisturbed water level, the crest of the investigated solitary wave is given by [15]

$$y = d + H \operatorname{sech}^2\left[\sqrt{\frac{3H}{4d^3}}x\right]. \tag{5.1}$$

Here, $H(= 2)$ and $d(= 10)$ denote the initial wave height and the still water depth, respectively. Initially, the velocities are given by

$$\begin{aligned} u &= \sqrt{gd}\frac{H}{d}\operatorname{sech}^2\left[\sqrt{\frac{3H}{4d^3}}x\right], \\ v &= \sqrt{3gd}\left(\frac{H}{d}\right)^{3/2}\left(\frac{y}{d}\right)\operatorname{sech}^2\left[\sqrt{\frac{3H}{4d^3}}x\right]\tanh\left[\sqrt{\frac{3H}{4d^3}}x\right], \end{aligned} \tag{5.2}$$

where $g(= 9.81)$ is the gravitational acceleration. In the current study, the initial distance between the neighbor particles is 0.8, and 3482 particles were used in the computation. For the wave propagating towards the right wall, the predicted run-up height on the right wall in Figure 3 is compared with the result given in [15]. The computed wave pressures at different times are shown in Figure 4.

5.2. Dam Break Flow

The investigated dambreak problem is schematic Figure 5, where $L(= 1)$ denotes the height and the width of the stillwater in the tank. The computed results were compared with the results in [16]. Figures 6(a)–6(f) show the results for the fluid flow with Re = 500. Figures 7(a)–7(f) are the results predicted in the case with Re = 1000. The red lines stand for the simulated free surfaces, and they are compared with those shown in [16].

6. Concluding Remarks

The idea of developing the proposed particle interaction model is to develop the kernel function which accommodates the property $\int_{r/r_e=-1}^{r/r_e=1} w(r)dr = 1$ embedded in the smoothed Dirac delta function. To justify the proposed kernel functions for simulating the realistic flow, we investigate two well-known benchmark problems for the validation sake. The predicted results of the dam break problem and the solitary wave problem clearly show that the solution predicted by the particle interaction model using the proposed kernel function can capture well the motion of the fluid flow subject to free surface.

Acknowledgments

The financial support by the National Science Council under Grants NSC96-2221-E-002-293-MY2 and NSC97-2628-M-002-022 and CQSE project 97R0066-69 are gratefully acknowledged.

References

[1] C. W. Hirt, A. A. Amsden, and J. L. Cook, "An arbitrary Lagrangian-Eulerian computing method for all flow speeds," *Journal of Computational Physics*, vol. 14, no. 3, pp. 227–253, 1974.
[2] F. H. Harlow and J. E. Welch, "Numerical calculation of time-dependent viscous incompressible flow of fluid with free surface," *Physics of Fluids*, vol. 8, no. 12, pp. 2182–2189, 1965.
[3] C. W. Hirt and B. D. Nichols, "Volume of fluid (VOF) method for the dynamics of free boundaries," *Journal of Computational Physics*, vol. 39, no. 1, pp. 201–225, 1981.
[4] S. Osher and R. P. Fedkiw, "Level set methods: an overview and some recent results," *Journal of Computational Physics*, vol. 169, no. 2, pp. 463–502, 2001.
[5] F. H. Harlow, "A machine calculation method for hydrodynamic problems," Los Alamos Scientific Laboratory Report LAMS-1956, 1955.
[6] L. B. Lucy, "A numerical approach to the testing of the fission hypothesis," *The Astrophysical Journal*, vol. 82, no. 12, pp. 1013–1024, 1977.
[7] R. R. Gingold and J. J. Monagham, "Smoothed particle hydrodynamics: theory and application to non-spherical stars," *The Astrophysical Journal*, vol. 181, pp. 375–389, 1977.
[8] J. J. Monaghan, "Simulating free surface flows with SPH," *Journal of Computational Physics*, vol. 110, no. 2, pp. 399–406, 1994.

[9] S. Koshizuka, H. Tamako, and Y. Oka, "A particle method for incompressible viscous flow with fluid fragmentation," *Computational Fluid Dynamics Journal*, vol. 4, no. 1, pp. 29–46, 1995.
[10] B. Ataie-Ashtiani and L. Farhadi, "A stable moving-particle semi-implicit method for free surface flows," *Fluid Dynamics Research*, vol. 38, no. 4, pp. 241–256, 2006.
[11] S. Koshizuka, A. Nobe, and Y. Oka, "Numerical analysis of breaking waves using the moving particle semi-implicit method," *International Journal for Numerical Methods in Fluids*, vol. 26, no. 7, pp. 751–769, 1998.
[12] T. Belytschko, Y. Krongauz, D. Organ, M. Fleming, and P. Krysl, "Meshless methods: an overview and recent developments," *Computer Methods in Applied Mechanics and Engineering*, vol. 139, no. 1-4, pp. 3–47, 1996.
[13] S. Koshizuka and Y. Oka, "Moving-particle semi-implicit method for fragmentation of incompressible fluid," *Nuclear Science and Engineering*, vol. 123, no. 3, pp. 421–434, 1996.
[14] B. Ramaswamy, "Numerical simulation of unsteady viscous free surface flow," *Journal of Computational Physics*, vol. 90, no. 2, pp. 396–430, 1990.
[15] T. W. H. Sheu and S. M. Lee, "Large-amplitude sloshing in an oil tanker with baffle-plate/drilled holes," *International Journal of Computational Fluid Dynamics*, vol. 10, no. 1, pp. 45–60, 1998.
[16] T. W. H. Sheu, C. H. Yu, and P. H. Chiu, "Development of a dispersively accurate conservative level set scheme for capturing interface in two-phase flows," *Journal of Computational Physics*, vol. 228, no. 3, pp. 661–686, 2009.

Hindawi Publishing Corporation
Journal of Applied Mathematics
Volume 2011, Article ID 673523, 18 pages
doi:10.1155/2011/673523

Research Article

Effects of Gravity and Inlet/Outlet Location on a Two-Phase Cocurrent Imbibition in Porous Media

M. F. El-Amin and Shuyu Sun

Computational Transport Phenomena Laboratory (CTPL), Physical Sciences and Engineering Division (PSE), King Abdullah University of Science and Technology (KAUST), Thuwal 23955-6900, Jeddah, Saudi Arabia

Correspondence should be addressed to M. F. El-Amin, mohamed.elamin@kaust.edu.sa

Received 15 December 2010; Accepted 8 January 2011

Academic Editor: Zhangxin Chen

Copyright © 2011 M. F. El-Amin and S. Sun. This is an open access article distributed under the Creative Commons Attribution License, which permits unrestricted use, distribution, and reproduction in any medium, provided the original work is properly cited.

We introduce 2D numerical investigations of the problem of gravity and inlet/outlet location effects of water-oil two-phase cocurrent imbibition in a porous medium. Three different cases of side-, top-, and bottom-inlet location are considered. Two-dimensional computations are carried out using the finite element method. Intensive comparisons are done between considering and neglecting gravity effect on water saturation, pressures of water and oil as well as water velocity. Results are introduced either in curves or as 2D visualization graphs. The results indicate that the buoyancy effects due to gravity force take place depending on inlet location. So, the buoyancy force in the momentum equations of the co-current imbibition model cannot be neglected as done by several previous studies. Also, we note that the 2D zero gravity model has a uniform flow and may be represented as 1D flow unlike the 2D nonzero gravity model showing a nonuniform flow.

1. Introduction

Oil recovery by imbibition mechanism, from fractured reservoirs, is a significant research area in multiphase flow in porous media especially for water-flooding process in fractured oil reservoir. Fractured reservoirs are composed of the fracture network and matrix. Fractures have a high permeability and very low volume compared to the matrix, whose permeability is very low but it contains the majority of the oil. Water-flooding is used to increase oil recovery by increasing water pressure in fractures since water quickly surrounds oil saturated matrices of lower permeability. The water-flooding performance works well with the water-wet condition, and imbibition can lead to significant recoveries, while poor recoveries and early water breakthrough occur with oil-wet condition. Imbibition is defined as displacement of the nonwetting phase (oil) by the wetting phase (water) with dominant

effect of the capillary force in porous media. Imbibition can occur in both countercurrent and cocurrent flow modes, depending on the fracture network and the water injection rates. In cocurrent imbibition, water pushes oil out of the matrix thus, both water and oil flows are in the same direction. Countercurrent imbibition is whereby a wetting phase imbibes into a porous matrix (rock), displacing the nonwetting phase out from one open boundary. Cocurrent imbibition is faster and more efficient than countercurrent imbibition. Countercurrent imbibition is often the only possible displacement mechanism for cases where a region of the matrix is completely surrounded by water in the fractures [1–5]. Imbibition has been investigated by many more authors either for cocurrent or countercurrent flows or both of them together [6–9]. Reis and Cil [10] introduced a one-dimensional model for oil expulsion by countercurrent water imbibition in rocks. Scaling of time imbibition was estimated by many of authors in terms of fluid and rock properties (e.g., see [11, 12]) while, recently, El-Amin and Sun [13] suggested a scaling law in terms of characteristic velocity (e.g., injection velocity), which may be useful for water-flooding mechanisms. Morrow and Mason [14] introduced a comprehensive review on recovery of oil by spontaneous imbibition. Kashchiev and Firoozabadi [15] gave analytical solutions for 1D countercurrent imbibition in water-wet media. Analytical analysis of oil recovery during countercurrent imbibition in strongly water-wet system was given by Tavassoli et al. [16]. The Barenblatt's model of spontaneous countercurrent imbibition was investigated by Silin and Patzek [17]. Behbahani et al. [18] have performed a simulation of countercurrent imbibition in water-wet fractured reservoirs.

In many of imbibition studies, authors have neglected the gravity force effect by dropping the gravity force term from the flow equations especially for the oil-water modeling. Wilkinson [19] studied the percolation model of immiscible displacement in the presence of buoyancy forces. Analytical and numerical solutions of gravity-imbibition and gravity-drainage processes were given by Bech et al. [20]. Tavassoli et al. [21] have introduced analysis of countercurrent imbibition with gravity in weakly water-wet system. A pore-scale study of gravity, capillary, and viscous forces during drainage in a two-dimensional porous medium was introduced by Løvoll et al. [22]. Effect of injection rate, initial water saturation and gravity on water injection in slightly water-wet fractured porous media was examined experimentally by Karimaie and Torsæter [23]. Ruth et al. [24] provided an approximate analytical solution for countercurrent spontaneous imbibition. The problems of buoyancy-driven vertical migration of fluids have been treated analytically or numerically by some researchers such as, recently, Silin et al. [25] have introduced simple analytical solutions in a model of gas flow driven by a combination of buoyancy, viscous, and capillary forces of a problem of two-phase countercurrent fluid flow. Akin and Kovscek [26] studied spontaneous cocurrent water imbibition into diatomite samples (with low-permeability porous media) at various initial water saturations. Cai et al. [27] have considered the fractal characterization of spontaneous cocurrent imbibition in porous media. They introduced analytical expressions for characterizing a spontaneous cocurrent imbibition process of wetting fluid into gas-saturated porous media proposed based on the fractal characters of porous media. Recently, El-Amin and Sun [28] introduced 1D/2D numerical investigations of the problem of gravity and inlet location effects of a water-oil two-phase countercurrent imbibition in a porous medium.

The purpose of this study is to investigate the influence of gravity acceleration for different locations of the inlet of a water-oil two-phase immiscible incompressible 2D flow cocurrent imbibition in a homogenous porous medium. It is assumed that the flow is combined capillary and buoyancy driven.

2. Basic Equations

In this section, we introduce the basic equations of water-oil two-phase flow of immiscible fluids. We assume that flow is incompressible governed by the equations of mass conservation for each phase and the generalized Darcy's law, respectively, as:

$$\begin{aligned} \frac{\partial(\varphi\rho_\alpha S_\alpha)}{\partial t} &= -\nabla\cdot(\rho_\alpha u_\alpha) + q_\alpha, \quad \alpha = w, o, \\ u_\alpha &= -\frac{Kk_{r\alpha}}{\mu_\alpha}(\nabla\cdot p_\alpha + \rho_\alpha g\nabla z), \quad \alpha = w, o. \end{aligned} \tag{2.1}$$

The index α denotes to the water (wetting-phase, w) and oil (nonwetting, nw), respectively. S, p, q, u, k_r, ρ, and μ are the phase saturation, pressure, mass flow rate, Darcy velocity, relative permeability, density and viscosity, respectively. The saturation S_α of the phases are constrained by,

$$S_w + S_o = 0. \tag{2.2}$$

One may defined the phase saturation as the fraction of the void volume of a porous medium filled by this fluid phase. The mass flow rate $q_{i\alpha}$, describe sources or sinks and can be neglected in the current study. The quantity

$$k_\alpha = Kk_{r\alpha}, \quad \alpha = w, o \tag{2.3}$$

is known as effective permeability of the phase α. The relative permeability of a phase is a dimensionless measure of the effective permeability of that phase. It is the ratio of the effective permeability of that phase to the absolute permeability. Also, it is interesting to define the quantities m_w and m_o which are known as mobility ratios of wetting and nonwetting phases, respectively, given by

$$m_\alpha = \frac{k_\alpha}{\mu_\alpha}, \quad \alpha = w, o. \tag{2.4}$$

The normalized wetting phase saturation S is given by,

$$S = \frac{S_w - S_{iw}}{1 - S_{or} - S_{iw}}, \quad 0 < S < 1, \tag{2.5}$$

where S_{iw} is the irreducible (minimal) wetting phase saturation and S_{or} is the residual (minimal) nonwetting phase (oil) saturation. The expression of relation between the relative permeabilities and the normalized wetting phase saturation S given as

$$\begin{aligned} k_{rw} &= k_{rw}^0 S^a, \\ k_{ro} &= k_{ro}^0 (1 - S)^b. \end{aligned} \tag{2.6}$$

The empirical parameters a and b can be obtained from measured data either by optimizing to analytical interpretation of measured data, or by optimizing using a core flow numerical simulator to match the experiment. $k_{rw}^0 = k_{rw}(S = 1)$ is the endpoint relative permeability to water, and $k_{ro}^0 = k_{ro}(S = 0)$ is the endpoint relative permeability to the nonwetting phase.

The capillary pressure p_c is defined as a difference between the nonwetting and wetting phase pressures,

$$p_c = p_o - p_w, \tag{2.7}$$

the total velocity defined as

$$u = u_w + u_o, \tag{2.8}$$

the total mobility is given by

$$m = m_w + m_o, \tag{2.9}$$

the fractional flow functions are

$$f_w(S) = \frac{m_w(S)}{m(S)}, \qquad f_o(S) = \frac{m_o(S)}{m(S)}, \tag{2.10}$$

and the density difference is,

$$\Delta\rho = \rho_o - \rho_w. \tag{2.11}$$

Using (2.1)–(2.2), and (2.7)–(2.10) with some mathematical manipulation one can find [29]

$$\frac{\partial(\varphi\rho_w S_w)}{\partial t} = -\nabla\cdot\rho_w f_w(S)\left\{Km_o(S)\left(\frac{dp_c}{dS_w}\nabla S_w - \Delta\rho g\nabla z\right) + u\right\}, \tag{2.12}$$

where u is total velocity given by

$$u = -Km(S)\left\{\nabla p - \left[\rho_w f_w(S) + \rho_o f_o(S)\right]g\nabla z\right\}. \tag{2.13}$$

Alternatively, using (2.7), the governing equation (2.1) may be rewritten in the form

$$\begin{aligned}
\frac{\partial(\varphi\rho_w S_w)}{\partial p_c}\left(\frac{\partial p_o}{\partial t} - \frac{\partial p_w}{\partial t}\right) &= \nabla\cdot\rho_w\left[Km_w(\nabla p_w - \rho_w g\nabla z)\right],\\
\frac{\partial(\varphi\rho_o(1 - S_w))}{\partial p_c}\left(\frac{\partial p_o}{\partial t} - \frac{\partial p_w}{\partial t}\right) &= \nabla\cdot\rho_o\left[Km_o(\nabla p_o - \rho_o g\nabla z)\right].
\end{aligned} \tag{2.14}$$

Both models, (2.12) and (2.14) are used intensively especially in the field of oil reservoir simulations.

The capillary pressure function is dependent on the pore geometry, fluid physical properties and phase saturations. The two phase capillary pressure can be expressed by Leverett dimensionless function $J(S)$ which is a function of the normalized saturation S,

$$p_c = \gamma\left(\frac{\varphi}{K}\right)^{1/2} J(S). \tag{2.15}$$

The $J(S)$ function typically lies between two limiting (drainage and imbibition) curves which can be obtained experimentally. Correlation of the imbibition capillary pressure data depends on the type of application. For example, for water-oil system, [3, 15], the capillary pressure and the normalized wetting phase saturation are correlated as

$$p_c = -B \ln S, \tag{2.16}$$

where B is the capillary pressure parameter, which is equivalent to $\gamma(\varphi/K)^{1/2}$, in the general form of the capillary pressure, (2.15), thus $B \equiv \gamma(\varphi/k)^{1/2}$, and $J(S) \equiv \ln S$. Note that $J(S)$ is a scalar nonnegative function.

The purpose of this section of study is to investigate the influence of gravity acceleration for different locations of the inlet of a two-phase immiscible incompressible flow in a homogenous porous medium for cocurrent imbibition.

It is assumed that the flow is combined capillary and buoyancy driven. Consider a rectangular core at irreducible water saturation, has inlet one face and outlet is on the opposite face, while all around surface except inlet and outlet is closed (cocurrent imbibition). The two-dimensional simplification case of the cylindrical core is a Cartesian rectangle of dimensions, $x = W$, $z = H$. Assuming that flow is incompressible and there is no mass transfer between the two phases. Under these assumptions the governing equations may be rewritten in the form

$$\begin{aligned} \varphi\frac{\partial S_w}{\partial p_c}\left(\frac{\partial p_o}{\partial t} - \frac{\partial p_w}{\partial t}\right) - \nabla\cdot\left[Km_w(\nabla p_w - \rho_w g\nabla z)\right] = 0, \\ \varphi\frac{\partial S_w}{\partial p_c}\left(\frac{\partial p_o}{\partial t} - \frac{\partial p_w}{\partial t}\right) + \nabla\cdot\left[Km_o(\nabla p_o - \rho_o g\nabla z)\right] = 0, \end{aligned} \tag{2.17}$$

which is the combined Darcy's law and the equations of mass conservation for each phase in 2D. In order to consider a specific case of study we may use an empirical formula of the capillary pressure in terms of normalized saturation function. The capillary pressure and the normalized wetting phase saturation are correlated as in (2.16).

3. Initial and Boundary Conditions

For the cocurrent imbibition in which the only open end is initially in contact with oil at ambient pressure, say, zero pressure (gauge pressure). The water pressure in the core is given by the capillary pressure relationship, (2.15)-(2.16), which at $t = 0$ leads to

$$\begin{gathered} p_o = 0, \quad t = 0, \quad 0 \le x \le W, \quad 0 \le z \le H, \\ p_w = p_o - p_c(S_{iw}) = -p_c(S_{iw}), \quad t = 0, \quad 0 \le x \le W, \quad 0 \le z \le H. \end{gathered} \tag{3.1}$$

It is worth mentioning that the equilibrium static pressure $p_c = \Delta\rho g z$ may be considered in the initial condition as well as $p_c = \Delta\rho g H$ in the bottom as a boundary condition. But it is negligible quantities because the domain is small-scale (we tested it), but it may has a significant effect for a large-scale simulation which will be the future work.

As the cocurrent imbibition process begins the oil in the open-end is replaced by water at the ambient pressure, so if one assumes zero capillary pressure at this open face. In this study we consider three different locations of the inlet and outlet, at side, top or bottom, namely, Cases 1, 2 and 3, as follows.

Case 1. Side inlet and opposite side outlet

$$\begin{gathered} p_w = p_o = 0, \quad t > 0, \quad x = 0, \quad 0 \le z \le H \quad \text{(Inlet)}, \\ q_w = q_o = 0, \quad t > 0, \quad 0 \le x \le W, \quad z = 0, \end{gathered} \tag{3.2a}$$

$$\begin{gathered} q_w = q_o = 0, \quad t > 0, \quad 0 \le x \le W, \quad z = H, \\ q_w = p_o = 0, \quad t > 0, \quad x = W, \quad 0 \le z \le H \quad \text{(Outlet)}, \end{gathered} \tag{3.2b}$$

where q_w and q_o are the water and oil flow rate, respectively.

Case 2. Top inlet and bottom outlet

$$\begin{gathered} q_w = q_o = 0, \quad t > 0, \quad x = 0, \quad 0 \le z \le H, \\ q_w = p_o = 0, \quad t > 0, \quad 0 \le x \le W, \quad z = 0 \quad \text{(Outlet)}, \end{gathered} \tag{3.3a}$$

$$\begin{gathered} p_w = p_o = 0, \quad t > 0, \quad 0 \le x \le W, \quad z = H \quad \text{(Inlet)}, \\ q_w = q_o = 0, \quad t > 0, \quad x = W, \quad 0 \le z \le H. \end{gathered} \tag{3.3b}$$

Case 3. Bottom inlet and top outlet

$$\begin{gathered} q_w = q_o = 0, \quad t > 0, \quad x = 0, \quad 0 \le z \le H, \\ p_w = p_o = 0, \quad t > 0, \quad 0 \le x \le W, \quad z = 0 \quad \text{(Inlet)}, \end{gathered} \tag{3.4a}$$

$$\begin{gathered} q_w = p_o = 0, \quad t > 0, \quad 0 \le x \le W, \quad z = H \quad \text{(Outlet)}, \\ q_w = q_o = 0, \quad t > 0, \quad x = W, \quad 0 \le z \le H. \end{gathered} \tag{3.4b}$$

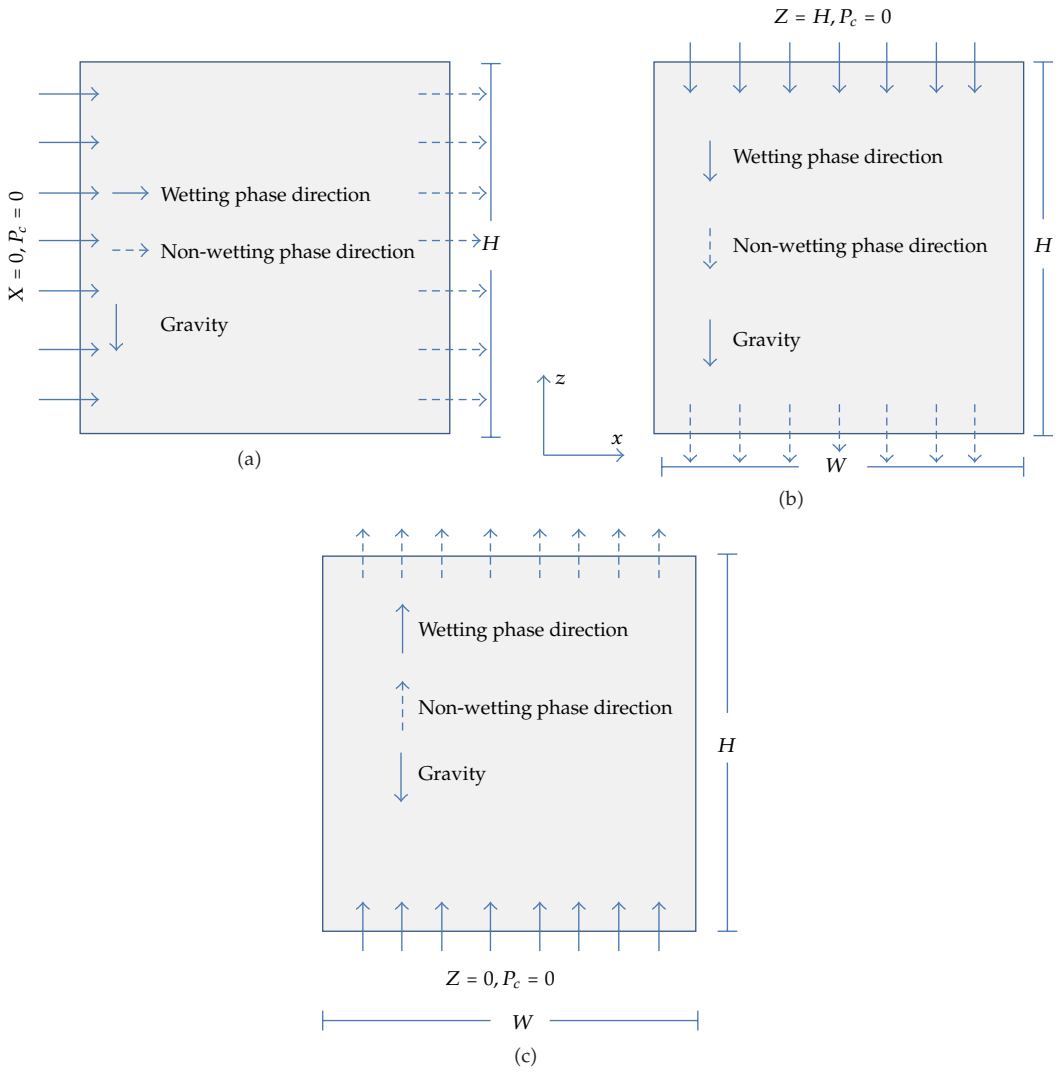

Figure 1: Schematic diagram of cocurrent imbibition for different inlet locations: (a) side, (b) top, and (c) bottom.

4. Results and Discussion

Figures 1(a), 1(b), and 1(c) show schematic diagrams of the problem of the two-phase cocurrent imbibition with gravity effect and different locations of the inlet (side, top and bottom) and the outlet is located opposite. Wetting phase imbibes inwards in a porous medium of height H and width W with zero capillary pressure at the inlet, and exits from the outlet at the opposite side and no-flow boundary at the other two boundaries.

Figures 2(a) and 2(b) show mesh distributions for Cases 1, 2, and 3, respectively, with a fine mesh on the inlet and outlet edges. Case 1 of a dimensional domain $(0.2, 0.2)$ m is meshed by 10439 nodes and 19968 triangle elements, corresponding to more than 81690 DOF (quadratic Lagrange elements), while Cases 2 and 3 of dimensional domain $(0.2, 0.2)$ m are meshed by 10591 nodes and 20272 triangle elements, corresponding to more than 82906 DOF

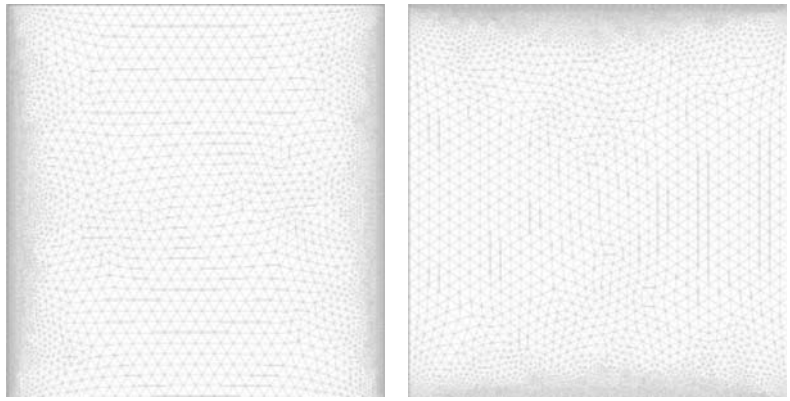

(a) (b)

Figure 2: Mesh distribution for: (a) Case 1, (b) Cases 2 and 3.

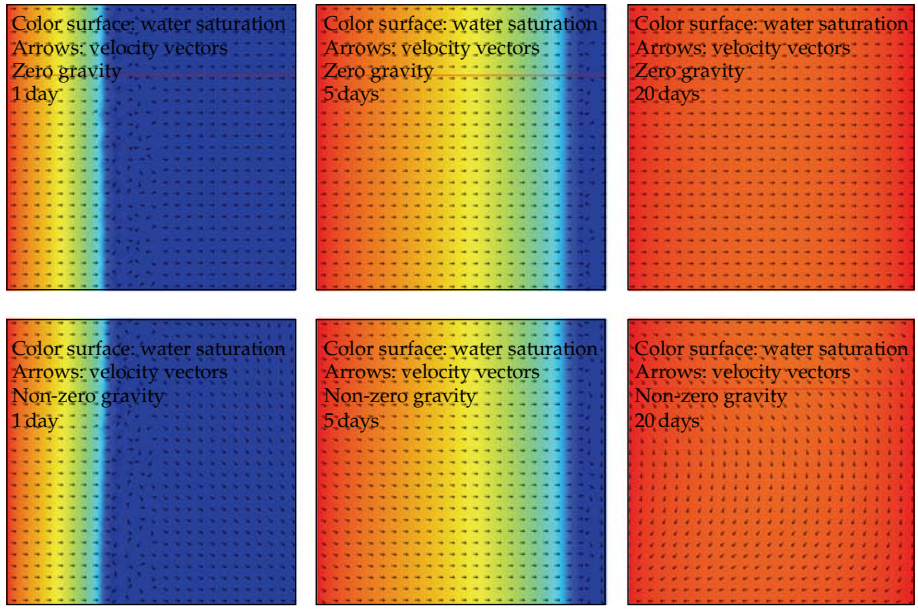

Figure 3: Distributions of water saturation and velocity vectors of zero, nonzero gravity of side-inlet case.

(quadratic Lagrange elements). All computations have been performed using the commercial software COMSOL version 3.5a with the direct solver UMFPACK, and were running on multi(8)-core workstation using SMP mode of parallel computation.

Figure 3 show distributions of water saturation and velocity vectors of zero, nonzero gravity of side-inlet case, at time imbibition of 1, 5, and 20 days. One can note that velocity vector of the zero-gravity case indicates has a uniform flow, while, the opposite is true for the case of nonzero gravity case shows a nonuniform flow.

Comparison between considering and neglecting gravity force on water saturation against x-axis of Case 1 (side-inlet), at $z = 0.15$ m is plotted in Figure 4. We can note that there is a slight difference, of water saturation profile, between the considering and neglecting

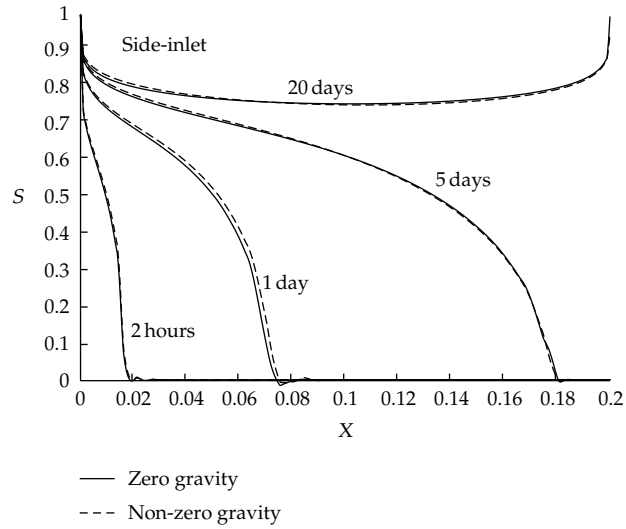

Figure 4: Comparison between considering and neglecting gravity effect on water saturation for the side-inlet case, at $z = 0.15$ m.

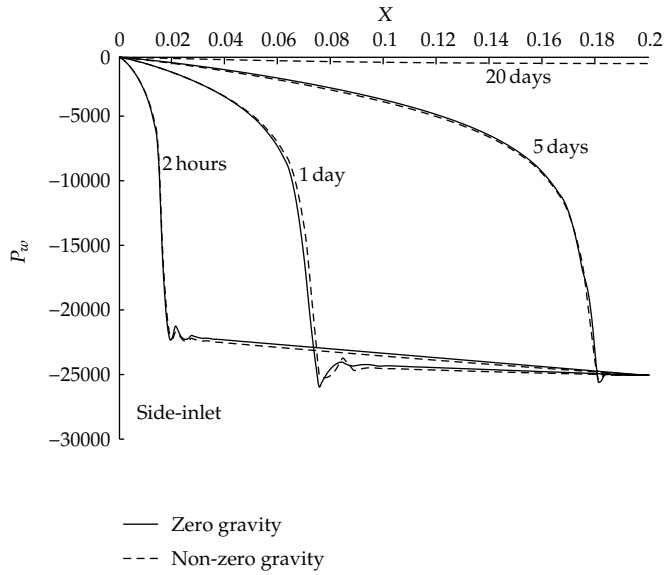

Figure 5: Comparison between considering and neglecting gravity effect on water pressure for the side-inlet case, at $z = 0.15$ m.

of the gravity force on the model. Figure 5 shows a comparison between considering and neglecting gravity effect on water pressure against x-axis of Case 1, at $z = 0.15$ m. Also, the difference between zero and nonzero gravity cases is small, of the water pressure, especially for early imbibition time, while, the difference is a bit significant at big imbibition time (20 days). Comparisons between considering and neglecting gravity effect on oil pressure against x-axis of Case 1, at $z = 0.15$ m, are plotted in Figure 6.

It is interesting to note a significant difference between zero and nonzero gravity cases, of oil pressure, at all imbibition time. It is clear that gravity force reduces the oil pressure and

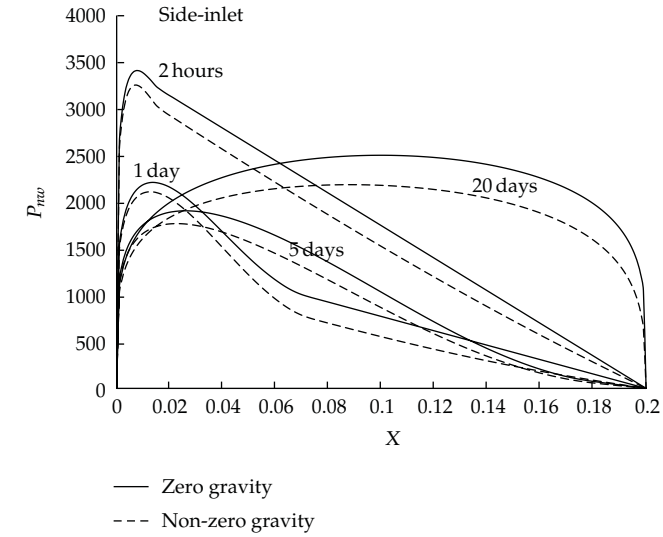

Figure 6: Comparison between considering and neglecting gravity effect on oil pressure for the side-inlet case, at $z = 0.15$ m.

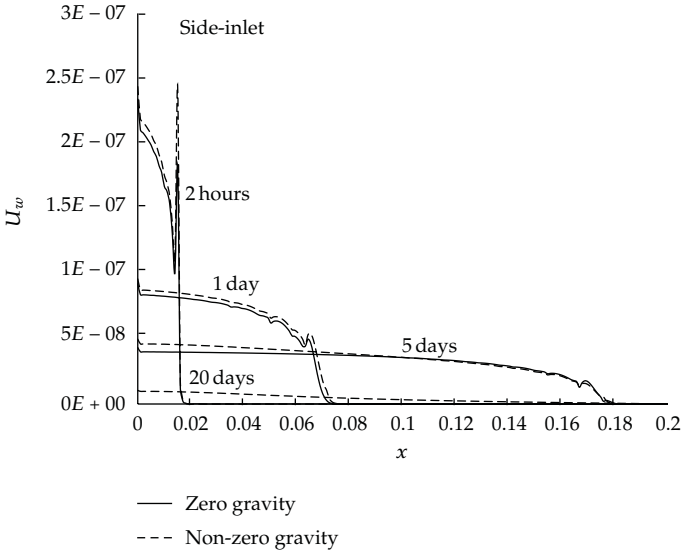

Figure 7: Comparison between considering and neglecting gravity effect on water x-velocity for the side-inlet case, at $z = 0.15$ m.

consequently reduces the capillary pressure of the side-inlet case. In Figure 7, a comparison between considering and neglecting gravity effect on water x-velocity is plotted against x-axis of Case 1, at $z = 0.15$ m. From this figure, we may note a significant difference between the two cases especially for small x (near to the inlet). This may be interpreted as the water imbibes inside medium pores the velocity is resisted by pores boundaries. Also, gravity has a significant effect after long imbibition time, so a quite big difference is noted at time 20 days between considering and neglecting gravity force.

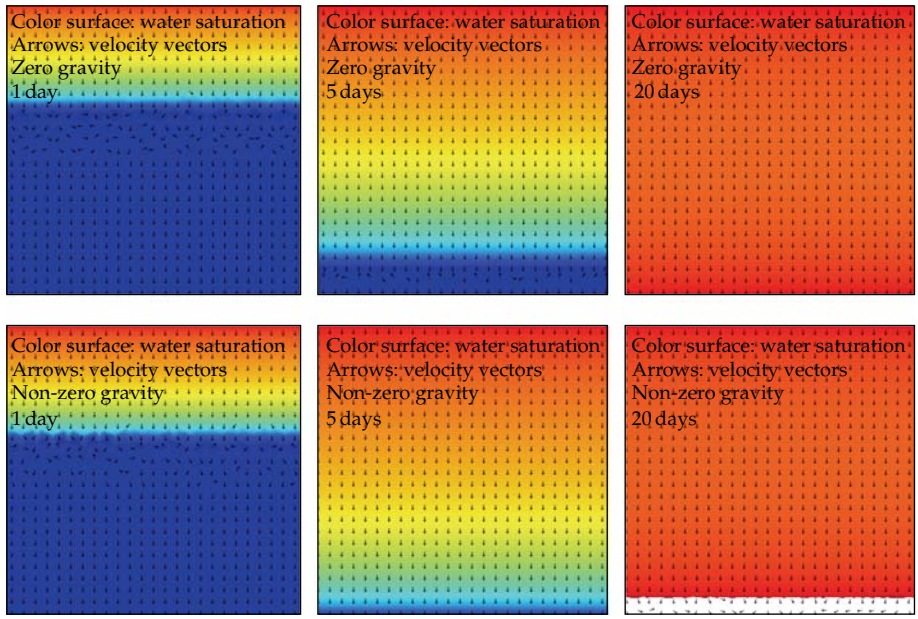

Figure 8: Distributions of water saturation and velocity vectors of zero, nonzero gravity for the top-inlet case.

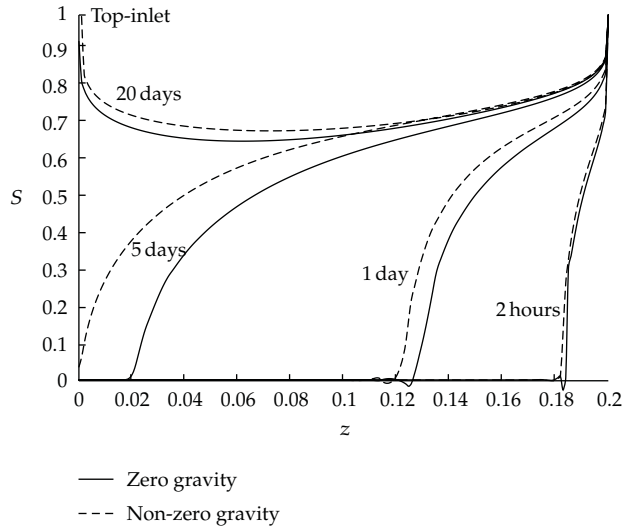

Figure 9: Comparison between considering and neglecting gravity effect on water saturation for the top-inlet case, at $x = 0.1$ m.

Figure 8 shows distributions of water saturation and velocity vectors of zero and nonzero gravity of top-inlet case, at time imbibition of 1, 5 and 20 days. From these figures we note that flow of the top-inlet case is uniform. Figure 9 illustrates a comparison between considering and neglecting gravity effect on water saturation against z-axis, at $x = 0.1$ m of top-inlet (Case 2).

It is interesting to note that the gravity force enhances water saturation for the top-inlet case, thus, one can say that flow is gravity assisting. Water pressure profiles are plotted

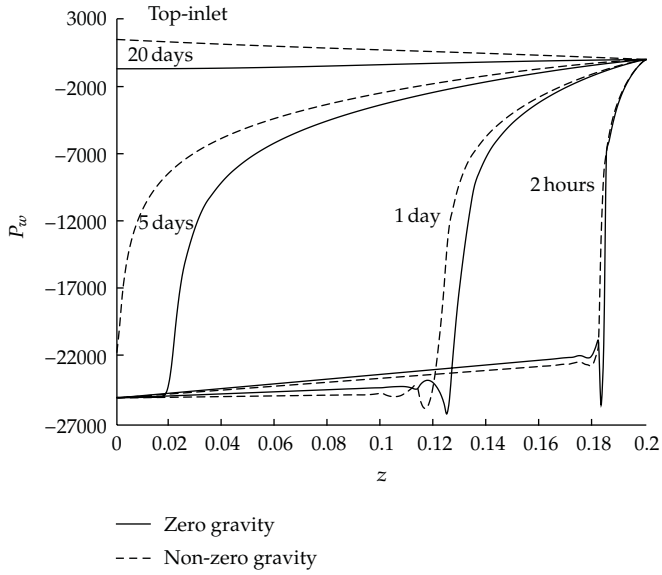

Figure 10: Comparison between considering and neglecting gravity effect on water pressure for the top-inlet case, at $x = 0.1$ m.

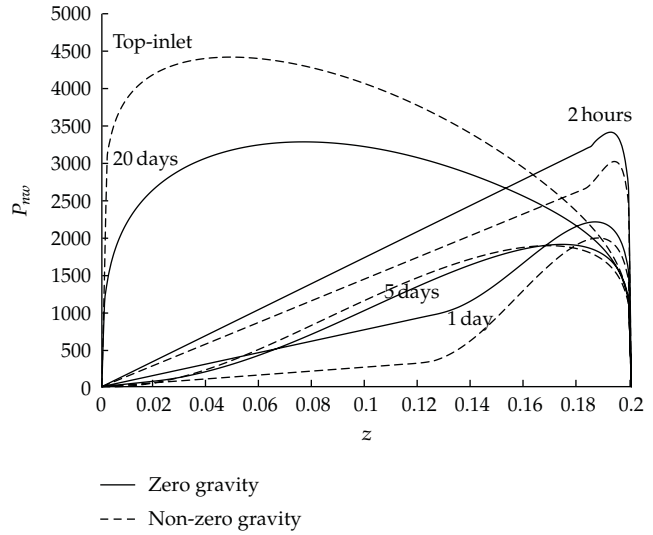

Figure 11: Comparison between considering and neglecting gravity effect on oil pressure for the top-inlet case, at $x = 0.1$ m.

in Figure 10 for zero and nonzero gravity for the top-inlet case. It can be seen from this figure that the gravity force enhances water pressure for the top-inlet case and after a quite long imbibition time the water pressure becomes positive. The positive values of water pressure may be lead to the negative capillary pressure under certain conditions in a big depth. It is worth mentioning that the phenomenon of negative capillary pressure appeared in a number of experimental tests.

Comparison between considering and neglecting gravity effect on oil pressure against z-axis of Case 2, at $x = 0.1$ m, is plotted in Figure 11. This figure indicates that the gravity

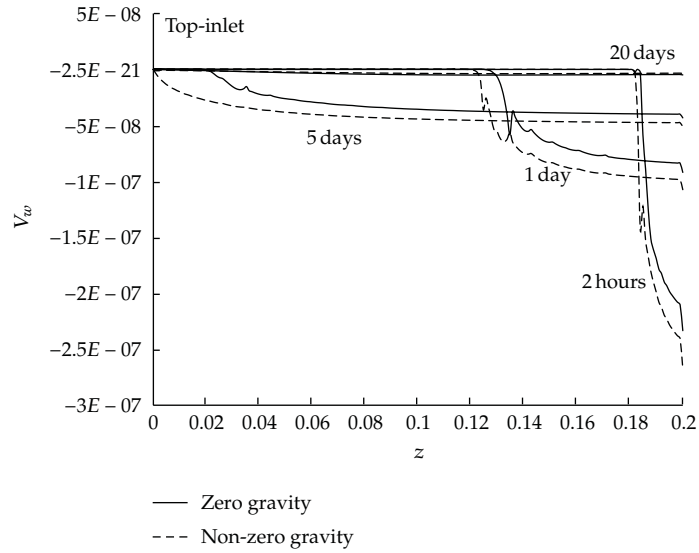

Figure 12: Comparison between considering and neglecting gravity effect on water z-velocity for the top-inlet case, at $x = 0.1$ m

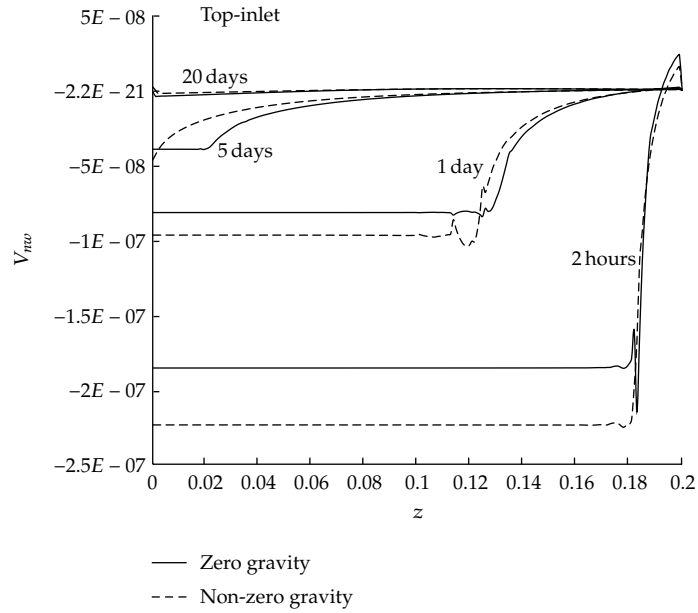

Figure 13: Comparison between considering and neglecting gravity effect on oil z-velocity for the top-inlet case, at $x = 0.1$ m.

force has irregular effect on the oil pressure. In Figure 12 comparisons between considering and neglecting gravity effect on water z-velocity are plotted against z-axis of the top-inlet case. This figure shows a significant difference between the two cases especially for small time imbibition. Also, the oil z-velocity is plotted in Figure 13 against z-axis of the top-inlet case for zero and nonzero gravity. Also, we note a significant difference between the two cases for small time imbibition.

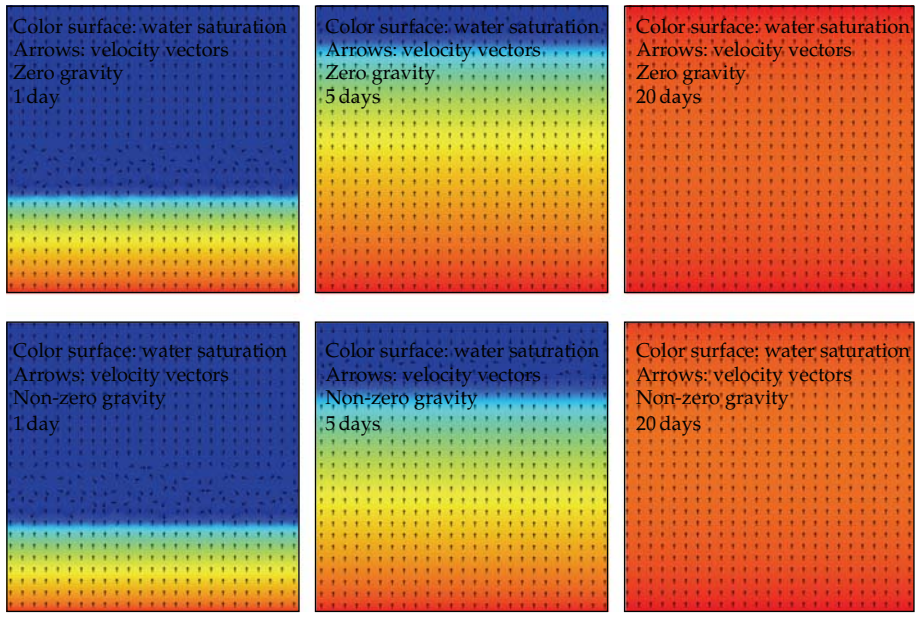

Figure 14: Distributions of water saturation and velocity vectors of zero, nonzero gravity for the bottom-inlet case.

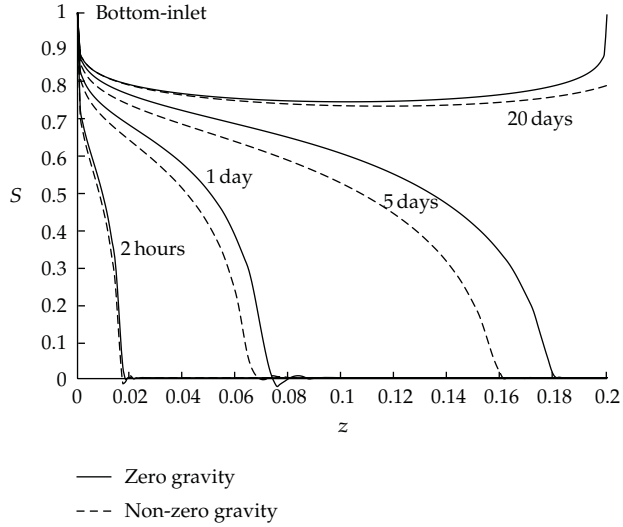

Figure 15: Comparison between considering and neglecting gravity effect on water saturation for the bottom-inlet case, at $x = 0.1$ m.

Distributions of water saturation and velocity vectors for zero and nonzero gravity of bottom-inlet case, at time imbibition of 1, 5 and 20 days, are plotted in Figure 14. It can be seen from these figures we note that flow of the bottom-inlet case is uniform. In Figure 15 the water saturation profiles are plotted against z-axis, at $x = 0.1$ m of bottom-inlet case. It can be seen from this figure that gravity reduces water saturation for the bottom-inlet case, and the flow is gravity opposing.

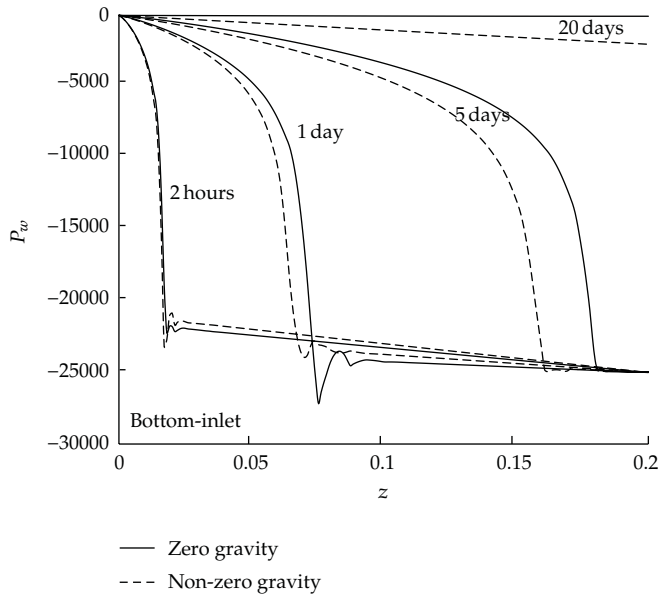

Figure 16: Comparison between considering and neglecting gravity effect on water pressure for the bottom-inlet case, at $x = 0.1$ m.

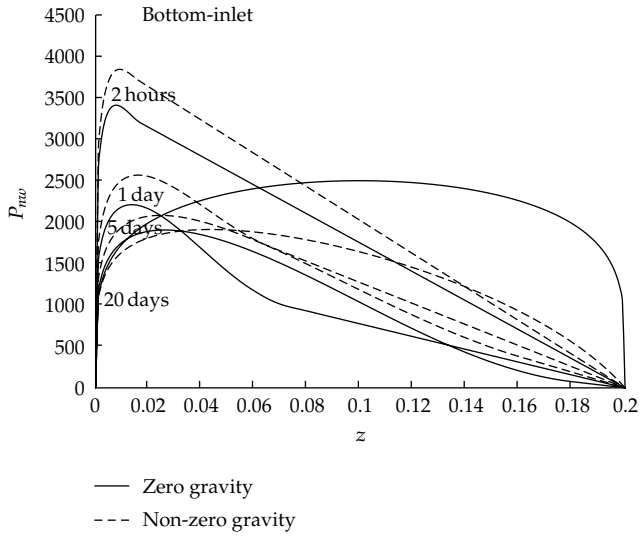

Figure 17: Comparison between considering and neglecting gravity effect on oil pressure for the bottom-inlet case, at $x = 0.1$ m.

Figure 16 shows a comparison between considering and neglecting gravity effect on water pressure against z-axis of Case 3, at $x = 0.1$ m. This figure indicates that the gravity force reduces water pressure. Oil pressure profiles with zero and nonzero gravity are shown in Figure 17, for bottom-inlet case. Again, as the top-inlet case, the gravity force has irregular effect on the oil pressure for the bottom-inlet case. In Figure 18, water z-velocity is plotted

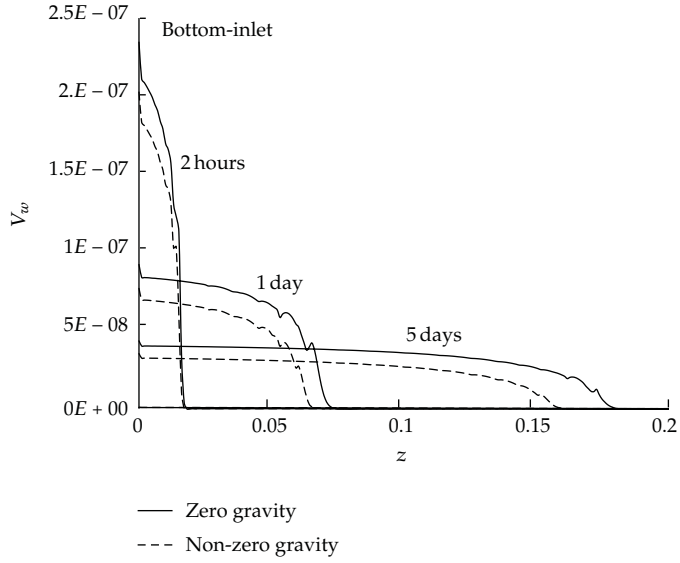

Figure 18: Comparison between considering and neglecting gravity effect on water z-velocity for the bottom-inlet case, at $x = 0.1$ m.

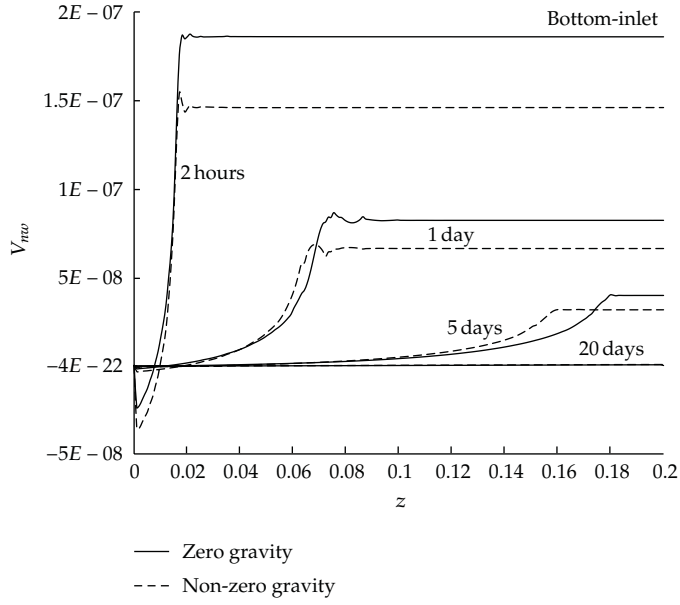

Figure 19: Comparison between considering and neglecting gravity effect on oil z-velocity for the bottom-inlet case, at $x = 0.1$ m.

against z-axis of the bottom-inlet case, for zero and nonzero gravity. Also, the oil z-velocity is plotted in Figure 19 against z-axis of the bottom-inlet case for zero and nonzero gravity. Again, we note a significant difference between zero and nonzero gravity as shown in the two Figures 18 and 19.

5. Conclusions

In this investigation we assure for including the gravity term in the mathematical model of two-phase cocurrent imbibition in a porous medium, and it cannot be ignored as done by several authors in the field. For this purpose we have considered three different cases of inlet location, namely, side, top and bottom. Numerical simulation was running of the water-oil system for maximum 20 days real imbibition time. Also, we have noted that the buoyancy effects due to gravity force take place depending on inlet/outlet location and a nonuniform 2D flow which is more realistic is detected. The current results will be useful for oil reservoir simulation and other similar simulation such as CO_2 sequestration.

References

[1] B. J. Bourblaux and F. J. Kalaydjian, "Experimental study of cocurrent and countercurrent flows in natural porous media," *SPE Reservoir Engineering*, vol. 5, no. 3, pp. 361–368, 1990.

[2] M. E. Chimienti, S. N. Illiano, and H. L. Najurieta, "Influence of temperature and interfacial tension on spontaneous imbibition process," in *Proceedings of the Latin American and Caribbean Petroleum Engineering Conference*, vol. 53668, SPE, Caracas, Venezuela, April 1999.

[3] M. Pooladi-Darvish and A. Firoozabadi, "Cocurrent and countercurrent imbibition in a water-wet matrix block," *SPE Journal*, vol. 5, no. 1, pp. 3–11, 2000.

[4] H. L. Najurieta, N. Galacho, M. E. Chimienti, and S. N. Illiano, "Effects of temperature and interfacial tension in different production mechanisms," in *Proceedings of the Latin American and Caribbean Petroleum Engineering Conference*, vol. 69398, SPE, Buenos Aires, Argentina, 2001.

[5] G. Q. Tang and A. Firoozabadi, "Effect of pressure gradient and initial water saturation on water injection in water-wet and mixed-wet fractured porous media," *SPE Reservoir Evaluation and Engineering*, vol. 4, no. 6, pp. 516–524, 2001.

[6] R. W. Parsons and P. R. Chaney, "Imbibition model studies on water-wet carbonate rocks," *SPE Journal*, pp. 26–34, 1966.

[7] R. Iffly, D. C. Rousselet, and J. L. Vermeulen, "Fundamental study of imbibition in fissured oil fields," in *Proceedings of the Annual Technical Conference*, vol. 4102, SPE, Dallas, Tex, USA, 1972.

[8] G. Hamon and J. Vidal, "Scaling-up the capillary imbibition process from laboratory experiments on homogeneous samples," in *Proceedings of the SPE European Petroleum Conferenc*, vol. 15852, London, UK, October 1986.

[9] S. Al-Lawati and S. Saleh, "Oil recovery in fractured oil reservoirs by low IFT imbibition process," in *Proceedings of the Annual Technical Conference and Exhibition*, vol. 36688, SPE, Denver, Colo, USA, 1996.

[10] J. C. Reis and M. Cil, "A model for oil expulsion by counter-current water imbibition in rocks: one-dimensional geometry," *Journal of Petroleum Science and Engineering*, vol. 10, no. 2, pp. 97–107, 1993.

[11] T. Babadagli, "Scaling of cocurrent and countercurrent capillary imbibition for surfactant and polymer injection in naturally fractured reservoirs," *SPE Journal*, vol. 6, no. 4, pp. 465–478, 2001.

[12] D. Zhou, L. Jia, J. Kamath, and A. R. Kovscek, "Scaling of counter-current imbibition processes in low-permeability porous media," *Journal of Petroleum Science and Engineering*, vol. 33, no. 1–3, pp. 61–74, 2002.

[13] M. F. El-Amin and S. Sun, "Scaling of a two-phase countercurrent imbibition using characteristic velocity," *Transport in Porous Media*. Submitted.

[14] N. R. Morrow and G. Mason, "Recovery of oil by spontaneous imbibition," *Current Opinion in Colloid and Interface Science*, vol. 6, no. 4, pp. 321–337, 2001.

[15] D. Kashchiev and A. Firoozabadi, "Analytic solutions for 1D countercurrent imbibition in water-wet media," *SPE Journal*, vol. 8, no. 4, pp. 401–408, 2003.

[16] Z. Tavassoli, R. W. Zimmerman, and M. J. Blunt, "Analytic analysis for oil recovery during counter-current imbibition in strongly water-wet systems," *Transport in Porous Media*, vol. 58, no. 1-2, pp. 173–189, 2005.

[17] D. Silin and T. Patzek, "On Barenblatt's model of spontaneous countercurrent imbibition," *Transport in Porous Media*, vol. 54, no. 3, pp. 297–322, 2004.

[18] H. S. Behbahani, G. D. Donato, and M. J. Blunt, "Simulation of counter-current imbibition in water-wet fractured reservoirs," *Journal of Petroleum Science and Engineering*, vol. 50, no. 1, pp. 21–39, 2006.

[19] D. Wilkinson, "Percolation model of immiscible displacement in the presence of buoyancy forces," *Physical Review A*, vol. 30, no. 1, pp. 520–531, 1984.

[20] N. Bech, O. K. Jensen, and B. Nielsen, "Modeling of gravity-imbibition and gravity-drainage processes: analytic and numerical solutions," *SPE Reservoir Engineering*, vol. 6, no. 1, pp. 129–136, 1991.

[21] Z. Tavassoli, R. W. Zimmerman, and M. J. Blunt, "Analysis of counter-current imbibition with gravity in weakly water-wet systems," *Journal of Petroleum Science and Engineering*, vol. 48, no. 1-2, pp. 94–104, 2005.

[22] G. Løvoll, Y. Méheust, K. J. Måløy, E. Aker, and J. Schmittbuhl, "Competition of gravity, capillary and viscous forces during drainage in a two-dimensional porous medium, a pore scale study," *Energy*, vol. 30, no. 6, pp. 861–872, 2005.

[23] H. Karimaie and O. Torsæter, "Effect of injection rate, initial water saturation and gravity on water injection in slightly water-wet fractured porous media," *Journal of Petroleum Science and Engineering*, vol. 58, no. 1-2, pp. 293–308, 2007.

[24] D. W. Ruth, Y. Li, G. Mason, and N. R. Morrow, "An approximate analytical solution for counter-current spontaneous imbibition," *Transport in Porous Media*, vol. 66, no. 3, pp. 373–390, 2007.

[25] D. Silin, T. Patzek, and S. M. Benson, "A model of buoyancy-driven two-phase countercurrent fluid flow," *Transport in Porous Media*, vol. 76, no. 3, pp. 449–469, 2009.

[26] S. Akin and A. R. Kovscek, "Imbibition studies of low-permeability porous media," in *Proceedings of the Western Regional Meeting*, vol. 54590, SPE, Anchorage, Ala, USA, May 1999.

[27] J. Cai, B. Yu, M. Zou, and L. Luo, "Fractal characterization of spontaneous co-current imbibition in porous media," *Energy and Fuels*, vol. 24, no. 3, pp. 1860–1867, 2010.

[28] M. F. El-Amin and S. Sun, "Effects of gravity and open-boundary location on a two-phase countercurrent imbibition in porous media," *Journal of Porous Media*. Submitted.

[29] Z. Chen, *Reservoir Simulation: Mathematical Techniques in Oil Recovery*, SIAM, Philadelphia, Pa, USA, 2007.

Hindawi Publishing Corporation
Journal of Applied Mathematics
Volume 2011, Article ID 325690, 14 pages
doi:10.1155/2011/325690

Research Article

Modeling and Analysis of Material Flows in Re-Entrant Supply Chain Networks Using Modified Partial Differential Equations

Fenglan He,[1] Ming Dong,[2] and Xiaofeng Shao[2]

[1] *Department of Industrial Engineering, School of Mechanical Engineering, Shanghai Jiao Tong University, 800 Dongchuan Road, Shanghai 200240, China*
[2] *Department of Operations Management, Antai College of Economics & Management, Shanghai Jiao Tong University, 535 Fahua Zhen Road, Shanghai 200052, China*

Correspondence should be addressed to Ming Dong, mdong@sjtu.edu.cn

Received 12 December 2010; Accepted 8 January 2011

Academic Editor: Shuyu Sun

Copyright © 2011 Fenglan He et al. This is an open access article distributed under the Creative Commons Attribution License, which permits unrestricted use, distribution, and reproduction in any medium, provided the original work is properly cited.

The basic partial differential equation (PDE) models for supply chain networks with re-entrant nodes and their macroscopic are proposed. However, through numerical examples, the basic continuum models do not perform well for multiple re-entrant systems. Then, a new state equation considering the re-entrant degree of the products is introduced to improve the effectiveness of the basic continuum models. The applicability of the modified continuum models for re-entrant supply chains is illustrated through numerical examples. Finally, based on the modified continuum model, numerical examples of different re-entrant degrees are given, meanwhile, the changes in the WIP and outflux are analyzed in details for multiple re-entrant supply chain systems.

1. Introduction

In recent years, factories and production systems have become larger and more complicated. The re-entrant manufacturing system is a typical example, which indicates that work in process (WIP) repeatedly passes through the same workstation at different stages of the process routes. Figure 1 gives a simplified model of re-entrant systems. The model consists of three workstations and five buffers; the arrows in the figure indicate the processing path of a lot. From Figure 1, it can be seen that the lot passes through the same workstations M_1 and M_2 twice, which is a typical situation of a re-entrant system. A re-entrant supply chain network consists of many such manufacturing systems. Understanding the behavior of large supply chains under different policies and scenarios is a major issue for many businesses

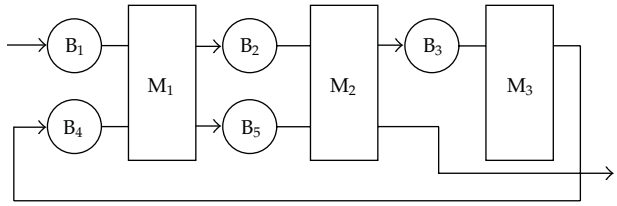

Figure 1: A simplified model for a re-entrant system.

today. In large factories, no experiments can be done involving whole supply chains. Therefore, simulation models are developed, which substitute for the real environment. There are several methods to model the multiple re-entrant production flows: Petrinet, queuing network, fluid network, and partial differential equation (PDE).

Petrinet is a mathematical tool to describe and analyze the logical relations of state changes for discrete event dynamic systems. It has been widely used in modeling, simulating, analyzing, and controlling of the discrete event dynamic systems. Compared with some other description tools, Petrinet model is especially easy to describe concurrent phenomena and simulate the parallel systems. On account of directly describing production processes, Petrinet model has been used to model the re-entrant manufacturing systems. However, it is extremely hard to solve the analytic solutions with the increase of system complexity. Wang and Wu [1] put forward an object-oriented hybrid Petrinet model of semiconductor manufacturing lines. Lin et al. [2] established a model of the re-entrant semiconductor production lines using Petrinets and studied on the stability of the system using buffer-boundless approach. Dong and Chen [3] developed a modular modeling approach based on object-oriented predicate/transition nets (OPTNs) for the analysis of supply chain process models.

Queuing network model treats each workstation as an individual discrete queue, then these independent queues are connected to form queuing networks according to the production flow. Queuing network model can directly describe the process of production lines and supply chain networks. A methodology for supply chain inventory analysis and optimization was presented by linking production authorization (PA) strategy to queueing models [4]. The statistics of arrival flow of the fluid model in queuing systems has been studied [5, 6]. Dong and Chen [7] proposed a network of inventory-queue models for the performance modeling and analysis of an integrated supply chain network. S. Kumar and P. R. Kumar [8] focused on the analysis of queuing theory of the re-entrant manufacturing systems. However, the analytic solution could be obtained only for the small-size systems based on the queuing models. When the scale of production systems or supply chain networks become large, the number of system states would grow exponentially and a combinatorial explosion problem would occur. Therefore, the queuing models have some difficulties in analysis of the real large-scale re-entrant supply chain networks. Most of the queuing models can only be used to evaluate the stability of some scheduling policies and difficult to be used directly for the real-world supply chains.

Since most supply chains deal with individual parts and the processes that those parts undergo, the above two discrete event models can describe a lot of details of the studied system. While discrete event simulators have been highly successful to simulate single factories, they are computationally too expensive to simulate even a moderately complicated

supply chains. Meanwhile, they are not scalable to a full supply chain. Therefore, a new modeling method called approximate modeling appears.

There are two kinds of approximate models: one is the so-called fluid model. It comes from traffic theory and was introduced by Newell [9] to approximately solve queuing problems. It treats the queue length $l(t)$ as a continuous variable. The change rate of a queue length is equal to the arrival rate $\lambda(t)$ minus the processing rate $\mu(t)$ when the queue length is not 0, otherwise the change rate of a queue length is 0. Hence, fluid models can quickly obtain the results by solving the ordinary differential equations. The time required for computing is not affected with the increase of material flows. The fluid models can be used not only to optimize the control system but also to reflect the long-term performance behavior of the system in the dynamic states.

However, one of the most important shortcomings of fluid models is that they cannot reflect the stochasticity of the production processes very well, that is, in the above equation, if $\lambda(t)$ and $\mu(t)$ are mean rates, then this is a fully deterministic system, stochasticity is not modeled at all. Otherwise, if $\lambda(t)$ and $\mu(t)$ are stochastic processes, then some theoretical analysis will be allowed. But this will degrade the advantages of a continuum models as a simulation tool [10].

Dai and Weiss [11] analyzed the relationship between the stability of the fluid model and the stability of the scheduling policies for the related queuing networks. Here, the stability of the fluid models is expressed by the boundedness of the fluid variables for a fixed influx. Göttlich [12] deduced the conservation laws under the form of ordinary differential and proved the existence of its solution based on the fluid models of supply chain networks.

The other approximate model is called partial differential equation (PDE) model. PDE models are actually continuum limit of fluid models. PDE models do have several advantages, that is, they are scalable; more detailed results can be found as compared to fluid models, and more importantly, they are amenable to optimization and control [13].

Recently, the continuous models have been applied to many fields and have achieved some significant research results. Anderson [14] established the basic continuous model for supply chains and described production flow of the system using rate equations macroscopically. Lee et al. [15] studied the supply chain simulation with combined discrete-continuous modeling method. It integrates the wide applicability of the discrete event simulation (DES) and fast computation of the continuum models together. Armburster et al. [16] introduced the concept of materials' density and established the continuous model of large-scale re-entrant manufacturing systems and proposed new state equations so that the continuous model could be used to the real production systems. Compared with a DES model, van den Berg et al. [17] verified the validity of the continuous model of simple serial production systems and then solved the optimal control problems with consideration of the demand growth. Unver et al. [18] presented a continuum (traffic flow like) model for the flow of products through complex production networks, based on statistical information obtained from extensive observations of the system. The resulting model consists of a system of hyperbolic conservation laws, which exhibit the correct diffusive properties given by the variance of the observed data.

In this paper, in order to accurately describe the multiple re-entrant supply chain networks from macroscopic perspective, a modified model is proposed, which can reflect how the re-entrant degree of a product impacts the system performance. Based on the queuing theory, we restrict our attention on establishing a new state equation considering the re-entrant degrees of jobs or products, meanwhile, we will also verify the validity of the modified PDE model for multiple re-entrant semiconductor supply chain systems by

a numerical experiment. And finally, the changes of the WIP and outflux in the case of different re-entrant factors are analyzed based on the modified PDE model.

The structure of this paper is organized as follows: in Section 2, the basic continuum model is presented and a numerical experiment is carried out to verify the validity of the basic model. Section 3 introduces the concept of re-entrant factor to improve the basic continuum model and verifies its effectiveness through an example. In Section 4, based on the modified continuous model, the WIP profile and outflux are analyzed in the case of different re-entrant factors. Finally, some conclusions are given in Section 5.

2. The Basic Continuum Model

2.1. Basic Model

Recently, continuum models for large-scale multiple re-entrant production systems have become an important research topic. Such a description is appropriate for a semiconductor manufacturing fab involving a large number of items in many stages. As $\rho(x,t)$ is the conserved variable, it is the density of the products with units [units/space] in the system. Here, x denotes the completion variable, $x = 0$ describes raw products that have just entered into the factory, and $x = 1$ denotes finished products that are ready to exit from the system. So, in the closed interval $x \in [0,1]$. The total number of products in the system can be found by taking the integral of density $\rho(x,t)$ of products over the stage variable x from 0 to 1. Therefore, the total WIP $W(t)$ as a function of time can be obtained as follows:

$$W(t) = \int_0^1 \rho(x,t)dx. \tag{2.1}$$

According to the conservation law, assuming that there is a unique entry and exit for the system and the yield is 100%, PDE models can be given by

$$\frac{\partial \rho(x,t)}{\partial t} + \frac{\partial\left(v\left(\rho(x,t)\right)\rho(x,t)\right)}{\partial x} = 0, \quad x \in [0,1],\ t \in (0,\infty), \tag{2.2}$$

where $v(\rho(x,t))$ is a velocity function that depends on the density $\rho(x,t)$ only. For a re-entrant supply chain system, we assume that $v(\rho(x,t))$ can be described by a state equation of the following form:

$$v\left(\rho(x,t)\right) = v_0\left(1 - \frac{W(t)}{W_{\max}}\right). \tag{2.3}$$

Here, v_0 is the velocity for the empty supply chain system and $W_{\max}$ is the maximal load (capacity of the supply chain system). Clearly, the velocity $v(\rho(x,t))$ is determined by the total WIP. The boundary condition for the start rate $\lambda(t)$ of products entering the supply chain system at $x = 0$ is then defined as

$$\lambda(t) = \rho(0,t)v(t). \tag{2.4}$$

An arbitrary initial condition for the density of the products can be expressed as

$$\rho(x,0) = \rho_0(x). \tag{2.5}$$

The production process in the supply chain network is described as an equivalent $M/M/1$ queue. The state variable ρ_{eq} denotes the equilibrium density of the supply chain system as a whole. Let $\rho = \rho_{\text{eq}}$, then $\rho(0,t) = \rho_{\text{eq}}$ and $v = v_{\text{eq}} = 1/\tau$. Correspondingly, the associated cycle time in steady state is $\tau = 1/v_{\text{eq}}$. Since a job arriving at a queue with a processing rate is $\mu = 1/v_{\max}$, the cycle time $\tau = \mu(1 + L)$ can be obtained according to the queuing theory; therefore, the equilibrium velocity becomes

$$v(\rho) = \frac{v_{\max}}{1 + \int_0^1 \rho(x,t)dx} = \frac{v_{\max}}{1 + w(t)}. \tag{2.6}$$

Equation (2.6) is a widely used expression between v and ρ for large-scale multiple re-entrant supply chain systems; note that the velocity v only depends upon the WIP at stage x. Therefore, Equation (2.2) can be rewritten as

$$\frac{\partial \rho(x,t)}{\partial t} + v\frac{\partial \rho(x,t)}{\partial x} = 0, \quad x \in [0,1],\ t \in (0,\infty). \tag{2.7}$$

Hence, assuming an initial WIP distribution $\rho_0(x)$ in the factory is given, the resulting full PDE model for the single-product multiple re-entrant supply chain systems is given as follows

$$\begin{aligned} \frac{\partial \rho(x,t)}{\partial t} + v(\rho)\frac{\partial \rho(x,t)}{\partial x} &= 0 \\ \rho(x,0) &= \rho_0(x), \\ \rho(0,t)v(t) &= \lambda(t), \\ v(\rho) &= \frac{v_{\max}}{1 + \int_0^1 \rho(x,t)dx}. \end{aligned} \tag{2.8}$$

If the influx $\lambda(\text{t})$ and the initial condition $\rho_0(x)$ are nonnegative, then the density will remain nonnegative. We use an upwind scheme [19] to discretize the PDE which is given by the following equation:

$$\rho(x_i, t_{j+1}) = \rho(x_i, t_j) - \frac{\Delta t}{\Delta x} v(t_j)\left[\rho(x_i, t_j) - \rho(x_{i-1}, t_j)\right], \tag{2.9}$$

where $i = 1, 2, \ldots, N$, and $\text{j} = 0, 1, \ldots, M - 1$. Δt and Δx are the step sizes in time and space, respectively. Based on the boundary condition, the propagation scheme is given by

$$\rho(x_0, t_{j+1}) = \rho(x_0, t_j) - \frac{\Delta t}{\Delta x}\left[v(t_j)\rho(x_0, t_j) - \lambda(t_j)\right]. \tag{2.10}$$

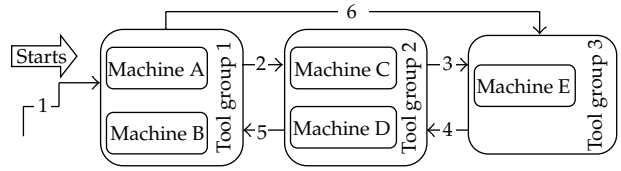

Figure 2: Process flow diagram of the Mini-Fab.

Since the Courant-Friedrich-Levy (CFL) condition is necessary for stability, the time step Δt and the space step Δx must satisfy the formulation as follows: $|(\Delta t/\Delta x)v_{\max}(t)| \leq 1$. Here, $v_{\max}(t)$ is the maximum of all occurring velocities in the system at time t.

Based on the above formula, the density distribution of each moment $\rho(x_i, t_j)$ can be obtained. Therefore, the system throughput rate $q(x_N, t_j)$ of each moment can also be computed as follows:

$$q(x_N, t_j) = \rho(x_N, t_j)v(\rho(x_N, t_j)). \tag{2.11}$$

Furthermore, the total WIP $w(t) = \int_0^1 \rho(x,t)dx$ can be obtained via the extended Simpson's rule quadrature, then the following equation can be obtained:

$$w(t) = \int_0^1 \rho(x,t)dx = \frac{h}{48}\Bigg[17\rho(x_0,t) + 59\rho(x_1,t) + 43\rho(x_2,t) + 49\rho(x_3,t) + 48\sum_{i=4}^{N-4}\rho(x_i,t) + 49\rho(x_{N-3},t) + 43\rho(x_{N-2},t) + 59\rho(x_{N-1},t) + 17\rho(x_N,t)\Bigg]. \tag{2.12}$$

Finally, the density distribution $\rho(x_i, t_j)$ and throughput $q(x_N, t_j)$ of each moment can be obtained.

2.2. Numerical Experiments

Mini-Fab is a simplified model of the semiconductor production line, which has all the important features of the re-entrant semiconductor manufacturing systems, such as re-entrant, different processing time, and batch production. Currently, many scholars have done a lot of research work based on the Mini-Fab. The Mini-Fab contains 5 machines grouped into 3 tool sets; the product comprises of 6 processing steps, each tool set is visited twice, which is shown in Figure 2 [20].

For convenience, we make the following basic assumptions on the model:

(1) the product yield rate is 100%, namely, there is no rework problem;

(2) the system is a continuous production process for 24 hours a day;

(3) the system does not take into account the time of carrying, loading and discharging, adjusting equipment, and premaintaining equipment and downtime.

Table 1: Processing time of the product D at each step.

Machining centers	Processing time (hours)	
Machines A & B	Step 1: 1.5	Step 5: 1.5
Machines C & D	Step 2: 0.5	Step 4: 1
Machine E	Step 3: 1	Step 6: 0.5

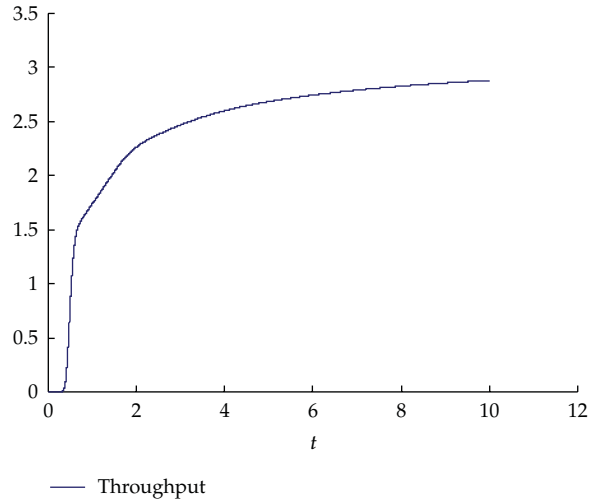

Figure 3: Throughput as a function of time for the PDE simulation.

Now it is assumed that there is one product D in the Mini-Fab, processing steps and processing time shown in Table 1.

Based on the basic continuous model, the parameters are assumed as follows: $P = 0.25$ (days), $v_{\max} = 4$ (units/day), $\lambda = 5$ (units/day). We typically start up with an empty production system; the total running time of the production lines is 10 (days). Let $\Delta t = 0.001$ and $\Delta x = 0.01$, then Δx and Δt satisfy the CFL stability condition $(\Delta t/\Delta x)v_{\max} < 1$. The system throughput can be obtained through the simulation based on the basic PDE model of (2.8). Figure 3 indicates that the system throughput is about 3.2 (units/day) during the steady state.

Once the throughput of the basic continuous models is obtained, the corresponding Mini-Fab simulation model can be built using simulation package ExtendSim [21] to verify the validity of the models with a period of one year. As can be seen from Figure 4 that the throughput during the steady state is about 5 (units/day) through the ExtendSim simulation.

Comparing Figure 3 with Figure 4, it is obviously found that there are some differences between the throughput results of the two models. This is because the basic continuous model of (2.8) is built on the basis of a large number of materials, and many re-entrant steps in the systems and some important characteristics of semiconductor production systems are not captured. Therefore, the further investigation is needed to explore more precise models for multiple re-entrant production systems.

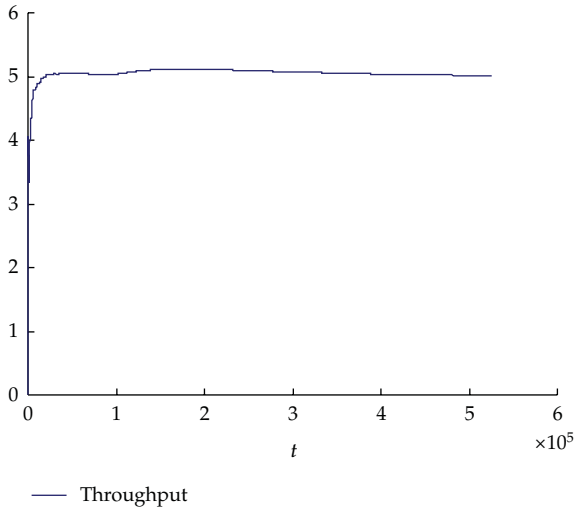

Figure 4: Throughput as a function of time for the ExtendSim simulation.

3. The Modified Continuum Model

3.1. Modified Model

It is worth noting that the state equations can reflect the characteristics of systems—any change of the multiple re-entrant production systems may lead to a different state equation. Equation (2.6) is a quite general state equation, in order to capture some important features of multiple re-entrant supply chain systems, so a more specified relationship is required for computing velocities numerically. Lefeber and Armbruster [22] presented a more sophisticated re-entrant factory model through the use of integration kernels. For the general supply chain systems (non-re-entrant systems), Sun and Dong [23] described several kinds of state equations and the corresponding cycle times. Although there are many kinds of continuum models for describing the re-entrant production system currently, they do not reflect how the re-entrant degree of the product impacts the system performance. Hence, a new concept reflecting the re-entrant degree of the products is introduced.

Definition 3.1. Let α be a product re-entrant factor, α equals the ratio of the product processing time of re-entrant steps and the product total processing time.

Re-entrant factor α is the property of product process flows, with the increase of re-entrant factor α, the degree of re-entrant of the product becomes larger and larger. Let P be the total processing time, let P_1 be the re-entrant processing time, and let P_2 be the non-re-entrant processing time. According to the above definition, we can obtain the following formula:

$$\alpha = \frac{P_1}{P_1 + P_2} = \frac{P_1}{P}. \tag{3.1}$$

In reality, the velocity of products in the system is not only related with the WIP level but also with the re-entrant factor. Let $w(t)$ be the WIP level in the system at a given time t, let

$w(\Delta x, t)$ be the WIP level at interval Δx at time t, let Δx be the interval of the completion of the product, and let Δt be the processing time required to complete the interval Δx. Assume that $w(\Delta x, t)$ is proportional to Δt and the system consists of two parts: re-entrant processes and non-re-entrant processes, hence, $\alpha w(t)$ is the WIP level of the re-entrant processes at a given time t and also referred to as re-entrant WIP. Similarly, $(1-\alpha)w(t)$ is the WIP level of non-re-entrant processes at a given time t and also called as non-re-entrant WIP.

According to the queuing theory, the processing cycle time of the re-entrant process τ_1 can be expressed as follows:

$$\tau_1 = [1 + \alpha w(t)]P_1. \tag{3.2}$$

As for the non-re-entrant processes, assuming the total number of workstations is m, $a_1, a_2, \ldots, a_m$ are the corresponding processing times at each workstation, respectively, and τ_2 is the non-re-entrant processing cycle time, then we have

$$\begin{gathered} P_2 = a_1 + a_2 + \cdots + a_m, \\ \tau_2 = \sum_{i=1}^{m}\left(1 + \frac{a_i}{P}w(t)\right)a_i = \sum_{i=1}^{m} a_i + \sum_{i=1}^{m}\frac{a_i^2}{P}w(t) = P_2 + \sum_{i=1}^{m}\frac{a_i^2}{P}w(t), \end{gathered} \tag{3.3}$$

so the total cycle time τ can be written in the following form:

$$\tau = \tau_1 + \tau_2 = [1 + \alpha w(t)]P_1 + \left[P_2 + \sum_{i=1}^{m}\frac{a_i^2}{P}w(t)\right] = P + \left(\alpha^2 + \sum_{i=1}^{m}\frac{a_i^2}{P^2}\right)w(t)P. \tag{3.4}$$

Then, the resulting new state equation for the velocity will be given by

$$v = \frac{1}{\tau} = \frac{1}{P + \left(\alpha^2 + \sum_{i=1}^{m}\left(a_i^2/P^2\right)\right)w(t)P}. \tag{3.5}$$

In order to avoid computational complexity of $\sum_{i=1}^{m}(a_i^2/P^2)$, an approximate method is proposed to deal with the non-re-entrant process. Suppose that WIP in non-re-entrant processes follows the uniform distribution in each workstation, then the mean processing time P_2/m and the mean WIP level at each workstation $((1-\alpha)/m)w(t)$ can be obtained. According to the queuing theory, the mean cycle time of the non-re-entrant processes at each workstation is $[1 + ((1-\alpha)/m)w(t)](P_2/m)$, and the total cycle time of the non-re-entrant

processes τ_2 is $[1 + ((1-\alpha)/m)w(t)]P_2$. Therefore, the total cycle time τ can be expressed as follows:

$$\begin{aligned}\tau = \tau_1 + \tau_2 &= [1 + \alpha w(t)]P_1 + \left[1 + \frac{(1-\alpha)}{m} w(t)\right] P_2 \\ &= P_1 + P_2 + \left[\alpha P_1 + \frac{(1-\alpha)}{m} P_2\right] w(t) \\ &= P + \left[\alpha \cdot \alpha P + (1-\alpha) \cdot \frac{(1-\alpha)P}{m}\right] w(t) \\ &= P + \left[\alpha^2 + \frac{(1-\alpha)^2}{m}\right] w(t)P.\end{aligned} \tag{3.6}$$

The corresponding new state equation can be obtained as follows:

$$v = \frac{1}{\tau} = \frac{1}{P + \left[\alpha^2 + (1-\alpha)^2/m\right] w(t)P}. \tag{3.7}$$

Therefore, the resulting modified whole PDE model is given below:

$$\begin{aligned}\frac{\partial \rho(x,t)}{\partial t} + v(\rho)\frac{\partial \rho(x,t)}{\partial x} &= 0, \\ \rho(x,0) &= \rho_0(x), \\ \rho(0,t)v(t) &= \lambda(t), \\ v = \frac{1}{\tau} &= \frac{v_{\max}}{1 + \left[\alpha^2 + (1-\alpha)^2/m\right] w(t)}.\end{aligned} \tag{3.8}$$

3.2. Validity of the Modified Model

Once the new state equation is obtained, the same example in the previous section can be used to verify the validity of the modified models. According to Figure 2, the total number of workstations is $m = 3$, the steps 4 to 6 are re-entrant steps. From Table 1, the products' re-entrant factor $\alpha = 0.5$ can be easily obtained by definition. Assume that the influx λ is 5 (units/day) and the total running time is 10 (days), the system starts running from an empty state. With $\Delta t = 0.001$, $\Delta x = 0.01$, then Δx and Δt satisfy the CFL stability condition: $v_{\max} \cdot \Delta t/\Delta x < 1$. Similarly, the modified continuous model (3.8) can be solved via the upwind scheme, and the throughput of the modified models can be obtained, which is plotted in Figure 5.

It can be seen that the throughput is initially zero for the re-entrant system. This is due to the time delay and the system initialization (the system starts up with an empty factory), then the system begins to have throughput about 0.25 (days) and increases drastically until

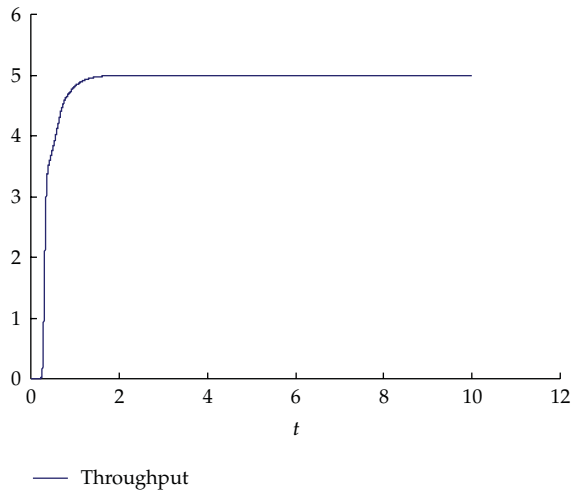

Figure 5: Throughput as a function of time for the modified PDE model.

the throughput reaches a stable value of 5 (units/day) about 1.5 days. It is obvious that the results are basically consistent with the simulation results obtained from ExtendSim. Therefore, it can be seen that the modified models are more effective for multiple re-entrant supply chain systems.

4. Case Studies for the Different Re-Entrant Factors

In order to analyze the influence of the re-entrant degree on the WIP profile and outflux for the multiple re-entrant supply chain systems, several scenarios of the different re-entrant factors are presented in this section. Same as the previous section, let $v_{\max} = 4$ (units/day), a uniform time step size $\Delta t = 0.001$ (days), and a uniform spatial interval length $\Delta x = 0.01$, then Δx and Δt also satisfy the CFL stability condition $(\Delta t/\Delta x)v_{\max} < 1$. We assume that the varying influx is prescribed first, as shown in Figure 6.

Taking the multiple re-entrant production systems as an example, the system begins to run from an empty factory. We observe the changes of the WIP and outflux in the case of different re-entrant factors. As shown in Figure 7, black and red lines indicate the WIP and outflux, respectively.

From Figure 7, we can observe that, roughly, the WIP of the modified PDE model shows an increasing trend gradually first to reach the maximum and then it has a decreasing trend until it reaches the stable value. Meanwhile, the outflux of the modified PDE model rises slowly and then sharply reaches the maximum, after that the outflux shows a sudden decrease and then slowly reaches a stable value. Additionally, it is easy to see that the maximum WIP occures a small decrease first and then rises slowly with the increase of the re-entrant factor. Correspondingly, the maximum outflux appears a small increasing trend at first; when the WIP reaches a certain value, the maximum outflux becomes smaller and smaller with the increase of the re-entrant factor. These results are almost consistent with the actual situation; meanwhile, the materials flow can be better controlled according to the WIP profile and outflux.

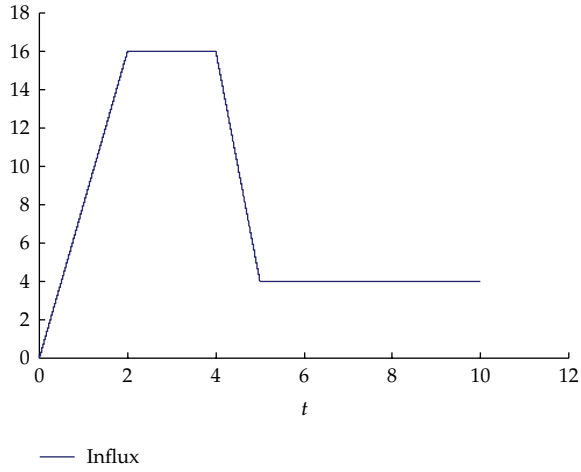

Figure 6: Influx as a function of time for the modified PDE model.

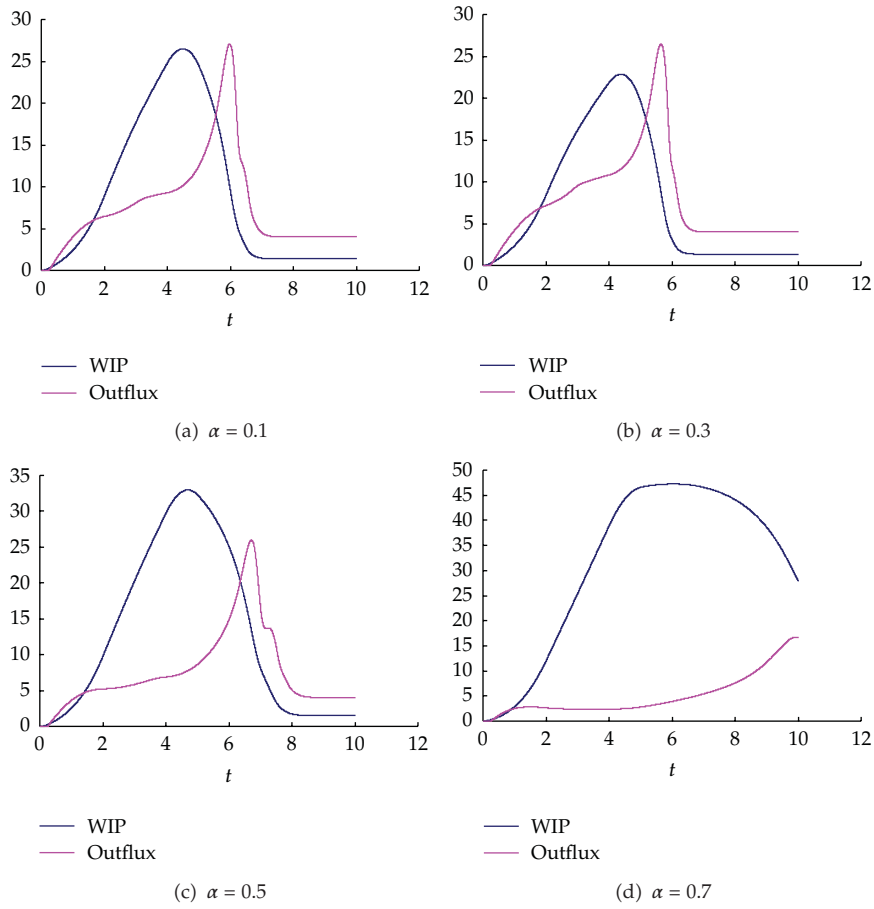

Figure 7: WIP and Throughput as a function of time for the modified PDE model.

5. Conclusions

In this paper, the basic continuum models for material flows are first proposed, and its low accuracy for the multiple re-entrant supply chain networks is explained by a numerical experiment. In order to model such systems more precisely, this paper presents a new state equation that takes into account the re-entrant degree of the product. The applicability of the modified continuum model for multiple re-entrant supply chain systems is also illustrated through a numerical example. Afterwards, based on the modified continuum models, some numerical examples on different re-entrant factors are provided, and the impacts of different re-entrant factors on the WIP profile and outflux changes are studied. Meanwhile, some interesting observations are discussed. The proposed model can be used to obtain more accurate results for material flows of the multiple re-entrant supply chain networks from macroscopic perspective.

Acknowledgments

The work presented in this paper has been supported by a Grant from the National High-Tech Research and Development Program (863 Program) of China (no. 2008AA04Z104) and a Grant from National Natural Science Foundation of China (no. 70871077).

References

[1] Z. Wang and Q. Wu, "Object-oriented hybrid PN model of semiconductor manufacturing line," in *Proceedings of the 4th World Congress on Intelligent Control and Automation*, pp. 1354–1358, June 2002.

[2] C. Lin, M. Xu, D. C. Marinescu, F. Ren, and Z. Shan, "A sufficient condition for instability of buffer priority policies in re-entrant lines," *IEEE Transactions on Automatic Control*, vol. 48, no. 7, pp. 1235–1238, 2003.

[3] M. Dong and F. F. Chen, "Process modeling and analysis of manufacturing supply chain networks using object-oriented Petri nets," *Robotics and Computer-Integrated Manufacturing*, vol. 17, no. 1-2, pp. 121–129, 2001.

[4] M. Dong, "Inventory planning of supply chains by linking production authorization strategy to queueing models," *Production Planning and Control*, vol. 14, no. 6, pp. 533–541, 2003.

[5] M. Li, "Fractal time series—a tutorial review," *Mathematical Problems in Engineering*, vol. 2010, Article ID 157264, 26 pages, 2010.

[6] M. Li, W. Zhao, and S. Y. Chen, "mBm-based scalings of traffic propagated in internet," *Mathematical Problems in Engineering*, vol. 2011, Article ID 389803, 21 pages, 2011.

[7] M. Dong and F. F. Chen, "Performance modeling and analysis of integrated logistic chains: an analytic framework," *European Journal of Operational Research*, vol. 162, no. 1, pp. 83–98, 2005.

[8] S. Kumar and P. R. Kumar, "Queueing network models in the design and analysis of semiconductor wafer fabs," *IEEE Transactions on Robotics and Automation*, vol. 17, no. 5, pp. 548–561, 2001.

[9] G. F. Newell, "Scheduling, location, transportation, and continuum mechanics: some simple approximations to optimization problems," *SIAM Journal on Applied Mathematics*, vol. 25, no. 3, pp. 346–360, 1973.

[10] D. Armbruster, D. E. Marthaler, C. Ringhofer, K. Kempf, and T. C. Jo, "A continuum model for a re-entrant factory," *Operations Research*, vol. 54, no. 5, pp. 933–950, 2006.

[11] J. G. Dai and G. Weiss, "Stability and instability of fluid models for reentrant lines," *Mathematics of Operations Research*, vol. 21, no. 1, pp. 115–134, 1996.

[12] S. Göttlich, M. Herty, and A. Klar, "Network models for supply chains," *Communications in Mathematical Sciences*, vol. 3, no. 4, pp. 545–559, 2005.

[13] J. Nocedal and S. J. Wright, *Numerical Optimization*, Springer Series in Operations Research and financial Engineering, Springer, New York, NY, USA, 2006.

[14] E. J. Anderson, "A new continuous model for job shop scheduling," *International Journal of Systems Science*, vol. 12, no. 12, pp. 1469–1475, 1981.

[15] Y. H. Lee, M. K. Cho, S. J. Kim, and Y. B. Kim, "Supply chain simulation with discrete-continuous combined modeling," *Computers and Industrial Engineering*, vol. 43, no. 1-2, pp. 375–392, 2002.

[16] D. Armbruster, C. Ringhofer, and T. C. Jo, "Continuous models for production flows," in *Proceedings of the American Control Conference (AAC '04)*, pp. 4589–4594, July 2004.

[17] R. van den Berg, E. Lefeber, and K. Rooda, "Modeling and control of a manufacturing flow line using partial differential equations," *IEEE Transactions on Control Systems Technology*, vol. 16, no. 1, pp. 130–136, 2008.

[18] A. Unver, C. Ringhofer, and D. Armbruster, "A hyperbolic relaxation model for product flow in complex production networks," *Discrete and Continuous Dynamical Systems*, supplement 2009, pp. 790–799, 2009.

[19] R. J. LeVeque, *Finite Difference Methods for Ordinary and Partial Differential Equations*, Society for Industrial and Applied Mathematics, Philadelphia, Pa, USA, 2007.

[20] H. Vogt, "FabSim Mini-fab example," 2007, http://www.fabsim.com/index.html.

[21] T. B. Qin and Y. F. Wang, *Application Oriented Simulation Modeling and Analysis with ExtendSim*, Tsinghua University Press, Beijing, China, 2009.

[22] E. Lefeber and D. Armbruster, *Aggregate modeling of manufacturing systems*, Systems Engineering Group, 2007.

[23] S. Sun and M. Dong, "Continuum modeling of supply chain networks using discontinuous Galerkin methods," *Computer Methods in Applied Mechanics and Engineering*, vol. 197, no. 13–16, pp. 1204–1218, 2008.

Hindawi Publishing Corporation
Journal of Applied Mathematics
Volume 2011, Article ID 129724, 16 pages
doi:10.1155/2011/129724

Research Article

A Stabilized Mixed Finite Element Method for Single-Phase Compressible Flow

Liyun Zhang[1] and Zhangxin Chen[2,3]

[1] *School of Science, Xi'an Jiaotong University, Xi'an 710049, China*
[2] *Center for Computational Geosciences, Xi'an Jiaotong University, Xi'an 710049, China*
[3] *Department of Chemical and Petroleum Engineering, Schulich School of Engineering, University of Calgary, 2500 University Drive, NW Calgary, Canada AB T2N 1N4*

Correspondence should be addressed to Zhangxin Chen, zhachen@ucalgary.ca

Received 6 December 2010; Accepted 2 January 2011

Academic Editor: Shuyu Sun

Copyright © 2011 L. Zhang and Z. Chen. This is an open access article distributed under the Creative Commons Attribution License, which permits unrestricted use, distribution, and reproduction in any medium, provided the original work is properly cited.

We present and study a stabilized mixed finite element method for single-phase compressible flow through porous media. This method is based on a pressure projection stabilization method for multiple-dimensional incompressible flow problems by using the lowest equal-order pair for velocity and pressure (i.e., the $\mathbf{P}_1 - P_1$ pair). An optimal error estimate in divergence norm for the velocity and suboptimal error estimates in the L^2-norm for both velocity and pressure are obtained. Numerical results are given in support of the developed theory.

1. Introduction

The mixed finite element method is frequently used to obtain approximate solutions to more than one unknown. For example, the Stokes equations are often solved to obtain both pressure and velocity simultaneously. Accordingly, we need a finite element space for each unknown. These two spaces must be chosen carefully so that they satisfy an inf-sup stability condition for the mixed method to be stable. Examples of an appropriate choice for the mixed spaces for the Stokes equations include the $\mathbf{P}_2 - P_1$ pair (i.e., the Taylor-Hood element [1, 2]) and the MINI-element [1, 3] (i.e., the $\mathbf{P}_1 - P_1$ pair with the addition of the cubic bubble functions on triangles to the $\mathbf{P}_1$-velocity space), where P_r stands for the space of polynomials of degree $r \geq 0$. For second-order partial differential problems of the Darcy flow type, many special mixed finite element spaces have been established, such as those of Nedelec [4], Raviart and Thomas [5], Brezzi et al. [6], Brezzi et al. [7], Chen and Douglas Jr. [8], and Brezzi et al. [9]. These mixed spaces do not include the equal-order pairs such as $\mathbf{P}_r - P_r$.

Although the equal-order pairs of mixed finite element spaces do not satisfy the inf-sup stability condition [10], they offer some computational advances such as they are simple and have practical uniform data structure and adequate accuracy. Much attention has recently been attracted to using the equal-order finite element pairs for the fluid mechanics equations, particularly for the Stokes and Navier-Stokes equations [10–16]. Many stabilization techniques have been used to stabilize these element pairs such as penalty, pressure projection, and residual stabilization methods [16–19]. Among these methods, the pressure projection stabilization method is a preferable choice in that it is free of stabilization parameters, does not require any calculation of high-order derivatives or edge-based data structures, and can be implemented at the element level [10, 12, 14, 15]. These recent studies have been focused on stabilization of the lowest equal-order finite element pair $\mathbf{P}_1 - P_1$ (or $\mathbf{Q}_1 - Q_1$, the bilinear function pair) using the pressure projection stabilization method for second-order elliptic problems of the Darcy flow type and the Stokes and Navier-Stokes problems [10, 12, 15, 20]. This pressure projection stabilization method involves the introduction of a local projection of the pressure into a scalar finite element space.

In this paper, we extend the pressure projection stabilization method to solving the single-phase compressible flow problem in porous media that is described by a second-order parabolic equation. We first define this stabilized method using the equal-order pair of mixed finite element spaces $\mathbf{P}_1 - P_1$. Then we derive error estimates for this method; optimal error estimates in the divergence norm for velocity and suboptimal error estimates in the L^2-norm for pressure and velocity are obtained. For more information on the better features of the present pressure projection stabilization method over other stabilized mixed methods, please refer to [21]. This is the first time that this method is used for the numerical solution of the single-phase compressible flow problem in porous media.

The rest of this paper is organized as follows. In the next section, the basic notation, the differential equation, and its mixed formulation are stated. Then, in the third section, the stabilized mixed finite element method is shown. Error estimates for this stabilized method are derived in the fourth section, and a superconvergence result is proved in the fifth section. In the final section, numerical experiments are given to illustrate the theoretical results.

2. Function Setting

The dynamical problem we consider is single-phase compressible flow in a porous medium domain $\Omega \subset \mathcal{R}^d, d \geq 2$, with a Lipschitz-continuous boundary Γ. The system is governed by

$$cp_t - \nabla \cdot (K \nabla p) = f, \quad \text{in } \Omega \times (0, T], \tag{2.1}$$

$$p = p_0, \quad \text{in } \Omega \times \{0\}, \tag{2.2}$$

$$p = 0, \quad \text{on } \Gamma \times (0, T], \tag{2.3}$$

where $p(\mathbf{x}, t)$ is the pressure, $c(\mathbf{x}, t)$ the compressibility factor, $f(\mathbf{x}, t)$ the source or sink function, $p_0(\mathbf{x})$ the initial pressure, $K(\mathbf{x})$ the permeability (or mobility) of the medium, $T > 0$ the final time, and $p_t = \partial p / \partial t$. When gravity is ignored, the single-phase compressible flow problem reduces to (2.1)–(2.3) [22]. We assume that $c(\mathbf{x}, t)$ is a smooth function:

$$0 < c_0 \leq c(\mathbf{x}, t) < \infty, \quad c_t(\mathbf{x}, t) < \infty, \quad \mathbf{x} \in \Omega, \quad 0 \leq t \leq T. \tag{2.4}$$

Furthermore, assume that $K = (k_{ij})_{i,j=1}^{d}$ is a bounded, symmetric, and positive definite matrix in Ω; that is, there exist positive constants α_1 and α_2 such that

$$\alpha_1\|\boldsymbol{\xi}\|^2 \le \boldsymbol{\xi}^T K\boldsymbol{\xi} \le \alpha_2\|\boldsymbol{\xi}\|^2, \quad \forall \boldsymbol{\xi} \in \mathcal{R}^d,\ d \ge 2, \tag{2.5}$$

where $\boldsymbol{\xi}^T$ is the transpose of $\boldsymbol{\xi}$.

In order to introduce a mixed formulation on Ω, set

$$\mathbf{V} = \mathbf{H}(\mathrm{div};\Omega) = \left\{\mathbf{v} \in \left(L^2(\Omega)\right)^d : \mathrm{div}\,\mathbf{v} \in L^2(\Omega)\right\}, \quad W = L^2(\Omega), \tag{2.6}$$

with the norms

$$\|\mathbf{v}\|_{\mathbf{H}(\mathrm{div};\Omega)} = \left(\|\mathbf{v}\|_0^2 + \|\mathrm{div}\,\mathbf{v}\|_0^2\right)^{1/2}, \quad \|q\|_W = \|q\|_0, \quad \mathbf{v} \in \mathbf{V}, \quad q \in W. \tag{2.7}$$

Introduce $\mathbf{u} = -K\nabla p$ and transform (2.1) and (2.3) into the standard mixed form: for any $t \in [0,T]$, find $\mathbf{u}(t) \in \mathbf{V}$ and $p(t) \in W$ such that

$$(cp_t, q) + (\mathrm{div}\,\mathbf{u}, q) = (f, q), \quad \forall q \in W, \tag{2.8}$$

$$\left(K^{-1}\mathbf{u}, \mathbf{v}\right) - (p, \mathrm{div}\,\mathbf{v}) = 0, \quad \forall \mathbf{v} \in \mathbf{V}. \tag{2.9}$$

This is the mixed variational form of (2.1) and (2.3). The initial condition (2.2) remains valid. A generalized bilinear form on $(\mathbf{V}, W) \times (\mathbf{V}, W)$ is defined by

$$B((\mathbf{u},p),(\mathbf{v},q)) = \left(K^{-1}\mathbf{u}, \mathbf{v}\right) - (p, \mathrm{div}\,\mathbf{v}) + (\mathrm{div}\,\mathbf{u}, q), \quad (\mathbf{u},p),(\mathbf{v},q) \in \mathbf{V} \times W. \tag{2.10}$$

Consequently, the system (2.8) and (2.9) is written as follows: for any $t \in [0,T]$, find $\mathbf{u}(t) \in \mathbf{V}$ and $p(t) \in W$ such that

$$(cp_t, q) + B((\mathbf{u},p),(\mathbf{v},q)) = (f, q), \quad \forall (\mathbf{v},q) \in \mathbf{V} \times W, \tag{2.11}$$

$$p(\mathbf{x}, 0) = p_0(\mathbf{x}), \quad \forall \mathbf{x} \in \Omega. \tag{2.12}$$

For convenience, we state the Gronwall Lemma that will be used later.

Lemma 2.1. *Let $g(t), l(t)$, and $\xi(t)$ be three nonnegative functions satisfying, for $t \in [0,T]$,*

$$\xi(t) + G(t) \le C + \int_0^t l\,ds + \int_0^t g\xi\,ds, \tag{2.13}$$

where $G(t)$ is a nonnegative function on $[0,T]$ and C is a number. Then

$$\xi(t) + G(t) \le \left(C + \int_0^t l\,ds\right)\exp\left(\int_0^t g\,ds\right), \quad t \in [0,T]. \tag{2.14}$$

Lemma 2.2. *In addition to the assumptions* (2.4) *and* (2.5), *if*

$$\|p_0\|_0 + \left(\int_0^t \|f(s)\|_0^2 ds\right)^{1/2} \le C, \quad t \in [0,T], \tag{2.15}$$

then the following stability estimate holds

$$\sup_{0\le s\le t}\left(\|p(s)\|_0^2 + \|\mathbf{u}(s)\|_0^2\right) + \int_0^t \left(\|p_t(s)\|_0^2 + \|\mathbf{u}(s)\|_0^2 + \|\operatorname{div}\mathbf{u}(s)\|_0^2\right) ds \le C, \tag{2.16}$$

for $t \in [0,T]$.

Proof. We divide the proof into three parts.

(1) Taking $q = p$ and $\mathbf{v} = \mathbf{u}$ in (2.8) and (2.9), respectively, and adding the resulting equations, we obtain

$$\frac{1}{2}\frac{d}{dt}\|\sqrt{c}p\|_0^2 + \left(K^{-1}\mathbf{u},\mathbf{u}\right) = (f,p) + \frac{1}{2}(c_t p, p) \le \left\|c^{-1/2}f\right\|_0 \|\sqrt{c}p\|_0 + C\|p\|_0^2, \tag{2.17}$$

which, along with Gronwall's inequality, (2.4), and (2.5), gives

$$\sup_{0\le s\le t}\|p(s)\|_0^2 + \int_0^t \|\mathbf{u}(s)\|_0^2 ds \le C, \quad t \in [0,T]. \tag{2.18}$$

(2) Taking $q = p_t$ in (2.8), differentiating (2.9) with respect to t, taking $\mathbf{v} = \mathbf{u}$, and adding the resulting equations, we see that

$$\|\sqrt{c}p_t\|_0^2 + \frac{1}{2}\frac{d}{dt}\left\|\sqrt{K^{-1}}\mathbf{u}\right\|_0^2 = (f,p_t) \le \left\|c^{-1/2}f\right\|_0 \|\sqrt{c}p_t\|_0, \tag{2.19}$$

which, along with Gronwall's inequality, (2.4), and (2.5), implies

$$\sup_{0\le s\le t}\|\mathbf{u}(s)\|_0^2 + \int_0^t \|p_t(s)\|_0^2 ds \le C, \quad t \in [0,T]. \tag{2.20}$$

(3) Taking $q = \operatorname{div}\mathbf{u}$ in (2.8), we obtain

$$\|\operatorname{div}\mathbf{u}\|_0^2 = (f, \operatorname{div}\mathbf{u}) - (cp_t, \operatorname{div}\mathbf{u}) \le \left(\|f\|_0 + \|cp_t\|_0\right)\|\operatorname{div}\mathbf{u}\|_0, \tag{2.21}$$

which, along with (2.20), yields

$$\int_0^t \|\operatorname{div}\mathbf{u}(s)\|_0^2\, ds \le C. \tag{2.22}$$

The proof has been completed. □

3. The Stabilized Mixed Finite Element Method

For $h > 0$, we introduce finite-dimensional subspaces $(\mathbf{V}_h, W_h) \subset (\mathbf{V}, W)$, which are associated with Γ_h, a triangulation of Ω into triangles, assumed to be regular in the usual sense [1, 23]. This paper focuses on the unstable velocity-pressure pair of the lowest equal-order finite element spaces:

$$\begin{aligned} \mathbf{V}_h &= \left\{\mathbf{v} \in \mathbf{V} : \mathbf{v}|_T \in (P_1(T))^2,\ \forall T \in \Gamma_h\right\}, \\ W_h &= \left\{q \in W : q|_T \in P_1(T),\ \forall T \in \Gamma_h\right\}. \end{aligned} \tag{3.1}$$

As noted earlier, this choice of the approximate spaces $\mathbf{V}_h$ and W_h does not satisfy the inf-sup condition uniformly in h [10]:

$$\sup_{\mathbf{v}\in\mathbf{V}_h} \frac{(\operatorname{div}\mathbf{v}, q)}{\|\mathbf{v}\|_{\mathbf{H}(\operatorname{div};\Omega)}} \ge \beta\|q\|_0, \quad \forall q \in W_h, \tag{3.2}$$

where the constant $\beta > 0$ is independent of h. The pressure projection stabilization method for elliptic problems and the Stokes and Navier-Stokes problems [10, 12, 15, 20] will be adopted.

Let $\Pi_h : W \to \overline{W}_h$ be the standard L^2-projection, which satisfies

$$\begin{aligned} (p, q) &= (\Pi_h p, q), \quad \forall p \in W,\ q \in \overline{W}_h, \\ \|\Pi_h p\|_0 &\le \|p\|_0, \quad \forall p \in W, \end{aligned} \tag{3.3}$$

where $\overline{W}_h = \{q \in W : q|_T \in P_0(T),\ \forall T \in \Gamma_h\}$. We introduce the pressure projection stabilization term

$$G(p, q) = (p - \Pi_h p, q - \Pi_h q), \quad p, q \in W. \tag{3.4}$$

Now, the stabilized mixed finite element method reads as follows: for any $t \in [0, T]$, find $\mathbf{u}_h(t) \in \mathbf{V}_h$ and $p_h(t) \in W_h$ such that

$$\begin{aligned} (cp_{ht}, q) + (\operatorname{div}\mathbf{u}_h, q) + G(p_h, q) &= (f, q), \quad \forall q \in W_h, \\ \left(K^{-1}\mathbf{u}_h, \mathbf{v}\right) - (p_h, \operatorname{div}\mathbf{v}) &= 0, \quad \forall \mathbf{v} \in \mathbf{V}_h. \end{aligned} \tag{3.5}$$

Introduce the bilinear form

$$\mathcal{B}((\mathbf{u}_h,p_h),(\mathbf{v},q)) = \left(K^{-1}\mathbf{u}_h,\mathbf{v}\right) - (p_h,\operatorname{div}\mathbf{v}) + (\operatorname{div}\mathbf{u}_h,q) + G(p_h,q), \quad (\mathbf{u}_h,p_h),(\mathbf{v},q) \in \mathbf{V}_h \times W_h. \tag{3.6}$$

Using this notation, the stabilized mixed method of problem (2.8) and (2.9) reads as follows: find $(\mathbf{u}_h,p_h) \in \mathbf{V}_h \times W_h$, $t \in [0,T]$, such that, for all $(\mathbf{v},q) \in \mathbf{V}_h \times W_h$,

$$(cp_{ht},q) + \mathcal{B}((\mathbf{u}_h,p_h),(\mathbf{v},q)) = (f,q), \tag{3.7}$$

$$p_h(0) = p_{0h}, \tag{3.8}$$

where p_{0h} is a proper approximation of p_0 in W_h. The next theorem can be found in [20], which shows the well-posedness of problem (3.7).

Theorem 3.1. *Under the assumption* (2.5) *and with* $(\mathbf{V}_h,W_h)$ *defined as above, there exist positive constants* C *and* β*, independent of* h*, such that*

$$\left|\mathcal{B}((\mathbf{u}_h,p_h),(\mathbf{v}_h,q_h))\right| \le C\left(\|\mathbf{u}_h\|_{\mathbf{H}(\operatorname{div};\Omega)} + \|p_h\|_0\right) \times \left(\|\mathbf{v}_h\|_{\mathbf{H}(\operatorname{div};\Omega)} + \|q_h\|_0\right), \tag{3.9}$$

$$\sup_{(\mathbf{v}_h,q_h)\in(\mathbf{V}_h,W_h)} \frac{\left|\mathcal{B}((\mathbf{u}_h,p_h),(\mathbf{v}_h,q_h))\right|}{\|\mathbf{v}_h\|_{\mathbf{H}(\operatorname{div};\Omega)} + \|q_h\|_0} \ge \beta\left(\|\mathbf{u}_h\|_{\mathbf{H}(\operatorname{div};\Omega)} + \|p_h\|_0\right), \quad \forall (\mathbf{u}_h,p_h),(\mathbf{v}_h,q_h) \in (\mathbf{V}_h,W_h). \tag{3.10}$$

4. Error Analysis

To derive error estimates for the mixed finite element solution $(\mathbf{u}_h,p_h)$, we define the mixed method elliptic projection operator $(R_h,Q_h) : (\mathbf{V},W) \to (\mathbf{V}_h,W_h)$ by

$$\mathcal{B}((R_h(\mathbf{v},q),Q_h(\mathbf{v},q)),(\mathbf{v}_h,q_h)) = B((\mathbf{v},q),(\mathbf{v}_h,q_h)), \quad \forall (\mathbf{v},q) \in (\mathbf{V},W), \quad (\mathbf{v}_h,q_h) \in (\mathbf{V}_h,W_h), \tag{4.1}$$

which is well defined by Theorem 3.1 and satisfies the following approximation properties, where we define $(\mathbf{u}_{0h},p_{0h}) = (R_h(\mathbf{u}_0,p_0),Q_h(\mathbf{u}_0,p_0))$ for simplicity of the presentation. The elliptic projection corresponds to the elliptic problem (without the time differentiation term) of the system (2.8) and (2.9).

Lemma 4.1. *Under the assumption of Theorem 3.1, the projection operator* (R_h,Q_h) *satisfies*

$$\|\mathbf{v} - R_h(\mathbf{v},q)\|_{\mathbf{H}(\operatorname{div};\Omega)} + \|q - Q_h(\mathbf{v},q)\|_0 \le Ch(\|\mathbf{v}\|_1 + \|\operatorname{div}\mathbf{v}\|_1 + \|q\|_1), \quad \forall (\mathbf{v},q) \in (\mathbf{V},W). \tag{4.2}$$

Proof. Let I_h denote the standard P_1-interplant. Then we see from the definition of (R_h, Q_h), the triangle inequality, (3.9), and (3.10) that

$$\begin{aligned}
&\left\|\mathbf{v} - R_h(\mathbf{v},q)\right\|_{\mathbf{H}(\mathrm{div};\Omega)} + \left\|q - Q_h(\mathbf{v},q)\right\|_0 \\
&\quad\le \|\mathbf{v} - I_h\mathbf{v}\|_{\mathbf{H}(\mathrm{div};\Omega)} + \left\|q - \Pi_h q\right\|_0 + \left\|I_h\mathbf{v} - R_h(v,q)\right\|_{\mathbf{H}(\mathrm{div};\Omega)} + \|\Pi_h q - Q_h(\mathbf{v},q)\|_0 \\
&\quad\le \|\mathbf{v} - I_h\mathbf{v}\|_{\mathbf{H}(\mathrm{div};\Omega)} + \left\|q - \Pi_h q\right\|_0 \\
&\qquad + \beta^{-1} \sup_{(\mathbf{x}_h,y_h)\in(\mathbf{V}_h,W_h)} \frac{\left|\mathcal{B}\left(\left(I_h\mathbf{v} - R_h(\mathbf{v},q), \Pi_h q - Q_h(\mathbf{v},q)\right), (\mathbf{x}_h,y_h)\right)\right|}{\|\mathbf{x}_h\|_{\mathbf{H}(\mathrm{div};\Omega)} + \left\|y_h\right\|_0} \\
&\quad\le \|\mathbf{v} - I_h\mathbf{v}\|_{\mathbf{H}(\mathrm{div};\Omega)} + \left\|q - \Pi_h q\right\|_0 \\
&\qquad + \beta^{-1} \sup_{(\mathbf{x}_h,y_h)\in(\mathbf{v}_h,W_h)} \frac{\left|B\left(\left(\mathbf{v} - I_h\mathbf{v}, q - \Pi_h q\right), (\mathbf{x}_h,y_h)\right)\right|}{\|\mathbf{x}_h\|_{\mathbf{H}(\mathrm{div};\Omega)} + \left\|y_h\right\|_0} \\
&\quad\le C\left(\|\mathbf{v} - I_h\mathbf{v}\|_{\mathbf{H}(\mathrm{div};\Omega)} + \left\|q - \Pi_h q\right\|_0\right) \\
&\quad\le Ch\left(\|\mathbf{v}\|_1 + \|\mathrm{div}\,\mathbf{v}\|_1 + \left\|q\right\|_1\right),
\end{aligned} \tag{4.3}$$

which completes the proof. □

Lemma 4.2. *Under the assumptions of Lemma 2.2 and Theorem 3.1, it holds that*

$$\left\|p(t) - p_h(t)\right\|_0^2 + \int_0^t \|\mathbf{u}(s) - \mathbf{u}_h(s)\|_0^2 ds \le Ch^2, \quad t \in [0,T]. \tag{4.4}$$

Proof. Subtracting (3.7) from (2.11) with $(\mathbf{v},q) = (\mathbf{v}_h, q_h)$, we have

$$\left(c\left[p_t - p_{ht}\right], q_h\right) + \mathcal{B}\left(\left(\mathbf{u} - \mathbf{u}_h, p - p_h\right), \left(\mathbf{v}_h, q_h\right)\right) = G(p, q_h), \tag{4.5}$$

for all $(\mathbf{v}_h, q_h) \in (\mathbf{V}_h, W_h)$. Setting $(\boldsymbol{\epsilon}_h, \eta_h) = (R_h(u,p) - \mathbf{u}_h, Q_h(u,p) - p_h)$, $E = p - Q_h(\mathbf{u},p)$, and $(\mathbf{v}_h, q_h) = 2(\boldsymbol{\epsilon}_h, \eta_h)$ in (4.5) and using (4.1), we see that

$$\begin{aligned}
\frac{d}{dt}\left\|\sqrt{c}\eta_h\right\|_0^2 + 2\left(K^{-1}\boldsymbol{\epsilon}_h, \boldsymbol{\epsilon}_h\right) + 2G(\eta_h,\eta_h) &= -2(cE_t, \eta_h) + (c_t\eta_h, \eta_h) \\
&\le 2\left\|c^{-1/2}E_t\right\|_0 \left\|\sqrt{c}\eta_h\right\|_0 + (c_t\eta_h, \eta_h).
\end{aligned} \tag{4.6}$$

Then, by integrating (4.6) from 0 to t and noting that $\eta_h(0) = 0$, we obtain

$$\left\|\eta_h\right\|_0^2 + \int_0^t \left(\left(K^{-1}\boldsymbol{\epsilon}_h, \boldsymbol{\epsilon}_h\right) + G(\eta_h,\eta_h)\right) ds \le C\left(\int_0^t \|E_t\|_0^2 ds + \int_0^t \left\|\eta_h\right\|_0^2 ds\right). \tag{4.7}$$

Applying Lemmas 2.1, 2.2, and 4.1 to (4.7) gives

$$\|\eta_h\|_0^2 + \int_0^t \left(\left(K^{-1}\boldsymbol{\epsilon}_h, \boldsymbol{\epsilon}_h \right) + G(\eta_h, \eta_h) \right) ds \le Ch^2. \tag{4.8}$$

As a result, (4.4) follows from Lemma 4.1 and the triangle inequality. □

Lemma 4.3. *Under the assumption of Lemma 2.2 and Theorem 3.1, it holds that*

$$\|\mathbf{u}(t) - \mathbf{u}_h(t)\|_0^2 + \int_0^t \|p_t - p_{ht}\|^2 ds \le Ch^2, \quad t \in [0,T]. \tag{4.9}$$

Proof. Differentiating the term $(K^{-1}(\mathbf{u} - \mathbf{u}_h), \mathbf{v}_h) - (p - p_h, \operatorname{div} \mathbf{v}_h)$ in (4.5) with respect to time t and taking $(\mathbf{v}_h, q_h) = (\boldsymbol{\epsilon}_h, \eta_{ht})$ in (4.5), we see that

$$\|\sqrt{c}\eta_{ht}\|_0^2 + \frac{1}{2}\frac{d}{dt}\left(\left(K^{-1}\boldsymbol{\epsilon}_h, \boldsymbol{\epsilon}_h \right) + G(\eta_h, \eta_h) \right) = -(cE_t, \eta_{ht}). \tag{4.10}$$

Using the Young inequality, we have

$$\|\eta_{ht}\|_0^2 + \frac{d}{dt}\left(\left(K^{-1}\boldsymbol{\epsilon}_h, \boldsymbol{\epsilon}_h \right) + G(\eta_h, \eta_h) \right) \le C\|E_t\|_0^2. \tag{4.11}$$

Then, integrating (4.11) from 0 to t and using Lemma 4.1, we obtain

$$\left(K^{-1}\boldsymbol{\epsilon}_h, \boldsymbol{\epsilon}_h \right) + G(\eta_h, \eta_h) + \int_0^t \|\eta_{ht}\|_0^2 ds \le C \int_0^t \|E_t\|_0^2 ds \le Ch^2, \tag{4.12}$$

which, together with Lemma 4.1 and the triangle inequality, implies (4.9). □

Theorem 4.4. *Under the assumptions* (2.4), (2.5), *and* (2.15), *it holds that*

$$\|\mathbf{u}(t) - \mathbf{u}_h(t)\|_0 + \|p(t) - p_h(t)\|_0 \le Ch, \quad t \in [0,T]. \tag{4.13}$$

This theorem follows from Lemmas 4.2 and 4.3.
Next, we will estimate $\|\mathbf{u}(t) - \mathbf{u}_h(t)\|_{\mathbf{H}(\operatorname{div};\Omega)}$. For this, we assume

$$\|p_0\|_0 + \left(\int_0^T \|f_t(t)\|_0^2 dt \right)^{1/2} \le C. \tag{4.14}$$

Differentiating (2.8) and (2.9) with respect to t, the following result follows from a similar proof to that of Lemma 2.2.

Lemma 4.5. *Under the assumptions* (2.4), (2.5), *and* (4.14), *the following estimate holds*

$$\sup_{0\le t\le T}\left(\left\|p_t(t)\right\|_0^2+\|\mathbf{u}_t(t)\|_0^2\right)+\int_0^T\left(\left\|p_{tt}(t)\right\|_0^2+\|\mathbf{u}_t(t)\|_0^2+\|\operatorname{div}\mathbf{u}_t(t)\|_0^2\right)dt\le C. \tag{4.15}$$

Lemma 4.6. *Under the assumptions of Lemma 4.5, it holds that*

$$\left\|p_t(t)-p_{ht}(t)\right\|_0^2+\int_0^t\|\mathbf{u}_t(s)-\mathbf{u}_{ht}(s)\|_0^2ds\le Ch^2,\quad t\in[0,T]. \tag{4.16}$$

Proof. Differentiating (4.5) with respect to time t, using (4.1), and taking $(\mathbf{v}_h,q_h)=2(\boldsymbol{\epsilon}_{ht},\eta_{ht})$ give

$$\begin{aligned}\frac{d}{dt}\left\|\sqrt{c}\eta_{ht}\right\|_0^2+2\left(K^{-1}\boldsymbol{\epsilon}_{ht},\boldsymbol{\epsilon}_{ht}\right)+2G(\eta_{ht},\eta_{ht})&=-2(c_tE_t,\eta_{ht})-2(cE_{tt},\eta_{ht})-(c_t\eta_{ht},\eta_{ht})\\&\le C\left(\|E_t\|_0+\|E_{tt}\|_0+\left\|\eta_{ht}\right\|_0\right)\left\|\eta_{ht}\right\|_0.\end{aligned} \tag{4.17}$$

Then, by integrating (4.17) from 0 to t, we see that

$$\left\|\eta_{ht}\right\|_0^2+\int_0^t\left(\left(K^{-1}\boldsymbol{\epsilon}_{ht},\boldsymbol{\epsilon}_{ht}\right)+G(\eta_{ht},\eta_{ht})\right)ds\le C\int_0^t\left(\|E_t\|_0^2+\|E_{tt}\|_0^2+\left\|\eta_{ht}\right\|_0^2\right)ds. \tag{4.18}$$

Applying Lemmas 2.1, 4.1, and 4.5 to (4.18) gives

$$\left\|\eta_{ht}\right\|_0^2+\int_0^t\left(\left(K^{-1}\boldsymbol{\epsilon}_{ht},\boldsymbol{\epsilon}_{ht}\right)+G(\eta_{ht},\eta_{ht})\right)ds\le Ch^2. \tag{4.19}$$

As a result, (4.16) comes from Lemma 4.1 and the triangle inequality. □

Lemma 4.7. *Under the assumptions of Lemma 4.5, it holds that*

$$\|\mathbf{u}-\mathbf{u}_h\|_{\mathbf{H}(\operatorname{div};\Omega)}\le Ch,\quad t\in[0,T]. \tag{4.20}$$

Proof. It follows from the inf-sup condition (3.10), Theorem 3.1, and (4.5) that

$$\begin{aligned}\|\boldsymbol{\epsilon}_h\|_0+\|\operatorname{div}\boldsymbol{\epsilon}_h\|_0+\left\|\eta_h\right\|_0&\le\beta^{-1}\sup_{(\mathbf{v}_h,w_h)\in(\mathbf{V}_h,W_h)}\frac{\left|\mathcal{B}\left((\boldsymbol{\epsilon}_h,\eta_h),(\mathbf{v}_h,w_h)\right)\right|}{\|\mathbf{v}_h\|_{\mathbf{H}(\operatorname{div};\Omega)}+\|w_h\|_0}\\&\le C\left\|p_t-p_{ht}\right\|_0.\end{aligned} \tag{4.21}$$

Consequently, using Lemmas 4.1 and 4.6 and the triangle inequality, we complete the proof. □

Theorem 4.8. *Under the assumptions* (2.4), (2.5), (2.15), *and* (4.14), *it holds that, for* $t \in [0,T]$,

$$\|\mathbf{u}(t)-\mathbf{u}_h(t)\|_0+\|\operatorname{div}(\mathbf{u}(t)-\mathbf{u}_h(t))\|_0+\|p(t)-p_h(t)\|_0\le Ch. \tag{4.22}$$

This theorem follows from Lemmas 4.2 and 4.7.

The result in Theorem 4.8 is optimal for $\mathbf{u}$ in the divergence norm and suboptimal for $\mathbf{u}$ and p in the L^2-norm in terms of the convergence rates. These are the best estimates one can obtain with method (3.7). The reason is that the approximation property of the lower-order space $\overline{W}_h$ always pollutes the global accuracy.

5. Superconvergence

Set

$$e_h(t)=\Pi_h\big(p(t)-p_h(t)\big),\quad t\in[0,T]. \tag{5.1}$$

Then, by the definition of the projection operator Π_h and the fact that $\operatorname{div}\mathbf{V}_h=\overline{W}_h$, the error equation (4.5) can be written as

$$\big(c[p_t-p_{ht}],q_h\big)+\mathcal{B}\big((\mathbf{u}-\mathbf{u}_h,e_h),(\mathbf{v}_h,q_h)\big)=G(p,q_h),\quad (\mathbf{v}_h,q_h)\in(\mathbf{V}_h,W_h). \tag{5.2}$$

We recall the projection operator (4.1) as follows:

$$\begin{aligned}B\big((\mathbf{v}-R_h(\mathbf{v},q),\Pi_h(q-Q_h(\mathbf{v},q))\big),(\mathbf{v}_h,q_h)\big)&=G(q,q_h),\\ \forall(\mathbf{v},q)\in(\mathbf{V},W),\quad (\mathbf{v}_h,q_h)&\in(\mathbf{V}_h,W_h).\end{aligned} \tag{5.3}$$

Under the assumption of Lemma 2.2, it follows from [20] that

$$\|\Pi_h(p-Q_h(\mathbf{u},p))\|_0\le Ch^2. \tag{5.4}$$

For simplicity of the presentation, we assume that the coefficient c is piecewise constant in the next theorem; for a variable coefficient c the same result holds if it is projected into the space $\overline{W}_h$ using the projection operator Π_h.

Theorem 5.1. *Under the assumptions* (2.4), (2.5), *and* (2.15), *it holds that*

$$\|\Pi_h(p(t)-p_h(t))\|_0\le Ch^2,\quad t\in[0,T]. \tag{5.5}$$

Proof. Setting $(\boldsymbol{\epsilon}_h,\eta_h)=(R_h(\mathbf{u},p)-\mathbf{u}_h,Q_h(\mathbf{u},p)-p_h)$, $E=p-Q_h(\mathbf{u},p)$, and $(\mathbf{v}_h,q_h)=2(\boldsymbol{\epsilon}_h,\Pi_h\eta_h)$ in (5.2) and using (5.3), we see that

$$\frac{d}{dt}\|\sqrt{c}\Pi_h\eta_h\|_0^2+2\Big(K^{-1}\boldsymbol{\epsilon}_h,\boldsymbol{\epsilon}_h\Big)\le C\|\Pi_hE_t\|_0\|\Pi_h\eta_h\|_0. \tag{5.6}$$

Table 1: Errors and convergence rates for the velocity.

$1/h$	$\mathbf{u}_{L^2}$ error	$\mathbf{u}_{L^2}$ rate	$\mathbf{u}_{\mathrm{div}}$ error	$\mathbf{u}_{\mathrm{div}}$ rate
8	0.0626682		0.0953064	
16	0.0175218	1.83858	0.0514547	0.889269
24	0.00819644	1.87377	0.0355113	0.914632
32	0.0047615	1.88798	0.027229	0.923136
40	0.00311895	1.89594	0.0221371	0.927761

Then, by integrating (5.6) from 0 to t and noting that $\eta_h(0) = 0$, we obtain

$$\left\|\Pi_h\eta_h\right\|_0^2 + \int_0^t \left(K^{-1}\boldsymbol{\epsilon}_h, \boldsymbol{\epsilon}_h\right) ds \le C\left(\int_0^t \|\Pi_h E_t\|_0^2 ds + \int_0^t \left\|\Pi_h\eta_h\right\|_0^2 ds\right). \tag{5.7}$$

Applying Lemmas 2.1 and 2.2 and (5.4) to (5.7) gives

$$\left\|\Pi_h\eta_h\right\|_0^2 + \int_0^t \left(K^{-1}\boldsymbol{\epsilon}_h, \boldsymbol{\epsilon}_h\right) ds \le Ch^4. \tag{5.8}$$

As a result, (5.5) comes from (5.4) and the triangle inequality. □

6. Numerical Results

Numerical results are presented to check the theory developed in the previous sections. In all the experiments, the triangulations Γ_h are based on the partition of the unit square $\Omega = [0,1] \times [0,1]$ into triangles. In the first example, the accuracy of the stabilized mixed finite element method is checked; in the second example, a single-phase flow problem is calculated using this method.

6.1. Accuracy

The purpose of this example is to check the convergence rates for the solution p and $\mathbf{u}$. Here, let $c = 1$ and the coefficient tensor K be the identity tensor. We choose the exact solution as follows:

$$p(x,y) = x^2(x-1)y(y-1)\cos(t). \tag{6.1}$$

The numerical experiments have been performed by using the equal-order finite element pair $\mathbf{P}_1 - P_1$ for velocity and pressure, as defined in the third section. The backward Euler scheme is used for the time discretization. To check the numerical accuracy in space, we use a small time step $dt = 0.0005$; the final time is $T = 1$.

Detailed numerical results are shown in Tables 1 and 2, which clearly present the expected convergence rates. In these tables, the p_{L^2} error, for example, is defined by

$$p_{L^2} \text{ error} = \left\|p - p_h\right\|_0. \tag{6.2}$$

Table 2: Errors and convergence rates for the pressure.

$1/h$	p_{L^2} error	p_{L^2} rate	Π_{hL^2} error	Π_{hL^2} rate
8	0.0303817		0.0200016	
16	0.00742562	2.03262	0.00464606	2.10603
24	0.00328428	2.01198	0.00203124	2.04055
32	0.00184548	2.00363	0.00113789	2.01428
40	0.00118171	1.9977	0.000728781	1.99673

Table 3: Parameters for a reservoir.

Item	Description	Unit	Value
k	Permeability	md	88.7
μ	Oil viscosity	cp	10
H	Thickness	ft	100
c	Compressibility	1/psi	0.0002
ϕ	Porosity	fraction	0.2
p_0	Initial pressure	psia	4,000
q	Oil flow rate	STB/D	400
r_w	Radius of wellbore	ft	0.25
B	Oil FVF	RB/STB	1
α_c	Transmissibility conversion factor	—	1.127
β_c	Volume conversion factor	—	5.614583
$x_{\max}$	Length in the x-direction	ft	4,000
$y_{\max}$	Length in the y-direction	ft	4,000

A selected numerical pressure and velocity for this example at $T = 1$ are shown in Figure 1. From these tables, better computational results, up to the convergence of order $O(h^2)$ for p and $\mathbf{u}$ in the L^2-norm, occur.

6.2. A Single-Phase Flow Problem

Here, we consider the unsteady-state single-phase flow of oil taking place in a two-dimensional, homogeneous, isotropic, horizontal reservoir, with its property parameters given in Table 3 [22]. At the internal boundary, there is a well producing at a constant flow rate. On the other hand, at the external boundary, the pressure remains constant.

The basic differential equation describing this reservoir is

$$\frac{\phi\mu c}{\beta_c\alpha_c k}\frac{\partial p}{\partial t} = \frac{\partial^2 p}{\partial x^2} + \frac{\partial^2 p}{\partial y^2}. \tag{6.3}$$

In Figure 2, we display the rectangular domain, boundary conditions, and mesh adopted in the simulation.

In Figures 3 and 4, the numerical results are shown. Figures 3(a)–3(c) show the variation of the pressure with respect to time; Figure 4 gives the pressure distribution in

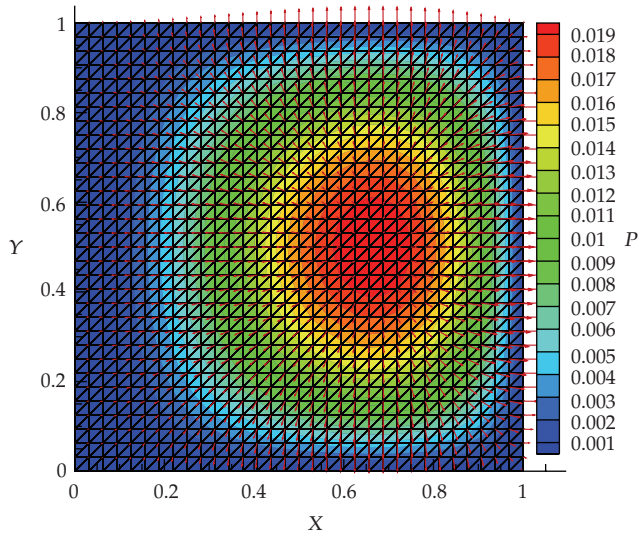

(a) The pressure and velocity

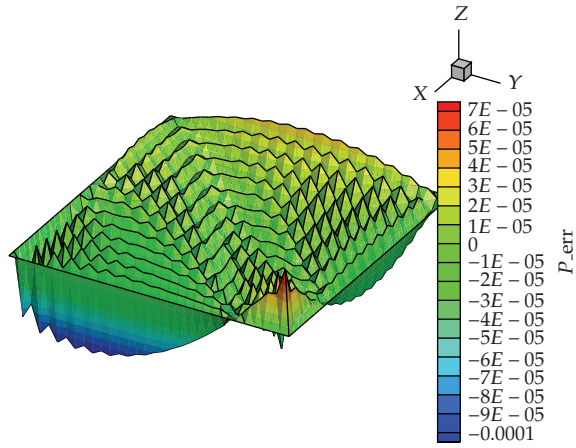

(b) The pointwise pressure error

Figure 1: Numerical results on a 32 × 32 uniform triangular mesh.

the reservoir at $r = r_w$ and $r = 200$ ft after 20 days. The pressure decreases as time progresses, which is reasonable; as the well produces, the reservoir pressure decreases.

7. Conclusions

A stabilized mixed finite element method for an unsteady-state single-phase flow problem in a porous medium has been developed and analyzed. An optimal error estimate in divergence norm for the velocity and suboptimal error estimates in the L^2-norm for both velocity and pressure have been proven. A superconvergence result for the pressure has been obtained as well. The numerical results to check the accuracy of this method and calculate single-phase flow have been presented.

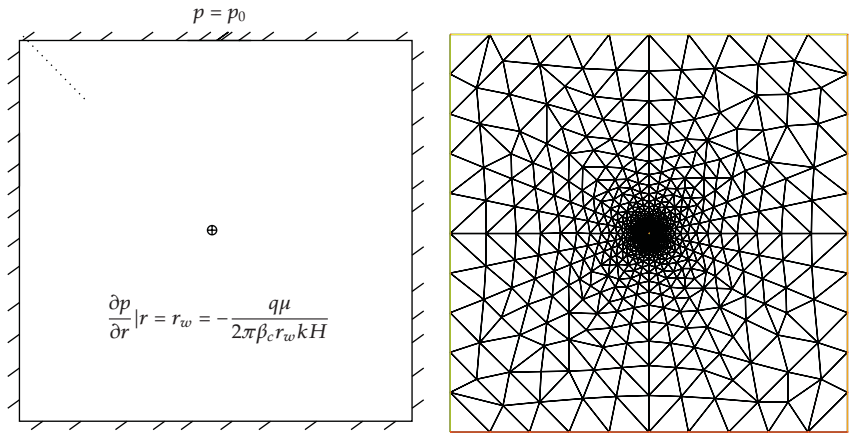

(a) Domain and boundary condition (b) Base triangles

Figure 2: Conditions adopted in simulation.

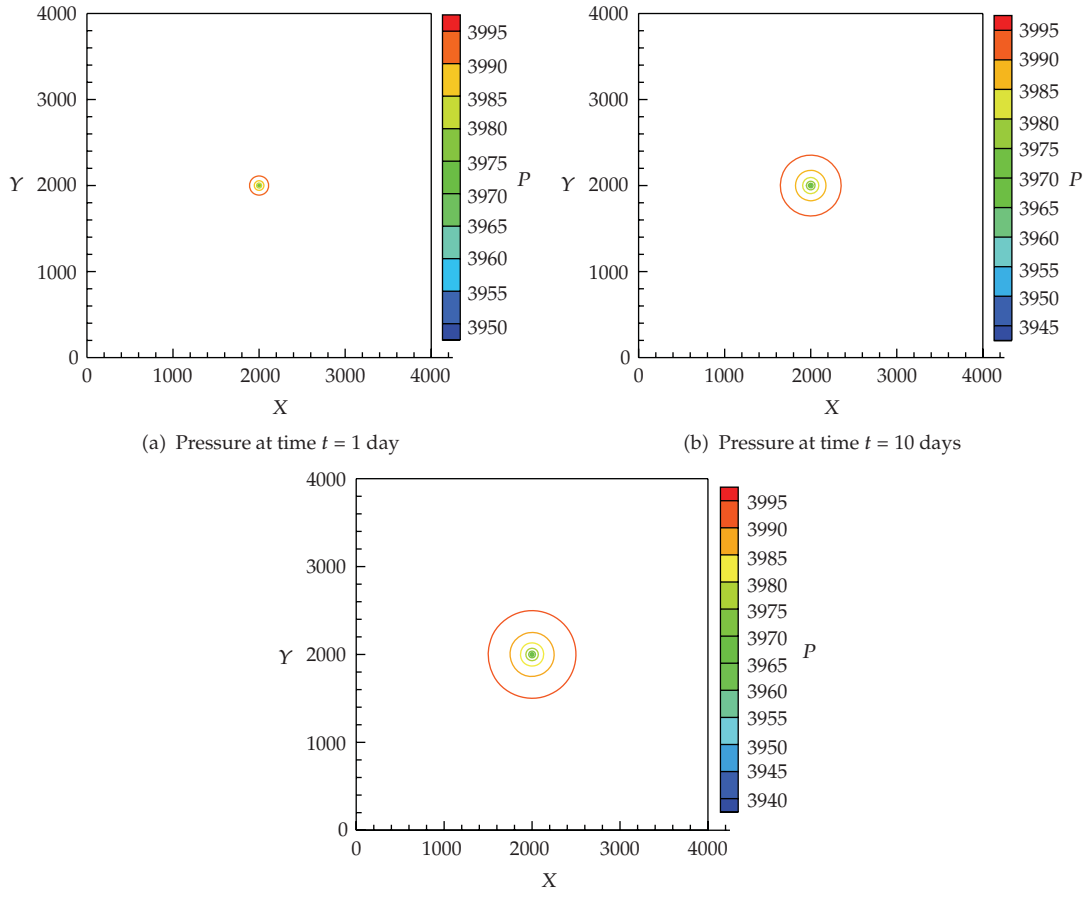

(a) Pressure at time $t = 1$ day

(b) Pressure at time $t = 10$ days

(c) Pressure at time $t = 20$ days

Figure 3: Numerical results (pressure contours) with respect to time.

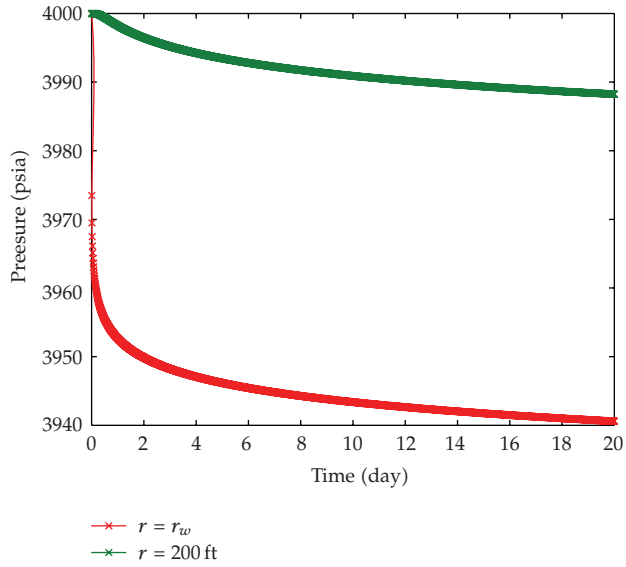

Figure 4: Numerical results at $r = r_w$ and $r = 200$ ft.

Acknowledgment

This work is supported in part by the NSERC/AERI/iCORE/Foundation CMG Chair Funds in Reservoir Simulation.

References

[1] Z. Chen, *Finite Element Methods and Their Applications*, Scientific Computation, Springer, Berlin, Germany, 2005.
[2] V. Girault and P. A. Raviart, *Finite Element Methods for Navier-Stokes Equations*, vol. 5 of *Springer Series in Computational Mathematics*, Springer, Berlin, Germany, 1986.
[3] D. N. Arnold, F. Brezzi, and M. Fortin, "A stable finite element for the Stokes equations," *Calcolo*, vol. 21, no. 4, pp. 337–344, 1984.
[4] J.-C. Nedelec, "Mixed finite elements in R^3," *Numerische Mathematik*, vol. 35, no. 3, pp. 315–341, 1980.
[5] R. A. Raviart and J. M. Thomas, "A mixed FInite element method for 2nd order elliptic problems," in *Mathematical Aspects of Finite Element Methods*, I. Galligani and E. Magenes, Eds., vol. 606 of *Lecture Notes in Mathematics*, pp. 292–315, Springer, New York, NY, USA, 1997.
[6] F. Brezzi, J. Douglas, Jr., and L. D. Marini, "Two families of mixed finite elements for second order elliptic problems," *Numerische Mathematik*, vol. 47, no. 2, pp. 217–235, 1985.
[7] F. Brezzi, J. Douglas, Jr., R. Durán, and M. Fortin, "Mixed finite elements for second order elliptic problems in three variables," *Numerische Mathematik*, vol. 51, no. 2, pp. 237–250, 1987.
[8] Z. Chen and J. Douglas, Jr., "Prismatic mixed finite elements for second order elliptic problems," *Calcolo*, vol. 26, no. 2–4, pp. 135–148, 1989.
[9] F. Brezzi, M. Fortin, and L. D. Marini, "Mixed finite element methods with continuous stresses," *Mathematical Models & Methods in Applied Sciences*, vol. 3, no. 2, pp. 275–287, 1993.
[10] J. Li and Y. He, "A new stabilized finite element method based on local Gauss integration techniques for the Stokes equations," *Journal of Computational and Applied Mathematics*, vol. 214, pp. 58–65, 2008.
[11] R. Becker and M. Braack, "A finite element pressure gradient stabilization for the Stokes equations based on local projections," *Calcolo*, vol. 38, no. 4, pp. 173–199, 2001.
[12] P. Bochev, C. R. Dohrmann, and M. D. Gunzburger, "Stabilization of low-order mixed finite elements for the Stokes equations," *SIAM Journal on Numerical Analysis*, vol. 44, no. 1, pp. 82–101, 2006.

[13] F. Brezzi and M. Fortin, "A minimal stabilisation procedure for mixed finite element methods," *Numerische Mathematik*, vol. 89, no. 3, pp. 457–491, 2001.
[14] C. R. Dohrmann and P. Bochev, "A stabilized finite element method for the Stokes problem based on polynomial pressure projections," *International Journal for Numerical Methods in Fluids*, vol. 46, no. 2, pp. 183–201, 2004.
[15] J. Li, Y. He, and Z. Chen, "A new stabilized finite element method for the transient Navier-Stokes equations," *Computer Methods in Applied Mechanics and Engineering*, vol. 197, no. 1–4, pp. 22–35, 2007.
[16] D. Silvester, "Stabilized mixed finite element methods," Numerical Analysis Report 262, 1995.
[17] R. Falk, "An analysis of the penalty method and extrapolation for the stationary Stokes equations," in *Advances in Computer Methods for Partial Differential Equations*, R. Vichnevetsky, Ed., pp. 66–69, AICA, 1975.
[18] T. J. R. Hughes, W. Liu, and A. Brooks, "Finite element analysis of incompressible viscous flows by the penalty function formulation," *Journal of Computational Physics*, vol. 30, no. 1, pp. 1–60, 1979.
[19] A. Masud and T. J. R. Hughes, "A stabilized mixed finite element method for Darcy flow," *Computer Methods in Applied Mechanics and Engineering*, vol. 191, no. 39-40, pp. 4341–4370, 2002.
[20] Z. Chen, Z. Wang, and J. Li, "Analysis of the pressure projectionstabilization method for second-order elliptic problems," to appear.
[21] J. Li, Y. He, and Z. Chen, "Performance of several stabilized finite element methods for the Stokes equations based on the lowest equal-order pairs," *Computing. Archives for Scientific Computing*, vol. 86, no. 1, pp. 37–51, 2009.
[22] Z. Chen, G. Huan, and Y. Ma, *Computational Methods for Multiphase Flows in Porous Media*, SIAM, Philadelphia, Pa, USA, 2006.
[23] P. G. Ciarlet, *The Finite Element Method for Elliptic Problems*, North-Holland, Amsterdam, The Netherlands, 1978.

Hindawi Publishing Corporation
Journal of Applied Mathematics
Volume 2011, Article ID 493014, 14 pages
doi:10.1155/2011/493014

Research Article

An Analytical Solution of the Advection Dispersion Equation in a Bounded Domain and Its Application to Laboratory Experiments

M. Massabó,[1] R. Cianci,[2] and O. Paladino[1,3]

[1] *CIMA Research Foundation, Via Magliotto 2, 17100 Savona, Italy*
[2] *Department of Engineering Production, Thermoenergetic and Mathematical Models, DIPTEM, University of Genoa, Piazzale Kennedy, Pad. D, 16129 Genoa, Italy*
[3] *Department of Communication Computer and System Sciences, DIST, University of Genoa, Via Opera Pia 13, 16145 Genoa, Italy*

Correspondence should be addressed to R. Cianci, cianci@unige.it

Received 6 September 2010; Accepted 1 November 2010

Academic Editor: Juergen Geiser

Copyright © 2011 M. Massabó et al. This is an open access article distributed under the Creative Commons Attribution License, which permits unrestricted use, distribution, and reproduction in any medium, provided the original work is properly cited.

We study a uniform flow in a parallel plate geometry to model contaminant transport through a saturated porous medium in a semi-infinite domain in order to simulate an experimental apparatus mainly constituted by a chamber filled with a glass beads bed. The general solution of the advection dispersion equation in a porous medium was obtained by utilizing the Jacobi θ_3 Function. The analytical solution here presented has been provided when the inlet (Dirac) and the boundary conditions (Dirichelet, Neumann, and mixed types) are fixed. The proposed solution was used to study experimental data acquired by using a noninvasive technique.

1. Introduction

The contamination of groundwater by substances of various kinds and the study of the behavior of compounds into natural or artificial porous media is a topic of growing interest. Laboratory flow experiments have been used in several works to study solute flow and transport phenomena at different spatial and temporal scales. Transmissive or reflective imaging techniques, in conjunction with dye tracer, allow to monitor the solute plume in a porous medium confined in a transparent box, satisfying the requirements of high spatial resolution and accuracy and achieving two or three orders of magnitude additional sampling points if compared to conventional analysis methods.

A growing number of applications of imaging technique to investigate solute transport in porous media are present in the literature [1–8]. Experimental measurements are compared with simplified theoretical models, based upon advection-dispersion equation, and they show reasonable agreement [3, 4].

The advection-dispersion equation is commonly used as governing equation for transport of contaminants, or more generally solutes, in saturated porous media [9]. Often the solution of this equation with particular boundary conditions requires the application of numerical methods. In other cases, where an analytical approach is possible, the solutions often deal with constant velocities. Many analytical solutions for constant velocity and dispersion coefficients and different boundary conditions are available. Lee in [10] offers exhaustive list of references and explanation of derivation techniques.

Analytical solutions in semi-infinite domain with different initial and boundary conditions have been derived by several authors [11–14]. Extension to domain with finite thickness has been derived by Sim and Chrysikopoulos [15] and Park and Zhan [16]. Batu in [17, 18] proposes a two-dimensional analytical solution for solute transport in a bounded aquifer by adopting Fourier analysis and Laplace transform. Chen et al. [19] derive an analytical solution in finite thickness domain with zero gradient boundary condition at the outlet of the domain and also consider a nonconstant dispersion coefficient. Analytical solutions for time-dependent dispersion coefficients have been derived by Aral and Liao [20] for a two-dimensional system and infinite domain. An analytical solution for the 2D steady-state convection-dispersion equation with nonconstant velocity and dispersion coefficients is given in [21]; the authors obtained the solution at steady state by the application of the Dupuit-Forchheimer approximation. Analytical solutions in cylindrical geometry, bounded domain and different source conditions are presented in [22]; these solutions, recovered by using a Bessel function expansion, have been used in order to estimate transport parameters [23, 24]. In this work an exact analytical solution of the advection-dispersion equation for the two-dimensional semi-infinite and laterally bounded domain is derived. The mathematical model wants to represent typical laboratory flow tank experiments where a tracer is injected in the porous medium and the domain is finite. The availability of an analytical solution taking into account the effects of the lateral borders and the influence of the upstream boundary condition in relation to the injection point can be necessary if one wants to use the whole set of experimental data acquired in the physical domain and if one wants to verify the experimental conditions for some fluctuations of the operative variables.

The proposed analytical solution is discussed by means of comparison with the well-known two-dimensional infinite domain solution proposed by Bear [9] and with some limit analytical solutions. The influence of the boundary conditions on the solution is also discussed in terms of Péclet numbers, and some suggestions are given in order to choose the right analytical model depending on the experimental conditions. Finally, the analytical solution is compared with experimental data obtained from an experimental apparatus based on a noninvasive measuring technique, designed and constructed by some of the authors of [8].

2. Problem Formulation

Mass conservation of nonreactive solutes transported through porous media is described by a partial differential equation known as advection-dispersion equation. Here we consider the transport of a solute through a thin chamber filled with a homogeneous porous medium.

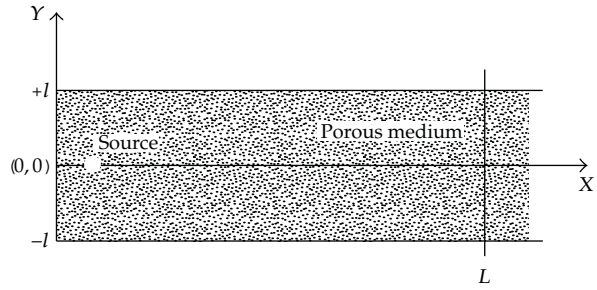

Figure 1: A schematization of the experimental apparatus and mathematical domain considered. L represents the length of the domain.

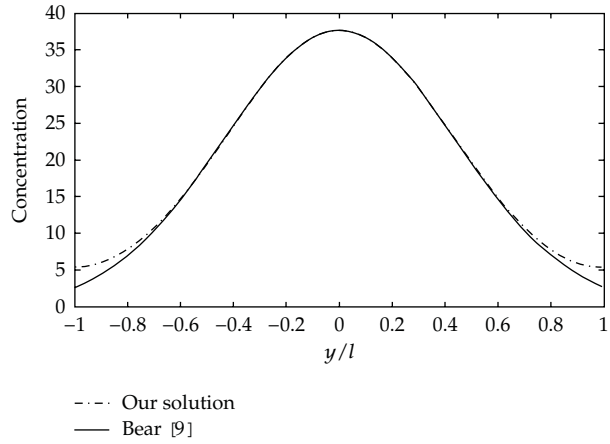

Figure 2: Effects of the lateral boundary conditions on our solution and comparison with the Bear one in a transverse cross-section at $x/L = 1$ and $t = (x - q)/u$ ($\mathrm{Pe}_L^{(\mathrm{ch})} = 5$ and $\mathrm{Pe}_T^{(\mathrm{ch})} = 10$).

Figure 1 shows a graphical representation of the problem: the water flow is along the x coordinate, the length of the chamber is L, and the chambers width is $2l$. Fresh water is fed from the inlet of the chamber while a pulse injection of solute mass is initially provided from a source placed at a distance q from the inlet. For thin chambers, where the thickness is much smaller than the other two dimensions in which the transport phenomenon occurs, the governing equation of solute concentration can be expressed by the two-dimensional advection-dispersion equation as follows [9]:

$$\frac{\partial C}{\partial t} + u\frac{\partial C}{\partial x} = D_L\frac{\partial^2 C}{\partial x^2} + D_T\frac{\partial^2 C}{\partial y^2}, \tag{2.1}$$

where $u[L/T]$ is the pore scale velocity, $C[M/L3]$ is the resident fluid solute concentration, and $D_L[L2/T]$ and $D_T[L2/T]$ are the longitudinal and transverse dispersion coefficients which are related to the pore scale velocity by [9]

$$D_L = d_{wm}^p + \alpha_L u, \qquad D_T = d_{wm}^p + \alpha_T u, \tag{2.2}$$

where d_{wm}^{p} is the molecular diffusion coefficient in a porous medium, where $d_{wm}^{p} \equiv \varepsilon d_{wm}$ is the molecular diffusion coefficient of the solute in water and $d_{wm}\varepsilon$ is the porosity. D_L and D_T are the longitudinal and transverse dispersivity, respectively.

Initial and boundary conditions are to be set in order to solve (2.1). No solute flux across the lateral boundaries has to be imposed; the condition can be expressed as a second-type boundary condition as follows:

$$\left.\frac{\partial C}{\partial y}\right|_{y=\pm L} = 0. \tag{2.3}$$

Concerning the longitudinal domain, two boundary conditions must be imposed. Exhaustive discussion of physical meaning of boundary condition is reported by Kreft and Zuber [25] and Parker and Van Genuchten [26]. The boundary condition for the inlet section ($x = 0$) is represented by a mass balance equation, thus the solute flux across the left size of the section equals the flux from the right. The mass balance across $x = 0$ is expressed in terms of resident concentration as [25]

$$[uC]_{x=0^-} = \left[uC - D_L \frac{\partial C}{\partial x}\right]_{x=0^+}, \tag{2.4}$$

where $C_{x=0^+}$ is the concentration of the inlet stream, which is zero in our case since the chamber is fed with pure water. In regard to the mass balance, the resulting boundary condition is then expressible as a mixed boundary value problem as follows:

$$\left[uC - D_L \frac{\partial C}{\partial x}\right]_{x=0^+} = 0. \tag{2.5}$$

It is important to notice that this boundary condition takes into account the fact that even if the source position is set in $x = q$, the solute can reach the inlet section by dispersion, so $C_{x=0^-}$ can be different from zero. Thus, the previous condition could represent a fresh groundwater that could be polluted by a spill located in a section relatively near to the inlet one, at a certain temporal instant. Similarly, mass balance should be imposed at $x = l$ resulting in

$$\left[uC - D_L \frac{\partial C}{\partial x}\right]_{x=l^-} = [uC]_{x=l^+}, \tag{2.6}$$

where $C_{x=l^+}$ is the concentration at the outlet section, which cannot be known a priori, thus the problem cannot be solved unless simplifications are assumed. Two different ways exist in order to treat this issue, the most common in chemical engineering is to assume that concentrations are continuous across the outlet section [27], namely, $C_{x=l^-} = C_{x=l^+}$, resulting in

$$\left.\frac{\partial C}{\partial x}\right|_{x=l^-} = 0. \tag{2.7}$$

The second way is to assume an infinite chamber in the longitudinal direction (x axis for the problem considered). This assumption can be reasonably chosen when one is interested in the plume profile far from the outlet boundary condition. In this case we get a first type boundary condition expressed as

$$\lim_{x\to+\infty} C(x,y,t) = 0. \tag{2.8}$$

Finally, the initial condition for the point pulse injection at $y = 0$ and $x = q$ yields

$$C(x,y,0) = M\delta(y)\delta(x-q), \tag{2.9}$$

where δ represents the Dirac delta function. Note that M is the total mass per unit thickness of the chamber injected in the porous medium.

3. The Analytical Solution

The derivation of an analytical solution of (2.1) subject to boundary conditions (2.3), (2.5), and (2.8) and initial condition (2.9) is here illustrated. Due to the symmetry of both the transversal boundaries and the injection position with respect to the longitudinal axis, the solution of the PDE will be symmetric as well, resulting in $C(x,y,t) = C(x,-y,t)$.

Starting from this consideration, we consider a cosine Fourier series expansion for the solution, and we write

$$C(x,y,t) = \frac{1}{2}a_0(x,t) + \sum_{n=1}^{+\infty} a_n(x,t)\cos\left(\frac{n\pi y}{l}\right), \tag{3.1}$$

where the coefficients of the expansion are

$$a_n(x,t) = \frac{1}{l}\int_{-l}^{+l} C(x,y,t)\cos\left(\frac{n\pi y}{l}\right)dy, \quad \text{for } n = 0,1,2,\ldots. \tag{3.2}$$

It is important to notice that (3.1) satisfies the no-flux boundary condition (2.3). By substituting (3.1) into (2.1) we get a set of partial different equations for the coefficients:

$$\frac{\partial^2 a_n(x,t)}{\partial x^2} - \frac{n^2\pi^2 D_T}{l^2 D_L}a_n(x,t) - \frac{u}{D_L}\frac{\partial a_n(x,t)}{\partial x} - \frac{1}{D_L}\frac{\partial a_n(x,t)}{\partial \mathrm{t}} = 0. \tag{3.3}$$

Similarly, boundaries and initial conditions (2.5), (2.8), and (2.9) may be written as

$$\left[u\ a_n(x,t) - D_L\frac{\partial a_n(x,t)}{\partial x}\right]_{x=0^+} = 0, \tag{3.4}$$

$$\lim_{x\to+\infty} a_n(x,t) = 0, \tag{3.5}$$

$$a_n(x,0) = \frac{M}{L}\delta(x-q). \tag{3.6}$$

The solution of (3.3) subject to (3.4), (3.5), and (3.6) is obtained by applying the Laplace transform. Details are reported in the appendix for completeness. By substituting (A.14) in (3.1) $C(x,y,t)$ becomes

$$C(x,y,t) = \frac{1}{2}a_0(x,t)\left(1 + 2\sum_{n=0}^{+\infty}\cos\left(\frac{n\pi y}{l}\right)e^{-(n^2\pi^2 D_T t/l^2)}\right). \tag{3.7}$$

The expansion present in this equation gives rise to the Jacobi function $\theta_3(z,r)$ whose definition can be found, for example, in the work of Abramowitz and Stegun [28] as

$$\theta_3(z,r) = 1 + 2\sum_{n=1}^{+\infty} r^{n^2}\cos(2nz). \tag{3.8}$$

By using this definition, we obtain the final expression for $C(x,y,t)$:

$$C(x,y,t) = \frac{M}{4l}\theta_3\left(\frac{\pi y}{2l}, e^{(D_T\pi^2/l^2)}\right)\left(\frac{1}{\sqrt{D_L\pi t}}\left[e^{((x-q-ut)^2/4D_T t)-(uq/D_L)} - e^{((x+q-ut)^2/4D_T t)}\right] - \frac{u}{D_L}\operatorname{erfc}\left(\frac{x+q+ut}{2\sqrt{D_L t}}\right)\right). \tag{3.9}$$

4. Influence of Boundary Conditions

The transport phenomenon into the chamber is mainly regulated by two time scales: the advection time scale related to the transport of the fluid from the inlet section to the outlet section and the dispersion time scale related to the dispersion of the solute from the source position in all the directions. The ratio between the longitudinal $t^{(\mathrm{ch})}_{L\mathrm{disp}} = l^2/D_L$ dispersion time scale and the advection time scale of the chamber $t^{(\mathrm{ch})}_{\mathrm{adv}} = l/u$ is the longitudinal Péclet number, and it is defined as $\mathrm{Pe}^{(\mathrm{ch})}_L = ul/D_L$ (where the superscript ch stands for chamber).

The ratio between the transverse dispersion time scale $t^{(\mathrm{ch})}_{T\mathrm{disp}} = l^2/D_T$ and the advection time scale of the chamber $t^{(\mathrm{ch})}_{\mathrm{adv}} = l/u$ is the transversal Péclet number, and it is defined as $\mathrm{Pe}^{(\mathrm{ch})}_T = t^{(\mathrm{ch})}_{T\mathrm{disp}}/t^{(\mathrm{ch})}_{\mathrm{adv}} = ul^2/LD_T$.

The aim of this section is to evaluate the influence of lateral and upstream boundary conditions on the proposed solution. In order to illustrate this point the new solution has been compared with the solution of a 2D transport problem in a unbounded domain for a pulse injection point at $x = q$ presented by [9]

$$C(x,y,t) = \frac{M}{4\pi t\sqrt{D_T}\sqrt{D_L}}e^{((x-q-ut)^2/4D_L t)-(y^2/4D_T t)}. \tag{4.1}$$

In principle, for $\mathrm{Pe}^{(\mathrm{ch})}_T \gg 1$ the lateral boundary condition has no influence on the solution since the transport of the solute by transversal dispersion is much slower than the transport by advection, and during the passage into the chamber the solute does not reach the borders.

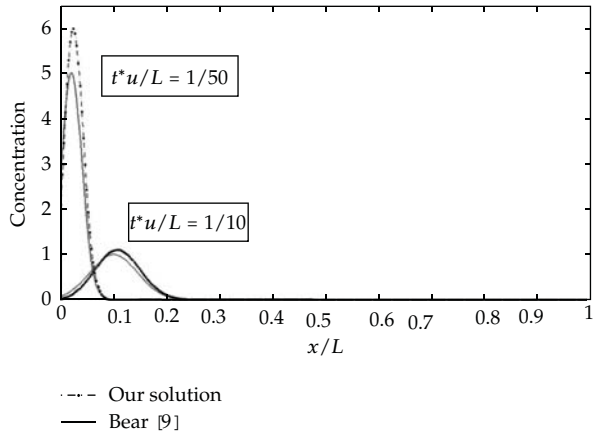

Figure 3: Effects of the upstream boundary condition on our solution and comparison with the Bear one in a longitudinal cross-section at $y = 0$ and two different times ($\mathrm{Pe}_L^{(\mathrm{ch})} = .1$ and $\mathrm{Pe}_T^{(\mathrm{ch})} = 10$).

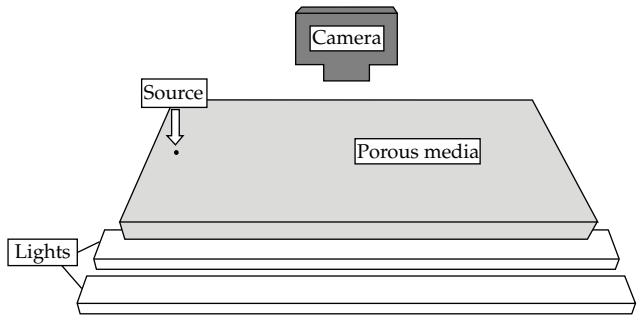

Figure 4: A schematization of the experimental apparatus and imaging set up.

Figure 2 shows the concentration profiles of the two solutions for $\mathrm{Pe}_T^{(\mathrm{ch})} = 5$ and $\mathrm{Pe}_T^{(\mathrm{ch})} = 10$ at $x/L = 1$ and $t = ((x - q)/u)$. Note that the series appearing in the Jacobi θ_3 function of Equation (18) converge very fast [28] for

$$\exp\left(-\frac{\mathrm{D}_T \pi^2 t}{l^2}\right) < 1, \tag{4.2}$$

which is always satisfied for arbitrary positive t.

The concentration profile of Figure 2 roughly corresponds to the passage of the peak of the plume. The influence of the lateral boundary condition is, obviously, mainly evident close to the edge of the chamber and it is maximum at $y/l = 1$. The difference between the two solutions becomes less than 1% at $\mathrm{Pe}_T^{(\mathrm{ch})}$ greater than about 20. The influence of the lateral boundaries is much more evident at small $\mathrm{Pe}_T^{(\mathrm{ch})}$. Small $\mathrm{Pe}_T^{(\mathrm{ch})}$ means that the transverse dispersion coefficient is high or that the lateral dimension of the chamber is smaller than the longitudinal one. In this last case, the solution of our bounded two-dimensional analytical solution tends to the monodimensional solution.

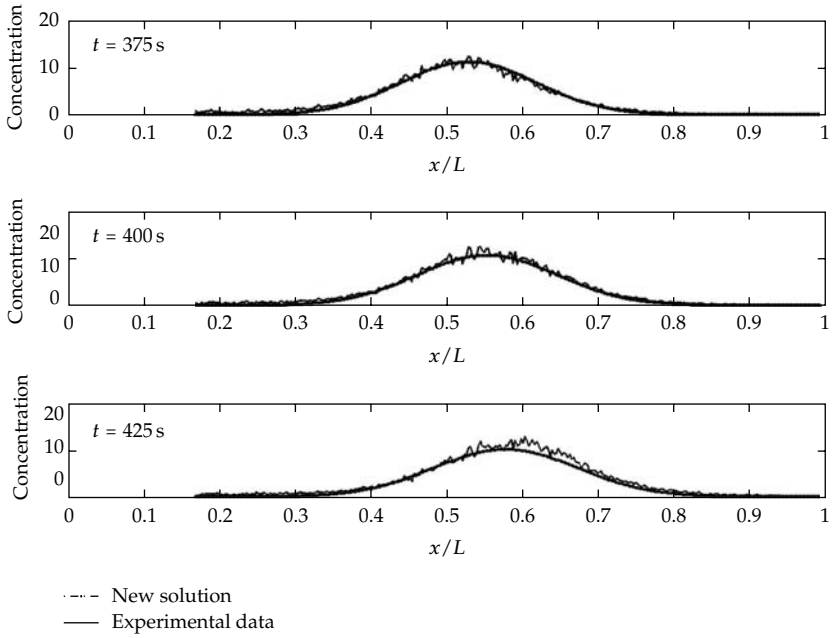

Figure 5: Comparison between analytical simulations and experimental data, for different times and fixed longitudinal cross-section at $y = 0$.

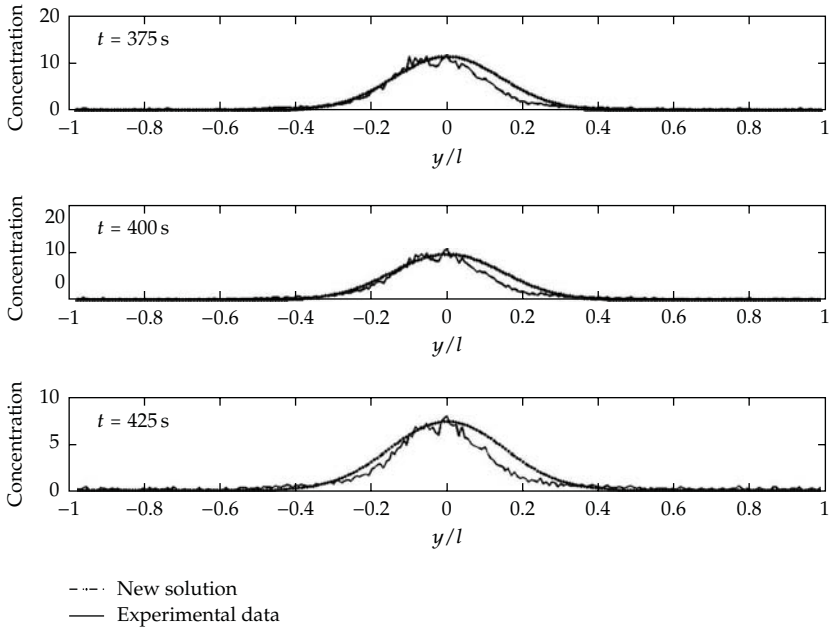

Figure 6: Comparison between analytical simulations and experimental data, for different times and fixed transverse cross-section at $x = 0.14$ m.

The influence of the upstream boundary condition is regulated by both advection and dispersion longitudinal time scales but defined taking into account the position of the source injection. The advection time scale $t_{\text{adv}}^{(s)}$ (where the superscript s stands for source) is related to the transport of the fluid from the inlet section to the source position and the dispersion time scale $t_{\text{disp}}^{(s)}$ is related to the dispersion of the solute from the source position and so on, also back to the inlet section.

We define another longitudinal Péclet number, related to the source position, as the dimensionless ratio between $t_{\text{disp}}^{(s)}$ and $t_{\text{adv}}^{(s)}$, namely,

$$\text{Pe}_L^{(s)} = \frac{t_{\text{disp}}^{(s)}}{t_{\text{adv}}^{(s)}} = \frac{q^2/D_L}{q/u} = \frac{uq}{D_L}. \tag{4.3}$$

The $\text{Pe}_L^{(s)}$ can be easily related to $\text{Pe}_L^{(\text{ch})}$ through $\text{Pe}_L^{(s)} = \text{Pe}_L^{(\text{ch})}(q/L)$. In principle, for $\text{Pe}_L^{(s)} \gg 1$ the time scale of advection is smaller than the time scale of back dispersion and the upstream boundary condition does not influence the solution.

Figure 3 shows the longitudinal profiles of the concentration solutions at $y = 0$ for $\text{Pe}_L^{(s)} = 0.1$. The chamber longitudinal Péclet number is 100. It is possible to notice that, close to the inlet section, the profile of the new solution is different from the Bear one in both magnitude of the concentration (10% in the case proposed in Figure 3) and position of the center of mass. Both the former and the latter differences are induced by the presence of the upstream boundary condition which rebounds the solute back to the chamber. The influence of this boundary condition decreases with increasing the distance from the source injection point due to the longitudinal dispersion.

Several simulations allowed to verify that the effect of the upstream boundary condition is still significant in proximity of the source for $\text{Pe}_L^{(s)}$ between 1 and 2, while negligible effects are present for $\text{Pe}_L^{(s)} > 2$ in any section.

For experimental application, it is important to put in evidence that small $\text{Pe}_L^{(s)}$ means either that the longitudinal dispersion coefficient is high or the velocity is small, or, equivalently, the injection point is very close to the inlet section (q/L small).

5. Application to Laboratory Experiments

The authors designed and constructed a laboratory scale flow chamber made of a Perspex box and filled it with transparent glass beads to study solute transport. The physical model represents a quasi-2-dimensional porous medium; indeed the thickness of the chamber is much smaller than the horizontal direction. The chamber is a Perspex box of internal dimension $200 \times 280 \times 10\,\text{mm}^3$ and is packed with glass beads of uniform diameter (1 mm).

The solute is introduced by a pulse-like injection. The model is illuminated by a diffuse backlight UV source and uses the transmitted light technique to detect the dye emission (visible light) by a CCD camera; a scheme of the experimental apparatus is shown in Figure 4. The acquired images are processed to estimate the 2D distribution of tracer concentrations by using a pixel-by-pixel calibration curve linking fluorescent intensity to concentration and taking into account the influence of the most common sources of errors due to the optical detection technique (photo-bleaching, nonuniform illumination, and vignetting).

Sodium fluorescent (formula: $C_{20}H_{10}Na_2O_5$) has been chosen as tracer for experimental tests. It has a moderately high resistance to sorption [29]. Details of the experimental apparatus, illumination, imaging processing, and concentration estimation can be found in [8].

The experimental campaign allows to obtain a complete set of fluorescein concentration data in the real domain. The dimension of the chamber and the solute mass are known, while pore-scale velocity (u) and the dispersion coefficients (D_L and D_T) are unknown.

The proposed analytical solution has been used to simulate the experimental campaign. For the conducted experimental campaign the estimated pore-scale velocity (from flow-rate and porosity measurements) was $u = 2.9 \times 10^{-4}$ m/s and the ratio between q and L was 0.1786. $\mathrm{Pe}_L^{(\mathrm{ch})}$ and $\mathrm{Pe}_T^{(\mathrm{ch})}$ have been estimated by residual minimization and least square best fit of Equation (25) and experimental data. $\mathrm{Pe}_L^{(\mathrm{ch})}$ and $\mathrm{Pe}_T^{(\mathrm{ch})}$ resulted to be, respectively, 87.3 and 37.5. Under these conditions, as stated in the previous paragraph, the lateral and the upstream borders should not influence the plume behavior at least at low times.

In Figures 5 and 6 the analytical simulations and the experimental data are compared, by considering the curves representative of the plume characteristics in the middle longitudinal cross-section ($y = 0$) at different times ($t_1 = 375$ s, $t_2 = 400$ s, and $t_3 = 425$ s) and at a fixed transverse cross-section in the middle part of the longitudinal domain ($x = 0.14$ m) for the same three times previously chosen. Domains have been scaled.

From Figure 4 it is possible to notice that the real plume at longer times is more advanced—in the longitudinal direction—than the analytical one. This happens in spite of using our analytical solution that gives, as discussed in paragraph 3, plume profiles whose center of mass is put forward with respect to the profile obtained with the Bear solution. This difference in position can be ascribed to the fact that the homogeneity of the porous medium is difficult to achieve in experiments, hence local heterogeneity of the hydraulic conductivity, which is not accounted for in the model, may produce local pore-scale velocity variation and hence the observed deviation of the center of mass.

By observing Figure 6 it is possible to notice again the effect of local medium heterogeneities (present in the physical domain of the experimental apparatus). Figure 6 is a transverse profile of plume concentration at different times; Figure 6 shows that the experimental plume has a slightly deviated shape with respect to the theoretical profile—in particular for $t = 425$ s, the deviation may be ascribed to local heterogeneity that is responsible of plume meandering [24] and deviation of the transverse coordinate of the center of mass. However the fitting of experimental data and model solution is acceptable.

6. Conclusions

This study principally concerns the development of a new analytical solution of the advection-dispersion equation in 2D by taking into account a semi-infinite and laterally bounded domain and a point-like injection. The simulated domain is considered as constituted by a chamber filled with a porous medium, and the advective velocity is fixed as constant. The solution proposed, where both upstream and lateral boundaries are considered, shows a good applicability to real cases of typical flow tank experiments. In the second part of the present paper, a brief analysis of the new solution is given in terms of Péclet numbers, and some typical experimental situations are discussed.

Finally, a comparison between the new solution and real experimental data is performed. Results show that the analytical solution correctly simulate the processes

considered in all the physical domains chosen. With this analytical solution it will be possible to perform data analysis for parameters estimation using all the experimental data obtained by relatively long time experimental campaigns and also data taken near the injection point.

Appendix

In this appendix we give some details of the procedure necessary to get the solution of (3.3) subject to boundaries and initial conditions (3.4), (3.5), and (3.6). The Laplace transform of a_n is defined as

$$A_n(x,s) = \int_0^{+\infty} e^{-st} a_n(x,t)\,dt, \tag{A.1}$$

where s is the frequency variable of the Laplace transform. By applying the Laplace transform to (3.3) and rearranging, we get

$$\frac{\partial^2 A_n(x,s)}{\partial x^2} - \frac{u}{D_L}\frac{\partial A_n(x,s)}{\partial x} - \left(\frac{s}{D_L} + \frac{n^2\pi^2\ D_T}{l^2 D_L}\right) A_n(x,s) = -\frac{1}{D_L} a_n(x,0), \quad n = 0,1,2,\ldots, \tag{A.2}$$

where $a_n(x,0)$ is expressed by (3.6). Initial and boundary conditions then become

$$\left[u\ a_n(x,s) - D_l \frac{\partial A_n}{\partial x}\right]_{x=0^+} = 0, \quad n = 0,1,2,\ldots, \tag{A.3}$$

$$\lim_{x\to+\infty} A_n(x,s) = 0, \quad n = 0,1,2,\ldots. \tag{A.4}$$

Equation (A.2) is a nonhomogeneous ordinary differential equation that can be solved with classical methods. The general solution of (A.2) is

$$\begin{aligned} A_n(x,s) = {} & e^{u(x-q)/2D_L}\left[Q_n(s)\ e^{(x\sqrt{W_n^2+4D_L s})/2D_L} + P_n(s) e^{-(x\sqrt{W_n^2+4D_L s})/2D_L}\right] \\ & - \frac{2M}{l\sqrt{W_n^2+4D_L s}} \sinh\left(\frac{(x-q)\sqrt{W_n^2+4D_L s}}{2D_L}\right) e^{u(x-q)/2D_L} H(x-q) \end{aligned} \tag{A.5}$$

for each $n = 0,1,2,\ldots,$ where $H(x)$ is the Heaviside function and W_n^2 is defined as follows:

$$W_n^2 = u^2 + 4\frac{n^2 D_L D_T \pi^2}{l^2}, \quad n = 0,1,2,\ldots. \tag{A.6}$$

The functions $Q_n(s)$ and $P_n(s)$ have to be determined by using boundaries conditions of (A.3) and (A.4). $Q_n(s)$ can be computed by using the right boundary condition for the longitudinal domain (A.4). If we compute the limits for $x \to +\infty$, we get

$$\lim_{s\to+\infty} A_n(x,s) = \lim_{s\to+\infty} e^{u(x-q)/2D_L} e^{(x\sqrt{W_n^2+4D_Ls})/2D_L} \left[Q_n(s) - \frac{Me^{-(q\sqrt{W_n^2+4D_Ls})/2D_L}}{l\sqrt{W_n^2+4D_Ls}} \right]. \tag{A.7}$$

By imposing in (A.7) that the limit of A_n is zero for $x \to +\infty$, the terms $Q_n(s)$ can be found:

$$Q_n(s) = -\frac{Me^{-(q\sqrt{W_n^2+4D_Ls})/2D_L}}{l\sqrt{W_n^2+4D_Ls}}. \tag{A.8}$$

The terms $P_n(s)$ can be computed by using the upstream boundary condition (3.4). By substituting $A_n(x,s)$ in (A.3) and rearranging, we get

$$-\exp^{-uq/2D_L} \times \frac{\left(Q_n(s)\left(W_n^2+4sD_L-u\sqrt{W_n^2+4D_Ls}\right)-P_n(s)\left(W_n^2+4sD_L+u\sqrt{W_n^2+4D_Ls}\right)\right)}{2\sqrt{W_n^2+4D_Ls}} = 0. \tag{A.9}$$

The expressions for $P_n(s)$ can be found from (A.9):

$$P_n(s) = \frac{Q_n(s)\left(W_n^2+4sD_L-u\sqrt{W_n^2+4D_Ls}\right)}{u\sqrt{W_n^2+4D_Ls}+W_n^2+4sD_L} \tag{A.10}$$

or, explicitly,

$$P_n(s) = -\frac{M}{l}\ \frac{u-\sqrt{W_n^2+4D_Ls}}{u\sqrt{W_n^2+4D_Ls}+W_n^2+4sD_L}\ e^{-(q\sqrt{W_n^2+4D_Ls})/2D_L}. \tag{A.11}$$

The final expressions for $A_n(x,s)$, $n = 0,1,2,\ldots$, can be written as follows:

$$A_n(x,s) = \frac{Z_0(x)H(q-x)\ e^{((x-q)\sqrt{W_n^2+4D_Ls})/2D_L}}{\sqrt{W_n^2+4D_Ls}} - \frac{Z_0(x)ue^{(-(x+q)\sqrt{W_n^2+4D_Ls})/2D_L}}{W_n^2+4D_Ls+u\sqrt{W_n^2+4D_Ls}}$$
$$+\frac{Z_0(x)\ e^{(-(x+q)\sqrt{W_n^2+4D_Ls})/2D_L}}{u+\sqrt{W_n^2+4D_Ls}} + \frac{Z_0(x)H(x-q)e^{(-(x-q)\sqrt{W_n^2+4D_Ls})/2D_L}}{\sqrt{W_n^2+4D_Ls}}, \tag{A.12}$$

where we have set

$$Z_0(x) = \frac{M}{l}\, e^{u(x-q)/2D_L}. \tag{A.13}$$

It is possible now to obtain the final solution by computing the inverse Laplace transform of $A_n(x,s)$; so doing, we get

$$a_n(x,t) = a_0(x,t)\, e^{-n^2\pi^2 D_l t/l^2} \tag{A.14}$$

$$a_0(x,t) = \frac{M}{2l}\left[\frac{1}{\sqrt{D_L\pi t}}\left(e^{-(x-q-ut)^2/4D_L t} + e^{-(x+q-ut)^2/4D_L t-(uq/D_L)}\right) - \frac{u}{D_L}e^{ux/D_L}\,\operatorname{erfc}\left(\frac{x+q+ut}{2t\sqrt{D_L}}\right)\right]. \tag{A.15}$$

References

[1] M. Y. Corapcioglu and P. Fedirchuk, "Glass bead micromodel study of solute transport," *Journal of Contaminant Hydrology*, vol. 36, no. 3-4, pp. 209–230, 1999.

[2] C. Jia, K. Shing, and Y. C. Yortsos, "Visualization and simulation of non-aqueous phase liquids solubilization in pore networks," *Journal of Contaminant Hydrology*, vol. 35, no. 4, pp. 363–387, 1999.

[3] W. E. Huang, C. C. Smith, D. N. Lerner, S. F. Thornton, and A. Oram, "Physical modelling of solute transport in porous media: evaluation of an imaging technique using UV excited fluorescent dye," *Water Research*, vol. 36, no. 7, pp. 1843–1853, 2002.

[4] M. A. Theodoropoulou, V. Karoutsos, C. Kaspiris, and C. D. Tsakiroglou, "A new visualization technique for the study of solute dispersion in model porous media," *Journal of Hydrology*, vol. 274, no. 1–4, pp. 176–197, 2003.

[5] P. Gaganis, E. D. Skouras, M. A. Theodoropoulou, C. D. Tsakiroglou, and V. N. Burganos, "On the evaluation of dispersion coefficients from visualization experiments in artificial porous media," *Journal of Hydrology*, vol. 307, no. 1–4, pp. 79–91, 2005.

[6] E. H. Jones and C. C. Smith, "Non-equilibrium partitioning tracer transport in porous media: 2-D physical modelling and imaging using a partitioning fluorescent dye," *Water Research*, vol. 39, no. 20, pp. 5099–5111, 2005.

[7] J. D. McNeil, G. A. Oldenborger, and R. A. Schincariol, "Quantitative imaging of contaminant distributions in heterogeneous porous media laboratory experiments," *Journal of Contaminant Hydrology*, vol. 84, no. 1-2, pp. 36–54, 2006.

[8] F. Catania, M. Massabó, M. Valle, G. Bracco, and O. Paladino, "Assessment of quantitative imaging of contaminant distributions in porous media," *Experiments in Fluids*, vol. 44, no. 1, pp. 167–177, 2008.

[9] J. Bear, *Dynamics of Fluids in Porous Media*, Elsevier, New York, NY, USA, 1972.

[10] T. C. Lee, *Applied Mathematics in Hydrogeology*, Lewis, Boca Raton, Fla, USA, 1999.

[11] F. J. Leij and J. H. Dane, "Analytical solutions of the one-dimensional advection equation and two- or three-dimensional dispersion equation," *Water Resources Research*, vol. 26, no. 7, pp. 1475–1482, 1990.

[12] F. J. Leij, E. Priesack, and M. G. Schaap, "Solute transport modeled with Green's functions with application to persistent solute sources," *Journal of Contaminant Hydrology*, vol. 41, no. 1-2, pp. 155–173, 2000.

[13] F. J. Leij, T. H. Skaggs, and M. T. Van Genuchten, "Analytical solutions for solute transport in three-dimensional semi-infinite porous media," *Water Resources Research*, vol. 27, no. 10, pp. 2719–2733, 1991.

[14] D. D. Walker and J. E. White, "Analytical solutions for transport in porous media with Gaussian source terms," *Water Resources Research*, vol. 37, no. 3, pp. 843–848, 2001.

[15] Y. Sim and C. V. Chrysikopoulos, "Analytical solutions for solute transport in saturated porous media with semi-infinite or finite thickness," *Advances in Water Resources*, vol. 22, no. 5, pp. 507–519, 1999.

[16] E. Park and H. Zhan, "Analytical solutions of contaminant transport from finite one-, two-, and three-dimensional sources in a finite-thickness aquifer," *Journal of Contaminant Hydrology*, vol. 53, no. 1-2, pp. 41–61, 2001.

[17] V. Batu, "A generalized two-dimensional analytical solution for hydrodynamic dispersion in bounded media with the first-type boundary condition at the source," *Water Resources Research*, vol. 25, no. 6, pp. 1125–1132, 1989.

[18] V. Batu, "A generalized two-dimensional analytical solute transport model in bounded media for flux-type finite multiple sources," *Water Resources Research*, vol. 29, no. 8, pp. 2881–2892, 1993.

[19] J. Chen, C. F. Ni, and C. P. Liang, "Analytical power series solutions to the two-dimensional advection-dispersion equation with distance-dependent dispersivities," *Hydrological Processes*, vol. 22, pp. 4670–4678, 2008.

[20] M. M. Aral and B. Liao, "Analytical solutions for two-dimensional transport equation with time-dependent dispersion coefficients," *Journal of Hydrologic Engineering*, vol. 1, no. 1, pp. 20–32, 1996.

[21] D. Tartakowsky and V. Di Federico, "An analytical solution for contaminant transportin non uniform flow," *Transport in Porous Media*, vol. 27, pp. 85–97, 1997.

[22] M. Massabó, R. Cianci, and O. Paladino, "Some analytical solutions for two-dimensional convection-dispersion equation in cylindrical geometry," *Environmental Modelling and Software*, vol. 21, no. 5, pp. 681–688, 2006.

[23] F. Catania, M. Massabó, and O. Paladino, "Estimation of transport and kinetic parameters using analytical solutions of the 2D advection-dispersion-reaction model," *Environmetrics*, vol. 17, no. 2, pp. 199–216, 2006.

[24] M. Massabó, F. Catania, and O. Paladino, "A new method for laboratory estimation of the transverse dispersion coefficient," *Ground Water*, vol. 45, no. 3, pp. 339–347, 2007.

[25] A. Kreft and A. Zuber, "On the physical meaning of the dispersion equation and its solutions for different initial and boundary conditions," *Chemical Engineering Science*, vol. 33, no. 11, pp. 1471–1480, 1978.

[26] J. C. Parker and M. T. Van Genuchten, "Flux-averaged and volume-averaged concentrations in continuum approaches to solute transport," *Water Resources Research*, vol. 20, no. 7, pp. 866–872, 1984.

[27] P. V. Danckwerts, "Continuous flow systems. Distribution of residence times," *Chemical Engineering Science*, vol. 2, no. 1, pp. 1–13, 1953.

[28] M. Abramowitz and I. Stegun, *Handbook of Mathematical Functions with Formulas, Graphs, and Mathematical Tables*, Dover, New York, NY, USA, 1972.

[29] P. L. Smart and I. M. S. Laidlaw, "An evaluation of some fluorescent dyes for water tracing," *Water Resources Research*, vol. 13, no. 1, pp. 15–33, 1977.